



**HAL**  
open science

# Physical modelling of electrostimulated transdermal drug delivery

Georgios Kougkolos

► **To cite this version:**

Georgios Kougkolos. Physical modelling of electrostimulated transdermal drug delivery. Material chemistry. Université Paul Sabatier - Toulouse III, 2023. English. NNT : 2023TOU30324 . tel-04576810

**HAL Id: tel-04576810**

**<https://theses.hal.science/tel-04576810>**

Submitted on 15 May 2024

**HAL** is a multi-disciplinary open access archive for the deposit and dissemination of scientific research documents, whether they are published or not. The documents may come from teaching and research institutions in France or abroad, or from public or private research centers.

L'archive ouverte pluridisciplinaire **HAL**, est destinée au dépôt et à la diffusion de documents scientifiques de niveau recherche, publiés ou non, émanant des établissements d'enseignement et de recherche français ou étrangers, des laboratoires publics ou privés.

Université Fédérale



Toulouse Midi-Pyrénées

# THÈSE

En vue de l'obtention du  
**DOCTORAT DE L'UNIVERSITÉ DE TOULOUSE**  
Délivré par l'Université Toulouse 3 - Paul Sabatier

---

Présentée et soutenue par  
**Georgios KOUGKOLOS**

Le 6 décembre 2023

**Modélisation physique de la délivrance transdermique  
électrostimulée de médicaments**

---

Ecole doctorale : **SDM - SCIENCES DE LA MATIERE - Toulouse**

Spécialité : **Sciences et Génie des Matériaux**

Unité de recherche :

**CIRIMAT - Centre Interuniversitaire de Recherche et d'Ingénierie des  
Matériaux**

Thèse dirigée par

**Emmanuel FLAHAUT et Zarel VALDEZ-NAVA**

Jury

M. Antoni IVORRA, Rapporteur  
Mme Marie FRENEA ROBIN, Rapporteuse  
Mme Sylvie DAGREOU, Examinatrice  
M. Emmanuel FLAHAUT, Directeur de thèse  
M. Zarel VALDEZ-NAVA, Co-directeur de thèse  
M. Christophe VIEU, Président

## Preface

The current PhD thesis is part of the ongoing research effort for an efficient, practical and non-invasive drug delivery through the skin. Non-invasive delivery through the skin presents some important advantages over conventional drug delivery routes. Pills taken orally undergo the first-pass effect, which means that they are degraded by the gastric fluids, passage through the intestine walls and enzyme metabolism in the liver. As a result, some drugs (for example insulin, lidocaine) with significant first-pass effects have to be injected. At the same time, injections are associated with a risk of infection, needlestick injuries and pain. Non-invasive transdermal delivery has the potential to overcome these limits by overpassing first-pass metabolism and limiting pain. The main obstacle to this delivery route is the barrier function of the skin, and more specifically its outermost layer, the stratum corneum, which only allows small, relatively lipophilic molecules to pass.

To overcome this barrier, we are building on skin electroporation, a biological phenomenon where the application of short-duration electric pulses temporarily permeabilizes the skin and allows the passage of therapeutic molecules through a combination of passive diffusion and electrophoretic transport. Our novelty, is the attempt to combine drug storage and electrical contact into a single two-in-one reservoir-electrode platform, in the form of a hydrophilic and electrically-conductive hydrogel, which can contain the medicine to be administered. We are involved in the full procedure, from the preparation of the hydrogel platforms, material characterizations, to experimentation with skin models, electrical response measurements, numerical modeling, and modeling molecule delivery through electroporation. As a result, the experimental procedure involves specialization in three different domains: materials chemistry, electrical engineering and biology (biophysics). For this reason, the current work is the fruit of the collaboration of three different labs, CIRIMAT, LAPLACE and IPBS, all geographically situated on the campus of Rangueil, Toulouse.

The current work is the third PhD that has resulted from the above collaboration. The first one was defended in 2017, by Jean-François Guillet and the second one in 2022 by Juliette Simon. Consequently, we have built, to some extent, on their results and tried to go further. Jean-François Guillet elaborated the nanocomposite agarose hydrogel platform, performed some electrical characterizations and demonstrated the delivery of a fluorophore on mouse skin, as a proof of concept. Juliette Simon further tested some different compositions and processing methods (including classical freezing) for the nanocomposite hydrogels and studied the impact of molecule size and charge on the delivery through electroporation. Here, we continued the characterization tests on the nanocomposite hydrogels, measured the electrical properties of the skin model during electroporation, numerically simulated the drug delivery system and tested different electric pulse amplitudes and their impact on molecule delivery and electrical properties.

In the following chapters, we introduce the key concepts necessary to understand the experimental part and briefly present the state of the art of skin electroporation and conductive nanocomposite hydrogels. The experimental conditions and protocols are described in details in the section *materials and methods*. The results section includes the material characterizations of the nanocomposite hydrogel platform and the skin models; the *in situ* electrical measurements of the skin models during *ex vivo* drug delivery through electroporation; a numerical model of the electric field distribution in the skin model, during the pulse application, and the delivery of fluorescent molecules through the skin for different experimental conditions. Lastly, conclusions and future perspectives are presented.

## Acknowledgements

Throughout the three years and few months of the current research work, I had the opportunity to interact with many remarkable people, on a scientific as well as a social level. These interactions nurtured my curiosity and deepened my understanding of sciences and life, in general. I would like to thank my supervisors Emmanuel and Zarel, the scientific advisors Lionel and Muriel, and all of the other members of the CARBO2DERM project. All together, they created a perfect team for stimulating research through their insightful comments and critiques, aid with experimental work, and precise feedback. On the more social level, I am really grateful for meeting L. and L., colleagues at the lab who made life more interesting through exciting side projects and refreshing discussions. And outside the lab, of course, S., for being my partner in life.

On the financial part, this research work was funded by the French national research agency (ANR - Agence Nationale de la Recherche) under the project CARBO2DERM – Carbon nanotubes for the transdermal delivery of therapeutic molecules (grant ANR-19-CE09-0007).



**The CARBO2DERM team.** From left to right: Marie-Pierre Rols, Zarel Valdez-Nava, Muriel Golzio, Morgan Legnani, Emmanuel Flahaut, Sorin Dinculescu, Lionel Laudebat, Alicia Weibel, Yorgos Kougkolos, Audrey Tourette, Brigitte Soula, Anne-Marie Larssonner-Galibert, Juliette Simon and Bastien Jouanmiqueou. Other members not in the photo include Geraldine Alberola, Jelena Kolosnjaj-Tabi and Cherif Moslah.



## Summary

Skin electroporation for transdermal drug delivery involves the application of Pulsed Electric Fields (PEFs) on the skin to disrupt its barrier function in a temporary and non-invasive manner, increasing the uptake of drugs. It represents a potential alternative to conventional delivery methods that are invasive (*e.g.* injections) or limited (orally-taken medication undergoes first-pass metabolism). Advantages include increased bioavailability, sustained steady-state blood concentration levels, painless self-administration and reduced frequency of dosing, which in turn improve patient compliance and quality of life.

We have developed a nanocomposite hydrogel drug delivery system by combining the hydrophilic and biocompatible agarose polymer with electrically conductive double-wall carbon nanotubes. The hydrogel acted as a reservoir for the drug and as a conductive electrode for the application of electrical pulses on the skin. The hydrogels were air-dried and then swollen in an aqueous solution with a molecule of interest, absorbing 2.7 times their dry mass. The incorporation of double-wall carbon nanotubes in the agarose hydrogels increased their electrical conductivity by two orders of magnitude. In parallel, we tested the impact of numerous parameters (nanomaterial concentration, processing method, dispersing agent, polymer) on the swelling ratio and electrical conductivity of the hydrogels.

We employed a multi-scale approach to investigate the drug delivery system on a mouse skin model, through electrical measurements, numerical modeling and fluorescence microscopy (**Figure 0.1**). Electrical properties indicated a highly nonlinear skin electrical behavior. The average resistance of the skin decreased with increasing applied voltage, and the instantaneous resistance decreased during the application of the electrical pulses. The current and voltage measurements were used to study skin recovery after electroporation and to validate the numerical model. The simulation of electric field distribution in the skin calculated electric field strengths in the range of reversible tissue electroporation (400-1200 V/cm) in the viable skin layers, for PEFs of 300 V. Fluorescence microscopy revealed increased uptake of fluorescent molecules (used as drug models) compared to the non-pulsed control. We reported three domains of effect of PEFs on the skin: (1) already at 50 V PEF conductive pathways were formed through the epidermis, decreasing the resistance of the skin, (2) at 100 V PEF, the first local transport regions appeared in the extracellular lipids of the stratum corneum, demonstrated by an increased uptake of lucifer yellow, a small hydrophilic fluorophore and (3) at 300 V PEF, the first permeabilization of nucleated cells occurred, evidenced by the increased fluorescence of propidium iodide, a membrane-impermeable DNA intercalating agent.

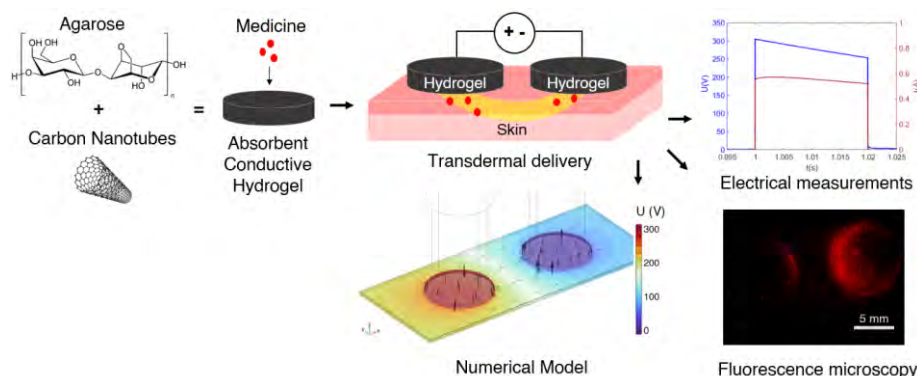


**Figure 0.1** – Graphical abstract. An absorbent and conductive hydrogel was prepared with agarose and carbon nanotubes. The hydrogel was used as a patch for transdermal drug delivery through skin electroporation. The delivery system was studied through electrical measurements, numerical modeling and fluorescence microscopy.

## Résumé en français (Summary in French)

L'électroporation de la peau pour l'administration transdermique de médicaments comprend l'application de champs électriques pulsés (PEF) sur la peau pour perturber sa fonction de barrière de manière temporaire et non invasive, augmentant ainsi l'absorption des médicaments. Elle représente une alternative potentielle aux méthodes d'administration conventionnelles qui sont invasives (par exemple les injections) ou limitées (les médicaments pris par voie orale subissent un métabolisme de premier passage). Parmi ses avantages, on note une biodisponibilité accrue, des concentrations sanguines stables et soutenues, une auto-administration indolore et une réduction de la fréquence des prises, ce qui améliore le respect de la prescription par le patient et donc sa qualité de vie.

Nous avons mis au point un système d'administration de médicaments par hydrogel nanocomposite en combinant le polymère d'agarose hydrophile et biocompatible avec des nanotubes de carbone bipolaires conducteurs d'électricité. L'hydrogel a servi de réservoir pour le médicament et d'électrode conductrice pour l'application d'impulsions électriques sur la peau. Les hydrogels ont été séchés à l'air puis gonflés dans une solution aqueuse avec une molécule d'intérêt, absorbant 2,7 fois leur masse sèche. L'incorporation de nanotubes de carbone dans les hydrogels d'agarose a augmenté leur conductivité électrique de deux ordres de grandeur. En parallèle, nous avons testé l'impact de nombreux paramètres (concentration en nanomatériaux, méthode de traitement, agent dispersant, polymère) sur le taux de gonflement et la conductivité électrique des hydrogels.

Nous avons utilisé une approche multi-échelle pour étudier le système d'administration de médicaments sur un modèle de peau de souris, au travers de mesures électriques, de la modélisation numérique et de la microscopie à fluorescence (Figure 0.1). Les propriétés électriques ont révélé un comportement électrique fortement non linéaire de la peau. La résistance moyenne de la peau diminue avec l'augmentation de la tension appliquée, et la résistance instantanée diminue pendant l'application des impulsions électriques. Les mesures de courant et de tension ont été utilisées pour étudier la récupération de la peau après l'électroporation et pour valider le modèle numérique. La simulation de la distribution du champ électrique dans la peau a permis de calculer des intensités de champ électrique dans la gamme de l'électroporation tissulaire réversible (400-1200 V/cm) dans les couches de peau viables, pour des PEF de 300 V. La microscopie à fluorescence a révélé une absorption accrue de molécules fluorescentes (utilisées comme modèles de médicaments) par rapport au contrôle non pulsé. Nous avons observé trois domaines d'effets des PEF sur la peau : (1) dès 50 V PEF, des voies conductrices se sont formées à travers l'épiderme, diminuant la résistance de la peau, (2) à 100 V PEF, les premières régions de transport local sont apparues dans les lipides extracellulaires de la couche cornée, (2) à 100 V PEF, les premières régions de transport local sont apparues dans les lipides extracellulaires de la couche cornée, démontrées par un marquage accru de Lucifer Yellow, un petit fluorophore hydrophile et (3) à 300 V PEF, la première perméabilisation des cellules nucléées s'est produite, démontrée par la fluorescence accrue de l'iodure de propidium, un agent d'intercalation de l'ADN imperméable à la membrane.

## Résumé détaillé en français (Extended summary in French)

Ces travaux de thèse s'inscrivent dans le cadre des recherches en cours sur l'administration efficace, pratique et non invasive de médicaments à travers la peau. Ils ont été réalisés dans le cadre du projet ANR Carbo<sup>2</sup>Derm impliquant 3 laboratoires Toulousains, le CIRIMAT, le LAPLACE et l'IPBS. L'administration transdermique non invasive présente des avantages importants par rapport aux voies d'administration de médicaments conventionnelles. Les pilules prises par voie orale subissent l'effet dit "de premier passage", ce qui signifie qu'elles sont dégradées par les fluides gastriques, le passage à travers les parois de l'intestin et le métabolisme enzymatique dans le foie. Par conséquent, certains médicaments (par exemple l'insuline, la lidocaïne) ayant des effets de premier passage importants doivent être injectés. Par ailleurs, les injections sont associées à la douleur, au risque d'infection et aux blessures liées à la mise en œuvre d'aiguilles. L'administration transdermique non invasive a le potentiel de surmonter ces limites en dépassant le métabolisme de premier passage et en limitant la douleur. Les avantages comprennent une biodisponibilité accrue, des niveaux de concentration sanguine stables et soutenus, une auto-administration indolore, ce qui améliore le suivi de la prescription, et par conséquent la qualité de vie des patients.

Le principal obstacle à cette voie d'administration est la fonction de barrière de la peau, et plus particulièrement de sa couche externe, le *stratum corneum* (SC) agit comme une barrière protégeant l'organisme de la pénétration de substances exogènes et de microbes et limitant la perte d'eau. La diffusion passive de médicaments à travers la peau n'est possible que pour des molécules de faible poids moléculaire (<400-500 Da) et relativement lipophiles ( $\log P$  autour de 2 à 3). Plusieurs méthodes chimiques et physiques sont en cours de développement, permettant à des molécules plus grosses et/ou hydrophiles de traverser la barrière cutanée. Parmi celles-ci, l'électroporation de la peau consiste à appliquer des impulsions de champ électrique de haute tension (50 à 3000 V) et de courte durée (5  $\mu$ s à 100 ms) à la surface de la peau, perméabilisant le SC de manière non invasive et temporaire (réversible).

L'électroporation est un phénomène biophysique qui consiste à perméabiliser une bicouche lipidique par l'application d'un Champ Electrique Pulsé (CEP) [1], [2]. En fonction des paramètres du champ électrique (intensité, durée, forme d'onde, nombre et fréquence des répétitions) et de la configuration de l'électrode, la perméabilisation peut être transitoire (réversible) ou permanente (irréversible). L'électroporation de la peau pour l'administration non invasive de médicaments par voie transdermique a été suggérée pour la première fois par Prausnitz *et al.* en 1993. Ils ont démontré que l'application de la CEP sur la peau humaine, *ex vivo*, et sur la peau de souris sans poils, *in vivo*, conduisait à une augmentation temporaire et multiple de l'absorption de trois molécules fluorescentes de taille petite à moyenne, chargées négativement (lucifer yellow, calcéine, dérivé d'érythrosine), par rapport à un contrôle non pulsé [3]. Depuis, de nombreuses études ont été publiées sur l'électroporation de la peau pour l'administration transdermique de médicaments, élargissant les résultats à une gamme plus large de molécules (charge et taille) et testant différentes configurations d'électrodes et paramètres d'impulsion, sur une variété de modèles de peau (souris, porc, humain reconstruit, humain) [4], [5], [6], [7], [8], [9], [10], [11], [12]. Cependant, très peu d'études sont parvenues à tester cette méthode d'administration *in vivo* sur l'homme [13], [14]. Un certain nombre de limitations empêchent l'électroporation transdermique pour l'administration de médicaments d'atteindre les essais cliniques. Il s'agit notamment de l'irrégularité des quantités de médicaments délivrées, de configurations d'électrodes peu pratiques, de seuils de douleur peu clairs pour les CEP,

de l'incapacité à délivrer des molécules à fort poids moléculaire et d'une compréhension généralement limitée des mécanismes sous-jacents. Pour se développer, l'administration transdermique non invasive de médicaments doit être indolore, pratique, totalement réversible et doit délivrer des quantités constantes de molécules thérapeutiques en quantités appropriées, dans des délais raisonnables.

Le paramètre critique de l'électroporation des bicouches lipidiques est la différence de potentiel électrique à travers la bicouche (qui possède des propriétés diélectriques). L'application d'un champ électrique externe charge cette dernière, jusqu'à un seuil critique où l'électroporation est observée. Pour les membranes plasmiques, ce seuil est calculé expérimentalement à environ 250 mV, pour les cellules eucaryotes [15]. L'électroporation est observée par la perte des propriétés de barrière de la bicouche (transport de l'eau et des solutés à travers celle-ci) et une diminution rapide du potentiel à travers cette dernière. Bien que le mécanisme exact de l'électroporation au niveau moléculaire ne soit pas entièrement élucidé, il est proposé qu'il soit causé par un réarrangement structural des lipides, formant des pores aqueux, des modifications chimiques des chaînes lipidiques induites par l'électricité ou une combinaison de ces éléments [2]. Des simulations de dynamique moléculaire de bicouches lipidiques soumises à des champs électriques puissants ont mis en évidence la formation de pores aqueux de courte durée [16]. Au niveau des tissus, un champ électrique supérieur à 400 V/cm peut perméabiliser les membranes plasmiques des cellules à l'intérieur du tissu [17]. À partir d'environ 1200 V/cm, l'application de CEP peut induire une perméabilisation permanente et la mort cellulaire, c'est-à-dire *que* l'électroporation est irréversible [17].

L'application d'un champ électrique externe peut perturber la fonction de barrière de la peau en créant des régions de transport local (RTL), c'est-à-dire des voies aqueuses à travers la peau [17], [18]. Les RTL sont des régions où la mobilité ionique et le transfert de masse des solutés sont accrues, avec une conductivité électrique et une perméabilité augmentée. Leur apparition s'accompagne d'une diminution rapide de la résistivité de la peau (jusqu'à trois ordres de grandeur [19]), d'une augmentation de la perte d'eau trans-épidermique et d'une perméabilité accrue aux composés hydrophiles [11], [20]. La forte densité de courant qui circule dans les RTL peut provoquer un échauffement par effet Joule et la fonte des lipides à proximité, ce qui augmente encore leur taille pour des durées d'impulsion plus longues. Des tensions appliquées plus élevées augmentent la densité des RTL, et des durées plus longues (durée de l'impulsion et nombre de répétitions) augmentent leur diamètre [5], [18]. Pour certains paramètres électriques, la tension étant le principal, ces changements sont en grande partie ou totalement réversibles. Récemment, Gupta et Rai ont visualisé la formation de pores sur les bicouches lipidiques extracellulaires du SC grâce à des simulations de dynamique moléculaire [21].

Une fois que les RTL sont formées, l'administration de médicaments à travers la peau peut avoir lieu. Les forces motrices du transfert de masse des solutés sont (1) l'entraînement électrophorétique (pour les entités chargées), (2) l'électro-osmose et (3) le gradient de concentration. [5]. Dans le cas de l'électroporation de la peau pour l'administration de médicaments, trois voies sont possibles : (1) la voie paracellulaire, une voie tortueuse à travers la matrice lipidique extracellulaire du SC ; (2) la voie transcellulaire, une voie plus directe à travers les cornéocytes (implique la perméabilisation de leurs enveloppes cornées), et (3) le passage par les annexes cutanées I, en suivant les follicules pileux ou les canaux sudoripares de la peau. [4], [22]. Le transport de molécules peut inclure une combinaison de ces voies, mais la voie paracellulaire est généralement acceptée comme la voie dominante [5], [11], [21].

L'originalité de notre approche réside dans la tentative de combiner le stockage de médicaments et le contact électrique en une seule plateforme réservoir-électrode deux-en-un, sous la forme d'un hydrogel hydrophile et électriquement conducteur, qui peut contenir le médicament à administrer. Nous avons travaillé sur l'ensemble de la procédure, depuis la préparation des plateformes d'hydrogel, la caractérisation des matériaux, l'expérimentation avec des modèles de peau, les mesures de la réponse électrique, la modélisation numérique et la modélisation de l'administration de molécules par électroporation (Fig. 1). Par conséquent, la procédure expérimentale combine une spécialisation dans trois domaines différents : la chimie des matériaux, l'ingénierie électrique et la biologie (biophysique). Pour cette raison, ces travaux sont le fruit de la collaboration de trois laboratoires différents, le CIRIMAT, le LAPLACE et l'IPBS, tous situés géographiquement sur le campus de Rangueil, à Toulouse.

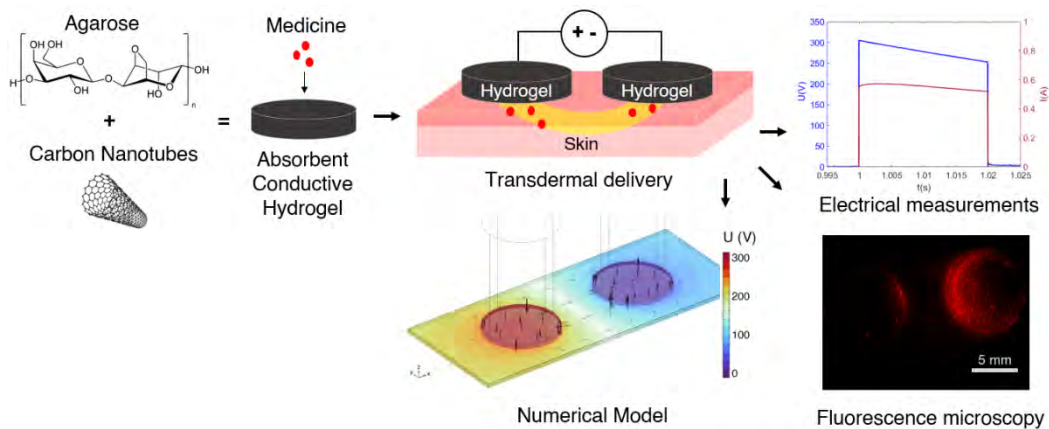


**Fig. 1.** Résumé graphique. Un hydrogel nanocomposite absorbant et conducteur a été préparé avec de l'agarose et des nanotubes de carbone. L'hydrogel a été utilisé comme patch pour l'administration transdermique de médicaments par électroporation de la peau. Le système d'administration a été étudié par des mesures électriques, la modélisation numérique et la microscopie à fluorescence.

Ces plates-formes réservoirs-électrodes doivent répondre aux critères suivants :

- Capacité à stocker et à libérer des médicaments
- Conductivité électrique
- Biocompatibilité
- Stabilité / résistance mécanique
- Conservation
- Praticité / facilité de fabrication

Les travaux de notre consortium ont permis la mise au point d'un système nanocomposite d'administration de médicaments par hydrogel en combinant l'agarose, polymère hydrophile et biocompatible, avec des nanotubes de carbone à double paroi (NTC), conducteurs électriques. L'hydrogel a servi de réservoir pour le médicament et d'électrode conductrice pour l'application d'impulsions électriques sur la peau. Les hydrogels ont été séchés à l'air puis gonflés dans une solution aqueuse contenant une molécule d'intérêt, absorbant les médicaments modèles (fluorophores de différentes tailles et de différentes charges). L'incorporation de NTC dans les hydrogels d'agarose a augmenté leur conductivité électrique. En parallèle, nous avons testé l'impact de nombreux paramètres (concentration en nanomatériaux, méthode de séchage, agent dispersant, polymère) sur le taux de gonflement et la conductivité électrique des hydrogels.



Les hydrogels d'agarose à une concentration de polymère de 2,5 % m/m présentent des propriétés mécaniques adéquates (module de compression de  $\sim 200$  kPa) et sont faciles à manipuler, sans être ni trop mous ni trop cassants. Une petite taille d'hydrogel a été choisie, des disques cylindriques de 10 mm de diamètre et de 2 mm d'épaisseur, adaptés à la petite taille des modèles de peau expérimentaux (peau de souris et épiderme humain reconstruit) et susceptibles de contenir une quantité pertinente de médicament pour les applications envisagées. Les hydrogels ont été séchés rapidement à 70 °C (60 min) ou à 50 °C (100 min). Une fois secs, les matériaux ont absorbé l'eau assez rapidement, atteignant 60 % de la valeur d'absorption finale en 10 minutes. L'analyse thermogravimétrique a montré que les hydrogels d'agarose secs contenaient encore environ 5,7 % d'eau.

En ce qui concerne la capacité d'absorption, les hydrogels d'agarose seule ont absorbé  $4,6 \pm 0,7$  fois leur masse sèche, tandis que les hydrogels nanocomposites, contenant des NTC représentant 10 % en poids du polymère, ont absorbé  $2,7 \pm 0,6$ . Les nanotubes de carbone ont diminué le taux de gonflement des hydrogels d'agarose mais aussi d'alginate/chitosane. Des concentrations plus élevées de NTC ont encore diminué la capacité d'absorption, mais dans une moindre mesure. Les NTC ont formé un réseau dans la matrice de l'hydrogel polymère, rigidifiant la structure et limitant ainsi la capacité d'expansion lors de l'absorption d'eau. En outre, les NTC ont des surfaces très hydrophobes, qui repoussent les molécules d'eau. L'impact de différentes méthodes de traitement, telles que le séchage à l'air et la congélation, a été testé. La congélation des hydrogels a augmenté leur taux de gonflement, et la congélation directionnelle (contact unilatéral avec une source de froid) l'a encore augmenté, permettant d'atteindre  $14,7 \pm 1,9$  (**Fig. 2**). Lorsque les hydrogels ont été refroidis en dessous de la température de cristallisation de l'eau, l'eau au sein des hydrogels a commencé à former des cristaux de glace. Ces cristaux se sont formés dans toute la matrice de l'hydrogel, de manière aléatoire (en commençant autour des particules ou des surfaces de nucléation). Sous l'effet de l'expansion des cristaux de glace, la matrice polymère s'est réorganisée, déplacée par l'expansion des cristaux. Ensuite, lorsque les cristaux de glace ont fondu, des pores ont été laissés en place. Ces pores augmentent la capacité de gonflement des hydrogels, d'une manière similaire aux éponges poreuses. Dans le cas de la lyophilisation directionnelle, nous avons contrôlé la direction, la croissance et la taille des cristaux de glace. Les hydrogels coulés par lyophilisation directionnelle présentaient des macropores alignés verticalement avec un diamètre médian de 150  $\mu\text{m}$  et des capacités d'absorption exceptionnelles, associées à une cinétique de gonflement/relargage très rapide.

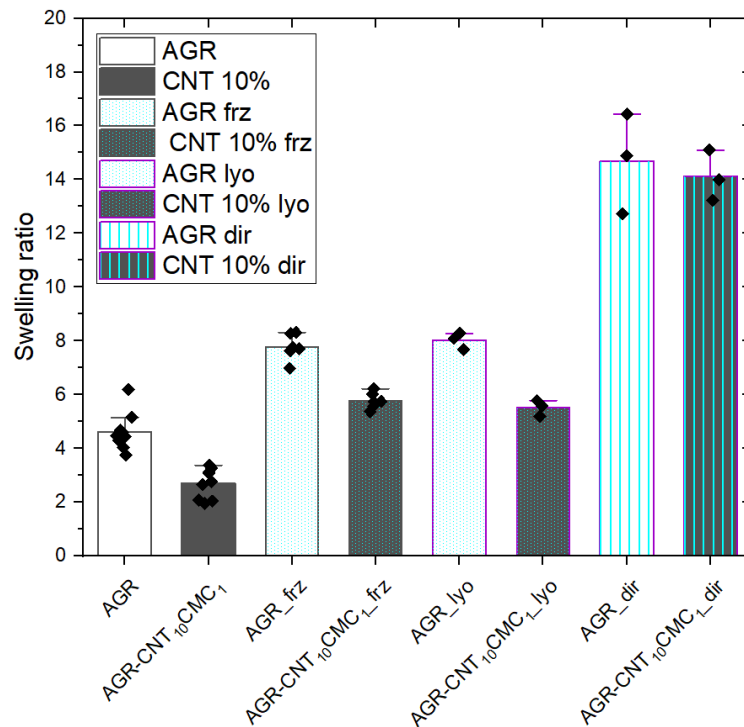


**Fig . 2.** Impact de la méthode de traitement sur le taux de gonflement. Blanc : hydrogels d'agarose simples. Gris foncé : hydrogels d'agarose nanocomposites (NTC 10 % en poids du polymère). n=3-10.

Une étude de cyclabilité des étapes de séchage/regonflement a démontré que les hydrogels étaient réutilisables, au moins jusqu'à 6 fois, avec seulement une perte mineure de capacité d'absorption ( $\leq 15\%$ ). Les hydrogels d'alginate/chitosan qui ont été testés, afin d'étudier le rôle de la matrice polymère sur les propriétés de l'hydrogel, avaient des capacités d'absorption bien moins importantes, n'absorbant que  $0,3 \pm 0,1$  fois leur masse sèche (32 %). Ce résultat a été attribué à la matrice de chitosan chimiquement réticulée, qui a limité la capacité d'expansion du réseau de chaînes de polymère interconnectées.

Les caractérisations électriques en courant continu (DC) ont montré que l'incorporation de NTC à double paroi augmentait la conductivité des hydrogels d'agarose gonflés de deux ordres de grandeur, passant ainsi de  $1,1 \times 10^{-6}$  à  $3,4 \times 10^{-4}$  S/m (**Fig. 3B**). D'autres types de NTC (multi-parois, oxydés) ont eu un effet similaire. Le seuil de percolation des NTC se situe entre 0,125 et 0,25 % p/p (0,07 et 0,14 % v/v). Les suspensions aqueuses de NTC avaient un seuil de percolation plus bas, à 0,025 % m/m, et des conductivités électriques (AC) plus élevées que les échantillons d'hydrogel.

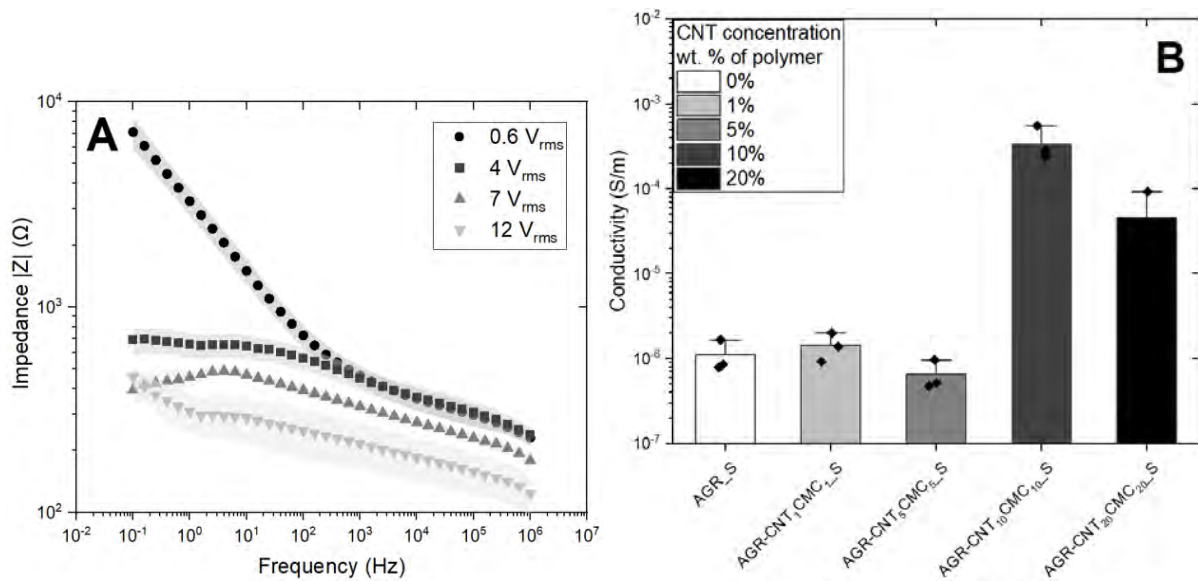


**Fig. 3.** Propriétés électriques des hydrogels nanocomposites. **(A)** Spectroscopie d'impédance d'hydrogels nanocomposites frais, à des tensions croissantes, de 0,6 à 12 V<sub>rms</sub>. n=4. (A) Impédance absolue en fonction de la fréquence. **(B)** Impact de la concentration en NTC sur la conductivité électrique de l'hydrogel. Conductivité électrique des hydrogels d'agarose gonflés en fonction de la concentration en NTC (n=3-4).

Les NTC ont des surfaces très hydrophobes. Ils ont tendance à former des agglomérats dans les suspensions aqueuses et ont le plus souvent une faible compatibilité interfaciale avec les matrices polymères. La carboxyméthylcellulose (CMC) est un polysaccharide utilisé dans l'industrie alimentaire qui peut être adsorbé sur la surface des NTC grâce à des interactions non covalentes entre le motif de l'unité glucose de la CMC et la surface hydrophobe des NTC [23]. Les groupes hydroxyles et carboxyliques présents dans la CMC rendent les nanotubes plus hydrophiles et les répulsions électrostatiques entre les chaînes de polymères anioniques de la CMC limitent l'agglomération des nanotubes [24]. Sans dispersant, l'incorporation de NTC dans des hydrogels d'agarose a eu un effet moindre sur la conductivité mesurée en courant continu. Un autre dispersant également testé, la polydopamine, a augmenté la conductivité DC des hydrogels nanocomposites, mais dans une moindre mesure en comparaison avec la carboxyméthylcellulose. La polydopamine a des propriétés semi-conductrices et l'augmentation de la conductivité a été attribuée à ces dernières.

Les solutions ioniques n'ont pas affecté la conductivité DC des hydrogels d'agarose. Les hydrogels d'alginate/chitosan avaient une conductivité plus élevée que les hydrogels d'agarose, à  $(4,1 \pm 0,3) \times 10^{-4}$  S/m, mais l'incorporation de NTC ne l'a pas augmentée davantage. Les hydrogels d'agarose gonflés qui avaient été préalablement congelés présentaient une conductivité électrique accrue,  $(2,4 \pm 1,4) \times 10^{-5}$  S/m. Cette conductivité a encore augmenté,  $(5,5 \pm 1,1) \times 10^{-4}$  S/m, pour les hydrogels d'agarose ayant subi une congélation directionnelle (mesure dans la direction de congélation). Les hydrogels d'agarose nanocomposites ont également présenté une dépendance modérée à la température, la conductivité DC passant de  $(9 \pm 5) \times 10^{-5}$  S/m à 10 °C à  $(4,1 \pm 1,9) \times 10^{-4}$  à 35 °C.

La conductivité électrique des hydrogels n'est pas constante, et elle augmente avec l'intensité du champ électrique. Cela était particulièrement vrai pour les hydrogels nanocomposites, dont l'impédance continuait à diminuer à mesure que nous augmentions la tension appliquée. Les systèmes nanocomposites peuvent présenter des propriétés électriques non linéaires, en raison de

changements dans la conductance à effet tunnel des électrons et/ou d'une éventuelle reconfiguration géométrique des nanomatériaux au sein de la matrice polymère.

Les différentes compositions d'hydrogel et méthodes de traitement explorées ont présenté des propriétés prometteuses pour une utilisation en tant que plates-formes conductrices de délivrance transdermique. Certains compromis ont dû être faits entre la conductivité électrique, la capacité d'absorption, la cytotoxicité potentielle, les propriétés mécaniques, la conservation, la réutilisation et la facilité de fabrication. Sur la base des travaux antérieurs de l'équipe et de nos propres travaux, nous avons choisi de travailler avec les hydrogels "Agarose 2,5 % p/p - CNT 10 % p/p de polymère - CMC 1 % p/p de polymère", qui ont un taux de gonflement de  $2,7 \pm 0,6$ , une conductivité DC de  $3,4 \times 10^{-4}$  S/m et une impédance décroissante avec l'augmentation du champ électrique (**Fig. 3A**).

Ces hydrogels ont été séchés à l'air puis gonflés dans une solution aqueuse contenant des médicaments modèles (molécules fluorophores). L'administration de médicaments a été testée sur deux types de peaux modèles : la peau fraîchement extraite de souris sans poils et l'épiderme humain reconstruit, cultivé en laboratoire au sein de notre consortium. Pour les expériences d'électroporation, la peau a été placée au-dessus d'une gaze imbibée de solution tampon phosphate salin. Deux hydrogels chargés de fluorophores ont été placés sur la peau, côte à côte, à 14 mm l'un de l'autre (centre à centre). Les hydrogels ont été connectés à un générateur électrique. Pendant le traitement CEP, le générateur a été réglé pour appliquer 8 impulsions d'une durée de 20 ms, d'une fréquence de 1 Hz et d'une tension allant de 0 (contrôle) à 400 V.

Nous avons mesuré le courant, la tension et la résistance instantanée du système lors de l'application du CEP, ainsi que les changements dans les propriétés électriques passives (conductivité DC) et l'augmentation de la température résultant du traitement (**Fig. 4**). En ce qui concerne les mesures I-V, trois observations majeures ont été faites : (1) la résistance moyenne du système (mesurée pendant la dernière des huit impulsions) a diminué pour des tensions CEP croissantes, de façon très importante entre 50 et 200 V, puis dans une moindre mesure entre 200 et 300 V, (2) la résistance instantanée du système a diminué pendant l'application des impulsions électriques, et (3) les changements de résistance ont été spécifiquement attribués à la peau, puisque le système sans la peau (hydrogels et gaze humide) a eu une résistance instantanée constante. Grâce aux mesures électriques, nous avons également confirmé que les hydrogels nanocomposites établissent un contact électrique efficace entre les contacts électriques métalliques et la peau. Cela élimine la nécessité d'utiliser un gel conducteur, car la résistance du système est restée inchangée indépendamment de la présence d'un gel conducteur.

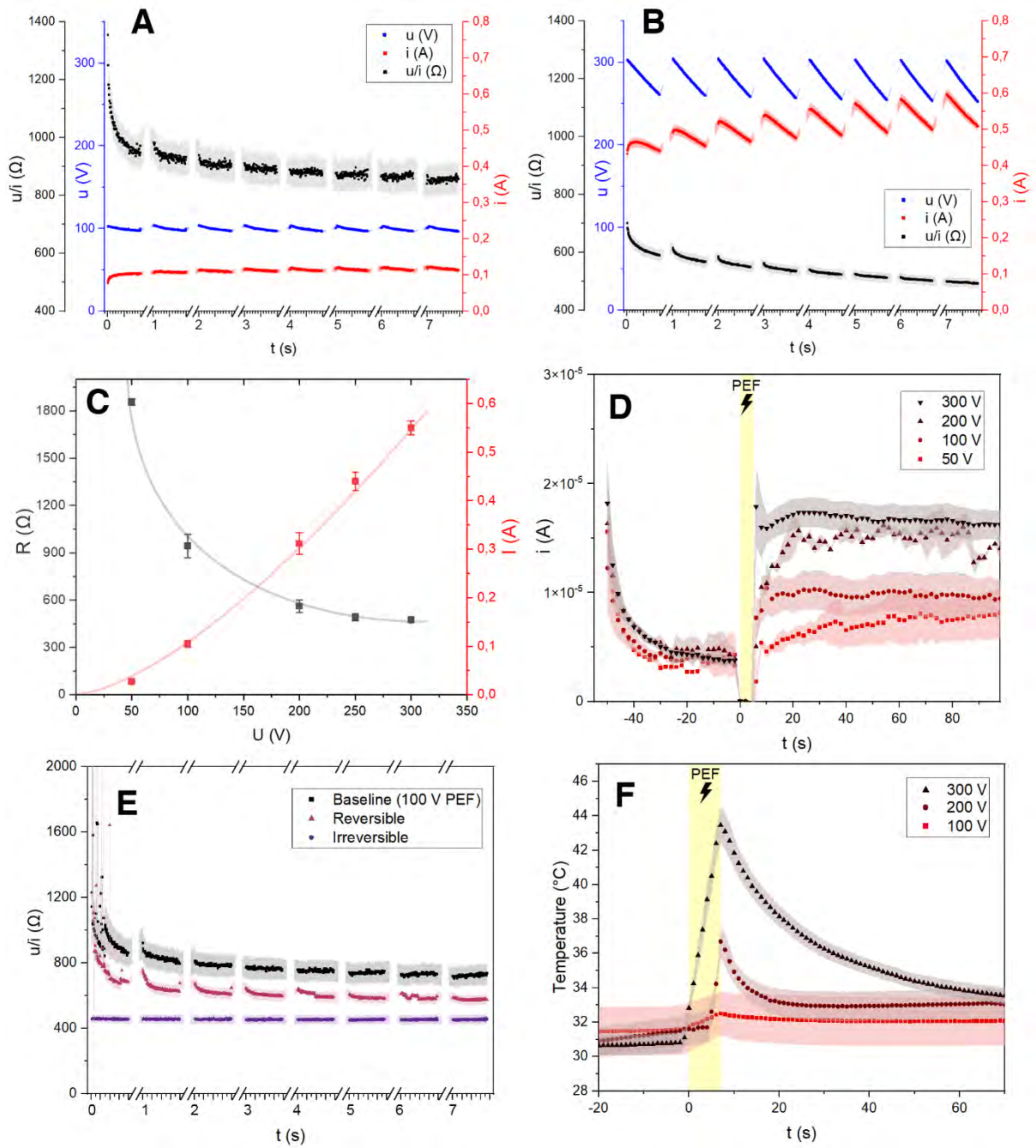


**Fig. 4.** Propriétés électriques et augmentation de la température du modèle de peau de souris *ex vivo* pendant l'application de CEP. **(A), (B)** Tension, courant et résistance instantanée ( $u/i$ ) des systèmes pendant l'application de champs électriques pulsés (CEP) de 100 V ( $n=5$ ) et 300 V ( $n=12$ ). Dans les deux cas, la résistance instantanée du système diminue pendant l'application de l'impulsion, principalement pendant les 5-7 premières ms. **(C)** Courbes I-V et R-V du système, démontrant un comportement non linéaire ( $n=2-18$ ). **(D)** Courant électrique résultant de l'application de 1V DC, avant et après CEP ( $n=2-11$ ). La zone ombrée en jaune correspond à l'application du CEP. Après un CEP de 50 V, le courant ne change pas de manière substantielle. Après un CEP de 100 à 300 V, une augmentation du courant électrique a été observée. **(E)** Résistance instantanée du système *ex vivo* à 100 V, pour une série d'applications CEP ( $n=3-4$ ). La résistance instantanée de la peau après une CEP à faible tension (jusqu'à 150 V) se rapproche de la valeur de base. Après une série de CEP à haute tension (jusqu'à 400 V), la peau perd son caractère dynamique. **(F)** Augmentation de la température de la peau pendant l'application de CEP ( $n=3-9$ ). La zone ombrée en jaune correspond à l'application du CEP. L'augmentation de la



température est minime pour un CEP de 100 V, mais augmente considérablement pour 200 et 300 V. Dans tous les cas, les zones ombrées et les barres d'erreur représentent le SEM.

Les mesures de courant et de tension ont été utilisées pour étudier la réversibilité du traitement CEP. La résistance instantanée des échantillons de peau exposés à des tensions faibles à modérées, jusqu'à 150 V, est presque revenue aux valeurs de base en l'espace d'une heure. En revanche, la résistance instantanée des échantillons de peau exposés à des CEP multiples, jusqu'à 400 V, a diminué de façon permanente (**Fig. 4E**).

L'application de CEP à 100 V et plus a modifié les propriétés électriques passives de la peau, en augmentant sa conductivité en courant continu. L'augmentation de la conductivité a été plus importante pour les tensions CEP les plus élevées. L'augmentation de la conductivité en courant continu a été durable. L'application des CEP a augmenté la température des échantillons de peau jusqu'à +12 °C, principalement pour les tensions les plus élevées de 200 et 300 V. La température de la peau est restée inférieure au seuil de douleur thermique chez les humains en bonne santé (50 à 55 °C, **Fig. 4F**).

Grâce à nos observations, nous émettons les hypothèses suivantes concernant l'impact des CEP sur la peau :

1. La diminution de la résistance moyenne de la peau est liée à la formation de RTL à travers l'épiderme. Des tensions appliquées plus élevées ont induit une plus grande densité de RTL, diminuant ainsi la résistance de la peau dans une plus large mesure.
2. La diminution de la résistance instantanée du système était liée à une augmentation de la conductivité dans les RTL déjà formées dans l'épiderme. Cette augmentation de la conductivité peut être due à l'expansion du rayon des RTL ou à des changements locaux induits par la chaleur dans l'organisation des lipides à l'intérieur des RTL. Pour les courants supérieurs à 0,25 A (correspondant à des tensions de 200 V et plus), l'augmentation de la température du système, et en particulier de la gaze humide, a également joué un rôle.
3. Les modifications de la conductivité électrique de la peau peuvent être temporaires, durables ou permanentes. La conductivité DC de la peau n'a pas changé après un CEP de 50 V, mais la résistance instantanée de la peau a diminué pendant son application. Cela montre que, pour des tensions plus faibles, des voies conductrices sont formées à travers la peau uniquement pendant l'application du champ électrique, sans impact sur les propriétés électriques passives de la peau. Cependant, des tensions CEP plus élevées induisent des changements durables sur la conductivité DC.
4. Une série de tensions CEP faibles à modérées (jusqu'à 150 V) a eu un impact mineur sur la résistance instantanée de base des échantillons de peau, tandis qu'une série de CEP à haute tension (jusqu'à 400 V) a augmenté de manière irréversible la conductivité de la peau. Nous supposons que dans le premier cas, les voies conductrices formées à travers la peau ont retrouvé leur résistivité d'origine. L'augmentation mineure et permanente de la conductivité peut être liée à l'électroporation irréversible des régions à plus forte densité de courant (par exemple les annexes cutanées (follicules pileux, canaux sudoripares, glandes sébacées). Dans le second cas, les voies conductrices ne se sont pas rétablies en raison de dommages électriques et éventuellement thermiques importants.
5. La distribution de la densité de courant à travers la peau n'était pas homogène. Les régions présentant une conductivité plus élevée, telles que les annexes cutanées et d'autres défauts

de l'épiderme dus à des blessures, étaient traversées par un courant plus important. Ces régions sont affectées de manière disproportionnée par le champ électrique. À des tensions plus faibles, en particulier, l'électroporation des cellules dans ces régions peut être responsable de l'augmentation globale de la conductivité [25].

Ces propriétés électriques ont également été utilisées pour optimiser et valider un modèle numérique du système d'électroporation. Nous avons développé une série de modèles numériques, de complexité croissante, pour décrire et comprendre les propriétés électriques du système d'administration de médicaments. Le premier modèle, bidimensionnel, a souligné le rôle de la conductivité électrique des plateformes d'hydrogel sur la distribution du champ électrique à travers le modèle de peau. Il a également révélé l'impact de la conductivité de la gaze humide et a confirmé que la densité de courant circulait à travers le SC, puis dans les couches profondes de la peau. Le deuxième modèle a été développé avec une géométrie tridimensionnelle qui correspondait au système complet d'administration du médicament. Nous avons corrigé les conductivités électriques des hydrogels nanocomposites et de la gaze humide, en nous basant sur les mesures I-V, et nous avons simulé le champ électrique à l'intérieur des différentes couches de la peau.

Le troisième modèle comprenait une dépendance non linéaire de la conductivité du SC par rapport au champ électrique. La conductivité du SC augmente considérablement grâce à la formation de voies conductrices, induites par le champ électrique appliqué. Nous avons utilisé les résultats expérimentaux du modèle 3D précédent et les mesures électriques effectuées sur la peau de souris *ex vivo* pour interpoler une fonction permettant de déterminer la dépendance de la conductivité du SC par rapport au champ électrique. Le modèle a décrit avec précision la diminution de la résistance du système avec l'augmentation des tensions CEP, produisant des résultats très proches des valeurs mesurées expérimentalement. Comme l'ont souligné Corovic *et al*, l'inclusion de la conductivité non linéaire du SC (c'est-à-dire que la conductivité dépend du champ électrique,  $\sigma(E)$ ) s'est avérée cruciale pour la distribution du champ électrique [17]. Avec une conductivité constante, le champ électrique semble se concentrer uniquement sur le SC, sans atteindre les couches cutanées plus profondes.

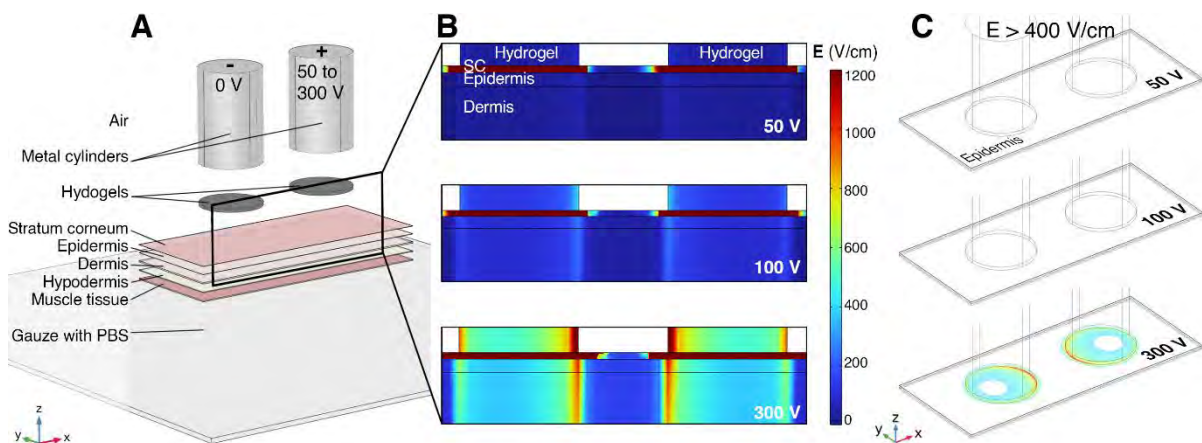


**Fig. 5.** Simulation numérique d'un modèle de peau de souris lors d'une stimulation électrique. **(A)** Le système d'administration de médicaments en 3D (aperçu des couches en cascade, colorisé). **(B)** Coupes XZ de la distribution du champ électrique pour une CEP de 50, 100 et 300 V. **(C)** Zone de peau viable (épiderme, sous le SC) où le champ électrique est supérieur à la valeur seuil pour la perméabilisation des cellules dans le tissu ( $\sim 400$  V/cm), pour une CEP de 50, 100 et 300 V. La légende des couleurs est commune pour B et C.

Le modèle numérique validé a montré que les cellules de l'épiderme et du derme pouvaient être perméabilisées de manière réversible ( $E > 400$  V/cm) pour des CEP de 300 V, dans une large zone sous les hydrogels (**Fig. 5**). L'intensité du champ électrique a atteint ses valeurs les plus élevées dans la zone en forme de croissant où les deux électrodes se font face. Avec des CEP de 400 V, la surface couverte par les champs électriques perméabilisants était plus importante, mais une fine région présentait des valeurs de champ électrique supérieures au seuil de perméabilisation irréversible (1200 V/cm). Le SC qui n'avait pas été perméabilisé a provoqué une chute de tension massive dans le système d'administration du médicament, limitant la différence de potentiel appliquée aux couches cutanées plus profondes. Pour les tensions CEP les plus faibles (50 V), cette chute de tension représentait 2/3 de la résistance du système. À des tensions plus élevées (300 V), la perméabilisation du SC a considérablement réduit sa contribution à la résistance du système. Pour les CEP de 300 V, la principale résistance du système provenait de la gaze humide. Cette résistance peut être diminuée en réduisant la distance entre les plates-formes d'hydrogel (actuellement, 6 mm d'un côté à l'autre). Cependant, en les rapprochant trop, on risque de provoquer un court-circuit avec la solution aqueuse qui est libérée des hydrogels lors de l'application des CEP.

Dans le contexte de l'administration de médicaments par voie transdermique, nous nous intéressons principalement aux trois premières couches de la peau, à savoir le stratum corneum, l'épiderme profond et le derme. Le SC est la couche limitante pour l'administration de molécules thérapeutiques. L'épiderme est la première couche contenant des cellules viables, avec des noyaux et des membranes plasmiques. Il comprend également des cellules immunitaires, ce qui en fait une cible adéquate pour les vaccinations. A titre d'exemple, les anesthésiques topiques tels que la lidocaïne pour insensibiliser la zone avant une intervention médicale et les rétinoïdes administrés localement pour le traitement de l'acné [13], [26] sont d'autres médicaments pouvant être administrés vers l'épiderme. Le derme comprend des cellules viables et des vaisseaux sanguins. Les médicaments délivrés dans le derme peuvent alors atteindre la circulation systémique grâce à la vascularisation du tissu. Le fentanyl pour le traitement de la douleur et l'insuline pour le métabolisme du glucose (diabète) sont des exemples de médicaments qui doivent atteindre la circulation systémique pour avoir un effet.

La conductivité électrique de la peau réelle n'est pas aussi homogène et isotrope que dans nos simulations. Elle contient des imperfections, telles que les follicules pileux et les canaux sudoripares, qui sont des régions où la conductivité est plus élevée [25]. En outre, l'alignement des cellules crée une conductivité électrique anisotrope. Ce phénomène est bien établi pour les tissus musculaires, où la conductivité longitudinale peut être jusqu'à 5 fois supérieure à la conductivité transversale [17] mais l'argument vaut également pour les cellules du SC et, dans une moindre mesure, pour l'ensemble de la peau. Pour toutes ces raisons, les valeurs précises obtenues à partir des simulations doivent être interprétées avec prudence.

Nous avons testé l'administration de molécules fluorescentes sur des modèles de peau de souris. Pour une gamme de tensions CEP étudiées, les trois fluorophores utilisés ont montré une émission de fluorescence significativement plus élevée par rapport au contrôle. Le Lucifer Yellow (LY) est un petit fluorophore (442 Da), hydrophile et chargé négativement. Nous l'avons utilisé comme marqueur de l'intégrité du SC. Sous l'électrode positive, il n'y a pas eu d'augmentation significative de l'absorption de LY pour aucune des tensions CEP testées. Sous l'électrode négative, dès une CEP de 100 V, le LY a présenté une augmentation statistiquement significative de la fluorescence ( $2,9 \pm 0,4$ ), par rapport au contrôle ( $1,4 \pm 0,1$ ). Une nouvelle augmentation de la tension CEP à 200 V a entraîné une augmentation

de l'émission de fluorescence ( $5,2 \pm 0,3$ ), tandis qu'à 300 V, la fluorescence n'a pas augmenté davantage ( $4,6 \pm 0,3$ ). L'iodure de propidium (IP) est un petit fluorophore (668 Da), hydrophile, chargé positivement, imperméable à la membrane et intercalant l'ADN, utilisé ici comme preuve de la perméabilisation de la membrane cellulaire. L'IP a montré une augmentation statistiquement significative de la fluorescence uniquement sous l'électrode positive, pour un CEP de 300 V ( $1,54 \pm 0,11$ , comparé à  $1,01 \pm 0,02$  pour le contrôle). L'isothiocyanate de fluorescéine-dextran (FD4) est un fluorophore hydrophile de grande taille (4000 Da de poids moléculaire moyen), avec peu de charges négatives (la fluorescéine est chargée négativement et le taux de substitution est d'environ 0,01 mole de FITC par mole de glucose). Nous l'avons utilisé comme molécule modèle pour l'insuline, qui a un poids moléculaire du même ordre de grandeur (5700 Da). Le FD4 n'a été testé qu'à 300 V, et a montré une augmentation statistiquement significative de la fluorescence sous l'électrode négative ( $2,3 \pm 0,3$ , contre  $0,96 \pm 0,01$  pour le contrôle).

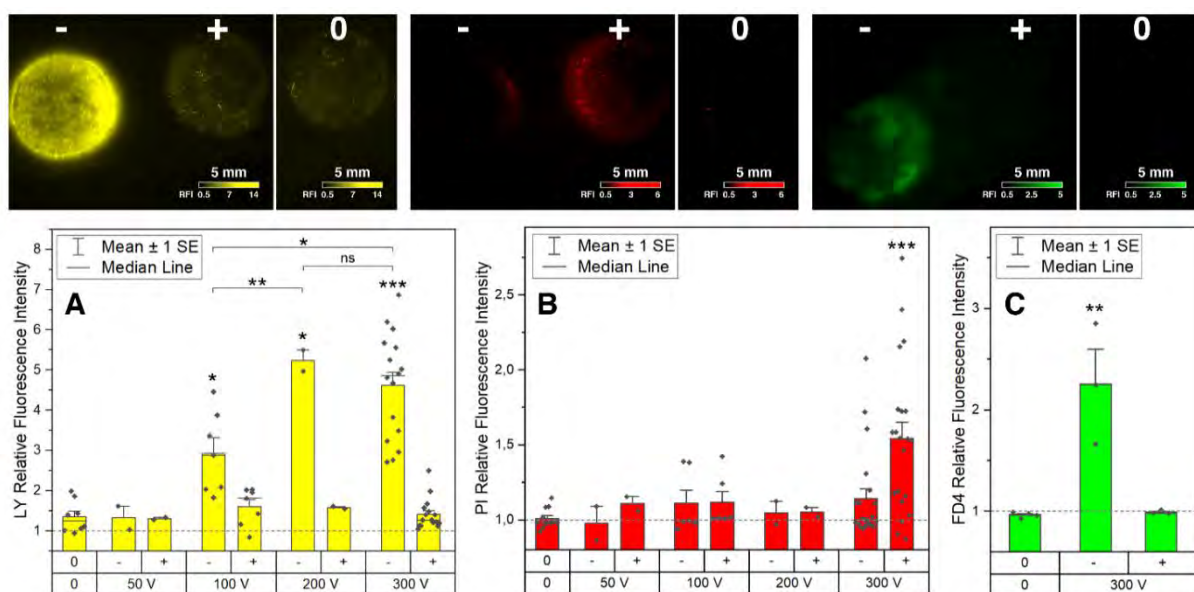


**Fig. 6.** Marquage de molécules fluorescentes sur le modèle de peau (vue de dessus) et graphiques de quantification de l'intensité relative de fluorescence. **(A)** Le Lucifer Yellow, un petit fluorophore (442 Da) chargé négativement, a pénétré la peau pour un CEP supérieur à 100 V (n=2-16). **(B)** L'iodure de propidium, un petit fluorophore (668 Da) chargé positivement et intercalant l'ADN, a perméabilisé les cellules nucléées pour une FPE de 300 V (n=2-20). **(C)** L'isothiocyanate de fluorescéine-dextran, un fluorophore de grande taille (4000 Da), légèrement chargé négativement, a été délivré à travers la peau avec 300 V CEP (n=3-4). Les barres d'erreur représentent l'erreur type. Traitement statistique : ANOVA à sens unique et tests post-hoc T3 de Dunnett (A, B) ou de Dunnett (C). Signification des codes : \* =  $p \leq 0,05$  ; \*\* =  $p \leq 0,01$  ; \*\*\* =  $p \leq 0,001$  ; pas de symbole ou ns = différence non significative ( $p > 0,05$ ). Les moyennes sont comparées au contrôle (0), sauf indication contraire entre parenthèses.

Parallèlement au modèle de peau animale, nous avons testé l'administration de médicaments sur un épiderme humain reconstruit et cultivé en laboratoire. Ce modèle présente les avantages de l'utilisation de cellules humaines, limitant l'inhomogénéité et la complexité par rapport à un modèle animal, tout en réduisant les dommages causés par l'expérimentation animale. Outre les modèles d'épiderme reconstruit, il est également possible de fabriquer des substituts de peau complets. Ils sont cultivés couche par couche en commençant par des feuillets dermiques. Cela offre une occasion unique d'étudier les propriétés électriques de couches de peau distinctes. Les données de la littérature dans ce domaine sont particulièrement rares et reposent sur quelques études présentant des niveaux

d'incertitude élevés. L'administration de médicaments sur des échantillons d'épiderme humain reconstruit a été testée avec LY et IP. Les échantillons ont montré une absorption accrue de LY (sous l'électrode négative) et de PI (sous l'électrode positive), par rapport à un contrôle non pulsé.

Nous avons cependant mis en évidence certaines limites. Les échantillons d'épiderme reconstruit présentaient une absorption accrue du fluorophore sans impulsions électriques, par rapport au modèle de peau animale. Il est possible qu'ils n'aient pas exactement les mêmes propriétés de barrière que la peau de souris *ex vivo*. Deuxièmement, ils ont montré une grande variabilité entre les différents échantillons. Ces deux limitations peuvent être liées au petit nombre d'échantillons testés et à leur manipulation difficile, combinée à leur nature fine et fragile. En outre, la tension CEP appliquée doit être adaptée à ces échantillons. Une CEP de 300 V a entraîné des courants électriques élevés (0,8 à 1,6 A). Compte tenu de la faible masse des échantillons d'épiderme reconstruits, des courants aussi élevés pendant 160 ms conduiraient à une augmentation importante de la température avec des dommages thermiques potentiellement irréversibles sur les échantillons de peau.

Dans des travaux antérieurs, la délivrance de molécules fluorescentes a été évaluée par des observations histologiques du modèle de peau de souris, après l'application de 300 V CEP [10]. Il a été démontré que le PI perméabilisait les cellules de l'épiderme, que le LY diffusait à travers le SC et l'épiderme jusqu'au derme alors que le FD4 pénétrait les premières couches du SC mais n'atteignait pas les couches plus profondes de l'épiderme et du derme.

En combinant les résultats des mesures électriques, du modèle numérique et de l'administration de molécules fluorescentes, nous distinguons trois domaines de tension ayant des effets différents sur la peau :

- Domaine 1 : CEP à basse tension (<100 V) - Formation de voies conductrices

Dans le domaine initial, où les CEP étaient inférieurs à 100 V, une augmentation de la mobilité ionique dans la peau a été observée. Cela s'est traduit par une réduction de la résistance instantanée pendant les CEP et une diminution de la résistance moyenne avec l'augmentation de la tension. Remarquablement, ces effets étaient perceptibles même à des CEP aussi faibles que 30 à 50 V. Cependant, aucun transfert de molécules à travers la peau n'a eu lieu à des tensions inférieures à 100 V. Nous avons émis l'hypothèse que les voies conductrices formées à l'intérieur de la peau augmentaient la mobilité des électrolytes, mais qu'elles étaient trop petites en rayon ou trop limitées en surface pour avoir un impact sur les propriétés de barrière de la peau (**Fig. 7B**). En outre, le courant continu mesuré avant et après l'application de CEP de 50 V a montré des altérations minimales, ce qui suggère que tout changement dans les propriétés électriques a été de courte durée. Dans ce domaine, la conductivité du SC est restée faible et l'intensité du champ électrique dans les couches cutanées plus profondes était minimale. Il a été difficile d'établir un seuil minimal précis de tension CEP pour la formation de voies conductrices, en se basant uniquement sur les propriétés électriques, car la résistance instantanée diminuait même aux tensions les plus faibles appliquées. Selon Chizmadzhev *et al*, à de faibles tensions (jusqu'à 30 V, équivalant à environ 100 V dans notre configuration), l'électroporation des cellules épithéliales dans les annexes cutanées contribue à la réduction observée de la résistance de la peau [23]. [25].

- Domaine 2 : CEPs à tension modérée (100-200 V) - Perturbation de la matrice extracellulaire lipidique et transport de molécules



En passant au deuxième domaine, englobant des CEP allant de 100 à 200 V, nous avons observé le transport de petites molécules hydrophiles à travers le SC et des changements durables dans les propriétés électriques passives de la peau. À ce stade, le CEP appliqué a perturbé l'organisation des lipides extracellulaires dans la couche cornée, ce qui a entraîné la formation de régions de transport local (RTL). Les molécules hydrophiles dont la diffusion passive à travers la peau est limitée, telles que LY, ont traversé la peau via les bicouches lipidiques désorganisées dans la région paracellulaire (**Fig. 7C**). En outre, nous avons noté une augmentation du courant continu de la peau après l'application du CEP, ce qui indique la création durable de voies conductrices. Cependant, l'intensité du champ électrique dans les couches de peau contenant des cellules viables est restée inférieure au seuil d'électroporation (400 V/cm) et aucune perméabilisation des membranes cellulaires ne s'est produite dans ce domaine.

- Domaine 3 : CEP à haute tension (300 V) - Perméabilisation de la membrane cellulaire

Dans le troisième domaine, correspondant à des CEP de 300 V, nous avons observé la perméabilisation des membranes cellulaires. À ce stade, la conductivité du SC a fortement augmenté et le champ électrique au niveau de l'épiderme et du derme (sous le SC) a atteint des valeurs supérieures à 400 V/cm. Il en résulte un potentiel transmembranaire dans les cellules nucléées de l'épiderme et/ou du derme dépassant le seuil de 250 mV, ce qui entraîne une perméabilisation de la membrane. L'iodure de propidium (PI) a pénétré dans l'espace intracellulaire et s'est ensuite intercalé avec l'ADN (**Fig. 6D**). Nos simulations numériques, malgré leurs simplifications, ont prédit avec précision la perméabilisation de la membrane cellulaire et la délivrance de molécules fluorescentes. Le courant continu a augmenté de 300 % après l'application du CEP, ce qui indique des changements majeurs dans les propriétés électriques passives de la peau.

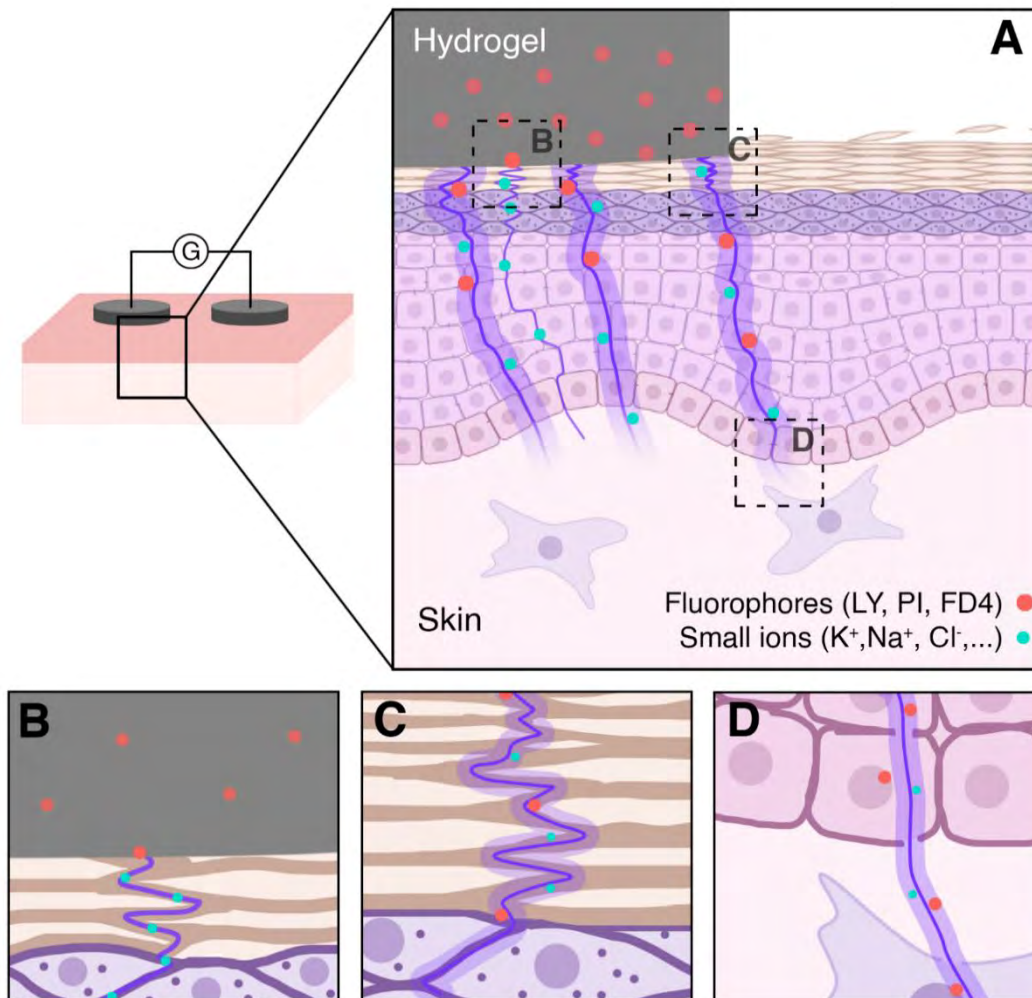


**Fig. 7.** Régions de transport local (RTL) et perméabilisation de la membrane cellulaire dans la peau. **(A)** Schéma de l'électroporation de la peau avec un hydrogel réservoir d'électrodes. **(B)** À des tensions CEP inférieures à 100 V, des voies conductrices se sont formées, augmentant la mobilité ionique. **(C)** À partir de 100 V CEP, la création de RTL dans les lipides extracellulaires de la couche cornée a permis la diffusion de fluorophores à travers la peau. **(D)** À 300 V CEP, les membranes cellulaires des cellules nucléées de l'épiderme et/ou du derme ont été perméabilisées et les fluorophores ont pénétré dans le cytoplasme.

Ces résultats ont montré l'existence de deux domaines distincts d'administration de médicaments, l'un consistant en la formation de RTL dans les lipides extracellulaires du SC permettant la diffusion de molécules hydrophiles, et l'autre consistant en la perméabilisation des membranes plasmiques des cellules nucléées (c'est-à-dire des cellules situées dans des couches plus profondes que le SC). Ces deux domaines sont importants dans le contexte de l'administration de médicaments à travers la peau. Certains médicaments tels que la lidocaïne et les corticostéroïdes peuvent être administrés localement, au niveau de l'épiderme, pour l'anesthésie locale et le traitement de l'inflammation cutanée. Les vaccins à base d'acide nucléique doivent pénétrer à l'intérieur des cellules afin d'exprimer l'antigène codé et de provoquer une réponse immunitaire. De même, les antibiotiques antitumoraux tels que la bléomycine doivent perméabiliser la membrane cellulaire pour avoir un effet. Le fentanyl et l'insuline doivent atteindre la circulation systémique pour traiter la douleur ou réguler le métabolisme du glucose, respectivement. Les paramètres exacts choisis pour l'électroporation de la peau dépendent de la cible d'administration, mais aussi des propriétés physicochimiques du

médicament (taille, charge, hydrophilie) et de leur adéquation avec les propriétés physicochimiques du matériau du patch.

Le dispositif expérimental que nous avons proposé ici (mesures *in situ* des propriétés électriques et de la température, modèle numérique et microscopie à fluorescence) peut servir de modèle pour de futures recherches sur l'électroporation de la peau. Une approche plus exhaustive inclurait les modifications suivantes : automatisation de la commutation entre les mesures du courant continu et de l'oscilloscope, permettant de surveiller le courant continu immédiatement après les impulsions et même entre celles-ci. Tentative de modélisation numérique de la dépendance temporelle et de la nature localisée des voies conductrices à travers la peau (au lieu d'une simulation macroscopique homogène). Combinaison de la macrofluo-microscopie avec des observations histologiques pour déterminer la profondeur de pénétration des fluorophores. Expérimentation avec un plus grand nombre de modèles de peau, y compris la peau humaine reconstruite et les tests *in vivo* sur les animaux.

# Table of Contents

<b>PREFACE</b> .....	<b>2</b>
<b>ACKNOWLEDGEMENTS</b> .....	<b>3</b>
<b>SUMMARY</b> .....	<b>4</b>
<b>RESUME EN FRANÇAIS (SUMMARY IN FRENCH)</b> .....	<b>5</b>
<b>RESUME DETAILLE EN FRANÇAIS (EXTENDED SUMMARY IN FRENCH)</b> .....	<b>6</b>
<b>TABLE OF CONTENTS</b> .....	<b>22</b>
<b>1 INTRODUCTION</b> .....	<b>32</b>
1.1 NON-INVASIVE, TRANSDERMAL DRUG DELIVERY .....	32
1.2 SKIN ANATOMY .....	33
1.3 SKIN BARRIER PROPERTIES .....	34
1.4 METHODS FOR NON-INVASIVE, TRANSDERMAL DRUG DELIVERY .....	35
1.5 ELECTROPORATION .....	36
1.5.1 <i>Lipid bilayer electroporation</i> .....	37
1.5.2 <i>Modeling cell membrane electroporation</i> .....	37
1.5.3 <i>Tissue electroporation</i> .....	39
1.5.4 <i>Skin electroporation</i> .....	40
1.6 HYDROGELS FOR DRUG DELIVERY .....	43
1.7 HYDROGELS.....	43
1.8 ELECTRICALLY CONDUCTIVE HYDROGELS FOR DRUG DELIVERY .....	45
1.9 CARBON-BASED NANOMATERIALS .....	47
1.9.1 <i>Carbon nanotubes</i> .....	47
1.10 ELECTRICAL PERCOLATION .....	48
1.10.1 <i>Percolation theory</i> .....	48
1.10.2 <i>Critical path approximation</i> .....	50
1.10.3 <i>Percolation of carbon nanotubes</i> .....	50
1.10.4 <i>Electrical percolation studies in hydrogels</i> .....	51
1.11 DISPERSION OF CONDUCTIVE NANOMATERIALS .....	51
1.12 ELECTRICAL CONDUCTIVITY AND CONDUCTION MECHANISMS .....	52
1.12.1 <i>Conductivity</i> .....	52
1.12.2 <i>Conduction mechanisms in dielectric materials under high electric fields</i> .....	52
1.12.3 <i>Ionic conduction</i> .....	52
1.12.4 <i>Electric current</i> .....	53
1.12.5 <i>Hydrogel water content and electrical conductivity</i> .....	53
1.13 MEASURING ELECTRICAL PROPERTIES .....	54
1.13.1 <i>Two-point and four-point probe methods</i> .....	55
1.13.2 <i>Alternating Current</i> .....	57
1.14 OVERVIEW .....	58
<b>2 MATERIALS AND METHODS</b> .....	<b>60</b>
2.1 MATERIALS CHARACTERIZATIONS .....	60
2.1.1 <i>CNT synthesis and extraction</i> .....	60
2.1.2 <i>Preparation of nanocomposite hydrogels</i> .....	60
2.1.3 <i>Drying and swelling</i> .....	62
2.1.4 <i>Preparation of alginate/chitosan hydrogels</i> .....	64
2.1.5 <i>DC conductivity</i> .....	65
2.1.6 <i>CNT conductivity in aqueous suspension</i> .....	67
2.1.7 <i>Impedance spectroscopy</i> .....	68
2.1.8 <i>Electrical conductivity of hydrogels with ionic solutions</i> .....	69

2.1.9	<i>Hydrogel nomenclature (sample naming conventions)</i> .....	69
2.2	SKIN MODELS.....	70
2.2.1	<i>Mouse skin model</i> .....	71
2.2.2	<i>Reconstructed human epidermis</i> .....	71
2.3	IN SITU MEASUREMENTS .....	72
2.3.1	<i>In-situ electrical response</i> .....	72
2.3.2	<i>Temperature monitoring</i> .....	74
2.4	FEM SIMULATIONS.....	74
2.5	DRUG DELIVERY.....	75
2.5.1	<i>Drug models</i> .....	75
2.5.2	<i>Fluorescence microscopy</i> .....	76
2.6	STATISTICAL TREATMENT .....	77
<b>3</b>	<b>MATERIALS CHARACTERIZATIONS.....</b>	<b>78</b>
3.1	HYDROGEL SPECIFICATIONS (DESIRED PROPERTIES) .....	78
3.1.1	<i>Ability to store and release medicine</i> .....	79
3.1.2	<i>Electrical conductivity</i> .....	79
3.1.3	<i>Biocompatibility</i> .....	79
3.1.4	<i>Mechanical strength / reusability</i> .....	80
3.1.5	<i>Preservation / stability</i> .....	80
3.1.6	<i>Practicality / ease of fabrication</i> .....	81
3.1.7	<i>Choice of drug delivery platform</i> .....	81
3.2	DIMENSIONS.....	81
3.3	THERMOGRAVIMETRIC ANALYSIS.....	84
3.4	SWELLING RATIO.....	85
3.4.1	<i>CNT concentration</i> .....	85
3.4.2	<i>Processing method</i> .....	86
3.4.3	<i>Drying – swelling cycles</i> .....	90
3.4.4	<i>Alginate/chitosan</i> .....	91
3.5	DRYING AND SWELLING KINETICS .....	93
3.6	MECHANICAL PROPERTIES .....	95
3.7	ELECTRICAL CHARACTERIZATIONS .....	97
3.7.1	<i>CNT conductivity in aqueous suspension</i> .....	97
3.7.2	<i>DC conductivity</i> .....	98
3.7.3	<i>Electrical conductivity of hydrogels with ionic solutions</i> .....	112
3.7.4	<i>Impedance spectroscopy</i> .....	114
3.8	SKIN MODEL .....	117
3.8.1	<i>DC conductivity of skin model</i> .....	117
3.8.2	<i>Impedance spectroscopy of skin model</i> .....	118
3.9	CHAPTER HIGHLIGHTS AND DISCUSSION ON MATERIALS CHARACTERIZATIONS .....	119
<b>4</b>	<b>IN SITU MEASUREMENTS .....</b>	<b>124</b>
4.1	ELECTRICAL RESPONSE .....	124
4.1.1	<i>I-V during PEF application</i> .....	124
4.1.2	<i>Conductive gel</i> .....	128
4.1.3	<i>DC resistance</i> .....	129
4.1.4	<i>Electrical recovery</i> .....	131
4.2	TEMPERATURE INCREASE.....	132
4.3	I-V MEASUREMENTS OF RECONSTRUCTED HUMAN EPIDERMIS.....	133
4.4	CHAPTER HIGHLIGHTS AND DISCUSSION ON <i>IN SITU</i> MEASUREMENTS .....	134
<b>5</b>	<b>NUMERICAL MODELING.....</b>	<b>137</b>
5.1	FIRST MODEL: 2D.....	137



5.2	SECOND MODEL: 3D .....	141
5.3	THIRD MODEL: 3D WITH NONLINEAR CONDUCTIVITY.....	143
5.4	CHAPTER HIGHLIGHTS AND DISCUSSION ON NUMERICAL MODELING .....	148
<b>6</b>	<b>DRUG DELIVERY .....</b>	<b>151</b>
6.1	FLUORESCENCE MICROSCOPY .....	151
6.1.1	<i>Molecule release on gauze .....</i>	<i>151</i>
6.1.2	<i>Molecule release on skin model .....</i>	<i>152</i>
6.2	RECONSTRUCTED HUMAN EPIDERMIS.....	157
6.3	MECHANISMS OF SKIN ELECTROPORATION .....	158
6.3.1	<i>Domain 1: low-voltage PEFs (&lt;100 V) - Conductive pathway formation.....</i>	<i>158</i>
6.3.2	<i>Domain 2: moderate-voltage PEFs (100-200 V) – Disruption of extracellular matrix and molecule transport.....</i>	<i>158</i>
6.3.3	<i>Domain 3: high-voltage PEFs (300 V) - Cell membrane permeabilization .....</i>	<i>159</i>
6.4	CHAPTER HIGHLIGHTS AND DISCUSSION ON DRUG DELIVERY.....	160
<b>7</b>	<b>CONCLUSIONS AND PERSPECTIVES .....</b>	<b>162</b>
<b>8</b>	<b>REFERENCES.....</b>	<b>167</b>
<b>9</b>	<b>ANNEXES.....</b>	<b>180</b>
9.1	POTENTIAL DIFFERENCE ACROSS SKIN .....	180
9.2	CONDUCTIVITY OF HYDROGELS AND WET GAUZE IN PEF CONDITIONS .....	181
9.3	CV AND SCIENTIFIC PRODUCTION .....	182
9.3.1	<i>Publications – Conferences.....</i>	<i>182</i>
9.3.2	<i>Teaching – supervision .....</i>	<i>182</i>
9.3.3	<i>Other activities .....</i>	<i>182</i>
9.3.4	<i>CV (en français) .....</i>	<i>183</i>
9.4	COMIC STRIP.....	184

## Abbreviations

AGR	Agarose
AL	Alginate
CC	Calcium Chloride
CNT	Carbon Nanotubes
CNTox	Oxidized Carbon Nanotubes
CS	Chitosan
D	Dry
DI	Deionized
dir	Directional Freeze-Casting
DWCNT	Double-Wall Carbon Nanotubes
EB	Electroporation Buffer
F	Fresh
FD4	Fluorescein Isothiocyanate Dextran (avg. MW 4 kDA)
FEM	Finite Element Method
FITC	Fluorescein Isothiocyanate
frz	Frozen
GO, rGO	Graphene Oxide, reduced GO
LTR	Local Transport Region
LY	Lucifer Yellow
lyo	Lyophilized
MWCNT	Multi-Wall Carbon Nanotubes
PB	Phosphate Buffer
PEF	Pulsed Electric Field
PI	Propidium Iodide
S	Swollen
SC	Stratum Corneum
SMU	Source-Measuring Unit
SWCNT	Single-Wall Carbon Nanotubes

## Table of figures

<b>Figure 0.1</b> – Graphical abstract. An absorbent and conductive hydrogel was prepared with agarose and carbon nanotubes. The hydrogel was used as a patch for transdermal drug delivery through skin electroporation. The delivery system was studied through electrical measurements, numerical modeling and fluorescence microscopy. ....	4
<b>Figure 1.1</b> - Schematic illustration of skin’s anatomy [10] .....	33
<b>Figure 1.2</b> - Scheme of human epidermis and stratum corneum. (A) layers and constituents of the epidermis. (B) Stratum corneum “brick and mortar” configuration. (C) Extracellular lipids stacked into lipid bilayer (“mortar”). Adapted from refs. [10] and [11]. ....	34
<b>Figure 1.3</b> – Schematic representation of possible pathways through the epidermis [13]. ....	35
<b>Figure 1.4</b> – Transdermal drug delivery methods. Adapted from refs. [19], [20]. ....	36
<b>Figure 1.5</b> - Proposed molecular mechanisms of electrically induced permeabilization of lipid bilayers, for increasing electric field, $E$ . (A) Formation of aqueous pores, (B) chemical changes of the phospholipid tails, (C) channels through membrane proteins. Adapted from [31]. ....	37
<b>Figure 1.6</b> – Transmembrane potential on cell under the influence of electric field. ....	39
<b>Figure 1.7</b> – Tissue electroporation. (A) Microscope image of connective tissue containing adipose cells. (B) 3D reconstruction of connective tissue with randomly positioned cells. (C) Electrical conductivity of cell membranes during exposition to 1000 V/cm electric field [40], [42]. ....	40
<b>Figure 1.8</b> – Skin electroporation. Formation of local transport regions through the application of an electric field to the skin .....	41
<b>Figure 1.9</b> - Configurations for skin electroporation. (A) Two-chamber. An <i>ex vivo</i> skin model is placed between two chambers, filled with an aqueous solution. The electrodes are immersed in the solutions. This configuration is only relevant for research. (B) Pinched skin with conductive gel. The skin model ( <i>ex vivo</i> or <i>in vivo</i> ) is pinched and placed between two electrodes. A Conductive gel placed between the metal electrodes and the skinfold ensures electrical contact. (C) Our configuration. Side by side hydrogels functioning as drug reservoirs and electrodes. ....	42
<b>Figure 1.10</b> – Transdermal drug delivery methods, including our approach to non-invasive skin electroporation with a two-in-one electrode-reservoir hydrogel platform. Images adapted from refs. [48], [63]–[65] .....	43
<b>Figure 1.11</b> - Conductive nanocomposite hydrogels for controlled drug delivery. (A) Electrical stimulation causes a methacrylic acid – graphene nanosheet hydrogel to shrink, releasing drug. <i>In vivo</i> release profile of $^{14}\text{C}$ sucrose on the blood plasma of mice implanted with sucrose-loaded hydrogels. Hydrogels with no nanomaterials (green), 0.2 mg/ml CNTs (red) and 0.2 mg/ml graphene (blue) were tested. A tension of 10 V DC is applied for 1 minute with a time interval of 2 h. The graphene-loaded hydrogel (which also had the highest conductivity) demonstrated a pulsatile release of sucrose, controlled by the electric field. Adapted from ref. [89]. (B) Reduced graphene oxide nanomaterials retain lidocaine hydrochloride within a polyvinyl alcohol hydrogel. Upon pulsatile electrical stimulation (on/off, 15 V DC) the nanocomposite hydrogels exhibit controlled drug release, while the blank gel does not change release profile. Adapted from ref. [67]. ....	46
<b>Figure 1.12</b> - Electrical conductivity vs nanofiller content. Percolation has three phases: initially the concentration of the nanomaterial is not enough to form an interconnecting network and the conductivity remains low. As the concentration increases, electrons can hop through the nanofillers with tunnelling and the conductivity increases. When the concentration reaches the percolation threshold, a network is formed throughout the whole system and the conductivity reaches a high plateau. Adapted from ref. [113]. ....	49
<b>Figure 1.13</b> - Conductivity of gellan gum hydrogels with CNTs (circles) and without (squares), over decreasing water content. The loss of water content densifies the polymer network restricting ion mobility but simultaneously increases the nanomaterial volume fraction and leads to percolation. Adapted from ref. [123]. ....	54
<b>Figure 1.14</b> - Circuit diagrams of (A) two-point probe and (B) four-point probe method. ....	55
<b>Figure 1.15</b> - Double-pulsed, controlled potential chronoamperometry. A square wave voltage initially causes a current peak, due to polarisation. The current then exponentially decays to the conduction current. The removal of the voltage may cause a brief reversed current peak. ....	56

<b>Figure 1.16</b> - Impedance spectroscopy results can be visualised with a Nyquist plot. (A) Typical Nyquist plot of simple RC circuit with one resistor and one capacitor in parallel. (B) Typical Nyquist plot of resistance in series with the parallel combination of a capacitance with a resistance and a Warburg diffusion element (also known as Randles circuit). .....	57
<b>Figure 1.17</b> – Overview of experimental work and manuscript organization. The 1 <sup>st</sup> chapter introduces the key concepts, focusing on skin electroporation and electrically conductive hydrogels. The 2 <sup>nd</sup> chapter presents the experimental conditions and protocols followed. The 3 <sup>rd</sup> chapter concentrates on the nanocomposite hydrogels and studies their absorption capacity (Swelling Ratio, <i>SR</i> ) and electrical conductivity ( $\sigma$ ). In the 4 <sup>th</sup> chapter we measure the voltage, current and temperature of the drug delivery system during electroporation. The 5 <sup>th</sup> chapter describes a numerical model of the drug delivery system. The 6 <sup>th</sup> chapter contains fluorescent molecule delivery through skin electroporation. The 7 <sup>th</sup> chapter summarizes the most important findings.....	59
<b>Figure 2.1</b> - Preparation of nanocomposite hydrogels .....	61
<b>Figure 2.2</b> - Mold casting and dimensions of hydrogels .....	61
<b>Figure 2.3</b> – Prepared agarose hydrogels. (A) Fresh agarose hydrogels, (B) fresh nanocomposite hydrogel, (C) dry nanocomposite hydrogel, after 48 h at 30 °C, (D) swollen nanocomposite hydrogel, after 24 h in water. ...	62
<b>Figure 2.4</b> – Scheme of the custom-made freeze-casting configuration [150]......	63
<b>Figure 2.5</b> – Directional freeze-cast aerogels. Plain agarose (A) and nanocomposite (B) aerogel. ....	63
<b>Figure 2.6</b> – Preparation of alginate/chitosan nanocomposite hydrogels.....	65
<b>Figure 2.7</b> – Mold casting and dimensions of alginate/chitosan nanocomposite hydrogels.....	65
<b>Figure 2.8</b> – Current – time curve for the application of DC voltages from 0.5 to 1 V. The last 10 points of the curve were used to calculate the conduction current. ....	66
<b>Figure 2.9</b> – DC conductivity measurement setup. (A) The Keithley 2410 source-measuring unit. (B) the 4-point configuration and the custom-made measurement cell. (C) Scheme of DC conductivity measurement setup...	67
<b>Figure 2.10</b> – CNT conductivity in aqueous suspension setup. (A) Conductivity meter (B) Conductivity probe. .	68
<b>Figure 2.11</b> – Impedance spectroscopy setup. (A) Broadband dielectric spectrometer with measurement cell in place. (B) AC measurement cell constituents and closed (C) and open (D) position. ....	68
<b>Figure 2.12</b> – How to read the hydrogel naming convention: The hydrogel in the example was prepared with 2.5 % w/w agarose, 10 wt. % of polymer double-wall carbon nanotubes, 1 wt. % of polymer carboxymethyl cellulose, is in the swollen state (dried, then placed in an aqueous solution), was frozen before air-drying and contains has been swollen in an electroporation buffer solution. ....	70
<b>Figure 2.13</b> – Reconstructed human epidermis. From top to bottom we observe the stratum corneum (deep red), the keratinocyte layer (pink) and the polycarbonate membrane (white). Image by Geraldine Alberola (IPBS). ....	71
<b>Figure 2.14</b> – Drug delivery configuration for the two skin models. (A) mouse skin. (B) reconstructed human epidermis. ....	72
<b>Figure 2.15</b> - Scheme of connections for <i>in situ</i> electrical measurements. Two hydrogels were placed on top of the skin model and connected to the pulse generator. An oscilloscope measured the voltage and current during the pulsed electric fields (PEF) application. Before, and after the PEF, the system was connected to a source-measuring unit (SMU) that measured the DC resistance. A manual switch allowed the transition between generator and SMU. The fiber optic temperature sensor was placed under the skin, at the center. ....	73
<b>Figure 2.16</b> – Electroporation device setup. (A) The full device with cables to be connected to generator. (B) Cell for skin sample. (C) Wet gauze, skin sample and two hydrogels (D) Skin sample in cell with plastic cross (guide) and two stainless steel cylinders (top view). ....	73
<b>Figure 2.17</b> – Programmed (theoretical) applied electric pulses. 8 square unipolar pulses of 20 ms duration and frequency of 1 Hz. ....	74
<b>Figure 2.18</b> – Mouse skin sample on fluorescent microscope with green filter cube. The two circles with intense fluorescence correspond to the electroporated region.....	77
<b>Figure 3.1</b> – Agarose hydrogels with microbial colonies. (A) hydrogels stored in deionized water. (B) A heavily colonized agarose hydrogel, after months of storage. ....	81
<b>Figure 3.2</b> – Mass of agarose and nanocomposite (AGR-CNT <sub>10</sub> CMC <sub>1</sub> ) agarose hydrogels in fresh (A), dry (B) and swollen (C) state. n=9.....	82
<b>Figure 3.3</b> - Height of agarose and nanocomposite (AGR-CNT <sub>10</sub> CMC <sub>1</sub> ) agarose hydrogels in fresh (A), dry (B) and swollen (C) state. n=6-9. ....	82

<b>Figure 3.4</b> – Swollen agarose (transparent) and nanocomposite (black) hydrogels (A) and thickness gauge (B).	84
<b>Figure 3.5</b> – Thermogravimetric analysis of dry agarose hydrogel.	84
<b>Figure 3.6</b> – Impact of CNT concentration on the Swelling Ratio of nanocomposite hydrogels. (A) Hydrogels with 0, 1 and 10 wt. % of polymer mass (agarose 2.5 % w/w). (B) Control experiment to monitor possible influence of the CNT dispersant used (carboxymethyl cellulose, CMC) on the swelling ratio.	86
<b>Figure 3.7</b> – Impact of processing method on swelling ratio. White: plain agarose hydrogels, AGR. Dark grey: nanocomposite agarose hydrogels (CNT 10 wt. % of polymer), AGR-CNT <sub>10</sub> CMC <sub>1</sub> . n=3-10.	87
<b>Figure 3.8</b> – Nanocomposite hydrogels after different processing methods. (A) Fresh hydrogel, (B) Air-dried hydrogel, (C) Air-dried, then swollen hydrogel, (D) Froze, air-dried and then swollen hydrogel, (E) lyophilized hydrogel.	88
<b>Figure 3.9</b> – Growth of ice crystals in freeze-casting. Adapted from [162].	89
<b>Figure 3.10</b> – SEM observations of macropores in directional freeze-cast nanocomposite hydrogel.	89
<b>Figure 3.11</b> – Macropore size distribution in directional freeze-cast nanocomposite hydrogel.	90
<b>Figure 3.12</b> – SEM observations of CNT bundles in directional freeze-cast nanocomposite hydrogel.	90
<b>Figure 3.13</b> – Swelling ratio of agarose and nanocomposite hydrogels over 9 dry / swell cycles. (A) Absolute values. (B) Percentage change of swelling ratio (compared to baseline).	91
<b>Figure 3.14</b> – Swelling ratio of alginate/chitosan hydrogels, compared to agarose hydrogels.	92
<b>Figure 3.15</b> – Drying kinetics of fresh agarose hydrogels at 50 °C (blue circles) and 70 °C (grey circles). n=2.	93
<b>Figure 3.16</b> – Mass and height variation of plain agarose (AGR) and nanocomposite hydrogels (AGR-CNT <sub>10</sub> CMC <sub>1</sub> ) during drying at 70 °C. (A) Mass variation of agarose (AGR, white circles) and nanocomposite (AGR-CNT <sub>10</sub> CMC <sub>1</sub> , black squares) hydrogels at 70 °C. n=2. (B) Height variation of agarose (white circles) and nanocomposite (black squares) hydrogels at 70 °C. n=1.	93
<b>Figure 3.17</b> – Water absorption over time for agarose and nanocomposite hydrogels. n=1 up to 700 s; n=10 for 24 h SR. (A) Swelling ratio. (B) Percentage of current swelling ratio over 24 h swelling ratio (SR <sub>t</sub> ).	94
<b>Figure 3.18</b> – Water release and swelling of nanocomposite directional freeze-cast hydrogel (AGR-CNT <sub>10</sub> CMC <sub>1</sub> _S_dir). The water-loaded hydrogel releases the water quasi-instantaneously, on contact with a humidified paper towel (A, B). The same hydrogel then rapidly (< 2 s) swells with water the moment it is submerged in an aqueous solution (C, D).	95
<b>Figure 3.19</b> – Mechanical properties of alginate/chitosan hydrogels. Compression module of alginate/chitosan hydrogels with increasing CNT concentration compared to compression modules of nanocomposite agarose and hydrogels. n=3.	96
<b>Figure 3.20</b> – Conductivity and electrical percolation of CNTs in aqueous suspension. Conductivity of double-wall CNTs (black squares, n=2) and oxidized double-wall CNTs (red circles, n=1).	97
<b>Figure 3.21</b> – Impact of CNT concentration on hydrogel electrical conductivity. Electrical conductivity of fresh (A, n=3-4) and swollen (B, n=3-4) agarose hydrogels with increasing CNT concentration.	99
<b>Figure 3.22</b> – SEM observations of dry nanocomposite hydrogel (AGR-CNT <sub>1</sub> ) and proposed parallel alignment of CNTs and polymer chains during drying. Adapted from ref. [153].	101
<b>Figure 3.23</b> – Impact of carboxymethyl cellulose (CMC, red border on graph) and polydopamine (pDA, green border on graph) on the dispersion and electrical conductivity of CNTs in fresh (A) and swollen (B) agarose nanocomposite hydrogels. The legend is common for both graphs.	103
<b>Figure 3.24</b> – Impact of dispersants alone (without CNTs) on the electrical conductivity of fresh (A) and swollen (B) agarose hydrogels.	104
<b>Figure 3.27</b> – Impact of different CNT types on the electrical conductivity of fresh agarose nanocomposite hydrogels.	105
<b>Figure 3.28</b> – Impact of ionic solutions (electroporation buffer and phosphate buffer) on the electrical conductivity of fresh (A) and swollen (B) agarose hydrogels.	106
<b>Figure 3.29</b> – Comparison of electrical conductivities of fresh agarose hydrogels prepared with deionized water, prepared with DI water and then immersed in phosphate buffer and prepared with phosphate buffer.	107
<b>Figure 3.30</b> – Impact of processing methods (air-drying, freezing, directional freeze-casting) on the electrical conductivities of swollen agarose hydrogels.	108
<b>Figure 3.31</b> – Comparison of electrical conductivities of nanocomposite hydrogels with different hydrophilic polymers (agarose and alginate/chitosan) in their fresh (A) and swollen (B) state.	109

<b>Figure 3.32</b> – Impact of other factors on the electrical conductivities of fresh agarose hydrogels. (A) Temperature. (B) Agarose polymer concentration. (C) hydrogels after slicing off outer layers. ....	111
<b>Figure 3.33</b> – Impedance spectroscopy graphs of fresh agarose (white circles, n=3) and nanocomposite (black squares, n=4) hydrogels, at 0.6 V <sub>rms</sub> . (A) Absolute impedance over frequency. (B) Phase angle over frequency. ....	114
<b>Figure 3.34</b> – Nyquist plots of fresh agarose (white circles and blue lines) and nanocomposite (grey squares) hydrogels, at 0.6 V <sub>rms</sub> , representing the real (Z') and the negative of the imaginative (-Z'') part of the impedance, over a frequency range from 10 <sup>6</sup> to 0.1 Hz. ....	115
<b>Figure 3.35</b> - Impedance spectroscopy graphs of fresh agarose hydrogels, at increasing voltages, from 0.6 to 12 V <sub>rms</sub> . n=3. (A) Absolute impedance vs. frequency. (B) Phase angle vs. frequency. ....	116
<b>Figure 3.36</b> - Impedance spectroscopy graphs of fresh nanocomposite hydrogels, at increasing voltages, from 0.6 to 12 V <sub>rms</sub> . n=4. (A) Absolute impedance vs. frequency. (B) Phase angle vs. frequency. ....	116
<b>Figure 3.37</b> – DC Electrical conductivity of mouse skin section, directly after excising and up to 16 h later. ....	118
<b>Figure 3.38</b> – Impedance spectroscopy graphs of excised mouse skin section, at 0.6 V <sub>rms</sub> . n=6. (A) Absolute impedance and relative permittivity over frequency. (B) Phase angle over frequency. ....	119
<b>Figure 3.39</b> – Chemical structures of agarose, alginate and chitosan hydrophilic biopolymers. ....	120
<b>Figure 3.40</b> - Nanocomposite hydrogel electrical conductivity vs. nanomaterial concentration. A nanomaterial concentration of 0 represents the electrical conductivity of the plain hydrogels (without conductive nanomaterials). GRM: Graphene-related materials; OPF: oligo(poly(ethylene glycol) fumarate); PAM: polyacrylamide; PEG: polyethylene glycol; PU: polyurethane. Adapted from ref. [171]. ....	122
<b>Figure 4.1</b> - Voltage, current and instantaneous resistance (u/i) of drug delivery setup during Pulsed Electric Fields (PEF) of voltages from 50 to 300 V. Shaded areas represent SEM. (50V,200V: n=3; 100V: n=5; 300V: n=12). ....	125
<b>Figure 4.2</b> - Voltage and current of the drug delivery setup without mouse skin (only hydrogels and gauze). n=3. Shaded areas represent SEM. ....	126
<b>Figure 4.3</b> - I-V curve of the system, demonstrating nonlinear behavior. n=2-18. Error bars represent SEM. ..	127
<b>Figure 4.4</b> - Voltage, current and instantaneous resistance (u/i) of drug delivery setup during Pulsed Electric Fields (PEF) of 30 V. ....	128
<b>Figure 4.5</b> - Instantaneous resistance (r=u/i) of drug delivery setup with skin and hydrogels only (black dots, n=12) and with skin, hydrogels and conductive gel between them (green dots, n=3), for 300 V PEF. Shaded areas represent SEM. ....	129
<b>Figure 4.6</b> - Electric current resulting from the application of 1V DC to the drug delivery system, before and after PEF (n=2-11). Yellow shaded area corresponds to PEF application. Shaded areas represent SEM. ....	130
<b>Figure 4.7</b> - Electric current resulting from the application of 1V DC, before and after PEF at 300 V. ....	130
<b>Figure 4.8</b> - Instantaneous resistance of <i>ex vivo</i> drug delivery system at 100 V, for a series of PEF applications (n=3-4). In black color, the baseline; in dark red, the instantaneous resistance of the skin after low-voltage PEF (up to 150 V); in purple, the instantaneous resistance of the skin, after a series of high-voltage PEF (up to 400 V). Shaded areas represent SEM. ....	131
<b>Figure 4.9</b> - Temperature increase of the skin during PEF application (n=3-9). Yellow shaded area corresponds to PEF application. Shaded areas represent SEM. ....	132
<b>Figure 4.10</b> - Voltage, current and instantaneous resistance (u/i) of drug delivery setup on reconstructed human epidermis, during Pulsed Electric Fields (PEF) of 300 V. Shaded areas represent SEM. n=3. ....	134
<b>Figure 5.1</b> – Geometry of 2D numerical simulation and mesh detail. ....	138
<b>Figure 5.2</b> – Electric field distribution in the skin for different hydrogel conductivities and zoom on first skin layers for 300 V pulse. (SC: Stratum Corneum, ED: Epidermis, D: Dermis). ....	139
<b>Figure 5.3</b> – Electric potential and current density on drug delivery system for 300 V and $\sigma_{hydrogel} = 10^{-4}$ S/m. Black arrows represent current density. ....	140
<b>Figure 5.4</b> – Electric potential and current density with varying gauze conductivities, for 300 V pulse and $\sigma_{hydrogel} = 0.15$ S/m. (A) $\sigma_{gauze} = 0.15$ S/m. (B) $\sigma_{gauze} = 1.5$ S/m. Black arrows represent current density. ....	140
<b>Figure 5.5</b> – The 3D drug delivery system in COMSOL (cascade layers preview, colorized). ....	141
<b>Figure 5.6</b> – Electric potential and current density (black arrows) on mouse skin model, at 300 V. ....	142
<b>Figure 5.7</b> – Electric field distribution at mouse skin model for 300 V PEF. Top: XZ slice. Bottom: Electric field at epidermis under SC. ....	142

<b>Figure 5.8</b> – Stratum Corneum (SC) nonlinear electrical conductivity. (A) The interpolated curve used for the relation between SC conductivity and the electric field, $\sigma_{sc}(E)$ . (B) the conductivity of the SC for applied PEFs from 50 to 300 V. ....	144
<b>Figure 5.9</b> - Average resistance of the <i>ex vivo</i> system for applied PEF voltages from 50 to 300 V, compared with the results of the numerical model. ....	145
<b>Figure 5.10</b> – XZ slices of electric field distribution in the skin for PEFs of 50 to 300 V. ....	145
<b>Figure 5.11</b> – Electric field distribution on surface of viable skin layers (Epidermis under SC). (A) Electric field distribution for PEFs from 50 to 300 V. (B) XY view (top view) of viable skin surface with $E > 400$ V/cm for PEFs from 100 to 300 V. ....	146
<b>Figure 5.12</b> - Electric field distribution on surface of viable skin layers (Epidermis under SC) at 400 V PEF. (A) Region over reversible electroporation threshold. (B) Region over irreversible electroporation threshold. ....	147
<b>Figure 5.13</b> – XZ slices of voltage (colored) and current density (black arrows) for PEFs of 50 V (A) and 300 V (B). Left: Full view (hydrogels, skin layers, gauze). Right: Zoom on first skin layers. ....	147
<b>Figure 6.1</b> – Fluorophore release from hydrogels after PEF application. The dotted line corresponds to relative fluorescence intensity of 1, meaning the same fluorescence as an area of the image without fluorophores. ...	151
<b>Figure 6.2</b> – Lucifer Yellow fluorescent marking on skin model (top view, 300 V and 0 V) and quantification of relative fluorescence intensity under negative and positive electrodes, for PEF from 0 to 300 V. n=2-16. Statistical treatment: one-way ANOVA and Dunnett’s T3 post-hoc test. Codes signification: * = $p \leq 0.05$ ; ** = $p \leq 0.01$ ; *** = $p \leq 0.001$ ; no symbol or ns = not significant difference ( $p > 0.05$ ). Means are compared to control (0), unless brackets indicate otherwise. ....	153
<b>Figure 6.3</b> – Propidium Iodide fluorescent marking on skin model (top view, 300 V and 0 V) and quantification of relative fluorescence intensity under negative and positive electrodes, for PEF from 0 to 300 V. n=2-20. Statistical treatment: one-way ANOVA and Dunnett’s T3 post-hoc test. Codes signification: * = $p \leq 0.05$ ; ** = $p \leq 0.01$ ; *** = $p \leq 0.001$ ; no symbol or ns = not significant difference ( $p > 0.05$ ). Means are compared to control (0), unless brackets indicate otherwise. ....	154
<b>Figure 6.4</b> - Fluorescein isothiocyanate–dextran marking on skin model (top view, 300 V and 0 V) and quantification of relative fluorescence intensity under negative and positive electrodes, for control (0 V) and 300 V PEF. n=3-4. Statistical treatment: one-way ANOVA and Dunnett’s post-hoc test. Codes signification: * = $p \leq 0.05$ ; ** = $p \leq 0.01$ ; *** = $p \leq 0.001$ ; no symbol or ns = not significant difference ( $p > 0.05$ ). Means are compared to control (0), unless brackets indicate otherwise. ....	155
<b>Figure 6.5</b> - Details of fluorescence microscopy images on skin model after PEF at 300 V. (A) Lucifer Yellow (LY) under negative electrode with optical zoom of 1.25x (left) and 3.2x (right); (B) LY under positive electrode with optical zoom of 1.25x (left) and 9.2x (right); (C) Propidium Iodide (PI) under positive electrode with optical zoom of 1.25x (left) and 9.2x (right); (D) Fluorescein isothiocyanate–dextran under negative electrode with optical zoom of 1.25x (left) and 9.2x (right). ....	156
<b>Figure 6.6</b> – Fluorescent molecule delivery on reconstructed human epidermis samples. ....	157
<b>Figure 6.7</b> – Local transport regions (LTR) and cell membrane permeabilization in skin. (A) Scheme of skin electroporation with electrode-reservoir hydrogel. (B) At PEF voltages lower than 100 V, conductive pathways were formed, increasing ionic mobility. (C) Starting at 100 V PEF, the creation of LTRs in the extracellular lipids of the stratum corneum, allowed the diffusion of fluorophores through the skin. (D) At 300 V PEF, the cell membranes of nucleated cells of the epidermis and/or dermis were permeabilized and fluorophores entered the cytoplasm. ....	159
<b>Figure 6.8</b> – Histological observations of fluorescent molecule delivery and penetration depth into mouse skin models. (A) Propidium Iodide (PI) reached permeabilized cells in the epidermis. (B) Lucifer Yellow (LY) reached all the way into the dermis. (C) Fluorescein isothiocyanate-dextran (FD4) was located in the stratum corneum and the outermost epidermis layers. Adapted from [47]. ....	161
<b>Figure 7.1 (printed version)</b> – Summary of experimental results on transdermal drug delivery, for applied PEFs of 50 to 300 V (8 pulses, 20 ms duration, 1 Hz). <b>In situ measurements.</b> Average resistance (U/I) during last pulse, DC current change after PEF, Temperature increase (max) during PEF. <b>Numerical model.</b> Electric field distribution on the skin, through validated, nonlinear model. XZ slices of first skin layers and areas where $E > 400$ V/cm (approximate threshold value for cell permeabilization in tissue) on viable skin layers. <b>Drug delivery.</b> Fluorescent marking of lucifer yellow (LY) and propidium iodide (PI) on skin, after PEF. <b>Discussion.</b> Proposed	



mechanisms for each voltage: creation of conductive pathways, formation of local transport regions and cell permeabilization. ....	165
<b>Figure 7.2 (screen version)</b> – Summary of experimental results on transdermal drug delivery, for applied PEFs of 50 to 300 V (8 pulses, 20 ms duration, 1 Hz). ....	166
<b>Figure 9.1</b> – I – V measurements of drug delivery system without skin model, at 150 V PEF. (A) Hydrogels and wet gauze. (B) Wet gauze only. ....	181

## Table of tables

<b>Table 2.1</b> – Nanocomposite hydrogels composition.....	61
<b>Table 2.2</b> – Summary of processing and drying methods. ....	63
<b>Table 2.3</b> – Naming conventions for prepared hydrogels.....	70
<b>Table 2.4</b> - Fluorescent molecules loaded into drug delivery hydrogels. ....	76
<b>Table 3.1</b> – Mass concentrations of fresh agarose hydrogel. ....	83
<b>Table 3.2</b> – Mass concentrations of fresh nanocomposite agarose hydrogel. ....	83
<b>Table 3.3</b> – Constituents and electrical conductivities of solvents used. ....	106
<b>Table 5.2</b> – Electric field distribution for different hydrogel conductivities ....	138
<b>Table 5.5</b> – Voltage drop in different components of the system for PEF of 50 and 300 V. ....	148

# 1 Introduction

<b>1</b>	<b>INTRODUCTION.....</b>	<b>32</b>
1.1	NON-INVASIVE, TRANSDERMAL DRUG DELIVERY .....	32
1.2	SKIN ANATOMY .....	33
1.3	SKIN BARRIER PROPERTIES .....	34
1.4	METHODS FOR NON-INVASIVE, TRANSDERMAL DRUG DELIVERY .....	35
1.5	ELECTROPORATION .....	36
1.5.1	<i>Lipid bilayer electroporation</i> .....	37
1.5.2	<i>Modeling cell membrane electroporation</i> .....	37
1.5.3	<i>Tissue electroporation</i> .....	39
1.5.4	<i>Skin electroporation</i> .....	40
1.6	HYDROGELS FOR DRUG DELIVERY .....	43
1.7	HYDROGELS.....	43
1.8	ELECTRICALLY CONDUCTIVE HYDROGELS FOR DRUG DELIVERY .....	45
1.9	CARBON-BASED NANOMATERIALS .....	47
1.9.1	<i>Carbon nanotubes</i> .....	47
1.10	ELECTRICAL PERCOLATION .....	48
1.10.1	<i>Percolation theory</i> .....	48
1.10.2	<i>Critical path approximation</i> .....	50
1.10.3	<i>Percolation of carbon nanotubes</i> .....	50
1.10.4	<i>Electrical percolation studies in hydrogels</i> .....	51
1.11	DISPERSION OF CONDUCTIVE NANOMATERIALS .....	51
1.12	ELECTRICAL CONDUCTIVITY AND CONDUCTION MECHANISMS .....	52
1.12.1	<i>Conductivity</i> .....	52
1.12.2	<i>Conduction mechanisms in dielectric materials under high electric fields</i> .....	52
1.12.3	<i>Ionic conduction</i> .....	52
1.12.4	<i>Electric current</i> .....	53
1.12.5	<i>Hydrogel water content and electrical conductivity</i> .....	53
1.13	MEASURING ELECTRICAL PROPERTIES .....	54
1.13.1	<i>Two-point and four-point probe methods</i> .....	55
1.13.2	<i>Alternating Current</i> .....	57
1.14	OVERVIEW .....	58

## 1.1 Non-invasive, transdermal drug delivery

The skin represents an accessible and convenient route for non-invasive drug delivery. Medicine administered through the skin avoids the first-pass metabolism and the gastrointestinal tract [27]. Transdermal delivery platforms, such as nicotine patches, can effectively administer drugs through the epidermis in a controlled manner. Advantages include increased bioavailability, sustained steady-state blood concentration levels, painless self-administration and reduced frequency of dosing, which in turn improve patient compliance and quality of life [5]. However, the skin, and more specifically its outermost layer, the stratum corneum (SC), acts as a barrier protecting the organism from the penetration of exogenous substances and microbes and limiting water loss. Passive diffusion of drugs through the skin is only achieved for low molecular weight ( $MW < 400-500$  Da), relatively lipophilic molecules ( $\log P$  around 2 to 3) [28]. Several chemical and physical methods are being developed, allowing bigger and/or hydrophilic molecules to cross the skin barrier. Among these, skin electroporation consists of applying electric field pulses with high voltage (50 to 3000 V) and short

duration (5  $\mu$ s to 100 ms) on the surface of the skin, permeabilizing the SC in a non-invasive and temporary manner [20], [29], [30].

## 1.2 Skin anatomy

In humans (and most mammals), the skin can be divided into three layers: the epidermis, the dermis and the hypodermis (**Figure 1.1**). The epidermis is a stratified epithelium consisting mainly of keratinocytes. These proliferate in the basal layer of the epidermis and progressively migrate outwards while terminally differentiating, forming the spinous layer, the granular layer and the stratum corneum (SC, or cornified layer). The keratinocytes of the SC are 15-20 layers of flattened, dead cells with a cornified envelope replacing their plasma membrane, and they form the layer responsible for the barrier function of the skin. The cells of the epidermis are constantly renewed in a dynamic equilibrium between desquamation of the outermost cornified cells and proliferation of cells in the basal layer [31]. The cornified envelope is a structure consisting of insoluble proteins, mostly keratin and filaggrin. The extracellular space in the SC is occupied by lipids (ceramides, fatty acids, cholesterol and cholesterol esters) that are attached to the cornified envelope and are largely organized in stacks of lipid bilayers [3], [31]. A common, simplified metaphor for the SC is the brick and mortar structure, where keratinocytes are the bricks and lipids in the extracellular space are the mortar (**Figure 1.2**). Other cells in the epidermis include melanocytes, Langerhans' cells and Merkel cells [32].

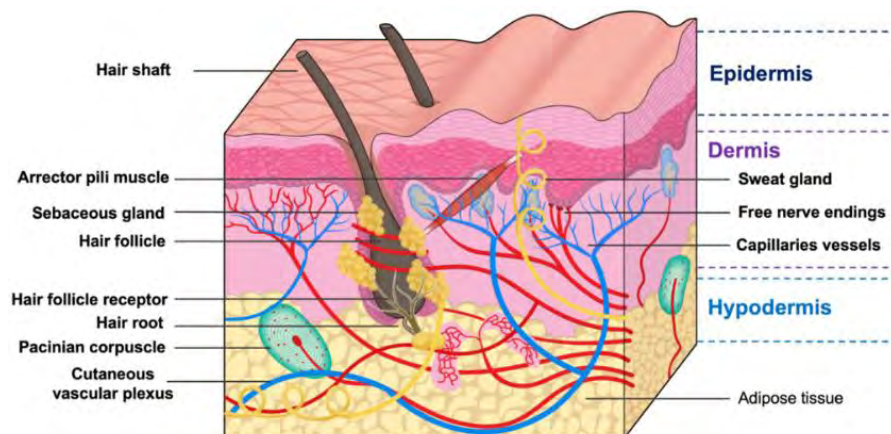


**Figure 1.1** - Schematic illustration of skin's anatomy [33]

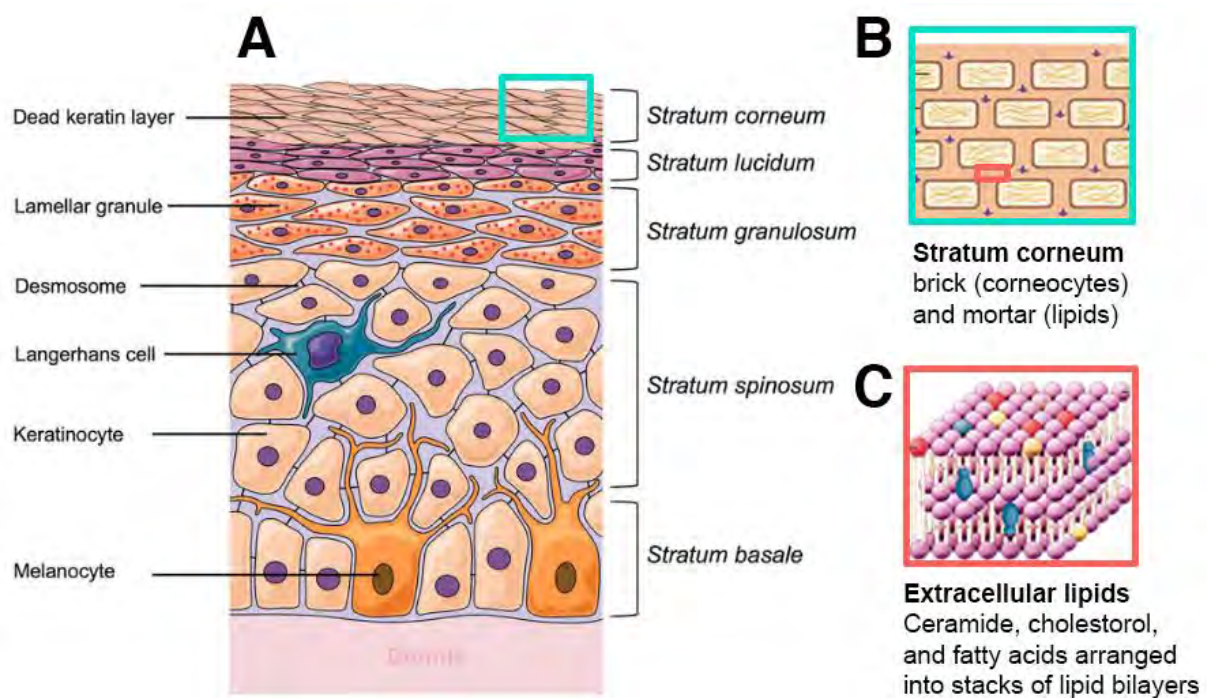


**Figure 1.2** - Scheme of human epidermis and stratum corneum. (A) layers and constituents of the epidermis. (B) Stratum corneum “brick and mortar” configuration. (C) Extracellular lipids stacked into lipid bilayer (“mortar”). Adapted from refs. [33] and [34].

The epidermis is connected to the dermis through the basement membrane, which serves as an anchor point for the cells of the epidermis, a barrier and a filter [32]. The dermis is a layer of connective tissue with high water content that provides nutrients to the epidermis and protects the organism against mechanical injury. It consists of a supporting matrix of polysaccharides and proteins [32]. The main protein constituent of the dermis is collagen, responsible for the high tensile strength, and secondly elastin, that provides elasticity to the tissue. On a cellular level, the most abundant cell type are fibroblasts, which produce the extracellular matrix components. Other cells include macrophages, mast cells and lymphocytes [32]. The dermis has a rich blood supply, provided by a highly branched network of blood vessels. The blood vessels in the dermis provide nutrients and oxygen to cells and play a role in regulating body temperature, by dilating or constricting. Both the dermis and the epidermis are also traversed by skin appendages, notably hair follicles, sebaceous glands and eccrine glands [35].

The subcutaneous tissue (or hypodermis) is located below the dermis. It is composed of loose connective tissue, including collagen and elastin fibres, as well as adipose tissue. Its main functions are temperature insulation, energy storage and further protection of organs from shock. The hypodermis is also vascularized and the blood vessels are generally larger than those found in the dermis. The cell constituents of the hypodermis are adipocytes, fibroblasts and immune cells [35].

### 1.3 Skin barrier properties

The epidermis acts as a physical barrier between the organism and the environment, limiting both inward and outward flows. This function protects the organism from the penetration of exogenous substances and pathogens, while maintaining the high water content of the interior layers by limiting

transepidermal water loss [36]. This function is ensured by the brick and mortar configuration and the physical properties of the SC, specifically the hydrophilic corneocytes composed mostly of keratin and the extracellular lipids (ceramides, cholesterol and fatty acids) arranged into stacks of lipid bilayers between them. The water content of the SC is very low, at *ca.* 15 % w/w [37].

In the case of transdermal drug delivery, three pathways through the epidermis are possible: (1) the intercellular (or paracellular) pathway, a tortuous pathway through the extracellular lipids of the SC; (2) the transcellular (or intracellular) pathway, a more direct pathway through the corneocytes (implies permeabilization of their cornified envelopes), and (3) the transappendageal pathway, following the hair follicles or the sweat ducts of the SC [4], [22] (**Figure 1.3**). Passive diffusion through the epidermis is only possible for molecules with adequate physicochemical properties (relatively lipophilic and small size) and takes place with very slow kinetics [28], [36]. It is generally accepted that small lipophilic molecules follow the intercellular pathways, through the lipids, while small hydrophilic molecules would follow the transcellular route, through the hydrated interior of the corneocytes [37]. The delivery of hydrophilic drugs poses a particular problem, due to the lipidic nature and low water content of the SC. Examples of hydrophilic therapeutic molecules are peptides (such as insulin), DNA or small-interfering RNA [38].

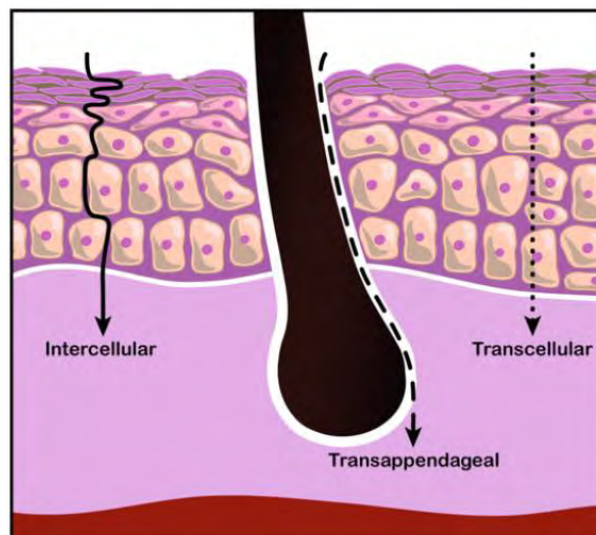


**Figure 1.3** – Schematic representation of possible pathways through the epidermis [36].

#### 1.4 Methods for non-invasive, transdermal drug delivery

Non-invasive transdermal drug delivery presents many advantages, while conventional drug delivery, such as oral administration and injections have some important limitations. Therefore, numerous research groups are working on methods for overcoming the skin barrier in a safe, effective and reversible manner. These methods can be classified according to their mechanism of action, into physical and chemical, or according to their chronology into 1<sup>st</sup>, 2<sup>nd</sup> and 3<sup>rd</sup> generation [39], [40].

Some representative examples of transdermal drug delivery without needles can be seen in **Figure 1.4**. These include injection techniques (jet injection and powder injection), microporation techniques (different types of microneedles and thermal microporation), Local Transport Region (LTR) techniques (electroporation and sonoporation), disruptive approaches (waxing and tape stripping) as well as passive approaches (hydrogels, liposomal formulations).



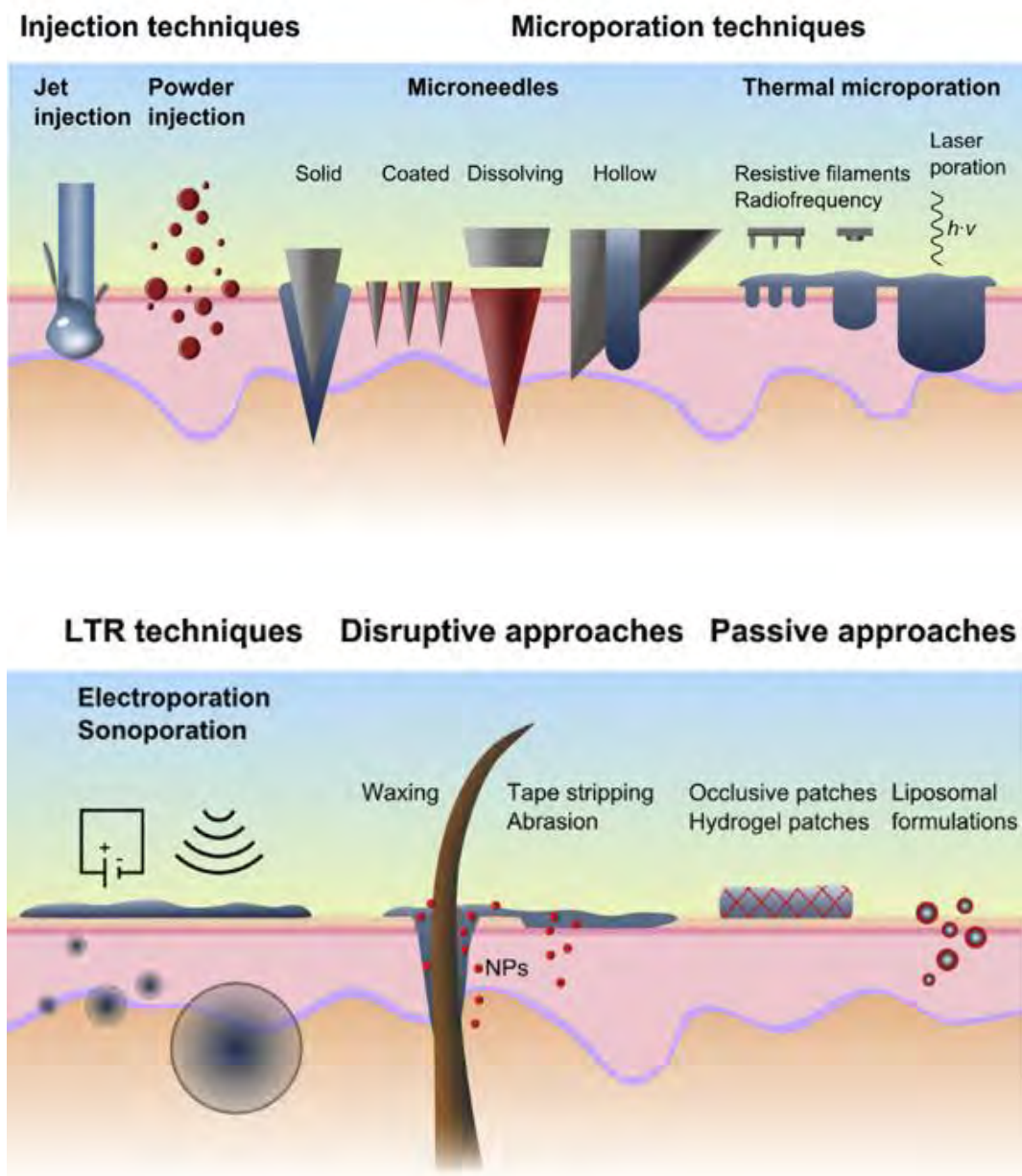


**Figure 1.4** – Transdermal drug delivery methods. Adapted from refs. [41], [42].

### 1.5 Electroporation

Electroporation is a bioelectrical phenomenon where a lipid bilayer is permeabilized through the application of an external electric field [1], [2]. Depending on the parameters of the electric field (strength, duration, waveform, number and frequency of repetitions in the case of PEF) and the electrode configuration, the permeabilization may be transient (reversible EP) or permanent (irreversible EP). Reversible electroporation has found numerous applications most notably in biotechnology, for inserting genes into cells (gene electro-transfer) [43] and for fusing cells (electrofusion) *in vitro* [44]; in medical applications for cancer treatment, through the uptake of membrane-impermeant drugs into cancer cells [45]; and in drug delivery through the needle-free

transport of molecules across the epidermis [5] or drug and nucleic acid administration through injection of the agents (drugs, vaccines) into tissue, followed by PEF application [46], [47].

### 1.5.1 Lipid bilayer electroporation

The critical parameter in lipid bilayer electroporation is the electric potential difference across the bilayer. The application of an external electric field charges the bilayer, which has dielectric properties, up to a critical threshold, when electroporation is observed. For plasma membranes, this threshold is experimentally calculated to be approximately 250 mV, in eukaryotic cells [15]. Electroporation is observed through the loss of the barrier properties of the bilayer (transport of water and solutes through it) and a rapid potential decrease across it. While the exact mechanism of electroporation at the molecular level is not fully elucidated, it is proposed that it may be caused by structural rearrangement of the lipids, forming aqueous pores, electrically-induced chemical modifications of the lipid chains, electrical breakdown of membrane proteins (in the case of plasma membranes) or a combination of these [2] (**Figure 1.5**). Molecular dynamics simulations of lipid bilayers under strong electric fields have pointed out towards the formation of short-lived aqueous pores [16]. The lipid bilayer is a dynamic structure, thus electrically induced changes should also be viewed as dynamic, rather than stable and targeted. The pulsed electric fields may not necessarily create pores in the structure but cause a more general loss of cohesion of the dynamic structure, allowing molecules to crawl their way through the bilayer [48].

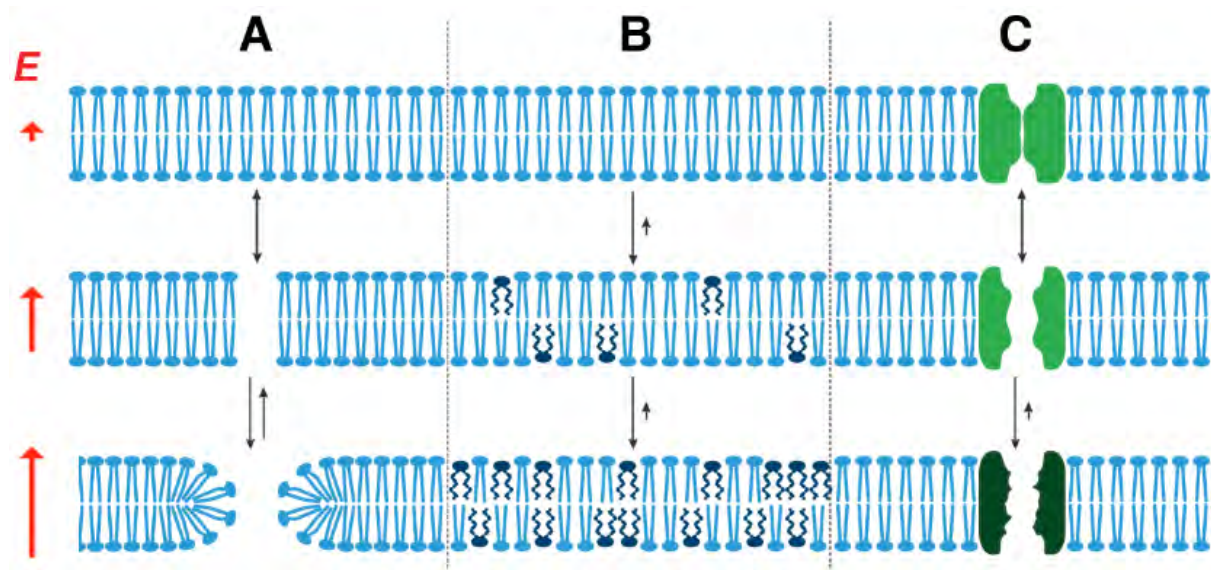


**Figure 1.5** - Proposed molecular mechanisms of electrically induced permeabilization of lipid bilayers, for increasing electric field,  $E$ . (A) Formation of aqueous pores, (B) chemical changes of the phospholipid tails, (C) channels through membrane proteins. Adapted from [49].

### 1.5.2 Modeling cell membrane electroporation

Electric fields induce a position-dependent change in the transmembrane potential difference,  $\Delta\psi$ , of the plasma membrane [50]. The transmembrane potential can be derived from the solution of the partial differential equation [51]

$$\nabla \left[ \left( \lambda + \varepsilon \frac{\partial}{\partial t} \right) \cdot \nabla \psi(x, y, z, t) \right] = 0 \quad (1.1)$$



where  $\lambda$  is the conductivity,  $\varepsilon$  the dielectric permittivity and  $\Psi$  the electric potential of a point in space  $(x,y,z)$  and time  $(t)$ .

For steady state conditions, the time derivative is zero and we get the Laplace equation

$$\nabla \cdot \nabla \Psi(x, y, z) = 0 \quad (1.2)$$

This equation can be easily solved for simple geometries. We will assume that the cells are perfect spheres. For a single cell, in steady state we get

$$\Delta \Psi_i = \frac{3}{2} \cdot g(\lambda) \cdot r \cdot E \cdot \cos\theta \quad (1.3)$$

where  $\Delta \Psi_i = \Psi_{in} - \Psi_{out}$  is the induced potential difference, caused by the electric field  $E$ .  $g(\lambda)$  is a factor that depends on the conductivities and morphological characteristics of the system,  $r$  the radius of the cell and  $\theta$  the angle between the normal to the membrane, in a given position, and the electric field  $E$ .

These steady state conditions are established on a very short time-scale after the onset of the electric field (on the range of 100 ns to 1 $\mu$ s [52]). To take into account the membrane charging time we use the equation

$$\Delta \Psi_i = \frac{3}{2} \cdot g(\lambda) \cdot r \cdot E \cdot \cos\theta \cdot (1 - e^{-\frac{t}{\tau_m}}) \quad (1.4)$$

where  $t$  is the time after the onset of the field and  $\tau_m$  is the time constant of the membrane charging.

The time constant of the membrane charging,  $\tau_m$  and the factor  $g(\lambda)$  depend on the electrical and morphological characteristics of the system, with the cell viewed as a spherical capacitor[48], [51], [53].

$$\tau_m = \frac{r \cdot \varepsilon_m}{2d \frac{\lambda_i \lambda_o}{\lambda_i + 2\lambda_o} + r \cdot \lambda_m} \quad (1.5)$$

$$g(\lambda) = \frac{\lambda_o \lambda_i \cdot 2 \frac{d}{r}}{(2\lambda_o + \lambda_i)\lambda_m + 2 \frac{d}{r} (\lambda_o - \lambda_m)(\lambda_i - \lambda_m)} \quad (1.6)$$

with  $r$  denoting the cell radius,  $\varepsilon_m$  the plasma membrane's dielectric permittivity,  $d$  the membrane thickness,  $\lambda_i$  the conductivity of the inside environment of the membrane (the cytoplasm),  $\lambda_o$  the conductivity of the outside environment (the extracellular medium, in our case the ZAP buffer) and  $\lambda_m$  the conductivity of the membrane.

The field-induced potential difference  $\Delta \Psi_i$  is added to the resting transmembrane potential  $\Delta \Psi_o$  [50].

$$\Delta \Psi = \Psi_i + \Psi_o \quad (1.7)$$

Permeabilization of the cell occurs after the transmembrane potential difference,  $\Delta \Psi$ , reaches a critical value,  $\Delta \Psi_{crit}$  [54].  $\Delta \Psi$  is position-dependent, because it varies according to the angle of the normal to the membrane and the electric field (**Figure 1.6**).

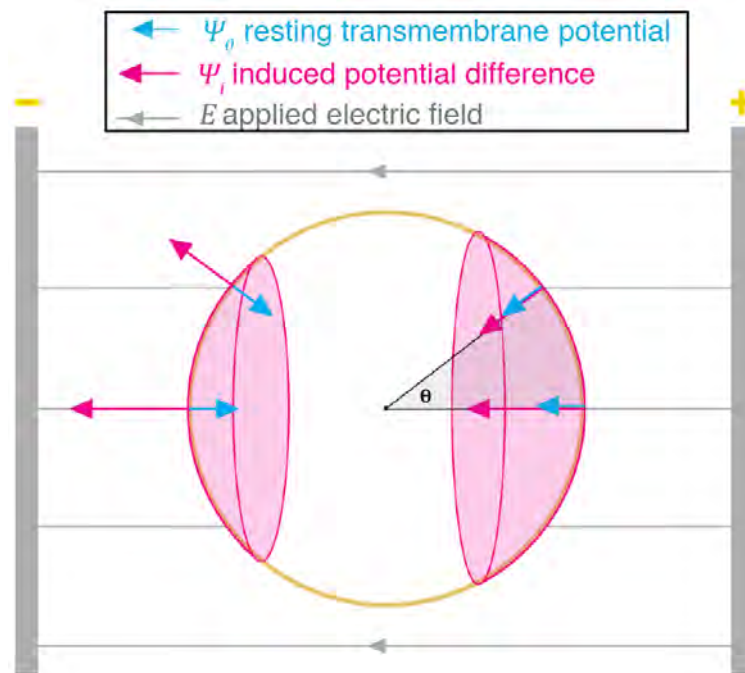


**Figure 1.6** – Transmembrane potential on cell under the influence of electric field.

### 1.5.3 Tissue electroporation

Tissue electroporation refers to the application of a PEF on the tissue level, in order to permeabilize multiple cells (reversible) or for non-thermal tissue ablation (irreversible). The reversible permeabilization of multiple cells is of particular interest in the context of inserting therapeutic molecules into cells. One application is gene therapy and DNA vaccination, through the injection of the therapeutic agent followed by tissue electroporation for the permeabilization of the cell membranes [55]. Another application of reversible tissue electroporation is for the treatment of cancer: cytotoxic agents, like bleomycin, are injected into a tumor followed by tissue electroporation for the insertion of the drug into the cells [45]. Alternatively, tumors can be treated with irreversible tissue electroporation, localized in the affected region [56]. A more recent application of irreversible tissue electroporation involves the non-thermal cardiac ablation for the treatment of cardiac arrhythmias [57].

For the purposes of understanding tissue electroporation, the tissue is typically modeled as a space with different densities and sizes of spherical cells surrounded by extracellular medium [58]. With the application of an external electric field, the transmembrane potentials of the cells increase in value. When the transmembrane potentials exceed a threshold value, the plasma membranes become permeabilized. The plasma membranes of permeabilized cells allow the passage of hydrophilic entities and have an increased electrical conductivity (**Figure 1.7**). The minimum electric field strength that leads to the permeabilization of plasma membranes in tissue is in the range of 300 to 700 V/cm. Starting at *ca.* 1200 V/cm and over, the permeabilization may be irreversible, leading to cell death [17].

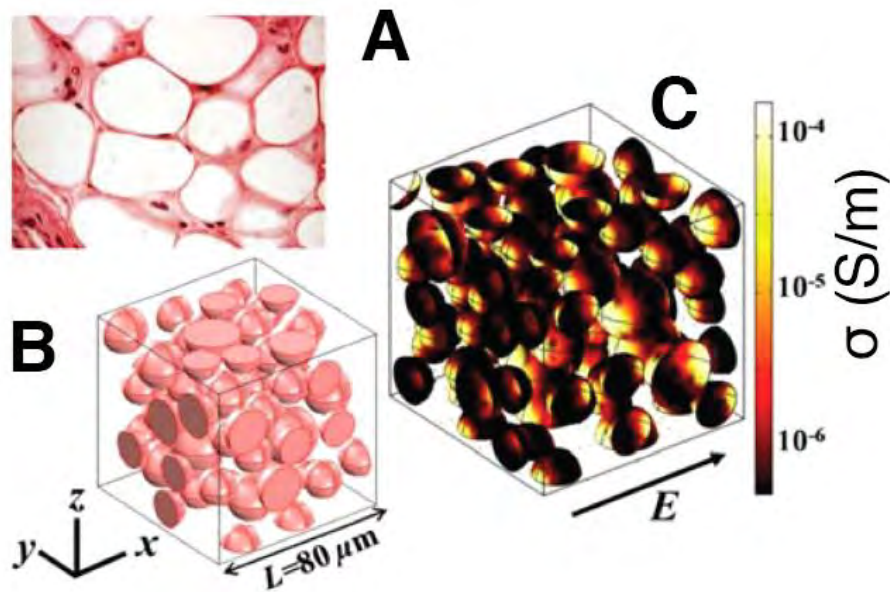


**Figure 1.7** – Tissue electroporation. (A) Microscope image of connective tissue containing adipose cells. (B) 3D reconstruction of connective tissue with randomly positioned cells. (C) Electrical conductivity of cell membranes during exposition to 1000 V/cm electric field [58], [59].

#### 1.5.4 Skin electroporation

Skin electroporation for non-invasive, transdermal drug delivery was first suggested by Prausnitz *et al.* in 1993. They demonstrated that the application of PEF on human skin, *ex vivo*, and hairless mouse skin, *in vivo*, lead to a temporary, multi-fold increase on the uptake of three small to medium-sized, negatively charged, fluorescent molecules (lucifer yellow, calcein, erythrosin derivative), compared to a non-pulsed control [3]. Since then, numerous studies have been published on skin electroporation for transdermal drug delivery, expanding the results to a wider range of molecules (charge and size) and testing different electrode configurations and pulse parameters, on a variety of skin models (mouse, pig, reconstructed human, human) [4], [5], [6], [7], [8], [9], [10], [11], [12]. However, very few studies have reached human *in vivo* testing of this delivery method [13], [14]. A number of limitations prevent transdermal electroporation for drug delivery from reaching clinical trials. These include inconsistent drug delivery quantities, unpractical electrode configurations, unclear pain thresholds for PEF, failure to deliver larger molecules and a general limited understanding of the underlying mechanisms. A successful non-invasive transdermal drug delivery has to be painless, practical, totally-reversible and must deliver consistent amounts of therapeutic molecules in relevant quantities, within reasonable timeframes.

At the skin level, the application of an external electric field can disrupt the barrier function of the stratum corneum. An electric field strength higher than *ca.* 400 V/cm, creates Local Transport Regions (LTRs), *i.e.* aqueous pathways through the skin (**Figure 1.8**) [17], [18]. LTRs are regions of increased ionic mobility and increased solute mass transfer, with enhanced electrical conductivity and permeability. Their appearance is accompanied by a rapid decrease in the resistivity of the SC (up to two orders of magnitude [17]), increase in transepidermal water loss, and increased permeability to hydrophilic compounds [11], [20]. The current density circulates through LTRs, and Joule heating causes melting of the lipids in their vicinity, further increasing their size for longer pulse durations. Higher applied voltages increase the density of LTRs and longer durations (pulse duration and number

of repetitions) increase their diameter [5]. For certain electrical parameters, with voltage being the most important, these changes are mostly or fully reversible.

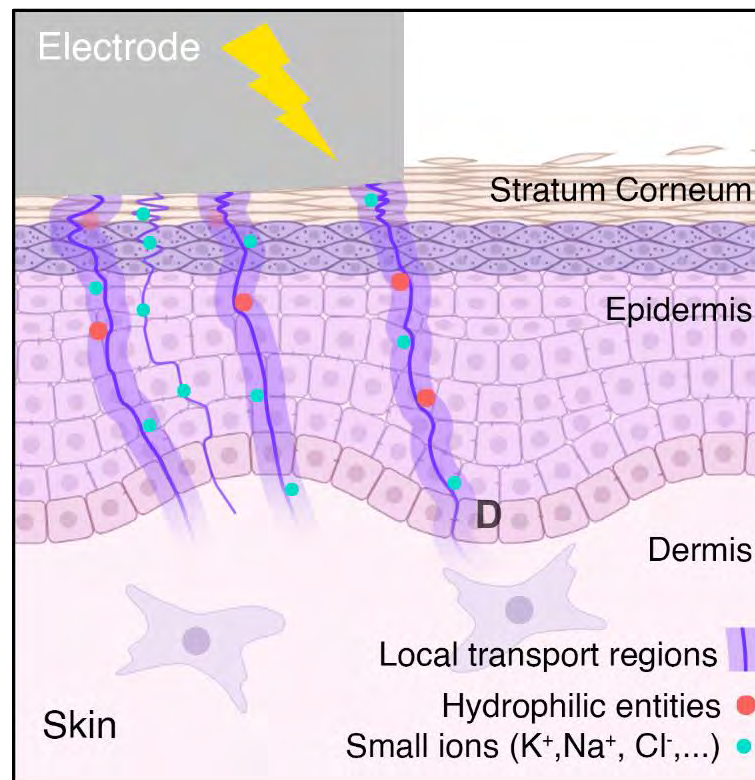


**Figure 1.8** – Skin electroporation. Formation of local transport regions through the application of an electric field to the skin

Once LTRs are formed, drug delivery across the skin can take place. The driving forces for the mass transfer of solutes are (1) electrophoretic drag (for charged entities), (2) electro-osmosis and (3) concentration gradient [5]. To this day, it is not fully clear how and where exactly these LTRs are formed in the SC. Three possibilities exist, each following a different pathway. The intercellular pathway is the pathway between the corneocytes, passing through the lipids of the extracellular region. These lipids are largely organized in stacks of lipid bilayers; thus, the electric field could act on them in a similar way as with cell membrane electroporation. However, some important differences exist: most importantly, in cell membrane electroporation the process includes the permeabilization of one lipid bilayer, which is surrounded by a humid and conductive environment (the cytoplasm and the extracellular space). In the case of the lipids of the SC, the process would entail the permeabilization of multiple stacked lipid layers in a row (*ca.* 70 to 100 [60]), all of which are surrounded by a vastly different environment (mostly lipophilic, resistive and low water content). Recently, Gupta and Rai visualized the pore formation on the extracellular lipid bilayers of the SC through molecular dynamics simulations [21]. The transcellular is the pathway through the corneocytes of the SC. This pathway involves the permeabilization of the cornified envelope of the corneocytes. The interior of the corneocytes is hydrophilic, thus this is the pathway with the shortest length of hydrophobic environment. Zewert *et al.* argued that high-voltage pulses can create straight-through, transcellular pathways by permeabilizing the corneocytes of the SC [61]. However, it seems unlikely that the cornified envelope, an insoluble protein structure, would behave in the same way as plasma membranes, under the application of an external electric field. The third possible pathway, the transappendageal, involves the transport of molecules through the permeabilization of the lining of

hair follicles and sweat ducts. The lining of hair follicles is comprised of only two cell layers. Additionally, skin appendages are regions with lower resistivity so higher current densities flow through them during PEF application [25]. Yet, the appendages cover only a very small part of the skin surface (0.001 to 0.01 % [62]) and imaging experiments have failed to point out a localized transport around them [18], [61]. Overall, transport of molecules may include a combination of these pathways but, more recently, the intercellular is generally accepted as the dominant one [5], [11], [21], [61].

The most common electrode configurations for skin electroporation are presented in **Figure 1.9**. These include the two-chamber configuration [3], the skinfold configuration [63] and our configuration [64], a two-in-one hydrogel electrode-reservoir platform. Some less common configurations include two cylindrical L-shaped electrodes side by side [65], multi-electrode arrays [66] and meander electrodes [67]. In general, the configurations include one (or more) positive electrode(s), one (or more) negative electrode(s), the model skin, the drug/model molecule formulation and (optionally) a conductive material to facilitate contact between the skin model and the electrodes. Some of these components may be combined.

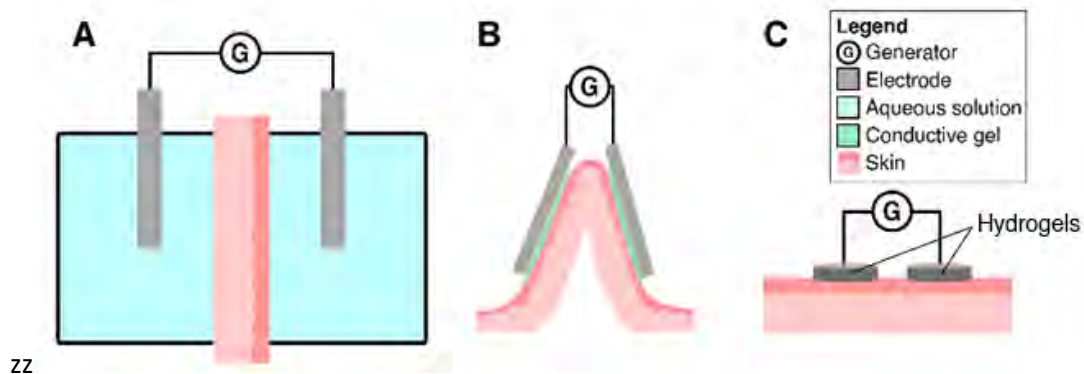


**Figure 1.9** - Configurations for skin electroporation. (A) Two-chamber. An *ex vivo* skin model is placed between two chambers, filled with an aqueous solution. The electrodes are immersed in the solutions. This configuration is only relevant for research. (B) Pinched skin with conductive gel. The skin model (*ex vivo* or *in vivo*) is pinched and placed between two electrodes. A Conductive gel placed between the metal electrodes and the skinfold ensures electrical contact. (C) Our configuration. Side by side hydrogels functioning as drug reservoirs and electrodes.

In previous works, we developed and characterized a nanocomposite hydrogel platform, serving as an electrode for the application of the electric pulses on the skin and as a reservoir to store the target drug (**Figure 1.10**) [64]. Subsequently, we demonstrated that the platform could be used to transiently increase the skin uptake of hydrophilic model drugs. The delivery of model drugs was found to be dependent on the molecule size and charge, while the main mechanism for transport through the permeabilized skin was electrophoretic force [10].



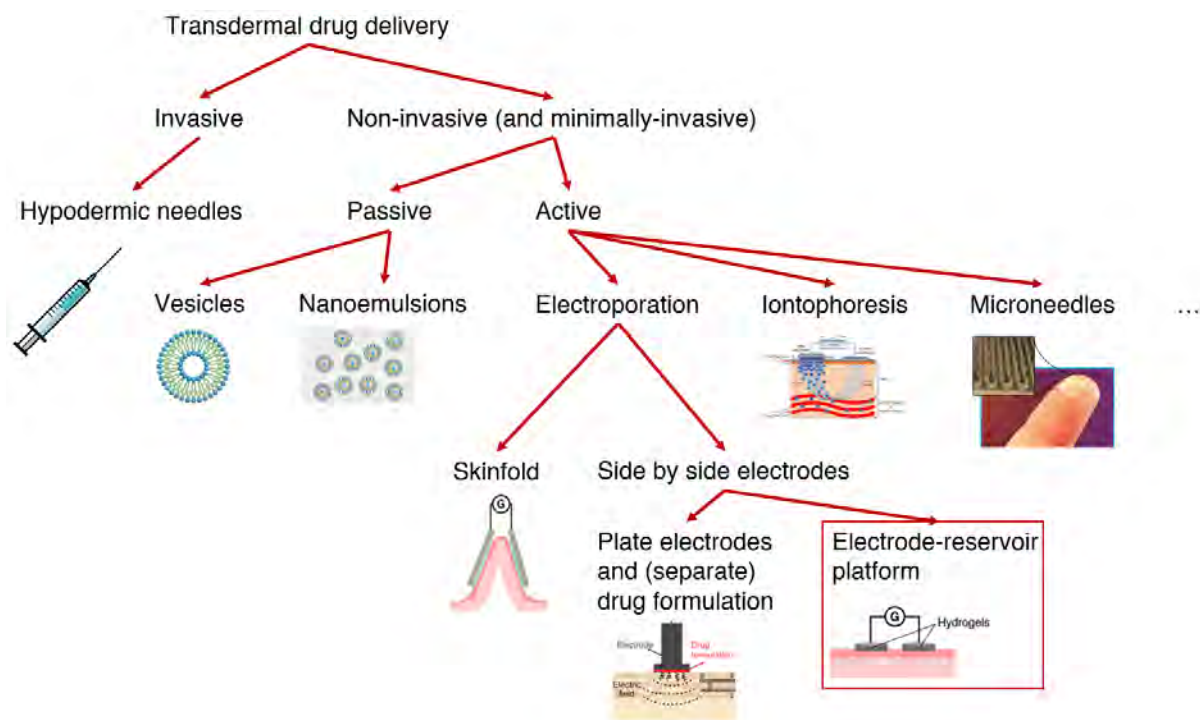


**Figure 1.10** – Transdermal drug delivery methods, including our approach to non-invasive skin electroporation with a two-in-one electrode-reservoir hydrogel platform. Images adapted from refs. [11], [68], [69], [70]

## 1.6 Hydrogels for drug delivery

Conventional drug delivery has a number of drawbacks including high dosages, limited bioavailability, repeated administration and potential toxicity [71]. Controlling how, when and where drugs are available to cells and tissues can increase the drug's efficiency and reduce the frequency and concentration of the doses, limiting the toxicity and improving patient compliance and life quality. Hydrogels are some of the most promising and widely considered platforms for controlled drug delivery. They are hydrophilic, biocompatible, have a large water retention capacity and can be stimuli-responsive. Typical mesh sizes of hydrogels range from 10 to 100 nm [71]. This means that most molecules can diffuse freely within the porosity of the hydrogel network. The mesh size can be decreased by increasing the polymer concentration and cross-linking, to delay the release rate by steric hindrance. To further reduce the release rate, active ingredients can form covalent, electrostatic or hydrophobic interactions with the polymer matrix [71]. Nanomaterials can also reduce the release rate of active ingredients [71], [72]. Hydrophilic drugs can be readily diffused within hydrogels while hydrophobic drugs can associate with hydrophobic domains (aliphatic chains, cyclodextrin) in the polymer network or be encapsulated in nanovesicles [71], [73]

## 1.7 Hydrogels

Hydrogels are three dimensional, viscoelastic networks of hydrophilic polymer chains, cross-linked in an aqueous environment. The water - polymer network is gelled through the association of polymer chains to form a continuous structure, that immobilises water within it and becomes resistant to flow [74]. The association of polymer chains occurs through a variety of mechanisms that can be classified into physical or chemical. Mechanisms of physical cross-linking include the physical entanglement of individual polymer chains, typically induced by solubility alterations in response to temperature changes; macromolecular self-assembly through non-covalent bonding (hydrogen bonds, Van der Waals forces, hydrophobic interactions); crystallization, the formation of microcrystals through a

freeze-and-thaw process, which then act as a cross-linking site; ionic gelation, polymer chains surround ions forming a crosslinking site; and electrostatic interaction of polymer chains with opposite charges [75], [76], [77], [78]. Chemical cross-linking involves the formation of covalent bonds between polymer chains through mechanisms including radical polymerization, chemical reactions of complementary groups (for example hydroxyl groups or amides with carboxylic acids), high energy irradiation, addition of chemical cross-linking agents (glutaraldehyde, epoxy compounds, isocyanates, metal ions) and enzymatic reactions [75], [76], [77], [79].

Physically cross-linked hydrogels are reversible, easy to produce and do not require the use of chemical cross-linking agents [76], [77]. Chemically cross-linked hydrogels generally have higher mechanical strength and offer more possibilities for control of the cross-linking process and customised design [75], [76]. However, they often make use of toxic cross-linkers which then have to be extracted to keep the hydrogel biocompatible [77]. The combination of physical and chemical cross-linking mechanisms offers the possibility for more precise control over the hydrogels' properties [75].

Hydrogels can be further classified according to their polymeric composition as: (1) single polymer networks (homo-polymers), derived from one type of monomer unit; (2) copolymers, derived from the cross-linking of two or more types of monomers, arranged in alternating, block or random configuration on the polymer chain; (3) semi-interpenetrating polymer networks, where a linear polymer is contained within an independent, cross-linked polymer network; and (4) interpenetrating polymer networks, derived from two independent, cross-linked polymer networks interlocked together [77], [78], [80]. In each case, at least one of the monomers must be hydrophilic, to render the network water swellable.

Hydrogels are rich in water (typically 80 to 95 % w/w but can span almost all range), flexible with viscoelastic behaviour and usually biocompatible [81], [82], [83]. These properties have fostered numerous applications in the domains of biomedicine, soft electronics and actuators [75]. Some of these properties can be straightforwardly modified to fit a specific application. For example, the rigidity and water content of hydrogels can be tuned by adjusting the polymer concentration and the cross-linking degree [84]. In an aqueous environment, a dynamic equilibrium exists between the interactions responsible for water sorption (capillary, osmotic and hydration forces) and the cross-linked polymer network resisting expansion [85].

In addition, hydrogels can be highly responsive to external stimuli. Small changes in environmental conditions such as temperature, pH, pressure, electric field or chemical agents can induce unexpected and mostly reversible changes in hydrogel properties such as volume, swelling degree, conductivity or permeability [86]. These stimuli-responsive or smart hydrogels can be engineered to sense external stimuli and transmit an electrical or optical signal, by modifying a readily readable property such as electrical conductivity or colour [86], [87]. Many hydrogels used in motion sensing devices change their electrical conductivity when strained, giving an electrical signal to the device [86]. Hydrogel membranes can selectively allow the transfer of molecules by swelling to open or block their pores, according to biochemical signals [88]. More recently, 3D printing of hydrogels has opened new possibilities for customized design [89].

Despite their remarkable properties and several possible applications, hydrogels have some important limitations. They generally have limited mechanical strength and are susceptible to irreversible deformation [90]. In addition, hydrogels from commonly used polymers intrinsically have very low



electrical conductivity. These limitations make conventional hydrogels unsuitable for applications that require robustness or electrical conductivity.

### 1.8 Electrically conductive hydrogels for drug delivery

Electrical conductivity, in particular, is an important property of hydrogels in biomedical applications. Applications of electrically conductive hydrogels include hydrogels used as substrates for the growth of electroactive cells, hydrogels which function as flexible strain sensors for health monitoring and wearable devices and drug-loaded hydrogels used for electro-stimulated drug delivery [91].

Hydrogels can be engineered to release part of their water content according to environmental stimuli [92]. Pulsatile drug release, in particular, can mimic the natural patterns of *in vivo* release of endogenous chemicals such as insulin, growth hormone and oestrogen [71], [93]. Externally applied electric fields can be used to control the release rate of drugs from conductive hydrogels. Servant *et al.* added ball-milled graphene nanosheets to methacrylic acid hydrogels, to improve their mechanical and electrical properties. A concentration of 0.2 mg/ml of graphene nanosheets increased the electrical conductivity of the hydrogel from  $2.9 \times 10^{-6}$  to  $10^{-5}$  S/m. The nanocomposite conductive hydrogels demonstrated controlled, pulsatile release of a small molecule (sucrose) upon the intermittent application of an electrical field (figure 5A) [94]. Additionally, nanomaterials can enhance electro-stimulated drug release. Liu *et al.* incorporated reduced graphene oxide (rGO) into poly(vinyl alcohol) hydrogels and loaded them with a drug (lidocaine). With no external stimulation, the rGO nanomaterials acted as a barrier, retaining the drug within the hydrogel, while the application of an electric field triggered the release of the drug. The addition of rGO negatively charged the polymer matrix, enhancing electro-osmosis. In contrast, a control hydrogel without conductive nanomaterials did not change the drug release profile with electric field application (figure 5B) [72]. Merino *et al.* reviewed the field of nanocomposite hydrogels for controlled drug delivery [92].

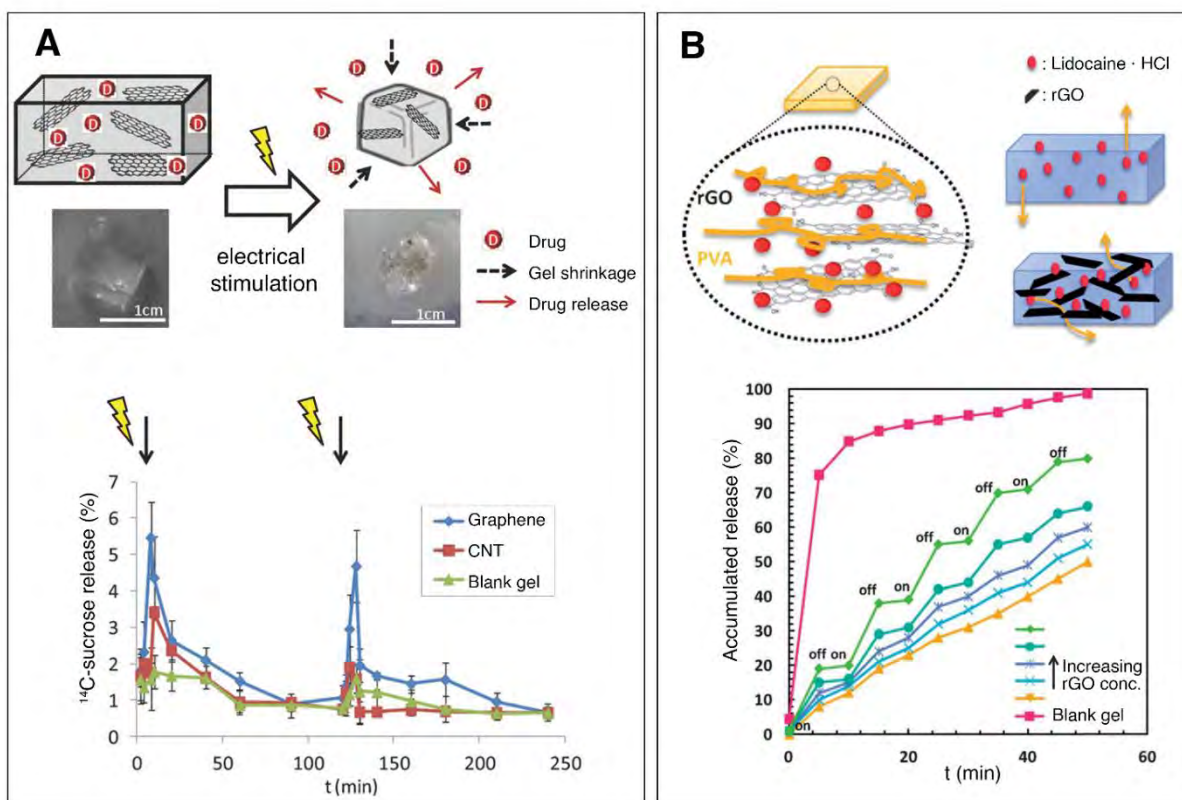


**Figure 1.11** - Conductive nanocomposite hydrogels for controlled drug delivery. (A) Electrical stimulation causes a methacrylic acid – graphene nanosheet hydrogel to shrink, releasing drug. *In vivo* release profile of  $^{14}\text{C}$  sucrose on the blood plasma of mice implanted with sucrose-loaded hydrogels. Hydrogels with no nanomaterials (green), 0.2 mg/ml CNTs (red) and 0.2 mg/ml graphene (blue) were tested. A tension of 10 V DC is applied for 1 minute with a time interval of 2 h. The graphene-loaded hydrogel (which also had the highest conductivity) demonstrated a pulsatile release of sucrose, controlled by the electric field. Adapted from ref. [94]. (B) Reduced graphene oxide nanomaterials retain lidocaine hydrochloride within a polyvinyl alcohol hydrogel. Upon pulsatile electrical stimulation (on/off, 15 V DC) the nanocomposite hydrogels exhibit controlled drug release, while the blank gel does not change release profile. Adapted from ref. [72].

In Electrically conductive hydrogels for drug delivery, two approaches are distinguished: electro-responsive hydrogels that release a drug upon application of an external electrical field and conductive hydrogels used as electrodes for transdermal drug delivery through skin electroporation [64], [92]. Electro-responsive hydrogels shrink or bend upon the application of an external electric field. A loaded drug is released through the contraction of the hydrogel as well as through electrophoretic forces. The electrically-induced contraction of hydrogels occurs through the combination of four mechanisms: (1) a stress gradient in the hydrogel, (2) electro-osmosis of water coupled with electrophoresis, (3) local pH changes near the electrodes due to water electrolysis and (4) a temperature gradient in the hydrogel due to resistive heating [92]. So far, there is no clear conductivity target for electro-responsive hydrogels in controlled drug release, however, the incorporation of conductive nanomaterials has been shown to enhance drug release [72], [94]. In the case of conductive hydrogels for transdermal drug delivery, the hydrogel functions as an electrode, for the application of pulsed electric field on the skin [64]. A higher conductivity ensures a more efficient distribution of the electric field into the skin, a prerequisite for skin electroporation [10], [64].

There are three approaches to prepare electrically conductive hydrogels: (1) using a conducting polymer in the hydrogel matrix, (2) increasing the ionic conductivity of the aqueous phase and (3) incorporating a conductive material in the hydrogel.

Conducting polymers are organic macromolecules with intrinsic electrical conductivity. Conducting polymers commonly used for preparing hydrogels are polypyrrole (PPy), polyaniline (PANI) and poly-(3,4-ethylenedioxythiophene) (PEDOT) [95]. They cannot form hydrogels themselves but have to be combined with a supporting polymer that provides hydrophilicity and mechanical strength [95]. They provide a conducting path of electronic conductivity due to the delocalized pi electrons of their conjugated systems, and can also increase the ionic conductivity of the aqueous phase by contributing ions [96], [97]. Guo and Ma reviewed materials for tissue engineering with conducting polymers, including hydrogels [98] and Stejskal reviewed conducting polymer hydrogels with a focus on preparation methods [95].

The ionic conductivity of the aqueous phase can be increased by preparing and/or swelling the hydrogel in an ion-rich aqueous solution. Free ions can be generated in water from acids, metal salts or ionic liquids [99]. Metal ions, in particular, can act both as cross-linking agents for polymer chains and electrolytes of ionic conductivity [100]. The cross-linking mechanism is metal-ligand interaction where the metal ions form coordinate covalent bonds with chelating agents (N, O, S) in the polymer chain [101]. In high concentrations, the free metal ions contribute to the ionic conductivity of the hydrogel [100]. Zhang *et al.* review the recent advances in metal ion hydrogels for biological applications [101]. Non-ionic polymer chains may impair the ionic conductivity of hydrogels, compared to polyelectrolyte hydrogels [102]. Polyelectrolytes are polymers which contain ionic and/or ionizable groups in a substantial portion of their constitutional units [103]. They can be cationic, anionic or ampholytic (containing both negative and positive charges; also called zwitterionic, commonly when the positive and negative charges are located in the same pendant group) [102], [103]. In low concentration electrolyte solutions, polycationic and polyanionic hydrogels exhibit the highest ionic conductivity, due to high concentrations of mobile counterions. In high concentration electrolyte solutions, polyzwitterionic hydrogels promote fast ion dissociation and transport due to the highly charged polar side groups [102], [104]. Wang *et al.* and Liu *et al.* reviewed polyelectrolyte [105] and polyzwitterionic [106] hydrogels for biomedical applications.

The incorporation of conductive materials aims to create a continuous network of electronic conduction throughout the hydrogel, through the dispersion of conductive nanomaterials and/or other conductive materials, such as metal microwires or carbon fibers, in the hydrogel framework.

## 1.9 Carbon-based nanomaterials

Carbon-based nanomaterials have high mechanical strength, electrical conductivity, surface area and chemical stability and are available in a variety of allotropes and forms [107]. They can usually combine these properties, which is rather unique. The carbon nanomaterials most commonly employed to increase the electrical conductivity of hydrogels include carbon nanotubes (CNTs) and graphene-related materials, and less often carbon black and graphite.

### 1.9.1 Carbon nanotubes

CNTs are one-dimensional, long, cylindrical nano-objects of  $sp^2$ -hybridized carbon atoms arranged in hexagonal arrays, with nanoscale diameters (figure 7A). They can be single-walled (SWCNT) or multi-walled (MWCNT), where multiple, concentric nanotubes with increasing diameters are held together

by Van der Waals forces. SWCNTs can have diameters of 0.4 to 4 nm with most of them being around 1.4 nm [108]. Their length can range from a few hundreds of nm up to centimeters, with most nanotubes length on the micro scale [109]. CNTs are known to have remarkable physical properties, notably heat and electrical conductivity, mechanical strength, optical properties and a large surface area, with numerous potential applications in electronics, biomedicine, optics, composite materials and more [108], [109], [110].

CNTs can be semi-conducting or metallic, depending on the diameter and the helicity of the nanotube. The electrical conductivity of isolated CNTs can reach values of  $10^5 - 10^8$  S/m [111], [112]. They are commonly implemented in nanocomposite hydrogels to increase their electrical conductivity because of their high intrinsic electrical conductivity, the ability to form percolation networks even at low concentration thanks to their high aspect ratio (typically from a few hundreds to tens of thousands) and the compliance with many polymer matrices [111]. Additionally, CNTs can also significantly reinforce the mechanical properties of nanocomposite hydrogels [113], [114].

Zhou *et al.* added SWCNT into a gelatin hydrogel and cross-linked them with glutaraldehyde. The hydrogel served as a scaffold for engineered cardiac tissue, aimed to treat myocardial infarction. Adding 0.15 % w/w of SWCNT into a hydrogel with 7.5 % w/w gelatin and 2.5 % w/w glutaraldehyde increased the electrical conductivity from  $3 \cdot 10^{-8}$  to  $5 \cdot 10^{-5}$  S/m and the shear modulus from 30 to 40 Pa. The SWCNT concentration was chosen as a compromise between conductivity and cytotoxicity; hydrogel scaffolds with higher SWCNT concentration significantly decreased cardiac cell viability. The conductive SWCNTs enhanced the contractile muscle tissue function and the formation of gap junction and globally improved heart function after myocardial infarction, as tested on rats [115].

Spizzirri *et al.* added MWCNTs into gelatin microgels by emulsion polymerization, in the presence of sodium methacrylate and N,N'-ethylenebisacrylamide. The microgels served as a drug reservoir for electro-stimulated release on the skin surface. It was found that 0.8 % w/w MWCNTs increased the hydrogel conductivity from  $1.3 \cdot 10^{-7}$  to  $2.6 \cdot 10^{-7}$  S/m. Lower concentrations of MWCNT had no effect on the conductivity, indicating that a percolation network was not formed. The microgels with MWCNTs showed no significant cytotoxic effect and increased the release rate of the drug, both with and without an external electric field [116].

## 1.10 Electrical Percolation

### 1.10.1 Percolation theory

Incorporation of a conducting filler in an insulating hydrogel matrix, increases the conductivity of the nanocomposite, with increasing filler concentration. Often, a point is observed where a small increase in filler concentration leads to a steep increase in conductivity, a shift of few orders of magnitude [111], [117]. Further increase in filler concentration has a limited effect on conductivity. The resultant graph of conductivity versus filler concentration exhibits a sigmoidal shape (**Figure 1.12**).

Percolation theory explains this jump-like transition. The conductivity increases steeply when the filler forms a continuous conducting network within the hydrogel. Individual clusters of filler particles come into contact with each other, to ultimately form a single cluster that extends throughout the system [117]. Electron transport takes place through the conductive filler network and the system's behaviour changes from insulating to conducting (**Figure 1.12**). The corresponding critical filler concentration is called percolation threshold. The percolation threshold of different nanocomposite hydrogels varies

widely and depends on the polymer matrix and the shape, size, orientation and dispersion of the filler [111]. Higher aspect ratios and better dispersions lead to lower percolation thresholds.

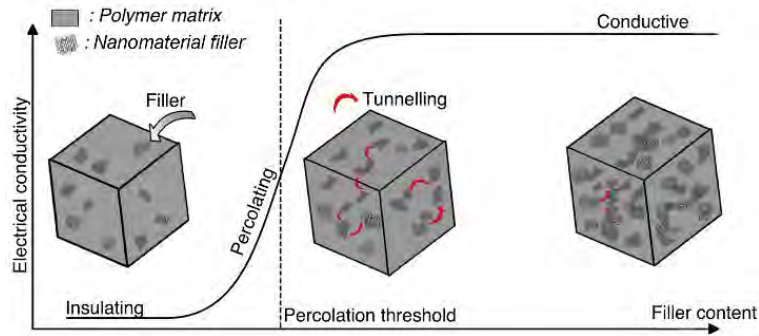


**Figure 1.12** - Electrical conductivity vs nanofiller content. Percolation has three phases: initially the concentration of the nanomaterial is not enough to form an interconnecting network and the conductivity remains low. As the concentration increases, electrons can hop through the nanofillers with tunnelling and the conductivity increases. When the concentration reaches the percolation threshold, a network is formed throughout the whole system and the conductivity reaches a high plateau. Adapted from ref. [118].

The electrical percolation threshold is an important parameter in percolating systems. Experimentally finding it and tuning it by changing the properties of the system can lead to the development of highly conductive nanocomposites with minimal filler concentration and desirable properties. For a random distribution of a well-dispersed filler, the statistical percolation theory can model the conductivity of composites [117], [119].

$$\sigma = \sigma_0(\Phi - \Phi_c)^t, \text{ for } \Phi > \Phi_c \quad (1.8)$$

Where  $\sigma$  is the electrical conductivity of the composite,  $\sigma_0$  the electrical conductivity of the filler in its bulk form,  $\Phi$  the filler volume fraction,  $\Phi_c$  the percolation threshold and  $t$  the critical power law exponent. The exponent  $t$  depends on the system dimensionality and takes values of *ca.* 1.3 for 2D systems and *ca.* 2 for 3D [118], [120]. The electrical percolation threshold can be determined experimentally or numerically.

Experimentally, the electrical percolation threshold can be deduced from a graph of electrical conductivity with increasing filler concentration. The threshold is the middle point of the S-shaped part of the graph. It can also be calculated by fitting equation (1.8) to experimental data.

Numerically, there are various models with increasing complexity for calculating the percolation threshold. The continuum percolation models can be applied for hydrogels, which have an amorphous structure and thus a random distribution of particles. The simplest models simulate the filler particles with interpenetrating objects. The electrical percolation threshold is calculated as the point where the filler particles form a continuous network, a cluster of particles that extends through the simulation space.

The calculated percolation thresholds from the above method can be higher than the experimental ones because it does not take into account two phenomena: the filler particles cannot penetrate into each other because of repulsive Van der Waals interactions and the electrical percolation threshold can occur before the geometrical percolation, due to electron tunnelling [121]. Geometrical percolation is when the filler particles form a network with physical contact. Electrical percolation can occur at lower filler concentrations, as electrons can be transferred through a thin film of dielectric

material that separates the filler particles. The electron tunnelling distance is in the order of few nm [122].

Another factor that differentiates experimental from numerical results is the non-randomness of real dispersions. In numerical models, the particles will be randomly distributed within the system's boundaries while in experiments particles tend to agglomerate/cluster and align, affected by particle interactions, the dispersion method and the thermal or mechanical processing history of the material [123]. This clustering and non-random alignment of nanomaterials can have substantial effects on the percolation concentration of the system [123], [124].

### 1.10.2 Critical path approximation

Percolation models assume a sharp cut-off point of electrical conductivity. Two individual particles are either electrically connected or not. Subsequently, a cluster of particles passes from disconnected (insulating) to percolated (electrically conductive), when the percolation threshold is reached. Ambrosetti *et al.* argue that this approach is well suited to explain the electrical conductivity in the extreme cases of low filler concentration (particles with no electrical contact) and high filler concentration (particles "touching" each other throughout the system) but fails to account for the conductivity changes in the intermediate regime, around the percolation concentration [125]. They model the conductivity changes in nanocomposite systems by focusing on the tunnelling conductance between conductive particles [125], [126]. The tunnelling conductance decays exponentially with distance, but does not include a sharp cut-off. This model can be solved numerically by simulating the conducting fillers as a network of particles that are all connected to each other through tunnelling processes (Global Tunnelling Network). An analytical solution for the conductivity  $\sigma$ , is given by the critical path approximation

$$\sigma \cong \sigma_0 \exp \left[ -\frac{2\delta_c(\varphi, a, b)}{\xi} \right] \quad (1.9)$$

Where  $\sigma_0$  a constant,  $\xi$  the characteristic tunnelling length and  $\delta_c$  a critical distance, which depends on the filler concentration  $\varphi$  and the geometric characteristics of the particles  $a$  and  $b$  ( $a/b$  is the aspect ratio). The solution of equation (1.9) reduces the conductivity of a nanocomposite system to the calculation of the geometrical parameter  $\delta_c$  and is in good accordance with the numerical solutions from the global tunnelling network model [125].

The implications of the critical path approximation are that the transition from insulating to conducting is no longer described by a power law increase in conductivity after the percolation threshold concentration, but rather as a crossover between the insulating matrix conductivity and the interparticle tunnelling conductivity [125].

### 1.10.3 Percolation of carbon nanotubes

CNTs have a high aspect ratio (generally *ca.* 1000 or higher), which allows for low percolation thresholds [111]. Kovacs *et al.* used the excluded volume concept to calculate a percolation threshold of

$$\Phi_c = \frac{1}{\eta} = \frac{1}{1000} = 0.1 \% w/w \quad (1.10)$$

where  $\eta$  is the aspect ratio of CNTs [120]. They argue that this percolation threshold is universal for CNTs in insulating polymer matrices (they reviewed solid nanocomposite polymers but their results are useful in the case of hydrogels too). Deviations with higher  $\Phi_c$  are attributed to poor dispersion



and lower  $\Phi_c$  are attributed to kinetic percolation, a state where the particles are free to move through diffusion, convection, shearing or external fields and form a conducting network at lower concentrations. The critical exponent  $t$  for CNTs, calculated from fitting the experimental data into equation (1.8) ranged from 0.9 to 7.6, peaking at  $t=2$  [120].

CNTs can be modelled as capped cylinders for the numerical simulations. The most sophisticated models take into account the electron tunneling distance, the non-random alignment, as well as the waviness of the nanotubes, which increases the percolation threshold [127].

#### 1.10.4 Electrical percolation studies in hydrogels

Most conductive hydrogel studies presented in this review did not report a percolation threshold. The ones commenting on percolation threshold concentration are grouped here. Ferris and Panhuis found a percolation threshold of 1.3 % w/w for gellan gum hydrogels containing multi-walled CNTs [128]. Mottet *et al.* report a percolation threshold of 0.5 % w/w for alginate hydrogels with CNTs. [129] Cui *et al.* report a percolation threshold of 0.015 % w/w for poly-ethyl acrylate hydrogels, with multi-walled CNTs [130]. Guillet *et al.* and Macdonald *et al.* found no percolation threshold for agarose – double-wall CNTs hydrogels for concentrations up to 1 % w/w and for collagen – SWCNTs for concentrations up 0.008 % w/w respectively [131], [132]. Alam *et al.* reported a percolation threshold of 0.4 % v/v for graphene incorporated in poly acrylic acid hydrogels [133]. Sayyar *et al.* and Qiu *et al.* both reported a percolation threshold of 0.1 % w/w for reduced graphene oxide fillers in chitosan and poly-isopropyl acrylamide hydrogels [134], [135].

In contrast, in studies of solid nanocomposite polymers, there are more publications reporting a clear electrical percolation threshold. We explain this by four factors: (1) there are fewer studies in total for nanocomposite hydrogels, (2) carbon-based materials which generally exhibit low percolation thresholds are highly hydrophobic resulting in the formation of aggregates and poor dispersions in aqueous media, (3) polymer chains may tend to wrap around nano-objects, limiting direct contact between the conductive phase, and (4) hydrogels are more complex systems consisting of at least three components (polymer matrix, water, filler) and two conduction mechanisms (ionic and electronic). This complicates the investigation of the percolation threshold. Rather than a clear cut-off point of several orders of magnitude increase in conductivity, many nanocomposite hydrogels present modest augmentations with increasing nanofiller content.

#### 1.11 Dispersion of conductive nanomaterials

Nanomaterials are introduced into nanocomposite hydrogels using one of three possible approaches: (1) dispersion of nanomaterials in an aqueous suspension of a monomer, followed by gelation, (2) dispersion of a nanomaterial precursor in an aqueous suspension of a monomer, followed by gelation and nanomaterial synthesis within the polymerized matrix, and (3) physical embedding of nanomaterials into a hydrogel matrix [136], [137]. The nanomaterials can significantly alter the properties of the nanocomposite hydrogels, thanks to the multiple physical and/or chemical interactions between the nanomaterials and the polymer. These include hydrogen bonds, van der Waals interactions and electrostatic interactions [136]. The dispersion of nanomaterials in the hydrogel network affects the system's electrical and mechanical properties. Poor dispersions, leading to nanomaterial agglomeration undermine the property-enhancing features of nano-engineering.

Carbon-based nanomaterials have highly hydrophobic surfaces. They form agglomerates in aqueous suspensions and have low interfacial compatibility with polymer matrices [136], [138]. The surface of



carbon nanotubes and graphene sheets can be functionalized with hydrophilic groups, such as -COOH and -OH, facilitating their dispersion in water through electrostatic repulsion (at slightly acidic pH and above, the carboxylic function is present as a negatively charged carboxylate) [139]. However, covalent functionalization disrupts the electronic structure of plain carbon-based nanomaterials, deteriorating their electrical conductivity [136]. Another route is the addition of surfactants. Lastly, physical methods, such as polymer wrapping and cellulose-assisted dispersion have also been developed. Polymer wrapping and surfactants improve dispersion but also cover the surface of carbon nanomaterials and may increase the distance between the nanomaterials, decreasing electron tunnelling conductance and negatively affecting the conductivity of the nanocomposite hydrogel [138].

## 1.12 Electrical conductivity and conduction mechanisms

### 1.12.1 Conductivity

Electrical conductivity is an intrinsic property of materials which measures how well they conduct electric current. It is the reciprocal of resistivity, the resistance of a material to the flow of electric current. When a potential difference is applied to a sample, an electric field  $E$  is created, and charges inside the sample have an electric force applied to them. For an isotropic and constant conductivity and a homogenous electric field, the current density  $J$  that results, depends on the sample's conductivity  $\sigma$ .

$$J = \sigma \cdot E \quad (1.11)$$

Electric current is conducted by charge carriers, which can be ions, electrons and holes. Electrical conductivity depends on the product of charge carrier concentration and mobility.

### 1.12.2 Conduction mechanisms in dielectric materials under high electric fields

When a sample is placed between two electrodes, charges are injected across the interface of the sample from the electrode materials, then pass through its volume and get out again from the interface of the sample with the other electrode. Localised charge movements also result in a measurable current, even if the charge carrier does not exit the sample. The limiting conduction mechanism is the determining one and this can fall into one of two categories: interface-limited (or electrode-limited) and volume-limited (or bulk-limited) [140]. Depending on the nature of the material and the applied electric field, one or more conduction mechanisms may contribute to the electric current transport.

Interface-limited conduction mechanisms depend on the electrical properties at the contact between the sample and the electrode. The most important parameters are the energy barrier height that the charge carrier has to overcome in order to get injected into the sample and the effective mass of the charge carriers [140], [141]. Volume-limited conduction mechanisms depend on the electrical properties of the sample. The most important parameter in volume-limited conduction are traps, locations in solids which restrict the movement of charge carriers. Trap energy level, trap spacing and concentration all affect volume-limited conduction. Other parameters include the electrical mobility and the dielectric relaxation time [140], [141].

### 1.12.3 Ionic conduction

Ionic conduction occurs when the charge carriers are ions. It is the dominant conduction mechanism in electrolyte solutions but also contributes to the electrical conductivity of solids. Fast ion conductors and solid electrolytes are examples of solid materials where ionic conduction is the main conduction

mechanism [142]. The ionic conduction mechanism consists of a series of jumps over potential barriers from one site to another [141]. Ions are several orders of magnitude bigger and heavier than electrons and consequently ion mobility, reduced by steric effects, is much lower than electron mobility. Ionic conduction depends on ion concentration, temperature, ion size and valency, electrical field magnitude, viscosity (in the case of solutions) and the height and spacing of potential barriers (in the case of solids).

#### 1.12.4 Electric current

The movement of charge carriers under the influence of an electric field is the conduction current. There are two more current types that can be measured. The diffusion current is created by the movement of charge carriers under the influence of their concentration gradient. The displacement current is a transitory current due to the variation of the electric field and is not linked to a charge movement inside the sample. It includes the polarisation current, a transitory current that arises from the orientation of dipoles with the electric field. The total current can be written as the sum of the above current types

$$j(t) = \underbrace{qn(x,t) \mu(E,t) E(x,t)}_{\text{Conduction}} - \underbrace{qD_n \frac{\partial n(x,t)}{\partial tx}}_{\text{Diffusion}} + \underbrace{\varepsilon_0 \frac{\partial E}{\partial t} + \frac{\partial P}{\partial t}}_{\text{Polarisation Displacement}} \quad (1.12)$$

where  $j$  is the current density,  $q$  the elemental charge,  $n$  the charge carrier concentration,  $\mu$  the charge carrier mobility,  $E$  the electric field  $D_n$  the diffusion constant of the charge carriers,  $\varepsilon_0$  the permittivity of vacuum and  $P$  is polarisation.

#### 1.12.5 Hydrogel water content and electrical conductivity

Nanocomposite hydrogels are complex systems consisting of at least three components: water, which comprises the largest part of the hydrogel, a cross-linked polymer network and the filler nanomaterials. The role of each constituent in the electrical conductivity of the system is still poorly understood. Deionised water is used for the fabrication of most hydrogel samples. Nevertheless, some ions will always be present, introduced to the system from the polymer, the nanomaterials and other impurities, the contact with air and labware and due to the non-perfect deionisation of water. These free ions contribute to the electrical conductivity of nanocomposite hydrogels by ionic conduction. However, the mobility of ions in hydrogels is restricted by the porous network of the polymer. The ion mobility inside a hydrogel depends on the concentration and charge of the polymer and the pore size and distribution and is significantly lower than the ion mobility in an aqueous solution. The total amount of water within hydrogels can be classified into three types, according to phase transition behavior: (1) non-freezing (bound) water, in the primary hydration shell of the hydrophilic polymer chains, (2) freezing bound water, in the secondary hydration shell and (3) freezing free water, which does not interact with the polymer matrix [143], [144]. These different states of water within the hydrogel framework can be distinguished through differential scanning calorimetry (DSC) [145]. Ionic mobility is expected to be much lower in the bound water fraction [146], [147]. Therefore, the ionic conductivity is mostly affected by the free water in the hydrogel matrix. The polymer network consists of electrically insulating polymer chains. The conduction mechanisms through it are expected to be equivalent to conduction through non-crystalline dielectric solids. Lastly, the nanomaterials studied in this review are embedded in hydrogels because of their metallic conduction properties. When they are present in a critically high concentration, they form a percolating network through the hydrogel

allowing for a steep increase in the system's conductivity. The conduction mechanism through a percolating network of conductive nanomaterials is ohmic conduction [131].

The water content of nanocomposite hydrogels directly affects their electrical conductivity. Lower water contents decrease ionic conduction by densifying the polymer network, leading to smaller pores and lower ion mobility. At the same time, a decrease in water content with the subsequent densification of the hydrogel, increases the volume fraction of the nanomaterials and thus the chances of forming a percolating network. Ferris and Panhuis measured the electrical conductivity of a gellan gum hydrogel embedded with multi-walled CNTs and a control gellan gum hydrogel (without nanomaterials), upon drying. They inserted the hydrogels between two electrodes, put it on a mass balance and placed all the system in a heated chamber, with the temperature increasing from 20 to 60 °C, over time. The device allowed for simultaneous mass and conductivity measurements. The initial conductivity for both hydrogels was  $10^{-3}$  S/m. At 95 % water content the conductivity of the nanocomposite hydrogel increased to  $10^{-2}$  S/m while the conductivity of the control hydrogel decreased dramatically to  $10^{-5}$  S/m (**Figure 1.13**) [128]. The initial hydrogel conductivity can be attributed to ionic conduction, while the differences in the behaviours for decreasing water content can be explained on the basis of electrical percolation of the CNTs and ion mobility restriction in the control hydrogel.

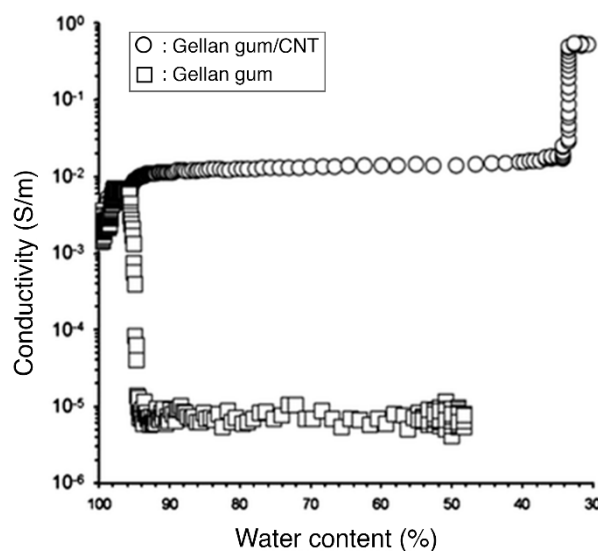


**Figure 1.13** - Conductivity of gellan gum hydrogels with CNTs (circles) and without (squares), over decreasing water content. The loss of water content densifies the polymer network restricting ion mobility but simultaneously increases the nanomaterial volume fraction and leads to percolation. Adapted from ref. [128].

### 1.13 Measuring electrical properties

The electrical conductivity of hydrogels can be measured from the relation between voltage and current. First, the sample hydrogel is placed between two electrodes. Then, an electrical stimulus is applied to the electrodes (known voltage or current) and the response of the system is observed. The electrical response of the system depends on the transport of charges within the material and the transfer of electrons to or from the atoms and ions of the sample at the electrode-sample interface. The total current flow will depend on the resistance of the sample and the reaction rates at the interface between the sample and electrodes. In addition, the electrical response will be affected by impurities on the sample and electrodes, possibly leading to oxidation or reduction reactions. Typically, these measures apply low voltages to the sample (50 mV to 1 V). Care has to be taken to not apply

over 1.23 V for an extended time period, which would lead to electrolysis of water molecules (oxidation, release of oxygen) and affect the results.

### 1.13.1 Two-point and four-point probe methods

The measuring device can be connected to the electrodes via a two-point or four-point system. Two-point probes are easier to handle but also measure the contact resistance, *i.e.* the resistance at the interface between the cables and the electrodes (**Figure 1.14 A**). A four-point system measures directly the resistance of the sample. The electrical stimulus is applied through two probes and the sample's response is measured through the two other probes, avoiding the contact resistance (**Figure 1.14 B**). However, in most cases of nanocomposite hydrogels, the sample's resistance is several orders of magnitude higher than the contact resistance, so the choice of a two- or four-point probe is of negligible impact.

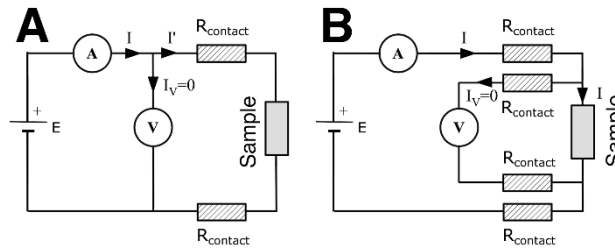


**Figure 1.14** - Circuit diagrams of (A) two-point probe and (B) four-point probe method.

#### 1.13.1.1 Ohmmeter

An ohmmeter calculates the resistance  $R$  of a sample by applying a fixed DC current of few mA and measuring the corresponding voltage.

$$R = \frac{V}{I} \quad (1.13)$$

where  $V$  is the measured tension and  $I$  the applied current.

For an isotropic conductivity and a homogenous electric field, and with a simple sample geometry, the conductivity is calculated as the reciprocal of resistivity.

$$\left. \begin{aligned} R &= \rho \frac{l}{A} \\ \sigma &= \frac{1}{\rho} \end{aligned} \right\} \Rightarrow \sigma = \frac{l}{A} \cdot \frac{1}{R} \quad (1.14)$$

where  $\rho$  the resistivity,  $l$  the length and  $A$  the surface of the sample

DC conductivity measurement with a multimeter is the most simple and straightforward way to measure the conductivity of a sample hydrogel. However, it doesn't provide any information about capacitive and inductive behaviour. Most works reviewed here use this measurement, since they only seek to demonstrate an increased electrical conductivity through the incorporation of nanomaterials.

#### 1.13.1.2 Chronoamperometry

In chronoamperometry, the electrical stimulus applied to the electrodes is a square-wave potential. The electrical response of the system is the current as a function of time  $I(t)$ . By applying a step potential difference on a hydrogel sample, a peak of current will be measured. This peak corresponds

to the sum of the conduction current and the polarisation current, *i.e.* the orientation of water and other polar molecules in the direction of the electric field. The polarisation current exponentially decays and the current then reaches a plateau corresponding to the conduction current, *i.e.* the movement of ions and electrons within the hydrogel. When the step voltage is removed, the measured current may briefly exhibit a reverse peak, before decaying to zero. This reverse current is the result of the return of the electric dipoles (polar molecules) to a random orientation, after the removal of the electric field (**Figure 1.15**).

From equation (1.11), we have  $\sigma = \frac{J}{E}$  and for a simple geometry with the normal of the electric field perpendicular to it

$$\sigma = \frac{J}{E} = \frac{I/A}{V/l} = \frac{I \cdot l}{V \cdot A} \quad (1.15)$$

where  $V$  is the tension,  $I$  the current,  $l$  the length and  $A$  the surface of the sample hydrogel.

To calculate the conductivity, the conduction current (the time-invariant part of the  $I(t)$  graph) is inserted into equation (1.15). Chronoamperometry also gives additional info about the sample's RC time constant.

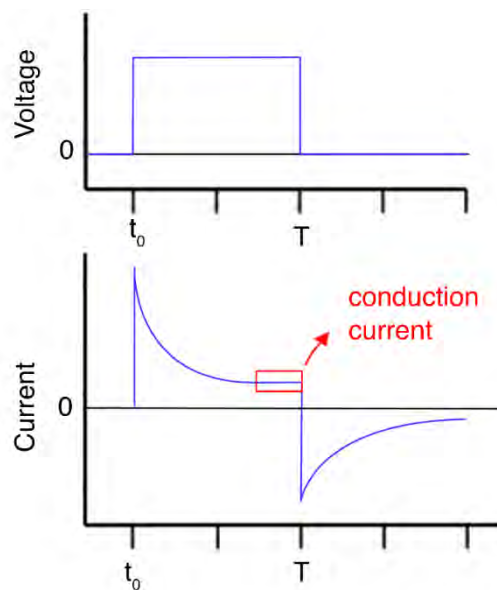


**Figure 1.15** - Double-pulsed, controlled potential chronoamperometry. A square wave voltage initially causes a current peak, due to polarisation. The current then exponentially decays to the conduction current. The removal of the voltage may cause a brief reversed current peak.

Guillet *et al.* studied the conduction mechanism of Agarose/CNTs nanocomposite hydrogels through chronoamperometry. They applied increasing voltage from 50 mV to 1.3 V and measured the current passing through the sample, *vs* time. By plotting the conduction current density *vs* the electric field (applied voltage divided by sample thickness) and comparing the graph with known equations of conduction mechanisms, they suggested that plain agarose hydrogels are dominated by an ionic conduction type, while nanocomposite hydrogels with CNTs most possibly exhibit a Poole-Frenkel conduction type [131].

## 1.13.2 Alternating Current

### 1.13.2.1 Impedance spectroscopy

In impedance spectroscopy, the electrical stimulus applied to the sample is a sinusoidal alternating voltage, over a range of frequencies (commonly between 0.1 and  $10^6$  Hz). The measured response of the system is the resulting current and the phase difference between signal and response [148]. For an electrical stimulus of  $v(t)=V_m \cdot \sin(\omega t)$ , with a frequency  $f=\omega/2\pi$ , the resulting current  $i(t)=I_m \cdot \sin(\omega t+\theta)$  is measured (for a linear behaviour). Here,  $\theta$  is the phase shift between the voltage and the current. It is equal to 0 for a purely resistive behaviour,  $\pi/2$  for a purely inductive and  $-\pi/2$  for purely capacitive. The conductive nanomaterials incorporated in hydrogels have a metallic conductivity, therefore phase shifts close to 0 degrees. In plain hydrogels, ionic conductivity dominates and the values of  $\theta$  are near -30 to -40 degrees.

From the amplitude and phase shift measurement, a complex impedance  $Z$  is deduced with  $Z'$  the real part (resistance) and  $Z''$  the imaginary part (reactance). Impedance expands the notion of resistance by taking reactance into account. While resistance leads to the dissipation of energy as heat, reactance stores energy and releases it after  $\pi/2$ . Capacitive reactance stores energy in the form of an electric field and inductive reactance stores energy in the form of a magnetic field.

The analysis of impedance spectroscopy data provides information about the electrical properties of the sample hydrogel. Different excitation frequencies will elicit different electrical responses from the material. For example, in low frequencies, electrons, ions and dipoles of different sizes will all move responding to the electric field. In higher frequencies ions and bigger dipoles do not have the time to move; only electrons respond to a rapidly changing electric field. Plotting the impedance data into a Nyquist plot (**Figure 1.16**) allows the visualization of electrical phenomena and the modelling of an equivalent circuit, *i.e.* a simplified theoretical model that retains all the electrical characteristics of the original, complex circuit [149]. The y-axis represents the negative of the imaginary part and the x-axis represents the real part of the complex impedance. The intersection of the curve with the x-axis designates the resistance of the hydrogel [150]. The conductivity is then calculated from equation (1.14).

In the case of nanocomposite hydrogels, the equivalent circuit seems to include a Warburg impedance element in series with a resistor [131], [151], [152]. The Warburg element models diffusion processes and is recognizable by a straight line with 45° slope, at low frequencies (figure 12B).

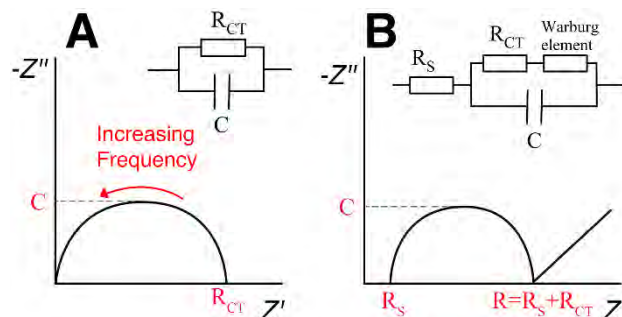


**Figure 1.16** - Impedance spectroscopy results can be visualised with a Nyquist plot. (A) Typical Nyquist plot of simple RC circuit with one resistor and one capacitor in parallel. (B) Typical Nyquist plot of resistance in series with the parallel combination of a capacitance with a resistance and a Warburg diffusion element (also known as Randles circuit).

Warren *et al.* used impedance spectroscopy to investigate the percolation behaviour of CNT-loaded gellan gum hydrogels [151]. They prepared the hydrogels by dissolving gellan gum powder into warm (80 °C) deionised water, dispersing CNTs in the solution through sonolysis and then cross-linking with  $\text{Ca}^{2+}$  ions. By varying the length of the hydrogel, they were able to distinguish between the sample's resistance and the contact resistance: the sample's resistance increases linearly with length, while the contact resistance remains invariable.

$$R_{measured} = \frac{1}{\sigma_{sample}} \frac{l}{A} + R_{contact} \quad (16)$$

Where  $\sigma_{sample}$  the conductivity of the sample (hydrogel),  $l$  the length and  $A$  the cross section.

Three different carbon nanomaterials were employed, single-wall CNTs, multi-wall CNTs and vapour-grown carbon nanofiber. The impedance analysis for all three carbon nanomaterials in a 0.9 % v/v concentration showed a similar modest increase in conductivity (final value 0.12 S/m; the original conductivity of gellan gum is not mentioned here but is reported as  $10^{-3}$  S/m in previous studies [128]). This concentration was deemed too low to have an effect on the conduction mechanism. The carbon filler concentration was further increased by selectively removing a part of the water content of the hydrogel, at a rate of 0.43 g/h, in a controlled temperature and humidity chamber. It was reported that at MWCNT concentration 1.4 % v/v the impedance was no longer dependent on frequency and the Warburg coefficient value rapidly decreased, witnessing the formation of a percolating network and the transition between transport dominated by ions to transport dominated by electrons [151].

#### 1.13.2.2 Conductivity meter

Another way to measure the electrical conductivity of hydrogels is the use of a conductivity meter with an adequate probe. These devices are optimized for fast conductivity measurements of aqueous, ionic solutions but can also work in the case of hydrogels. In conductivity meters, the electrical stimulus applied is a single-frequency alternating current (or voltage) and the produced voltage (or current) is read. The conductivity meters are calibrated with solutions of known conductivity and their output is directly the conductivity value. Koppes *et al.* used a conductivity meter to evaluate changes in conductivity induced by the incorporation of single-wall CNTs into collagen type I hydrogels. For the measurements, they submerged the conductivity meter probe in the hydrogel precursor solution, cross-linked the hydrogel and then measured the conductivity. A concentration of 0.01 % w/w of CNT increased the conductivity of collagen hydrogels from 1.4 to 2.4 S/m [153].

#### 1.14 Overview

In the current study, we evaluated the nanocomposite hydrogels and used them as platforms for transdermal drug delivery. The most important properties studied were their absorption capacity, to function as drug reservoirs, and electrical conductivity, to serve as electrodes for the application of electrical pulses on the skin. We set up an experimental configuration that allowed the monitoring of the current and voltage of the system, during electroporation conditions. Then, these measurements were used to refine a numerical model of the system. Lastly, we loaded the hydrogels with fluorescent molecules and made a series of delivery experiments, for different pulse amplitudes. **Figure 1.17** presents a visual summary of the experimental work.



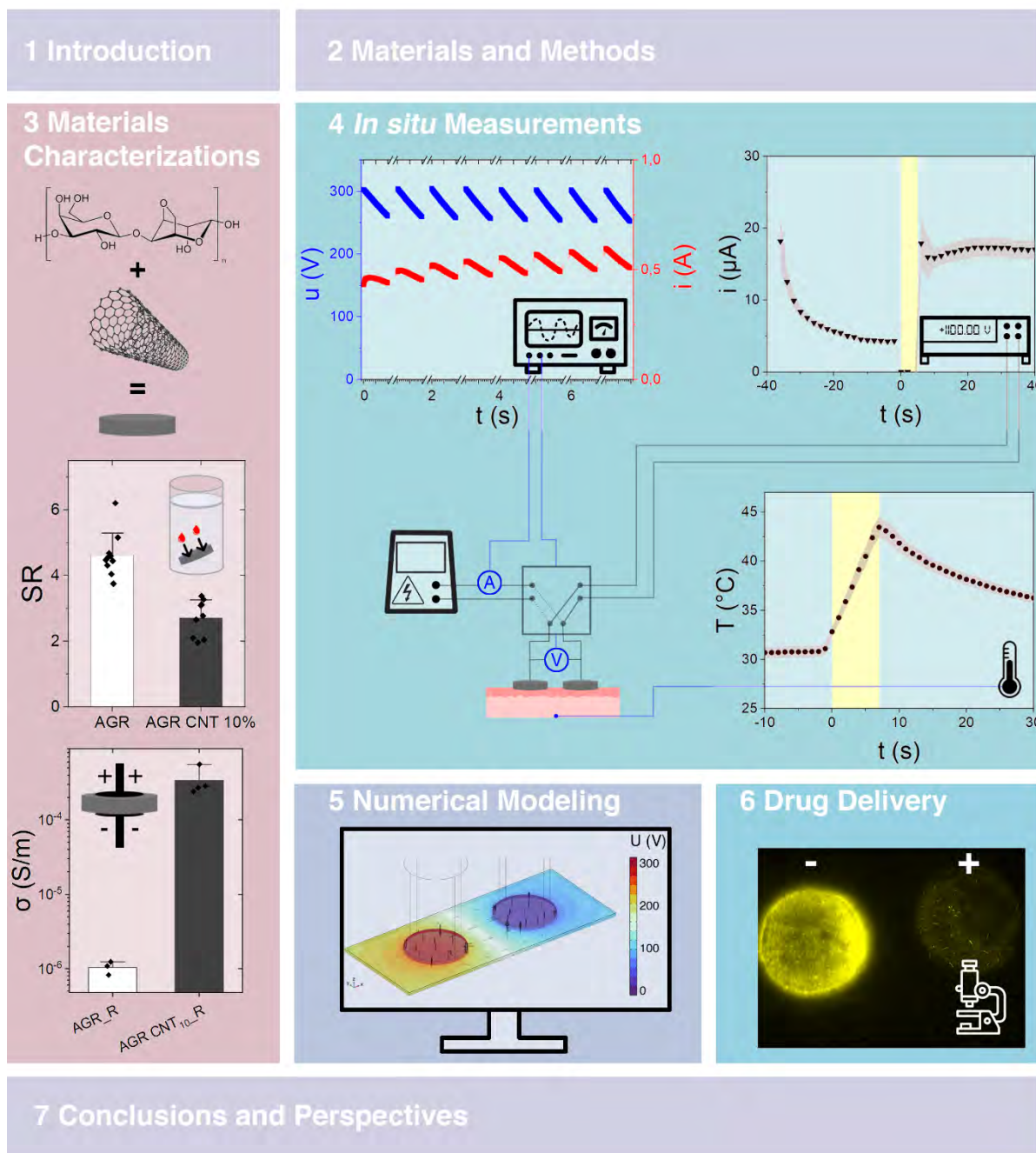


**Figure 1.17** – Overview of experimental work and manuscript organization. The 1<sup>st</sup> chapter introduces the key concepts, focusing on skin electroporation and electrically conductive hydrogels. The 2<sup>nd</sup> chapter presents the experimental conditions and protocols followed. The 3<sup>rd</sup> chapter concentrates on the nanocomposite hydrogels and studies their absorption capacity (Swelling Ratio,  $SR$ ) and electrical conductivity ( $\sigma$ ). In the 4<sup>th</sup> chapter we measure the voltage, current and temperature of the drug delivery system during electroporation. The 5<sup>th</sup> chapter describes a numerical model of the drug delivery system. The 6<sup>th</sup> chapter contains fluorescent molecule delivery through skin electroporation. The 7<sup>th</sup> chapter summarizes the most important findings.



## 2 Materials and methods

<b>2</b>	<b>MATERIALS AND METHODS</b>	<b>60</b>
2.1	MATERIALS CHARACTERIZATIONS	60
2.1.1	CNT synthesis and extraction	60
2.1.2	Preparation of nanocomposite hydrogels	60
2.1.3	Drying and swelling	62
2.1.4	Preparation of alginate/chitosan hydrogels	64
2.1.5	DC conductivity	65
2.1.6	CNT conductivity in aqueous suspension	67
2.1.7	Impedance spectroscopy	68
2.1.8	Electrical conductivity of hydrogels with ionic solutions	69
2.1.9	Hydrogel nomenclature (sample naming conventions)	69
2.2	SKIN MODELS	70
2.2.1	Mouse skin model	71
2.2.2	Reconstructed human epidermis	71
2.3	IN SITU MEASUREMENTS	72
2.3.1	In-situ electrical response	72
2.3.2	Temperature monitoring	74
2.4	FEM SIMULATIONS	74
2.5	DRUG DELIVERY	75
2.5.1	Drug models	75
2.5.2	Fluorescence microscopy	76
2.6	STATISTICAL TREATMENT	77

### 2.1 Materials characterizations

#### 2.1.1 CNT synthesis and extraction

The double-walled Carbon Nanotubes (DWCNTs) employed were prepared through catalytic chemical vapor deposition. The catalyst was  $\text{Mg}_{0.99}(\text{Co}_{3/4}\text{Mo}_{1/4})_{0.01}\text{O}$ . During the synthesis, a flux of methane and hydrogel gas was decomposed at high temperature (1000 °C). The CNTs started to grow on the metal nanoparticles (Co:Mo) generated *in situ* on the oxide support. At the end of the reaction a composite powder was obtained which contained around 11 % w/w CNTs [154]. A unique batch was prepared at the beginning of the PhD work to ensure that the DWCNTs would be strictly the same for all experiments. The CNTs were then extracted from the composite powder through acid dissolution. An excess of HCl was added on the powder, dissolving the catalyst and the support while leaving the CNTs intact. The suspension was then filtered through a cellulose nitrate membrane and washed with DI water until neutrality (pH 6-7, the pH of the suspension was monitored with pH paper. The CNTs were recovered wet.

#### 2.1.2 Preparation of nanocomposite hydrogels

Nanocomposite hydrogels were prepared by mixing a suspension of Carbon Nanotubes (CNTs) in deionised (DI) water with a solution of agarose in DI water (**Figure 2.1**). First, 1.25 g of agarose (Sigma-Aldrich, CAS: 9012-36-6) were dissolved into 25 ml of DI water at 90 °C, under magnetic stirring, while 125 mg of lab-produced double-wall CNTs were suspended into another 25 ml of DI water through 1 hour of probe sonication (Vibra Cell, Bioblock scientific, 12 mm diameter, 1s ON/1s OFF, 30 % amplitude, 750 W max power) and with the addition of 12.5 mg of carboxymethyl cellulose (Ultra-low

viscosity, Fluka, CAS: 9004-32-4), used as a dispersant. CNTs were used in wet form to ensure a better redispersion in DI water. The agarose solution and CNT suspension were then mixed together through 20 min of dispersion with a mini disperser (IKA ultra-turrax T10, 8000 rpm) and simultaneous magnetic stirring, before being cast into silicone molds of 10 mm diameter and 2 mm height, and left to cool down for 5-10 min. at room temperature (**Figure 2.2**). When cooled down, the agarose chains formed a solid hydrogel with water. A preselection step discarded the hydrogels with dimensions  $h < 1.8$  mm and  $h > 2.2$  mm. The nanocomposite hydrogels were then stored into DI water at 4 °C (in the fridge).

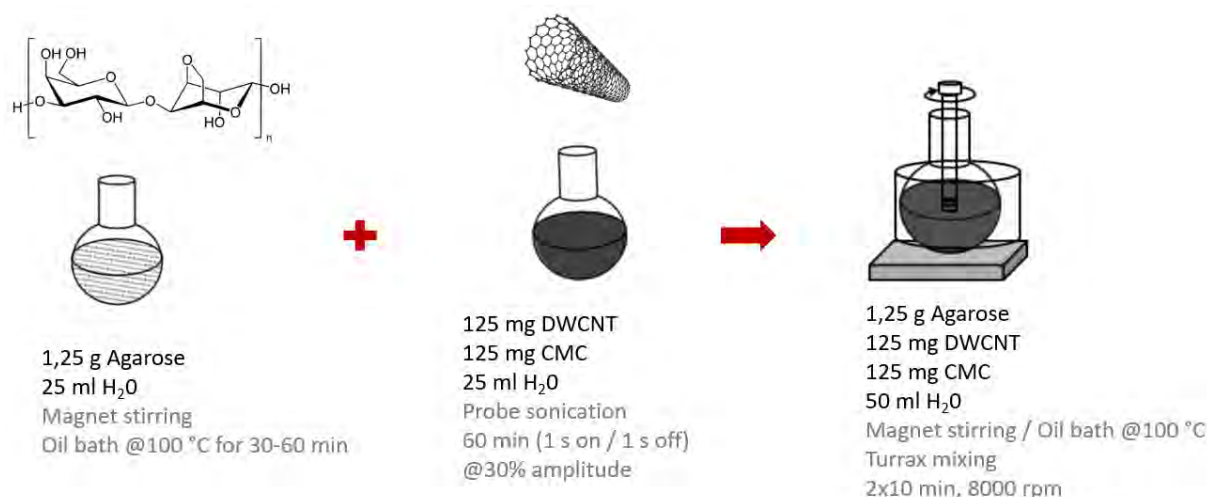


**Figure 2.1** - Preparation of nanocomposite hydrogels

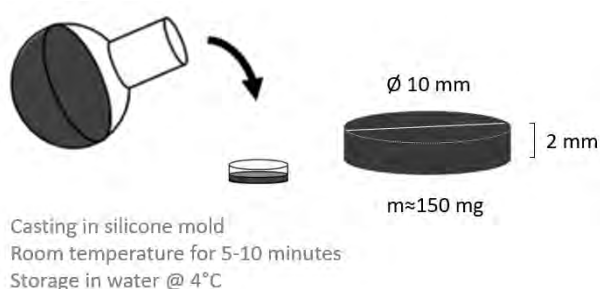


**Figure 2.2** - Mold casting and dimensions of hydrogels

The composition of the nanocomposite hydrogels is presented in the following table (**Table 2.1**). For the material characterization studies, hydrogels with different compositions were also prepared.

**Table 2.1** – Nanocomposite hydrogels composition

	H <sub>2</sub> O	AGR	CNT	CMC
<b>Mass (mg)</b>	49900	1250	125	12.5
<b>Concentration (mg/ml)</b>		25	2.5	0.25
<b>Density (g/cm<sup>3</sup>)</b>	0.998	1.64	1.8	1.6
<b>Concentration (% w/w)</b>	97.295	2.437	0.244	0.024
<b>Concentration (% v/v)</b>	98.349	1.499	0.137	0.015

### 2.1.3 Drying and swelling

Agarose hydrogels dry rapidly in air at room temperature. They could then be placed again in an aqueous solution and recovered part of their initial volume (**Figure 2.3**). We exploited this property to use them as drug reservoirs. The fresh hydrogels were air-dried at 30 °C for 48 h, then placed in an aqueous solution with a molecule of interest for 24 h - 48 h.

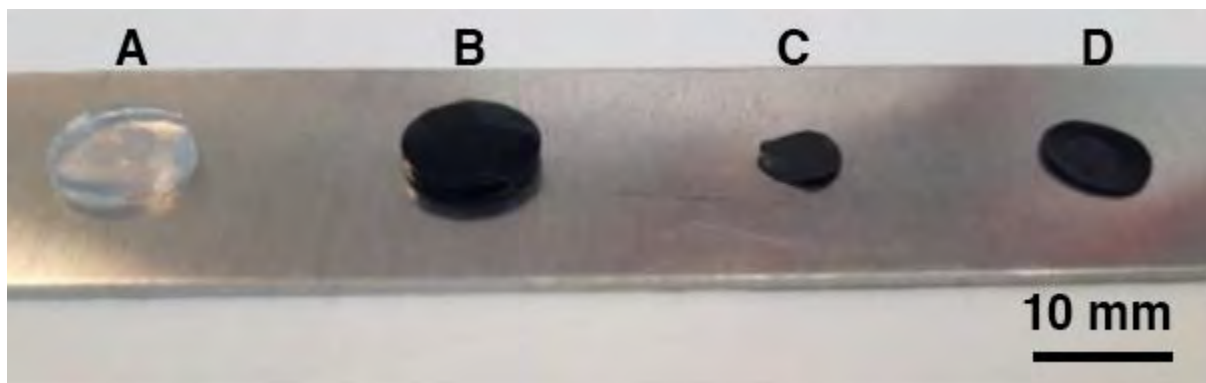


**Figure 2.3** – Prepared agarose hydrogels. (A) Fresh agarose hydrogels, (B) fresh nanocomposite hydrogel, (C) dry nanocomposite hydrogel, after 48 h at 30 °C, (D) swollen nanocomposite hydrogel, after 24 h in water.

For the material characterization studies, we investigated the influence of different processing and drying methods on the swelling ratio and electrical conductivity of the hydrogels.

#### 2.1.3.1 Air drying

Air drying was the simplest way of drying the hydrogels. Fresh hydrogels that were stored in DI water at 4 °C were briefly dried on a paper towel to remove excess water from both sides. They were then placed on a metallic (stainless steel) plate, and another smaller, flat, metal bar was placed on top of them. The metal bar on top ensured that the hydrogels stayed flat while drying, under the weight of the bar (the bar can be viewed in **Figure 2.3**). Without the bar on top, the hydrogels tended to curve while drying. The metal tray with the hydrogels and the metal bar(s) was then placed in a lab oven at 30 °C for 48 h. The oven contained silica gel desiccants to keep the humidity to a minimum and had a small hole for air circulation, but no mechanical ventilation. The volume of the oven was about 50 L.

#### 2.1.3.2 Freezing, then air-drying

In this processing method, fresh hydrogels were removed from water, briefly dried on a paper towel and then placed in a commercial freezer (-20 °C), on a plastic support (polystyrene) for at least 24 h. The frozen hydrogels were then removed from the freezer and air-dried as described in paragraph **2.1.3.1**.

#### 2.1.3.3 Freeze-drying (Lyophilization)

For the lyophilization process, hydrogels were removed from water, briefly dried on a paper towel and then placed in a commercial freezer (-20 °C), within a freeze-drying vial, for 24 h. The freeze-drying vials were then connected to the freeze-dryer (Alpha 2-4, Martin Christ) and the frozen water was sublimated at low pressure (around 1 Pa) and temperature (condenser at -85 °C) conditions for 48 h.

#### 2.1.3.4 Directional freeze casting, followed by freeze-drying

In this method, the goal was to create uni-directional macropores in the hydrogel. A collaboration with the PPB team (CIRIMAT) allowed us to test this processing method on our hydrogels (ENSIACET department of CIRIMAT). The directional freeze-casting procedure is described in detail in refs. [155], [156]. Briefly, the hydrogel precursor solution (or suspension) was cast into a cylindrical polymer mold, which was brought into contact with a cold source only from one side (**Figure 2.4**). This created ice crystals that expanded into the vertical direction from the cold source (-10 °C). The hydrogels were then freeze-dried. The oriented ice-crystals were sublimated leaving an aerogel with oriented macropores (**Figure 2.5**).

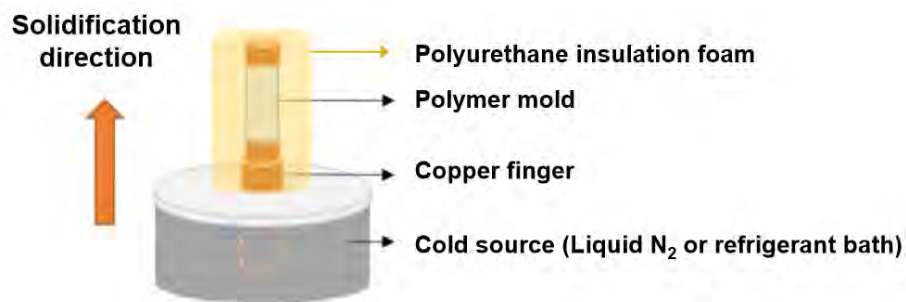


**Figure 2.4** – Scheme of the custom-made freeze-casting configuration [155].



**Figure 2.5** – Directional freeze-cast aerogels. Plain agarose (A) and nanocomposite (B) aerogel.

**Table 2.2** – Summary of processing and drying methods.

Drying method name	Procedure
Air drying	48 h @30 °C
Freezing, then air-drying	24 h @-20 °C then 48 h @30 °C
Freeze-drying (Lyophilization)	24 h @-20 °C then 48 h @1 Pa
Directional freeze casting, followed by freeze-drying	Few minutes @-10 °C from one direction, then 48 h @1 Pa

### 2.1.3.5 Swelling ratio

The swelling ratio corresponds to the ability of the hydrogel to absorb water. To calculate it, we measured the dry mass of the hydrogel,  $m_{dry}$ , after each of the drying / processing methods. The hydrogels were then placed into DI water for 24-48 h, and absorbed part of it. We then measured the mass of the hydrogel swollen with water,  $m_{swollen}$ . The swelling ratio is equal to:

$$\text{swelling ratio} = SR = \frac{m_{\text{absorbed water}}}{m_{\text{dry}}} = \frac{m_{\text{reswollen}} - m_{\text{dry}}}{m_{\text{dry}}} \left[ \frac{\text{mg water}}{\text{mg dry mass}} \right] \quad (2.1)$$

It can also be expressed as a percentage,  $SR\%$ , by multiplying SR by 100 %.

Special care has to be taken for the measurement of the absorbed mass of water through  $m_{swollen}$ . The mass should not include water on the surface of the hydrogel, but only water absorbed in it. A paper towel was used to dry the hydrogels before weighing. However, the dry absorbent towel tended to absorb water from the interior of the hydrogel too. Typical masses for dry hydrogels were around 5 mg and *ca.* 20 mg for swollen. Subsequently few water drops on the surface of the hydrogel, or some mg of water from the interior absorbed by the paper towel can make a big difference when measuring the swelling ratio. Our approach was to use a wet paper towel to wipe away the water from the surface of the hydrogel. In this way, the paper towel did not absorb important amounts of water from the interior of the hydrogel while still effectively removing the surface water.

### 2.1.3.6 Drying and swelling kinetics

For the drying kinetics, fresh hydrogels were placed in a lab oven at fixed temperature (ranging from 30 to 70 °C). For the kinetics experiments, hydrogels were removed from the oven briefly and their mass was measured on a precision scale, at fixed time intervals. The hydrogels were then returned to the oven for further drying.

For the swelling kinetics, dry hydrogels were placed in a DI water bath at ambient temperature. The hydrogels were removed from the water, the surface water was absorbed by a wet paper towel (see **paragraph 2.1.3.5** for details) and their mass was measured, at fixed time intervals.

### 2.1.4 Preparation of alginate/chitosan hydrogels

Alginate/chitosan hydrogels were prepared following an established protocol of the CREPEC research team at Polytechnique Montréal. Chitosan was dissolved into an acetic acid 0.1 M solution, at a concentration of 1 % w/w, through vortexing (3200 rpm) and ultrasonic bath until dissolution (10 – 20 minutes). Alginate was dissolved into warm (~60 °C) DI water at a concentration of 2 % w/w, through vortexing (3200 rpm) and ultrasonic bath until dissolution (10 – 20 minutes). The pH of the dissolved chitosan solution was then increased with the addition of 0.18 g of sodium bicarbonate to 4 ml of the chitosan/acetic acid solution. The chitosan and agarose solutions were mixed in a one-to-one ratio with the aid of an ultrasonic bath, for a total volume of 1.5 ml. To form the hydrogel, 150 µl of genipin 0.15 % w/w solution were added to chemically cross-link the chitosan polymer. This hydrogel precursor solution was then poured in the same mold we used for the agarose hydrogels (small cylindrical discs of 10-mm diameter and 2-mm height, **Figure 2.7**).

The hydrogel was left to cross-link for two days, in a humidity-saturated environment, at ambient temperature. Then, an excess of a 4 % w/w calcium chloride solution was poured onto the hydrogels, physically cross-linking the alginate network. The polymer concentrations in the hydrogels were 1 % w/w alginate and 0.5 % w/w chitosan. The hydrogels were stored in calcium chloride (4 % w/w) solution in the fridge (4 °C).

For the nanocomposite alginate/chitosan/CNT hydrogels, the same procedure was followed but with some modifications. CNTs were suspended in DI water with the aid of CMC (10 wt. % of CNT mass) and probe sonication (Vibra Cell, Bioblock scientific, 12 mm diameter, 1s ON/1s OFF, 30 % amplitude, 750 W max power). The hydrogel precursor solutions with chitosan and alginate were made with higher concentrations, chitosan at 1.5 % w/w and alginate at 3 % w/w. Then, the two solutions and the CNT suspension were mixed in a 1:1:1 ratio and homogenized with a vortex shaker (3200 rpm) and ultrasonic bath (10 minutes). The final concentrations of the hydrogels were 1 % w/w alginate, 0.5 % w/w chitosan and CNT content ranging from 0 to 0.25 % w/w (**Figure 2.6** and **Figure 2.7**).

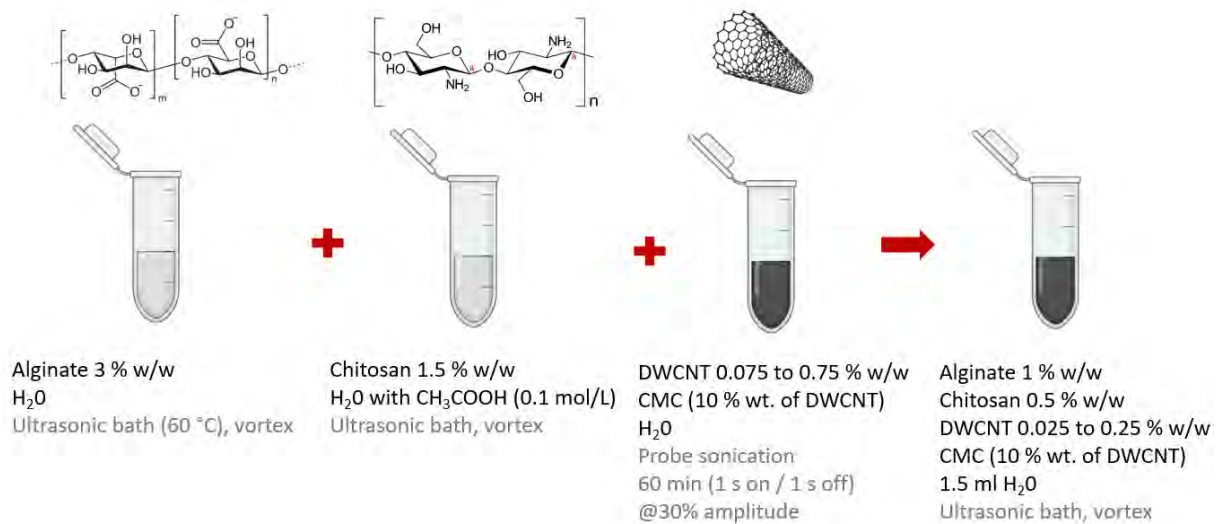


**Figure 2.6** – Preparation of alginate/chitosan nanocomposite hydrogels.

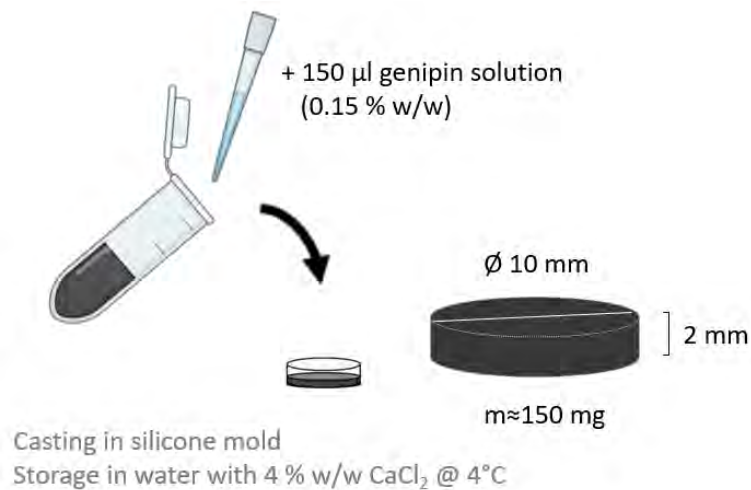


**Figure 2.7** – Mold casting and dimensions of alginate/chitosan nanocomposite hydrogels.

### 2.1.5 DC conductivity

The DC electrical conductivity of the samples was measured with a source-measuring unit (SMU, Keithley 2410, **Figure 2.9**, A). A DC voltage (ranging from 0.5 to 1V) was applied to the hydrogel during 240 s. The resulting electric current was read by the SMU every 5 s (**Figure 2.8**).

The conductivity was calculated from the average of the last ten points (last 50 s) of the  $I(t)$  curve, from the following equation:



$$\sigma = \frac{J}{E} = \frac{I/A}{V/l} = \frac{I \cdot e}{V \cdot S} \quad (2.2)$$

where  $V$  is the voltage,  $I$  the current,  $e$  the length and  $S$  the surface of the sample hydrogel.

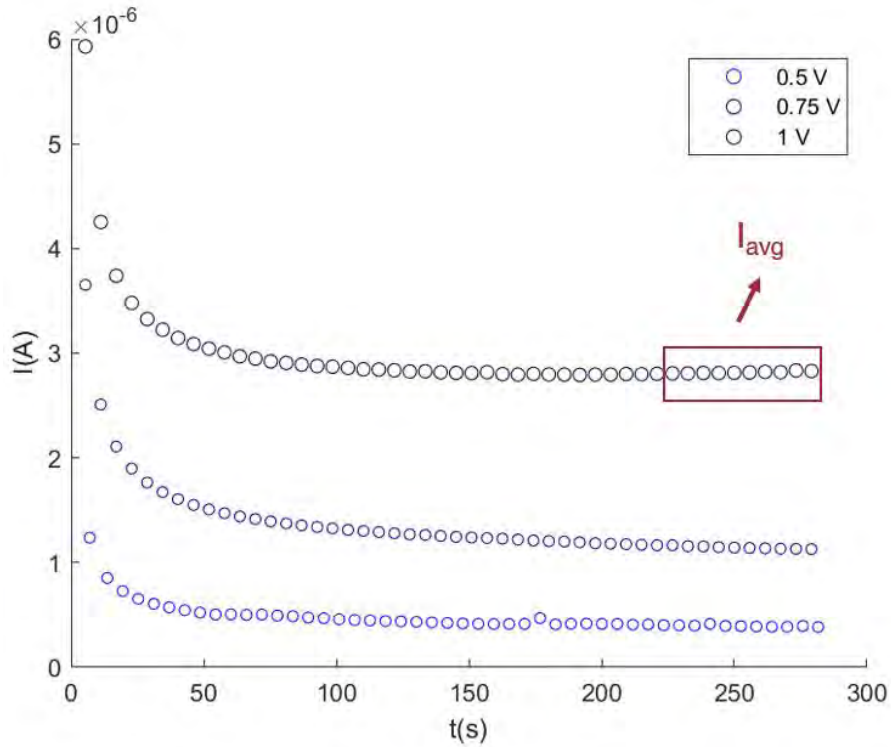


**Figure 2.8** – Current – time curve for the application of DC voltages from 0.5 to 1 V. The last 10 points of the curve were used to calculate the conduction current.

The samples were connected to the source-measuring unit through a 4-point probe configuration. The samples were placed inside a custom-made DC measurement cell (**Figure 2.9**, B and C). The cell ensured electrical contact during the measurement through a spring-like electrode and minimised water evaporation. All measures were conducted with controlled temperature (24 °C). The SMU was controlled through computer software (LabTracer, Tektronix). Each sample was measured for three different voltages, with a pause of two minutes between each measurement. Total measuring time was 16-20 min.

Within this timeframe the hydrogels generally shrank by 5-30 %, due to water evaporation and mechanical pressure by the spring-like electrode. We took this into account for the conductivity calculations, by measuring the hydrogel thickness before and after the experiment. The thickness used for each voltage was as follows: 1<sup>st</sup> voltage (0.5 V), thickness =  $e_0$ ; 2<sup>nd</sup> voltage (0.75 V), thickness =  $(e_0 - e_f)/2$ ; 3<sup>rd</sup> voltage (1 V), thickness =  $e_f$

Where  $e_0$  the hydrogel thickness at the beginning of the experiment and  $e_f$  the hydrogel thickness at the end.



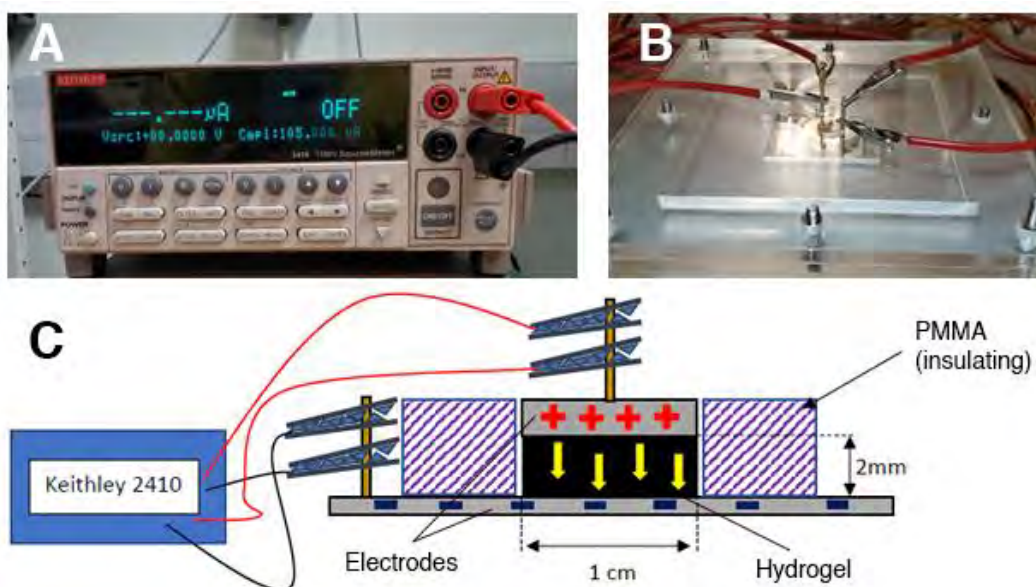


**Figure 2.9** – DC conductivity measurement setup. (A) The Keithley 2410 source-measuring unit. (B) the 4-point configuration and the custom-made measurement cell. (C) Scheme of DC conductivity measurement setup.

### 2.1.6 CNT conductivity in aqueous suspension

We measured the conductivity of CNT suspensions in DI water. Suspensions with concentrations ranging from 2.5 to 10 mg/ml were diluted down to concentrations of 0.01 mg/ml. The initial (mother) suspensions were dispersed through 20 minutes of probe sonication (12 mm diameter, 1s ON/1s OFF, 30 % amplitude). The suspensions were placed in an ice bath to prevent overheating. Subsequent suspensions were prepared by diluting the mother suspension, followed by 5 min ultrasonic bath.

The conductivity of the suspensions was measured with a conductometer (SevenExcellence Multiparameter conductivity meter, Mettler Toledo) and a graphite 4-point electrode with measuring capacity from 0.001 to 100 S/m (Mettler Toledo, **Figure 2.10**). The conductivity meter was calibrated with a commercial solution of fixed conductivity at  $8.4 \times 10^{-3}$  S/m. The volume used for the conductivity measurement was 4 ml. A 2 min ultrasonic bath and manual shaking preceded each conductivity measurement, to minimize CNT precipitation. All measurements were performed at ambient temperature, *ca.* 21 °C.

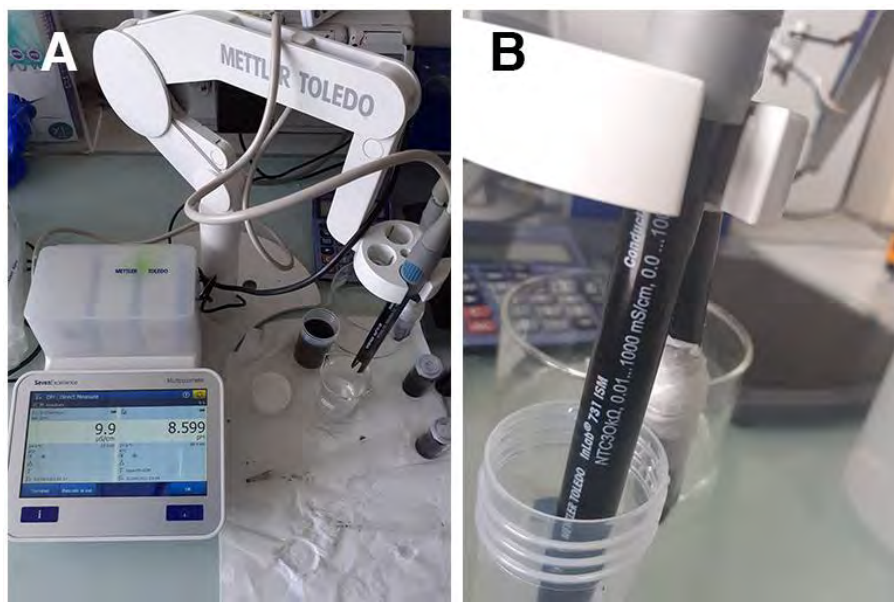


**Figure 2.10** – CNT conductivity in aqueous suspension setup. (A) Conductivity meter (B) Conductivity probe.

### 2.1.7 Impedance spectroscopy

Electrical characterization experiments were performed with a broadband dielectric spectrometer (Alpha analyser, Novocontrol technologies) on a frequency range between 0.1 and  $10^6 \text{ s}^{-1}$ . A sinusoidal alternating voltage ranging from 0.7 to 30  $V_{\text{rms}}$  was applied to the samples and the resulting current and phase shift were measured. The temperature of the spectrometer was controlled through a cold nitrogen gas flow and an electrical resistance heater. The samples were placed in a custom-made AC measurement cell. The cell ensured constant electric contact throughout the thickness variations of the samples, with the aid of a spring. Additionally, the cell allowed for an open setting, allowing air flow and water vapor evaporation through eight slits, or a closed setting, minimising air flow and water evaporation (**Figure 2.11**).

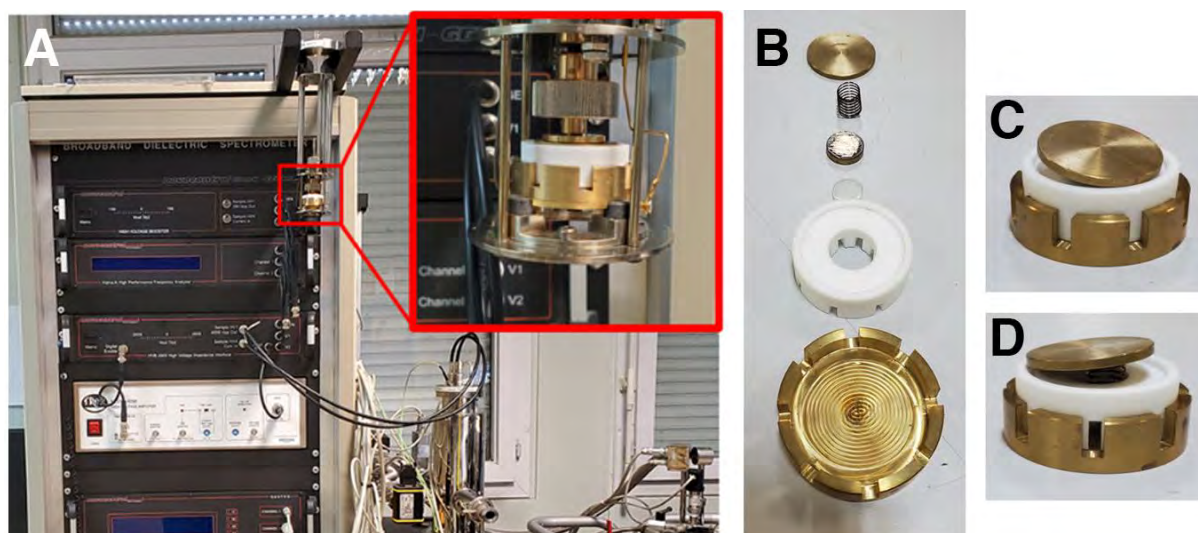


**Figure 2.11** – Impedance spectroscopy setup. (A) Broadband dielectric spectrometer with measurement cell in place. (B) AC measurement cell constituents and closed (C) and open (D) position.

### 2.1.8 Electrical conductivity of hydrogels with ionic solutions

A series of additional conductivity experiments on hydrogels with ionic solutions was made after the DC conductivity measurements revealed no differences between the solutions. We measured the conductivity of the hydrogels with an AC conductometer, through Impedance spectroscopy and with the application of a 50 V PEF.

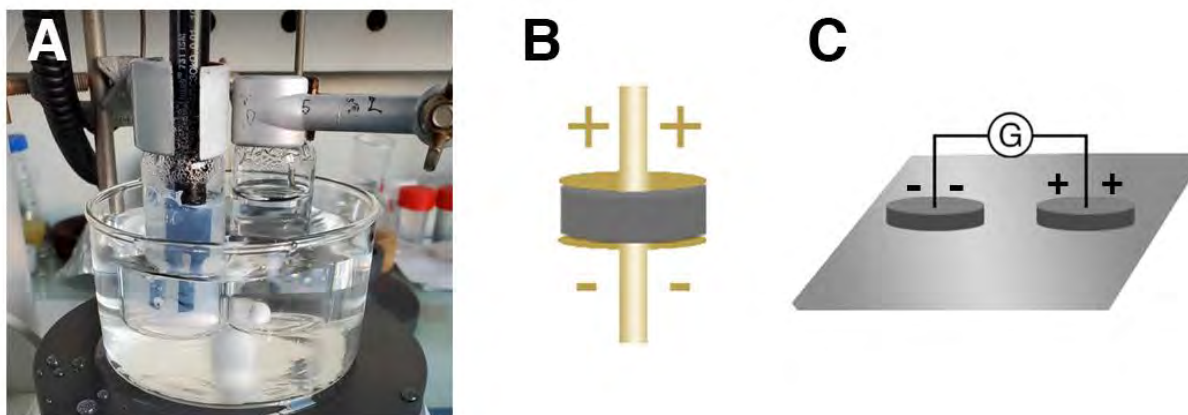


**Figure 2.12** – Electrode configurations for conductivity measurements of hydrogels with ionic solutions. (A) AC conductivity probe immersed in hydrogel. (B) Hydrogel between two flat metal electrodes. (C) Electroporation setup: two hydrogels on top of metal plate.

The AC conductometer was the same as previously described. An aqueous solution (DI water, electroporation buffer or phosphate buffer) was poured in a 15 ml glass vial and 2.5 % w/w agarose was added. The mixture was agitated with a small magnet and placed in a bath at 90 °C to solubilize the agarose. After solubilization, the solution was placed in a bath at 25 °C till hydrogel formation within the glass vial. The conductivity measurement was conducted by immersing the probe into the hydrogel. The Impedance spectroscopy was made as previously described, at 0.6  $V_{rms}$  and room temperature. For the PEF experiment, we used the electroporation device setup (**Figure 2.17**). A metal (stainless steel) plate served as an electrical contact under the hydrogels (instead of placing a mouse skin). A voltage of 50 V was applied, at room temperature. The resistance of the system was calculated as the average  $u(t)/i(t)$  during the 8 pulses.

### 2.1.9 Hydrogel nomenclature (sample naming conventions)

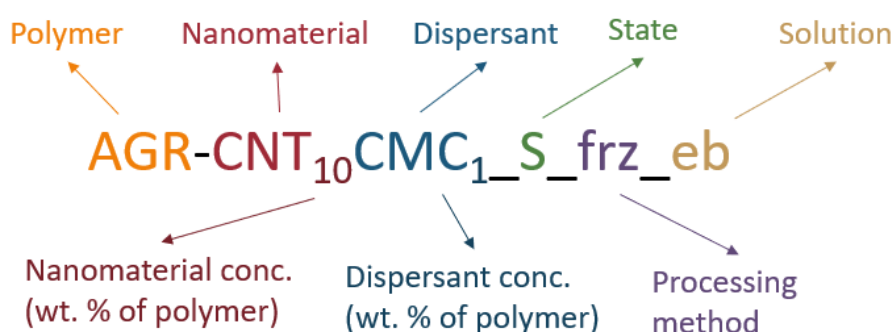
During the elaboration of the hydrogel platform for drug delivery, we investigated numerous parameters (polymer, nanomaterial, dispersant, concentration, processing methods, aqueous media) and their impact on selected properties (swelling ratio, electrical conductivity, mechanical strength). We did not investigate all possible combinations, nor did we perform all material characterizations on all samples, as this would exceed the scope of the current project. In the following table, we provide a comprehensive guide of the naming conventions employed, which are used in the chapter of materials characterizations, and **Figure 2.13** provides an example of how to read the hydrogel composition and processing methods.

**Table 2.3** – Naming conventions for prepared hydrogels

POLYMER		NANOMATERIAL		DISPERSANT	
AGR	Agarose (2.5 % w/w)	CNT	Double-wall carbon nanotubes	-	none
AL/CS	Alginate (1 % w/w) and Chitosan (0.5 % w/w)	CNT <sub>ox</sub>	Oxidized double-wall CNTs	CMC	Carboxymethyl cellulose
		8WCNT	8-wall CNTs	pDA	Polydopamine
		20WCNT <sub>ox</sub>	Oxidized 20-wall CNTs		

STATUS		PROCESSING METHOD		SOLUTION	
F	Fresh	-	Air-drying	-	Deionised water
D	Dry	lyo	Lyophilization (freeze-drying)	eb	Electroporation buffer
S	Swollen	frz	Frozen, then air- dried	pb	Phosphate buffer saline
		dir	Directional freeze-casting	cc	Calcium chloride solution (4 % w/w)



**Figure 2.13** – How to read the hydrogel naming convention: The hydrogel in this example was prepared with agarose 2.5 % w/w, double-wall carbon nanotubes 10 wt. % of polymer, carboxymethyl cellulose 1 wt. % of polymer, is in the swollen state (dried, then placed in an aqueous solution), was frozen before air-drying and has been swollen in electroporation buffer solution.

In the text, when we mention “agarose hydrogels”, or “plain agarose hydrogels” we refer to AGR and when we mention “nanocomposite hydrogels” or just “CNT” we refer to AGR-CNT<sub>10</sub>CMC<sub>1</sub> hydrogels.

## 2.2 Skin models

Two skin models were used for the drug delivery experiments: *ex vivo* mouse skin and lab-grown, human reconstructed epidermis. The vast majority of the experiments and characterizations were made with mice skin, because of availability and to be able to readily compare with the results of the previous studies in our group [157], [158]. For the electroporation experiments, the skin models were placed on top of a gauze soaked with phosphate buffer saline. The gauze served the purposes of: (1) keeping the skin humidified and viable, with an isotonic solution and (2) modeling the layers under the skin (muscle, connective tissue, interstitial fluid) and serving as an electrical contact.



### 2.2.1 Mouse skin model

Electroporation experiments were conducted on freshly-extracted, dorsal mouse skin. Two mice strains were used: female hairless SKH1 mice (Charles River, France) aged 8 to 16 weeks and weighing between 25 and 35 g, and male and female C57BL/6 mice, aged 8 to 16 weeks and weighing 20 to 30 g. With the latter, hair removal was performed two days before using a depilatory cream (Veet). The mice were anesthetized with isoflurane and euthanized prior to the skin extraction. The explanted mouse skin samples had a thickness of  $0.46 \pm 0.07$  mm. For the electrical characterization experiments, they were cut into discs with 8 - 10 mm diameter, while for the electroporation experiments, they were cut into rectangles with average dimensions  $14 \pm 1 \times 33 \pm 4$  mm. Experiments were performed 15 minutes to 2 hours after mice euthanasia and skin extraction.

### 2.2.2 Reconstructed human epidermis

The reconstructed human epidermis was produced at the IPBS lab. It was prepared by seeding a polycarbonate membrane with keratinocytes (from human donors), and growing them in a liquid growth medium. Afterwards, the keratinocytes were exposed to air from one side (forming a liquid/air interface). This initiated their differentiation to corneocytes, in a similar manner as with the healthy human skin differentiation procedure. The outer layer, which was in contact with air, formed an artificial stratum corneum with corneocytes (**Figure 2.14**).



**Figure 2.14** – Reconstructed human epidermis. From top to bottom we observe the stratum corneum (deep red), the keratinocyte layer (pink) and the polycarbonate membrane (white). Image by Geraldine Alberola (IPBS).

The diameter of the reconstructed human epidermis samples was 8 mm, matching with the average diameter of the swollen hydrogels. With the mouse skin samples, two hydrogels were placed side-by-side, 14 mm apart (center to center), on the top of the rectangular extracted mouse skin (See **Figure 2.17** for the experimental configuration). The application of the PEF, created an electric circuit with the current passing through the skin and the soaked gauze. The small size of the reconstructed epidermis samples did not allow the exact recreation of the configuration used with the mouse skin. As an alternative, we used two samples for each experiment, and the soaked gauze completed the electric circuit between the hydrogels (**Figure 2.15**).

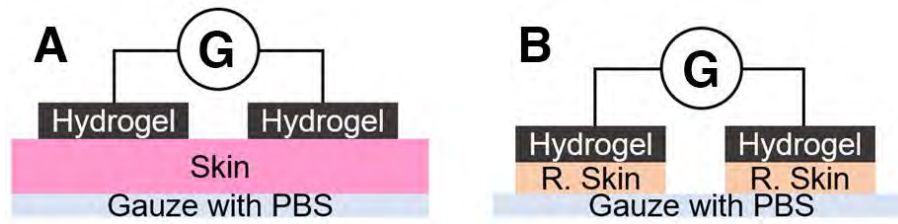


**Figure 2.15** – Drug delivery configuration for the two skin models. (A) mouse skin. (B) reconstructed human epidermis.

## 2.3 In situ measurements

### 2.3.1 In-situ electrical response

Freshly-extracted mouse skin was placed on a gauze soaked with commercial phosphate buffer saline (PBS without  $\text{Ca}^{2+}$  and  $\text{Mg}^{2+}$ , Eurobio Scientific), inside a plastic petri dish. An electrical heater under the petri dish kept the temperature of the skin at 32 °C, corresponding to the skin surface temperature of the human forearm [159]. Two hydrogel electrodes, loaded with fluorophores, were placed on the surface of the skin, 14 mm apart (center to center, see **Figure 2.17** for the experimental configuration). Stainless steel cylindrical electrical contacts were placed on top of each hydrogel and were connected to an electrical generator (ELECTRO cell B10 HVLV, Betatech).

The skin's response to a Pulsed Electric Field (PEF) can be categorized into three time-frames: immediate (during the pulse application), short-term (few seconds following the PEF), and long-term (minutes to hours after the PEF). To comprehensively understand these effects, we configured the electroporation setup for parallel data acquisition from three instruments: a source-measuring unit, a digital oscilloscope and a fiber optic thermometer (**Figure 2.16**). An electroporation device was fabricated to ensure the reproducibility of the experiments, allow the monitoring of the electrical response and facilitate the setup. The device consisted of two boxes with entry and exit ports for the cables, a manual switch to pass between the source-measuring unit and the oscilloscope and a cell for the skin sample. The cell was made of a plastic petri dish (PMMA: Poly(methyl methacrylate), 90 mm diameter), a plastic (PMMA) cross with holes on the positions where the hydrogels were placed (14 mm apart center-to-center), a printed circuit board (PCB) that connected the two stainless steel cylinders with the generator and a 50 g calibration weight placed on top of the PCB, applying an even and reproducible pressure to the hydrogels (**Figure 2.17**). The force applied on each hydrogel was approximately equal to 0.3 N (50 g weight divided by two + 5 g per metal cylinder, multiplied by  $g$ ).

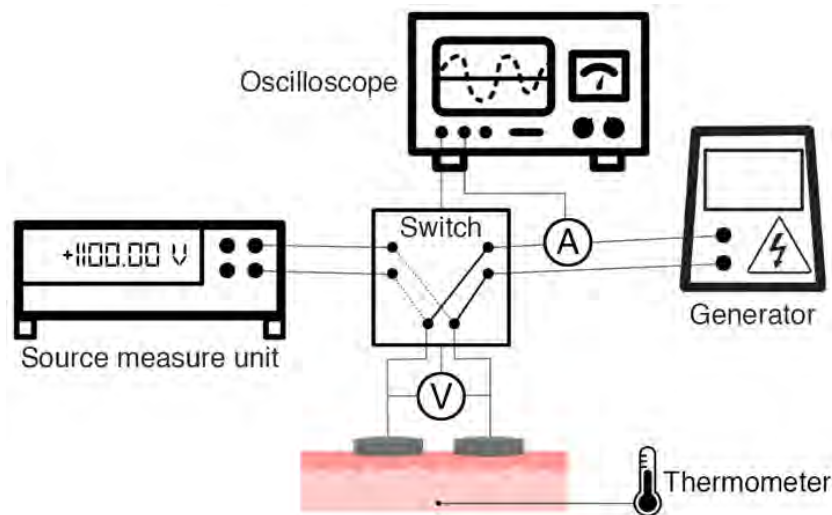


**Figure 2.16** - Scheme of connections for *in situ* electrical measurements. Two hydrogels were placed on top of the skin model and connected to the pulse generator. An oscilloscope measured the voltage and current during the pulsed electric fields (PEF) application. Before, and after the PEF, the system was connected to a source-measuring unit (SMU) that measured the DC resistance. A manual switch allowed the transition between generator and SMU. The fiber optic temperature sensor was placed under the skin, at the center.

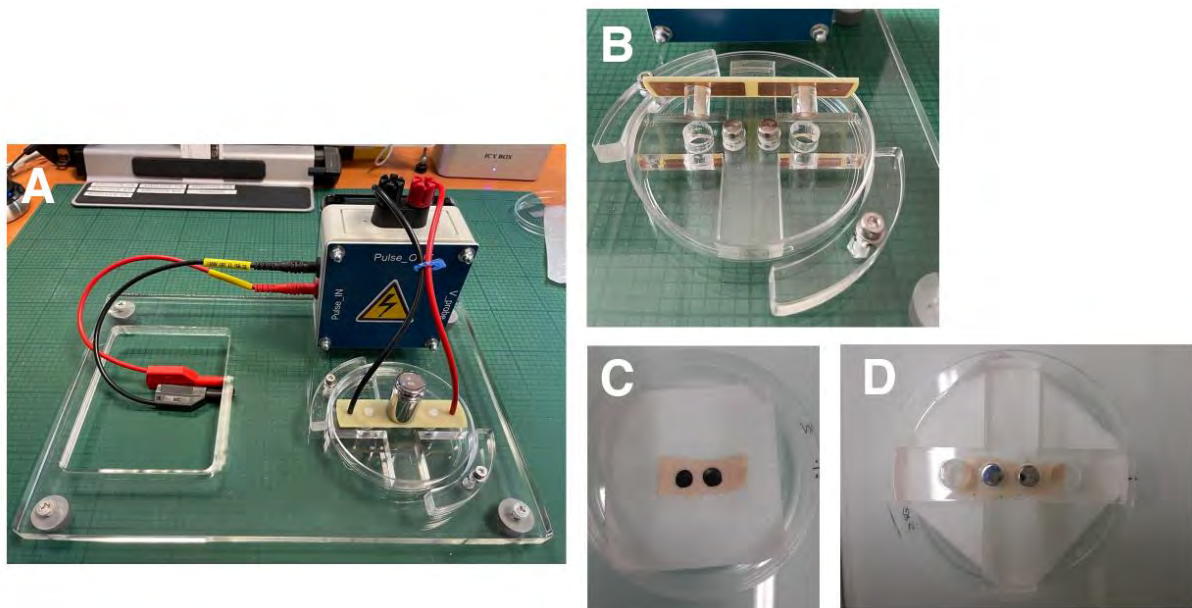


**Figure 2.17** – Electroporation device setup. (A) The full device with cables to be connected to generator. (B) Cell for skin sample. (C) Wet gauze, skin sample and two hydrogels (D) Skin sample in cell with plastic cross (guide) and two stainless steel cylinders (top view).

### 2.3.1.1 *I-V during PEF application*

The Pulsed Electric Field applied consisted of 8 square unipolar pulses of 20 ms duration, frequency of 1 Hz and a voltage of 0 (control) to 400 V (**Figure 2.18**), inspired from refs. [46], [160]. A digital oscilloscope (Tektronix MSO44), equipped with a high-voltage differential probe (Tektronix THDP0200) and an AC/DC current probe (Tektronix TCP0030A), measured the voltage applied on the electrodes and the current passing through the system during the application of the PEF.



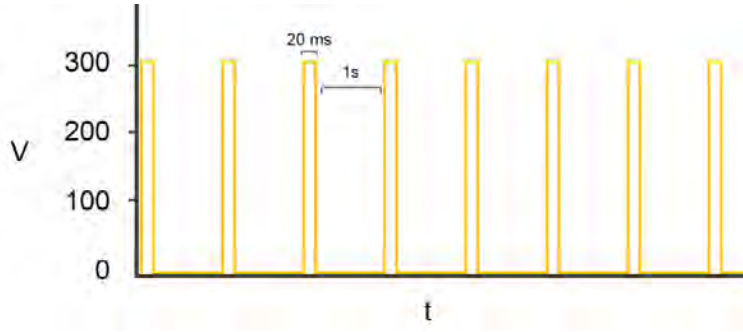


**Figure 2.18** – Programmed (theoretical) applied electric pulses. 8 square unipolar pulses of 20 ms duration and frequency of 1 Hz.

### 2.3.1.2 DC resistance

The potential difference and the current passing through the system were monitored before, during and after the application of PEF. A source-measuring unit (SMU, Keithley 2410) applied a constant DC voltage of 1 V and measured the resulting current every 2 s, before and after the PEF. A manual switch allowed the transition between generator and SMU.

### 2.3.1.3 Electrical recovery

The I-V measurements were also used to evaluate the electrical recovery of the skin samples. For the evaluation of the electrical recovery, a series of PEF were applied on the skin samples. First, a low-to-moderate voltage PEF was applied, which served as a baseline (50 to 100 V). Next, a series of PEF were applied with voltages ranging from 50 to 400 V. Rest time between the applications was 1-2 minutes, to allow the temperature to return to baseline, in order to minimize thermal damage to the skin. After the series of PEF applications, the skin samples were left to recover for 1 h in an incubator set at 37 °C. After the recovery, a subsequent low-voltage PEF (50 to 100 V) was applied and the electrical response was compared to the baseline.

## 2.3.2 Temperature monitoring

The temperature of the skin was monitored with a fiber optic temperature sensor (Neoptix Qualitrol), placed at the center, between the skin and the humidified gauze, at the point with the highest current density and temperature increase.

## 2.4 FEM simulations

The numerical model of the drug delivery system was developed with COMSOL, a Finite Element Method (FEM) software (COMSOL Multiphysics, v. 6.1, AC/DC Module). The module solved the following set of equations in time domain:

$$\vec{E}(t) = -\vec{\nabla}V \quad (2.3)$$

$$\vec{J}(t) = \sigma\vec{E}(t) + \frac{\partial\vec{D}(t)}{\partial t} \quad (2.4)$$

With  $\vec{E}(t)$  the electric field,  $V$  the voltage,  $\vec{J}(t)$  the current density,  $\sigma$  the conductivity and  $\vec{D}(t)$  the electric displacement. The boundary conditions were the voltages set on each electrical contact: the left electrode was set at 0 V (ground) and the right electrode was set at 50 to 300 V. For the purposes of the numerical simulation, the mouse skin was simulated as stacked homogeneous layers, with isotropic conductivity. Geometry and electrical properties of mouse skin were found in refs. [161],

[162]. In lack of data on the conductivity of specific mouse skin layers, the values from humans were used. As a convention, by “Epidermis” we refer to the deeper epidermis layers (the stratum lucidum, granulosum, spinosum and basale), without the stratum corneum.

**Table 1.** Geometry and electrical properties of the different elements of the system.

Material	Thickness (m)	Conductivity (S/m)
Nanocomposite hydrogel	$4 \times 10^{-4}$	$10^{-6}$ to 0.15
Stratum corneum	$9 \times 10^{-6}$	$10^{-4}$ to $5 \times 10^{-2}$
Epidermis	$1.8 \times 10^{-5}$	0.2
Dermis	$1.8 \times 10^{-4}$	0.2
Hypodermis	$10^{-4}$	0.05
Muscle tissue	$1.4 \times 10^{-4}$	0.5
Wet gauze	$1 \times 10^{-3}$	0.15 to 1.5

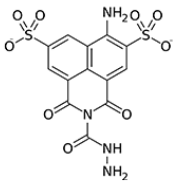
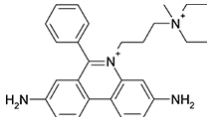
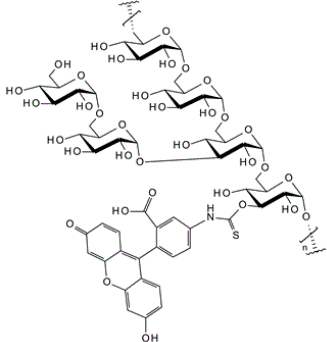
## 2.5 Drug delivery

### 2.5.1 Drug models

Drug delivery was tested through the use of fluorescent molecules, as models. We used three different fluorophores, with distinct properties (**Table 2.4**). The hydrogels were loaded with one or more of these molecules for the drug delivery experiments. The dry hydrogels were immersed for 48 h in electroporation buffer solution (8.1 mM  $K_2HPO_4$ , 1.9 mM  $KH_2PO_4$ , 1 mM  $MgCl_2$ , 250 mM saccharose;  $\sigma=0.15$  S/m) containing one or two types of fluorescent molecules. The fluorescent molecules used were Lucifer Yellow (LY, Sigma-Aldrich, CAS: 67769-47-5), at a concentration of 1 mM, Propidium Iodide (PI, Sigma-Aldrich, CAS: 25535-16-4) at a concentration of 0.1 mM, and Fluorescein isothiocyanate–dextran of average molecular weight 4 kDa (FD4, Sigma-Aldrich, CAS: 60842-46-8) at a concentration of 1 mM.

Lucifer Yellow (LY) is a small, negatively charged, hydrophilic molecule, used to evaluate the disruption of the skin’s barrier properties. Propidium Iodide (PI) is a small, positively charged, hydrophilic molecule that was used as a marker of cell permeabilization. PI increases its fluorescence by 20 to 30-fold when it binds to DNA [163]. Fluorescein isothiocyanate–dextran, is a large, slightly negatively charged (fluorescein is negatively charged and the substitution rate is *ca.* 0.01 mol FITC per mol of glucose) fluorescent marker, used here for its size (4000 Da), in the same range than therapeutic agents such as insulin (5734 Da). The passive diffusion of these three molecules, through the skin, is negligible.

**Table 2.4** - Fluorescent molecules loaded into drug delivery hydrogels.

Fluorophore	Molar mass (Da)	Charge	Notes	Chemical structure
<b>Lucifer Yellow (LY)</b>	442 (428 without 2 Li <sup>+</sup> )	-	Destabilization of extracellular matrix	
<b>Propidium Iodide (PI)</b>	668 (414 without 2 I <sup>-</sup> )	+	Cell permeabilization	
<b>Fluorescein isothiocyanate–dextran (FD4)</b>	4000 (avg)	Slightly -	Macromolecule delivery model	

### 2.5.2 Fluorescence microscopy

After PEF application, mouse skins were thoroughly rinsed with PBS to wash off the fluorescent molecules that had not penetrated into the skin. The skin surface was then visualized with an upright, wide-field fluorescence microscope (Light source EL6000, Leica Microsystems) equipped with a microscope camera (CoolSNAP HQ, Roper Scientific). The images were acquired through microscopy image analysis software (Metamorph, Molecular Devices) and treated through image processing software (ImageJ, National Institute of Health). A green filter cube (EX 480/40 nm, BS 505 nm, EM 527/30 nm; L5 filter, Leica Microsystems) was used for the FITC and LY fluorophores, and a red filter cube (EX 560/40 nm, BS 585 nm, EM 630/75 nm; mCH/TR, Leica Microsystems) was used for PI (**Figure 2.19**). Exposure time was 1 s. Relative Fluorescence Intensity (RFI) is presented as a ratio between the mean fluorescence intensity of the treated area (full area under the hydrogel) divided by the mean fluorescence intensity of an untreated area of the mouse skin.

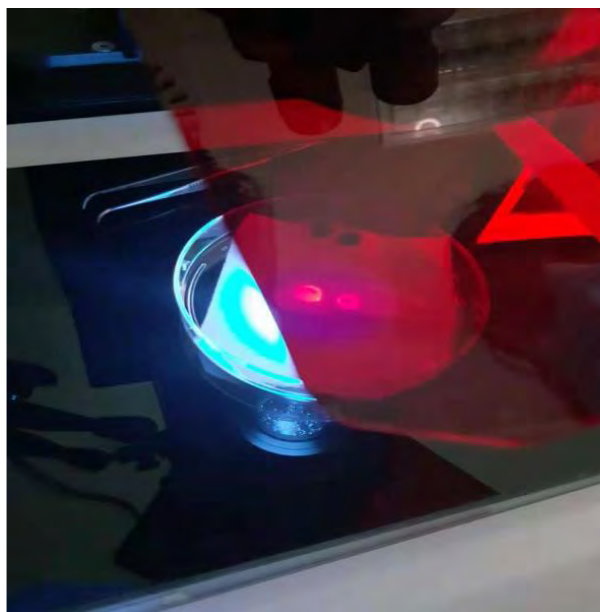


**Figure 2.19** – Mouse skin sample on fluorescent microscope with green filter cube. The two circles with intense fluorescence correspond to the electroperated region.

## 2.6 Statistical treatment

When relevant, we used statistical tests to compare data. We used the student's t-test to compare means between two samples and the p-values are indicated next to the comparisons. When necessary, the experimental data was tested for normality, with the Shapiro-Wilk test and the variance of the results was tested for equality with the Brown-Forsythe test. Comparisons between means of multiple treatment groups were made using one-way ANOVA, followed by the Dunnett's test, for the samples with equal variance, and the Dunnett's T3 post-hoc test, for the samples with unequal variance. Differences were considered significant for  $p \leq 0.05$ . The Dunnett's and Dunnett's T3 post-hoc tests are suitable for small groups and unequal sample sizes, which is the case for our fluorescence data. The Dunnett's test compares all groups to a control, while the Dunnett's T3 test compares all possible pairwise group differences and both tests are relatively conservative (limit false positives) [164]. Error bars, values given with plus minus their uncertainty, and shaded areas in graphs represent standard deviation, unless otherwise stated in the legend.

## 3 Materials characterizations

<b>3</b>	<b>MATERIALS CHARACTERIZATIONS</b>	<b>78</b>
3.1	HYDROGEL SPECIFICATIONS (DESIRED PROPERTIES)	78
3.1.1	<i>Ability to store and release medicine</i>	79
3.1.2	<i>Electrical conductivity</i>	79
3.1.3	<i>Biocompatibility</i>	79
3.1.4	<i>Mechanical strength / reusability</i>	80
3.1.5	<i>Preservation / stability</i>	80
3.1.6	<i>Practicality / ease of fabrication</i>	81
3.1.7	<i>Choice of drug delivery platform</i>	81
3.2	DIMENSIONS	81
3.3	THERMOGRAVIMETRIC ANALYSIS	84
3.4	SWELLING RATIO	85
3.4.1	<i>CNT concentration</i>	85
3.4.2	<i>Processing method</i>	86
3.4.3	<i>Drying – swelling cycles</i>	90
3.4.4	<i>Alginate/chitosan</i>	91
3.5	DRYING AND SWELLING KINETICS	93
3.6	MECHANICAL PROPERTIES	95
3.7	ELECTRICAL CHARACTERIZATIONS	97
3.7.1	<i>CNT conductivity in aqueous suspension</i>	97
3.7.2	<i>DC conductivity</i>	98
3.7.3	<i>Electrical conductivity of hydrogels with ionic solutions</i>	112
3.7.4	<i>Impedance spectroscopy</i>	114
3.8	SKIN MODEL	117
3.8.1	<i>DC conductivity of skin model</i>	117
3.8.2	<i>Impedance spectroscopy of skin model</i>	118
3.9	CHAPTER HIGHLIGHTS AND DISCUSSION ON MATERIALS CHARACTERIZATIONS	119

### 3.1 Hydrogel specifications (desired properties)

In this chapter we study the physical and electrical properties of the hydrogel platforms used for drug delivery. These two-in-one electrode-reservoir platforms must fulfill the following criteria:

- Ability to store and release medicine
- Electrical conductivity
- Biocompatibility
- Stability / mechanical strength
- Preservation
- Practicality / ease of fabrication

The choice of the nanocomposite hydrogels with agarose and CNTs was elaborated in previous works [157], [158]. To summarize, this system represents the best compromise between chemical stability, swelling/storage capacity, durability and safety. In this study, we further examine their properties, and investigate how different polymers, types of CNTs, concentrations, dispersants and processing methods affect these properties.

### 3.1.1 Ability to store and release medicine

The platforms should act as drug reservoirs, storing a medicine and releasing it timely. We assumed the case of hydrophilic therapeutic molecules, which is the case for numerous molecules relevant for transdermal delivery (insulin, morphine, nucleic acid vaccines). Different methods for making reservoirs exist, such as using an impermeable shell housing a liquid core or employing a hydrogel. Hydrogels are suitable because they are highly-absorbent, hydrophilic, and mostly biocompatible.

There are three approaches to loading up a hydrogel with medicine: (1) Preparation of the hydrogel with the therapeutic molecule in the precursor solution. (2) Solvent exchange of fresh hydrogels, by placing them in a solution with the therapeutic molecule. The medicine will diffuse within the hydrogel (depending on the mesh size of the hydrogel) due to concentration gradient. (3) Drying the hydrogel and then swelling it in a solution with the molecule of interest.

We chose the 3<sup>rd</sup> approach for three reasons: (1) **Preservation**. Dry hydrogels can be preserved for much longer than fresh ones. (2) **Possible degradation of therapeutic molecules**. In the process of fabricating the hydrogels, the precursor solution is heated up to 90 °C, to enable the solubilization of agarose. Most therapeutic molecules would be degraded by exposure to such high temperatures. (3) **Medical classification**. There is a juridical distinction of medical products into medicine or medical devices. A product that already contains the active ingredient is classified as medicine, and this involves different legal framework with rigorous safety evaluations and lengthy procedures. On the other hand, a platform that can be used for the administration of licensed medicine is considered a medical device, circumventing the previous procedure [158]. It must be clarified that the inclusion of nanomaterials (CNTs) is likely to place our system in a kind of intermediate situation.

We evaluated the reservoir function of the hydrogels through the absorption capacity (swelling ratio) and drying and swelling kinetics. The release profile without electrical stimulation has been investigated in previous works [157]. More indirectly, the reservoir function and release kinetics are also evaluated in chapter **6.1.1 Molecule release on gauze**.

### 3.1.2 Electrical conductivity

In addition to the reservoir function, the goal of the project was to create a conductive platform that can behave as an electrode for the application of the PEF on the skin. The electrical conductivity of the hydrogel plays an important role in the distribution of the electric field inside the skin. A resistive platform would induce a major voltage drop within it, minimizing the potential difference applied on the skin. On the other hand, a conductive platform entails minor voltage drop and ensures that the full potential difference applied by the generator reaches the skin. The electric field distribution is a critical parameter for electroporation. We evaluated the DC and AC electrical conductivities of different hydrogel platforms and the impact of processing methods on these properties. In chapter **5 Numerical Modeling**, we also modeled the voltage drop induced by the hydrogels at different conductivities and the effect of this parameter on the electric field distribution within the skin layers.

### 3.1.3 Biocompatibility

The drug delivery platforms come into contact with the skin so biocompatibility is a prerequisite. Additionally, PEF application increases the permeability of the skin, so the nanocomposite hydrogel should not release any non-biocompatible or toxic compounds. Agarose hydrogels are perfectly biocompatible. In fact, they are routinely used for cell cultures and tissue engineering and even eaten in the form of desserts in Japanese cuisine (with red bean paste and sugar). The dispersant used for



the CNTs, carboxymethyl cellulose (CMC) is also perfectly biocompatible. It is commonly used as a food additive (E466) for thickening liquids. Biocompatibility studies therefore focused on the use of CNTs. CNTs are potentially cytotoxic to skin cells [165]. In previous works, we evaluated the release of CNTs from the hydrogels [64] and the potential cytotoxicity of CNTs on skin cells. No traces of CNT were found to be released from the hydrogel platforms even under extreme (and not realistic) conditions: 24 h in artificial sweat at 50 °C [158]. Regarding the cytotoxicity of CNTs, they were tested on the three most common line cells of the skin (corneocytes, melanocytes and fibroblasts) and were found to substantially affect their viability only at high concentrations > 10 µg/ml for the melanocytes and > 20 µg/ml for the corneocytes and fibroblasts [157]. Such concentrations are highly unlikely.

#### 3.1.4 Mechanical strength / reusability

Even though mechanical strength was not a priority, the hydrogel platforms must be rigid enough to be handled with ease. Hydrogels with low polymer concentrations, short chains or low degree of cross-linking may be very fluid, with a liquid-like consistency, complicating experimental manipulation. On the other hand, some hydrogels with higher polymer concentrations and degree of cross-linking may be brittle, breaking into pieces during manipulation. This is the case for chemically cross-linked chitosan hydrogels, for example. This is especially true for the dried form of hydrogels. Therefore, the platform for drug delivery must have a sufficient mechanical strength to be manipulated and a certain degree of flexibility or softness to not be very brittle. In the scope of the current work, the mechanical properties evaluation was performed mostly by observation and manipulation. In previous works rheological tests were made [157] and in chapter **3.6 Mechanical properties** we also present some basic characterizations.

Another factor that was investigated was the reusability of hydrogels. In chapter **3.4.3 Drying – swelling cycles** we measured the swelling ratio of hydrogels over multiple cycles of drying and swelling.

#### 3.1.5 Preservation / stability

The drug delivery platforms must be stable over time and not degrade while in their storage conditions. Hydrogels are high water content and biocompatible systems, thus propitious to microbial infections (yeasts, bacteria). We observed that fresh hydrogels preserved in DI water tended to get colonies after few weeks, at ambient temperature, or after few months, in the fridge (4°C). This was visually observed only for agarose hydrogels, without CNTs (**Figure 3.1**). There are two possible explanations: either the CNTs hindered microbe growth [166], or the colonies were not visible on the black hydrogels. A closer observation of hydrogels with CNTs revealed that they may also be colonized by microbes, because of changes in water viscosity. We stored the hydrogels in a dry form, to avoid this issue.

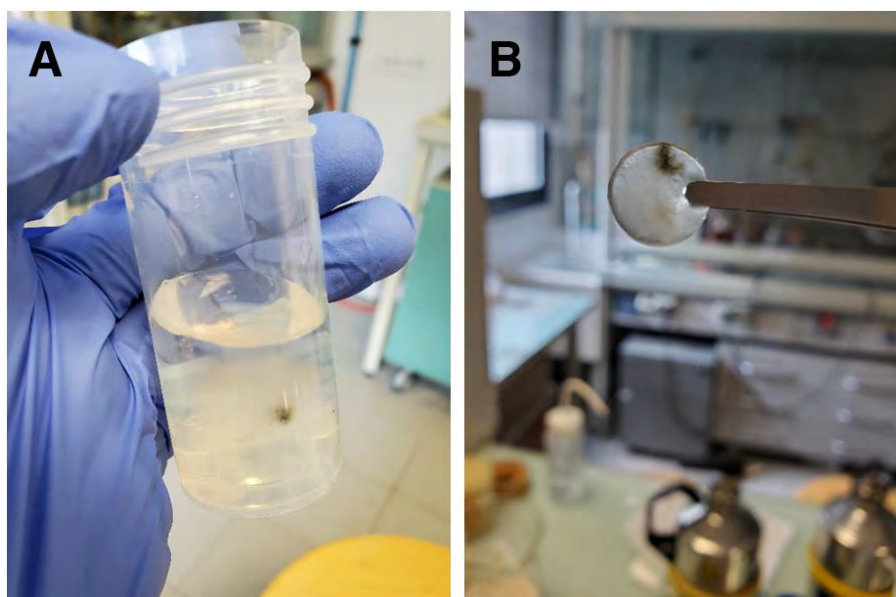


**Figure 3.1** – Agarose hydrogels with microbial colonies. (A) hydrogels stored in deionized water. (B) A heavily colonized agarose hydrogel, after months of storage.

### 3.1.6 Practicality / ease of fabrication

Ease of fabrication was also considered for the choice of the drug delivery platforms. Indeed, agarose is a hydrogel that can be readily physically cross-linked, without needing any (potentially toxic) chemical cross-linkers. This is reversible by heating again at 90°C in water.

### 3.1.7 Choice of drug delivery platform

Considering the previous criteria, the choice was made to work with agarose hydrogels incorporating double-wall CNTs and carboxymethyl cellulose. These hydrogels were air-dried and swollen in a solution with the molecules of interest, serving as drug models. In the current chapter we will elaborate on this choice, as well as investigate possible alternatives.

## 3.2 Dimensions

The hydrogels were prepared by mold-casting, in cylindrical molds with 10-mm diameter and 2-mm height. *Fresh (F)* hydrogels refers to humid hydrogels directly after mold-casting, or after storage in water. *Dry (D)* hydrogels were air-dried at 30 °C for 48 h and *Swollen (R)* hydrogels are dry hydrogels placed in a DI water solution for 24 h - 48 h. We measured the mass and height of agarose (AGR) and nanocomposite (AGR-CNT<sub>10</sub>CMC<sub>1</sub>) hydrogels (**Figure 3.2** and **Figure 3.3**). Fresh agarose hydrogels had a mass of  $149 \pm 3$  mg (range 144 – 155, n=9) and height of  $1.95 \pm 0.07$  mm (range 1.86 – 2.06, n=9) while fresh nanocomposite hydrogels weighed  $146 \pm 8$  mg (range 133 – 158, n=9) and measured  $1.92 \pm 0.08$  mm (range 1.81 – 2.02, n=9). In their dried form, agarose hydrogels weighed  $4.3 \pm 0.6$  mg (range 3.5 – 5.3, n=9) and measured  $0.26 \pm 0.06$  mm (range 0.16 – 0.34, n=6) whereas nanocomposite hydrogels were  $4.8 \pm 0.5$  mg (range 4.0 – 5.4, n=9) and  $0.26 \pm 0.07$  mm (range 0.17 – 0.35, n=6). When swollen in water, agarose hydrogels had a mass of  $24 \pm 2$  mg (range 20 – 27, n=9) and height of  $0.52 \pm 0.09$  mm (range 0.42 – 0.65, n=9) while nanocomposite hydrogels weighed  $18 \pm 2$  mg (range 15 – 20, n=9) and measured  $0.42 \pm 0.06$  mm (range 0.37 – 0.56, n=9).

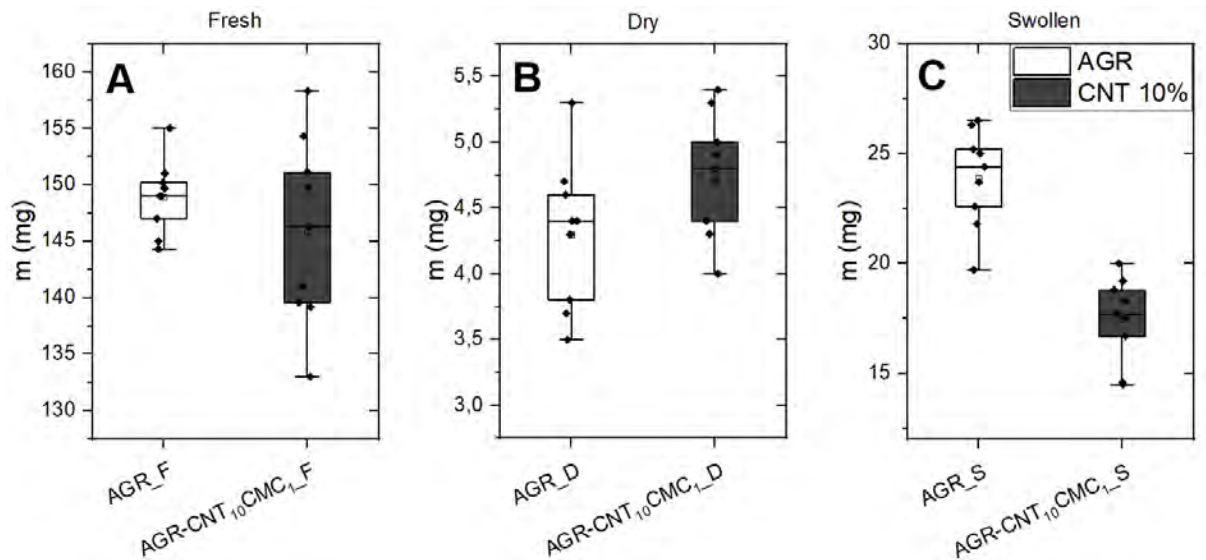


**Figure 3.2** – Mass of agarose and nanocomposite (AGR-CNT<sub>10</sub>CMC<sub>1</sub>) agarose hydrogels in fresh (A), dry (B) and swollen (C) state. n=9.

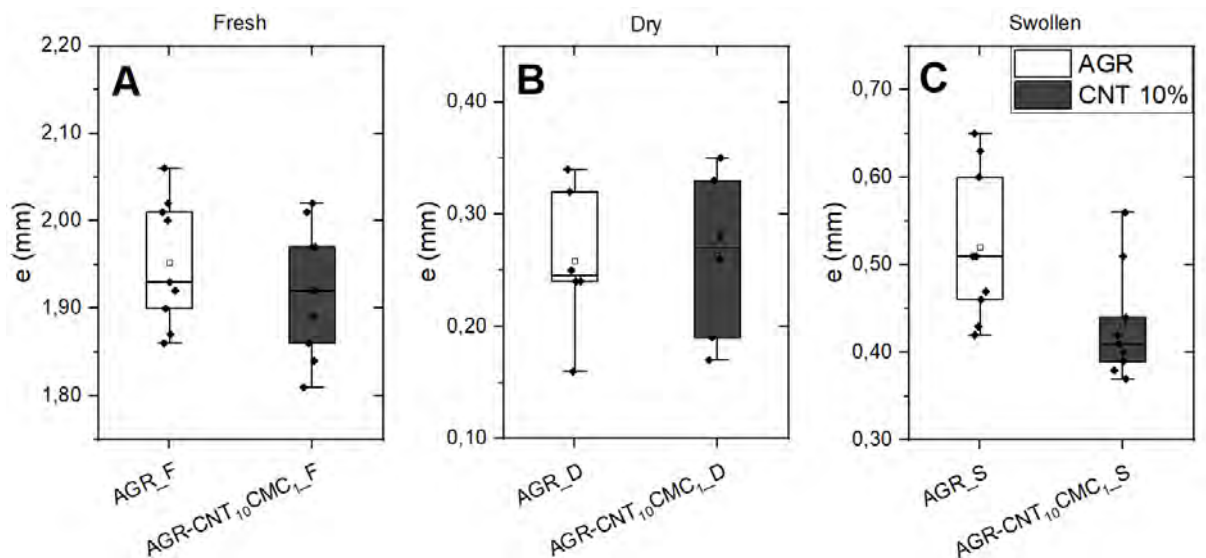


**Figure 3.3** - Height of agarose and nanocomposite (AGR-CNT<sub>10</sub>CMC<sub>1</sub>) agarose hydrogels in fresh (A), dry (B) and swollen (C) state. n=6-9.

The theoretical volume of the hydrogels was (according to the dimensions of the mold):

$$V_{th} = \pi \cdot \frac{d^2}{4} \cdot e = \pi \cdot \frac{10^2}{4} \cdot 2 = 157 \text{ mm}^3$$

The experimental volume was  $V_{AGR} = 153 \text{ mm}^3$  and  $V_{CNT} = 151 \text{ mm}^3$ . The small difference between theoretical and experimental volume is explained by three factors: (1) the experimental procedure, during which the hydrogel precursor solution that exceeded the 2 mm molds was scraped away, (2) the thickness-measuring device, which applied a small pressure and compressed slightly the hydrogels (**Figure 3.4**) and (3) evaporation of a small amount of water.

The following tables present the mass concentrations per hydrogel, taking into account the % w/w concentrations of the preparation protocol (**2.1.2 Preparation of nanocomposite hydrogels**) and the total mass measured experimentally.

**Table 3.1** – Mass concentrations of fresh agarose hydrogel.

AGR hydrogel	H <sub>2</sub> O	AGR	Total
Concentration % w/w	97.56	2.44	100
Mass (mg)	14.26	3.64	148.9

**Table 3.2** – Mass concentrations of fresh nanocomposite agarose hydrogel.

CNT hydrogel	H <sub>2</sub> O	AGR	CNT	CMC	Total
Concentration % w/w	97.30	2.4	0.24	0.02	100
Mass (mg)	141.08	3.53	0.35	0.04	145.8

By assuming that dry hydrogels lose 100 % of their water content, the mass of dry hydrogels was expected to be 3.6 mg for the agarose hydrogels and 3.9 mg (3.53 + 0.35 + 0.04) for the nanocomposite hydrogel. The experimental values were 4.3 and 4.8 mg, respectively. In the next chapter, **Thermogravimetric analysis**, we will see that in fact dry hydrogels still contained a small percentage of water.

We compared the means of agarose and nanocomposite hydrogels through Student's t-test. As expected, the mass and height of the fresh hydrogels did not differ significantly ( $p=0.313$  and  $p=0.385$  for mass and height respectively) between AGR\_F and AGR-CNT<sub>10</sub>CMC<sub>1</sub>\_F hydrogels. For dried hydrogels, the height did not differ ( $p=0.9$ ) but the mass of the AGR-CNT<sub>10</sub>CMC<sub>1</sub>\_D hydrogels was  $0.46 \pm 0.24$  mg higher than the mass of the AGR\_D hydrogels. This difference was significant at the 90 % confidence interval ( $p=0.08$ ). The mass of CNTs, at *ca.* 0.35 mg per hydrogel was too small to make a difference in the fresh hydrogels that contain mostly water, but was measurable for the dried hydrogels. The height of the dried hydrogels was most probably overestimated: the dried hydrogels were not totally flat and because of their stiffness and brittleness, the thickness gauge device measured a height slightly higher than the actual thickness.

The largest differences between plain and nanocomposite version were observed in the swollen hydrogels: the mass and height of AGR\_S hydrogels was significantly ( $p<0.001$  for both mass and height) larger than the AGR-CNT<sub>10</sub>CMC<sub>1</sub>\_S hydrogels. The nanocomposite hydrogels absorbed less water during the swelling. We will discuss this difference in details in chapter **3.4 Swelling ratio**.

These relatively small hydrogel dimensions were chosen to be adapted to the small size of the experimental animal model (mice). In addition, smaller volumes allow the preparation of a larger number of samples from a set number of reagents, limiting waste. These dimensions can be scaled up for subsequent human trials.

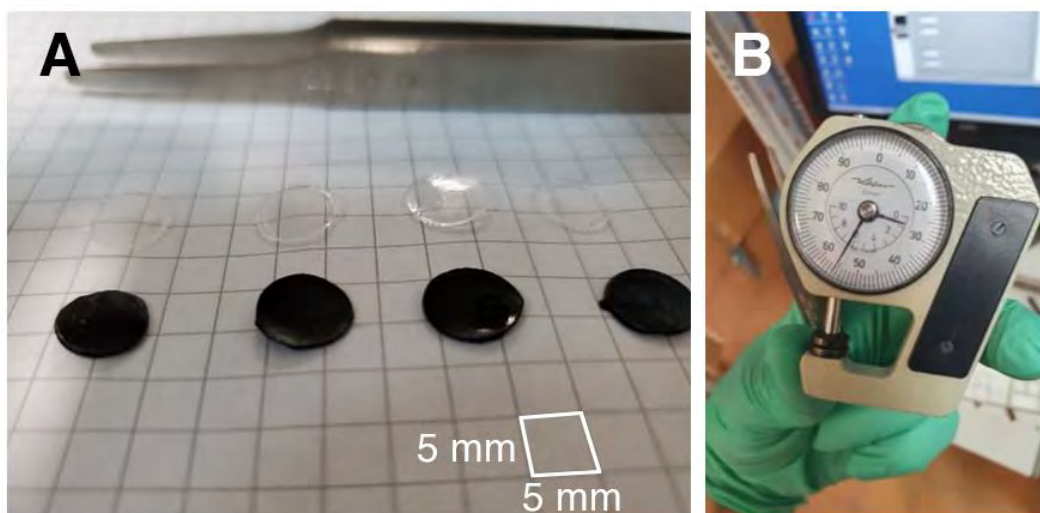


**Figure 3.4** – Swollen agarose (transparent) and nanocomposite (black) hydrogels (A) and thickness gauge (B).

Swollen hydrogels were not perfect circles (**Figure 3.4**). Their diameter was calculated by measuring their surface, through image analysis tools, and then inferring the diameter by assuming circular geometry. The diameter of AGR\_S hydrogels was  $8.2 \pm 0.5$  mm (range 7.6 – 8.5, n=4) and  $8.2 \pm 0.3$  mm (range 7.8 – 8.5, n=4) for AGR-CNT<sub>10</sub>CMC<sub>1</sub>\_S hydrogels.

### 3.3 Thermogravimetric analysis

Thermogravimetric analysis of a dry agarose hydrogel was conducted to evaluate the percentage of water in the hydrogel network after air-drying. The dry agarose hydrogel had an initial mass of 4.19 mg and the TGA was performed in nitrogen atmosphere, from room temperature up to 400 °C with a ramp of 1 °C/min. The results are displayed in **Figure 3.5**.

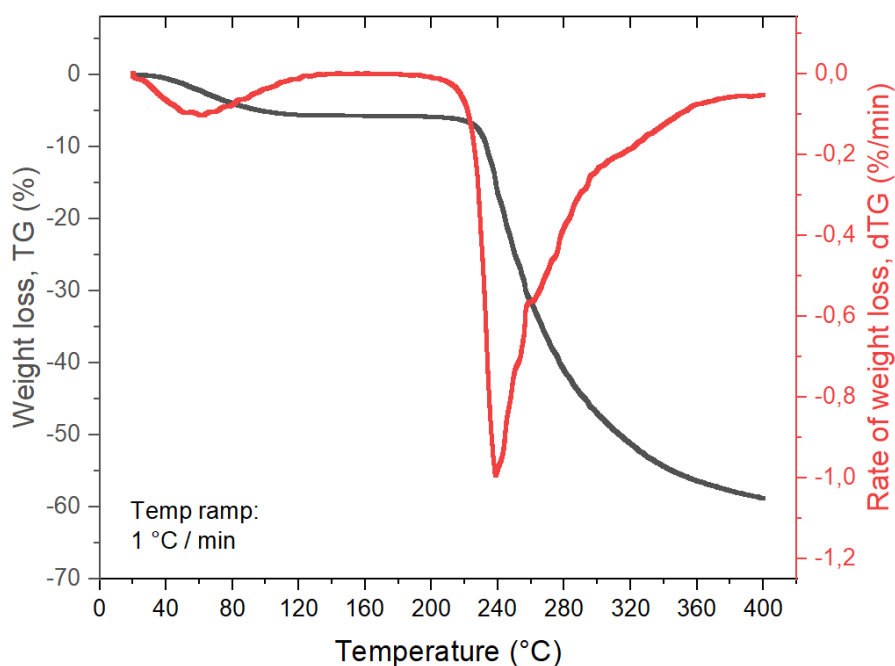


**Figure 3.5** – Thermogravimetric analysis of dry agarose hydrogel.

Two major mass loss regions were observed: one initial loss of 5.7 % at low temperatures, between 40 and 100 °C, peaking at 62 °C and a second, bigger mass loss of *ca.* 50 % between 230 and 400 °C, peaking at 240 °C.

We attributed the first mass loss of 5.7 % to the evaporation of water that remained in the air-dried hydrogel and the second mass loss corresponded to the thermal decomposition of agarose. Our results were in close agreement with the relevant literature. Ouyang *et al.* studied the thermal degradation of agar (agar contains  $\beta$ -1,3-linked galactopyranose and  $\alpha$ -1,4-linked 3,6-inner ether-L-galactopyranose while agarose, which is purified from agar, contains D-galactose and 3,6-anhydro-L-galactose [158], [167]) and found a 10 % mass loss between 50 and 110 °C, peaking at 100 °C, that corresponded to the evaporation of water from the sample and a larger mass loss of 55 % between 250 and 350 °C, peaking at 300 °C, that corresponded to the thermal degradation of the agar constituents [167]. Similarly, Wang *et al.* investigated the thermal stability of a palladium catalyst supported on agarose polymer and found an initial mass loss of 5 % from room temperature to 100 °C, and a larger mass loss of 75 % between 250 and 600 °C, corresponding to the decomposition of agarose. This also highlights the excellent thermal stability of agarose below 200°C, which is very interesting for device applications.

The 5.7 % of water content that remained in the air-dried agarose hydrogel was non-freezing bound water of the polymer network (see introduction paragraph **1.12.5 Hydrogel water content and electrical conductivity** for more details), possibly in combination with some water absorbed from ambient humidity.

### 3.4 Swelling ratio

The swelling ratio was the most important hydrogel characteristic for their function as drug reservoirs. Hydrogels with higher swelling ratios can absorb bigger quantities of aqueous solutions containing molecules of interest. We investigated the impact of numerous parameters on the swelling ratio of the hydrogel platforms.

#### 3.4.1 CNT concentration

CNTs were added to the agarose polymers in order to increase their electrical conductivity. The impact of CNT concentration on the swelling ratio of nanocomposite hydrogels is presented in **Figure 3.6**. The AGR hydrogels had a swelling ratio of  $4.6 \pm 0.7$  (range 3.8 – 6.2, n=10), the AGR-CNT<sub>1</sub>CMC<sub>1</sub> hydrogels had  $3.5 \pm 0.6$  (range 2.7 – 4.1, n=6) and the AGR-CNT<sub>10</sub>CMC<sub>1</sub> hydrogels had  $2.7 \pm 0.6$  (range 2.0 – 3.4, n=9).



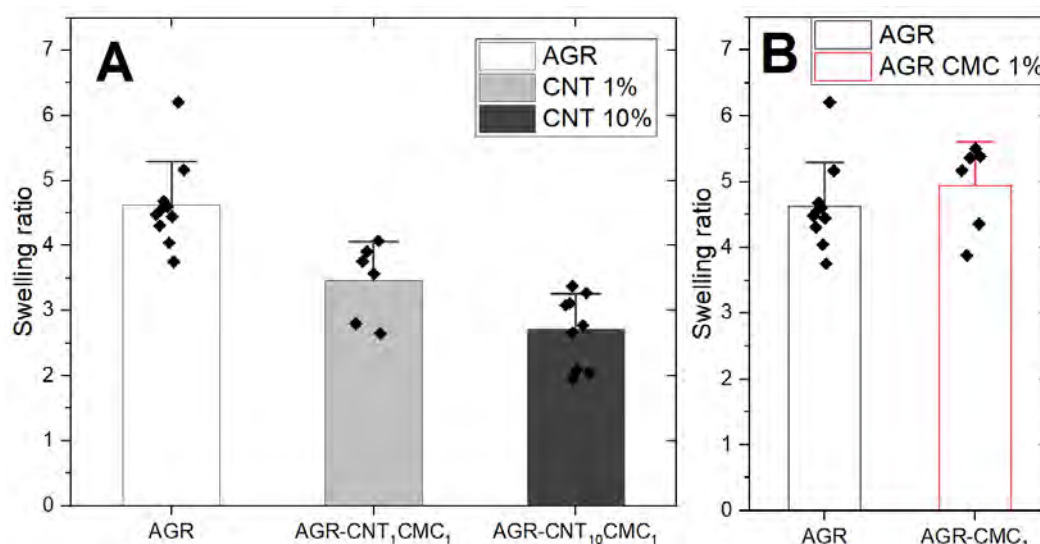


**Figure 3.6** – Impact of CNT concentration on the Swelling Ratio of nanocomposite hydrogels. (A) Hydrogels with CNTs 0, 1 and 10 wt. % of polymer mass (agarose 2.5 % w/w). (B) Control experiment to monitor possible influence of the CNT dispersant used (carboxymethyl cellulose, CMC) on the swelling ratio.

The incorporation of CNTs decreased the swelling ratio of plain agarose hydrogels. A CNT concentration of 1 wt. % of polymer decreased the swelling ratio by 25 % while a CNT concentration of 10 wt. % of polymer decreased the swelling ratio by 40 %. The decrease in swelling ratio was not linearly proportionate to CNT concentration.

In both cases, CMC at 1 wt. % of polymer was employed to disperse the CNT in the aqueous suspension. A control experiment demonstrated that the impact of CMC alone on the swelling ratio of agarose hydrogels was not significant ( $p=0.25$ , student's t-test).

There are two ways in which the incorporation of CNTs decreases the swelling ratio: densification of the polymer matrix and hydrophobicity of the nanomaterial. The CNTs are dispersed within the agarose polymer chains, rigidifying and densifying the network. Water absorption necessitates a flexible polymer network that will swell in the presence of water. Therefore, a denser network hinders water absorption. Secondly, CNTs have a highly hydrophobic surface. Agarose chains are hydrophilic but the inclusion of a dispersed hydrophobic phase repels some water from the surface of the hydrogel.

The fact that an important decrease in swelling ratio was observed already at a concentration of CNTs of 1 wt. % of polymer indicates that the most critical factor is the densification of the polymer network. It is unlikely that such a low concentration of hydrophobic material would have such an impact on the hydrophobicity of the hydrogel as a whole. Additionally, the dispersant added (CMC) renders the surface of CNTs more hydrophilic.

Even though the incorporation of CNTs moderately decreases the swelling ratio of the hydrogels for drug delivery, we have chosen to include them because of the substantial increase in electrical conductivity (See chapter 3.7.2.1 CNT concentration).

### 3.4.2 Processing method

Next, we investigated the impact of the processing methods on the swelling ratio of the hydrogels. The processing methods presented are air-drying, where the hydrogels are dried at 30 °C for 48 h; freezing,



where fresh hydrogels were first frozen at -20 °C, then air-dried; lyophilization, where fresh hydrogels were frozen at -20 °C, then the water phase was sublimated; and directional freeze casting, where the hydrogels were brought into contact with a cold source from one side only, creating perpendicular ice crystals, and the water phase was later sublimated.

The impact of processing method on the swelling ratio of hydrogels is presented in **Figure 3.7**. The frozen agarose hydrogels, AGR\_frz, had a swelling ratio of  $7.8 \pm 0.5$  (range 7.0 – 8.3, n=6), the lyophilized agarose hydrogels, AGR\_lyo, had a swelling ratio of  $8.0 \pm 0.3$  (range 7.7 – 8.3, n=6) and the directional freeze-cast agarose hydrogels, AGR\_dir, had a swelling ratio of  $14.7 \pm 1.8$  (range 12.7 – 16.4, n=3). The frozen nanocomposite hydrogels, AGR-CNT<sub>10</sub>CMC<sub>1</sub>\_frz, had a swelling ratio of  $5.8 \pm 0.3$  (range 5.4 – 6.2, n=6), the lyophilized nanocomposite hydrogels, AGR-CNT<sub>10</sub>CMC<sub>1</sub>\_lyo, had  $5.5 \pm 0.3$  (range 5.2 – 5.8, n=6) and the directional freeze-cast nanocomposite hydrogels had a swelling ratio of  $14.1 \pm 1.0$  (range 13.2 – 15.1, n=3).

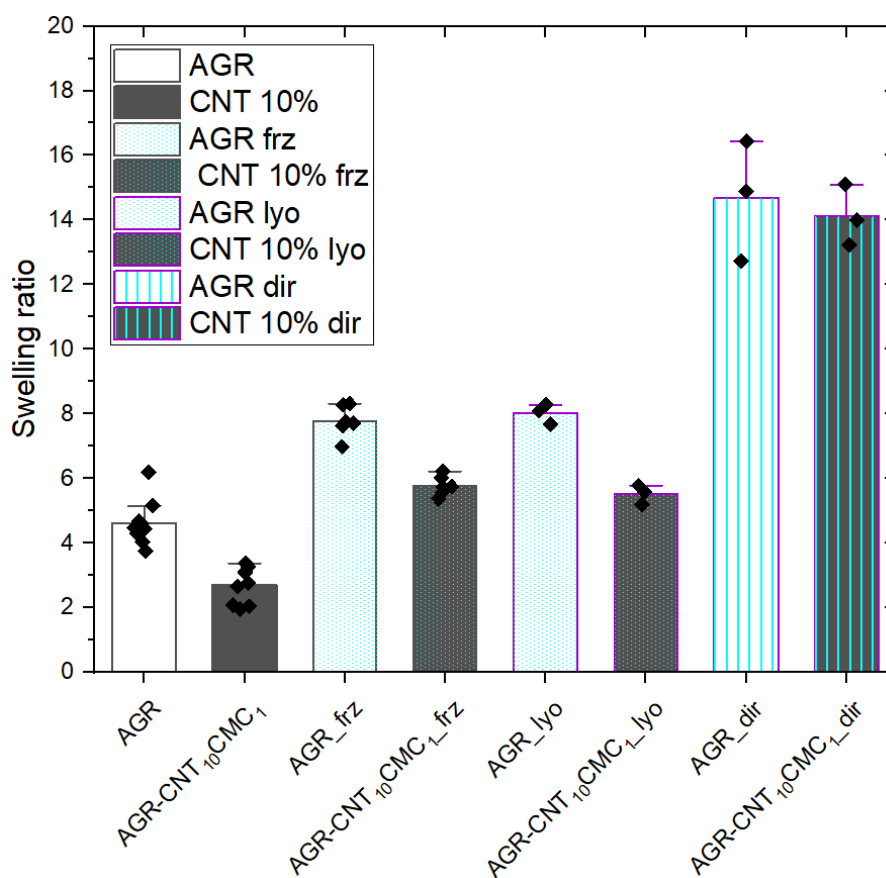


**Figure 3.7** – Impact of processing method on swelling ratio. White: plain agarose hydrogels, AGR. Dark grey: nanocomposite agarose hydrogels (CNT 10 wt. % of polymer), AGR-CNT<sub>10</sub>CMC<sub>1</sub>. n=3-10.

All three processing methods employed increased the swelling ratio of plain and nanocomposite hydrogels. Freezing and lyophilization both increased the swelling ratio of agarose hydrogels by 70 % and 90 %, respectively, while directional freeze-casting increased the swelling ratio of agarose hydrogels by 200 %. The nanocomposite hydrogels showed a similar trend: freezing and lyophilization increased the swelling ratio by 100 %, while directional freeze-casting increased the swelling ratio of nanocomposite hydrogels by 400 %.

Freezing the hydrogels was initially investigated as a preservation method. Changes in the hydrogel morphology were observed after freezing and air-drying, so it was decided to further study the impact of freezing on the hydrogel properties (**Figure 3.8**). Water within hydrogel networks can be classified into three types: non-freezing bound water, freezing bound water and freezing free water. When placed at  $-20\text{ }^{\circ}\text{C}$ , the freezing bound and free water started to crystallize. The ice crystals started to expand, pushing away the agarose chains and carbon nanotubes, creating ice regions within the hydrogel. When the hydrogel dried, this water melted away and evaporated (in air-drying) or sublimated (in freeze-drying), leaving behind numerous pores at the random positions of the ice crystals. These pores were big enough to affect the morphology of the hydrogel. These randomly positioned macropores in the network of the dry hydrogel were easily filled with water, increasing the overall swelling ratio.

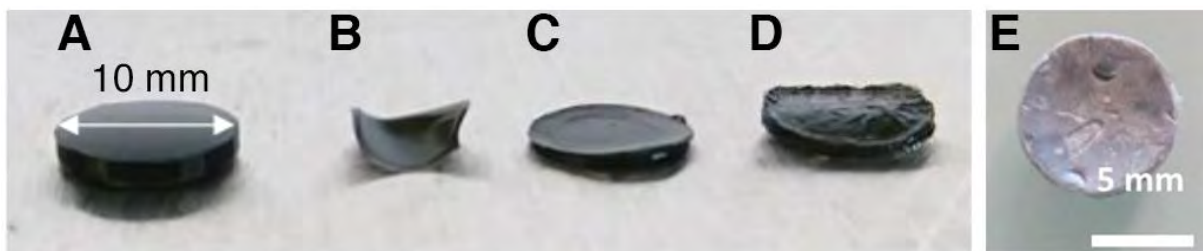


**Figure 3.8** –Nanocomposite hydrogels after different processing methods. (A) Fresh hydrogel, (B) Air-dried hydrogel, (C) Air-dried, then swollen hydrogel, (D) Froze, air-dried and then swollen hydrogel, (E) lyophilized hydrogel.

Dry, freeze-dried hydrogels are very different in their morphology from air-dried or frozen and then air-dried hydrogels. Freeze-drying preserved the approximate shape of the fresh hydrogel (diameter of 10 mm and height of 2 mm) while air-dried hydrogels were considerably smaller (diameter of 8.2 mm and height of 0.26 mm). Interestingly though, once the ice crystals were formed, melting and evaporation of water through air-drying or sublimation of water through freeze-drying did not make any statistically significant difference in the swelling ratio ( $p=0.44$  and  $p=0.288$ , student's t-test, for plain agarose and nanocomposite hydrogels, respectively). We therefore conclude that it is the formation of macropores through ice crystal formation within the hydrogel network that increased the swelling ratio, and not the lyophilization process in whole.

Freeze-casting creates a highly-oriented ice crystal formation. After sublimation, the dry hydrogel (or aerogel) is left with vertical macropores (**Figure 3.9**). The size of these pores can be controlled, to some extent, by the temperature of the cold source [155]. These hydrogels exhibited remarkable swelling properties, absorbing more than 14 times their dry mass in water. We attributed this property to the oriented macropores within the hydrogel that absorb water readily. While in every other processing method, nanocomposite hydrogels had lower swelling ratios than plain ones, in the freeze-cast hydrogels there was no observable difference (**Figure 3.7**). This indicated that the biggest part of absorbed water was absorbed within the vertical macropores.

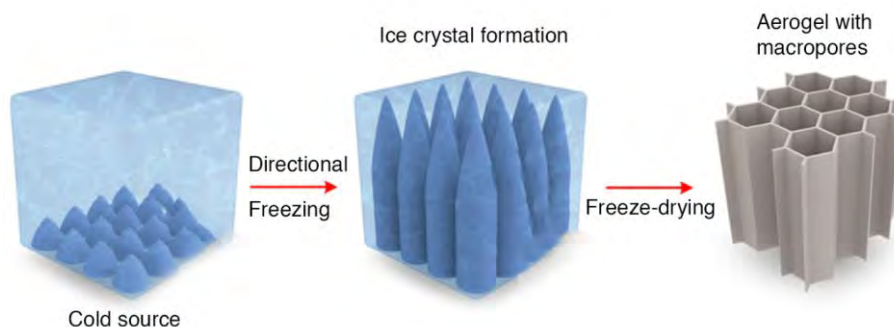


**Figure 3.9** – Growth of ice crystals in freeze-casting. Adapted from [168].

We also made some SEM observations to visualize the macropore orientation and distribution (**Figure 3.10**). The macropores of the hydrogel were already visible to the naked eye. The SEM observations revealed they had an elliptical cylinder shape, with approximate pentagonal and hexagonal symmetries. We performed an image analysis of a representative part of the sample (**Figure 3.10**, middle) to calculate the size distribution of the macropores, considering both the shortest and longest lengths within a pore (**Figure 3.11**). It gave a median of 148  $\mu\text{m}$  (range 40 – 708, Q1: 111, Q3:210,  $n=70$ ).

Further zooming in, allowed us to visualize the CNT bundles (**Figure 3.12**). The CNTs seemed well-dispersed in the agarose hydrogel matrix, with no visible big aggregates (CMC was also used). At the limit of the electronic microscope resolution, we measured a diameter of 32 nm for a CNT bundle. By assuming individual double-walled CNTs outer diameter at 1.5 to 3 nm [154], this roughly corresponded to CNT bundles of 10-20 nanotubes wrapped together.

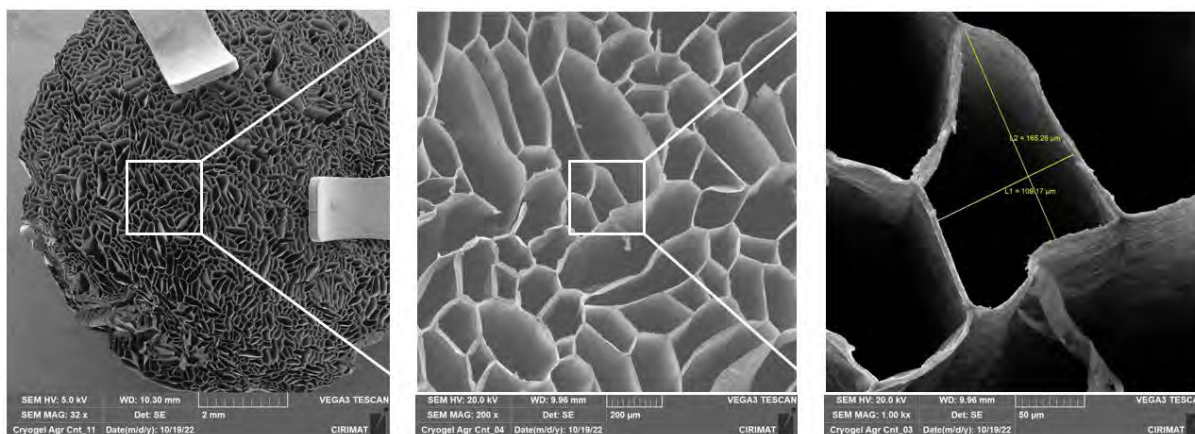


**Figure 3.10** – SEM observations of macropores in directional freeze-cast nanocomposite hydrogel.

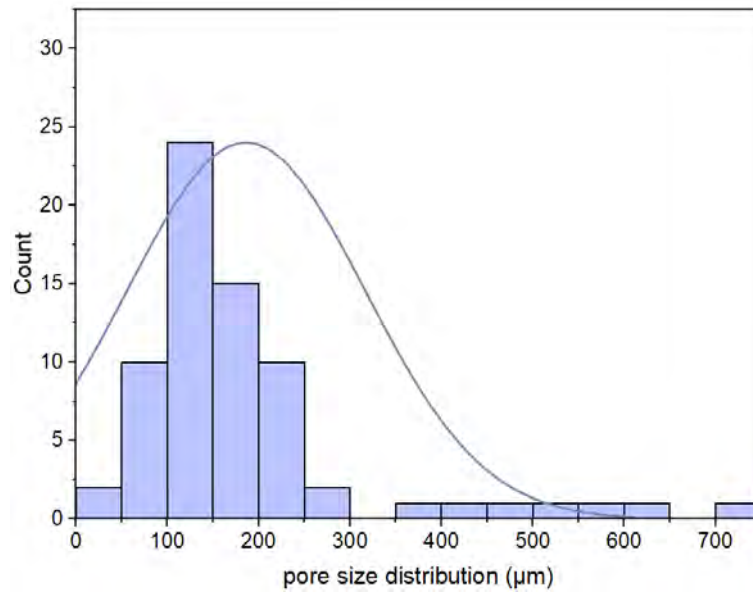


**Figure 3.11** – Macropore size distribution in directional freeze-cast nanocomposite hydrogel.

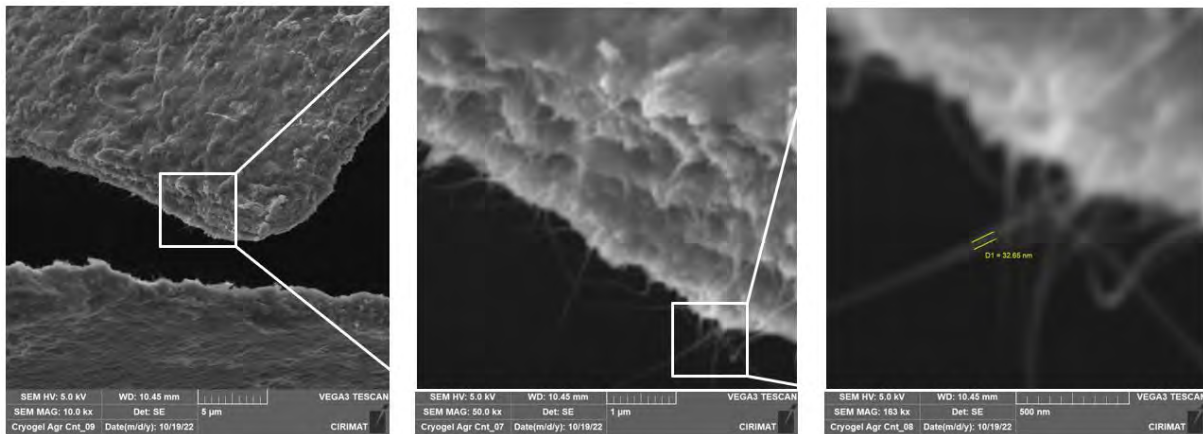


**Figure 3.12** – SEM observations of CNT bundles in directional freeze-cast nanocomposite hydrogel.

### 3.4.3 Drying – swelling cycles

The possible reusability of hydrogels was investigated, by calculating the swelling ratio after a number of drying and swelling cycles. The hydrogels were air-dried for 48 h at 30 °C, had their mass measured and were then placed in DI water to swell over 24 h. This procedure was repeated 9 times. The swelling ratio of the agarose hydrogels (AGR) started at  $4.8 \pm 0.6$  (range 4.3 – 5.5,  $n=3$ ) and the initial swelling ratio of the nanocomposite hydrogels (AGR-CNT<sub>10</sub>CMC<sub>1</sub>) was  $3.25 \pm 0.13$  (range 3.12 – 3.38,  $n=3$ ). At the end of the dry/swell cycles the swelling ratio of agarose hydrogels had dropped to  $2.59 \pm 0.12$  (range 2.50 – 2.72,  $n=3$ , 50 % of initial value) and of the nanocomposite hydrogels to  $1.92 \pm 0.09$  (range 1.86 – 2.02,  $n=3$ , 60 % of initial value). The results are presented in **Figure 3.13** A and B.

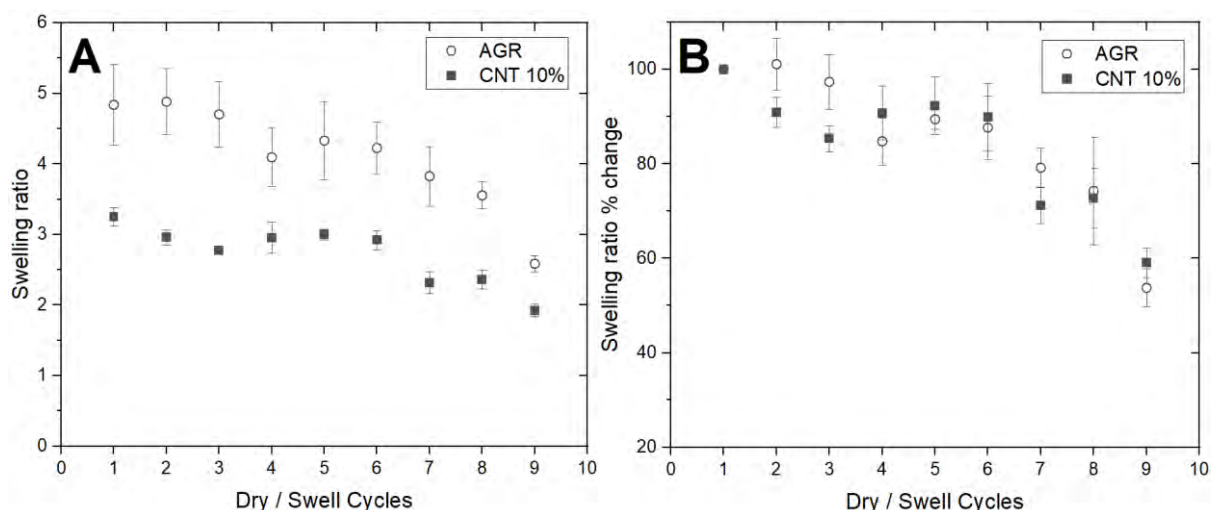


**Figure 3.13** – Swelling ratio of agarose and nanocomposite hydrogels over 9 dry / swell cycles. (A) Absolute values. (B) Percentage change of swelling ratio (compared to baseline).

In both cases there was a deterioration of the swelling capacity of hydrogels, after 9 cycles. In terms of percentage change, this deterioration was very similar in plain and nanocomposite hydrogels (**Figure 3.13 B**). In both cases, the most important deterioration started after the 7<sup>th</sup> dry/swell cycle. During the first 6 cycles, the swelling ratio remained within 85 % of the initial value. After the 7<sup>th</sup>, 8<sup>th</sup> and 9<sup>th</sup> cycle it rapidly deteriorated to 80 %, 75 %, 55 % and 70 %, 70 %, 60 % for the agarose and for the nanocomposite hydrogels, respectively. The reasons for this deterioration may be morphological changes in the polymer chain network, including progressive entanglement of agarose chains over the swelling / drying cycles. This resulted in a stiffer network, losing a part of its ability to expand.

We inferred that there is a reusability potential for the reservoir function of the hydrogels, at least for 5 to 6 cycles of use. However, in the following chapters we chose to not reuse the hydrogels in order to ensure repeatability and same starting conditions for the biological and electrical characterization experiments.

#### 3.4.4 Alginate/chitosan

Alginate/chitosan hydrogels were prepared in order to evaluate the influence of different polymers (others than agarose) on the properties of the hydrogel, and especially to tune its hydrophilicity and surface charge. This may be especially interesting to obtain a better match between the reservoir and the drug when the properties of the drug are modified. Alginate/chitosan hydrogels were prepared by modifying an existing protocol of hydrogels for entrapment of cancerous cells in the brain [169], [170]. The protocol was modified to include CNTs, dispersed in the hydrogel matrix and the hydrogel precursor solution was cast into our silicone molds (cylinders of 10 mm diameter and 2 mm height). We followed the same protocols for materials characterizations as with the agarose hydrogels.

We prepared four batches of alginate/chitosan hydrogels containing 1 % w/w alginate 0.5 % w/w chitosan (AL/CS) with increasing CNT concentrations. CMC was used as a dispersant. The swelling ratio of alginate/chitosan hydrogels and the impact of increasing CNT concentration on the swelling ratio are presented in **Figure 3.14**. Plain alginate/chitosan hydrogels (AL/CS) had a swelling ratio of  $0.33 \pm 0.06$  (range 0.26 – 0.39, n=4), AL/CS-CNT<sub>1.7</sub>CMC<sub>0.17</sub> hydrogels had  $0.16 \pm 0.06$  (range 0.08 – 0.21, n=4), AL/CS-CNT<sub>8.3</sub>CMC<sub>0.83</sub> hydrogels had  $0.17 \pm 0.03$  (range 0.14 – 0.22, n=4) and AL/CS-CNT<sub>16.7</sub>CMC<sub>1.67</sub> hydrogels had a swelling ratio of  $0.14 \pm 0.03$  (range 0.12 – 0.18, n=4).

The alginate/chitosan hydrogels had a very small swelling capacity, absorbing only 14 % to 32 % of their dry mass in water. This came in stark contrast with the agarose-based hydrogels, which absorbed 270 % to 460 %, depending on the CNT concentration. In alginate/chitosan hydrogels, similarly with the agarose ones, the incorporation of CNTs moderately decreased their swelling capacity by 50 % to 60 %. In the case of alginate-chitosan hydrogels, the decrease was similar on the three concentrations tested.

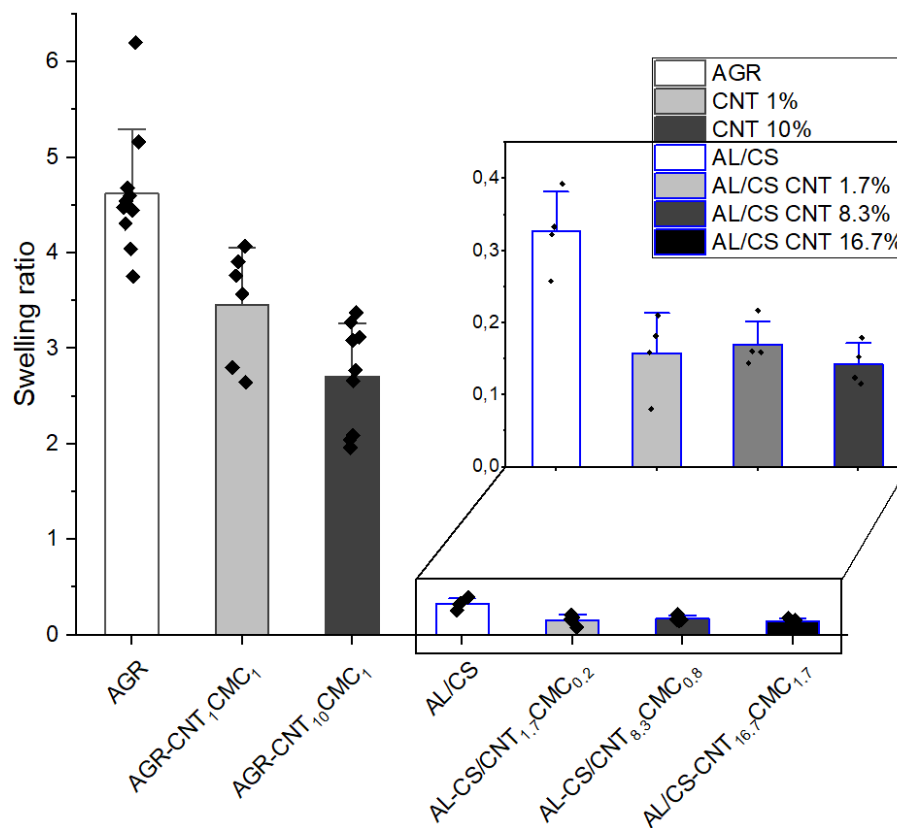


**Figure 3.14** – Swelling ratio of alginate/chitosan hydrogels, compared to agarose hydrogels.

The alginate/chitosan hydrogels formed an interpenetrating double network of alginate chains physically cross-linked with  $\text{Ca}^{2+}$  ions and chitosan chains chemically cross-linked with genipin. Alginate is a highly hydrophilic polymer and physical hydrogels prepared with alginate alone are known to have high swelling ratios [171]. Chitosan is also a hydrophilic polymer, but the covalent cross-linking of the chitosan chains rigidified the polymer matrix, restraining its expansion capacity. In the alginate/chitosan hydrogels, chemically cross-linked chitosan chains are found all over the polymer network, resulting in densely packed, rigid hydrogels with minor absorbing capacities.

Incorporation of CNTs in these hydrogels had the same effect as in agarose hydrogels: further rigidification of the polymer structure, combined with the hydrophobic surface of CNTs, moderately decreased the swelling ratio of nanocomposite alginate/chitosan hydrogels.

Physically cross-linked alginate hydrogels, at 1 to 1.5 % w/w concentration (without chitosan), did not possess adequate mechanical properties to be further investigated. They were fluid-like and difficult to manipulate. Increasing the alginate and/or cross-linker concentration ( $\text{Ca}^{2+}$  ions) could result in stronger hydrogels.



### 3.5 Drying and swelling kinetics

The drying and swelling kinetics of the hydrogels were briefly studied. We measured the mass loss of agarose hydrogels at 50 and 70 °C (**Figure 3.15**), and we compared the mass and height changes of agarose and nanocomposite hydrogels at 70 °C (**Figure 3.16**). We also studied the kinetics of water absorption in dry agarose and nanocomposite hydrogels (**Figure 3.17**).

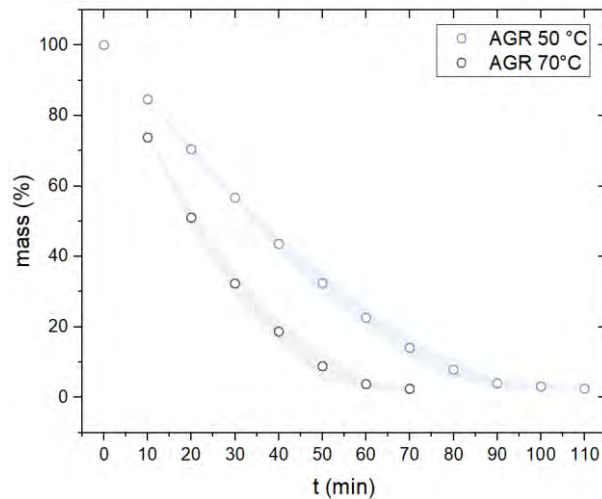


**Figure 3.15** – Drying kinetics of fresh agarose hydrogels at 50 °C (blue circles) and 70 °C (grey circles). n=2.

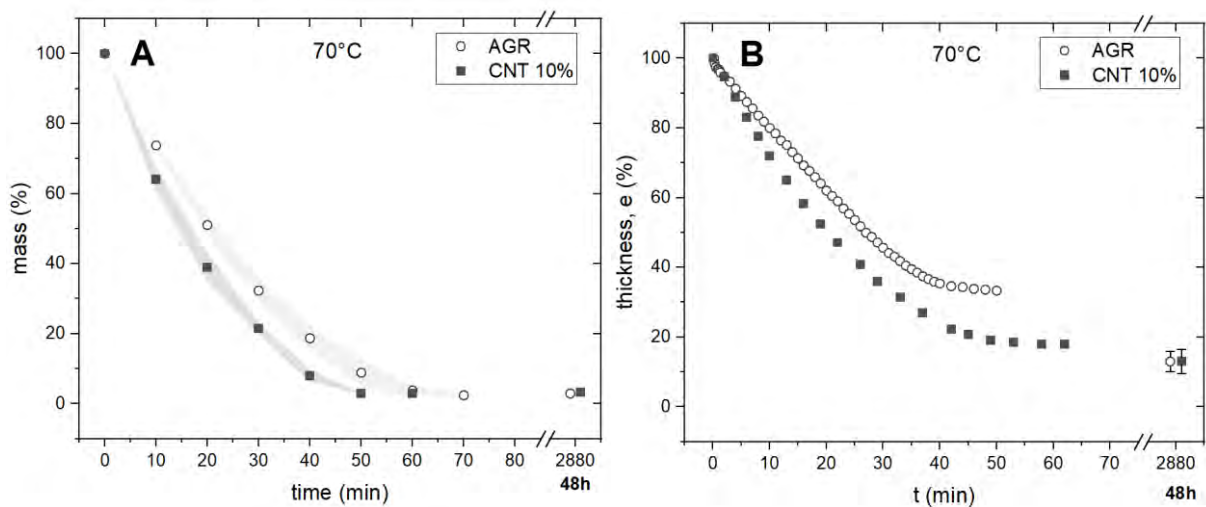


**Figure 3.16** – Mass and height variation of plain agarose (AGR) and nanocomposite hydrogels (AGR-CNT<sub>10</sub>CMC<sub>1</sub>) during drying at 70 °C. (A) Mass variation of agarose (AGR, white circles) and nanocomposite (AGR-CNT<sub>10</sub>CMC<sub>1</sub>, black squares) hydrogels at 70 °C. n=2. (B) Height variation of agarose (white circles) and nanocomposite (black squares) hydrogels at 70 °C. n=1.

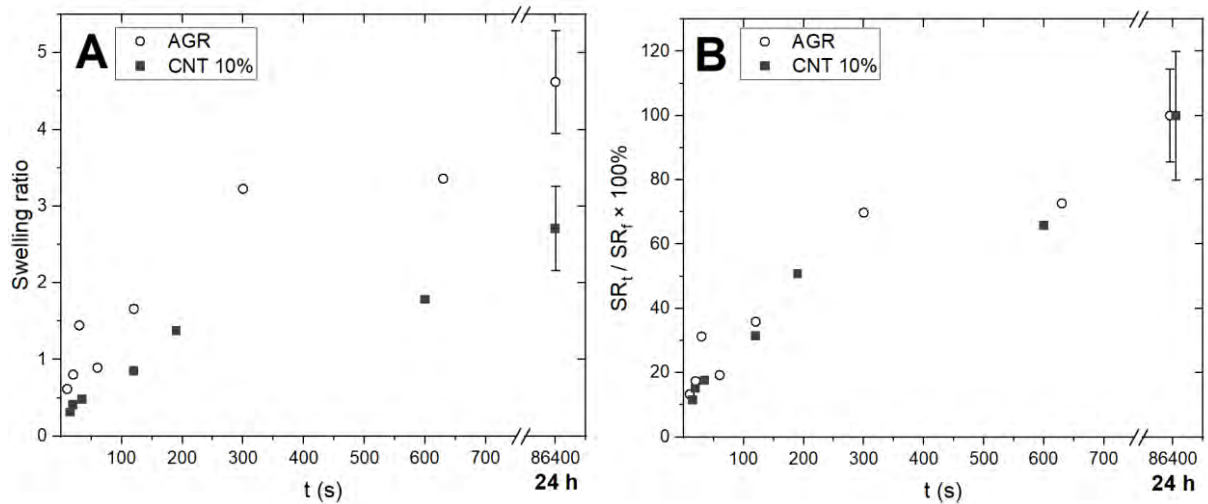


**Figure 3.17** – Water absorption over time for agarose and nanocomposite hydrogels.  $n=1$  up to 700 s;  $n=10$  for 24 h SR. (A) Swelling ratio. (B) Percentage of current swelling ratio over 24 h swelling ratio ( $SR_t$ ).

The agarose hydrogels dried over 100 min at 50 °C and 60 min at 70 °C. A small difference was observed on the drying speed and height loss between agarose and nanocomposite hydrogels, with nanocomposite hydrogels drying and losing height slightly faster than plain agarose hydrogels.

Water absorption was rapid in both types of hydrogels. Over 30 % of water absorption occurred within the first 2 minutes, and the largest water absorption (over 60 % of final value) occurred within 10 minutes. Nanocomposite hydrogels had lower swelling ratios over time, but when normalized to the final absorption values, the kinetics appeared to be similar in both types of hydrogels. Previous works showed that leaving the hydrogels to swell for 10 days, moderately increased the swelling ratio of agarose hydrogels by *ca.* 5 % compared to swelling for 24 h [157]. However, we decided to stick to the 24 h swelling protocol, as it was more practical and realistic for a clinical setting.

The kinetics of water absorption in directional freeze-cast hydrogels were too fast to be monitored. The following images shows the water release and absorption and the subsequent dimension change of a sample hydrogel (**Figure 3.18**).

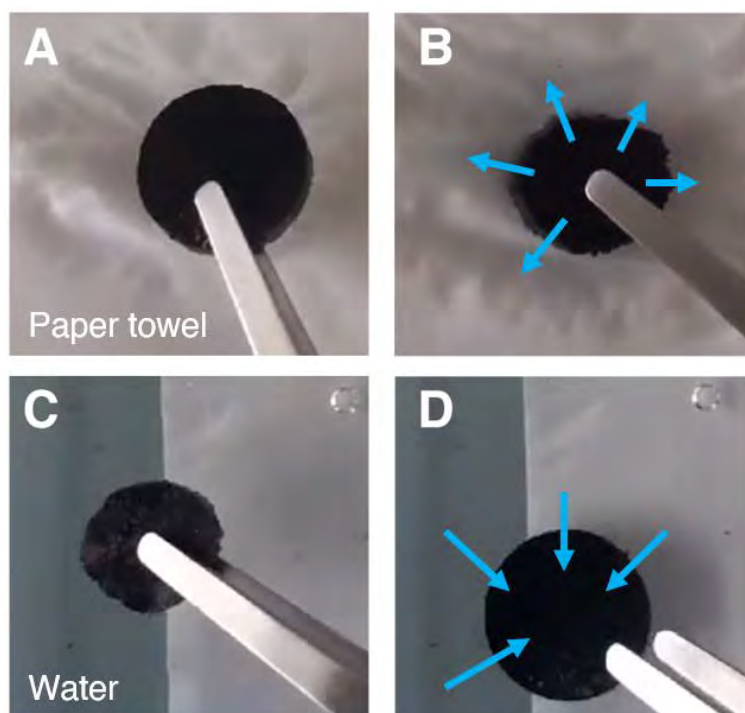


**Figure 3.18** – Water release and swelling of nanocomposite directional freeze-cast hydrogel (AGR-CNT<sub>10</sub>CMC<sub>1</sub>\_S\_dir). The water-loaded hydrogel releases the water quasi-instantaneously, on contact with a humidified paper towel (A, B). The same hydrogel then rapidly (< 2 s) swells with water the moment it is submerged in an aqueous solution (C, D).

### 3.6 Mechanical properties

The mechanical properties of some of our hydrogel samples were tested. In previous works, it was found that the CNTs incorporated into the hydrogels did not have a significant impact on the mechanical properties [157]. However, processing methods, such as freezing the hydrogels and then air-drying, before swelling had an impact on these properties, because of the creation of the macropores within the hydrogel network. The elastic and conservation modules of frozen hydrogels was found to be higher [157].

In the current work, we tested the impact of different polymers on the mechanical properties of the hydrogel matrix. We compared the compression module of agarose hydrogels with alginate/chitosan hydrogels, and we studied the impact of increasing CNT concentration on the compression module of alginate/chitosan hydrogels.

Plain alginate/chitosan hydrogels (AL/CS) had a compression module of  $40 \pm 30$  kPa (range 23 – 73, n=3), AL/CS-CNT<sub>1.7</sub>CMC<sub>0.17</sub> hydrogels had  $100 \pm 50$  kPa (range 48 – 157, n=3), AL/CS-CNT<sub>8.3</sub>CMC<sub>0.83</sub> hydrogels had  $50 \pm 30$  kPa (range 26 – 79, n=3) and AL/CS-CNT<sub>16.7</sub>CMC<sub>1.67</sub> hydrogels had  $17 \pm 5$  kPa (range 12 – 20, n=3). For comparison, agarose nanocomposite hydrogels (AGR-CNT<sub>10</sub>CMC<sub>1</sub>) had a compression module of  $200 \pm 100$  kPa (range 95 – 300, n=3).

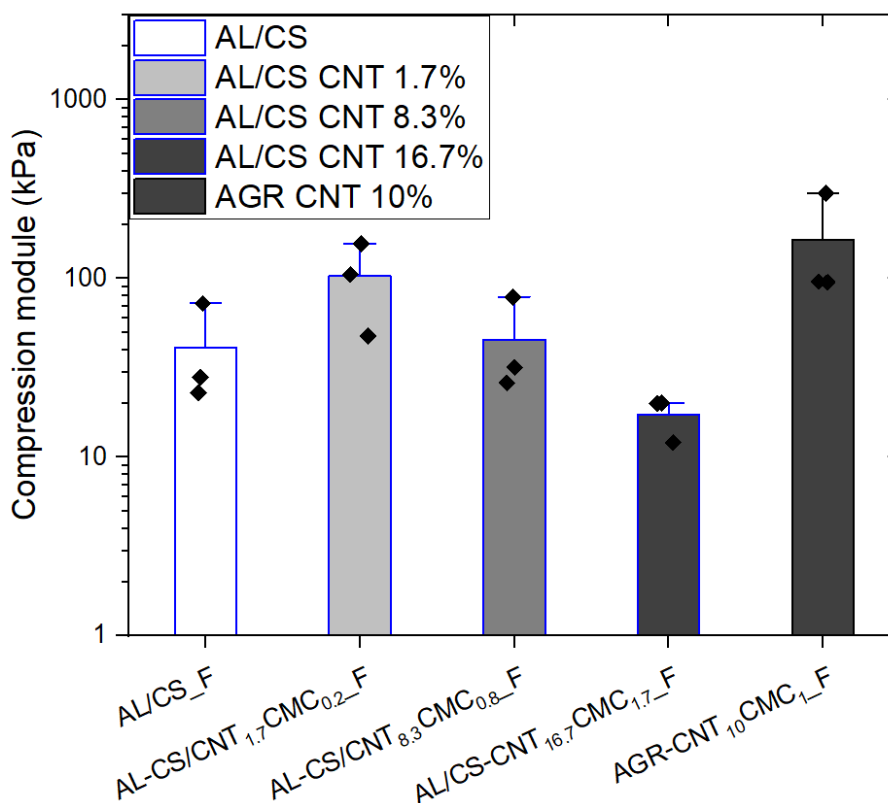


**Figure 3.19** – Mechanical properties of alginate/chitosan hydrogels. Compression module of alginate/chitosan hydrogels with increasing CNT concentration compared to compression modules of nanocomposite agarose and hydrogels. n=3.

The differences between the alginate/chitosan hydrogels with increasing CNT concentration were not statistically significant (for  $\alpha=0.05$ , Tukey's test). The hydrogel with CNTs 1.7 wt. % of polymer had a slightly higher compression module than the others. This behavior not uncommon in nanoreinforced polymers, *i.e.* increased mechanical strength at lower concentrations which then decreases over a threshold concentration. It is explained by the interactions between the nanomaterials and the polymer matrix at different concentrations. At low concentrations of nanomaterials, they may act as reinforcing agents, enhancing the mechanical properties of the polymer. This could be attributed to the effective dispersion of the nanomaterials within the polymer matrix, providing additional points of reinforcement that resist deformation and distribute stress more uniformly. As the concentration of nanomaterials increases, there is an optimal range where the interactions between the nanomaterials and polymer matrix are most effective in reinforcing the material. At higher concentrations, the nanomaterials start to agglomerate, leading to areas of weak bonding and reduced mechanical strength. These agglomerates act as stress concentrators, causing premature failure and a decrease in overall mechanical properties [172], [173]. However, our compression module measurements had high variances, thus our conclusion must be taken with caution. The small differences in mean values may well be due to random fluctuation between samples.

The agarose nanocomposite hydrogels had higher compression modules than the alginate/chitosan hydrogels with same CNT concentration per mass. This difference was significant at the 90 % level ( $p=0.098$ , Student's t-test). The agarose hydrogels had higher polymer concentrations (2.5 % w/w), in total, than the alginate/chitosan ones (1.5 % w/w)

## 3.7 Electrical characterizations

### 3.7.1 CNT conductivity in aqueous suspension

The electrical conductivity and percolation of CNTs in aqueous suspensions was investigated, aiming at better understanding the impact of CNTs on the electrical properties of hydrogels. The hydrogels we prepared had water contents >97 %, thus the electrical behavior of CNTs in aqueous suspensions is relevant for understanding the electrical properties of the nanocomposite hydrogels. CNTs in decreasing concentrations were dispersed into DI water through probe sonication and ultrasonic bath. No dispersant was used, as CMC addition would considerably increase the conductivity of the aqueous solution (The form in which we use it is salt form, sodium carboxymethyl cellulose).

For concentrations lower than 0.1 mg/ml, the electrical conductivity of the CNT suspensions remained constant at  $(1.6 - 2) \times 10^{-3}$  S/m. After CNT concentration of 0.25 mg/ml, the conductivity rapidly increased to  $(8 \pm 2) \times 10^{-3}$  S/m,  $(8 \pm 0.2) \times 10^{-2}$  S/m and  $0.49 \pm 0.12$  S/m for concentrations of 0.25, 1 and 2.5 mg/ml, respectively (**Figure 3.20**). The oxidized CNTs showed a similar trend.

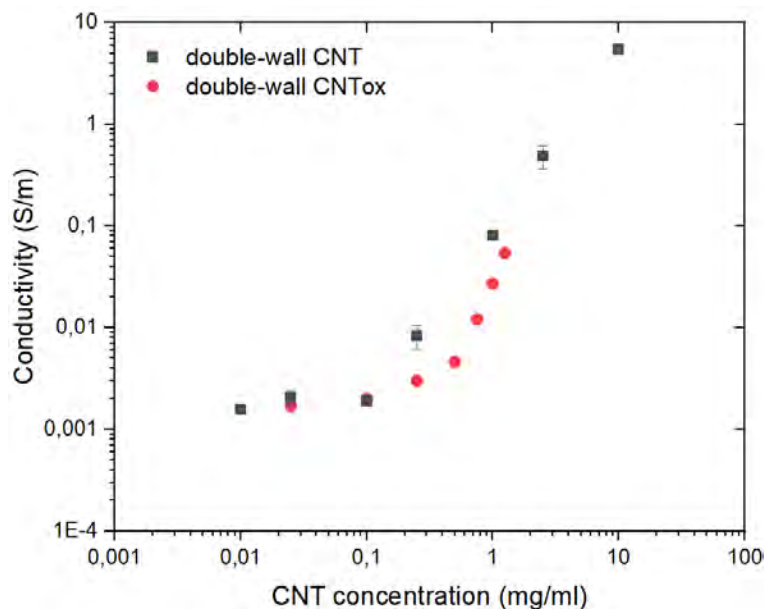


**Figure 3.20** – Conductivity and electrical percolation of CNTs in aqueous suspension. Conductivity of double-wall CNTs (black squares, n=2) and oxidized double-wall CNTs (red circles, n=1).

The electrical conductivity of the CNT suspensions increased in a non-linear manner. This was attributed to the electrical percolation of CNTs at a concentration between 0.1 and 0.25 mg/ml. At this concentration, the dispersed CNTs started to form a conductive network that extended all over the suspension. For lower concentrations, the conductivity was constant at  $(1.6 - 2) \times 10^{-3}$  S/m, higher than the conductivity of deionized water ( $5 \times 10^{-6}$  to  $5 \times 10^{-5}$  S/m). The increased conductivity at concentrations lower than the percolation threshold was due to ionic impurities present in the water. These may have originated from the CNTs suspension, or contact of the deionized water with labware and air.

The oxidized CNTs have hydrophilic groups in their surface, rendering them less hydrophobic. This facilitates their dispersion into aqueous suspensions, without the use of dispersing agents. The overall electrical conductivity of oxidized CNTs is moderately lower than that of pristine CNTs, because of the defects on their surface (oxygen, hydroxyl and carboxylic groups) [174]. In the current study we did

not observe any major difference in the electrical conductivity between oxidized and plain double-wall CNTs.

As we will see in the following chapters, the electrical conductivity of hydrogels with comparable CNT concentrations was considerably lower. Moreover, higher concentrations of CNTs were required in order to measure an increase in electrical conductivity. Even though hydrogels are mainly composed of water, there are two important differences, compared to aqueous suspensions: (1) in hydrogels, the CNTs are wrapped by isolating polymer chains, (2) CNTs in hydrogels are fixed to their positions to a much greater extent than in aqueous suspensions, where their movement is free. Bauhofer and Kovacs argued that the dynamic (kinetic) percolation threshold, *i.e.* the percolation threshold for nanomaterials that have a degree of free movement was lower than the statistical percolation threshold for nanocomposite polymers [175].

Lima *et al.* reported on the conductivity of CNTs in suspension [176]. They observed a percolation threshold around 0.1 mg/ml, depending on the type of CNT (single-wall, multi-wall, short/long), similar to our results. However, they reported a steeper increase in electrical conductivity, partly due to the fact that they dispersed the CNTs in chloroform, a perfectly insulating solvent, thus starting at very low conductivities (near  $10^{-8}$  S/m) [176].

### 3.7.2 DC conductivity

The electrical conductivity of the hydrogels for drug delivery is the most important parameter for their function as an electrode for the application of the electrical pulses. The distribution of the electric field within the skin depends on the potential difference applied on the surface of the skin, which in turn depends on the pulse amplitude produced by the generator and the voltage drop within the electrodes.

In the drug delivery experiments, the voltage applied consisted of millisecond-range square pulses of few hundreds of volts (50 – 400 V). We chose to study the conductivity of the hydrogel platforms in low-voltage (0.5 to 1 V) DC and AC, for the following reasons: (1) **Water electrolysis**. Applying voltages over 1.23 V for extended periods of time results in the electrolysis of water in the hydrogels, producing hydrogen (cathode) and oxygen (anode) gas. (2) **Comparability with literature**. Most electrical conductivity studies in hydrogels perform electrical characterizations at low voltages [177]. If we assume a linear conductivity for the hydrogels, the electrical conductivity values are the same regardless of the applied electric field (We will see later that this was not the case).

In the following paragraphs, we examine the impact of CNT concentrations, dispersion and type, as well as the impact of ionic solutions, processing methods and different polymers on the DC conductivity of hydrogels for drug delivery.

#### 3.7.2.1 CNT concentration

Double-wall carbon nanotubes were incorporated in the agarose hydrogels, with increasing concentrations. Carboxymethyl cellulose was added to facilitate the dispersion of CNTs in the aqueous suspension. Electrical conductivities were measured in the fresh state, for comparisons and as a more reproducible type of sample and also after being dried and swollen, which is most relevant for our application. The impact of increasing nanomaterial concentration on the electrical conductivities of the hydrogels is presented in **Figure 3.21**.



The electrical conductivity of plain agarose hydrogels was  $(2.0 \pm 1.3) \times 10^{-5}$  S/m in the fresh state and  $(1.1 \pm 0.7) \times 10^{-6}$  S/m in the swollen state. The incorporation of 1 % or 5 % (w/w of polymer) CNTs did not have an impact on the electrical conductivity of the hydrogels. A concentration of 10 % CNTs increased the electrical conductivity of fresh hydrogels to  $(3.3 \pm 0.5) \times 10^{-4}$  S/m and to  $(3.4 \pm 1.5) \times 10^{-4}$  S/m for the swollen hydrogels, an increase by one and two orders of magnitude, respectively. Increasing the CNT concentration to 20 % did not further increase the electrical conductivity of fresh hydrogels, while moderately decreased the conductivity of swollen hydrogels, compared to a concentration of 10 %.

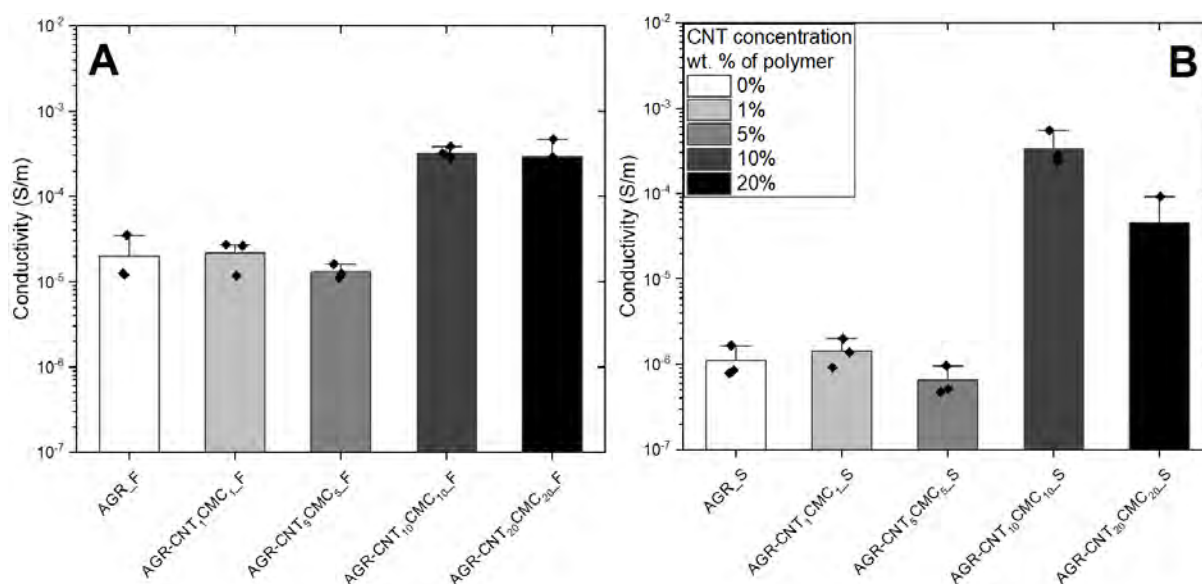


**Figure 3.21** – Impact of CNT concentration on hydrogel electrical conductivity. Electrical conductivity of fresh (A, n=3-4) and swollen (B, n=3-4) agarose hydrogels with increasing CNT concentration.

The percolation threshold concentration for our system is thus located between 5 % and 10 % of CNTs, expressed as a percentage of the polymer. Expressed as a percentage concentration of the whole system (polymer + water + nanomaterial + dispersant), this roughly corresponds to a concentration between 0.125 and 0.25 % w/w or between 0.07 and 0.14 % v/v. This was the critical concentration after which an interconnecting network of carbon nanotubes was formed within the hydrogel, increasing the electrical conductivity of the system thanks to electron conduction through the network of CNTs.

The qualitative behavior of the conductivity, with increasing nanomaterial concentration, is typical of a percolation system: no increase in conductivity for low concentrations, a jump-like transition after the percolation threshold and a high conductivity plateau, where higher concentrations of nanomaterial do not further increase the electrical conductivity. Quantitatively though, the conductivity increase was moderate: one to two orders of magnitude. The electrical conductivity increase of (monophasic) polymers with CNTs can reach several orders of magnitude [178]. However, in the case of hydrogels, the conductivity increase through the incorporation of conductive nanomaterials is lower than in solid polymer nanocomposites [177]. This was explained by numerous factors: hydrogels are less studied than solid polymers, poor dispersions of nanomaterials in aqueous systems and polymer chains within hydrogels may wrap around the nanomaterials, limiting the conductive contact.

Kovacs and Bauhofer (2009) reviewed hundreds of polymer/CNTs nanocomposite systems and suggested a quasi-global percolation threshold of 0.1 % w/w, with optimal dispersion [175]. Indeed, the percolation threshold mostly depends on the nanomaterials used, thus it is reasonable to propose a global percolation threshold by category of nanomaterial. However, the individual properties of the nanomaterials of the same type (for example CNT length) as well as the interactions of the nanomaterial with the polymer and other components of the system will also have a substantial impact on the percolation threshold. Our experimentally calculated threshold (between 0.125 and 0.25 % w/w CNT) was in close agreement with the suggested percolation threshold.

The electrical conductivities of hydrogels with concentrations lower than the percolation threshold (0, 1 % and 5 % CNTs) decreased by approximately one order of magnitude in the swollen state. This decrease is explained by the conduction mechanism, which is ionic conduction. Ionic conduction depends on the concentration and mobility of ions. Even though the agarose hydrogels are prepared with deionized water, they contain ions through reagent impurities, the dispersing agent, and contact with air and labware. Fresh hydrogels contain a greater water content than swollen hydrogels, thus the ionic mobility is greatly enhanced. Even if the swollen hydrogels contain a higher concentration of ions, their mobility is restricted because of the shrinkage of the water phase.

On the other hand, the nanocomposite hydrogel with a concentration of 10 % CNTs maintained its electrical conductivity in the swollen state. The conduction mechanism in this hydrogel was -at least partly- electronic conduction through the percolating nanomaterial network. The shrinkage of the water phase decreased the ionic mobility but did not affect the percolating network. It is possible that the hydrogels in swollen state have a denser network of nanomaterials. Indeed, swollen hydrogels lost a big part of their water content, increasing the concentration of the other constituents. The mass concentration of CNTs in swollen hydrogels was increased 6 to 8 times, from 0.025 % - 0.5 % w/w in fresh hydrogels up to 0.2 % – 4 % w/w in swollen ones. However, this increased concentration was not accompanied by an increase in electrical conductivity. One hypothesis is that the drying process created stratified parallel layers of polymer chains and CNTs. This hypothesis was first put forward by Guillet (2017), after the observation of dry nanocomposite hydrogels on the electronic microscope (**Figure 3.22**) [158]. Certainly, the alignment and orientation of nanomaterials plays an important role in the electrical properties and the percolation threshold.

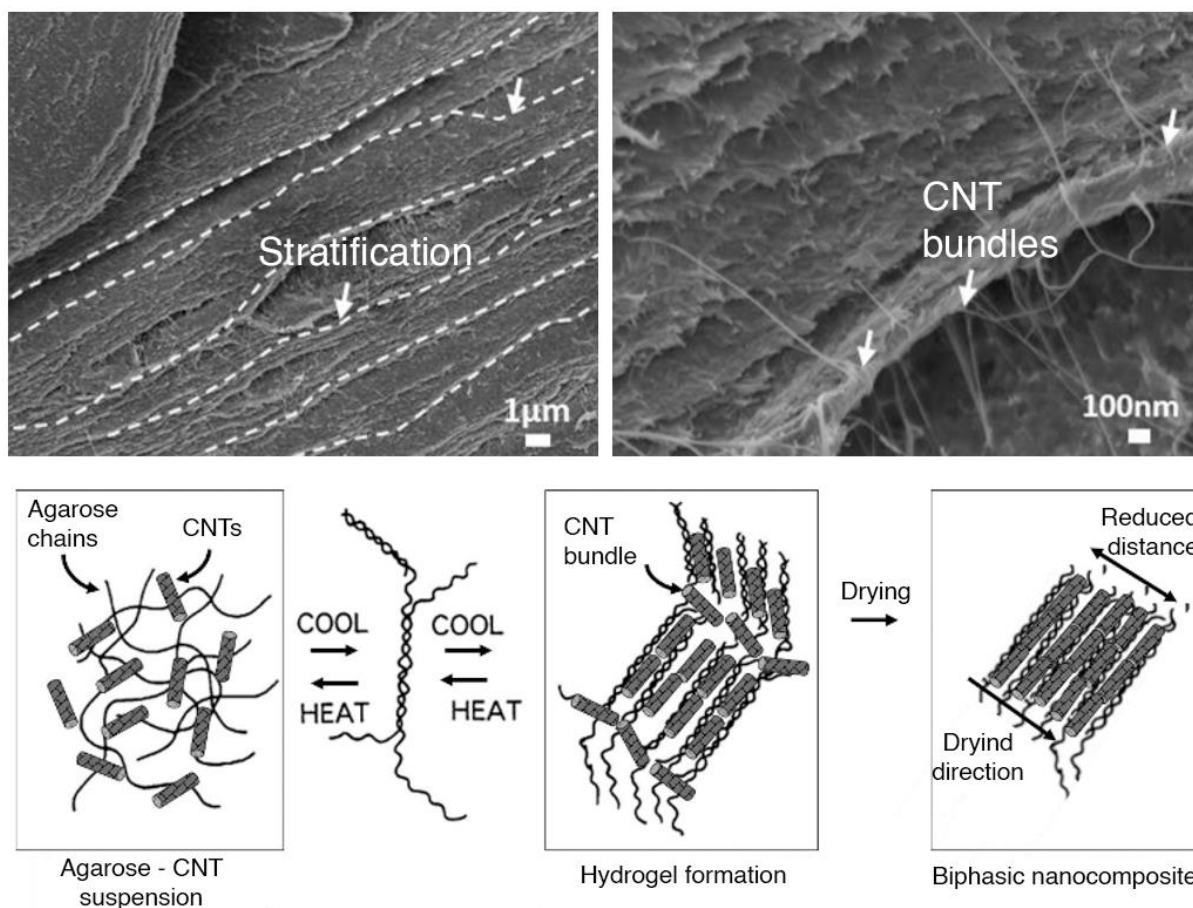


**Figure 3.22** – SEM observations of dry nanocomposite hydrogel (AGR-CNT<sub>1</sub>) and proposed parallel alignment of CNTs and polymer chains during drying. Adapted from ref. [158].

Lastly, we observed that the electrical conductivity of swollen nanocomposite hydrogels with 20 % CNTs was moderately lower than the swollen hydrogels at 10 % CNT concentration. This can be explained by the poor dispersion of high concentrations of CNTs in aqueous suspensions. Aqueous suspensions of CNTs with concentrations over 0.5 % w/w are very viscous. The dispersion methods (probe sonication, ultrasonic bath) become less effective and the nanomaterials form big aggregates. Furthermore, hydrogels with higher concentration of CNTs absorbed less water during the swelling procedure. This also contributed to limit the ionic mobility in the hydrogels with higher CNT concentrations.

### 3.7.2.2 CNT dispersion

Effective dispersion of nanomaterials is essential for their property-enhancing features. In particular, a substantial increase in electrical conductivity of nanocomposite hydrogels can only take place once the filler particles have formed a percolative network, and the agglomeration of nanomaterials dramatically increases the percolation threshold concentration.

Carbon-based nanomaterials, and in specific, CNTs, have highly hydrophobic surfaces and low interfacial compatibility with polymer matrices [177]. For these reasons, a dispersing agent was added to facilitate their dispersion in aqueous suspensions. Carboxymethyl cellulose (CMC) is a polysaccharide that can be adsorbed on the surface of CNTs through non-covalent interactions between the glucose ring of CMC and the hydrophobic surface of CNTs [23]. The hydroxyl and

carboxylic groups present in CMC render the nanotubes more hydrophilic and electrostatic repulsions between the anionic CMC polymer chains prevent agglomeration of nanotubes [24].

The electrical conductivity of hydrogels with 10 % CNTs but without dispersant, AGR-CNT<sub>10</sub>, was  $(7.5 \pm 1.2) \times 10^{-5}$  S/m in the fresh state and  $(2.1 \pm 0.5) \times 10^{-5}$  S/m in the swollen state. With the addition of 1 % CMC, this increased to  $(3.2 \pm 0.4) \times 10^{-4}$  S/m and  $(3.3 \pm 1.7) \times 10^{-4}$  S/m in the fresh and swollen state, respectively. Adding 10 % CMC did not further improve the electrical conductivity. The full results are presented in **Figure 3.23**.

Our results showed that the incorporation of CNTs alone was not enough to get higher values of electrical conductivity. The addition of CMC as a dispersing agent achieved the highest conductivity values for swollen hydrogels, at  $(3.3 \pm 1.7) \times 10^{-4}$  S/m. It did not make a difference if the quantity of CMC was 1 % or 10 %, with respect to the polymer. In the following chapters we used the 1 % concentration, which achieved the same results with less material.

We also tested a second dispersing agent, polydopamine, frequently employed to facilitate the dispersion of carbon-based nanomaterials in hydrogels used as biosensors [177]. Polydopamine coating is inspired by adhesive proteins secreted by mussels to attach to wet surfaces. Dopamine is a simple structural mimic of *Mytilus Edulis* foot protein 5 (Mefp-5) [179]. In an alkaline solution, it self-polymerizes into a thin surface-adherent polydopamine film through oxidation by dissolved oxygen [180], [181]. Polydopamine adheres to a large number of varied surfaces through covalent (Michael reaction of catechol with an amine or thiol) and non-covalent (hydrogen bonds and  $\pi$ - $\pi$  stacking) interactions [181]. In nanocomposite hydrogels, polydopamine coating is used to facilitate nanomaterial dispersion and to confer self-healing and adhesive properties to the hydrogel [139], [182].

We tested polydopamine (pDA) as an alternative dispersing agent to carboxymethyl cellulose (CMC). The dispersion of CNTs through the polymerization of dopamine on their surface, at 1 mg/ml (4 % in respect to the polymer concentration) moderately increased the electrical conductivities of the hydrogels. Hydrogels with 1 % CNTs and no dispersing agent, AGR-CNT<sub>1</sub>, had an electrical conductivity of  $(1.8 \pm 0.6) \times 10^{-5}$  S/m in the fresh state and  $(1.3 \pm 0.3) \times 10^{-6}$  S/m in the swollen state. With pDA, the electrical conductivity increased to  $(1.7 \pm 0.5) \times 10^{-4}$  S/m and  $(1.9 \pm 0.9) \times 10^{-5}$  S/m, in the fresh and swollen state respectively. Hydrogels with 10 % CNTs exhibited a lesser increase: from  $(7.5 \pm 1.2) \times 10^{-5}$  S/m to  $(2.4 \pm 0.2) \times 10^{-4}$  S/m in the fresh state and from  $(2.1 \pm 0.5) \times 10^{-5}$  S/m to  $(3.3 \pm 0.7) \times 10^{-5}$  S/m in the swollen state. The full results are presented in **Figure 3.23**.

Polydopamine had an effect on electrical conductivity of the hydrogels, already at the concentration of 1 % CNTs. This implied that the dispersing ability of pDA was superior than that of CMC, allowing the CNTs to form a percolating network at the lowest concentration. Carboxymethyl cellulose, on the other hand, achieved higher max conductivity, at 10 % CNTs, at the swollen state.

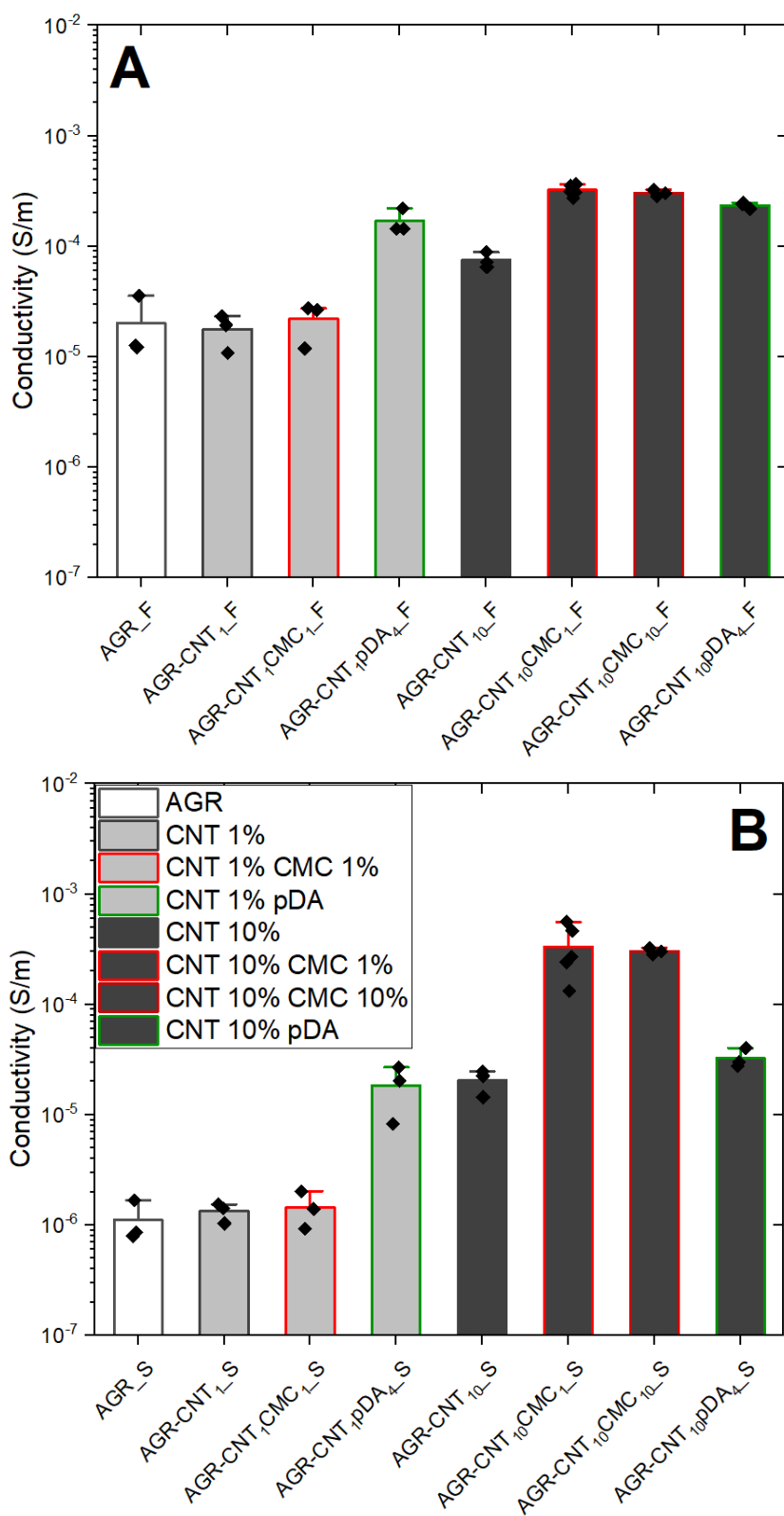


**Figure 3.23** – Impact of carboxymethyl cellulose (CMC, red border on graph) and polydopamine (pDA, green border on graph) on the dispersion and electrical conductivity of CNTs in fresh (A) and swollen (B) agarose nanocomposite hydrogels. The legend is common for both graphs.

As a control experiment, we studied the impact of the dispersing agents alone (without CNTs) on the electrical conductivity of agarose hydrogels (**Figure 3.24**). Carboxymethyl cellulose did not affect the

conductivity of fresh agarose hydrogels at any concentration. At the swollen state, the higher concentration of CMC (5 mg/ml at preparation or 20 wt. % of polymer) increased the conductivity of agarose hydrogels to  $(7.1 \pm 2.5) \times 10^{-6}$  S/m. Polydopamine alone, at a concentration of 1 mg/ml (4 wt. % of polymer) increased the conductivity of fresh agarose hydrogels to  $(1.2 \pm 0.5) \times 10^{-4}$  S/m and of swollen agarose hydrogels to  $(2.3 \pm 1.4) \times 10^{-5}$  S/m.

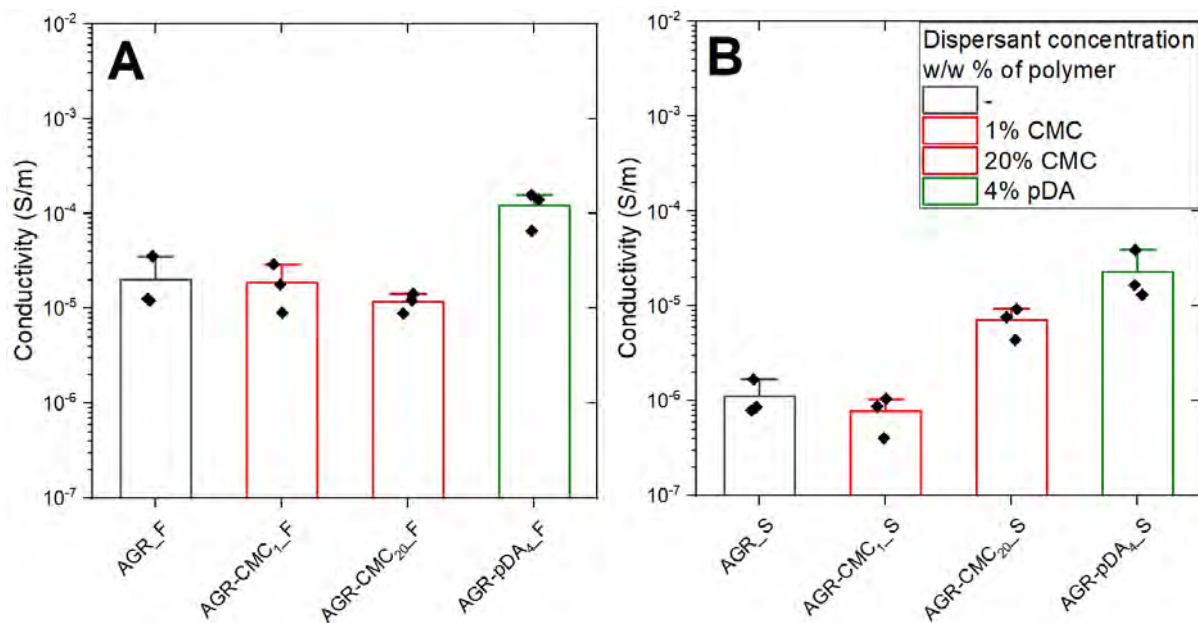


**Figure 3.24** – Impact of dispersants alone (without CNTs) on the electrical conductivity of fresh (A) and swollen (B) agarose hydrogels.

Carboxymethyl cellulose, at concentrations up to 1 %, did not have an impact on the electrical conductivity of the hydrogels. At 20 %, the conductivity increase was attributed to two factors: (1) The agarose hydrogels with 20 % CMC absorbed substantially more water, during swelling. Plain agarose hydrogels had a swollen mass of  $23.9 \pm 2.2$  mg while AGR-CMC<sub>20</sub>\_S hydrogels had a mass of  $34.2 \pm 0.9$  mg. (2) The dispersing agent, CMC, was added in its salt form, sodium carboxymethyl cellulose, imparting ions to the hydrogel. The combination of these two factors, higher water content and higher ion concentration was responsible for the increased conductivity of AGR-CMC<sub>20</sub>\_S hydrogels.

Polydopamine itself, has semiconducting properties, therefore the incorporation of pDA into agarose hydrogels increased their electrical conductivity [183]. As a dispersing agent, it was not clear if it facilitated the dispersion of CNTs. The electrical conductivities of the fresh hydrogels with pDA were similar, regardless of CNT concentration (0, 1 and 10 percent). Likewise, the conductivities of swollen hydrogels with pDA were similar, irrespective of CNT concentration. These findings put into question the dispersing effect, which may be masked under the semiconducting properties of polydopamine polymer itself. The polymerization of dopamine on the surface of CNTs was a complicated procedure, that depended on the reagent concentrations, the pH of the suspension and the sonication duration and power. We did not exclude a dispersing effect of pDA but further work would be necessary to study it in depth (investigation of multiple parameters, combined with microscope observations and conductivity tests).



### 3.7.2.3 CNT type

We tested the influence of two different types of commercial MWCNTs, eight-wall CNTs (Nanocyl, NC3100) and oxidized 20-wall CNTs (Nanothinx), on the electrical conductivity of fresh agarose hydrogels, at a concentration of 10 % w/w. In both cases, the electrical conductivity of the hydrogels was similar to the electrical conductivity obtained with double-wall CNTs (**Figure 3.25**).

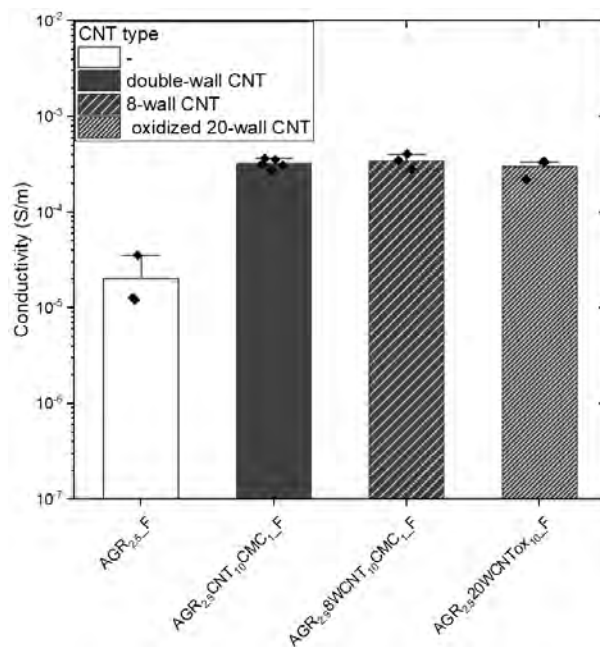


**Figure 3.25** – Impact of different CNT types on the electrical conductivity of fresh agarose nanocomposite hydrogels.

CMC was added, as a dispersing agent, for the 8WCNTs. No dispersing agent was added for the oxidized 20WCNTs. Oxidized nanotubes have hydrophilic functional groups on their surface. In addition, the 20WCNTs had shorter lengths than the DWCNTs. These two factors facilitated their dispersion in the aqueous suspension. The electrical conductivity achieved for the 20-wall CNTs was similar to the double-wall and 8-wall CNTs, but without the use of a dispersing agent.

### 3.7.2.4 Ionic solutions

There are three approaches for increasing the electrical conductivity of hydrogels: (1) incorporation of conductive nanomaterials, (2) using conducting polymers for the hydrogel network and (3) increasing the ionic conductivity of the aqueous phase.

Here, we explored the impact of ionic solutions on the DC electrical conductivity of agarose hydrogels. We added two ionic buffer solutions, a commercial phosphate buffer saline (PB) and a lab-produced electroporation buffer (EB). The electroporation buffer is an isotonic buffered solution very similar to the PB, with the main difference of substituting sodium for sucrose (**Table 3.3**).

**Table 3.3** – Constituents and electrical conductivities of solvents used.

Solvents	Constituents	Electrical conductivity (S/m)
Deionized water	H <sub>2</sub> O	$5 \times 10^{-6}$ to $5 \times 10^{-5}$
Phosphate buffer saline (pb)	137 mM NaCl, 2.7 mM KCl, 8 mM Na <sub>2</sub> HPO <sub>4</sub> , 2 mM KH <sub>2</sub> PO <sub>4</sub>	1.5
Electroporation buffer (eb)	250 mM sucrose, 1 mM MgCl, 8.1 mM K <sub>2</sub> HPO <sub>4</sub> , 1.9 mM KH <sub>2</sub> PO <sub>4</sub>	0.15

Fresh agarose hydrogels were placed into ionic solutions (EB and PB) and left for at least 24 h, to ensure solvent exchange. Swollen hydrogels were air-dried, then placed into ionic solutions for 24 h, swelling with EB and PB, instead of DI water. The impact of these ionic solutions was tested on plain agarose and nanocomposite hydrogels with 1 % CNT and 1 % CMC. CNTs at this concentration (AGR-CNT<sub>1</sub>CMC<sub>1</sub>) did not have an impact on the electrical conductivity.

Counterintuitively, the electrical conductivities of hydrogels with ionic solutions, did not increase, compared to DI water (**Figure 3.26**). This was the case for both ionic solutions studied, regardless of their intrinsic conductivity. The electrical conductivities of the fresh hydrogels did not differ significantly (one-way ANOVA,  $p > 0.05$ ), nor did the electrical conductivities of the swollen hydrogels (one-way ANOVA,  $p > 0.05$ ).

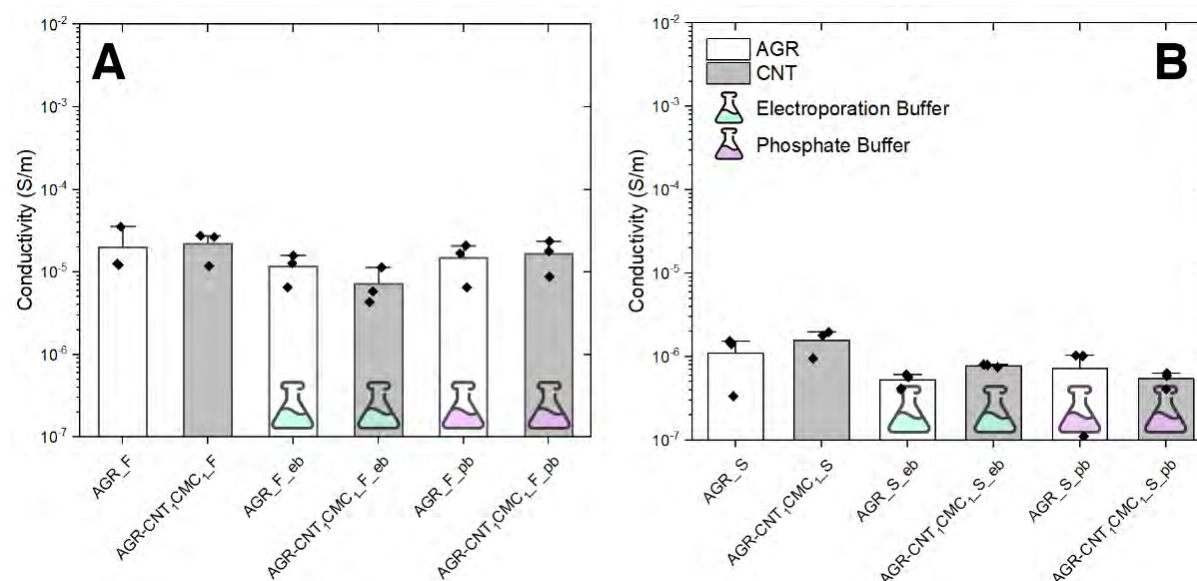


**Figure 3.26** – Impact of ionic solutions (electroporation buffer and phosphate buffer) on the electrical conductivity of fresh (A) and swollen (B) agarose hydrogels.

Typical agarose mesh sizes range from pore diameters between 50 and 600 nm, depending on concentration, polymer length and gelation temperature and kinetics [184], [185]. In our case, the concentration of 2.5 % w/w would place the mesh size towards the lower end of the spectrum. Anyhow, the ions from the ionic solutions used can easily enter the hydrogel pores. However, in order to exclude an inefficient solvent exchange effect, we performed a control experiment, where agarose

hydrogels were prepared with PB solution instead of DI water. In this case again, the ionic solution failed to increase the global electrical conductivity of the hydrogel (**Figure 3.27**).

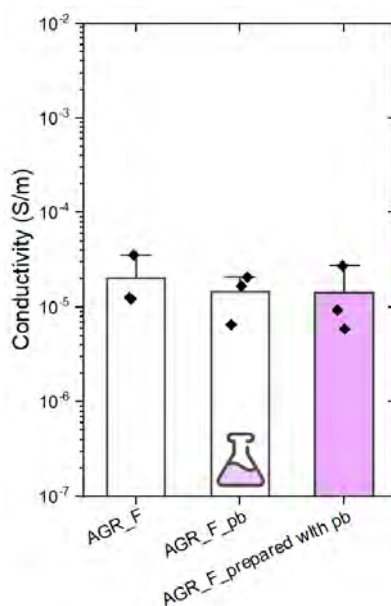


**Figure 3.27** – Comparison of electrical conductivities of fresh agarose hydrogels prepared with deionized water, prepared with DI water and then immersed in phosphate buffer and prepared with phosphate buffer.

How could we then explain the low conductivities of hydrogels with ionic solutions? We suggest that the key is in ion mobility. Electrical conductivity depends on the product of charge carrier concentration and mobility. In the case of agarose hydrogels in ionic solutions, the charge carriers are ions and their concentrations are high enough to confer high conductivities (0.15 and 1.5 S/m) to their ionic solutions. However, the ion mobility within the hydrogel network is severely restrained. Even though the mesh size is more than enough to allow for ion and even macromolecule transfer through the gel, this process has very slow kinetics. Slowly moving ions do not have a significant impact on the electrical conductivity of the hydrogels.

To give a more concrete example, agarose hydrogels are commonly used in molecular biology for DNA electrophoresis. DNA chains are transferred through an agarose gel, under the influence of an electric field. Differences in the size of DNA chains are translated into different travel rates, allowing the approximate identification of DNA base pair numbers. Typical residence times of DNA in agarose gels of few cm wide range from some minutes to few hours, for agarose gels at a concentration of 1 % w/w. Of course, DNA chains are orders of magnitude larger than the small mobile ions in our ionic solutions. However, in a similar manner, ionic mobility is restricted by the dense network of agarose chains, resulting in much lower electrical conductivities than in aqueous solutions.

The fact that electrical conductivities were globally lower in swollen hydrogels supports the above hypothesis. Swollen hydrogels have a denser polymer chain network and a lower water content. This further restriction of ionic mobility translated to a loss of *ca.* one order of magnitude in electrical conductivity.

Another reason may be that the experimental protocol we used was not well-adapted to measure the electrical conductivity of ions. The electrical conductivity of ionic solutions is typically measured with

AC conductometers, immersed in aqueous solutions. However, an increased conductivity due to ionic conduction should have also manifested in the DC conductivity of the samples.

### 3.7.2.5 Processing methods

The impact of different processing methods (air-drying, freezing, directional freeze-casting) on the electrical conductivity of agarose hydrogels was investigated. Freezing increased the electrical conductivity of swollen agarose hydrogels to  $(2.4 \pm 1.4) \times 10^{-5}$  S/m. Directional freeze-casting further increased the conductivity to  $(5.5 \pm 1.1) \times 10^{-4}$  S/m (along the freezing direction). As for the nanocomposite hydrogels with 10 % CNTs and 1 % CMC, air-drying and freezing had similar conductivities at  $(3.3 \pm 1.7) \times 10^{-4}$  S/m and  $(4.0 \pm 2.4) \times 10^{-4}$  S/m, respectively, while directional freeze-casting moderately increased this conductivity to  $(1.0 \pm 0.4) \times 10^{-3}$  S/m. This increase was significant at the 0.01 level, compared to the air-dried hydrogels (Student's t-test,  $p=0.008$ ).

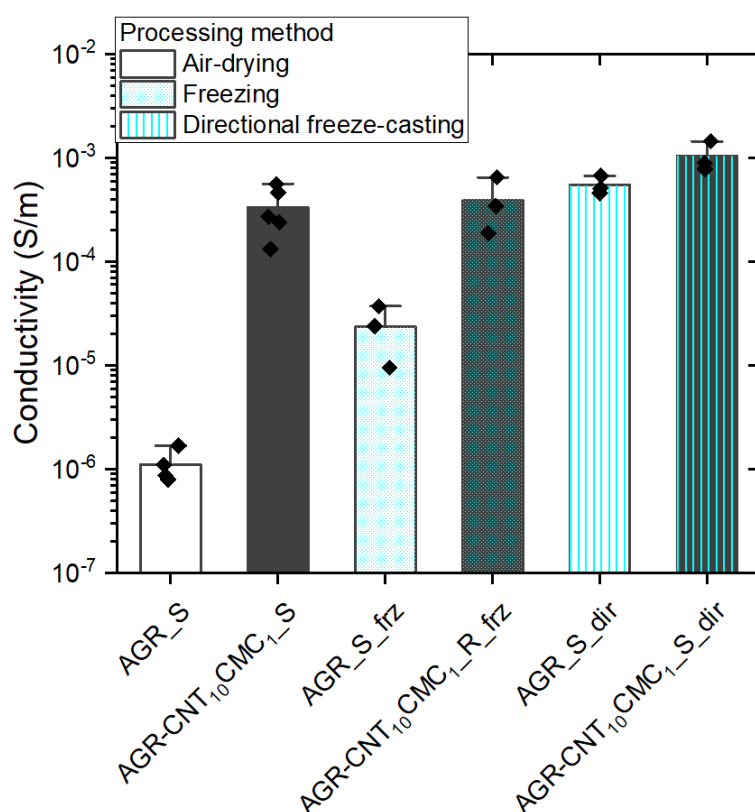


**Figure 3.28** – Impact of processing methods (air-drying, freezing, directional freeze-casting) on the electrical conductivities of swollen agarose hydrogels

Freezing the hydrogels created macropores within the hydrogel network, because of the formation of water crystals. These macropores were responsible for the higher swelling ratio observed in frozen hydrogels. Directional freeze-casting exploited this property to an even greater extent, with the creation of oriented macropores of *ca.* 150  $\mu$ m diameter. These macropores increased the water absorption capacity of the hydrogels. The macropore network also greatly enhanced the ionic mobility of the hydrogels. This was reflected on the electrical conductivity increase of agarose hydrogels by more than two orders of magnitude. In the case of nanocomposite hydrogels, the electrical conductivity was driven by electronic conduction through the CNT network. This conductivity was not affected by freezing. Directional freeze-casting moderately increased the conductivity, compared to air-drying. This was attributed to two factors: (1) a mixed ionic and electronic conductivity and (2) a

possible directional orientation of CNTs along the aligned macropores. Nanomaterials with high aspect ratios, such as nanotubes, can be aligned within the polymer matrix to further increase the conductivity in the alignment orientation [177], [186].

### 3.7.2.6 Alginate/chitosan

We prepared alginate/chitosan hybrid hydrogels in order to evaluate the influence of the hydrophilic polymer on the swelling and the electrical properties of the hydrogels. Four batches were prepared, with an increasing CNT concentration, ranging from 0 to 16.7 % w/w of the polymers (or 0.25 mg/ml).

The electrical conductivity of fresh plain alginate/chitosan hydrogels was  $(4.1 \pm 0.3) \times 10^{-4}$  S/m, higher than that of plain agarose hydrogels and similar to the conductivity of nanocomposite agarose hydrogels at 10 % CNT concentration. The incorporation of CNTs in the alginate/chitosan hydrogels in concentrations ranging from 1.7 % to 16.7 wt. % of polymer (0.025 to 0.25 mg/ml) did not have a significant impact on the electrical conductivity of the hydrogels (one-way ANOVA,  $p=0.3$ ). The conductivity of swollen alginate/chitosan hydrogels was  $(1.2 \pm 0.6) \times 10^{-5}$  S/m and slightly more for the nanocomposite alginate/chitosan hydrogel with the highest CNT concentration at  $(2.9 \pm 2.1) \times 10^{-5}$  S/m, but this difference was not significant at the 0.05 level (Student's t-test,  $p=0.2$ ). The full results are presented in **Figure 3.29**.

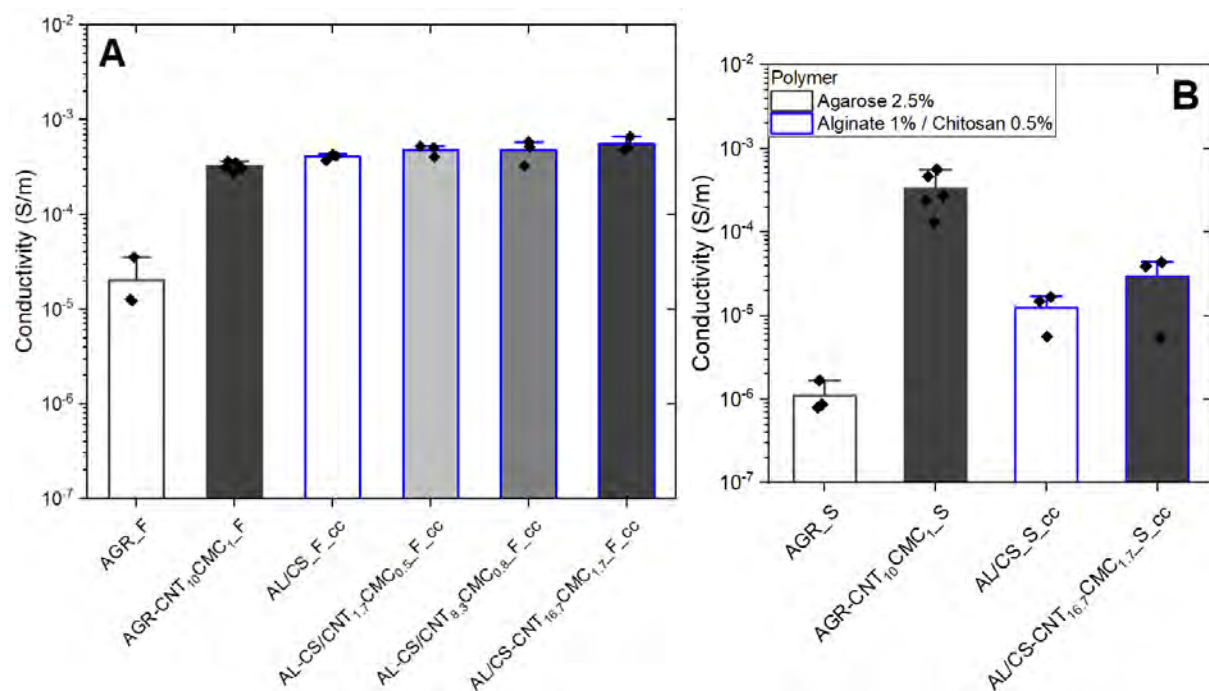


**Figure 3.29** – Comparison of electrical conductivities of nanocomposite hydrogels with different hydrophilic polymers (agarose and alginate/chitosan) in their fresh (A) and swollen (B) state.

The plain alginate/chitosan hydrogels had higher conductivity than the plain agarose hydrogels. We suggest this was due to two factors: (1) Alginate/chitosan hydrogels were cross-linked with, and stored in an ion-rich aqueous solution, more specifically,  $\text{CaCl}_2$  4 % w/w, with an approximate conductivity of 4 S/m. Yet, as we showed for the agarose hydrogels, ionic solutions did not have a significant impact on the overall conductivity because of restrained ion mobility, but this may not stand true for alginate/chitosan hydrogels that had a lower polymer concentration. (2) Different hydrophilic polymers confer different conductivity values to hydrogels. These values can range roughly from  $10^{-6}$  to 1 S/m [177]. In general, agarose and alginate-based hydrogels are more insulating than chitosan

hydrogels, which can have higher conductivity values. The alginate/chitosan hybrid hydrogels stand between the two, getting some conductivity boost from the chitosan network.

The incorporation of CNTs did not increase the electrical conductivity of alginate/chitosan hydrogels in any of the concentrations studied. This was attributed to three factors: (1) Inadequate CNT dispersion within the interpenetrating hydrogel matrix. We adapted the CNT dispersion protocol to the alginate/chitosan hydrogel preparation, by adding CMC and dispersing the CNTs in a small amount of DI water probe sonication. Nonetheless, the dispersion may have been inefficient due to the hydrophobicity of the CNTs and the high viscosity of the suspension. (2) The electrical conductivity of the alginate/chitosan hydrogels was already quite high, without the CNTs. It is likely that the impact of CNTs was masked behind this already high conductivity. (3) It is possible that an outer layer of alginate was formed during the preparation of the hydrogels. Briefly, the nanocomposite hydrogels were prepared as follows: CNTs were dispersed in water with CMC, then mixed with a solution of chitosan and a solution of alginate. In this precursor suspension, genipin was added, in order to chemically cross-link the chitosan chains. Afterwards, an excess of calcium chloride solution was added, to cross-link the alginate chains. During this step, part of the alginate moved from the core of the hydrogel by diffusion towards the calcium chloride solution, and cross-linked as an outer layer. This was visible at times, as a transparent outer layer on a dark black core. Such an insulating layer would substantially limit the conductivity of CNTs. Unfortunately, we did not achieve to slice it out due to the poor mechanical properties of the alginate/chitosan hydrogels.

#### 3.7.2.7 Other parameters (Temperature, polymer concentration and outer layer)

Lastly, we estimated the impact of some other parameters on the electrical conductivity of agarose hydrogels. Temperature is a parameter that is known to have an impact on electrical conductivity. Ionic conductivity increases, with increasing temperature, due to the increased ionic mobility, while metallic conduction decreases, with increasing temperature, due to the increased vibrations of metal cations which in turn decrease electron mobility. CNTs exhibit a minor increase in conductivity, with increasing temperature, both as individual nanotubes [112], or as part of a polymer nanocomposite [187].

We tested the effect of three different temperatures on the electrical conductivity of fresh agarose nanocomposite hydrogels, AGR-CNT<sub>10</sub>CMC<sub>1</sub>\_F (**Figure 3.30**, A). The conductivity moderately increased with increasing temperature from  $(9 \pm 5) \times 10^{-5}$  S/m at 10 °C, to  $(4.1 \pm 1.9) \times 10^{-4}$  S/m at 35 °C. The difference between 10 °C and 35 °C was significant at the 0.05 level (Student's t-test,  $p=0.006$ ).

Aqueous ionic solutions have a temperature coefficient of approximately 2 % conductivity increase per degree Celsius [188]. This corresponds to a 50 % conductivity increase between 10 °C and 35 °C. For individual CNTs, Ebbesen *et al.* reported a very moderate increase of 0.03 % per °C but noted a high degree of variability [112]. For a solid polymer nanocomposite (Poly Ether Ether Ketone – MWCNT), the findings of Mohiuddin and Hoa pointed towards a higher temperature coefficient at roughly 2.3 % per °C [187]. In our hydrogels, the experimentally-measured conductivity increase was close to 350 % for 25 °C (from 10 to 35 °C), corresponding to a temperature coefficient of ~15 % conductivity increase per degree Celsius. This relatively large increase was attributed to the hydrogel nature of our nanocomposite and the important changes in ionic mobility from 10 °C to 35 °C. The agarose hydrogel viscosity decreases with temperature, to a larger extent than the viscosity decrease of an aqueous solution. The next step would be to investigate the conductivity changes in even higher temperatures, after the gel-sol transition of agarose, but this would require adapting the measuring cell to be able to accommodate both solids and liquids.



The second parameter that was tested was agarose concentration. The hypothesis was that if the dense agarose polymer chain network restrained ionic mobility, a hydrogel with lower agarose concentration, with larger pores, would have increased ionic mobility. Agarose can form hydrogels in a wide range of concentrations, starting at 0.5 % w/w. Hydrogels with agarose concentrations less than 1 % w/w are very fluid-like and cannot be easily manipulated. We prepared a batch of agarose hydrogels at 1 % w/w and compared their electrical conductivity to the 2.5 % agarose hydrogels (**Figure 3.30, B**). No significant difference was observed (Student's t-test,  $p=0.9$ ).

Lastly, we measured the influence of the outer layer of the nanocomposite hydrogel. The hypothesis was that in the case of an inhomogeneous dispersion of CNTs within the hydrogel, an outer layer with lower concentrations would have a limiting impact on the global conductivity. To test this, we sliced a thin part of the upper and lower layer and measured the conductivity of the nanocomposite hydrogels (**Figure 3.30, C**). No significant difference was observed (Student's t-test,  $p=0.2$ ).

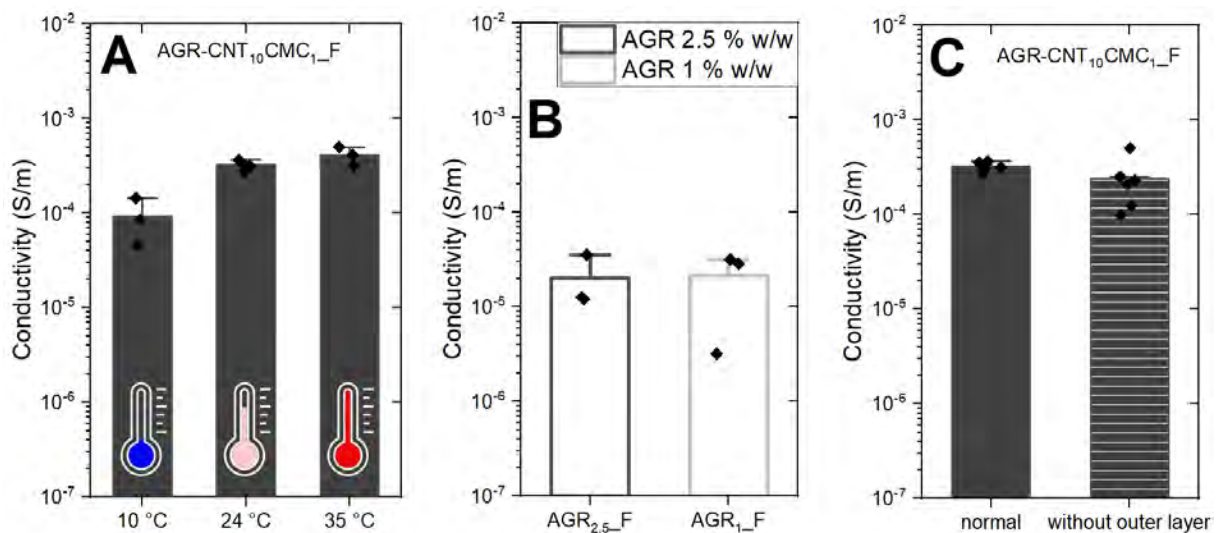


**Figure 3.30** – Impact of other factors on the electrical conductivities of fresh agarose hydrogels. (A) Temperature. (B) Agarose polymer concentration. (C) hydrogels after slicing off outer layers.

### 3.7.3 Electrical conductivity of hydrogels with ionic solutions

The DC conductivity measurements of hydrogels with ionic solutions failed to measure any significant differences between hydrogels with deionized water, electroporation buffer and phosphate buffer, even though these three aqueous solutions have different conductivities (3.7.2.4 Ionic solutions). We made a small series (fewer replicates) of additional experiments to confirm the influence of the ionic solutions: AC conductometer (Figure 3.31), impedance spectroscopy (Figure 3.32) and pulsed electric field (Figure 3.33).

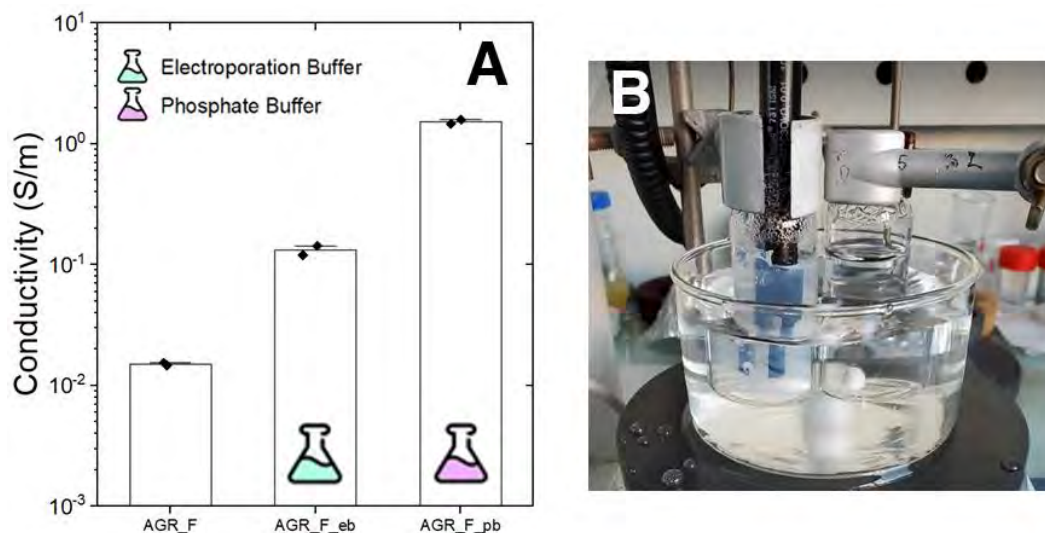


**Figure 3.31** – Conductivity of hydrogels with ionic solutions measured with AC conductometer. (A) Fresh agarose hydrogels with DI water, electroporation buffer and phosphate buffer (n=2). (B) Probe of AC conductometer immersed in agarose hydrogel.

The AC conductometer measured a conductivity of  $(1.51 \pm 0.06) \times 10^{-2}$  S/m for the agarose hydrogels with DI water,  $0.13 \pm 0.02$  S/m for the agarose hydrogels with electroporation buffer and  $1.53 \pm 0.08$  S/m for the agarose hydrogels with phosphate buffer (Figure 3.31). These values were much closer to the conductivities listed for the buffer solutions (Electroporation buffer: 0.15 S/m; Phosphate buffer: 1.5 S/m).

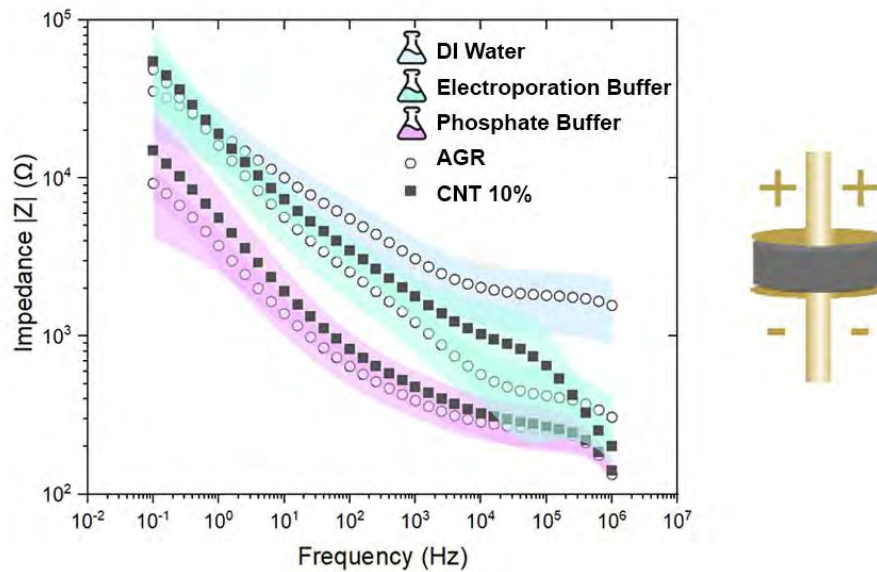


**Figure 3.32** – Absolute impedance over frequency at 0.6  $V_{rms}$  for swollen agarose (white circles) and nanocomposite (black squares) hydrogels, with DI water (light blue), electroporation buffer (green) and phosphate buffer (pink).  $n=3$ .

The absolute impedance of agarose hydrogels swollen in ionic solutions was lower than the impedance of hydrogels with DI water, and even more in the medium to high frequencies (from 10 Hz onwards approx.). There was little to no difference between the plain agarose and the nanocomposite hydrogels, in this case.

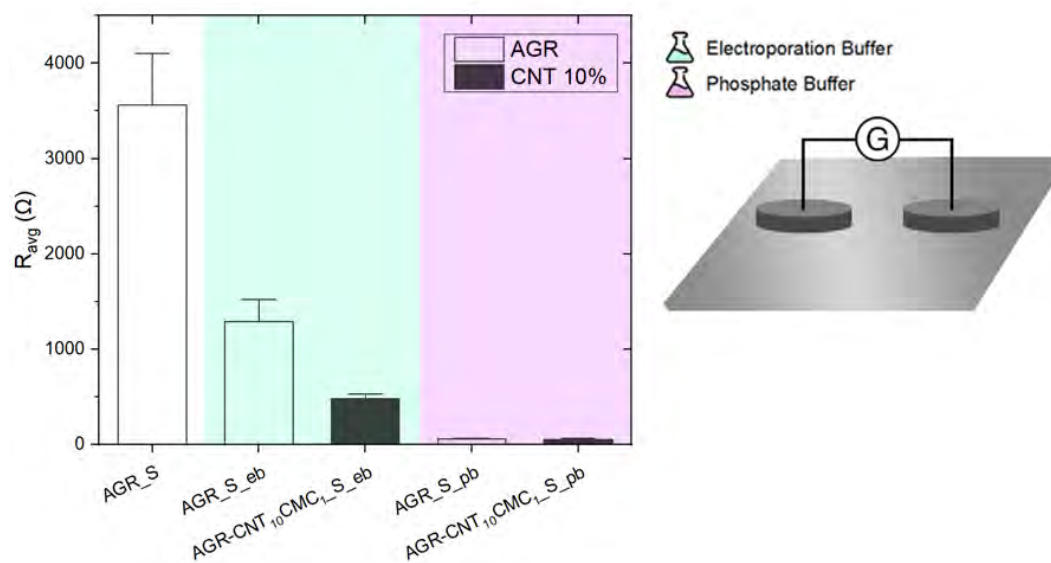


**Figure 3.33** – Average resistance of system consisting of two hydrogels placed on top of a metal (stainless steel) plate and connected with cylindrical electrical contacts. Hydrogels swollen in DI water, electroporation buffer or phosphate buffer. A PEF of 50 V was applied to the hydrogels and the resistance was calculated as the average  $u(t)/i(t)$ .  $n=2$ .

The average resistance of the system during the 50 V PEF application was  $3600 \pm 800 \Omega$  for the agarose hydrogels with DI water,  $1300 \pm 300 \Omega$  and  $480 \pm 70$  respectively for the plain agarose and nanocomposite hydrogels with electroporation buffer, and  $58 \pm 13 \Omega$  and  $55 \pm 17 \Omega$  respectively for the plain agarose and nanocomposite hydrogels with phosphate buffer.

In all cases, the conductivity of hydrogels with ionic solutions was higher than the conductivity of hydrogels with DI water. The increase was larger for solutions with higher ionic content (phosphate buffer). From these results, we infer that the DC conductivity experiments were not well-adapted for measuring the conductivity of hydrogels with ionic solutions. In DC conductivity, the electrode-electrolyte impedance may be considerable, due to the formation of an electrical double layer in the interface. The high impedance of this interface then dominates the conductivity measurement, masking the volume conductivity of the sample.

### 3.7.4 Impedance spectroscopy

Impedance spectroscopy allowed us to investigate the AC electrical properties of the hydrogels over a range of frequencies, from 0.1 to  $10^6$  Hz. The hydrogel samples studied in impedance spectroscopy were of two types: the plain agarose hydrogels (AGR\_F) and nanocomposite hydrogels with 10 % CNTs (AGR-CNT<sub>10</sub>CMC<sub>1</sub>\_F), which presented the most interesting electrical properties in DC.

#### 3.7.4.1 Low voltage

We compared the Bode plots of plain agarose and nanocomposite hydrogels (**Figure 3.34**). In the higher frequencies, from 1 MHz down to *ca.* 40 Hz, the impedance of the nanocomposite hydrogels was considerably lower, while a plateau was obtained from *ca.* 40 Hz for plain agarose. In lower frequencies, from 40 Hz down to 0.1 Hz, we observed a similar behavior of the two types of hydrogels. Passing onto the phase angle plot, we observed a similar qualitative behavior between the two hydrogel types. At higher frequencies the phase angle was between  $-15^\circ$  and  $0^\circ$ , demonstrating a resistive behavior. In the lower frequencies range, the phase angle decreased and stabilized near  $-40^\circ$ , for both types of hydrogels.

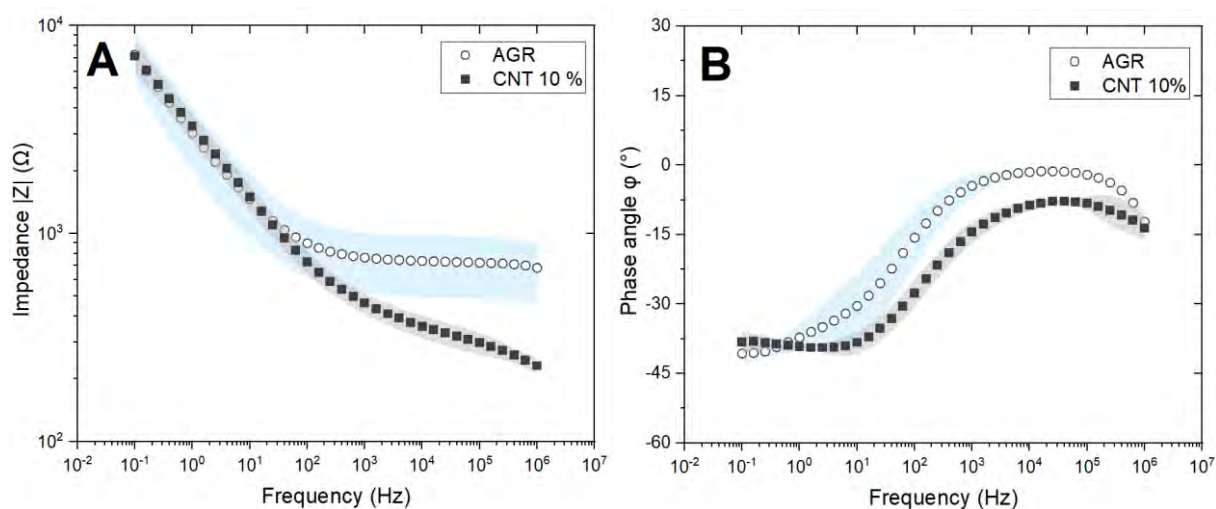


**Figure 3.34** – Impedance spectroscopy graphs of fresh agarose (white circles,  $n=3$ ) and nanocomposite (black squares,  $n=4$ ) hydrogels, at  $0.6 V_{rms}$ . (A) Absolute impedance over frequency. (B) Phase angle over frequency.

The incorporation of CNTs did not decrease the impedance of the hydrogels at lower frequencies. The impact of the CNTs was only visible at higher frequencies. In the phase angle plot, the CNT-loaded hydrogel exhibited lower values at higher frequencies. Through these observations we infer that the impact of CNTs was mostly of capacitive nature.

On the Nyquist plot (**Figure 3.35**, same data), we also observed similar trends between the plain agarose and the nanocomposite hydrogels. At lower frequencies, the points formed a straight line with

ca. 45° angle. This is a trait of the Warburg diffusion element, characteristic of ionic diffusion processes [148].

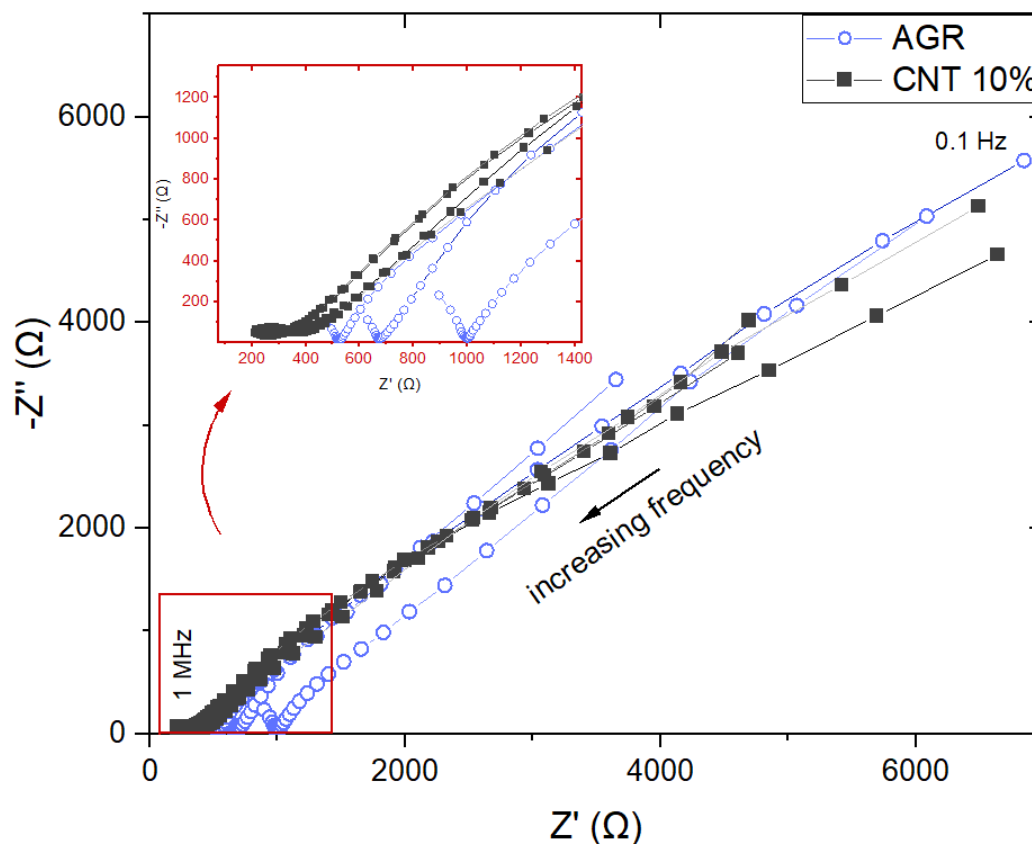


**Figure 3.35** – Nyquist plots of fresh agarose (white circles and blue lines) and nanocomposite (grey squares) hydrogels, at  $0.6 V_{rms}$ , representing the real ( $Z'$ ) and the negative of the imaginative ( $-Z''$ ) part of the impedance, over a frequency range from  $10^6$  to 0.1 Hz.

The Nyquist plot can be used to model an equivalent circuit of the system. In our case, the equivalent circuit appeared to include a Warburg impedance element in series with a resistor, and in parallel with a capacitor (See chapter **1.13.2.1 Impedance spectroscopy**). Studies of the electrical properties of nanocomposite hydrogels have also suggested that such an equivalent circuit best models their behavior [131], [151], [152]. We can calculate the resistor in this equivalent circuit as the point where the curve intersects with the x-axis (**Figure 3.35**, Visible in the zoomed red inset). The resistance was between 500 and 1000  $\Omega$  for the plain agarose hydrogels and between 250 and 400  $\Omega$  for the nanocomposite hydrogels. Considering the geometry of the hydrogels, this corresponded to an electrical conductivity of  $0.04 \pm 0.01$  S/m for the agarose hydrogels and  $0.08 \pm 0.02$  S/m for the nanocomposite hydrogels. Studied through impedance spectroscopy, the differences in electrical conductivity between plain agarose and nanocomposite hydrogels were still present, but noticeably smaller, compared to the DC electrical measurements. Besides, the ionic processes played an important role in the conductivity of our system, as highlighted by both the Bode and Nyquist plots.

### 3.7.4.2 Voltage sweep

The electrical properties of the hydrogels were measured at low voltages, typically 0.5 to 1 V. The practical application in which we are interested involves much higher voltages, in the range of 100 to 300 V. However, it was not possible to measure the electrical properties at such voltages, in DC or AC.



In DC, the constant application of higher voltages causes electrochemical reactions and joule heating. A voltage over 1.23 V ( $E_0$  O<sub>2</sub>/H<sub>2</sub>O / Normal Hydrogen Electrode) causes water electrolysis, producing hydrogen and oxygen. Actually, electrolysis of water has very slow kinetics without the use of an adequate catalyst [189], but constant higher voltages can lead to a number of other electrochemical reactions between the water and the electrodes as well as significant heating of the system. AC testing can reduce electrochemical reactions to some extent. We measured the electrical impedance of our hydrogels, over increasing voltage, from 0.6 to 12 V<sub>rms</sub>. We were limited to 12 V as the maximum voltage, because higher voltages produced more current than the dielectric spectrometer was designed to handle. The hydrogel samples had a thickness of *ca.* 2 mm, thus the associated electric field was in the range of 300 – 6000 V/m. The Bode plots of agarose hydrogels (**Figure 3.36**) and nanocomposite hydrogels (**Figure 3.37**) are shown below.

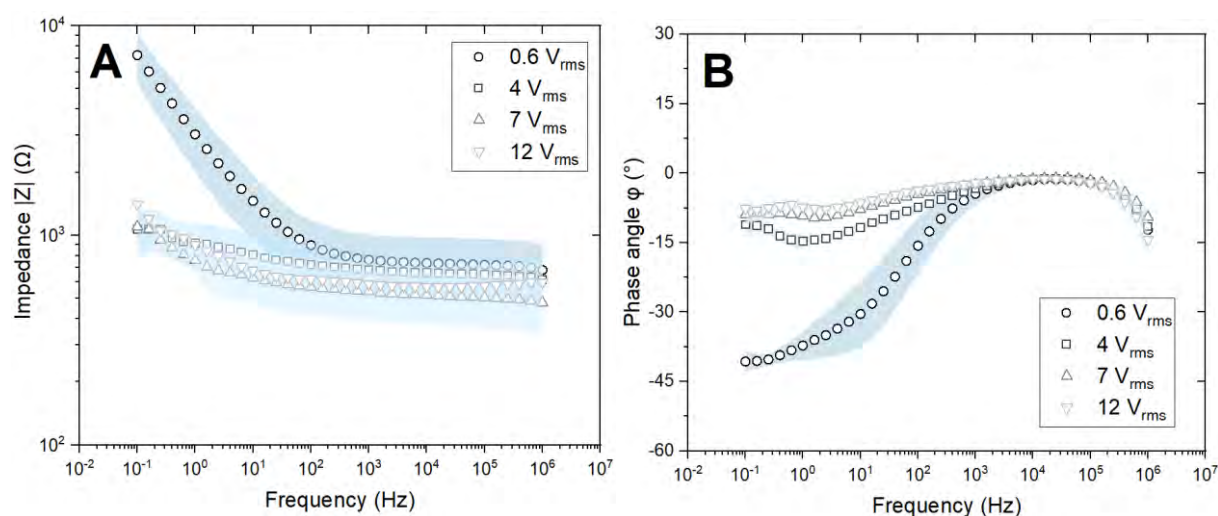


**Figure 3.36** - Impedance spectroscopy graphs of fresh agarose hydrogels, at increasing voltages, from 0.6 to 12 V<sub>rms</sub>. n=3. (A) Absolute impedance vs. frequency. (B) Phase angle vs. frequency.

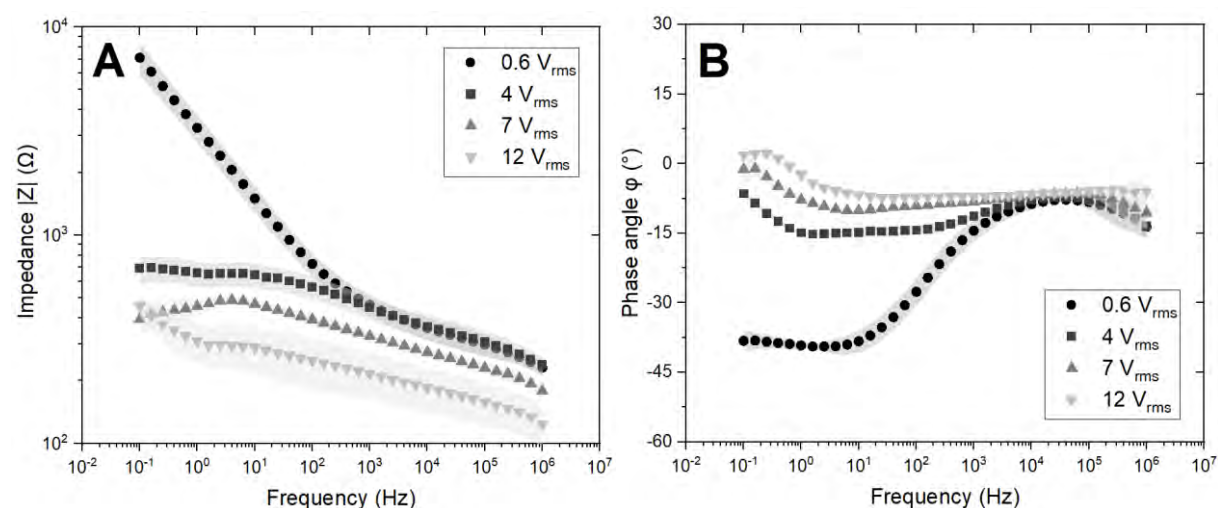


**Figure 3.37** - Impedance spectroscopy graphs of fresh nanocomposite hydrogels, at increasing voltages, from 0.6 to 12 V<sub>rms</sub>. n=4. (A) Absolute impedance vs. frequency. (B) Phase angle vs. frequency.

The electrical properties of both types of hydrogels varied with increasing voltage, demonstrating an electrical conductivity dependent on voltage level (nonlinear). In the case of plain agarose hydrogels, there was an important change between 0.6 and 4 V<sub>rms</sub>. At 4 V<sub>rms</sub>, the agarose hydrogels had a



decreased impedance, at lower frequencies. In addition, the phase angle of the agarose hydrogels shifted towards  $0^\circ$  at lower frequencies, indicating a resistive behavior. Further increase in RMS voltage did not have extra impact on the electrical properties of the fresh agarose hydrogels. In the case of nanocomposite hydrogels, a similar shift was observed between voltages of 0.6 and 4  $V_{rms}$ : at lower frequencies the impedance decreased and the phase angle tended towards  $0^\circ$ . The decrease in impedance between 0.6 and 4  $V_{rms}$  was higher for the nanocomposite hydrogel (decrease of one order of magnitude, *ca.*) than for the plain agarose hydrogels. More interestingly, in the case of nanocomposite hydrogels, the electrical properties continued to evolve with increasing applied voltage. The impedance decreased with increasing voltage, all over the frequency range studied. In parallel, the phase angle also evolved slightly with increasing voltage, approaching  $0^\circ$ .

Increasing the voltage revealed a nonlinear electrical behavior in both the plain agarose and nanocomposite hydrogels. In the case of plain hydrogels, the nonlinearity was limited to the transition between 0.6 and 4  $V_{rms}$ . It is possible that electrochemical reactions between the electrodes and the hydrogel took place, as the potential difference increased. These electrochemical reactions could be responsible for the modified electrical response of the system. However, in nanocomposite hydrogels, the nonlinearity persisted all over the voltage range studied (0.6 to 12  $V_{rms}$ ). The impedance of the hydrogels continued to decrease for increasing applied voltage. It is not uncommon for nanocomposite systems to display nonlinear electrical behavior [190]. In our system, the orientation of CNTs, as well as the electron tunneling distances can change with an increasing electric field, resulting in a highly nonlinear behavior [191], [192]. With this nonlinearity in mind, we hypothesized that the property-enhancing effect of the incorporation of CNTs may be even greater at the voltages used for our application (100 to 300 V).

### 3.8 Skin model

The electrical properties of the skin model were measured with DC and AC voltage. The mouse skin was excised, and then cylindrical discs of 8 mm diameter were punched out of the dorsal skin. The excised skin sections had a thickness of  $0.46 \pm 0.07$  mm.

#### 3.8.1 DC conductivity of skin model

The DC electrical conductivity of excised mouse skin was measured, at ambient temperature. The DC conductivity of freshly-extracted dorsal mouse skin was  $(2.9 \pm 1.1) \times 10^{-4}$  S/m (range  $1.4 - 4.7 \times 10^{-4}$  S/m,  $n=6$ ).

The electroporation experiments were performed *ex vivo*, with freshly-extracted mouse skin. The excised mouse skin was used up to two hours after euthanasia of the animal. After euthanasia and skin extraction, the skin begins to deteriorate, due to dehydration, lack of blood circulation (and thus oxygen and nutrient transfer) and loss of thermoregulation. To delay this deterioration, we kept the excised mouse skin on a humidified gauze, soaked with isotonic phosphate buffer saline, and heated it to  $32^\circ\text{C}$  during the electroporation experiments.

Through DC electrical conductivity, we subsequently tested if the deterioration of the mouse skin over time, had an important impact on its electrical properties. We compared the conductivities of freshly-extracted skin, two hours after extraction and 16 hours after extraction (**Figure 3.38**).

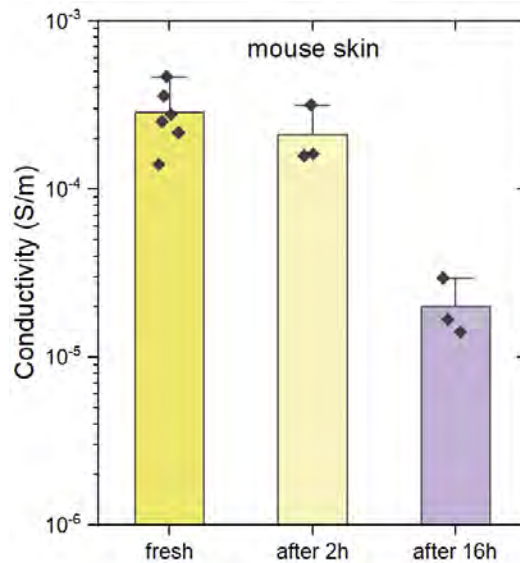


**Figure 3.38** – DC Electrical conductivity of mouse skin section, directly after excising and up to 16 h later.

Over the course of two hours, the conductivity of the skin was not significantly different from the freshly-extracted skin (Student's t-test,  $p=0.4$ ). However, within 16 hours, the DC electrical conductivity decreased by one order of magnitude, to  $(2.0 \pm 0.8) \times 10^{-5}$  S/m, a significant difference from the fresh skin (Student's t-test,  $p=0.006$ ). We hypothesized that dehydration was the most important factor that decreased the conductivity of the skin after 16 hours. Indeed, the 16-hour-old skin had a more wrinkled appearance, as a result of this dehydration. A decreased water content within the skin limited ionic mobility, increasing resistivity.

### 3.8.2 Impedance spectroscopy of skin model

Freshly-extracted mouse skin was also studied by impedance spectroscopy, at ambient temperature (**Figure 3.39**). At lower frequencies, the absolute impedance of the skin approached  $10^4 \Omega$ . Considering the geometry of the skin sample, this corresponded to a conductivity of  $9.15 \times 10^{-4}$  S/m. The phase angle was between  $-60$  and  $-30^\circ$ . At higher frequencies, the impedance of the skin decreased. The skin can be modeled as a tissue composed of cells, with capacitive plasma membranes, and intracellular and extracellular fluid, with resistive behavior. At lower frequencies, however, the current passes only through the limited extracellular space. In higher frequencies, the capacitive plasma membranes may also conduct current, decreasing the overall impedance of the tissue [193].

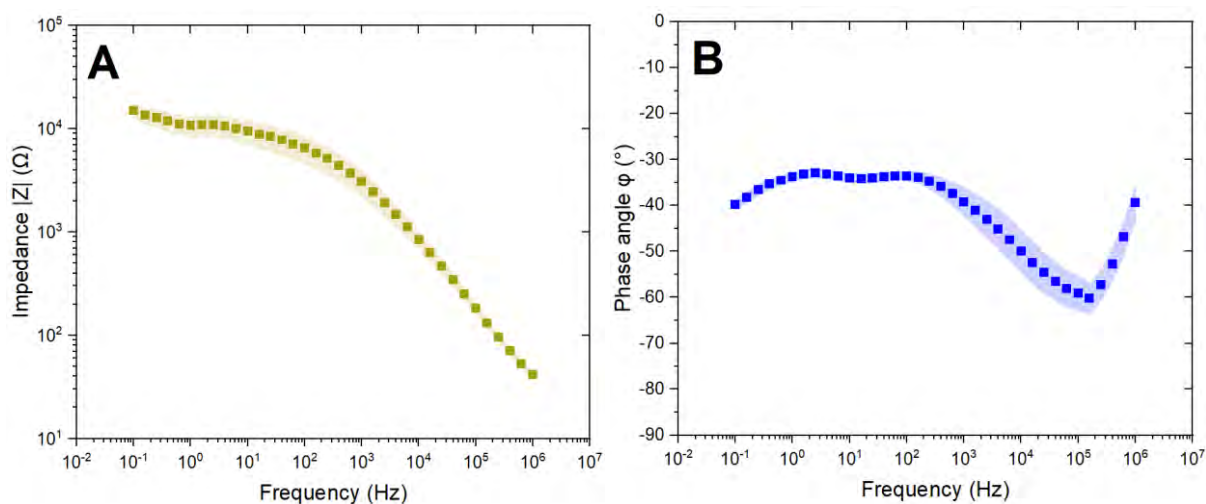


**Figure 3.39** – Impedance spectroscopy graphs of excised mouse skin section, at 0.6  $V_{rms}$ ,  $n=6$ . (A) Absolute impedance and relative permittivity over frequency. (B) Phase angle over frequency.

In the relevant literature, the deeper layers of the skin (dermis) are considered mostly resistive in nature, because of the high water content and the low relative permittivity [194]. But the outer layer, the epidermis, and more specifically the SC displays a capacitive behavior with high relative permittivity and very low conductivity, because of its low water content, large resistance and thin geometry [195].

### 3.9 Chapter highlights and discussion on materials characterizations

A series of materials characterizations were made to evaluate the usability of the hydrogels as platforms for transdermal drug delivery through skin electroporation. The hydrogels were made with agarose, a hydrophilic, biosourced and biocompatible polymer with a straightforward cross-linking mechanism (solubilization of agarose chains in hot water followed by physical entanglement of polymer chains during cooling down). It was chosen to work with dry hydrogels that can be placed in an aqueous solution with the molecules of interest (therapeutic molecules, fluorophores) where they swell, absorbing part of the solution, and thus of the molecule of interest. This choice was made considering the long preservation time of dry hydrogels and to avoid thermal degradation of therapeutic molecules during the preparation of agarose hydrogels (temperatures up to 90 °C).

The agarose hydrogels at 2.5 % w/w polymer concentration had adequate mechanical properties (compression module of ~200 kPa) and were easy to handle, without being too soft nor too brittle. A small hydrogel size was chosen, cylindrical discs of 10 mm diameter and 2 mm thickness, both suitable for the small size of the experimental skin models (mouse skin and reconstructed human epidermis) and likely to contain a relevant amount of drug for the possible applications we have in mind. The hydrogels dried rapidly at 70 °C (60 min) and 50 °C (100 min). We opted for a slower drying speed at 30°C (few hours) because it minimized deformation during drying. The dry hydrogels absorbed water rather quickly, reaching 60 % of the final absorption value within 10 minutes. In the experimental protocol, we increased these times to ensure complete drying and reproducible swelling each time: the hydrogels were dried over 48 h at 30°C and swollen over 24 h. The thermogravimetric analysis showed that dry agarose hydrogels still contained *ca.* 5.7 % of non-freezing bound water.

Regarding the absorption capacity, plain agarose hydrogels (AGR) absorbed  $4.6 \pm 0.7$  times their dry mass, while nanocomposite hydrogels (AGR-CNT<sub>10</sub>CMC<sub>1</sub>) absorbed  $2.7 \pm 0.6$ . Freezing the hydrogels

increased their swelling ratio, and directional freeze-casting increased it even more, up to  $14.7 \pm 1.9$ , while considerably accelerating the kinetics of loading and release. The drying/swelling cyclability study demonstrated that the hydrogel platforms were reusable, at least up to 6 times with only a minor loss of absorption capacity ( $\leq 15\%$ ). The alginate/chitosan hydrogels that were tested, in order to investigate the role of the polymer matrix on the hydrogel properties, had very minor absorption capacities, absorbing only  $0.3 \pm 0.1$  times their dry mass (32 %).

The swelling ratio of the tested agarose and nanocomposite agarose hydrogels varied from 2.7 to 14.7. Considering the size of these hydrogels (dry mass of *ca.* 5 mg), this corresponded to an absorption capacity of 13.5 to 73.5  $\mu\text{l}$  per hydrogel, or 27 to 147  $\mu\text{l}$  per pair of hydrogels. For comparison, typical volumes for intradermal injections are 100  $\mu\text{l}$  to 500  $\mu\text{l}$  and 100  $\mu\text{l}$  to 1500  $\mu\text{l}$  for subcutaneous injections [196], [197]. One unit of insulin is equivalent to 10  $\mu\text{l}$  of U100 insulin and insulin needs can vary considerably between patients, from insulin pumps injecting 1 unit to maximum size of injections holding 100 units (1 ml) [198], [199]. Currently, a pair of our hydrogels could hold up to 15 units of U100 insulin max, and the size can be easily upscaled for human subjects.

In total, the factors that affected the absorption capacity of the hydrogels were the following:

- **Polymer matrix and cross-linking.** Agarose absorbed much more water than alginate/chitosan hydrogels. All of these three polymers are highly hydrophilic due to the multiple hydrophilic functional groups in the polymer chains (four hydroxylic groups per repeating unit in agarose, three hydroxylic and two carboxylic groups in alginate, four hydroxylic groups and two amines in chitosan, **Figure 3.40**). In the case of the alginate/chitosan hydrogels, the chitosan polymer chains were chemically cross-linked with genipin. The chemical cross-linking rigidified the structure of the hydrogel, limiting expansion of the 3D polymer matrix and water swelling. Tuning the surface properties of the hydrogel with those of a specific drug is hypothesized to be very relevant.

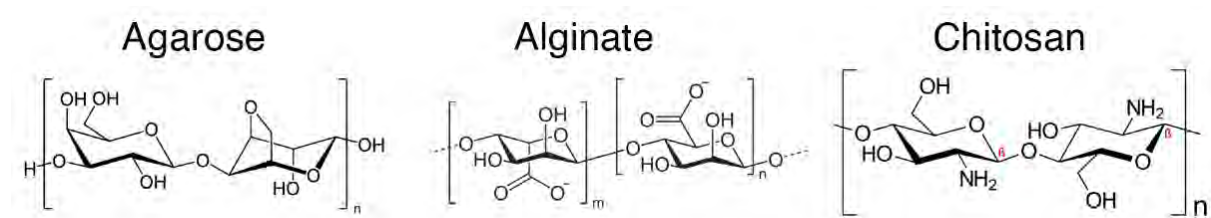


**Figure 3.40** – Chemical structures of agarose, alginate and chitosan hydrophilic biopolymers

- **Nanomaterial incorporation and concentration.** Carbon nanotubes decreased the swelling ratio of agarose and alginate/chitosan hydrogels. Higher concentrations of CNTs further decreased the absorption capacity, yet to a lesser extent. CNTs formed a network within the polymer hydrogel matrix, stiffening the structure, thus limiting the capacity to expand during water absorption. Additionally, CNTs have highly hydrophobic surfaces, repelling water molecules.
- **Freezing.** Freezing increased the swelling ratio of agarose hydrogels. When the hydrogels were cooled down to  $-20^{\circ}\text{C}$  in a freezer, the freezing free water and the freezing bound water started to form ice crystals. These crystals formed all over the hydrogel matrix, in random locations (starting around nucleating particles or surfaces). Through the expansion of the ice crystals,

the polymer matrix was rearranged, being pushed by the crystal expansion. Afterwards, when the ice crystals melted, pores were left behind. These pores increased the swelling capacity of the hydrogels, in a manner similar to porous sponges. In directional freeze-casting, we controlled the direction, growth and size of the ice crystals. Directional freeze-cast hydrogels had vertically aligned macropores with a median diameter of 150  $\mu\text{m}$  and outstanding absorption capacities, coupled with very fast swelling/release kinetics.

The DC electrical characterizations showed that the incorporation of double-wall CNTs increased the conductivity of swollen agarose hydrogels by two orders of magnitude, from  $1.1 \times 10^{-6}$  (AGR\_S) to  $3.4 \times 10^{-4}$  S/m (AGR-CNT<sub>10</sub>CMC<sub>1</sub>\_S). Other CNT types (multi-walled, oxidized) had a similar effect. The percolation threshold of CNTs was between 0.125 and 0.25 % w/w (0.07 and 0.14 % v/v). Aqueous suspensions of CNTs had a lower percolation threshold, at 0.025 % w/w, and higher (AC) electrical conductivities than hydrogel samples.

Without a dispersant, the incorporation of CNTs in agarose hydrogels, had a lesser effect on the DC conductivity. A different dispersant that was also tested, polydopamine, increased the DC conductivity of nanocomposite hydrogels, but less than carboxymethyl cellulose. Polydopamine has semiconducting properties, and the conductivity increase was attributed to these properties. Ionic solutions did not affect the conductivity of agarose hydrogels. Alginate/chitosan hydrogels had higher conductivity than agarose hydrogels, at  $(4.1 \pm 0.3) \times 10^{-4}$  S/m, but the incorporation of CNTs did not further increase it. Swollen agarose hydrogels that were previously frozen had an increased electrical conductivity,  $(2.4 \pm 1.4) \times 10^{-5}$  S/m. This increased even more,  $(5.5 \pm 1.1) \times 10^{-4}$  S/m, for directional freeze-cast agarose hydrogels (measured along the freezing direction). Nanocomposite agarose hydrogels also exhibited a moderate temperature dependence, with the DC conductivity increasing from  $(9 \pm 5) \times 10^{-5}$  S/m at 10 °C to  $(4.1 \pm 1.9) \times 10^{-4}$  at 35 °C.

Compared to the relevant literature on electrically conductive nanocomposite hydrogels, our AGR-CNT<sub>10</sub>CMC<sub>1</sub>\_F hydrogels are situated in the lower average of the nanomaterial concentration vs. conductivity graph (**Figure 3.41**). From the same graph, it can be seen that the DC electrical conductivity of nanocomposite hydrogels varies by several orders of magnitude. The conductivities of hydrogels of different polymers, without nanomaterials, already show an important variability. In our case, plain agarose hydrogels had one of the lowest conductivities reported. The conductivity increase that we measured (two orders of magnitude), through the incorporation CNTs, is situated towards the higher average of the reported values [177].

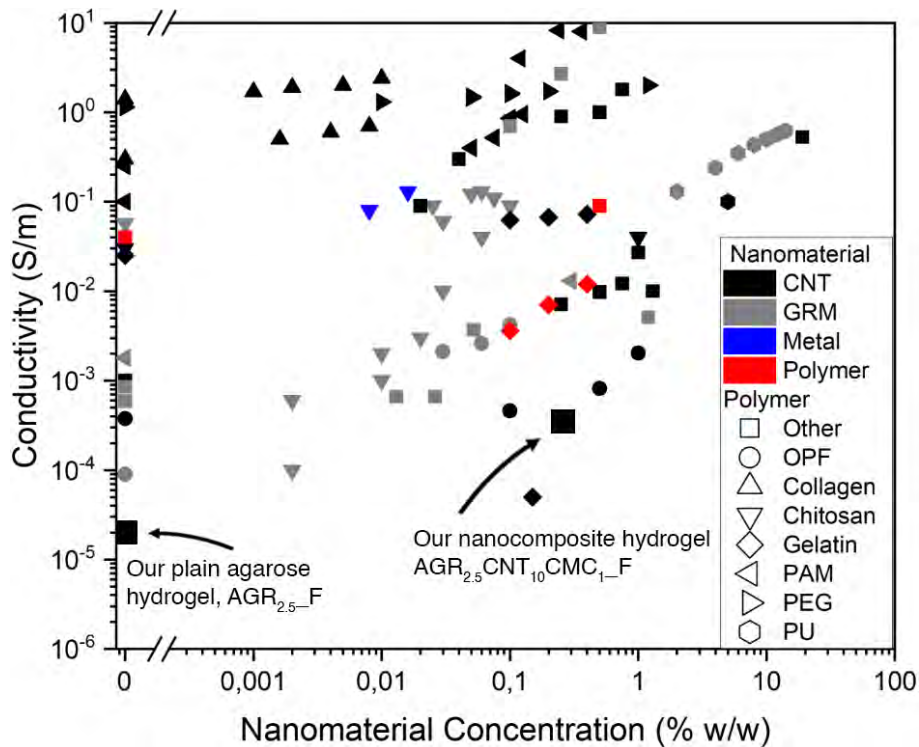


**Figure 3.41** - Nanocomposite hydrogel electrical conductivity vs. nanomaterial concentration. A nanomaterial concentration of 0 represents the electrical conductivity of the plain hydrogels (without conductive nanomaterials). GRM: Graphene-related materials; OPF: oligo(poly(ethylene glycol) fumarate); PAM: polyacrylamide; PEG: polyethylene glycol; PU: polyurethane. Adapted from ref. [177].

The low-voltage impedance spectroscopy ( $0.6 V_{rms}$ ) analysis of the hydrogels highlighted the ionic component of the electrical conductivity. The incorporation of CNTs (AGR-CNT<sub>10</sub>CMC<sub>1</sub>\_F) decreased the impedance of the agarose hydrogels (AGR\_F) only at higher frequencies, and the changes were mostly of capacitive nature. Based on the Nyquist plot, an equivalent circuit could be modelled as a resistor in series with a Warburg diffusion element, and in parallel with a capacitor. Increasing the voltage applied to the hydrogels revealed their nonlinear electrical behavior. The impedance of agarose hydrogels, at lower frequencies, decreased between 0.6 and 4  $V_{rms}$ , and remained stable at subsequent voltage increase. In the case of nanocomposite hydrogels, the impedance decreased all over the frequency range (0.1 Hz to 1 MHz) with increasing electric fields.

In total, the factors that affected the electrical conductivity of the hydrogels were the following:

- **Conductive nanomaterial concentration.** The incorporation of conductive CNTs, significantly increased the conductivity of the hydrogels, from a critical concentration (percolation threshold), above which the CNTs dispersed within the hydrogel formed an electron-conductive network through the delocalized  $\pi$  electrons of the CNTs. In agreement with percolation theory, further increase in CNT concentration over the percolation concentration did not have an impact on conductivity.
- **Nanomaterial dispersion.** Carbon nanotubes have highly hydrophobic surfaces and form large agglomerates in aqueous suspensions. Without an adequate dispersing method, the CNTs did not form an efficient conductive network. We used carboxymethyl cellulose (CMC) as a dispersing agent. It rendered the surface of the CNTs less hydrophobic and increased the conductivity of the hydrogels, in combination with the nanomaterial concentration. However,



as CMC was not removed, at least not willingly, it may have formed an additional interface in our system.

- **Water content.** Part of the electrical conductivity of the hydrogels was due to ionic conduction of ions within the water phase of the hydrogels. Hydrogels with lower water content (swollen hydrogels), had generally lower electrical conductivities (with the exception of AGR-CNT<sub>10</sub>CMC<sub>1\_S</sub> hydrogels where the CNT network was responsible for the higher conductivity).
- **Porosity.** Freezing the hydrogels created macropores within the hydrogel network due to the growth of ice crystals. These macropores then increased the ionic mobility within the hydrogel, increasing the conductivity. Hydrogels with aligned macropores (prepared through directional freeze-casting) had even higher electrical conductivities. In nanocomposite hydrogels, a second hypothesis may be that the ice crystal formation also reorganizes the CNT network, possibly leading to a more interconnected conductive network.
- **Polymer matrix.** Different polymers matrices have variable inherent electrical properties. It is expected that polymer chains with a large number of ionizable functional groups have higher conductivities. In our case, it was shown that alginate/chitosan hydrogels had higher conductivity than agarose.
- **Temperature.** Increasing temperature increased the conductivity of the hydrogels more than what would have been expected in an aqueous ionic solution. Agarose formed thermo-reversible hydrogels, meaning that heat can disassociate the agarose chains back into a sol state (gel to sol transition at 80 to 90 °C [200]). For this reason, the viscosity of agarose decreases considerably with temperature, augmenting the ionic mobility within the network.
- **Ionic solutions.** Hydrogels with ionic solutions (electroporation buffer or phosphate buffer) had higher electrical conductivities than hydrogels with DI water.
- **Electric field.** The electrical conductivity of hydrogels was not constant. Increasing electric field strength increased the conductivity. This was especially true for nanocomposite hydrogels (AGR-CNT<sub>10</sub>CMC<sub>1\_F</sub>), where the impedance continued to decrease as we increased the applied voltage. Nanocomposite systems can exhibit nonlinear electrical properties, due to changes in electron tunneling conductance and/or possible geometrical reconfiguration of nanomaterials within the polymer matrix.

The different hydrogel compositions and processing methods explored presented promising properties for use as conductive transdermal delivery platforms. Some compromises had to be made between electrical conductivity, absorption capacity, potential cytotoxicity, mechanical properties, preservation, reusability and ease of fabrication. In the following chapters we chose to work with the AGR-CNT<sub>10</sub>CMC<sub>1\_S</sub> hydrogels, that have a swelling ratio of  $2.7 \pm 0.6$ , a DC conductivity of  $3.4 \times 10^{-4}$  S/m and decreasing impedance with increasing electric field. To better understand this selection, the chronology of the materials characterizations should be considered: some results came in parallel, or after the drug delivery experiments, so they could not be considered for the final choice. Other promising options include the AGR-CNT<sub>10</sub>CMC<sub>1\_frz</sub> hydrogels with swelling ratio of  $5.8 \pm 0.3$  and DC conductivity of  $(4 \pm 0.4) \times 10^{-4}$  S/m, or even without CNTs, the AGR\_frz and AGR\_dir.

## 4 *In situ* measurements

<b>4</b>	<b>IN SITU MEASUREMENTS .....</b>	<b>124</b>
4.1	ELECTRICAL RESPONSE .....	124
4.1.1	<i>I-V during PEF application</i> .....	124
4.1.2	<i>Conductive gel</i> .....	128
4.1.3	<i>DC resistance</i> .....	129
4.1.4	<i>Electrical recovery</i> .....	131
4.2	TEMPERATURE INCREASE .....	132
4.3	I-V MEASUREMENTS OF RECONSTRUCTED HUMAN EPIDERMIS.....	133
4.4	CHAPTER HIGHLIGHTS AND DISCUSSION ON <i>IN SITU</i> MEASUREMENTS .....	134

We set up a measurement configuration to monitor the current and voltage running through the system before, during and after the PEF application, as well as the temperature increase. In the following sections, we used these measurements to understand and model the pathway creation through the skin and propose skin electroporation mechanisms.

### 4.1 Electrical response

The electrical response of the system was studied under DC and PEF electrical stimuli, with various configurations. Then, the observations were synthesized to form hypotheses on the mechanisms by which the electric field affects the skin model.

#### 4.1.1 I-V during PEF application

The voltage and the current traversing the system during the application of PEFs were measured using a digital oscilloscope (**Figure 4.1**). The data were plotted as  $u(t)$ ,  $i(t)$  and  $u/i(t)$  graphs, where the time scale was adapted to mostly include the pulse time. The first pulse started at  $t=0$  and the last pulse ended at  $t=7.02$  s.

The capacitive nature of the generator and the larger currents generated a limited voltage drop during the square pulses, for higher voltages. The voltage drop in the first pulse was not visible for a PEF of 50 V, equal to 5 V for 100 V PEF, 27 V for 200 V, and 42 V for 300 V pulses. For this reason, it is handier to use the resistance value ( $R=U/I$ ) to study the effects of the PEF. We define the instantaneous resistance of the system as  $r(t)=u(t)/i(t)$ . We also used the average resistance during the last pulse, for comparison between different experiments.

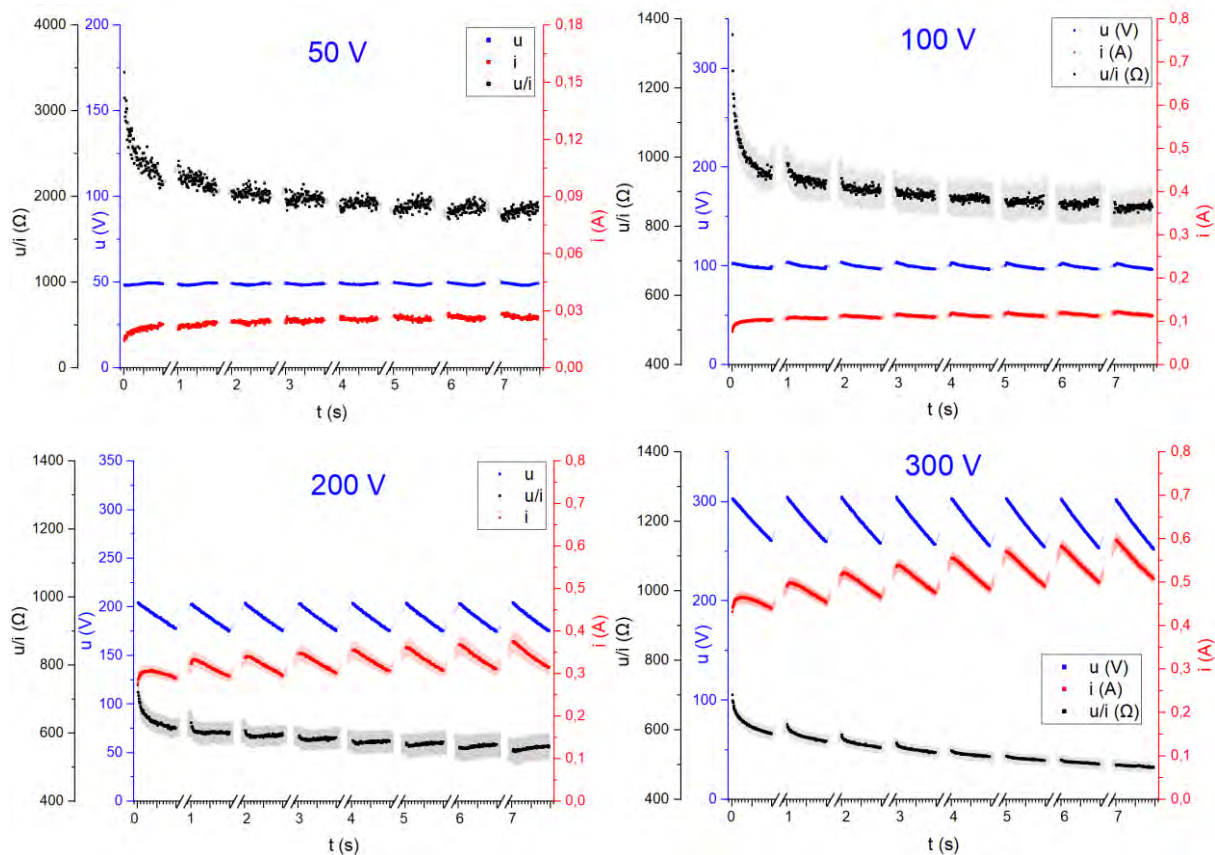


**Figure 4.1** - Voltage, current and instantaneous resistance ( $u/i$ ) of drug delivery setup during Pulsed Electric Fields (PEF) of voltages from 50 to 300 V. Shaded areas represent SEM. (50V,200V:  $n=3$ ; 100V:  $n=5$ ; 300V:  $n=12$ ).

The detailed electrical response obtained through the oscilloscope showed that the instantaneous resistance of the system decreased during the application of the pulses. A control experiment confirmed that the decrease in the instantaneous resistance of the system is attributed specifically to the skin, and not to the hydrogels or other components (wet gauze, metal cylinders, cables): the instantaneous resistance of our system without the skin remained constant during the application of PEF (**Figure 4.2**).

The application of a PEF, over a threshold value, permeabilizes the skin, creating aqueous pathways through the skin layers. These pathways allow the delivery of hydrophilic entities, such as hydrophilic drugs or fluorophores into the skin. At the same time, they also increase the conductivity of the skin by increasing the mobility of ions in the skin. Naturally present electrolytes ( $K^+$ ,  $Na^+$ ,  $Cl^-$  and others) give ionic conductive properties to tissues [193]. However, in the SC, their mobility is dramatically restricted by the tightly packed lipid layers, leading to a more resistive behavior ( $\sigma \approx 5 \times 10^{-4}$  S/m). At the onset of electroporation, a measurable and rapid decrease in the instantaneous resistance of the system occurs.

The largest resistance decrease was observed during the first 5-7 ms after PEF application. We therefore infer that the expansion of the local transport regions occurs within these first milliseconds. Further (lesser) decrease in instantaneous resistance may be attributed to conductivity changes within already formed and expanding LTR, due to local temperature increase and lipid phase transition. According to molecular dynamics simulations, the creation of pores in the lipid bilayers of the SC takes

place very rapidly, within few tens of nanoseconds (1-100 ns) [21]. It is possible that pores appear in the nanosecond range, but their expansion continues up to the millisecond range.

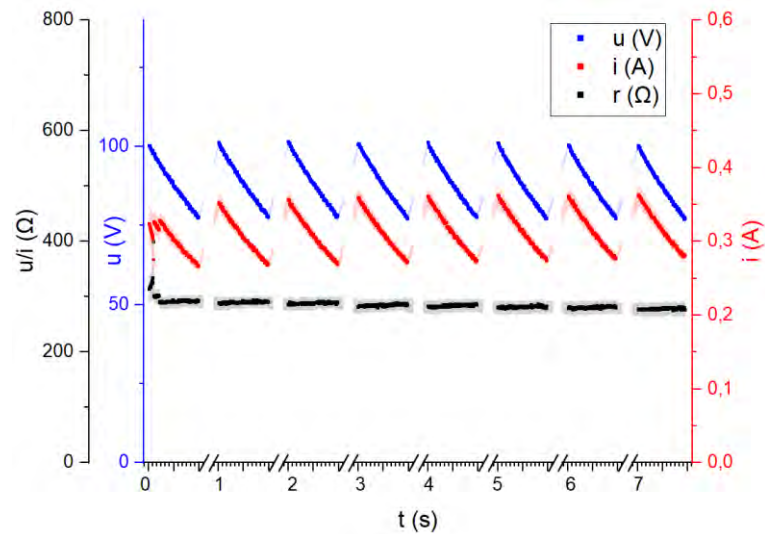


**Figure 4.2** - Voltage and current of the drug delivery setup without mouse skin (only hydrogels and gauze).  $n=3$ . Shaded areas represent SEM.

Moreover, the average resistance of the system varied considerably for different applied voltages. The  $I/U$  graph (**Figure 4.3**) shows the average current and average resistance of the system, during the last of 8 pulses. It ranged from  $1860 \pm 30 \Omega$  for PEF of 50 V, down to  $470 \pm 10 \Omega$  during the application of 300 V PEF, indicating a highly non-linear electric behavior. There was a rapid decrease of average resistance between PEF of 50 to 100 V, then a more modest decrease till 200 V and minor further decrease for PEF between 200 to 300 V. This multi-fold increase in conductivity was indicative of the extent of skin electroporation. We support the hypothesis that higher PEF voltages increase the density (the surface coverage) of LTRs in the skin, therefore increasing the overall conductivity.

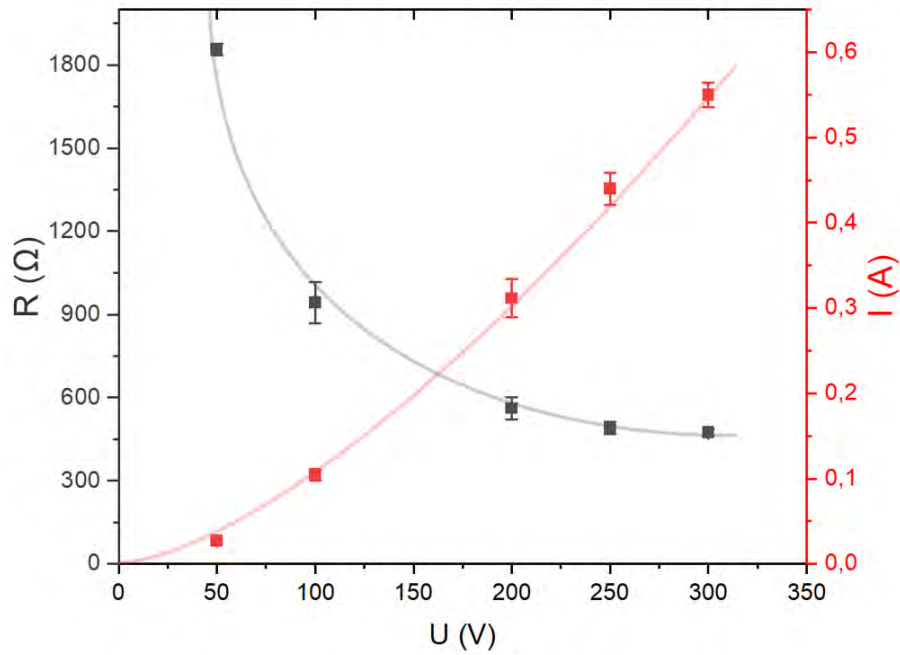


**Figure 4.3** - I-V curve of the system, demonstrating nonlinear behavior.  $n=2-18$ . Error bars represent SEM.

It was challenging to establish a precise minimum PEF voltage threshold for pathway formation, based solely on electrical properties, as instantaneous resistance decreased even at the lowest voltages applied. According to Chizmadzhev *et al.*, at low voltages (up to 30 V through the skin, equivalent to roughly 100 V in our configuration, according to the numerical model), electroporation of epithelial cells in appendageal ducts might contribute to the observed decrease in skin resistance. The appendageal ducts (hair follicles and sweat glands) are regions of higher current density and are lined by only two layers of epithelial cells [25]. Therefore, the plasma membranes of these cells are exposed to high electric fields, potentially over the electroporation threshold for transmembrane voltage (*ca.* 250 mV).

The lowest PEF voltage we could test with our configuration was 30 V, and the results included lots of noise (**Figure 4.4**). The electric current probe did not measure currents lower than 10 mA with adequate accuracy. For 30 V, we got an average resistance of *ca.* 4000 Ω, two times more than the resistance measured for 50 V PEF.

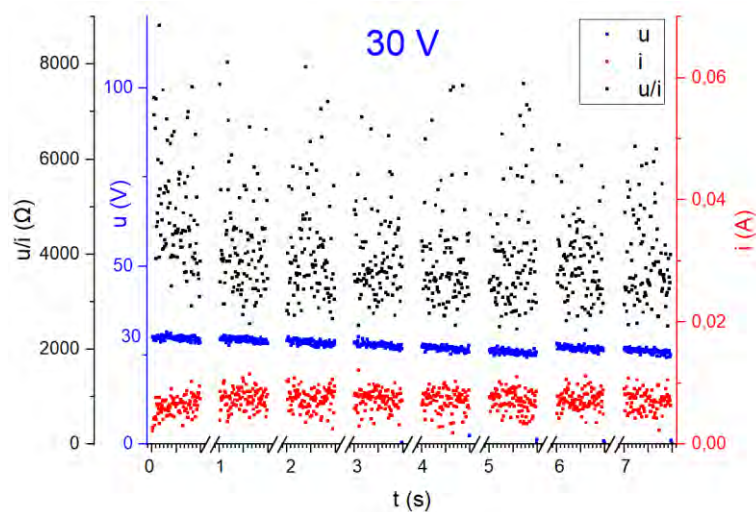


**Figure 4.4** - Voltage, current and instantaneous resistance ( $u/i$ ) of drug delivery setup during Pulsed Electric Fields (PEF) of 30 V.

#### 4.1.2 Conductive gel

In most applications of PEF on human skin, a conductive gel is placed between the skin and the electrodes to ensure optimal electrical contact. Metal electrodes are hard, solid and flat materials, while the skin is soft, elastic and rough. The contact between them is suboptimal: there are regions of the skin that do not touch the metal electrodes, air gaps and uneven contact. As a result, the electric field is not distributed uniformly. In addition, the sharp edges of metal electrodes become places of concentration of the electric field, creating localized high current densities. The conductive gel (also known as ultrasound gel; it is the same gel used in ultrasound imaging) is a viscous liquid with high ion concentration that is applied between the skin and the electrodes.

We hypothesized that hydrogels functioning as electrodes would minimize these contact issues and avoid altogether the need for use of an additional conductive gel. We tested this hypothesis by comparing the instantaneous resistance of the drug delivery system, with and without the use of a conductive gel. No substantial difference was observed in the instantaneous resistance of the system (**Figure 4.5**).



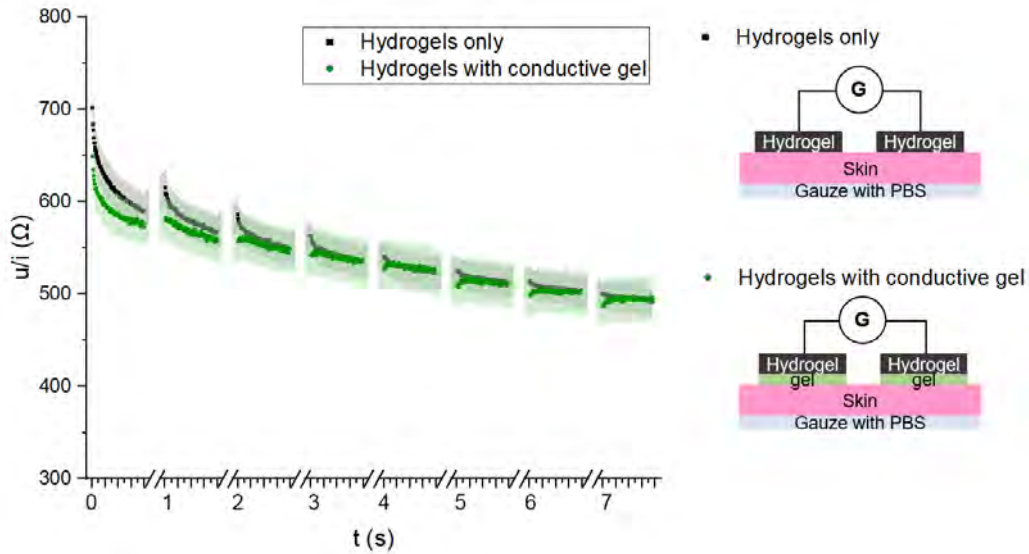


**Figure 4.5** - Instantaneous resistance ( $r=u/i$ ) of drug delivery setup with skin and hydrogels only (black dots,  $n=12$ ) and with skin, hydrogels and conductive gel between them (green dots,  $n=3$ ), for 300 V PEF. Shaded areas represent SEM.

The conductive gel did not improve the electrical contact. It is thus inferred that our hydrogels ensured optimal contact between the metal electrical contacts and the skin. Hydrogels are soft, visco-elastic materials with high water content, and have a good compatibility with the skin. On the drug delivery system, the hydrogels had a fixed weight of 60 g applied on them (this roughly amounts to 0.3 N or 6000 Pa per hydrogel). This force, in combination with the material characteristics, the water content and the conductivity of the hydrogels ensured optimal electrical contact and quasi-uniform distribution of the electric field.

#### 4.1.3 DC resistance

In parallel to the electrical response during PEF, we also measured the current flowing in the system, under a 1 V DC square step chronoamperometry ( $I(t)$ ), before and after the PEF (**Figure 4.6**). Upon DC voltage application, a brief current peak is observed, decaying swiftly to a steady value. This peak was attributed to the polarization of the system, while the steady state value corresponded to the conduction current.

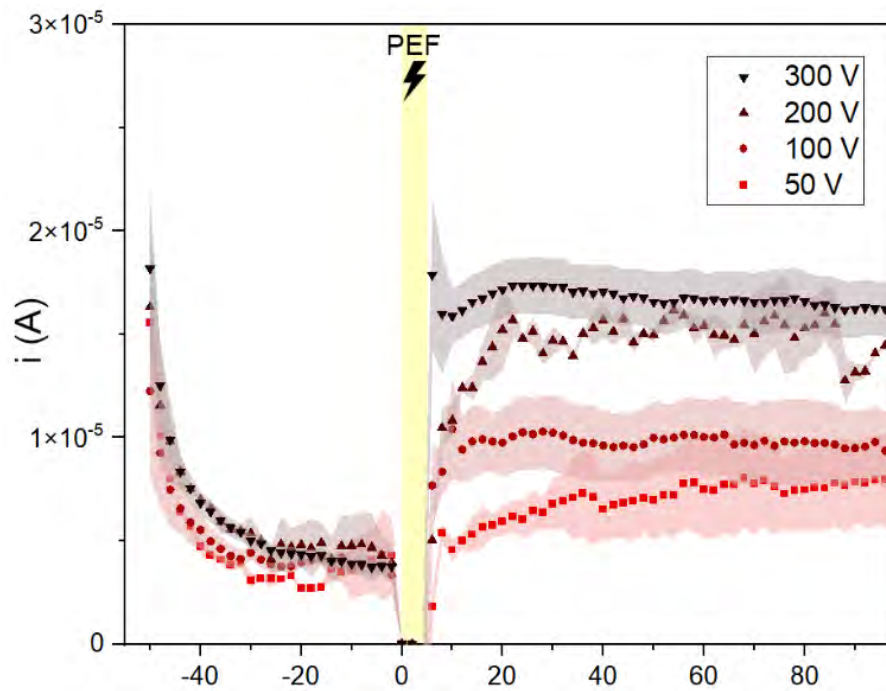


**Figure 4.6** - Electric current resulting from the application of 1V DC to the drug delivery system, before and after PEF (n=2-11). Yellow shaded area corresponds to PEF application. Shaded areas represent SEM.

The current increased after the PEF treatment, indicating prolonged changes in the conductivity of the skin. The conduction current was equal to  $4.0 \pm 0.1 \mu\text{A}$  before PEF application. After PEF application, the current increased with the voltage applied: we measured  $4.4 \pm 1.1 \mu\text{A}$  (+10 %) for 50 V,  $9.1 \pm 0.5 \mu\text{A}$  (+130 %) for 100 V,  $13.6 \pm 1.2 \mu\text{A}$  (+240 %) for 200 V, and  $16.3 \pm 0.3 \mu\text{A}$  (+310 %) for 300 V. The current did not regress towards the baseline (current before PEF), even after up to 12 minutes following the application of PEF (**Figure 4.7**).

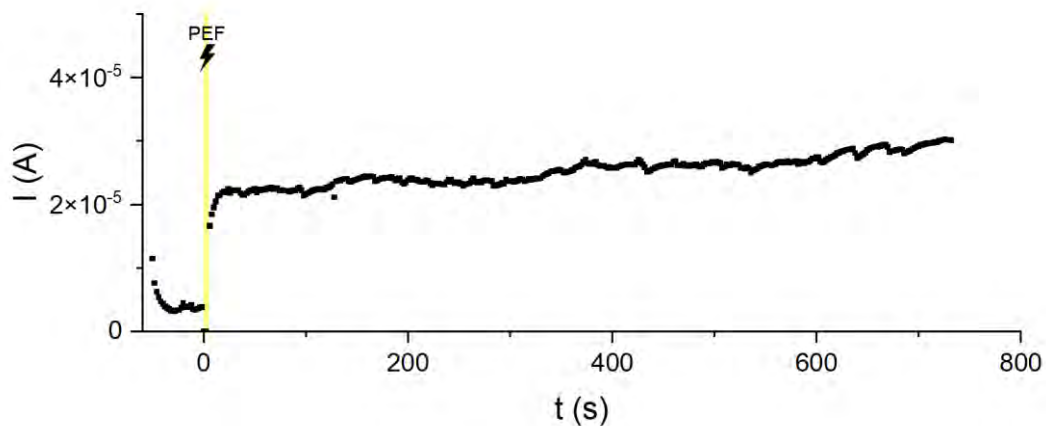


**Figure 4.7** - Electric current resulting from the application of 1V DC, before and after PEF at 300 V.

Unexpectedly, the DC electrical properties of the skin did not recover, after PEF, even for the lower voltages tested (100 V; 50 V did not induce any significant changes). Similar studies have reported a rapid recovery (*ca.* 20 s for the essential part [201]). Some possible but unlikely explanations could be

the *ex vivo* system, not attached to the living organism; an influence of the 1 V DC applied, inhibiting electrical recovery, or a recovery in a later period.

#### 4.1.4 Electrical recovery

Next, we studied the reversibility of the electrical response after the PEF application, by applying the PEF to the same skin model multiple times. The first PEF application at 100 V, served as a baseline. For the reversibility experiment, we applied two series of low-to-moderate voltage PEF from 100 up to 150 V. For the irreversibility experiment, we applied five series of high-voltage PEF from 200 up to 400 V. The skin models were then placed in an incubator at 37 °C and left to recover for one hour. After the recovery, subsequent PEF at 100 V were applied and the electrical response was compared to the baseline (**Figure 4.8**). The instantaneous resistance of the baseline measurement started at  $1200 \pm 200 \Omega$ , decreased to  $860 \pm 90 \Omega$  at the end of the 1<sup>st</sup> pulse and further decreased to  $730 \pm 60 \Omega$  at the last pulse. The reversible experiments revealed a similar behavior: the instantaneous resistance started at  $1100 \pm 100 \Omega$ , decreased to  $680 \pm 20 \Omega$  at the end of the 1<sup>st</sup> pulse and further decreased to  $580 \pm 30 \Omega$  at the last pulse. The baseline and the reversibility experiments resulted in a typical instantaneous resistance behavior, with a major decrease over the first pulse and lesser subsequent decrease over the next pulses (compare with **Figure 4.1**, 100V). Moreover, the reversibility experiments indicated that the electrical properties of the skin were recovered, albeit not to 100 % of the baseline values ( $R/R_0=86\%$ ). On the contrary, after the irreversibility experiments, the skin did not present a dynamic behavior and exhibited a constant instantaneous resistance of  $460 \pm 20 \Omega$  throughout the duration of the pulses ( $R/R_0=37\%$ ). These experiments showed that, under intense conditions (multiple PEF application in a short time interval, up to 400 V), the skin may be irreversibly damaged, losing its dynamic character. The low resistance indicated the permanent formation of aqueous pathways.

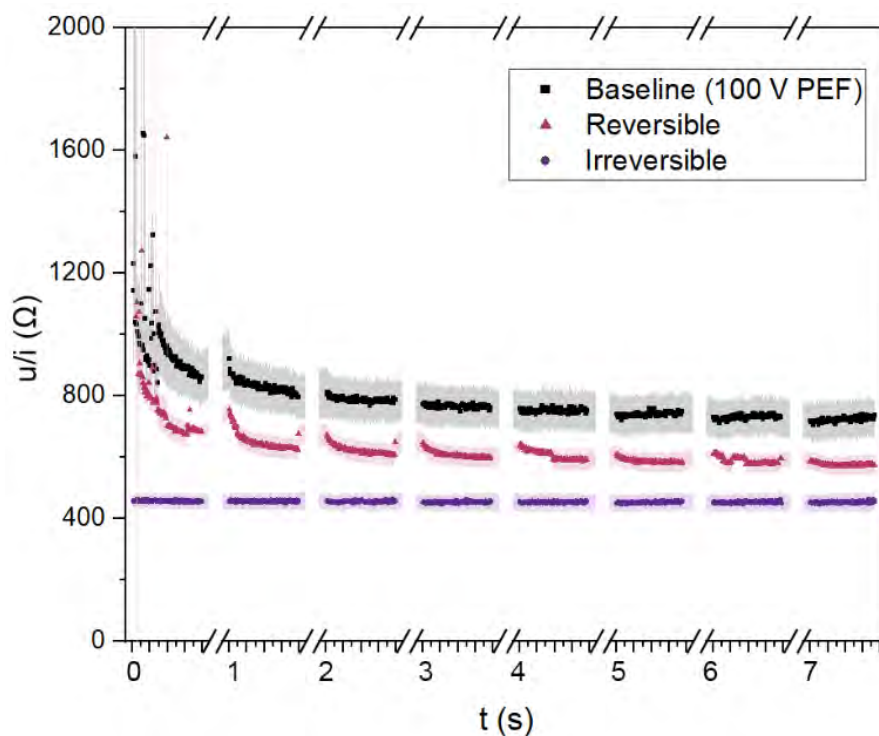


**Figure 4.8** - Instantaneous resistance of *ex vivo* drug delivery system at 100 V, for a series of PEF applications ( $n=3-4$ ). In black color, the baseline; in dark red, the instantaneous resistance of the skin after low-voltage PEF (up to 150 V); in purple, the instantaneous resistance of the skin, after a series of high-voltage PEF (up to 400 V). Shaded areas represent SEM.

Electrical properties measured through the oscilloscope, during PEF application, demonstrated recovery of instantaneous resistance for the reversibility experiment, reaching up to 86 % of the baseline value. The 14 % loss in instantaneous resistance may include permanent formation of some conductive pathways, in the center of LTRs, due to local thermal damage or irreversible electrically-induced changes. Noteworthy, the instantaneous resistance of the skin in the irreversibility experiment, not only did not recover to the baseline value, but also totally lost its dynamic character, and was assimilated to a dielectric material with a constant resistance, such as our system without the skin (consisting only of a humidified gauze and hydrogels, compare **Figure 4.8** with **Figure 4.2**). We infer that in this case, permanent conductive pathways were formed by a combination of electrical and thermal effects, in such a density and size, that no new pathways can be formed for a PEF of 100 V, *i.e.* virtually all of the current traversing the system passes through the pre-formed pathways.

#### 4.2 Temperature increase

We chose to regulate the temperature at 32 °C because this is the temperature of a healthy human forearm [159]. The measured baseline temperature of the skin model was  $31.2 \pm 0.4$  °C. During PEF application, the temperature of the explanted mouse skins increased rapidly throughout the duration of PEF, before regressing towards baseline within the next seconds (**Figure 4.9**). There was no measurable increase for a PEF of 50 V. The max temperature reached  $32.5 \pm 1.3$  °C for 100 V,  $36.7 \pm 0.9$  °C for 200 V and  $43.5 \pm 1$  °C for 300 V. In all cases, the maximum temperature was reached just after the last pulse of the PEF. The temperature decreased to less than 35 °C within 3 seconds, in the case of 200 V; and within 36 seconds, in the case of 300 V.

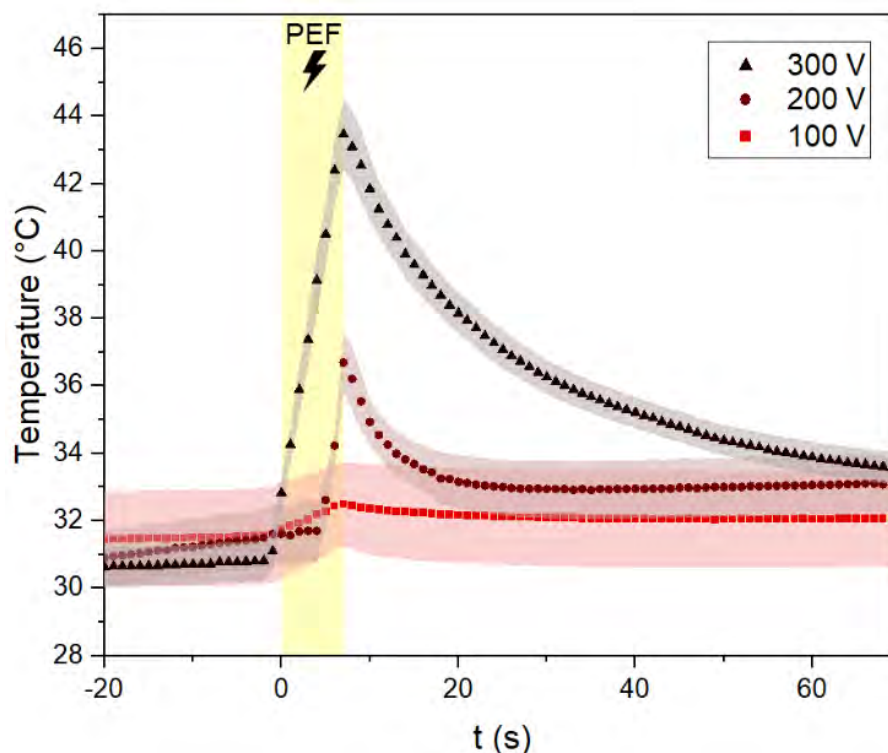


**Figure 4.9** - Temperature increase of the skin during PEF application (n=3-9). Yellow shaded area corresponds to PEF application. Shaded areas represent SEM.

Electroporation is generally understood to be a non-thermal phenomenon at the lipid bilayer level [202]. Yet Joule heating, local temperature increase and heat transfer play an important role during

the application of PEF on biological tissue. The current passing through the skin produces heat. At the place with the highest current density, according to our simulation, we measured a maximum temperature increase of  $+12.3 \pm 1$  °C for a 300 V PEF, below the heat pain threshold on healthy human skin (50-55 °C [203]). Some caution has to be taken here though, because the heat pain threshold is defined for the surface of the skin. In our case, the maximum temperature increase was under the skin, between the muscle and the wet gauze. It is not clear what is the heat pain threshold for temperatures *within* the skin, but it is possibly lower. For a fixed voltage, the temperature increase can be minimized by reducing the duration of the pulses and/or their frequency. A suggestion would be to limit the pulse duration to 5 ms; the observed decrease of instantaneous resistance mostly took place in these first 5 ms (**Figure 4.1**). *In vivo*, the temperature increase is expected to be lower, and the return to baseline faster, thanks to the mass of the organism that functions as a heat sink and blood circulation that contributes to thermoregulation. It must also be noted that the thermal properties of mouse and human (thicker) skins should differ.

The current density through the skin is not homogeneous. Our simulation assumes a homogeneous conductivity all over the skin layers. In the SC, the conductivity is a function of the electric field intensity,  $\sigma(E)$ . In reality though, the conductivity increase as a function of the electric field is not homogeneous. Most of the SC remains resistive, while local transport regions have a dramatically increased conductivity. As a result, the current density also preferentially passes through these regions. The local temperature at the center of the transport regions may reach much higher values. According to Pliquett *et al.* [204] and Becker [205], the temperature locally rises to over 70 °C, the phase transition temperature of lipids, contributing to the thermal expansion of the local transport region and the delivery of larger molecules. A local temperature increase as low as 45 °C may also contribute to the destabilization of the barrier function of the SC. At *ca.* 45 °C, the lipid packing evolves from orthorhombic to the less dense hexagonal packing [206]. In addition, Bulysheva *et al.* showed that moderately increased skin temperatures (43 °C) lead to more efficient gene electrotransfer, compared to a non-heated control (The temperature increase was independent from pulse application; they heated the skin through infrared laser heating) [207].

### 4.3 I-V measurements of reconstructed human epidermis

In parallel to the mouse skin model, we had the opportunity to test the drug delivery platform on a lab-grown, reconstructed human epidermis model. This model offers many advantages compared to the mouse skin. It is composed of human cell lines, so it is more relevant for the transdermal drug delivery on human subjects. The reconstructed epidermis presents a more simplified model of the human epidermis, composed only of keratinocytes and corneocytes. In this way, the complexity arising from the multitude of parameters (defects, pores, different kinds of cells) in the real skin, are avoided. In addition, the growth of the epidermis is strictly controlled (nutrients, temperature, time). This may lead to a smaller variation of experimental results than in the real skin of experimental animals which have a natural variability, both genetic (genes, mutations) and environmental (nutrition, humidity, temperature, injuries). Lastly, lab-grown models allow the minimization of killing and suffering associated with animal experimentation.

However, the reconstructed epidermis also had some differences compared to the mouse skin model, notably a much smaller size (both surface and thickness), and higher humidity than the real skin. We tested it with the same parameters used as with the mouse skin model, at 300 V PEF (**Figure 4.10**).

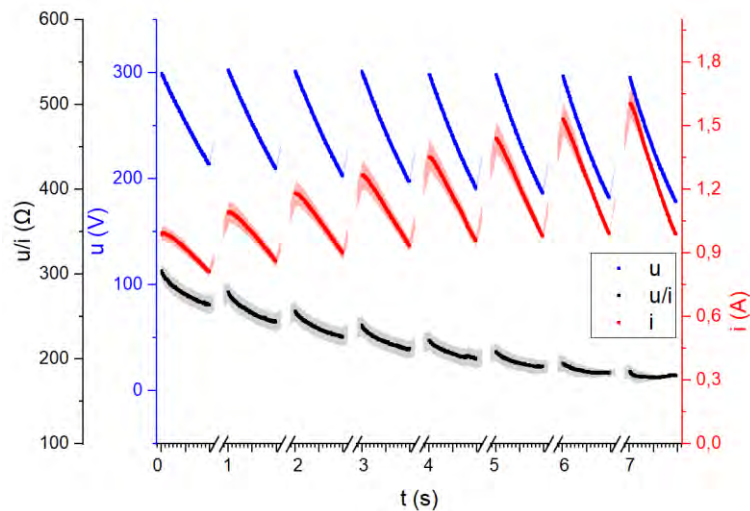


**Figure 4.10** - Voltage, current and instantaneous resistance ( $u/i$ ) of drug delivery setup on reconstructed human epidermis, during Pulsed Electric Fields (PEF) of 300 V. Shaded areas represent SEM.  $n=3$ .

Overall, the qualitative behavior of the reconstructed epidermis was similar to the mouse skin: the instantaneous resistance of the system decreased over the application of the PEF. But the system with the reconstructed epidermis model is much more conductive overall, leading to higher currents (up to 1.6 A) and lower resistance. The instantaneous resistance decreased from 300 to 180  $\Omega$  during the PEF. We did not monitor the temperature increase during these experiments, but the high current (0.8 to 1.6 A) implied an important temperature increase during the PEF treatment.

The thinner geometry and higher water content of the reconstructed epidermis model lead to a higher conductance. Therefore, the electric field distribution and the current resulting from 300 V PEFs was also not the same. In order to continue the experiments on this model, the PEF parameters must be adapted. The current PEF parameters (8 pulses of 20 ms at 300 V) heat up the system possibly over 70  $^{\circ}\text{C}$  locally, inducing permanent changes in the skin model. Some steps towards the optimization of the parameters for the reconstructed epidermis model would include testing a wider range of PEF voltages, coupled with a validated numerical model of the system.

#### 4.4 Chapter highlights and discussion on *in situ* measurements

We monitored the current, voltage and instantaneous resistance of the drug delivery system during PEF application, as well as the changes in passive electrical properties (DC conductivity) and temperature increase resulting from the treatment. Regarding the I-V measurements, there were three major observations: (1) the average resistance of the system (measured during the last of eight pulses) decreased for increasing PEF voltages, dramatically between 50 and 200 V, then to a lesser extent between 200 and 300 V, (2) the instantaneous resistance of the system decreased during the application of the electric pulses, and (3) the resistance changes were specifically attributed to the skin, since the system without the skin (hydrogels and wet gauze) had a constant instantaneous resistance. Through the electrical measurements, we also confirmed that the nanocomposite hydrogels establish effective electrical contact between the metal electrical contacts and the skin. This eliminates the necessity of using a conductive gel, as the resistance of the system remained unchanged regardless of the presence of a conductive gel.



Current – voltage measurements were used to study the reversibility of the PEF treatment. The instantaneous resistance of skin samples that were exposed to low-to-moderate voltages, up to 150 V, recovered back to almost the baseline values, within one hour. In contrast, the instantaneous resistance of skin samples exposed to multiple PEFs, up to 400 V was permanently decreased.

The application of PEFs at 100 V and over, modified the passive electrical properties of the skin, increasing its DC conductivity. There was a larger conductivity increase for higher PEF voltages. The increase in DC conductivity was long-lasting. The application of the PEFs increased the temperature of the skin samples up to +12 °C, mostly for the higher voltages of 200 and 300 V. The skin temperature remained under the heat pain threshold in healthy humans (50 to 55 °C). Reconstructed human epidermis presented numerous advantages over the mouse skin model. However, the PEF parameters must be reconsidered and optimized for this skin model, because of its higher conductance.

The most important factors that can affect the resistance of the system are the following:

1. **Creation and expansion of LTRs.** An electric field over a threshold value can create aqueous pathways through the skin, dramatically increasing ionic mobility. The formed local transport regions (LTRs) can expand in diameter under the application of longer pulsed electric fields.
2. **Electroporation of cell membranes.** An external electric field higher than *ca.* 400 V/cm in viable tissue can induce a transmembrane potential over the membrane electroporation threshold value (250 mV for most eukaryotic cells [15]), temporarily permeabilizing the cell membrane. Cell membranes have very low conductivities ( $10^{-6}$  S/m), therefore their permeabilization increases the overall conductance of a tissue.
3. **Temperature.** Temperature affects conductivity in different ways depending on the conduction mechanism of the material. In our case, the predominant conduction mechanism was ionic conduction. Higher temperatures increase the conductivity of aqueous ionic solution by *ca.* 2 % per degree Celsius [188].
4. **Changes in plasma membrane conductance.** The conductance of plasma membranes can change from an externally applied electric field, even before reaching the electroporation threshold, due to activation of voltage gated ion channels [193]. In addition, externally-induced changes to the transmembrane voltage of excitable cells (neurons, muscle cells) can trigger action potentials.
5. **Nonlinear conductivity.** Some materials have a nonlinear electrical conductivity, *i.e.* their current – voltage curve does not follow Ohm’s law. This is common in materials used in electronics such as semiconductors and varistors but also in nanocomposite materials [208] and in some cases also in electrolytes [209]. In chapter **3.7.4.2**, we studied the electrical properties of the nanocomposite hydrogels and observed that they behave as nonlinear materials, in the electric field range from 300 to 6000 V/m.
6. **Changes at the interface of materials.** Changes at the interfaces between the metal electrical contacts, the hydrogels and the skin can have an effect on the resistance of the system. These changes include formation of gas bubbles due to electrochemical reactions (water electrolysis) and/or temperature increase, corrosion of surface of the metal, and small-scale physical movements of the configuration due to the applied external electric field. The tissue contains muscles and nerves which can contract with the electric field, slightly moving the system and potentially affecting the electrical contacts.

Some of these factors are overlapping. As mentioned in paragraph **4.2 Temperature increase**, phase transition of lipids due to heat can play a role in the creation and expansion of LTRs. Additionally, increased temperatures can increase the electrical conductivity of aqueous pathways formed through electroporation. Creation and expansion of LTRs in the skin for high electric fields, is also itself a form of nonlinear conductivity. For simplicity reasons, in the following hypotheses we will focus on the first three factors, as the nonlinearity and the interfaces of materials cannot be predicted with accuracy. Their impact on conductivity is also less important than the creation of local transport regions, plasma membrane electroporation and temperature increase.

Through our observations, we make the following hypotheses for the impact of PEFs on the skin:

6. The decrease in average resistance of the skin was related to the formation of LTRs through the epidermis. Higher applied voltages induced a higher density of LTRs, thus decreasing the resistance of the skin to a larger extent.
7. The decrease in the instantaneous resistance of the system was related to an increasing conductivity within already formed LTRs in the epidermis. This increasing conductivity may be due to the expansion of the radius of the LTRs, or local heat-induced changes in lipid packing within LTRs. For currents over 0.25 A (corresponding to voltages of 200 V and over), the temperature increase of the system, and in particular the wet gauze, also played a role.
8. The changes in the electrical conductivity of the skin can be temporary, longer-lasting or permanent. The DC conductivity of the skin showed no changes after a PEF of 50 V, but the instantaneous resistance of the skin decreased during its application. This showed that, for lower voltages, conductive pathways are formed through the skin only during the application of the electric field, without impacting the passive electrical properties of the skin. However, higher PEF voltages induced long-lasting changes on the DC conductivity.
9. A series of low-to-moderate (up to 150 V) PEF voltages had a minor impact on the baseline instantaneous resistance of the skin samples, while a series of high voltage PEFs (up to 400 V) irreversibly increased the conductivity of the skin. We hypothesize that in the first case the conductive pathways formed through the skin, recovered their original resistivity. The minor, permanent conductivity increase may be connected to the irreversible electroporation of regions with higher current density (for example appendages). In the second case, the conductive pathways did not recover due to extensive electrical and possibly thermal damage.
10. The distribution of the current density through the skin was not homogeneous. Regions with higher conductivity, such as skin appendages (hair follicles, sweat ducts, sebaceous glands) and other defects of the epidermis due to injuries, had a higher current passing through them. These regions were disproportionately affected by the electric field. At lower voltages, particularly, the electroporation of the cells in these regions may be responsible for the overall conductivity increase [25].

## 5 Numerical Modeling

5.1	FIRST MODEL: 2D .....	137
5.2	SECOND MODEL: 3D .....	141
5.3	THIRD MODEL: 3D WITH NONLINEAR CONDUCTIVITY.....	143
5.4	CHAPTER HIGHLIGHTS AND DISCUSSION ON NUMERICAL MODELING .....	148

We developed a series of numerical models to simulate the electric field distribution in the system, with increasing complexity and accuracy. Through numerical modeling, we evaluated the impact of changing parameters (geometry, electrical properties) on electroporation conditions, predicted and then confirmed the delivery of fluorescent molecules and got a better understanding on the mechanisms behind skin electroporation. An experimentally-validated numerical model allowed to perform multiple virtual experiments, minimizing the need for experimental reagents and skin models (both animal skin and lab-grown human skin).

### 5.1 First model: 2D

The first numerical model we developed was a simplified, two-dimensional model of the drug delivery system. The model used a combination of literature and experimental values of electrical and geometrical properties and evaluated the impact of the conductivity of the hydrogel, and the soaked gauze, on the distribution of the electric field through the various skin layers.

The geometry was designed as a series of rectangular layers of varying width and electrical conductivity, representing the different skin layers (**Figure 5.1**). The two hydrogels were placed on top, and the voltage was applied at the top side of the hydrogels. The rest of the simulation area was filled with air, and the boundaries were considered electrically insulating. The fine mesh size allowed for simulation of skin layers with a thickness down to  $9 \times 10^{-6}$  m (stratum corneum).

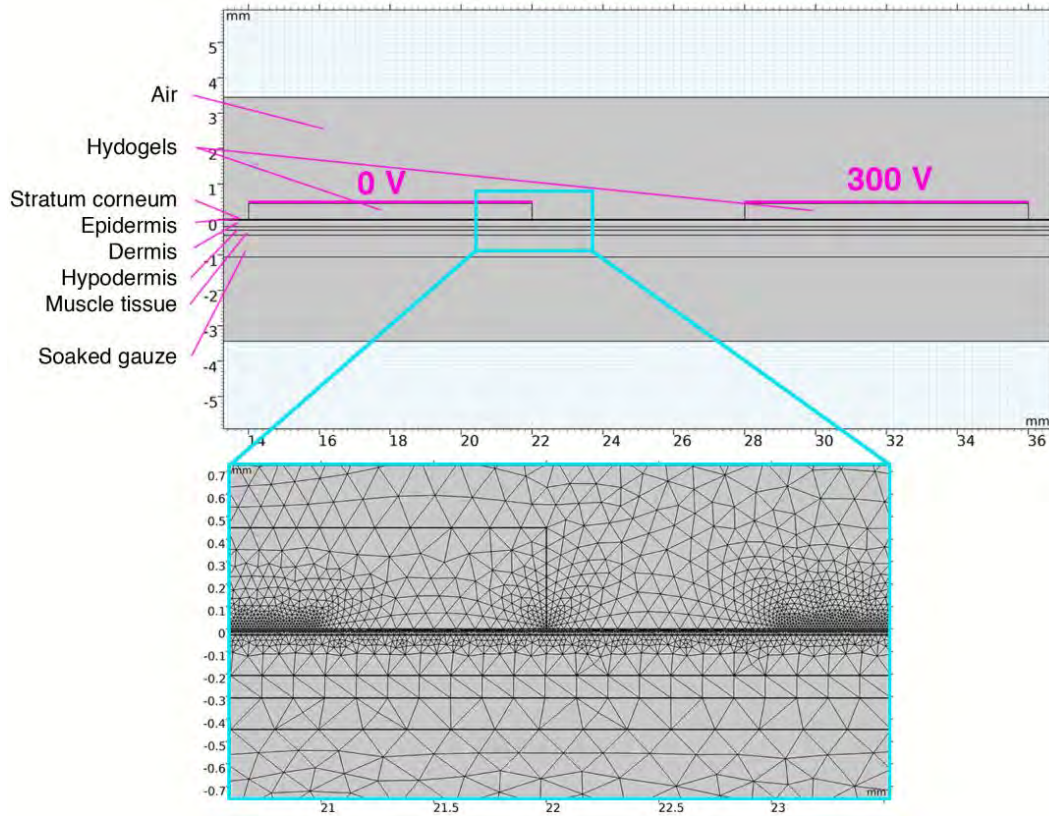


**Figure 5.1** – Geometry of 2D numerical simulation and mesh detail.

The distribution of the electric field is the most crucial parameter in skin electroporation. The threshold value for permeabilization of tissue is approximately 400 V/cm, while electric field strengths over 1200 V/cm can damage viable tissue irreversibly [17], [18]. This is the case for the skin layers with living cells; less is known for the electroporation threshold values of the stratum corneum, which contains dead, flattened corneocytes.

We simulated the electric field distribution for different hydrogel conductivities, from  $10^{-6}$  to 0.15 S/m, for a voltage of 300 V. The calculation time for this simplified model did not exceed some tens of seconds for each parametric run. At  $10^{-6}$  S/m, the conductivity of swollen plain agarose hydrogels, the electric field at the skin did not exceed 7 V/cm. At  $10^{-4}$  S/m, the conductivity of swollen nanocomposite hydrogels, the electric field at the SC reached 660 V/cm and 6-14 V/cm at the epidermis and dermis. At 0.15 S/m, the conductivity of the electroporation buffer in which the hydrogels are swollen, the electric field reached values of 30 – 70 kV/cm at the SC and 75 – 250 V/cm, at the epidermis and dermis (with the largest parts under 150 V/cm). The full results are displayed on the following table (**Table 5.1**) and **Figure 5.2**.

**Table 5.1** – Electric field distribution for different hydrogel conductivities

Hydrogel conductivity (S/m)	E (V/cm) @Stratum corneum	E(V/cm) @Epidermis and Dermis
$10^{-6}$	7	2-5
$10^{-4}$	640-660	6-14
0.15	30000-70000	75-250

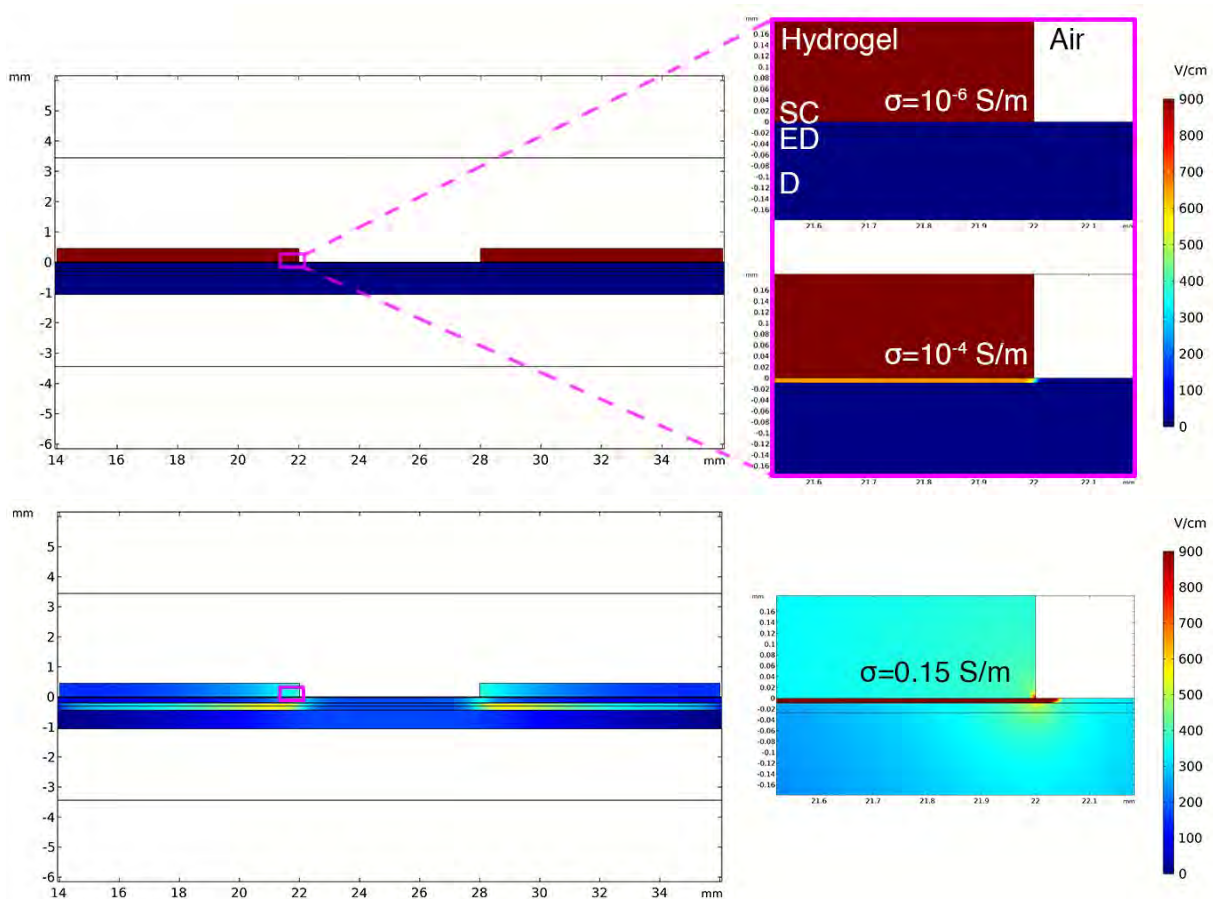


**Figure 5.2** – Electric field distribution in the skin for different hydrogel conductivities and zoom on first skin layers for 300 V pulse. (SC: Stratum Corneum, ED: Epidermis, D: Dermis).

It was clear from these results that the conductivity of the hydrogel played an important role in the distribution of the electric field in the skin. Resistive hydrogels produced an important voltage drop within the hydrogel, resulting in a severely decreased electric potential applied on the skin surface (**Figure 5.3**). Increasing the conductivity of the nanocomposite hydrogels, from  $10^{-6}$  to  $10^{-4}$  S/m had a positive impact on the distribution of the electric field, by increasing the field values of the SC. However, even for hydrogel conductivities up to 0.15 S/m, the electric field values at the epidermis and dermis did not reach the electroporation threshold values (*ca.* 400 V/cm for tissue).

The current density arrows traversed the SC virtually vertically and then traversed the deeper layers (dermis, muscle tissue, gauze) before exiting from the negative electrode ( $V=0$ ). The SC has a very high resistivity ( $\sim 2000 \Omega \cdot m$ ), thus the current density traverses it with the shortest pathway possible (vertical) before reaching the more conductive layers (**Figure 5.3**).

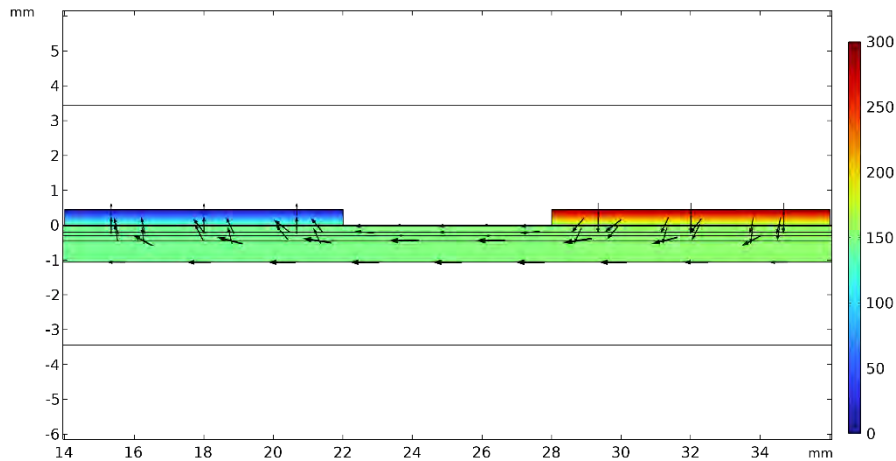


**Figure 5.3** – Electric potential and current density on drug delivery system for 300 V and  $\sigma_{\text{hydrogel}} = 10^{-4}$  S/m. Black arrows represent current density.

The impact of the conductivity of the soaked gauze was also tested. In the drug delivery configuration, the explanted mouse skin was placed on a gauze soaked with phosphate buffer saline (PB). The conductivity of this layer played a decisive role in the current density paths. A more resistive gauze, at 0.15 S/m saw a very small part of the current passing through it. Most of the current passed through the epidermis, the dermis and the muscle tissue. On the other hand, a more conductive gauze saw a bigger part of the current density traversing it. The current density passed mostly from the muscle, the gauze and the dermis (**Figure 5.4**).

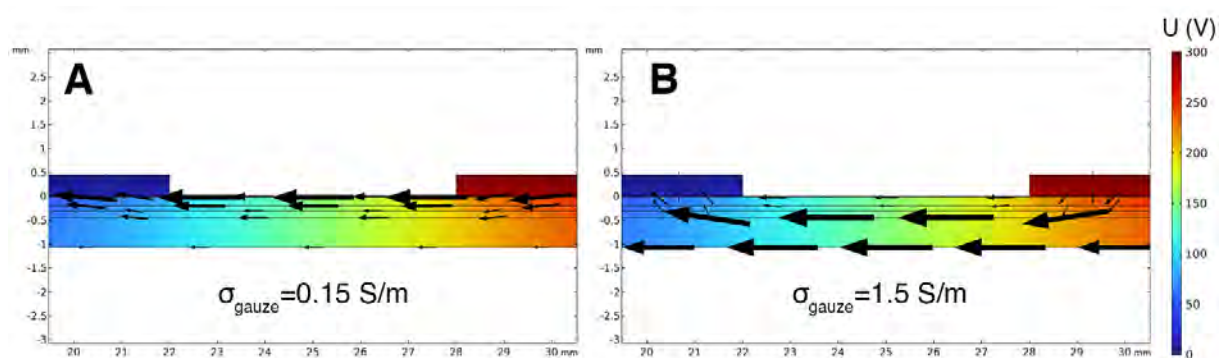


**Figure 5.4** – Electric potential and current density with varying gauze conductivities, for 300 V pulse and  $\sigma_{\text{hydrogel}} = 0.15$  S/m. (A)  $\sigma_{\text{gauze}} = 0.15$  S/m. (B)  $\sigma_{\text{gauze}} = 1.5$  S/m. Black arrows represent current density.

In the following chapters it was chosen to work with the most conductive gauze (soaked with PBS). This gauze achieved a higher current density and a more uniform distribution of the electric field. Furthermore, previous works of our group, as well as the first series of experiments for the current work used the PBS-soaked gauze [157], [158]. To ensure the comparability of current findings with the previous results it was chosen to not change this parameter.

This first 2D numerical modeling of our system gave us valuable insights into the role of the system's electrical and geometrical properties, on the distribution of the electric field and the current density paths. We confirmed that the conductivity of the hydrogels was of utmost importance. The hydrogel conductivity increase of two orders of magnitude (from  $10^{-6}$  to  $10^{-4}$  S/m), achieved through the incorporation of 10 % CNTs in the agarose hydrogels, resulted in a substantial increase in the electric field at the SC (from 7 to 660 V/cm). However, the electric field did not reach near the values for tissue



electroporation at the viable layers of the epidermis and dermis. In fact, even a very conductive hydrogel at 0.15 S/m did not lead to in values over the threshold for tissue electroporation (400 V/cm) at the deeper skin layers.

The current density arrows showed that the current crossed the SC virtually vertically, and traversed the skin through the deeper layers (epidermis, dermis, muscle, soaked gauze). This was expected because of the huge electrical conductivity differences of these layers ( $5 \times 10^{-4}$  S/m for the SC; 0.2 to 1.5 S/m for the deeper layers mentioned). Moreover, the simulations highlighted the impact of the soaked gauze on the resulting current density. This parameter had previously been disregarded as trivial.

The advantages of the 2D simulation were simplicity in modeling, rapid calculations even for a fine mesh (in general, less than a minute for each parameter) and straightforward visualization of results. Nonetheless, the two-dimensional simulation presented some important limitations. Firstly, the simulation cannot give us the calculated values of current and resistance, as these require three-dimensional objects. As a result, no comparisons with the experimentally acquired values could be made. Moreover, there was no information on the spatial distribution of the electric field on a surface under the hydrogels. For these reasons, we proceeded by simulating the full 3D environment of the drug delivery system.

## 5.2 Second model: 3D

For the second numerical model, a 3D simulation of the drug delivery system was recreated in its entirety (**Figure 5.5**). The conductivity of the wet gauze and the nanocomposite hydrogels were calculated through I- V measurements, at 150 V PEFs (Annex, section 9.1).

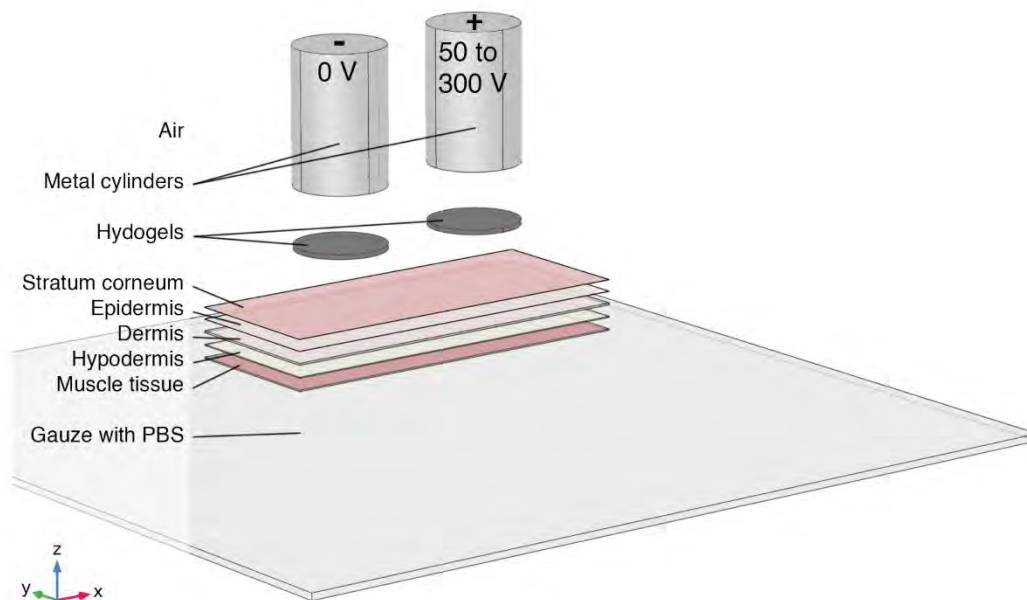


**Figure 5.5** – The 3D drug delivery system in COMSOL (cascade layers preview, colored).

The 3D model gave us the electric potential, current density and electric field distribution at the drug delivery system (**Figure 5.6** and **Figure 5.7**). The calculation time for the 3D model increased to several minutes (15-30 per parametric run).

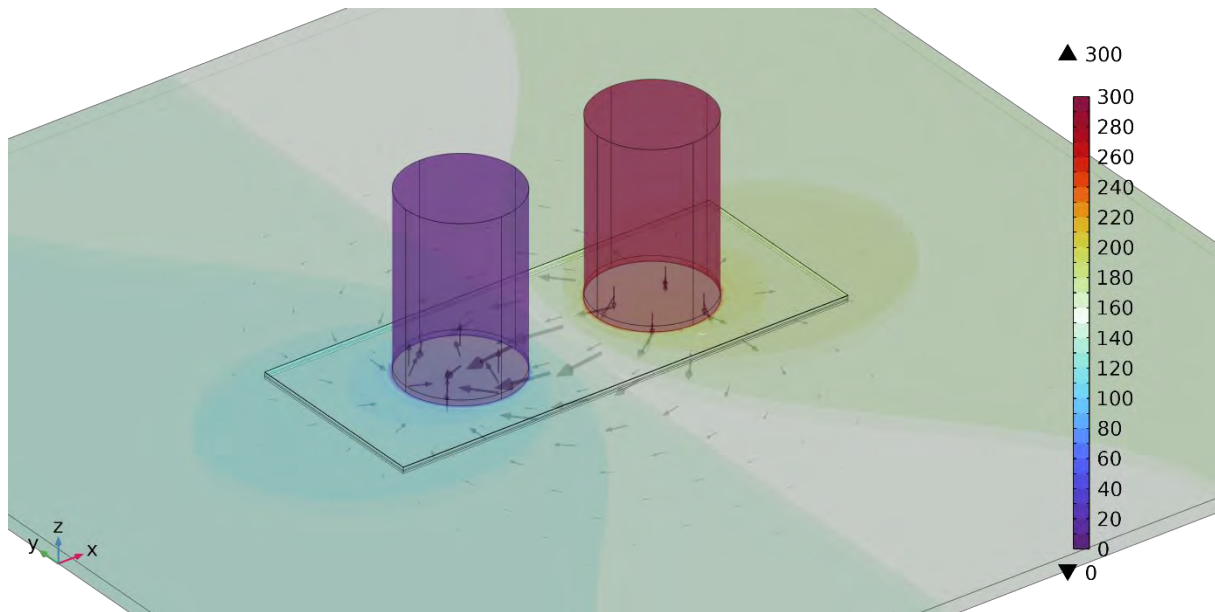


**Figure 5.6** – Electric potential and current density (black arrows) on mouse skin model, at 300 V.

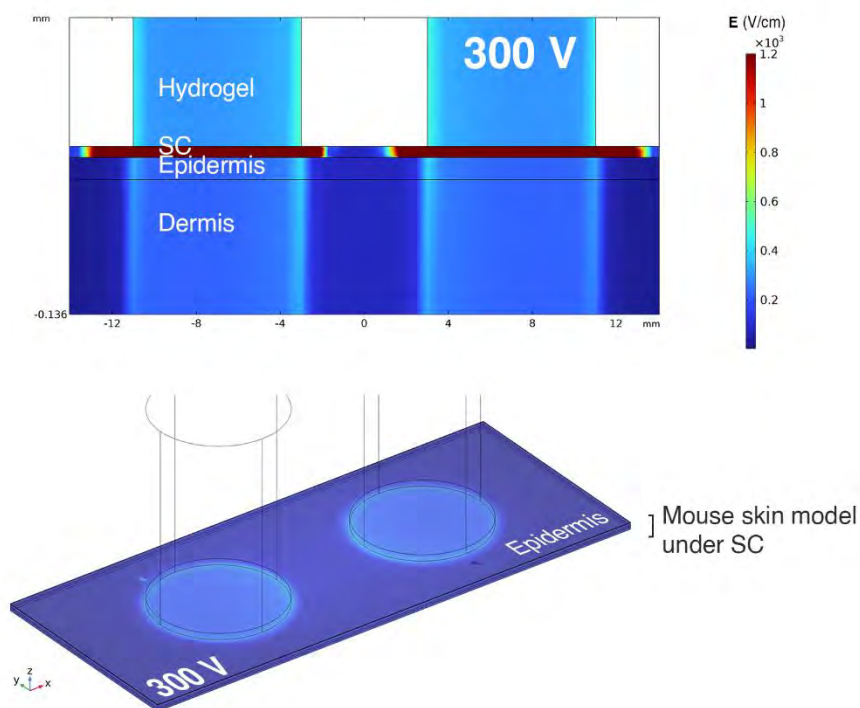


**Figure 5.7** – Electric field distribution at mouse skin model for 300 V PEF. Top: XZ slice. Bottom: Electric field at epidermis under SC.

The resistance of the system calculated through the second model ( $1250 \Omega$ ) was in the range of resistances measured through the I-V measurements, during the PEF application on mouse skin samples (*ca.* 500 to  $2000 \Omega$ ). The second model had two limitations:

1. **Constant resistance.** The resistance value calculated through the second numerical model was constant and independent of the applied electric field. As measured in the previous chapter,

the average resistance of the system varied for different applied voltages, decreasing for increasing PEF strengths.

2. **Electric field at low levels in viable skin layers.** The distribution of the electric field simulated through the second model, reached a maximum strength of 250 V/cm in the epidermis and the dermis, lower than the threshold for permeabilization of cells in tissue (400 V/cm [17]). However, our drug delivery experiments (Chapter 6 **Drug delivery**) demonstrated permeabilization of cells for 300 V PEFs.

For these reasons, we developed a third numerical model, with nonlinear electrical properties.

### 5.3 Third model: 3D with nonlinear conductivity

In the third numerical model, we included the nonlinear electrical conductivity of the SC in the simulation. We used the *ex vivo* results on the average skin resistance during the PEF application from the previous chapter, to validate the numerical model. The application of an electric field creates conductive pathways through the SC, increasing its conductivity in relation to the electric field strength. At the same time, the conductivity of the SC affects the distribution and strength of the electric field, so this is a nonlinear equation that has to be solved through iterations. The conductivity of the most resistive part of the skin, the stratum corneum, can be increased up to three orders of magnitude during electroporation conditions [17].

We used the electrical measurements to adjust the nonlinear conductivity of the SC for different electric fields, while remaining within the range of the reported literature values. The temporal simulation with nonlinear conductivity for a very thin domain (stratum corneum) was challenging, especially to have a well-adapted mesh, therefore the grid was refined during the simulation to get a convergence of the solution. The conductivity of the other skin layers also decreases through electroporation, but to a much lesser extent (factor of 2 to 4) [17]. This was not included in the simulation to save on computing power and because the changes in the resistance of the system would be minor (<10 %).

In the literature, few different ways have been reported to model the dependency of the conductivity of the SC to the electric field. These range from giving fixed values to the  $\sigma_{SC}$  for discrete ranges of electric fields (for example  $\sigma_{SC} = 5 \times 10^{-4}$  for  $E < 600$  V/cm,  $\sigma_{SC} = 10^{-3}$  for  $600 < E < 1200$  V/cm and  $\sigma_{SC} = 0.05$  for  $E > 1200$  V/cm) to analytical equations in the form of exponentials or logistic functions [17], [19]. We used our experimental results (*ex vivo* measurements and simulations from the second numerical model) to create a piecewise cubic interpolated function for  $\sigma_{SC}(E)$ , in COMSOL. The conductivity of the SC increased between the different applied PEFs, according to the interpolated function (**Figure 5.8**).

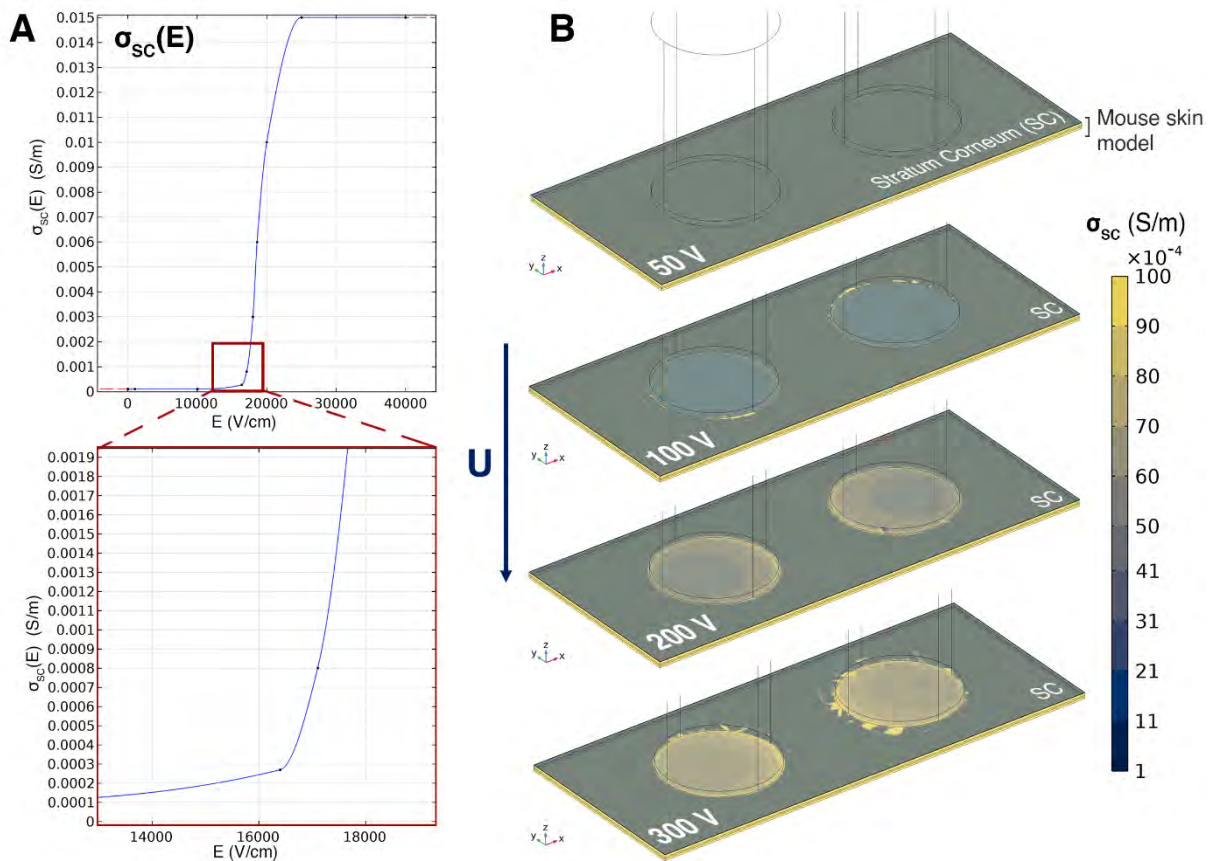


**Figure 5.8** – Stratum Corneum (SC) nonlinear electrical conductivity. (A) The interpolated curve used for the relation between SC conductivity and the electric field,  $\sigma_{sc}(E)$ . (B) the conductivity of the SC for applied PEFs from 50 to 300 V.

Through the  $\sigma_{sc}(E)$  curve we aligned the numerical model with the experimental results on the *ex vivo* mouse skin. There were two major observations from the *ex vivo* electrical measurements: (1) the average resistance of the system (measured during the last of eight pulses) decreased for increasing PEF voltages and (2) the instantaneous resistance of the system decreased during the application of the electric pulses. With the inclusion of the nonlinearity of the SC, the numerical model accurately predicted the 1<sup>st</sup> observation: the average resistance decreased for increasing PEF voltages. A comparison between the *ex vivo* and the simulation results is presented in **Figure 5.9**. We did not attempt to include the 2<sup>nd</sup> observation, the decrease in the instantaneous resistance during the PEF application, in the numerical model. The time-dependence of the resistance during PEF application is governed by a combination of electrical and biological phenomena which are not yet fully elucidated.

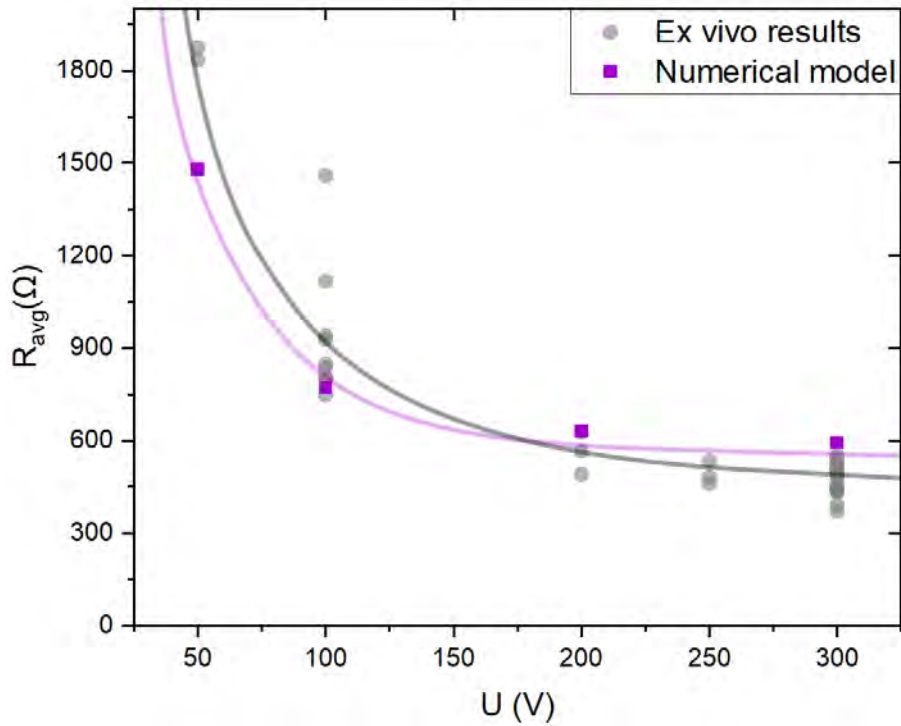


**Figure 5.9** - Average resistance of the *ex vivo* system for applied PEF voltages from 50 to 300 V, compared with the results of the numerical model.

Next, we used the validated numerical model, to simulate the distribution of the electric field on different skin layers, during the PEF application (**Figure 5.10**). Through the conductivity increase of the SC, the electric field reached the deeper skin layers. The calculation time stretched to few hours (1-4 hours) for each parametric run in the nonlinear, 3D model.

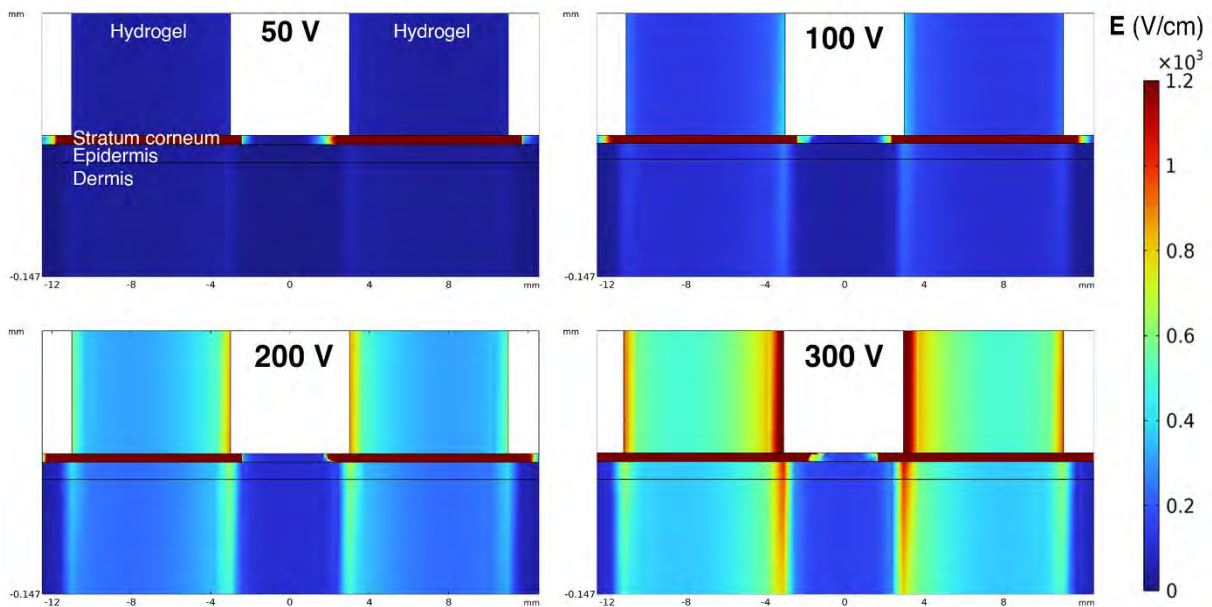


**Figure 5.10** – XZ slices of electric field distribution in the skin for PEFs of 50 to 300 V.

The layers which contain viable cells, that can be permeabilized through electroporation are the lower levels of the epidermis and the dermis. In the following figure, we simulated the distribution of the



electric field on the epidermis, under the SC (**Figure 5.11**). At 50 and 100 V, the electric field remained under the threshold for cell permeabilization (400 V/cm), all over the viable skin. For 200 V, there was a very thin crescent-shaped area, where the electrodes faced each other, where the electric field exceeded 400 V/cm. At 300 V, almost all the area under the hydrogels was over 400 V/cm.

For electric field strengths over 1200 V/cm, the cells of the epidermis and dermis may be permeabilized irreversibly [17]. In the context of transdermal drug delivery, irreversible permeabilization, leading to cell death, has to be avoided. For applied PEF voltages up to 300 V, no area of the epidermis and dermis reached electric field strengths higher than 1200 V/cm. For 300 V, the strongest electric field was 1100 V/cm, on a very thin, crescent-shaped, area where the electrodes faced each other.

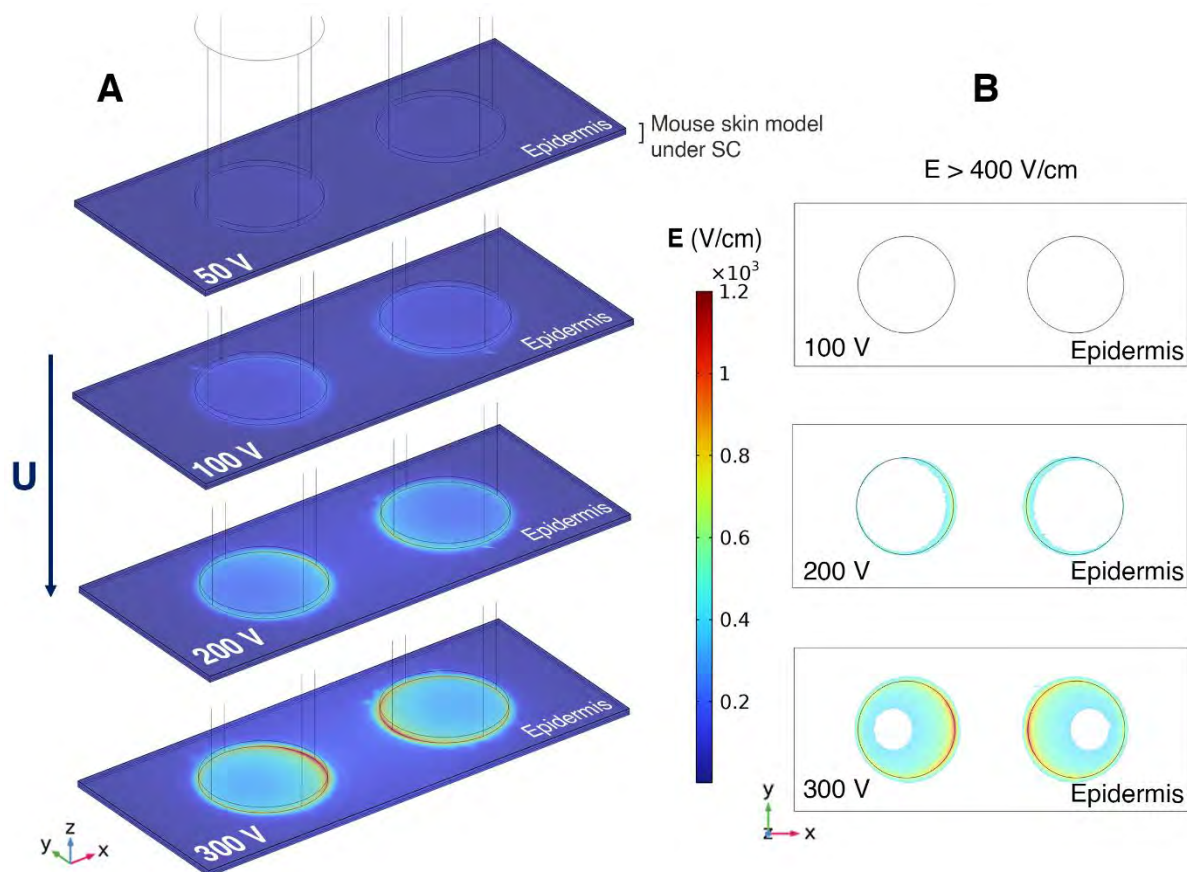


**Figure 5.11** – Electric field distribution on surface of viable skin layers (Epidermis under SC). (A) Electric field distribution for PEFs from 50 to 300 V. (B) XY view (top view) of viable skin surface with  $E > 400$  V/cm for PEFs from 100 to 300 V.

At 400 V PEF, the entire viable skin area under the hydrogels reached values over the threshold for reversible electroporation. However, on a thin area under the hydrogels, the electric field strength reached values over the threshold for irreversible electroporation (**Figure 5.12**).



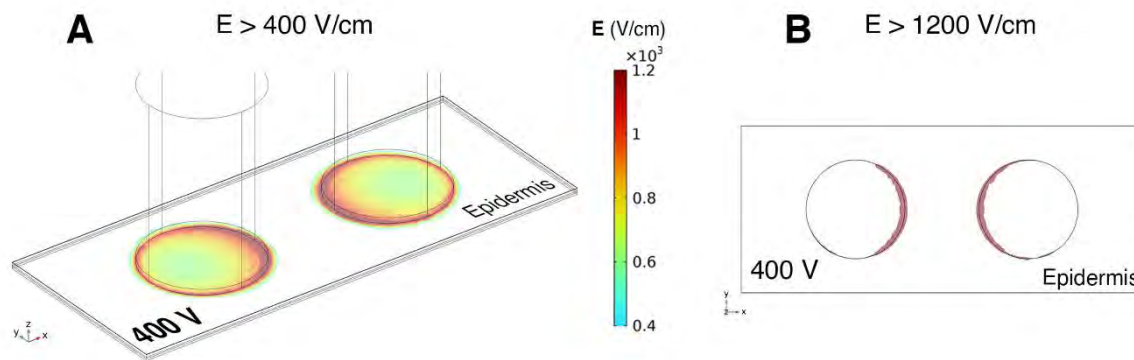


**Figure 5.12** - Electric field distribution on surface of viable skin layers (Epidermis under SC) at 400 V PEF. (A) Region over reversible electroporation threshold. (B) Region over irreversible electroporation threshold.

The numerical model was also used to evaluate the voltage drop along the current lines passing through the system (**Figure 5.13**). There was a small voltage drop within the hydrogels, then a substantial voltage drop within the SC and a smaller voltage drop within the deeper skin layers, followed by a larger voltage drop within the wet gauze.

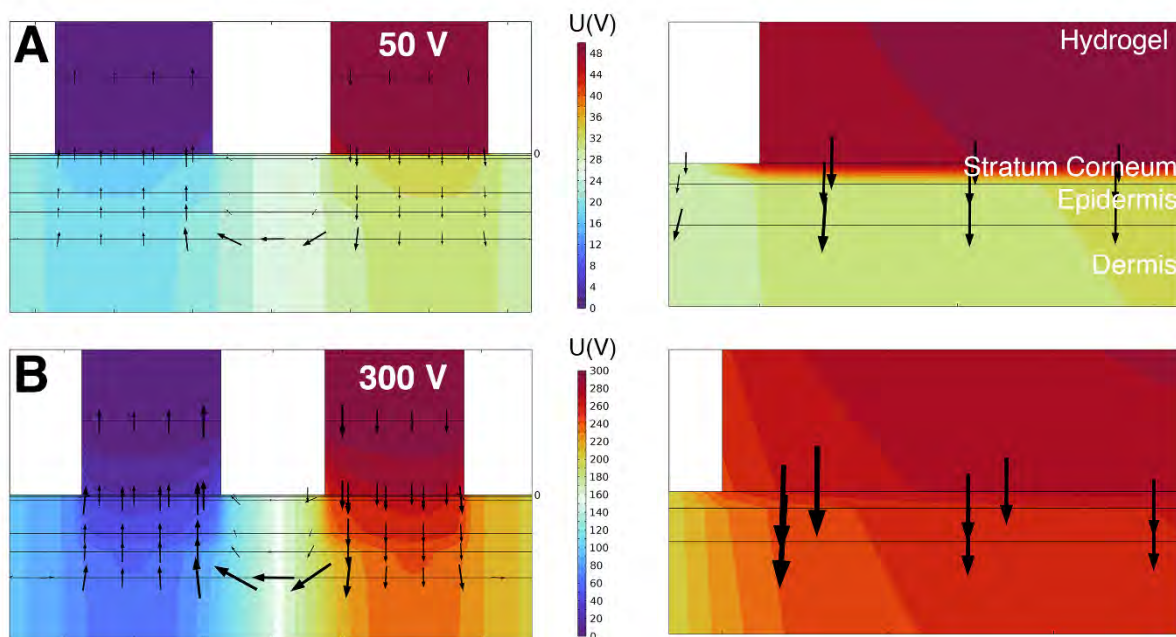


**Figure 5.13** – XZ slices of voltage (colored) and current density (black arrows) for PEFs of 50 V (A) and 300 V (B). Left: Full view (hydrogels, skin layers, gauze). Right: Zoom on first skin layers.

The nonlinear conductivity of the SC affected the contribution of the different components in the total resistance of the system. For a PEF of 50 V, no (or very few) conductive pathways were created through the SC, resulting in a high resistance. At 50 V, the SC alone accounted for 66 % of the system's resistance. With the formation of conductive pathways, the contribution of the SC to the total resistance of the system dropped to 12 %. At 300 V, the regions with the largest resistance drop were the hydrogels (24 %) and the wet gauze (47 %). The full results are presented in **Table 5.2**. The resistance of the skin with a permeabilized SC was very low because the deeper skin layers were fairly conductive and the total thickness was less than half a millimeter (0.47 mm).

**Table 5.2** – Voltage drop in different components of the system for PEF of 50 and 300 V.

Component	50 V		300 V	
	Voltage drop	% of total voltage drop	Voltage drop	% of total voltage drop
Metal cylinder (x2)	0	0	0	0
Hydrogel (x2)	5	10	72	24
Stratum Corneum (x2)	33	66	35	12
Epidermis (x2)	0	0	3	1
Dermis (x2)	1	2	12	4
Hypodermis (x2)	3	6	30	10
Muscle (x2)	0	0	6	2
Wet gauze (x1)	8	16	142	47
Sum	50	100	300	100

#### 5.4 Chapter highlights and discussion on numerical modeling

We developed a series of numerical models, with increasing complexity, to describe and understand the electrical properties of the drug delivery system. The first, two-dimensional, model underlined the role of the electrical conductivity of the hydrogel platforms, on the distribution of the electric field through the skin model. It also revealed the impact of the conductivity of the wet gauze and confirmed that the current density flowed through the SC, into the deeper skin layers. The second model was developed with a three-dimensional geometry that corresponded to the full drug delivery system. We corrected the electrical conductivities of the nanocomposite hydrogels and the wet gauze, with feedback from the I-V measurements, and simulated the electric field within the different skin layers.

The third model included a nonlinear dependence of the conductivity of the SC on the electric field. The conductivity of the SC increased dramatically through the formation of conductive pathways, induced by the applied electric field. We used experimental results from the previous 3D model and the electrical measurement on the *ex vivo* mouse skin to interpolate a function for the dependence of the SC's conductivity on the electric field. The model accurately described the decrease in the resistance of the system with increasing PEF voltages, producing results very close to the experimentally measured values. As pointed out by Corovic *et al.*, the inclusion of nonlinear conductivity of the SC (*i.e.* the conductivity is dependent on the electric field,  $\sigma(E)$ ) proved crucial for the electric field distribution. With a constant conductivity, the electric field appeared to concentrate only on the SC, without reaching the deeper skin layers.

The validated numerical model showed that cells in the epidermis and dermis could be permeabilized reversibly ( $E > 400$  V/cm) for PEFs of 300 V, in a large region under the hydrogels. The electric field strength reached its highest values at the crescent-shaped region where the two electrodes faced each other. At 400 V PEFs, the surface coverage of permeabilizing electric fields was larger, but a thin region had electric field values over the threshold for irreversible permeabilization (1200 V/cm). The SC that had not been permeabilized caused a massive voltage drop in the drug delivery system, limiting the potential difference applied to the deeper skin layers. For lower PEF voltages (50 V), this voltage drop accounted for 66 % of the resistance of the system. At higher voltages (300 V), the permeabilization of the SC drastically decreased its contribution to the system's resistance. For 300 V PEFs, the main resistance in the system originated from the wet gauze. This resistance may be decreased by

decreasing the distance between the hydrogel platforms (currently, 6 mm side to side). However, bringing them too close would risk causing a short-circuit with the aqueous solution that is released from the hydrogels during PEF application.

The wet gauze placed under the skin served for hydration of the tissue but it was also meant to simulate the layers under the hypodermis. These include muscle, connective tissue and interstitial fluid, with approximate conductivities of 0.5, 0.2 and 2 S/m, respectively [210], [211]. We wetted the gauze with phosphate buffer (1.5 S/m), rather on the higher conductivity side, in lack of acknowledged data. A drug delivery experiment with a full mouse could give us the conductivity value to be used for the gauze.

In the context of transdermal drug delivery, we are mostly interested in the first three skin layers, the SC the deeper epidermis and the dermis. The SC is the limiting layer for therapeutic molecule delivery. The epidermis is the first layer with viable cells, that contain nuclei and plasma membranes. It also includes immune cells, making it an adequate target for vaccinations. Some other examples of drugs that can be delivered to the epidermis include topical anesthetics such as lidocaine for numbing the area before a medical procedure and retinoids delivered locally for acne treatment [13], [26]. The dermis includes viable cells and also blood vessels. Drugs delivered into the dermis can then reach systemic circulation through the vascularization of the tissue. Examples of drugs that have to reach systemic circulation to have an effect include morphine for pain treatment and insulin for glucose metabolism (diabetes).

The interpolated function that we used to describe the conductivity of the SC, included very high electric field values, in the range of 14 to 18 kV/cm. How do we explain such high threshold values for the creation of LTRs? Both in the electroporation of the SC and of plasma membranes, the basis of the phenomenon lies in the permeabilization of lipid bilayers, through the buildup of electric potential across the bilayer followed by a sort of dielectric breakdown, caused by an external electric field. However, their environment is drastically different: the extracellular lipids of the SC are arranged into dense stacks of lipid bilayers (70 to 100 stacks in the human SC [60]) in an electrically resistive ( $5 \times 10^{-4}$  S/m) and relatively dry environment, while the plasma membranes of cells in tissue are less densely packed and are surrounded by electrically conductive, water-rich medium from both sides (cytoplasm and extracellular medium). Cell membranes are permeabilized when the transmembrane potential  $\Delta\psi$  reaches a value of *ca.* 250 mV [15]. For eukaryotic cells in an aqueous suspension, or cells that are part of a biological tissue, this roughly corresponds to a homogeneous electric field in the range of 400 to 700 V/cm [17], [212]. These values are commonly used as the critical electric field strength for electroporation of tissue in general, including the SC [161], [213]. However, it is clear that the electrical and morphological properties of the lipid bilayer environment play an important role on the critical electric field strength for electroporation. Therefore, there is no reason to expect that the electroporation threshold value for cell permeabilization would be the same as the threshold value for the creation of LTRs through the SC. Our findings pointed out toward the existence of two distinct critical electric field strength values in the context of skin electroporation: a strength of roughly 14-18 kV/cm at the SC for the creation of LTR and a strength of *ca.* 400 V/cm at the epidermis and dermis for cell permeabilization. This second electric field strength threshold is in agreement with previously reported values [17].

The electric field within the SC builds up to very high values, even for moderate voltages, because of its geometrical and electrical characteristics of being a very thin and resistive layer surrounded by more

conductive layers. In real conditions, the increased conductivity, localized in the LTRs would prevent a buildup of the electric field strength at the SC. It is possible to take into account the individual LTR but the incomplete literature data on LTR density, conductivity, shape and density, as well as the imposed decreased model size due to computer power limitations, present their own shortcomings [214], [215].

The electrical conductivity of the skin is not homogeneous and isotropic, as simulated. Real skin contains imperfections, such as hair follicles and sweat ducts, which are regions with higher conductivities [25]. Moreover, the alignment of cells creates an anisotropic electrical conductivity. This is well established for muscle tissue, where the longitudinal conductivity can be up to 5 times higher than the transversal one [17], but the argument holds true for the cells of the SC too, and to a lesser extent, all of the skin. For all these reasons, the precise values obtained from the simulations should be interpreted with caution.

## 6 Drug delivery

<b>6</b>	<b>DRUG DELIVERY</b>	<b>151</b>
6.1	FLUORESCENCE MICROSCOPY	151
6.1.1	Molecule release on gauze	151
6.1.2	Molecule release on skin model	152
6.2	RECONSTRUCTED HUMAN EPIDERMIS	157
6.3	MECHANISMS OF SKIN ELECTROPORATION	158
6.3.1	Domain 1: low-voltage PEFs (<100 V) - Conductive pathway formation	158
6.3.2	Domain 2: moderate-voltage PEFs (100-200 V) – Disruption of extracellular matrix and molecule transport	158
6.3.3	Domain 3: high-voltage PEFs (300 V) - Cell membrane permeabilization	159
6.4	CHAPTER HIGHLIGHTS AND DISCUSSION ON DRUG DELIVERY	160

The nanocomposite hydrogels (AGR-CNT<sub>10</sub>CMC<sub>1</sub>S<sub>eb</sub>) were loaded with electroporation buffer and low concentrations of fluorescent molecules, serving as drug models. We used three hydrophilic fluorophores with different electrical charges, sizes and properties. The loaded hydrogels were placed on top of the skin models, and a PEF of 0 (control) to 300 V was applied.

### 6.1 Fluorescence microscopy

#### 6.1.1 Molecule release on gauze

We first tested the release of the fluorescent molecules on a wet gauze, in the absence of a skin model. We used the same configuration and PEF conditions as in the delivery experiments, to study the solute transfer from the hydrogels onto the wet gauze. The fluorescein isothiocyanate–dextran (FD4) and the lucifer yellow (LY) exhibited an increased fluorescence under the negative electrode, and decreased under the positive electrode, compared to a non-pulsed control (**Figure 6.1**, A, B). When we applied bipolar pulses to the LY-loaded hydrogels, the fluorescence on the gauze was more or less equivalent to the non-pulsed control, under each electrode (**Figure 6.1**, C). Propidium Iodide (PI) has a negligible fluorescence when it is not intercalated to DNA; we just wanted to confirm this and ensure that the PEF application did not affect its fluorescence (**Figure 6.1**, D).

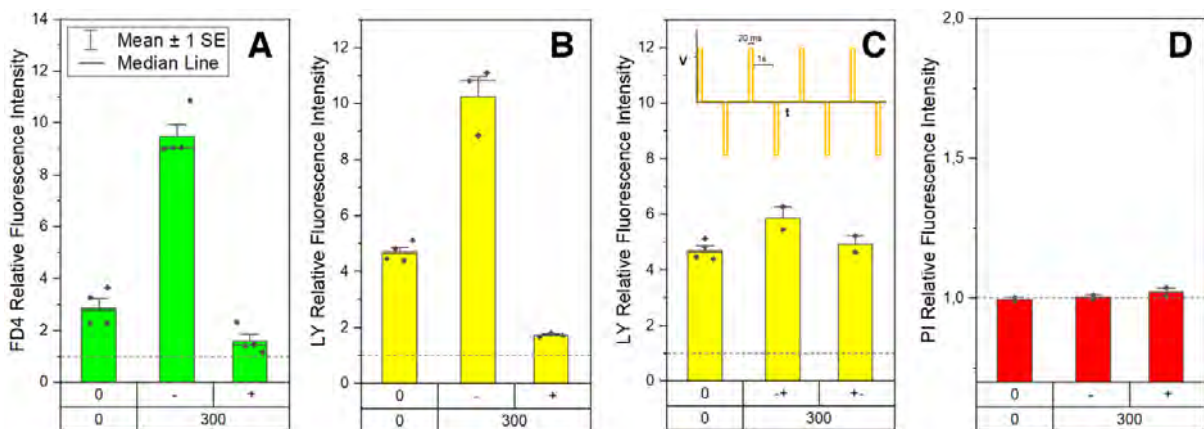


**Figure 6.1** – Fluorophore release from hydrogels after PEF application. The dotted line corresponds to relative fluorescence intensity of 1, meaning the same fluorescence as an area of the image without fluorophores.

From these results it is inferred that electrophoretic transport of the charged solutes played an important role in mass transfer [10]. Passive diffusion due to concentration gradients was also present, as evidenced by the increased fluorescence of the gauze under non-pulsed hydrogels. Other mass transfer mechanisms of the fluorophores during PEFs include electro-osmosis, and possible contraction (shrinkage) of the hydrogel due to the applied electric field.

### 6.1.2 Molecule release on skin model

Next, we tested the fluorescent molecule delivery on the mouse skin models. For a range of PEF voltages studied, all three fluorophores demonstrated significantly higher fluorescence emission compared to the control. Lucifer Yellow (LY) is a small (442 Da), hydrophilic, negatively charged fluorophore. We used it as a marker of the integrity of the SC. Under the positive electrode, there was no significant increase in the LY uptake for any of the PEF voltages tested. Under the negative electrode, already at a PEF of 100 V, LY exhibited a statistically significant ( $p=0.03$ ; Dunnett's T3) increase in fluorescence ( $2.9 \pm 0.4$ ), compared to the control ( $1.4 \pm 0.1$ ). Further increase in the PEF voltage at 200 V resulted in an increased fluorescence emission ( $5.2 \pm 0.3$ ), while at 300 V, the fluorescence did not increase more ( $4.6 \pm 0.3$ ) (**Figure 6.2**).



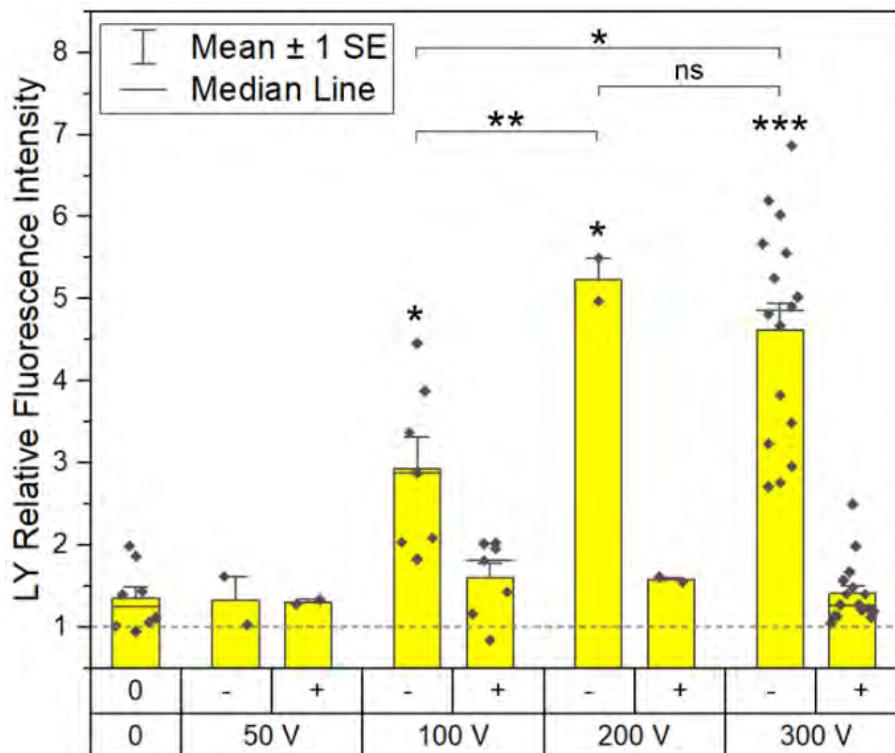
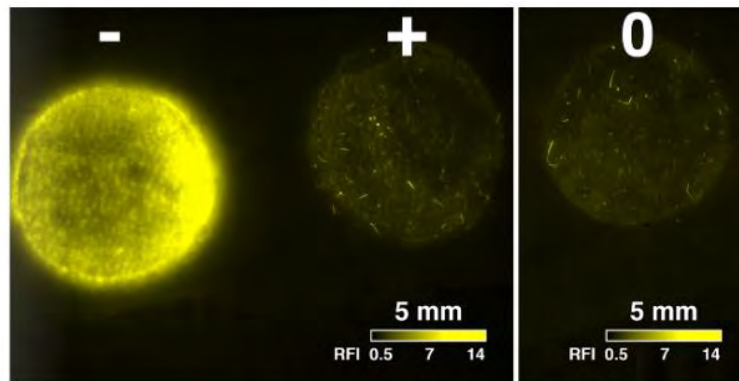


**Figure 6.2** – Lucifer Yellow fluorescent marking on skin model (top view, 300 V and 0 V) and quantification of relative fluorescence intensity under negative and positive electrodes, for PEF from 0 to 300 V. n=2-16. Statistical treatment: one-way ANOVA and Dunnett’s T3 post-hoc test. Codes signification: \* =  $p \leq 0.05$ ; \*\* =  $p \leq 0.01$ ; \*\*\* =  $p \leq 0.001$ ; no symbol or ns = not significant difference ( $p > 0.05$ ). Means are compared to control (0), unless brackets indicate otherwise.

Propidium Iodide (PI) is a small (668 Da), hydrophilic, positively-charged, membrane-impermeable, DNA-intercalating fluorophore, used here as evidence of cell membrane permeabilization. PI showed a statistically significant ( $p = 0.0008$ ; Dunnett’s T3) increase in fluorescence only under the positive electrode, for a PEF of 300 V ( $1.54 \pm 0.11$ , compared to  $1.01 \pm 0.02$  for the control, **Figure 6.3**).

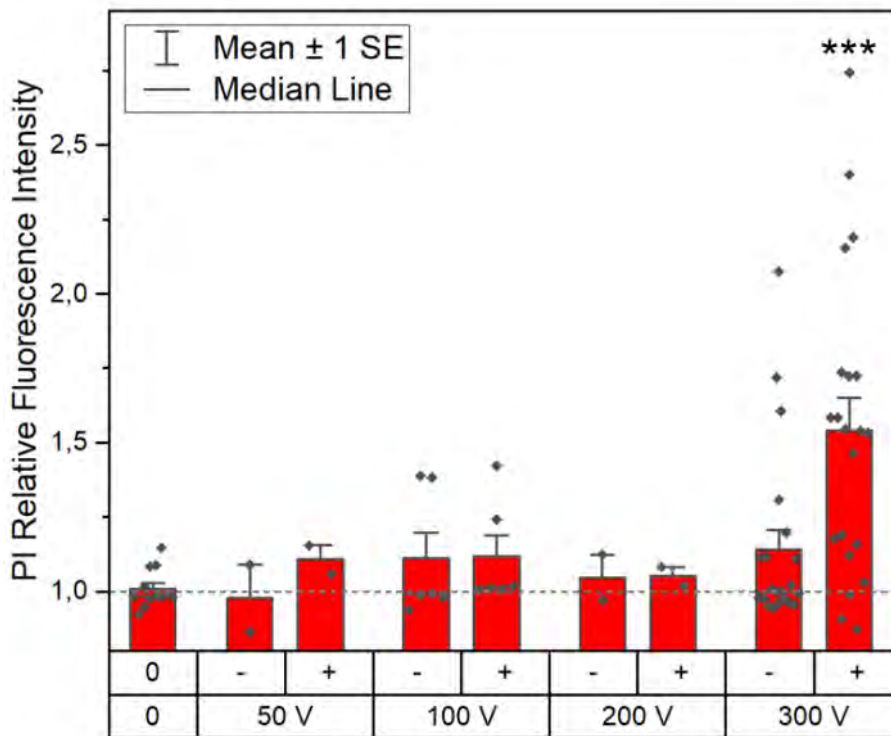
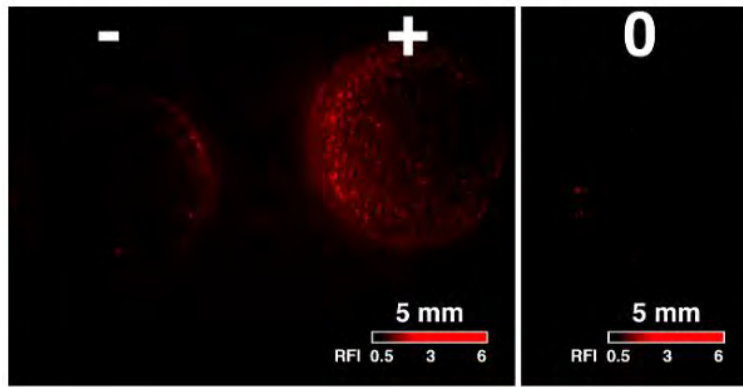


**Figure 6.3** – Propidium Iodide fluorescent marking on skin model (top view, 300 V and 0 V) and quantification of relative fluorescence intensity under negative and positive electrodes, for PEF from 0 to 300 V. n=2-20. Statistical treatment: one-way ANOVA and Dunnett’s T3 post-hoc test. Codes signification: \* =  $p \leq 0.05$ ; \*\* =  $p \leq 0.01$ ; \*\*\* =  $p \leq 0.001$ ; no symbol or ns = not significant difference ( $p > 0.05$ ). Means are compared to control (0), unless brackets indicate otherwise.

Fluorescein isothiocyanate–dextran (FD4), is a large (4000 Da average molecular weight), hydrophilic fluorophore, with sparse negative charges (fluorescein is negatively charged and the substitution rate is *ca.* 0.01 mol FITC per mol glucose). We used it as a model molecule for insulin, that has a comparable molecular weight (5700 Da). FD4 was only tested at 300 V, and showed a statistically significant ( $p=0.002$ ; Dunnett’s) increase in fluorescence, under the negative electrode ( $2.3 \pm 0.3$ , compared to  $0.96 \pm 0.01$  for the control, **Figure 6.4**).

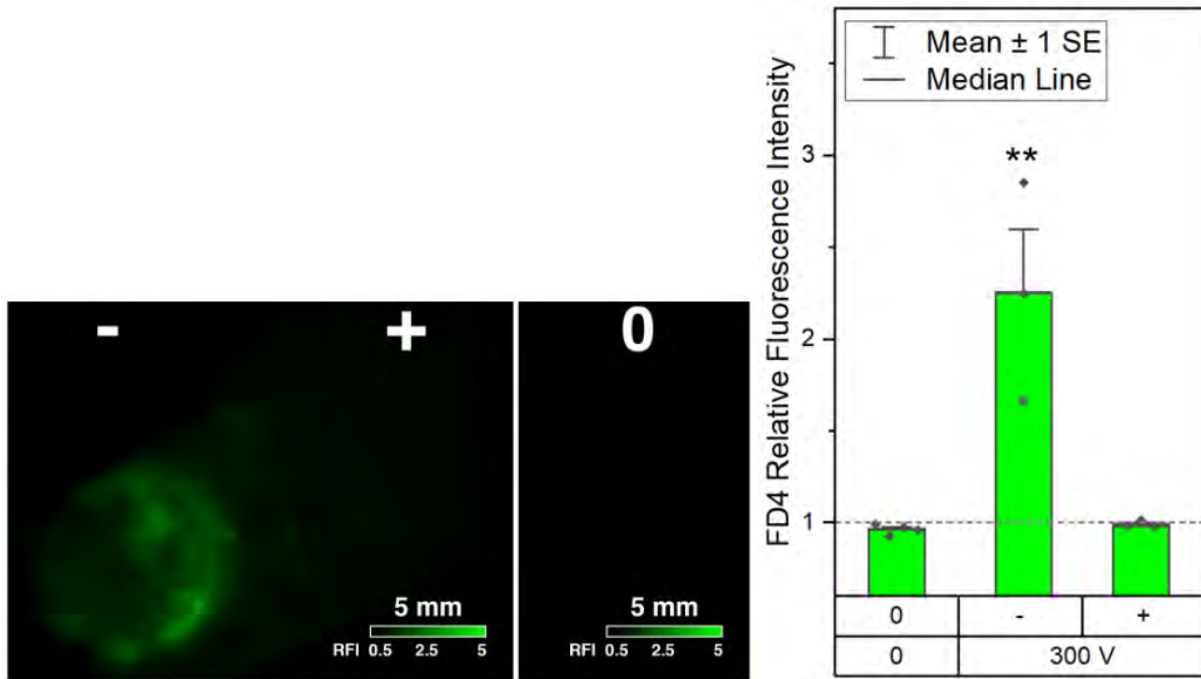


**Figure 6.4** - Fluorescein isothiocyanate–dextran marking on skin model (top view, 300 V and 0 V) and quantification of relative fluorescence intensity under negative and positive electrodes, for control (0 V) and 300 V PEF. n=3-4. Statistical treatment: one-way ANOVA and Dunnett’s post-hoc test. Codes signification: \* =  $p \leq 0.05$ ; \*\* =  $p \leq 0.01$ ; \*\*\* =  $p \leq 0.001$ ; no symbol or ns = not significant difference ( $p > 0.05$ ). Means are compared to control (0), unless brackets indicate otherwise.

In all three cases, the charge of the fluorophore played a determining role in the delivery: negatively charged fluorophores marked the skin under the negative electrode and the positively charged PI mostly marked the skin under the positive electrode [10]. This was true even for FD4, whose total electric charge was marginal. LY was the only fluorophore that exhibited some fluorescence in the control experiment. Indeed, the limit for passive diffusion through the SC, for hydrophilic molecules is *ca.* 500 Da. Molecules close to this limit, such as LY, have a very slow diffusion rate, but a small quantity may penetrate into the SC. However, the fluorescence of LY was greatly enhanced already with a PEF of 100 V. We hypothesized that the application of a PEF of 100 V, destabilized the extracellular lipids between the cells of the SC, allowing the fluorophore to pass through the paracellular pathway. An increase to 200 V nearly doubled the fluorescence intensity, while 300 V did not further increase it. The disorganization of the extracellular matrix peaked at 200 V, for our configuration. However, there was no cell membrane permeabilization for PEF lower than 300 V. Indeed, PI, a marker of cell permeabilization only exhibited enhanced fluorescence at 300 V. PI is a DNA intercalating agent, increasing its fluorescence by 20 to 30-fold when it binds to DNA [163]. The cells of the SC do not contain a nucleus, thus the PI fluorescence originated in cells in deeper layers of the epidermis or the dermis. Lastly, FD4, a macromolecule of 4kDa, exhibited significantly increased fluorescence, demonstrating the potential of skin electroporation for the delivery of therapeutic molecules of large size, such as insulin.

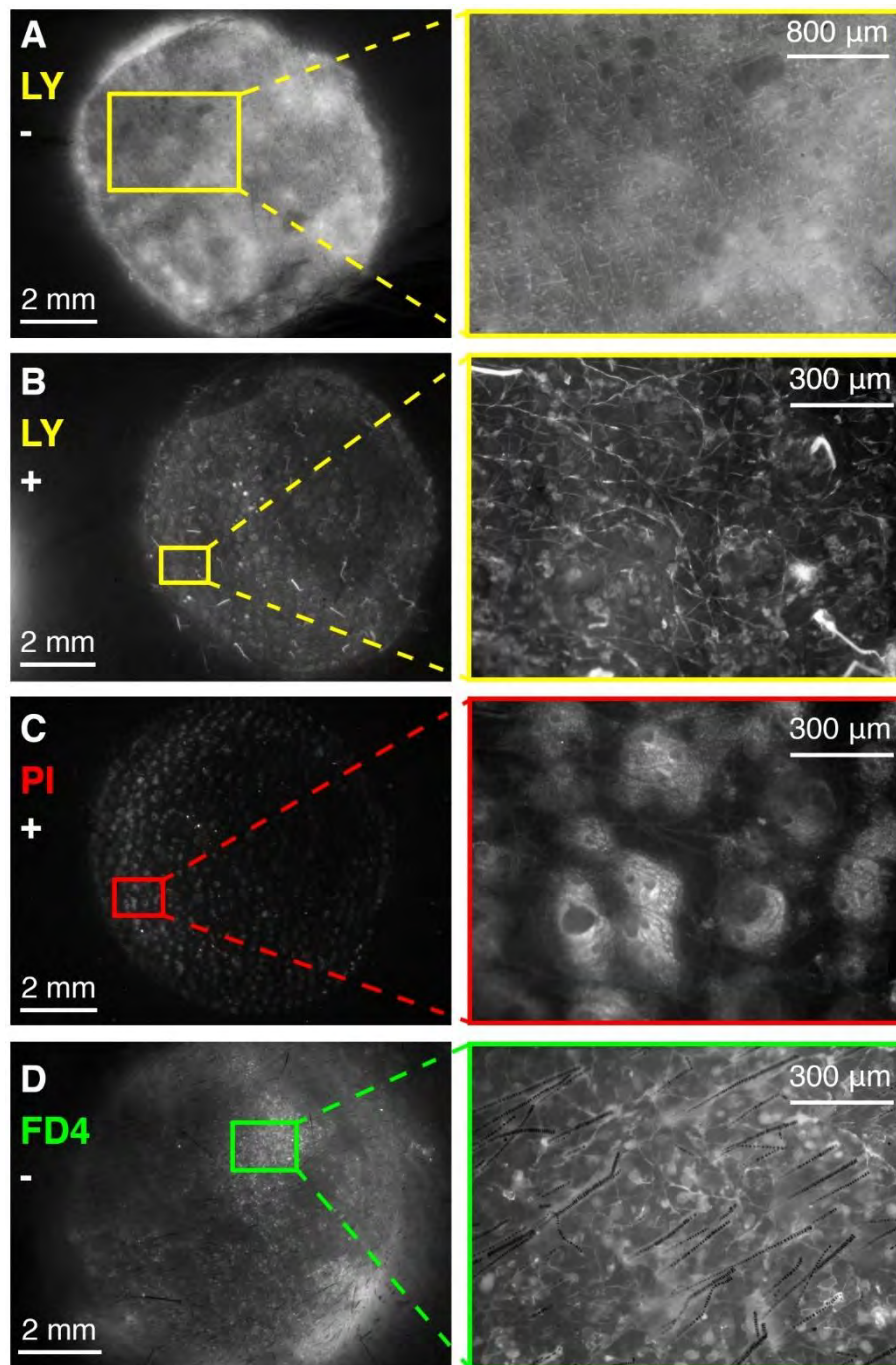


**Figure 6.5** - Details of fluorescence microscopy images on skin model after PEF at 300 V. (A) Lucifer Yellow (LY) under negative electrode with optical zoom of 1.25x (left) and 3.2x (right); (B) LY under positive electrode with optical zoom of 1.25x (left) and 9.2x (right); (C) Propidium Iodide (PI) under positive electrode with optical zoom of 1.25x (left) and 9.2x (right); (D) Fluorescein isothiocyanate–dextran under negative electrode with optical zoom of 1.25x (left) and 9.2x (right).

Visible light penetrates into the skin, at a depth of few hundred  $\mu\text{m}$ , typically 100  $\mu\text{m}$  to 1 mm, depending on the wavelength [216]. Therefore, fluorescence emission captured by the camera does not only originate from the SC, but also from deeper layers, at least down to parts of the dermis. Under the negative electrode, the fluorescence of LY appeared mostly concentrated at the regions between cells. Additionally, a diffuse, out-of-focus fluorescence was observed, originating from LY deeper into

the skin (**Figure 6.5A**). Under the positive electrode, where LY did not benefit from the electrophoretic force, it was clearly seen concentrated on the paracellular regions, with much less diffuse light from deeper layers (**Figure 6.5B**). PI was observed within skin cells (**Figure 6.5C**). The cells of the SC are anucleated, thus PI fluorescence originated from cells deeper in the epidermis and/or dermis. Similar to LY, FD4 appeared to fluoresce from the paracellular regions, with some diffuse light from deeper layers (**Figure 6.5D**). In most cases, the fluorescence intensity was higher in the crescent-shaped areas where electrodes faced each other. This can be explained by the electric field strength calculated through the simulations, which was higher in these areas (**Figure 5.11**).

## 6.2 Reconstructed human epidermis

In parallel to the experiments with animal skin models, we also tested the drug delivery on lab-grown reconstructed human epidermis samples. These present numerous advantages, notably the use of human cell lines and the strict control of the growth conditions, theoretically leading to a skin model with lower variability. The drug delivery on reconstructed human epidermis samples was tested with LY and PI. The samples showed an increased uptake of both LY (under the negative electrode) and PI (under the positive electrode), compared to a non-pulsed control. The full results are presented in **Figure 6.6**.

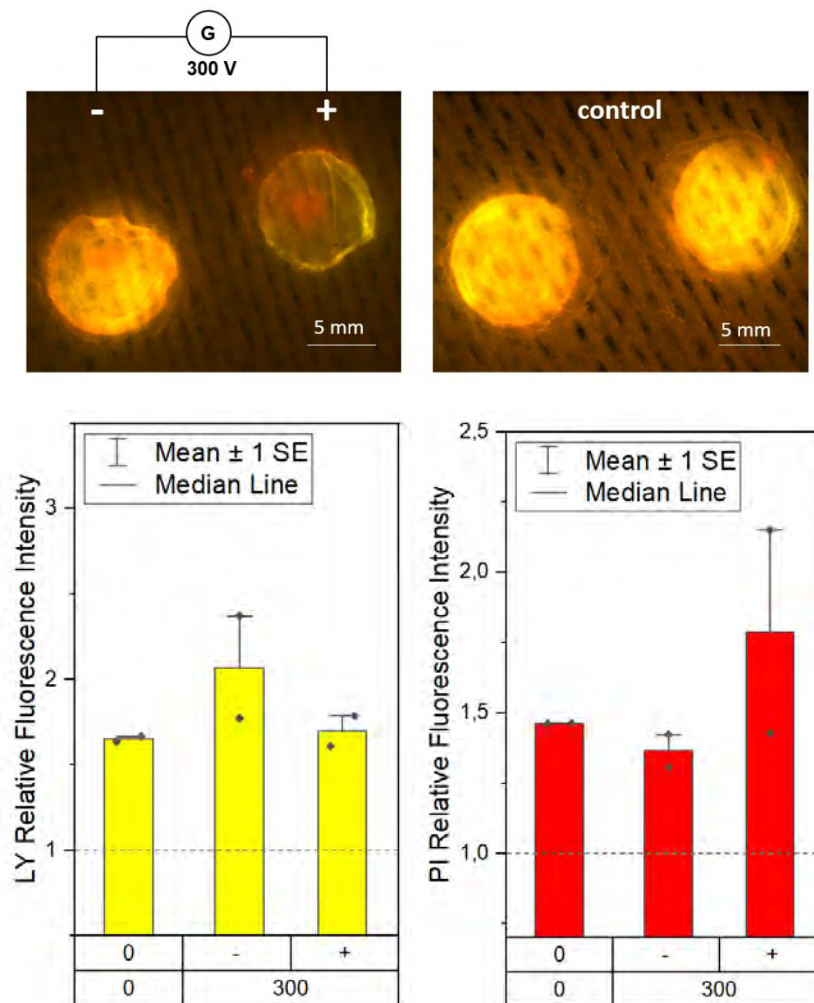


**Figure 6.6** – Fluorescent molecule delivery on reconstructed human epidermis samples.



There were however some limitations. The reconstructed epidermis samples had an increased fluorophore uptake without electrical pulses, compared to the animal skin model. It is possible that they do not have exactly the same barrier properties as the *ex vivo* mouse skin. Secondly, they showed a high variance between the different samples. Both of these limitations may be related to the small number of samples tested and their difficult handling, combined with their thin and fragile nature.

In addition, as mentioned in section **I-V measurements of reconstructed human epidermis**, the PEF voltage applied has to be adapted to these samples. The PEF of 300 V resulted in high electrical currents (0.8 to 1.6 A). Considering the small mass of the reconstructed epidermis samples, such high currents during 160 ms would lead to an important temperature increase with potentially irreversible thermal damage skin samples.

### 6.3 Mechanisms of skin electroporation

We evaluated skin electroporation, for applied PEFs of 50 to 300 V, on five different levels: (1) electrical measurements during the pulses, (2) DC current before and after the pulses, (3) FEM simulations on a three-dimensional, nonlinear numerical model validated with *ex vivo* results (4) fluorescent microscopy of LY, a fluorophore indicating destabilization of extracellular matrix, and (5) fluorescent microscopy of PI for cell membrane permeabilization. Combining our findings, we distinguish three voltage domains with different effects on the skin.

#### 6.3.1 Domain 1: low-voltage PEFs (<100 V) - Conductive pathway formation

In the initial domain, where PEFs were below 100 V, an increase in ionic mobility within the skin was observed. This was evidenced by a reduction in instantaneous resistance during PEFs and a decline in average resistance with increasing voltage. Remarkably, these effects were noticeable even at PEFs as low as 30 to 50 V. However, no molecule transfer through the skin occurred at voltages less than 100 V. We hypothesized that the conductive pathways formed within the skin increased the mobility of electrolytes but were too small in radius or limited in surface coverage to impact the skin's barrier properties (**Figure 6.7**, B). Additionally, the DC current measured before and after applying 50 V PEFs showed minimal alterations, suggesting that any changes in electrical properties were short-lived. In this domain, the conductivity of the SC remained low, and the electric field strength in deeper skin layers was minimal. It was challenging to establish a precise minimum PEF voltage threshold for conductive pathway formation, based solely on electrical properties, as instantaneous resistance decreased even at the lowest voltages applied. According to Chizmadzhev *et al.*, at low voltages (up to 30 V, equivalent to *ca.* 100 V in our configuration. See Annex, section **9.1** for the calculation), electroporation of epithelial cells in appendageal ducts contributes to the observed reduction in skin resistance.

#### 6.3.2 Domain 2: moderate-voltage PEFs (100-200 V) – Disruption of extracellular matrix and molecule transport

Moving to the second domain, encompassing PEFs ranging from 100 to 200 V, we observed the transport of small hydrophilic molecules through the stratum corneum (SC) and enduring changes in the skin's passive electrical properties. At this stage, the applied PEF disrupted the organization of extracellular lipids in the SC, resulting in the formation of local transport regions (LTRs). Hydrophilic molecules with limited passive diffusion through the SC, such as LY, traversed the SC via the disorganized lipid bilayers in the paracellular region (**Figure 6.7**, C). Moreover, we noted an increase in the skin's DC current following PEF application, indicating the sustained creation of conductive LTRs.



Still, the electric field strength in skin layers with viable cells remained lower than the electroporation threshold (400 V/cm) and no permeabilization of cell membranes occurred within this domain.

### 6.3.3 Domain 3: high-voltage PEFs (300 V) - Cell membrane permeabilization

In the third domain, corresponding to PEFs of 300 V, we observed the permeabilization of cell membranes. At this point, the conductivity of the SC was greatly increased and the electric field at the epidermis and the dermis (beneath the SC) reached values exceeding 400 V/cm. This resulted in a transmembrane potential within nucleated cells in the epidermis and/or dermis surpassing the threshold of 250 mV, leading to membrane permeabilization. Propidium Iodide (PI) entered into the intracellular space, followed by its subsequent intercalation with DNA (**Figure 6.7**, D). Our numerical simulations, despite their simplifications, accurately predicted cell membrane permeabilization and the delivery of fluorescent molecules. The DC current increased by 300 % after the PEF application, indicating major changes in the passive electrical properties of the skin.

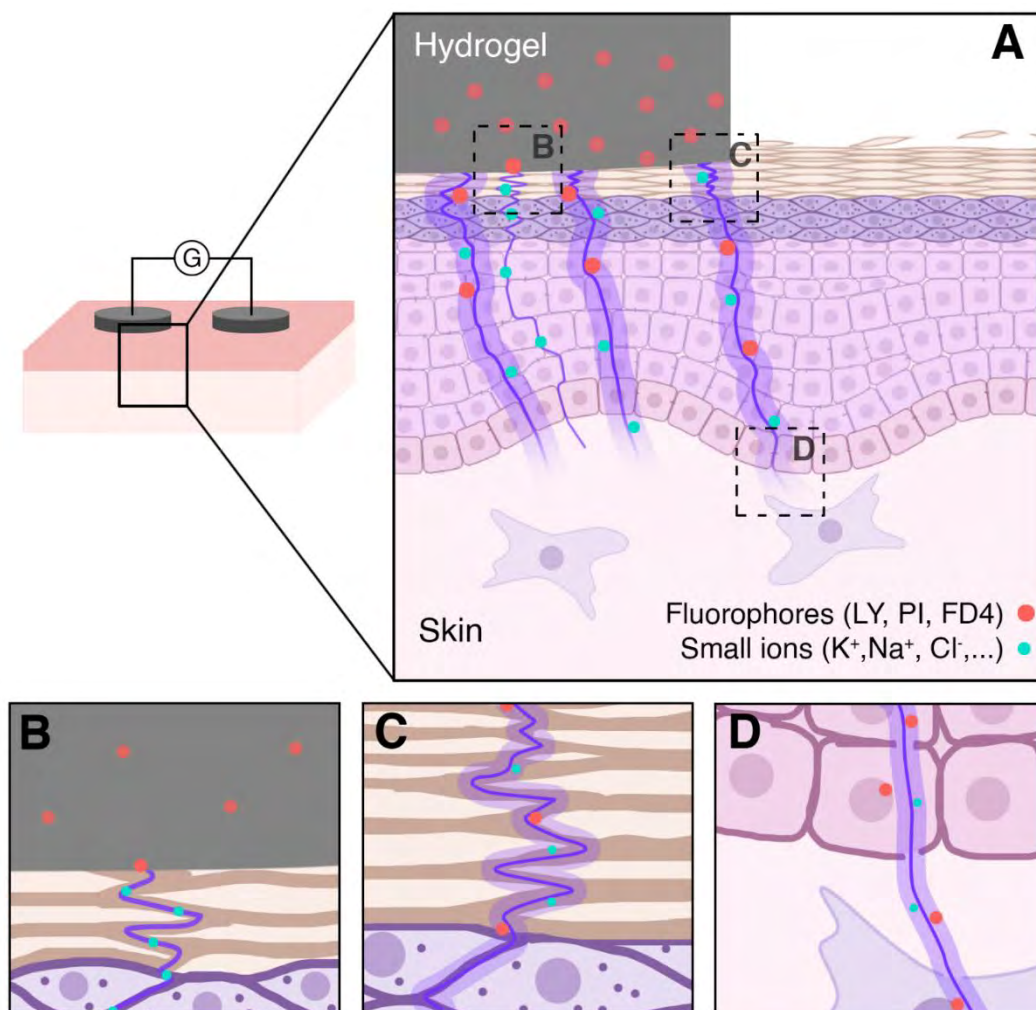


**Figure 6.7** – Local transport regions (LTR) and cell membrane permeabilization in skin. (A) Scheme of skin electroporation with electrode-reservoir hydrogel. (B) At PEF voltages lower than 100 V, conductive pathways were formed, increasing ionic mobility. (C) Starting at 100 V PEF, the creation of LTRs in the extracellular lipids of the stratum corneum, allowed the diffusion of fluorophores through the skin. (D) At 300 V PEF, the cell membranes of nucleated cells of the epidermis and/or dermis were permeabilized and fluorophores entered the cytoplasm.

## 6.4 Chapter highlights and discussion on drug delivery

Molecule release experiments from loaded hydrogels showed that the PEFs apply a considerable electrophoretic force on charged fluorophores. This was the case even for molecules with minor electric charge, like the FD4 used here. The FD4 was a large molecule, but it did not show any steric effects during its release from the hydrogel mesh, for an agarose polymer concentration of 2.5 % w/w. In the absence of an electric field, diffusion driven by concentration gradients accounted for the molecule release from the hydrogel onto the wet gauze.

In total the mechanisms that favor molecule release from the hydrogel, during the application of a PEF, are the following:

- **Electrophoretic force.** The main release mechanism for charged fluorophores. The molecules were pushed away or towards the metal electrical contacts.
- **Diffusion.** Passive diffusion of the fluorophores occurred when the concentration within the hydrogel was higher than the concentration at the interface with the skin model or gauze.
- **Electro-osmosis.** The movement of ions within a solvent creates a force that can drag other non-charged entities.
- **Contraction of the hydrogel.** The nanocomposite hydrogels may contract during the PEF application, thus forcing their contents (solvent + solutes) to be released. The contraction can be the result of an electrically-induced stress gradient, water electro-osmosis, local pH changes or thermal gradient due to resistive heating [177].

The drug delivery experiments showed an increased uptake of fluorescent molecules, under the effect of PEFs. LY delivery started already at a PEF of 100 V, while the delivery of PI to cell nuclei started at 300 V. FD4 was tested at 300 V and exhibited an increased fluorescence, compared to a non-pulsed control. The emission intensity of fluorescent molecules can be influenced by some other factors too, such as temperature and pH. FD4, in particular, is sensitive to pH changes exhibiting higher fluorescence in alkaline environment [217]. The application of unipolar PEFs causes local pH changes near the electrodes. The pH under the negative electrode increased during PEF application, and the pH under the positive electrode decreased [157]. Therefore, we cannot exclude an amplification of FD4 fluorescence due to pH increase at the negative electrode. In contrast, LY is insensitive to pH changes and PI is not particularly sensitive either [218].

In previous works, the fluorescent molecule delivery was evaluated by histological observations of the mouse skin model, after the application of 300 V PEFs [10]. It was shown that PI permeabilized cells in the epidermis, LY diffused through the SC and epidermis till the dermis and FD4 penetrated the first layers of the SC but did not reach into the deeper layers of the epidermis and dermis (**Figure 6.8**). The fluorescent marking was more pronounced in the areas where the electrodes face each other. These observations are in agreement with our results, and predicted by the numerical model, to some extent. The same study indicated an asymmetrically increased uptake of LY, under the negative electrode, when the fluorophore was added *after* the PEF application (and thus presumed independent of electrophoretic forces). To this day we do not have a clear explanation for this observation. It is possibly related to local pH changes under the two electrodes. Mauro *et al.* showed that the recovery of the skin's barrier function is slower in alkaline pH [219]. The electrical measurements and the numerical model cannot be used to explain this asymmetry because they do not distinguish between the two electrodes (other than in electric field vector direction) and do not take into account electrophoretic transport of molecules and electrochemical reactions.

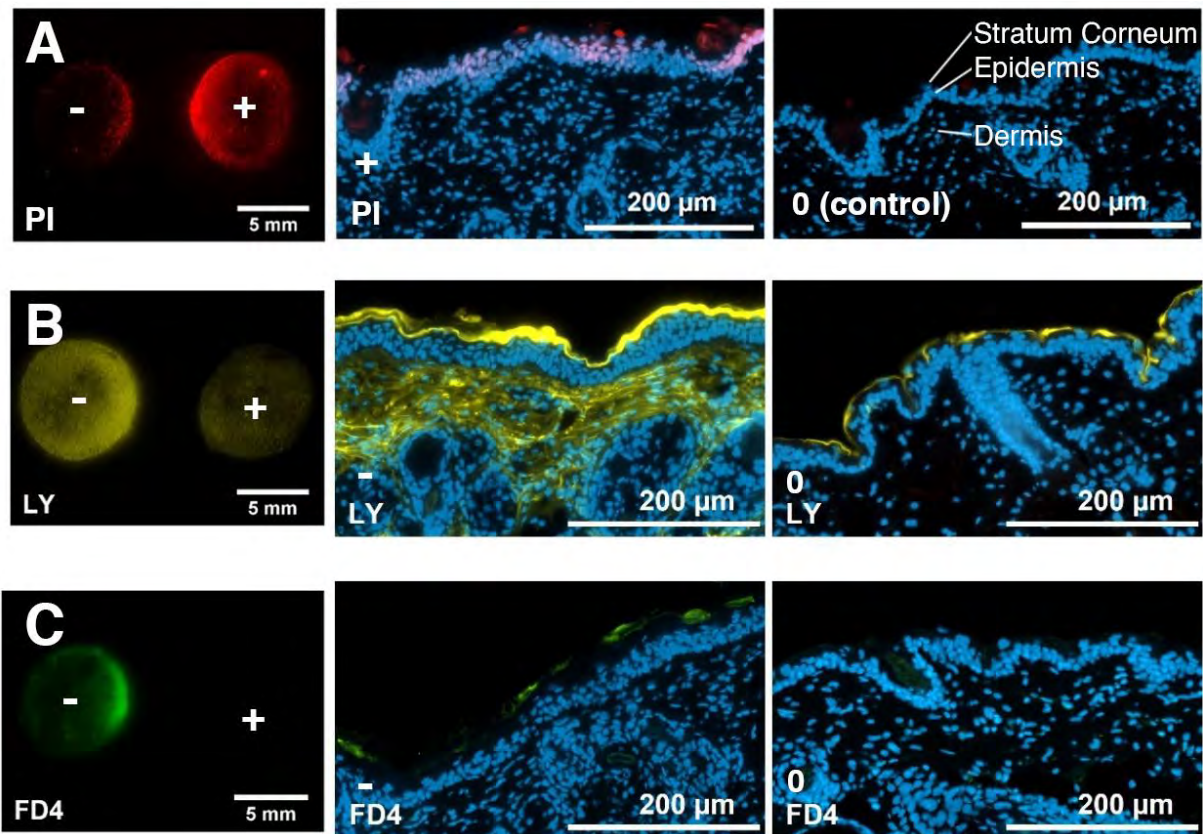


**Figure 6.8** – Histological observations of fluorescent molecule delivery and penetration depth into mouse skin models. (A) Propidium Iodide (PI) reached permeabilized cells in the epidermis. (B) Lucifer Yellow (LY) reached all the way into the dermis. (C) Fluorescein isothiocyanate-dextran (FD4) was located in the stratum corneum and the outermost epidermis layers. Adapted from [10].

## 7 Conclusions and perspectives

We studied a novel method for non-invasive drug delivery through skin electroporation, consisting of two conductive hydrogels, placed side-to-side, that contained the model medication and ensured conductive contact between electrodes and the skin. We applied a multi-scale approach to evaluate skin electroporation and drug delivery: FEM simulations of our system and *in situ* measurements of electrical properties and temperature before, during and after the application of a PEF, coupled with fluorescence microscopy to evaluate the delivery of model molecules. The hydrogels were prepared with agarose, a hydrophilic, biosourced and biocompatible polymer with thermo-reversible cross-linking. We added double-wall CNTs to the hydrogels to increase their electrical conductivity, so they can serve as electrodes for the application of electrical pulses to the skin. Therapeutic or fluorescent molecules were incorporated into the hydrogel by drying it and then placing it in an aqueous solution with the molecules of interest. In this way, the hydrogels could be used for a wide variety of molecule delivery, were preserved indefinitely in dry form and thermal degradation of medicine was avoided.

We measured the absorption capacity and electrical properties of the hydrogels and studied the impact of numerous parameters (polymer matrix, nanomaterial concentration and type, dispersion, processing methods, temperature) on the aforementioned properties. The dispersion of CNTs within the agarose hydrogel matrix moderately decreased its absorption capacities, because of matrix rigidification and CNT hydrophobicity. Freezing the hydrogels increased their swelling ratio, thanks to the macropore network created by the growth of ice crystal within the hydrogel matrix. Directional freeze-casting, increased the absorption capacity of agarose hydrogels even more, through the controlled formation of aligned macropores. Alginate/chitosan hydrogels presented very limited absorption capacities, possibly due to the strong chemical cross-linking of chitosan with genipin. The DC electrical conductivity of swollen agarose hydrogels was increased by two orders of magnitude, through the incorporation of CNTs. Carboxymethyl cellulose was used to render the surface of the CNTs more hydrophilic and facilitate their dispersion. Without the use of a dispersant, the electrical conductivity was lower. The nanocomposite hydrogels presented a combination of ionic conductivity, through the transport of ions in the water phase, and electronic conductivity, through electron transport in the CNT network. Increasing the water content, the porosity (through freezing) and the temperature were factors that increased the DC conductivity. Impedance spectroscopy measurements confirmed the ionic nature of the hydrogel's conductivity. The impact of CNT reinforcement in decreasing the impedance of the hydrogels was only visible at higher frequencies. Based on the Nyquist plot of the hydrogels, an equivalent circuit could be modelled containing a Warburg impedance element in series with a resistor, and in parallel with a capacitor. The hydrogels exhibited a nonlinear electrical behavior, with decreasing impedance for higher electric fields. This was especially true for the nanocomposite hydrogels, which had decreased impedance all over the frequency range, with increasing applied voltages. The hydrogels chosen for the drug delivery experiments, agarose hydrogels with CNTs and dispersant, presented a compromise between the desired properties and ease of fabrication, with an increased weight on the electrical conductivity.

We monitored the current, voltage and instantaneous resistance of the drug delivery system during the application of the Pulsed Electric Field (PEF), along with the changes in passive electrical properties (DC conductivity) and temperature increase resulting from the treatment. Regarding the I-V measurements, there were three major observations: (1) the average resistance of the system (measured during the last of eight pulses) decreased for increasing PEF voltages, (2) the instantaneous

resistance of the system decreased during the application of the electric pulses, and (3) the resistance changes of the system were specifically attributed to the skin, and not to the other components. The decrease in the average resistance of the skin for increasing PEF voltages was attributed to the formation of conductive pathways, with an increasing density, while the decrease in instantaneous resistance during the pulses was attributed to the expansion of the formed conductive pathways. The current – voltage measurements were also used to confirm the effective electrical contact between the metal cylinders and the skin, eliminating the necessity of using a conductive gel, but also to monitor the reversibility of the PEF treatment. As a proof of concept, we presented a series of low-voltage PEF applications that maintained the resistance and the dynamic electrical properties of the skin versus a high-voltage series of PEF applications that damaged the skin irreversibly by creating permanent conductive pathways. The application of PEFs at 100 V and over, modified the passive electrical properties of the skin, increasing its the DC conductivity. For PEFs of 200 V and over, the temperature of skin samples was also measurably increased, but remained under the limit of heat pain threshold in humans.

A three-dimensional, nonlinear numerical model of the drug delivery system was developed and validated through *ex vivo* data. The model used data from previous FEM simulations and electrical measurements to interpolate a function for the dependence of the conductivity of the SC on the electric field. We assumed homogeneous and isotropic electrical properties. The model accurately described the decrease in the resistance of the skin with increasing PEF voltages, producing results very close to the experimentally measured values. According to the simulation of the electric field distribution in the viable skin layers, the cells in the epidermis and the dermis could be reversibly permeabilized for PEF strengths over 200 V and irreversibly at PEF strengths over 400 V. The numerical model calculated increased electric field strengths in the crescent-shaped areas where the electrodes faced each other.

The drug delivery experiments demonstrated an increased uptake of hydrophilic fluorescent molecules, after the application of electric pulses. Lucifer yellow, a small negatively charged fluorophore passed through the intercellular spaces of the SC already at PEFs of 100 V. Propidium iodide, a small (only slightly larger than LY) positively charged fluorophore permeabilized the plasma membranes of cells in the epidermis and/or dermis at PEFs of 300 V, as predicted by the numerical model. Fluorescein isothiocyanate-dextran (4 kDa), a molecule with comparable size to insulin, passed through the first skin layers at a PEF of 300 V, but previous results showed that it remained contained in the SC. In most cases, the fluorescence was most intense in the crescent-shaped interior areas, where the calculated electric field was stronger.

Combining the results on transdermal drug delivery, three domains were distinguished:

- **PEF < 100 V.** The PEFs formed conductive pathways through the skin, increasing the ionic mobility of the SC. The pathways were too small to allow for molecule transfer and too short-lived to have any lasting effect.
- **100 < PEF < 200 V.** The PEFs disrupted the organization of the extracellular lipid at the SC, forming local transport regions, which increased ionic mobility and diffusion of small hydrophilic molecules. Long-lasting changes were observed in the passive electrical properties of the skin and a small temperature increase was recorded.
- **PEF > 300 V.** The PEFs penetrated into the deeper skin layers, through the formation of the local transport regions at the SC, reversibly permeabilizing cells in the viable skin layers. Both

the passive electrical properties and the temperature increased considerably after the PEF application.

Even though the formation of LTR within the lipid bilayers of the extracellular matrix of the SC was demonstrated for PEFs starting at 100 V, no permeabilization of nucleated cells was observed for PEF lower than 300 V. A table with the summarized results is presented in **Figure 7.1**. These results showed the existence of two distinct drug delivery domains, one consisting in the formation of LTRs in the extracellular lipids of the SC allowing the diffusion of hydrophilic molecules, and a second one, consisting in the permeabilization of the plasma membranes of nucleated cells (*i.e.* cells in layers deeper than the SC). Both of these domains are relevant in the context of drug delivery through the skin. Some drugs such as lidocaine and corticosteroids can be administered locally, to the epidermis, for local anesthesia and to treat skin inflammation. Nucleic acid vaccinations have to enter inside cells in order to express the encoded antigen and elicit an immune response. Similarly, antitumor antibiotic medicine such as bleomycin, have to permeabilize the cell membrane to have an effect. Morphine and insulin have to reach systemic circulation to treat pain or regulate glucose metabolism, respectively. The exact parameters chosen for skin electroporation depend on the delivery target but also the drug's physicochemical properties (size, charge, hydrophilicity) and how they match with the physicochemical properties of the patch material.

The experimental setup that we proposed here (*in situ* measurements of electrical properties and temperature, numerical model and fluorescence microscopy) can serve as a model for future investigations of skin electroporation. A more exhaustive approach would include the following modifications: Automation of the switch between DC current and oscilloscope measurements, allowing the monitoring of DC current immediately after the pulses and even in between them. Attempt to numerically model the time-dependence and localized nature of conductive pathways through the skin (instead of a macroscopic, homogeneous simulation). Combination of macrofluorescence microscopy with histological observations to determine the penetration depth of fluorophores. Experimentation with a wider range of skin models, including reconstructed human skin and *in vivo* animal testing.

In parallel to the animal skin model, we tested the drug delivery on lab-grown, reconstructed human epidermis. This model presented the advantages of using human cells, limiting inhomogeneity and complexity, compared to an animal model, and reducing the harm caused by animal experimentation. Moreover, in addition to the reconstructed epidermis models, full skin substitutes can also be made. They are grown layer by layer starting with dermal sheets. This presents a unique opportunity for the study of the electrical properties of separate skin layers. The literature data on this domain is particularly scarce, relying on few studies with high levels of uncertainty. The electrical properties of individual skin layers could help update the numerical model of the drug delivery system, which can then be used to adapt the electric field strength to each skin model.



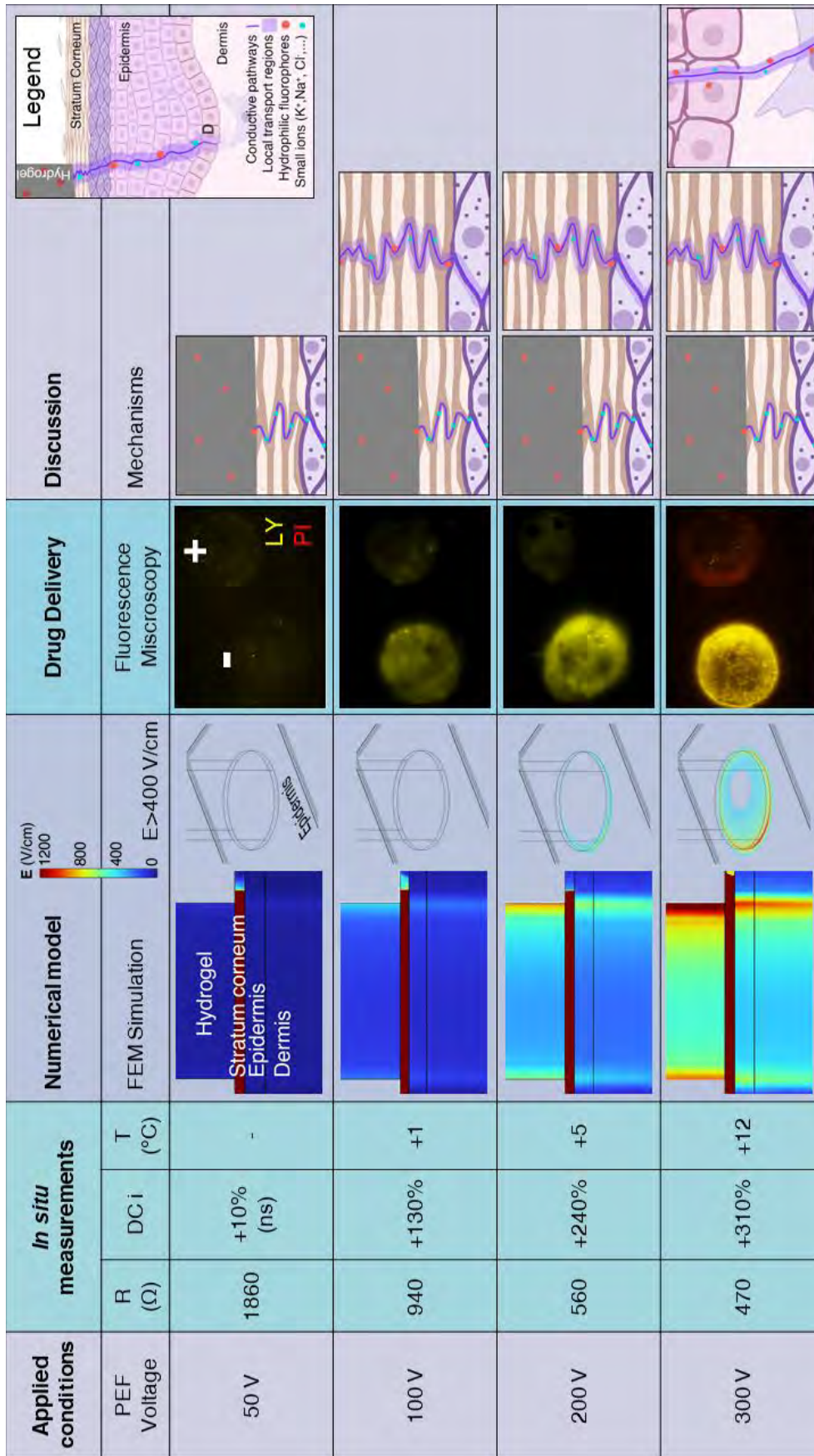


**Figure 7.1 (printed version)** – Summary of experimental results on transdermal drug delivery, for applied PEFs of 50 to 300 V (8 pulses, 20 ms duration, 1 Hz). **In situ measurements.** Average resistance (U/I) during last pulse, DC current change after PEF, Temperature increase (max) during PEF. **Numerical model.** Electric field distribution on the skin, through validated, nonlinear model. XZ slices of first skin layers and areas where  $E > 400$  V/cm (approximate threshold value for cell permeabilization in tissue) on viable skin layers. **Drug delivery.** Fluorescent marking of lucifer yellow (LY) and propidium iodide (PI) on skin, after PEF. **Discussion.** Proposed mechanisms for each voltage: creation of conductive pathways, formation of local transport regions and cell permeabilization.

Applied conditions	In situ measurements			Numerical model
	PEF Voltage	R ( $\Omega$ )	DC i	
50 V	1860	+10% (ns)	-	
100 V	940	+130%	+1	
200 V	560	+240%	+5	
300 V	470	+310%	+12	

**Figure 7.2 (screen version)** – Summary of experimental results on transdermal drug delivery, for applied PEFs of 50 to 300 V (8 pulses, 20 ms duration, 1 Hz).

**In situ measurements.** Average resistance (U/I) during last pulse, DC current change after PEF, Temperature increase (max) during PEF.

**Numerical model.** Electric field distribution on the skin, through validated, nonlinear model. XZ slices of first skin layers and areas where  $E > 400$  V/cm (approximate threshold value for cell permeabilization in tissue) on viable skin layers.

Applied conditions	Drug Delivery	Discussion	
PEF Voltage	Fluorescence Microscopy	Mechanisms	
50 V			
100 V			
200 V			
300 V			

**Drug delivery.** Fluorescent marking of lucifer yellow (LY) and propidium iodide (PI) on skin, after PEF.

**Discussion.** Proposed mechanisms for each voltage: creation of conductive pathways, formation of local transport regions and cell permeabilization.

## 8 References

- [1] E. Neumann et K. Rosenheck, « Permeability changes induced by electric impulses in vesicular membranes », *J. Membr. Biol.*, vol. 10, n° 1, p. 279-290, déc. 1972, doi: 10.1007/BF01867861.
- [2] T. Kotnik, L. Rems, M. Tarek, et D. Miklavčič, « Membrane Electroporation and Electropermeabilization: Mechanisms and Models », *Annu. Rev. Biophys.*, vol. 48, n° 1, p. 63-91, 2019, doi: 10.1146/annurev-biophys-052118-115451.
- [3] M. R. Prausnitz, V. G. Bose, R. Langer, et J. C. Weaver, « Electroporation of mammalian skin: a mechanism to enhance transdermal drug delivery. », *Proc. Natl. Acad. Sci.*, vol. 90, n° 22, p. 10504-10508, nov. 1993, doi: 10.1073/pnas.90.22.10504.
- [4] B. M. Medi, B. Layek, et J. Singh, « Electroporation for Dermal and Transdermal Drug Delivery », in *Percutaneous Penetration Enhancers Physical Methods in Penetration Enhancement*, N. Dragicevic et H. I. Maibach, Éd., Berlin, Heidelberg: Springer, 2017, p. 105-122. doi: 10.1007/978-3-662-53273-7\_7.
- [5] A.-R. Denet, R. Vanbever, et V. Prétat, « Skin electroporation for transdermal and topical delivery », *Adv. Drug Deliv. Rev.*, vol. 56, n° 5, p. 659-674, mars 2004, doi: 10.1016/j.addr.2003.10.027.
- [6] R. Vanbever, N. Lecouturier, et V. Prétat, « Transdermal Delivery of Metoprolol by Electroporation », *Pharm. Res.*, vol. 11, n° 11, p. 1657-1662, nov. 1994, doi: 10.1023/A:1018930425591.
- [7] A. Jadoul, N. Lecouturier, J. Mesens, W. Caers, et V. Prétat, « Transdermal alniditan delivery by skin electroporation », *J. Controlled Release*, vol. 54, n° 3, p. 265-272, août 1998, doi: 10.1016/S0168-3659(97)00195-8.
- [8] V. Regnier, N. De Morre, A. Jadoul, et V. Prétat, « Mechanisms of a phosphorothioate oligonucleotide delivery by skin electroporation », *Int. J. Pharm.*, vol. 184, n° 2, p. 147-156, juill. 1999, doi: 10.1016/S0378-5173(98)00085-4.
- [9] T.-W. Wong, T.-Y. Chen, C.-C. Huang, J.-C. Tsai, et S. W. Hui, « Painless Skin Electroporation as a Novel Way for Insulin Delivery », *Diabetes Technol. Ther.*, vol. 13, n° 9, p. 929-935, sept. 2011, doi: 10.1089/dia.2011.0077.
- [10] J. Simon, B. Jouanmiquieu, M.-P. Rols, E. Flahaut, et M. Golzio, « Transdermal Delivery of Macromolecules Using Two-in-One Nanocomposite Device for Skin Electroporation », *Pharmaceutics*, vol. 13, n° 11, Art. n° 11, nov. 2021, doi: 10.3390/pharmaceutics13111805.
- [11] N. Kis, A. Kovács, M. Budai-Szűcs, G. Erős, E. Csányi, et S. Berkó, « The effect of non-invasive dermal electroporation on skin barrier function and skin permeation in combination with different dermal formulations », *J. Drug Deliv. Sci. Technol.*, vol. 69, p. 103161, mars 2022, doi: 10.1016/j.jddst.2022.103161.
- [12] M. Madi, M.-P. Rols, et L. Gibot, « Efficient In Vitro Electropermeabilization of Reconstructed Human Dermal Tissue », *J. Membr. Biol.*, vol. 248, n° 5, p. 903-908, oct. 2015, doi: 10.1007/s00232-015-9791-z.
- [13] M. S. Wallace, B. Ridgeway, E. Jun, G. Schulteis, D. Rabussay, et L. Zhang, « Topical Delivery of Lidocaine in Healthy Volunteers by Electroporation, Electroincorporation, or Iontophoresis: An Evaluation of Skin Anesthesia », *Reg. Anesth. Pain Med.*, vol. 26, n° 3, p. 229-238, mai 2001, doi: 10.1053/rapm.2001.22633.
- [14] U. Pliquet et J. C. Weaver, « Feasibility of an electrode-reservoir device for transdermal drug delivery by noninvasive skin electroporation », *IEEE Trans. Biomed. Eng.*, vol. 54, n° 3, p. 536-538, mars 2007, doi: 10.1109/TBME.2006.886828.
- [15] J. Teissié et M. P. Rols, « An experimental evaluation of the critical potential difference inducing cell membrane electropermeabilization. », *Biophys. J.*, vol. 65, n° 1, p. 409-413, juill. 1993.
- [16] M. Tarek, « Membrane Electroporation: A Molecular Dynamics Simulation », *Biophys. J.*, vol. 88, n° 6, p. 4045-4053, juin 2005, doi: 10.1529/biophysj.104.050617.



- [17] S. Corovic, I. Lackovic, P. Sustaric, T. Sustar, T. Rodic, et D. Miklavcic, « Modeling of electric field distribution in tissues during electroporation », *Biomed. Eng. OnLine*, vol. 12, n° 1, p. 16, févr. 2013, doi: 10.1186/1475-925X-12-16.
- [18] U. F. Pliquett, T. E. Zewert, T. Chen, R. Langer, et J. C. Weaver, « Imaging of fluorescent molecule and small ion transport through human stratum corneum during high voltage pulsing: localized transport regions are involved », *Biophys. Chem.*, vol. 58, n° 1, p. 185-204, janv. 1996, doi: 10.1016/0301-4622(95)00098-4.
- [19] N. Pavšelj, V. Prémat, et D. Miklavčič, « A Numerical Model of Skin Electroporabilization Based on In Vivo Experiments », *Ann. Biomed. Eng.*, vol. 35, n° 12, p. 2138-2144, déc. 2007, doi: 10.1007/s10439-007-9378-7.
- [20] J. Dermol-Černe, E. Pirc, et D. Miklavčič, « Mechanistic view of skin electroporation – models and dosimetry for successful applications: an expert review », *Expert Opin. Drug Deliv.*, vol. 17, n° 5, p. 689-704, mai 2020, doi: 10.1080/17425247.2020.1745772.
- [21] R. Gupta et B. Rai, « Electroporation of Skin Stratum Corneum Lipid Bilayer and Molecular Mechanism of Drug Transport: A Molecular Dynamics Study », *Langmuir*, vol. 34, n° 20, p. 5860-5870, mai 2018, doi: 10.1021/acs.langmuir.8b00423.
- [22] B. Zorec, V. Prémat, D. Miklavčič, et N. Pavselj, « Active enhancement methods for intra- and transdermal drug delivery: a review. », *ZdravVestn*, 2013, doi: 10.6016/1889.
- [23] I. Riou, P. Bertoncini, H. Bizot, J. Y. Mevellec, A. Buléon, et O. Chauvet, « Carboxymethylcellulose/Single Walled Carbon Nanotube Complexes », *J. Nanosci. Nanotechnol.*, vol. 9, n° 10, p. 6176-6180, oct. 2009, doi: 10.1166/jnn.2009.1573.
- [24] T. Takahashi, K. Tsunoda, H. Yajima, et T. Ishii, « Dispersion and Purification of Single-Wall Carbon Nanotubes Using Carboxymethylcellulose », *Jpn. J. Appl. Phys.*, vol. 43, n° 6R, p. 3636, juin 2004, doi: 10.1143/JJAP.43.3636.
- [25] Y. A. Chizmadzhev, A. V. Indenbom, P. I. Kuzmin, S. V. Galichenko, J. C. Weaver, et R. O. Potts, « Electrical Properties of Skin at Moderate Voltages: Contribution of Appendageal Macropores », *Biophys. J.*, vol. 74, n° 2, p. 843-856, févr. 1998, doi: 10.1016/S0006-3495(98)74008-1.
- [26] J. Leyden, L. Stein-Gold, et J. Weiss, « Why Topical Retinoids Are Mainstay of Therapy for Acne », *Dermatol. Ther.*, vol. 7, n° 3, p. 293-304, juin 2017, doi: 10.1007/s13555-017-0185-2.
- [27] G. W. Cleary, « Transdermal Delivery Systems: A Medical Rationale », in *Topical Drug Bioavailability, Bioequivalence, and Penetration*, V. P. Shah et H. I. Maibach, Éd., Boston, MA: Springer US, 1993, p. 17-68. doi: 10.1007/978-1-4899-1262-6\_2.
- [28] S. Wiedersberg et R. H. Guy, « Transdermal drug delivery: 30+ years of war and still fighting! », *J. Controlled Release*, vol. 190, p. 150-156, sept. 2014, doi: 10.1016/j.jconrel.2014.05.022.
- [29] R. Vanbever et V. Prémat, « In vivo efficacy and safety of skin electroporation », *Adv. Drug Deliv. Rev.*, vol. 35, n° 1, p. 77-88, janv. 1999, doi: 10.1016/s0169-409x(98)00064-7.
- [30] M. R. Prausnitz, « A practical assessment of transdermal drug delivery by skin electroporation », *Adv. Drug Deliv. Rev.*, vol. 35, n° 1, p. 61-76, janv. 1999, doi: 10.1016/s0169-409x(98)00063-5.
- [31] E. Candi, R. Schmidt, et G. Melino, « The cornified envelope: a model of cell death in the skin », *Nat. Rev. Mol. Cell Biol.*, vol. 6, n° 4, Art. n° 4, avr. 2005, doi: 10.1038/nrm1619.
- [32] J. A. McGrath, R. a. J. Eady, et F. M. Pope, « Anatomy and Organization of Human Skin », in *Rook's Textbook of Dermatology*, John Wiley & Sons, Ltd, 2004, p. 45-128. doi: 10.1002/9780470750520.ch3.
- [33] D. Ramadon, M. T. C. McCrudden, A. J. Courtenay, et R. F. Donnelly, « Enhancement strategies for transdermal drug delivery systems: current trends and applications », *Drug Deliv. Transl. Res.*, vol. 12, n° 4, p. 758-791, avr. 2022, doi: 10.1007/s13346-021-00909-6.
- [34] Neopharm, « ZEROID Professional Solution for Healthy Skin ». Consulté le: 19 juillet 2023. [En ligne]. Disponible sur: <http://zeroid.com/main/contents.asp?cate=272&Pcate=267&Mcate=269>

- [35] Y. Gilaberte, L. Prieto-Torres, I. Pastushenko, et Á. Juarranz, « Chapter 1 - Anatomy and Function of the Skin », in *Nanoscience in Dermatology*, M. R. Hamblin, P. Avci, et T. W. Prow, Éd., Boston: Academic Press, 2016, p. 1-14. doi: 10.1016/B978-0-12-802926-8.00001-X.
- [36] B. Godin et E. Touitou, « Dermal and Transdermal Delivery », in *Encyclopedia of Nanotechnology*, B. Bhushan, Éd., Dordrecht: Springer Netherlands, 2014, p. 1-12. doi: 10.1007/978-94-007-6178-0\_81-2.
- [37] J. T. Huzil, S. Sivaloganathan, M. Kohandel, et M. Foldvari, « Drug delivery through the skin: molecular simulations of barrier lipids to design more effective noninvasive dermal and transdermal delivery systems for small molecules, biologics, and cosmetics », *WIREs Nanomedicine Nanobiotechnology*, vol. 3, n° 5, p. 449-462, 2011, doi: 10.1002/wnan.147.
- [38] M. R. Prausnitz et R. Langer, « Transdermal drug delivery », *Nat. Biotechnol.*, vol. 26, n° 11, Art. n° 11, nov. 2008, doi: 10.1038/nbt.1504.
- [39] J. P. Atkinson, H. I. Maibach, et N. Dragicevic, « Targets in Dermal and Transdermal Delivery and Classification of Penetration Enhancement Methods », in *Percutaneous Penetration Enhancers Chemical Methods in Penetration Enhancement: Drug Manipulation Strategies and Vehicle Effects*, N. Dragicevic et H. I. Maibach, Éd., Berlin, Heidelberg: Springer, 2015, p. 93-108. doi: 10.1007/978-3-662-45013-0\_8.
- [40] M. R. Prausnitz et R. Langer, « Transdermal drug delivery », *Nat. Biotechnol.*, vol. 26, n° 11, p. 1261-1268, nov. 2008, doi: 10.1038/nbt.1504.
- [41] L. Engelke, G. Winter, S. Hook, et J. Engert, « Recent insights into cutaneous immunization: How to vaccinate via the skin », *Vaccine*, vol. 33, n° 37, p. 4663-4674, sept. 2015, doi: 10.1016/j.vaccine.2015.05.012.
- [42] S. Mitragotri, « Immunization without needles », *Nat. Rev. Immunol.*, vol. 5, n° 12, Art. n° 12, déc. 2005, doi: 10.1038/nri1728.
- [43] S. Chabot, C. Rosazza, M. Golzio, A. Zumbusch, J. Teissié, et M.-P. Rols, « Nucleic acids electrotransfer: from bench to bedside », *Curr. Drug Metab.*, vol. 14, n° 3, p. 300-308, mars 2013, doi: 10.2174/1389200211314030005.
- [44] I. P. Sugar, W. Förster, et E. Neumann, « Model of cell electrofusion: Membrane electroperoration, pore coalescence and percolation », *Biophys. Chem.*, vol. 26, n° 2, p. 321-335, mai 1987, doi: 10.1016/0301-4622(87)80033-9.
- [45] L. M. Mir *et al.*, « Effective treatment of cutaneous and subcutaneous malignant tumours by electrochemotherapy », *Br. J. Cancer*, vol. 77, n° 12, Art. n° 12, juin 1998, doi: 10.1038/bjc.1998.388.
- [46] S. Pedron-Mazoyer, J. Plouët, L. Hellaudais, J. Teissie, et M. Golzio, « New anti angiogenesis developments through electro-immunization: optimization by in vivo optical imaging of intradermal electro gene transfer », *Biochim. Biophys. Acta*, vol. 1770, n° 1, p. 137-142, janv. 2007, doi: 10.1016/j.bbagen.2006.09.014.
- [47] L. Pasquet *et al.*, « Safe and efficient novel approach for non-invasive gene electrotransfer to skin », *Sci. Rep.*, vol. 8, n° 1, Art. n° 1, nov. 2018, doi: 10.1038/s41598-018-34968-6.
- [48] J. Teissie, M. Golzio, et M. P. Rols, « Mechanisms of cell membrane electropermeabilization: A minireview of our present (lack of ?) knowledge », *Biochim. Biophys. Acta BBA - Gen. Subj.*, vol. 1724, n° 3, p. 270-280, août 2005, doi: 10.1016/j.bbagen.2005.05.006.
- [49] T. Kotnik, L. Rems, M. Tarek, et D. Miklavčič, « Membrane Electroperoration and Electropermeabilization: Mechanisms and Models », *Annu. Rev. Biophys.*, vol. 48, n° 1, p. 63-91, mai 2019, doi: 10.1146/annurev-biophys-052118-115451.
- [50] J.-M. Escoffre, T. Portet, L. Wasungu, J. Teissié, D. Dean, et M.-P. Rols, « What is (still not) known of the mechanism by which electroperoration mediates gene transfer and expression in cells and tissues », *Mol. Biotechnol.*, vol. 41, n° 3, p. 286-295, mars 2009, doi: 10.1007/s12033-008-9121-0.
- [51] T. Kotnik, P. Kramar, G. Pucihar, D. Miklavcic, et M. Tarek, « Cell membrane electroperoration- Part 1: The phenomenon », *IEEE Electr. Insul. Mag.*, vol. 28, n° 5, p. 14-23, sept. 2012, doi: 10.1109/MEI.2012.6268438.

- [52] Z. Vasilkoski, A. T. Esser, T. R. Gowrishankar, et J. C. Weaver, « Membrane electroporation: The absolute rate equation and nanosecond time scale pore creation », *Phys. Rev. E*, vol. 74, n° 2, p. 021904, août 2006, doi: 10.1103/PhysRevE.74.021904.
- [53] J. Teissie et D. Zerbib, « Cell Membrane Electropermeabilization », p. 9, 2018.
- [54] J. Teissié et M. P. Rols, « An experimental evaluation of the critical potential difference inducing cell membrane electropermeabilization. », *Biophys. J.*, vol. 65, n° 1, p. 409-413, juill. 1993.
- [55] L. Lambricht, A. Lopes, S. Kos, G. Sersa, V. Prémat, et G. Vandermeulen, « Clinical potential of electroporation for gene therapy and DNA vaccine delivery », *Expert Opin. Drug Deliv.*, vol. 13, n° 2, p. 295-310, févr. 2016, doi: 10.1517/17425247.2016.1121990.
- [56] B. Al-Sakere *et al.*, « Tumor Ablation with Irreversible Electroporation », *PLOS ONE*, vol. 2, n° 11, p. e1135, nov. 2007, doi: 10.1371/journal.pone.0001135.
- [57] A. Sugrue *et al.*, « Irreversible electroporation for the treatment of cardiac arrhythmias », *Expert Rev. Cardiovasc. Ther.*, vol. 16, n° 5, p. 349-360, mai 2018, doi: 10.1080/14779072.2018.1459185.
- [58] M. Essone Mezeme, G. Pucihar, M. Pavlin, C. Brosseau, et D. Miklavčič, « A numerical analysis of multicellular environment for modeling tissue electroporation », *Appl. Phys. Lett.*, vol. 100, n° 14, p. 143701, avr. 2012, doi: 10.1063/1.3700727.
- [59] S. Huclova, D. Erni, et J. Fröhlich, « Modelling effective dielectric properties of materials containing diverse types of biological cells », *J. Phys. Appl. Phys.*, vol. 43, n° 36, p. 365405, août 2010, doi: 10.1088/0022-3727/43/36/365405.
- [60] S. W. Hui, « Low voltage electroporation of the skin, or is it iontophoresis? », *Biophys. J.*, vol. 74, n° 2 Pt 1, p. 679-680, févr. 1998.
- [61] T. E. Zewert, U. F. Pliquett, R. Vanbever, R. Langer, et J. C. Weaver, « Creation of transdermal pathways for macromolecule transport by skin electroporation and a low toxicity, pathway-enlarging molecule », *Bioelectrochem. Bioenerg.*, vol. 49, n° 1, p. 11-20, oct. 1999, doi: 10.1016/S0302-4598(99)00056-2.
- [62] M. R. Prausnitz *et al.*, « Transdermal transport efficiency during skin electroporation and iontophoresis », *J. Controlled Release*, vol. 38, n° 2, p. 205-217, févr. 1996, doi: 10.1016/0168-3659(95)00121-2.
- [63] G. A. Hofmann, W. V. Rustrum, et K. S. Suder, « Electro-incorporation of microcarriers as a method for the transdermal delivery of large molecules », *Bioelectrochem. Bioenerg.*, vol. 38, n° 1, p. 209-222, août 1995, doi: 10.1016/0302-4598(95)01827-2.
- [64] J.-F. Guillet, E. Flahaut, et M. Golzio, « A Hydrogel/Carbon-Nanotube Needle-Free Device for Electrostimulated Skin Drug Delivery », *ChemPhysChem*, vol. 18, n° 19, p. 2715-2723, 2017, doi: <https://doi.org/10.1002/cphc.201700517>.
- [65] S. Mazères *et al.*, « Non invasive contact electrodes for in vivo localized cutaneous electropulsation and associated drug and nucleic acid delivery », *J. Control. Release Off. J. Control. Release Soc.*, vol. 134, n° 2, p. 125-131, mars 2009, doi: 10.1016/j.jconrel.2008.11.003.
- [66] S. Guo, A. Donate, G. Basu, C. Lundberg, L. Heller, et R. Heller, « Electro-gene transfer to skin using a noninvasive multielectrode array », *J. Control. Release Off. J. Control. Release Soc.*, vol. 151, n° 3, p. 256-262, mai 2011, doi: 10.1016/j.jconrel.2011.01.014.
- [67] L. Zhang, L. Li, Z. An, R. M. Hoffman, et G. A. Hofmann, « In vivo transdermal delivery of large molecules by pressure-mediated electroincorporation and electroporation: a novel method for drug and gene delivery », *Bioelectrochem. Bioenerg.*, vol. 42, n° 2, p. 283-292, mai 1997, doi: 10.1016/S0302-4598(96)05128-8.
- [68] S. Aryal, « Vesicles- Definition, Structure, Functions and Diagram ». Consulté le: 10 octobre 2023. [En ligne]. Disponible sur: <https://microbenotes.com/vesicles-structure-types-and-functions/>
- [69] T. Sheth, S. Seshadri, T. Prileszky, et M. E. Helgeson, « Multiple nanoemulsions », *Nat. Rev. Mater.*, vol. 5, n° 3, Art. n° 3, mars 2020, doi: 10.1038/s41578-019-0161-9.



- [70] « Microneedles are promising devices for painless drug delivery with minimal side effects | University of Helsinki ». Consulté le: 10 octobre 2023. [En ligne]. Disponible sur: <https://www.helsinki.fi/en/news/healthier-world/microneedles-are-promising-devices-painless-drug-delivery-minimal-side-effects>
- [71] J. Li et D. J. Mooney, « Designing hydrogels for controlled drug delivery », *Nat. Rev. Mater.*, vol. 1, n° 12, Art. n° 12, oct. 2016, doi: 10.1038/natrevmats.2016.71.
- [72] H.-W. Liu, S.-H. Hu, Y.-W. Chen, et S.-Y. Chen, « Characterization and drug release behavior of highly responsive chip-like electrically modulated reduced graphene oxide–poly(vinyl alcohol) membranes », *J. Mater. Chem.*, vol. 22, n° 33, p. 17311-17320, juill. 2012, doi: 10.1039/C2JM32772D.
- [73] K. Elkhoury, P. Koçak, A. Kang, E. Arab-Tehrany, J. Ellis Ward, et S. R. Shin, « Engineering Smart Targeting Nanovesicles and Their Combination with Hydrogels for Controlled Drug Delivery », *Pharmaceutics*, vol. 12, n° 9, Art. n° 9, sept. 2020, doi: 10.3390/pharmaceutics12090849.
- [74] M. J. Lewis, « 5 - Solid rheology and texture », in *Physical Properties of Foods and Food Processing Systems*, M. J. Lewis, Éd., in Woodhead Publishing Series in Food Science, Technology and Nutrition. , Woodhead Publishing, 1996, p. 137-166. doi: 10.1533/9781845698423.137.
- [75] Y. S. Zhang et A. Khademhosseini, « Advances in engineering hydrogels », *Science*, vol. 356, n° 6337, mai 2017, doi: 10.1126/science.aaf3627.
- [76] K. Varaprasad, G. M. Raghavendra, T. Jayaramudu, M. M. Yallapu, et R. Sadiku, « A mini review on hydrogels classification and recent developments in miscellaneous applications », *Mater. Sci. Eng. C*, vol. 79, p. 958-971, oct. 2017, doi: 10.1016/j.msec.2017.05.096.
- [77] F. Ullah, M. B. H. Othman, F. Javed, Z. Ahmad, et H. Md. Akil, « Classification, processing and application of hydrogels: A review », *Mater. Sci. Eng. C*, vol. 57, p. 414-433, déc. 2015, doi: 10.1016/j.msec.2015.07.053.
- [78] N. A. Peppas et A. S. Hoffman, « 1.3.2E - Hydrogels », in *Biomaterials Science (Fourth Edition)*, W. R. Wagner, S. E. Sakiyama-Elbert, G. Zhang, et M. J. Yaszemski, Éd., Academic Press, 2020, p. 153-166. doi: 10.1016/B978-0-12-816137-1.00014-3.
- [79] W. Wagermaier et P. Fratzl, « 9.03 - Collagen », in *Polymer Science: A Comprehensive Reference*, K. Matyjaszewski et M. Möller, Éd., Amsterdam: Elsevier, 2012, p. 35-55. doi: 10.1016/B978-0-444-53349-4.00247-8.
- [80] E. M. Ahmed, « Hydrogel: Preparation, characterization, and applications: A review », *J. Adv. Res.*, vol. 6, n° 2, Art. n° 2, mars 2015, doi: 10.1016/j.jare.2013.07.006.
- [81] J. P. Gong, « Friction and lubrication of hydrogels—its richness and complexity », *Soft Matter*, vol. 2, n° 7, p. 544-552, juin 2006, doi: 10.1039/B603209P.
- [82] H. Li, Y. S. Choi, M. W. Rutland, et R. Atkin, « Nanotribology of hydrogels with similar stiffness but different polymer and crosslinker concentrations », *J. Colloid Interface Sci.*, vol. 563, p. 347-353, mars 2020, doi: 10.1016/j.jcis.2019.12.045.
- [83] A. S. Hoffman, « Hydrogels for biomedical applications », *Adv. Drug Deliv. Rev.*, vol. 64, p. 18-23, déc. 2012, doi: 10.1016/j.addr.2012.09.010.
- [84] A. Doderò, L. Pianella, S. Vicini, M. Alloisio, M. Ottonelli, et M. Castellano, « Alginate-based hydrogels prepared via ionic gelation: An experimental design approach to predict the crosslinking degree », *Eur. Polym. J.*, vol. 118, p. 586-594, sept. 2019, doi: 10.1016/j.eurpolymj.2019.06.028.
- [85] S. J. Buwalda, K. W. M. Boere, P. J. Dijkstra, J. Feijen, T. Vermonden, et W. E. Hennink, « Hydrogels in a historical perspective: From simple networks to smart materials », *J. Controlled Release*, vol. 190, p. 254-273, sept. 2014, doi: 10.1016/j.jconrel.2014.03.052.
- [86] D. Zhang et al., « From design to applications of stimuli-responsive hydrogel strain sensors », *J. Mater. Chem. B*, vol. 8, n° 16, p. 3171-3191, 2020, doi: 10.1039/C9TB02692D.
- [87] G. Isapour et M. Lattuada, « Bioinspired Stimuli-Responsive Color-Changing Systems », *Adv. Mater.*, vol. 30, n° 19, p. 1707069, 2018, doi: 10.1002/adma.201707069.

- [88] I. Tokarev *et al.*, « Stimuli-Responsive Hydrogel Membranes Coupled with Biocatalytic Processes », *ACS Appl. Mater. Interfaces*, vol. 1, n° 3, p. 532-536, mars 2009, doi: 10.1021/am800251a.
- [89] T. Distler et A. R. Boccaccini, « 3D printing of electrically conductive hydrogels for tissue engineering and biosensors – A review », *Acta Biomater.*, vol. 101, p. 1-13, janv. 2020, doi: 10.1016/j.actbio.2019.08.044.
- [90] Lh. Yahia, « History and Applications of Hydrogels », *J. Biomed. Sci.*, vol. 04, n° 02, 2015, doi: 10.4172/2254-609X.100013.
- [91] B. W. Walker, R. P. Lara, E. Mogadam, C. H. Yu, W. Kimball, et N. Annabi, « Rational Design of Microfabricated Electroconductive Hydrogels for Biomedical Applications », *Prog. Polym. Sci.*, vol. 92, p. 135-157, mai 2019, doi: 10.1016/j.progpolymsci.2019.02.007.
- [92] S. Merino, C. Martín, K. Kostarelos, M. Prato, et E. Vázquez, « Nanocomposite Hydrogels: 3D Polymer–Nanoparticle Synergies for On-Demand Drug Delivery », *ACS Nano*, vol. 9, n° 5, p. 4686-4697, mai 2015, doi: 10.1021/acsnano.5b01433.
- [93] S. Murdan, « Electro-responsive drug delivery from hydrogels », *J. Controlled Release*, vol. 92, n° 1, p. 1-17, sept. 2003, doi: 10.1016/S0168-3659(03)00303-1.
- [94] A. Servant *et al.*, « Graphene-Based Electroresponsive Scaffolds as Polymeric Implants for On-Demand Drug Delivery », *Adv. Healthc. Mater.*, vol. 3, n° 8, p. 1334-1343, 2014, doi: <https://doi.org/10.1002/adhm.201400016>.
- [95] J. Stejskal, « Conducting polymer hydrogels », *Chem. Pap.*, vol. 71, n° 2, Art. n° 2, févr. 2017, doi: 10.1007/s11696-016-0072-9.
- [96] K. Liu, S. Wei, L. Song, H. Liu, et T. Wang, « Conductive Hydrogels—A Novel Material: Recent Advances and Future Perspectives », *J. Agric. Food Chem.*, vol. 68, n° 28, p. 7269-7280, juill. 2020, doi: 10.1021/acs.jafc.0c00642.
- [97] A. Malti *et al.*, « An Organic Mixed Ion–Electron Conductor for Power Electronics », *Adv. Sci.*, vol. 3, n° 2, p. 1500305, 2016, doi: 10.1002/advs.201500305.
- [98] B. Guo et P. X. Ma, « Conducting Polymers for Tissue Engineering », *Biomacromolecules*, vol. 19, n° 6, Art. n° 6, juin 2018, doi: 10.1021/acs.biomac.8b00276.
- [99] Q. Peng *et al.*, « Recent advances in designing conductive hydrogels for flexible electronics », *InfoMat*, vol. 2, n° 5, p. 843-865, 2020, doi: 10.1002/inf2.12113.
- [100] D. Liang, G. Zhou, Y. Hu, C. Zhao, et C. Chen, « Metal cation-ligand interaction modulated mono-network ionic conductive hydrogel for wearable strain sensor », *J. Mater. Sci.*, vol. 56, n° 26, p. 14531-14541, sept. 2021, doi: 10.1007/s10853-021-06242-0.
- [101] X. Zhang *et al.*, « A review of recent advances in metal ion hydrogels: mechanism, properties and their biological applications », *New J. Chem.*, vol. 46, n° 29, p. 13838-13855, juill. 2022, doi: 10.1039/D2NJ02843C.
- [102] C.-J. Lee *et al.*, « Ionic Conductivity of Polyelectrolyte Hydrogels », *ACS Appl. Mater. Interfaces*, vol. 10, n° 6, p. 5845-5852, févr. 2018, doi: 10.1021/acsaami.7b15934.
- [103] M. Hess *et al.*, « Terminology of polymers containing ionizable or ionic groups and of polymers containing ions (IUPAC Recommendations 2006) », *Pure Appl. Chem.*, vol. 78, n° 11, p. 2067-2074, janv. 2006, doi: 10.1351/pac200678112067.
- [104] J. Cardoso, A. Huanosta, et O. Manero, « Ionic conductivity studies on salt-polyzwitterion systems », *Macromolecules*, vol. 24, n° 10, p. 2890-2895, mai 1991, doi: 10.1021/ma00010a039.
- [105] C.-G. Wang *et al.*, « Polyelectrolyte Hydrogels for Tissue Engineering and Regenerative Medicine », *Chem. – Asian J.*, vol. 17, n° 18, p. e202200604, 2022, doi: 10.1002/asia.202200604.
- [106] S. Liu, J. Tang, F. Ji, W. Lin, et S. Chen, « Recent Advances in Zwitterionic Hydrogels: Preparation, Property, and Biomedical Application », *Gels*, vol. 8, n° 1, Art. n° 1, janv. 2022, doi: 10.3390/gels8010046.
- [107] K. Zhou, *Carbon Nanomaterials : Modeling, Design, and Applications*. CRC Press, 2019. doi: 10.1201/9781351123587.

- [108] M. Monthieux *et al.*, « Introduction to Carbon Nanotubes », in *Springer Handbook of Nanotechnology*, B. Bhushan, Éd., in Springer Handbooks. , Berlin, Heidelberg: Springer, 2010, p. 47-118. doi: 10.1007/978-3-642-02525-9\_3.
- [109] M. F. L. D. Volder, S. H. Tawfick, R. H. Baughman, et A. J. Hart, « Carbon Nanotubes: Present and Future Commercial Applications », *Science*, vol. 339, n° 6119, p. 535-539, févr. 2013, doi: 10.1126/science.1222453.
- [110] J. Simon, E. Flahaut, et M. Golzio, « Overview of Carbon Nanotubes for Biomedical Applications », *Materials*, vol. 12, n° 4, Art. n° 4, janv. 2019, doi: 10.3390/ma12040624.
- [111] C.-W. Nan, Y. Shen, et J. Ma, « Physical Properties of Composites Near Percolation », *Annu. Rev. Mater. Res.*, vol. 40, n° 1, p. 131-151, 2010, doi: 10.1146/annurev-matsci-070909-104529.
- [112] T. W. Ebbesen, H. J. Lezec, H. Hiura, J. W. Bennett, H. F. Ghaemi, et T. Thio, « Electrical conductivity of individual carbon nanotubes », *Nature*, vol. 382, n° 6586, Art. n° 6586, juill. 1996, doi: 10.1038/382054a0.
- [113] F. Xie, P. Weiss, O. Chauvet, J. Le Bideau, et J. F. Tassin, « Kinetic studies of a composite carbon nanotube-hydrogel for tissue engineering by rheological methods », *J. Mater. Sci. Mater. Med.*, vol. 21, n° 4, p. 1163-1168, avr. 2010, doi: 10.1007/s10856-009-3984-x.
- [114] X. Liu, J. C. Kim, A. Lee Miller, B. E. Waletzki, et L. Lu, « Electrically conductive nanocomposite hydrogels embedded with functionalized carbon nanotubes for spinal cord injury », *New J. Chem.*, vol. 42, n° 21, Art. n° 21, 2018, doi: 10.1039/C8NJ03038C.
- [115] J. Zhou *et al.*, « Engineering the heart: Evaluation of conductive nanomaterials for improving implant integration and cardiac function », *Sci. Rep.*, vol. 4, n° 1, Art. n° 1, janv. 2014, doi: 10.1038/srep03733.
- [116] U. G. Spizzirri *et al.*, « Spherical gelatin/CNTs hybrid microgels as electro-responsive drug delivery systems », *Int. J. Pharm.*, vol. 448, n° 1, p. 115-122, mai 2013, doi: 10.1016/j.ijpharm.2013.03.013.
- [117] A. Aharony et D. Stauffer, *Introduction To Percolation Theory : Second Edition*. Taylor & Francis, 2018. doi: 10.1201/9781315274386.
- [118] A. J. Marsden *et al.*, « Electrical percolation in graphene–polymer composites », *2D Mater.*, vol. 5, n° 3, p. 032003, juin 2018, doi: 10.1088/2053-1583/aac055.
- [119] J. W. Essam, « Percolation theory », *Rep. Prog. Phys.*, vol. 43, n° 7, p. 833, juill. 1980, doi: 10.1088/0034-4885/43/7/001.
- [120] W. Bauhofer et J. Z. Kovacs, « A review and analysis of electrical percolation in carbon nanotube polymer composites », *Compos. Sci. Technol.*, vol. 69, n° 10, Art. n° 10, août 2009, doi: 10.1016/j.compscitech.2008.06.018.
- [121] L. Berhan et A. M. Sastry, « Modeling percolation in high-aspect-ratio fiber systems. I. Soft-core versus hard-core models », *Phys. Rev. E*, vol. 75, n° 4, p. 041120, avr. 2007, doi: 10.1103/PhysRevE.75.041120.
- [122] J. R. Winkler et H. B. Gray, « Long-Range Electron Tunneling », *J. Am. Chem. Soc.*, vol. 136, n° 8, p. 2930-2939, févr. 2014, doi: 10.1021/ja500215j.
- [123] A. P. Chatterjee, « A lattice model for connectedness percolation in mixtures of rods and disks », *J. Phys. Condens. Matter*, vol. 27, n° 31, p. 315303, juill. 2015, doi: 10.1088/0953-8984/27/31/315303.
- [124] A. P. Chatterjee, « A percolation-based model for the conductivity of nanofiber composites », *J. Chem. Phys.*, vol. 139, n° 22, p. 224904, déc. 2013, doi: 10.1063/1.4840098.
- [125] G. Ambrosetti, C. Grimaldi, I. Balberg, T. Maeder, A. Danani, et P. Ryser, « Solution of the tunneling-percolation problem in the nanocomposite regime », *Phys. Rev. B*, vol. 81, n° 15, Art. n° 15, avr. 2010, doi: 10.1103/PhysRevB.81.155434.
- [126] V. Ambegaokar, B. I. Halperin, et J. S. Langer, « Hopping Conductivity in Disordered Systems », *Phys. Rev. B*, vol. 4, n° 8, p. 2612-2620, oct. 1971, doi: 10.1103/PhysRevB.4.2612.

- [127] L. Berhan et A. M. Sastry, « Modeling percolation in high-aspect-ratio fiber systems. II. The effect of waviness on the percolation onset », *Phys. Rev. E*, vol. 75, n° 4, p. 041121, avr. 2007, doi: 10.1103/PhysRevE.75.041121.
- [128] C. John Ferris et M. in het Panhuis, « Conducting bio-materials based on gellan gum hydrogels », *Soft Matter*, vol. 5, n° 18, Art. n° 18, 2009, doi: 10.1039/B909795C.
- [129] L. Mottet *et al.*, « A conductive hydrogel based on alginate and carbon nanotubes for probing microbial electroactivity », *Soft Matter*, vol. 14, n° 8, p. 1434-1441, févr. 2018, doi: 10.1039/C7SM01929G.
- [130] Z. Cui *et al.*, « A study of conductive hydrogel composites of pH-responsive microgels and carbon nanotubes », *Soft Matter*, vol. 12, n° 18, p. 4142-4153, mai 2016, doi: 10.1039/C6SM00223D.
- [131] J.-F. Guillet, Z. Valdez-Nava, M. Golzio, et E. Flahaut, « Electrical properties of double-wall carbon nanotubes nanocomposite hydrogels », *Carbon*, vol. 146, p. 542-548, mai 2019, doi: 10.1016/j.carbon.2019.01.090.
- [132] R. A. MacDonald, C. M. Voge, M. Kariolis, et J. P. Stegemann, « Carbon nanotubes increase the electrical conductivity of fibroblast-seeded collagen hydrogels », *Acta Biomater.*, vol. 4, n° 6, p. 1583-1592, nov. 2008, doi: 10.1016/j.actbio.2008.07.005.
- [133] A. Alam *et al.*, « Electrically conductive, mechanically robust, pH-sensitive graphene/polymer composite hydrogels », *Compos. Sci. Technol.*, vol. 127, p. 119-126, avr. 2016, doi: 10.1016/j.compscitech.2016.02.024.
- [134] L. Qiu *et al.*, « Mechanically robust, electrically conductive and stimuli-responsive binary network hydrogels enabled by superelastic graphene aerogels », *Adv. Mater. Deerfield Beach Fla*, vol. 26, n° 20, p. 3333-3337, mai 2014, doi: 10.1002/adma.201305359.
- [135] S. Sayyar *et al.*, « Processable conducting graphene/chitosan hydrogels for tissue engineering », *J. Mater. Chem. B*, vol. 3, n° 3, p. 481-490, déc. 2014, doi: 10.1039/C4TB01636J.
- [136] T. Chen, K. Hou, Q. Ren, G. Chen, P. Wei, et M. Zhu, « Nanoparticle–Polymer Synergies in Nanocomposite Hydrogels: From Design to Application », *Macromol. Rapid Commun.*, vol. 39, n° 21, p. 1800337, 2018, doi: 10.1002/marc.201800337.
- [137] P. Thoniyot, M. J. Tan, A. A. Karim, D. J. Young, et X. J. Loh, « Nanoparticle–Hydrogel Composites: Concept, Design, and Applications of These Promising, Multi-Functional Materials », *Adv. Sci.*, vol. 2, n° 1-2, Art. n° 1-2, 2015, doi: <https://doi.org/10.1002/advs.201400010>.
- [138] A. Hajian, S. B. Lindström, T. Pettersson, M. M. Hamed, et L. Wågberg, « Understanding the Dispersive Action of Nanocellulose for Carbon Nanomaterials », *Nano Lett.*, vol. 17, n° 3, p. 1439-1447, mars 2017, doi: 10.1021/acs.nanolett.6b04405.
- [139] X. Jing, H.-Y. Mi, B. N. Napiwocki, X.-F. Peng, et L.-S. Turng, « Mussel-inspired electroactive chitosan/graphene oxide composite hydrogel with rapid self-healing and recovery behavior for tissue engineering », *Carbon*, vol. 125, p. 557-570, déc. 2017, doi: 10.1016/j.carbon.2017.09.071.
- [140] C. Kittel, *Introduction to Solid State Physics*, 8th éd. Wiley, 2005. Consulté le: 5 juillet 2021. [En ligne]. Disponible sur: <https://www.wiley.com/en-us/Introduction+to+Solid+State+Physics%2C+8th+Edition-p-9780471415268>
- [141] F.-C. Chiu, « A Review on Conduction Mechanisms in Dielectric Films », *Adv. Mater. Sci. Eng.*, vol. 2014, p. e578168, févr. 2014, doi: 10.1155/2014/578168.
- [142] H. L. Tuller et P. K. Moon, « Fast ion conductors: future trends », *Mater. Sci. Eng. B*, vol. 1, n° 2, p. 171-191, nov. 1988, doi: 10.1016/0921-5107(88)90018-9.
- [143] C. Lin et I. Gitsov, « Synthesis and Physical Properties of Reactive Amphiphilic Hydrogels Based on Poly(p-chloromethylstyrene) and Poly(ethylene glycol): Effects of Composition and Molecular Architecture », *Macromolecules*, vol. 43, n° 7, p. 3256-3267, avr. 2010, doi: 10.1021/ma9026564.
- [144] V. M. Gun'ko, I. N. Savina, et S. V. Mikhalovsky, « Properties of Water Bound in Hydrogels », *Gels*, vol. 3, n° 4, Art. n° 4, déc. 2017, doi: 10.3390/gels3040037.

- [145] T. Hatakeyama et F. X. Quinn, *Thermal analysis: fundamentals and applications to polymer science*, 2nd ed. Chichester ; New York: Wiley, 1999.
- [146] A. R. Khare et N. A. Peppas, « Investigation of hydrogel water in polyelectrolyte gels using differential scanning calorimetry », *Polymer*, vol. 34, n° 22, p. 4736-4739, janv. 1993, doi: 10.1016/0032-3861(93)90710-R.
- [147] H. B. Lee, M. S. Jhon, et J. D. Andrade, « Nature of water in synthetic hydrogels. I. Dilatometry, specific conductivity, and differential scanning calorimetry of polyhydroxyethyl methacrylate », *J. Colloid Interface Sci.*, vol. 51, n° 2, p. 225-231, mai 1975, doi: 10.1016/0021-9797(75)90107-1.
- [148] J. R. Macdonald et W. B. Johnson, « Fundamentals of Impedance Spectroscopy », in *Impedance Spectroscopy*, John Wiley & Sons, Ltd, 2018, p. 1-20. doi: 10.1002/9781119381860.ch1.
- [149] N. Bonanos *et al.*, « Applications of Impedance Spectroscopy », in *Impedance Spectroscopy*, John Wiley & Sons, Ltd, 2018, p. 175-478. doi: 10.1002/9781119381860.ch4.
- [150] P. Pissis et A. Kyritsis, « Electrical conductivity studies in hydrogels », *Solid State Ion.*, vol. 97, n° 1, Art. n° 1, mai 1997, doi: 10.1016/S0167-2738(97)00074-X.
- [151] H. Warren, R. D. Gately, P. O'Brien, R. Gorkin, et M. in het Panhuis, « Electrical conductivity, impedance, and percolation behavior of carbon nanofiber and carbon nanotube containing gellan gum hydrogels », *J. Polym. Sci. Part B Polym. Phys.*, vol. 52, n° 13, Art. n° 13, 2014, doi: 10.1002/polb.23497.
- [152] C. Dispenza, C. L. Presti, C. Belfiore, G. Spadaro, et S. Piazza, « Electrically conductive hydrogel composites made of polyaniline nanoparticles and poly(N-vinyl-2-pyrrolidone) », *Polymer*, vol. 47, n° 4, Art. n° 4, févr. 2006, doi: 10.1016/j.polymer.2005.12.071.
- [153] A. N. Koppes *et al.*, « Robust neurite extension following exogenous electrical stimulation within single walled carbon nanotube-composite hydrogels », *Acta Biomater.*, vol. 39, p. 34-43, juill. 2016, doi: 10.1016/j.actbio.2016.05.014.
- [154] E. Flahaut, R. Bacsa, A. Peigney, et C. Laurent, « Gram-scale CCVD synthesis of double-walled carbon nanotubes », *Chem. Commun.*, n° 12, p. 1442-1443, nov. 2003, doi: 10.1039/B301514A.
- [155] P. Lagarrigue *et al.*, « Poly(d,l-lactide)-Grafted Bioactive Glass Nanoparticles: From Nanobricks to Freeze-Cast Scaffolds for Bone Substitution », *ACS Appl. Nano Mater.*, vol. 5, n° 4, p. 5278-5291, avr. 2022, doi: 10.1021/acsanm.2c00313.
- [156] M. ScharDOSim *et al.*, « Freeze-casting for PLGA/carbonated apatite composite scaffolds: Structure and properties », *Mater. Sci. Eng. C*, vol. 77, p. 731-738, août 2017, doi: 10.1016/j.msec.2017.03.302.
- [157] J. Simon, « CARBODERM : NANOTUBES DE CARBONE POUR LA DELIVRANCE TRANSDERMIQUE ELECTROSTIMULEE DE MOLECULES THERAPEUTIQUES », These en préparation, Toulouse 3, 2022. Consulté le: 5 juin 2022. [En ligne]. Disponible sur: <https://www.theses.fr/s294653>
- [158] J.-F. Guillet, « Nanotubes de carbone pour la délivrance transdermique électro-stimulée de substances biologiquement actives », These de doctorat, Toulouse 3, 2017. Consulté le: 6 avril 2021. [En ligne]. Disponible sur: <http://www.theses.fr/2017TOU30348>
- [159] C. M. Lee, S.-P. Jin, E. J. Doh, D. H. Lee, et J. H. Chung, « Regional Variation of Human Skin Surface Temperature », *Ann. Dermatol.*, vol. 31, n° 3, p. 349-352, juin 2019, doi: 10.5021/ad.2019.31.3.349.
- [160] M. P. Rols, C. Delteil, M. Golzio, P. Dumond, S. Cros, et J. Teissie, « In vivo electrically mediated protein and gene transfer in murine melanoma », *Nat. Biotechnol.*, vol. 16, n° 2, p. 168-171, févr. 1998, doi: 10.1038/nbt0298-168.
- [161] N. Pavselj et D. Miklavcic, « Numerical Models of Skin Electropermeabilization Taking Into Account Conductivity Changes and the Presence of Local Transport Regions », *Plasma Sci. IEEE Trans. On*, vol. 36, p. 1650-1658, sept. 2008, doi: 10.1109/TPS.2008.928715.
- [162] K. Sato, K. Sugibayashi, et Y. Morimoto, « Species Differences in Percutaneous Absorption of Nicorandil », *J. Pharm. Sci.*, vol. 80, n° 2, p. 104-107, févr. 1991, doi: 10.1002/jps.2600800203.

- [163] D. J. Arndt-Jovin et T. M. Jovin, « Chapter 16 Fluorescence Labeling and Microscopy of DNA », in *Methods in Cell Biology*, vol. 30, D. L. Taylor et Y.-L. Wang, Éd., in Fluorescence Microscopy of Living Cells in Culture Part B. Quantitative Fluorescence Microscopy—Imaging and Spectroscopy, vol. 30. , Academic Press, 1989, p. 417-448. doi: 10.1016/S0091-679X(08)60989-9.
- [164] D. C. Sauder et C. E. DeMars, « An Updated Recommendation for Multiple Comparisons », *Adv. Methods Pract. Psychol. Sci.*, vol. 2, n° 1, p. 26-44, mars 2019, doi: 10.1177/2515245918808784.
- [165] S. Vankoningsloo *et al.*, « Cytotoxicity of multi-walled carbon nanotubes in three skin cellular models: Effects of sonication, dispersive agents and corneous layer of reconstructed epidermis », *Nanotoxicology*, vol. 4, n° 1, p. 84-97, mars 2010, doi: 10.3109/17435390903428869.
- [166] L. Giraud, A. Tourrette, et E. Flahaut, « Carbon nanomaterials-based polymer-matrix nanocomposites for antimicrobial applications: A review », *Carbon*, vol. 182, p. 463-483, sept. 2021, doi: 10.1016/j.carbon.2021.06.002.
- [167] Q.-Q. Ouyang *et al.*, « Thermal degradation of agar: Mechanism and toxicity of products », *Food Chem.*, vol. 264, p. 277-283, oct. 2018, doi: 10.1016/j.foodchem.2018.04.098.
- [168] Y. Si, X. Wang, L. Dou, J. Yu, et B. Ding, « Ultralight and fire-resistant ceramic nanofibrous aerogels with temperature-invariant superelasticity », *Sci. Adv.*, vol. 4, n° 4, p. eaas8925, avr. 2018, doi: 10.1126/sciadv.aas8925.
- [169] C. Safi *et al.*, « Effect of Chitosan on Alginate-Based Macroporous Hydrogels for the Capture of Glioblastoma Cancer Cells », *ACS Appl. Bio Mater.*, vol. 5, n° 9, p. 4531-4540, sept. 2022, doi: 10.1021/acsbm.2c00598.
- [170] A. G. Solano *et al.*, « An alginate-based macroporous hydrogel matrix to trap cancer cells », *Carbohydr. Polym.*, vol. 266, p. 118115, août 2021, doi: 10.1016/j.carbpol.2021.118115.
- [171] C. K. Kuo et P. X. Ma, « Maintaining dimensions and mechanical properties of ionically crosslinked alginate hydrogel scaffolds in vitro », *J. Biomed. Mater. Res. A*, vol. 84A, n° 4, p. 899-907, 2008, doi: 10.1002/jbm.a.31375.
- [172] Q. Wu, W. Miao, Y. Zhang, H. Gao, et D. Hui, « Mechanical properties of nanomaterials: A review », *Nanotechnol. Rev.*, vol. 9, n° 1, p. 259-273, janv. 2020, doi: 10.1515/ntrev-2020-0021.
- [173] C. Thongchom *et al.*, « An Experimental Study on the Effect of Nanomaterials and Fibers on the Mechanical Properties of Polymer Composites », *Buildings*, vol. 12, n° 1, Art. n° 1, janv. 2022, doi: 10.3390/buildings12010007.
- [174] V. H. R. Souza, E. Flahaut, et A. J. G. Zarbin, « Conducting, transparent and flexible substrates obtained from interfacial thin films of double-walled carbon nanotubes », *J. Colloid Interface Sci.*, vol. 502, p. 146-152, sept. 2017, doi: 10.1016/j.jcis.2017.04.084.
- [175] W. Bauhofer et J. Z. Kovacs, « A review and analysis of electrical percolation in carbon nanotube polymer composites », *Compos. Sci. Technol.*, vol. 69, n° 10, Art. n° 10, août 2009, doi: 10.1016/j.compscitech.2008.06.018.
- [176] M. D. Lima, M. J. Andrade, V. Skákalová, C. P. Bergmann, et S. Roth, « Dynamic percolation of carbon nanotubes in liquid medium », *J. Mater. Chem.*, vol. 17, n° 46, Art. n° 46, 2007, doi: 10.1039/B710417K.
- [177] G. Kougkoulos, M. Golzio, L. Laudebat, Z. Valdez-Nava, et E. Flahaut, « Hydrogels with electrically conductive nanomaterials for biomedical applications », *J. Mater. Chem. B*, vol. 11, n° 10, p. 2036-2062, mars 2023, doi: 10.1039/D2TB02019J.
- [178] V. Tishkova *et al.*, « Electrical conductivity and Raman imaging of double wall carbon nanotubes in a polymer matrix », *Compos. Sci. Technol.*, vol. 71, n° 10, p. 1326-1330, juill. 2011, doi: 10.1016/j.compscitech.2011.05.001.
- [179] H. Lee, S. M. Dellatore, W. M. Miller, et P. B. Messersmith, « Mussel-Inspired Surface Chemistry for Multifunctional Coatings », *Science*, vol. 318, n° 5849, p. 426-430, oct. 2007, doi: 10.1126/science.1147241.



- [180] Y. Liang, X. Zhao, T. Hu, Y. Han, et B. Guo, « Mussel-inspired, antibacterial, conductive, antioxidant, injectable composite hydrogel wound dressing to promote the regeneration of infected skin », *J. Colloid Interface Sci.*, vol. 556, p. 514-528, nov. 2019, doi: 10.1016/j.jcis.2019.08.083.
- [181] J. H. Ryu, P. B. Messersmith, et H. Lee, « Polydopamine Surface Chemistry: A Decade of Discovery », *ACS Appl. Mater. Interfaces*, vol. 10, n° 9, p. 7523-7540, mars 2018, doi: 10.1021/acsami.7b19865.
- [182] L. Han *et al.*, « A Mussel-Inspired Conductive, Self-Adhesive, and Self-Healable Tough Hydrogel as Cell Stimulators and Implantable Bioelectronics », *Small*, vol. 13, n° 2, p. 1601916, 2017, doi: 10.1002/smll.201601916.
- [183] H. Coskun *et al.*, « Chemical vapor deposition - based synthesis of conductive polydopamine thin-films », *Thin Solid Films*, vol. 645, p. 320-325, janv. 2018, doi: 10.1016/j.tsf.2017.10.063.
- [184] M. Trudicova *et al.*, « Multiscale Experimental Evaluation of Agarose-Based Semi-Interpenetrating Polymer Network Hydrogels as Materials with Tunable Rheological and Transport Performance », *Polymers*, vol. 12, n° 11, p. 2561, oct. 2020, doi: 10.3390/polym12112561.
- [185] J. Narayanan, J.-Y. Xiong, et X.-Y. Liu, « Determination of agarose gel pore size: Absorbance measurements vis a vis other techniques », *J. Phys. Conf. Ser.*, vol. 28, n° 1, p. 83, janv. 2006, doi: 10.1088/1742-6596/28/1/017.
- [186] S. Ahadian *et al.*, « Hybrid hydrogel-aligned carbon nanotube scaffolds to enhance cardiac differentiation of embryoid bodies », *Acta Biomater.*, vol. 31, p. 134-143, févr. 2016, doi: 10.1016/j.actbio.2015.11.047.
- [187] M. Mohiuddin et S. V. Hoa, « Temperature dependent electrical conductivity of CNT-PEEK composites », *Compos. Sci. Technol.*, vol. 72, n° 1, p. 21-27, déc. 2011, doi: 10.1016/j.compscitech.2011.08.018.
- [188] D. M. Gray, T. Associates, et A. C. Bevilacqua, « CATION CONDUCTIVITY TEMPERATURE COMPENSATION », présenté à International Water Conference, Pittsburgh, PA, USA, 1997.
- [189] S. Wang, A. Lu, et C.-J. Zhong, « Hydrogen production from water electrolysis: role of catalysts », *Nano Converg.*, vol. 8, n° 1, p. 4, févr. 2021, doi: 10.1186/s40580-021-00254-x.
- [190] A. C. Ortiz, « Epoxy-based SiC micro- and nano-composites with nonlinear electrical properties for electric field grading applications : an experimental and modeling study », phdthesis, Université Paul Sabatier - Toulouse III, 2022. Consulté le: 21 septembre 2023. [En ligne]. Disponible sur: <https://theses.hal.science/tel-03924726>
- [191] C. Kohlfürst, F. Queisser, et R. Schützhold, « Dynamically assisted tunneling in the impulse regime », *Phys. Rev. Res.*, vol. 3, n° 3, p. 033153, août 2021, doi: 10.1103/PhysRevResearch.3.033153.
- [192] J. Ramón-Azcón *et al.*, « Dielectrophoretically Aligned Carbon Nanotubes to Control Electrical and Mechanical Properties of Hydrogels to Fabricate Contractile Muscle Myofibers », *Adv. Mater.*, vol. 25, n° 29, Art. n° 29, 2013, doi: 10.1002/adma.201301300.
- [193] A. Ivorra, « Tissue Electroporation as a Bioelectric Phenomenon: Basic Concepts », in *Irreversible Electroporation*, B. Rubinsky, Éd., in Series in Biomedical Engineering. , Berlin, Heidelberg: Springer, 2010, p. 23-61. doi: 10.1007/978-3-642-05420-4\_2.
- [194] S. Gabriel, R. W. Lau, et C. Gabriel, « The dielectric properties of biological tissues: III. Parametric models for the dielectric spectrum of tissues », *Phys. Med. Biol.*, vol. 41, n° 11, p. 2271, nov. 1996, doi: 10.1088/0031-9155/41/11/003.
- [195] H. S. Hershkovich, N. Urman, O. Yesharim, A. Naveh, et Z. Bomzon, « The dielectric properties of skin and their influence on the delivery of tumor treating fields to the torso: a study combining in vivo measurements with numerical simulations », *Phys. Med. Biol.*, vol. 64, n° 18, p. 185014, sept. 2019, doi: 10.1088/1361-6560/ab33c6.
- [196] G. R. Doyle et J. A. McCutcheon, « 7.3 Intradermal and Subcutaneous Injections », nov. 2015, Consulté le: 30 septembre 2023. [En ligne]. Disponible sur:

<https://opentextbc.ca/clinicalskills/chapter/6-7-intradermal-subcutaneous-and-intramuscular-injections/>

- [197] I. Usach, R. Martinez, T. Festini, et J.-E. Peris, « Subcutaneous Injection of Drugs: Literature Review of Factors Influencing Pain Sensation at the Injection Site », *Adv. Ther.*, vol. 36, n° 11, p. 2986-2996, 2019, doi: 10.1007/s12325-019-01101-6.
- [198] B. Paldus, M. H. Lee, et D. N. O'Neal, « Insulin pumps in general practice », *Aust. Prescr.*, vol. 41, n° 6, p. 186-190, déc. 2018, doi: 10.18773/austprescr.2018.056.
- [199] T. J. Church et S. T. Haines, « Treatment Approach to Patients With Severe Insulin Resistance », *Clin. Diabetes Publ. Am. Diabetes Assoc.*, vol. 34, n° 2, p. 97-104, avr. 2016, doi: 10.2337/diaclin.34.2.97.
- [200] N. Ichinose et H. Ura, « Concentration dependence of the sol-gel phase behavior of agarose-water system observed by the optical bubble pressure tensiometry », *Sci. Rep.*, vol. 10, n° 1, Art. n° 1, févr. 2020, doi: 10.1038/s41598-020-58905-8.
- [201] U. Pliquett, R. Langer, et J. C. Weaver, « Changes in the passive electrical properties of human stratum corneum due to electroporation », *Biochim. Biophys. Acta BBA - Biomembr.*, vol. 1239, n° 2, p. 111-121, nov. 1995, doi: 10.1016/0005-2736(95)00139-T.
- [202] U. F. Pliquett, G. T. Martin, et J. C. Weaver, « Kinetics of the temperature rise within human stratum corneum during electroporation and pulsed high-voltage iontophoresis », *Bioelectrochemistry Amst. Neth.*, vol. 57, n° 1, p. 65-72, juill. 2002, doi: 10.1016/s1567-5394(01)00177-3.
- [203] A. Pertovaara, T. Kauppila, et M. M. Hämäläinen, « Influence of skin temperature on heat pain threshold in humans », *Exp. Brain Res.*, vol. 107, n° 3, p. 497-503, janv. 1996, doi: 10.1007/BF00230429.
- [204] U. Pliquett, Ch. Gusbeth, et R. Nuccitelli, « A propagating heat wave model of skin electroporation », *J. Theor. Biol.*, vol. 251, n° 2, p. 195-201, mars 2008, doi: 10.1016/j.jtbi.2007.11.031.
- [205] S. Becker, « Transport Modeling of Skin Electroporation and the Thermal Behavior of the Stratum Corneum », *Int. J. Therm. Sci. - INT J THERM SCI*, vol. 54, janv. 2011, doi: 10.1016/j.ijthermalsci.2011.10.022.
- [206] N. Pavšelj et D. Miklavčič, « Resistive heating and electropermeabilization of skin tissue during in vivo electroporation: A coupled nonlinear finite element model », *Int. J. Heat Mass Transf.*, vol. 54, n° 11, p. 2294-2302, mai 2011, doi: 10.1016/j.ijheatmasstransfer.2011.02.035.
- [207] A. Bulysheva *et al.*, « Coalesced thermal and electrotransfer mediated delivery of plasmid DNA to the skin », *Bioelectrochemistry Amst. Neth.*, vol. 125, p. 127-133, févr. 2019, doi: 10.1016/j.bioelechem.2018.10.004.
- [208] A. Can-Ortiz, L. Laudebat, Z. Valdez-Nava, et S. Diahm, « Nonlinear Electrical Conduction in Polymer Composites for Field Grading in High-Voltage Applications: A Review », *Polymers*, vol. 13, n° 9, Art. n° 9, janv. 2021, doi: 10.3390/polym13091370.
- [209] E. Karimi-Sibaki, A. Kharicha, M. Wu, A. Ludwig, et J. Bohacek, « Confrontation of the Ohmic approach with the ionic transport approach for modeling the electrical behavior of an electrolyte », *Ionics*, vol. 24, n° 7, p. 2157-2165, juill. 2018, doi: 10.1007/s11581-018-2460-3.
- [210] J. H. Lee *et al.*, « In vivo electrical conductivity measurement of muscle, cartilage, and peripheral nerve around knee joint using MR-electrical properties tomography », *Sci. Rep.*, vol. 12, n° 1, Art. n° 1, janv. 2022, doi: 10.1038/s41598-021-03928-y.
- [211] M. J. Peters, J. G. Stinstra, et I. Leveles, « The Electrical Conductivity of Living Tissue: A Parameter in the Bioelectrical Inverse Problem », in *Modeling and Imaging of Bioelectrical Activity: Principles and Applications*, B. He, Éd., in Bioelectric Engineering, Boston, MA: Springer US, 2005, p. 281-319. doi: 10.1007/978-0-387-49963-5\_9.
- [212] G. Pucihar, T. Kotnik, J. Teissié, et D. Miklavčič, « Electropermeabilization of dense cell suspensions », *Eur. Biophys. J.*, vol. 36, n° 3, p. 173-185, mars 2007, doi: 10.1007/s00249-006-0115-1.

- [213] S. M. Becker, « Skin Electroporation With Passive Transdermal Transport Theory: A Review and a Suggestion for Future Numerical Model Development », *J. Heat Transf.*, vol. 133, n° 1, sept. 2010, doi: 10.1115/1.4002362.
- [214] N. Pavselj et D. Miklavcic, « A Numerical Model of Permeabilized Skin With Local Transport Regions », *IEEE Trans. Biomed. Eng.*, vol. 55, n° 7, p. 1927-1930, juill. 2008, doi: 10.1109/TBME.2008.919730.
- [215] J. Dermol-Černe et D. Miklavčič, « From Cell to Tissue Properties—Modeling Skin Electroporation With Pore and Local Transport Region Formation », *IEEE Trans. Biomed. Eng.*, 2018, doi: 10.1109/TBME.2017.2773126.
- [216] L. Finlayson *et al.*, « Depth Penetration of Light into Skin as a Function of Wavelength from 200 to 1000 nm », *Photochem. Photobiol.*, vol. 98, n° 4, p. 974-981, 2022, doi: 10.1111/php.13550.
- [217] F. Le Guern, V. Mussard, A. Gaucher, M. Rottman, et D. Prim, « Fluorescein Derivatives as Fluorescent Probes for pH Monitoring along Recent Biological Applications », *Int. J. Mol. Sci.*, vol. 21, n° 23, p. 9217, déc. 2020, doi: 10.3390/ijms21239217.
- [218] J. Coppeta et C. Rogers, « Dual emission laser induced fluorescence for direct planar scalar behavior measurements », *Exp. Fluids*, vol. 25, n° 1, p. 1-15, juin 1998, doi: 10.1007/s003480050202.
- [219] T. Mauro *et al.*, « Barrier recovery is impeded at neutral pH, independent of ionic effects: implications for extracellular lipid processing », *Arch. Dermatol. Res.*, vol. 290, n° 4, p. 215-222, avr. 1998, doi: 10.1007/s004030050293.

## 9 Annexes

<b>9</b>	<b>ANNEXES.....</b>	<b>180</b>
9.1	POTENTIAL DIFFERENCE ACROSS SKIN .....	180
9.2	CONDUCTIVITY OF HYDROGELS AND WET GAUZE IN PEF CONDITIONS .....	181
9.3	CV AND SCIENTIFIC PRODUCTION .....	182
9.3.1	<i>Publications – Conferences.....</i>	182
9.3.2	<i>Teaching – supervision .....</i>	182
9.3.3	<i>Other activities .....</i>	182
9.3.4	<i>CV (en français) .....</i>	183
9.4	COMIC STRIP.....	184

### 9.1 Potential difference across skin

We employed our numerical model (**5.3 Third model: 3D with nonlinear conductivity**) to calculate the potential difference across the skin within our specific setup. Our calculations indicated that a 100 V PEF would result in an estimated potential difference of approximately 30 V across the skin. It's important to note that due to the non-uniform electric field resulting from the side-by-side electrode configuration, this estimation is approximate.

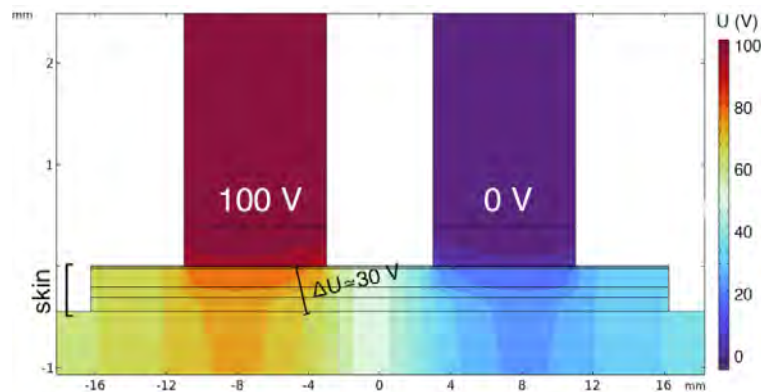


**Figure 9.1** – Potential difference across skin for 100 V PEF.

## 9.2 Conductivity of hydrogels and wet gauze in PEF conditions

A series of I – V experiments were carried out to determine the conductivity of the nanocomposite hydrogels and the wet gauze, in PEF conditions (**Figure 9.2**). The resistance of the drug delivery systems without the skin (hydrogels and wet gauze) was 300  $\Omega$ . The resistance of the wet gauze only was 200  $\Omega$ . For the nanocomposite hydrogels, this corresponded to a resistance of 50  $\Omega$  per hydrogel. Considering their geometry, the conductivity of the nanocomposite hydrogels during the PEFs was *ca.* 0.15 S/m, equivalent to the conductivity of the electroporation buffer with which they were loaded. For the wet gauze, the geometry alone was not enough to calculate the conductivity, because the electric field was not homogeneous. We made a FEM simulation of the wet gauze, with a thickness of 1 mm, and the two metal electrodes placed on top. Through the simulation, we obtained a conductivity of 1.7 S/m for the wet gauze. We corrected this conductivity to 1.5 S/m to match the conductivity of the phosphate buffer saline with which the gauze was wetted.

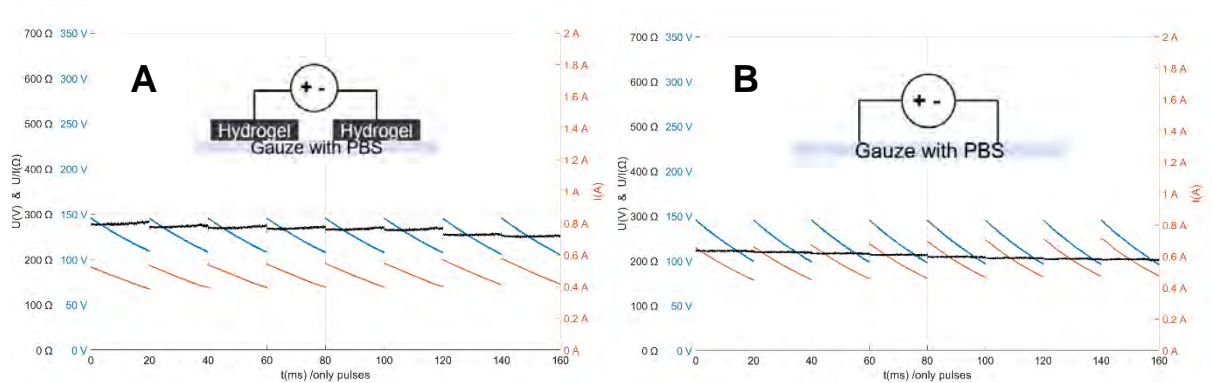


**Figure 9.2** – I – V measurements of drug delivery system without skin model, at 150 V PEF. (A) Hydrogels and wet gauze. (B) Wet gauze only.

## 9.3 CV and scientific production

### 9.3.1 Publications – Conferences

Nov 2021	Poster presentation at scientific workshop, <b>EBTT21 (Ljubljana, Slovenia)</b> <b>“Modelling of non-invasive drug delivery through skin electroporation”</b> - <b>Electroporation-Based Technologies and Treatments</b>
Jun 2022	<b>Oral presentation at national conference</b> , JCGE – SEEDS 22 (Le Croisic, France) “Physical modeling of non-invasive transdermal drug delivery through skin electroporation” - Conférence des Jeunes Chercheurs en Génie Electrique – GDR Systèmes d’énergie électrique dans leurs dimensions sociétales
Oct 2022	<b>Oral presentation at international conference</b> , 4WCE (Copenhagen, Denmark) “Physical modelling of non-invasive transdermal drug delivery through skin electroporation” - 4th World Congress on Electroporation & Pulsed Electric Fields in Biology, Medicine, Food and Environmental Technologies
Oct 2022	<b>Oral presentation at international francophone conference</b> , Matériaux 2022 (Lille, France) “Hydrogel nanocomposite conducteur électrique pour l’administration transdermique de médicaments” - conférence internationale de Matériaux
Feb 2023	<b>Publication of review article at scientific journal</b> “Hydrogels with electrically conductive nanomaterials for biomedical applications” - Journal of Materials Chemistry B (IF 7.6) doi: <a href="https://doi.org/10.1039/D2TB02019J">10.1039/D2TB02019J</a>
Oct 2023 (ongoing)	<b>Publication of research article at scientific journal</b> “Non-invasive drug delivery through skin electroporation: coupling electrical measurements with numerical modeling and molecule delivery” The article will be submitted soon.

### 9.3.2 Teaching – supervision

Apr 2021 - Jun 2021	Supervision of intern DUT Physical Measurements <b>“Electrical characterization of nanocomposites for electro-stimulated transdermal drug delivery”</b>
Oct 2021- Dec 2021	<b>Preparation and teaching at tutor group (TD)</b> , <i>Faculté Sciences et Ingénierie, UPS</i> (Toulouse, France) “Solid chemistry” - Licence 1 Sciences numériques
Apr 2022 - Jun 2022	<b>Supervision of two interns Master 1 Materials science and engineering</b> “Preparation of nanocomposite hydrogels and evaluation of their electrical properties”
Feb 2022 - May 2022 & Feb 2023 - May 2023	<b>Preparation and teaching of lab classes (TP)</b> , <i>Faculté Sciences et Ingénierie, UPS</i> (Toulouse, France) “Polymer materials” - Licence 3 Chimie Parcours Matériaux

### 9.3.3 Other activities

Nov 2022 - Dec 2022	Research internship, <b>Polytechnique Montréal (Montréal, Canada)</b> <b>Alginate/chitosan hydrogels and agarose electrospinning for drug delivery</b>
Feb 2023 - Sep 2023	<b>Science vulgarisation - designs/illustrations</b> , ANR Connects
Sep 2023	<b>Science vulgarisation – animation</b> , European night of researchers (Cité de l’espace, Toulouse, France)



## 9.3.4 CV (en français)


### Georgios KOUKKOLOS

 gkoukol@live.com

 07 53 30 15 90

 6 boulevard des Minimes  
31200, Toulouse

 [www.researchgate.net/profile/  
Georgios-Koukoulos-2](http://www.researchgate.net/profile/Georgios-Koukoulos-2)

 [www.orcid.org/  
0000-0001-6677-3514](http://www.orcid.org/0000-0001-6677-3514)

### Profil

Doctorant avec expérience de recherche et d'enseignement. Diplômé en génie chimique avec une spécialisation en science des matériaux et en applications biomédicales. Très autonome, capable de prendre des initiatives, de travailler de manière indépendante et en groupe, et de résoudre des problèmes avec une approche pluridisciplinaire.

### Compétences informatiques

MatLab, COMSOL Multiphysics,  
Origin Pro, ImageJ, MS Office Suite

Blender, Adobe Photoshop  
et Illustrator

### Langues

Anglais (bilingue)  
Français (indépendant)  
Grec (natale)

### Loisirs / Autres

Permis A et B, vélo  
musique (batterie), photographie,  
graphisme, lecture, écriture

### Éducation

2020 - **Doctorat en chimie des matériaux et biophysique**, intitulé « Modélisation physique de la délivrance transdermique électro-stimulée des médicaments ». *CIRIMAT, LAPLACE, IPBS, Université Toulouse III – Paul Sabatier*

2018 - **Master en Ingénierie des membranes** – Biotechnologies, santé et alimentation  
2020 *Université de Montpellier, Université Toulouse III, Université de Chimie et Technologie (Prague, CZ), Nouvelle université de Lisbonne (PT), INSA (Toulouse, FR)*

2011 - **Diplôme en génie chimique**, *Université Aristote de Thessalonique (GR)*  
2017

### Expérience

oct 2020 - **Thèse, Centre Inter-universitaire de Recherche et d'Ingénierie des Matériaux (CIRIMAT), Laboratoire plasma et conversion d'énergie (LAPLACE), Institut de Pharmacologie et Biologie Structurale (IPBS) (Toulouse, FR)**

« Modélisation physique de la délivrance transdermique électro-stimulée des médicaments »  
Préparation et caractérisation des hydrogels nanocomposites, Nanomatériaux carbonés (synthèse, caractérisation, dispersion), Caractérisations électriques (spectroscopie d'impédance, conductivité DC), Simulations numériques FEM, Expériences ex vivo avec des peaux de souris, Microscopie de fluorescence, Electroporation de la peau

oct 2021 - **Enseignement** comme Doctorant Contractuel Chargé d'Enseignement (DCCE),  
mai 2023 *Faculté Sciences et Ingénierie, UPS (Toulouse, FR)*

Préparation et encadrement de Travaux Pratiques, « Matériaux Polymères » - Licence 3 Chimie Parcours Matériaux (64h), Préparation et encadrement de Travaux Dirigés, « Chimie du Solide » - Licence 1 Sciences numériques (32h)

jan 2020 - **Mémoire/Stage de Master 2, Toulouse Biotechnology Institute (TBI), Institut de Pharmacologie et Biologie Structurale (IPBS) (Toulouse, FR)**

« Étude de la réponse de la paroi et de la membrane cellulaire de *S. Cerevisiae* sous champ électrique pulsé »

Biophysique et biologie cellulaire, Electroporation, Microscopie optique (champ clair, contraste de phase, fluorescence), Microbiologie (travail en milieu aseptique, inoculation), Biologie moléculaire (PCR, électrophorèse d'ADN et des protéines)

oct 2017 - **Stage, Institut de l'ingénierie médicale appliqué, RWTH Université Aachen (DE)**

jan 2018 « Nouvelles approches sur le traitement de l'intoxication par monoxyde de carbone »

Expériences d'échange de gaz, Tomodensitométrie et bio-impression 3D, Mesures PIV pour la simulation de l'écoulement sanguin

fev 2017 - **Mémoire de fin d'études, Université Aristote de Thessalonique (GR)**

sep 2017 « Étude de l'effet de la viscosupplémentation sur les propriétés biomécaniques du liquide synovial équin, obtenu à partir d'articulations saines »

Mesures rhéologiques (modules de conservation et dissipation, courbes contrainte-déformation, balayage de fréquence)

### Publications - Conférences

fev 2023 **Publication d'article** de revue en journal scientifique

"Hydrogels with electrically conductive nanomaterials for biomedical applications"  
- *Journal of Materials Chemistry B* (IF 7.6) doi: 10.1039/D2TB02019J

oct 2022 **Présentation orale** en conférence internationale, 4WCE (Copenhague, DK)

"Physical modelling of non-invasive transdermal drug delivery through skin electroporation"  
- 4th World Congress on Electroporation & Pulsed Electric Fields in Biology, Medicine, Food and Environmental Technologies

oct 2022 **Présentation orale** en conférence internationale francophone, Matériaux 2022 (Lille, FR)

« Hydrogel nanocomposite conducteur électrique pour l'administration transdermique de médicaments » - conférence internationale de Matériaux

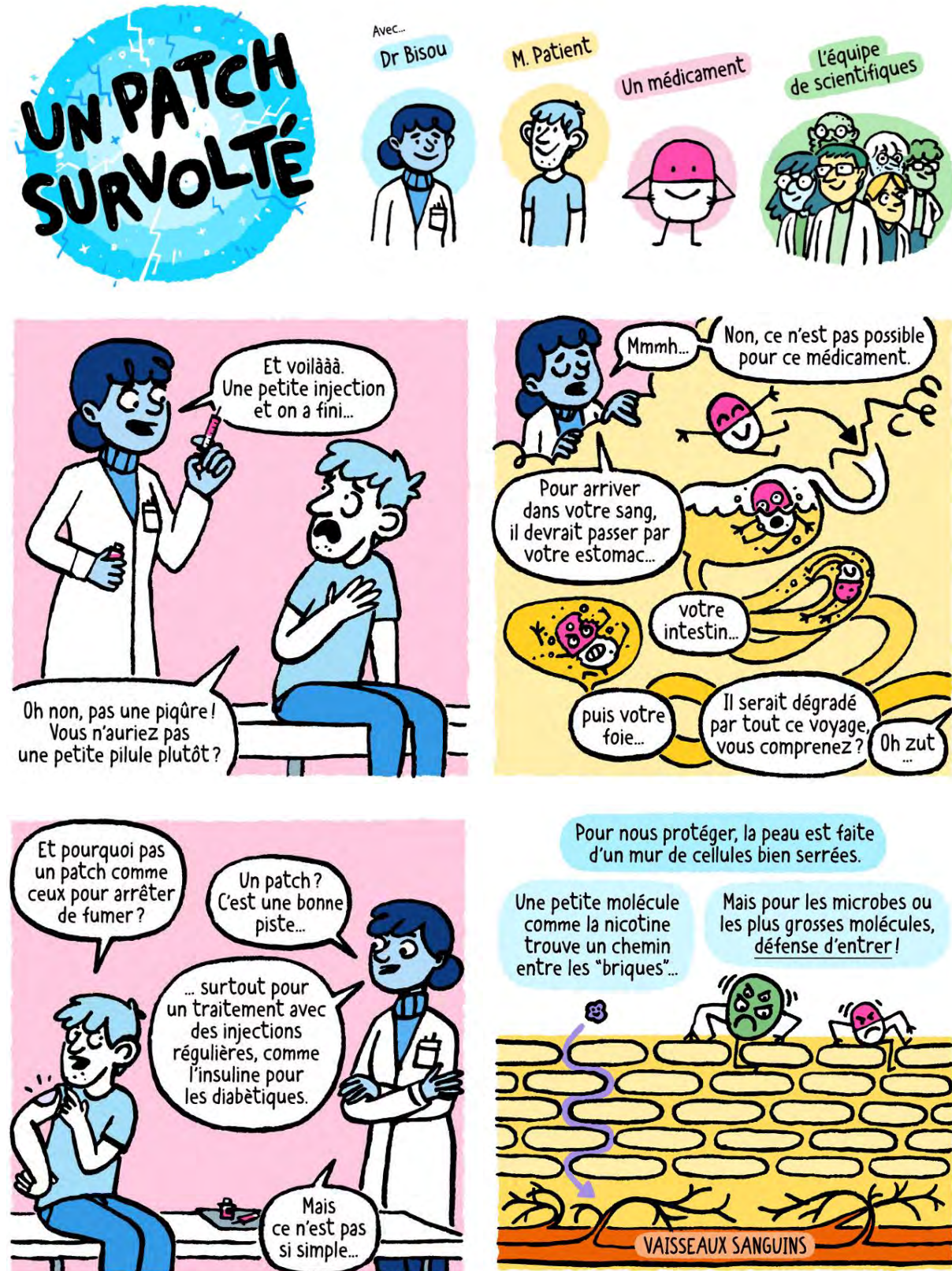
juin 2022 **Présentation orale** en conférence nationale, JCGE – SEEDS 22 (Le Croisic, FR)

"Physical modelling of non-invasive transdermal drug delivery through skin electroporation"  
- Conférence des Jeunes Chercheurs en Génie Electrique – GDR Systèmes d'énergie électrique dans leurs dimensions sociétales



## 9.4 Comic strip

We created a comic strip that summarized the research project for a general audience (in French), in collaboration with the [explorer](#) team from University of Toulouse and designer [Perceval Barrier](#).

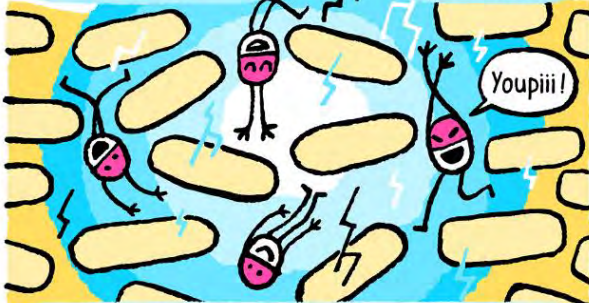




Pour passer ce mur sans abîmer la peau, des scientifiques misent sur une technique: "l'électroporation".

On applique sur la peau un champ électrique très bref...

... ce qui la rend temporairement perméable.



De plus grandes molécules ont alors le temps de passer entre les briques pour atteindre directement le sang.

Cette technique pourrait être proposée sous la forme d'un patch conducteur "2 en 1" servant à la fois d'électrode et de réservoir pour le médicament.



Le patch serait relié à une batterie de la taille d'une montre.



C'est parfait, alors faites-moi ça plutôt!

Un instant, j'appelle le labo.

Oui, bonjour Yorgos, mon patient est très intéressé par votre patch à électroporation, est-ce qu'il fonctionne bien?



Hum... presque! Nous obtenons déjà des résultats très positifs sur la peau artificielle.

BIOLOGISTE

PHYSICIENNE

Ça sent le cramé non?

CHIMISTE

Vérifiez le réglage, le champ électrique était un peu fort...

Les scientifiques doivent encore s'assurer de l'efficacité et de la sécurité de cette technique médicale...



Entendu, je vais le lui dire... Merci et bonne journée!

Désolée Monsieur, mais aujourd'hui ce sera une petite piqûre!

Il faudra encore être un peu patient avant que ce patch prometteur soit disponible...



Cite this: *J. Mater. Chem. B*, 2023, 11, 2036

## Hydrogels with electrically conductive nanomaterials for biomedical applications†

Georgios Kougkolos,<sup>ab</sup> Muriel Golzio,<sup>c</sup> Lionel Laudebat,<sup>bd</sup> Zarel Valdez-Nava<sup>bd\*</sup> and Emmanuel Flahaut<sup>bd\*</sup>

Hydrogels, soft 3D materials of cross-linked hydrophilic polymer chains with a high water content, have found numerous applications in biomedicine because of their similarity to native tissue, biocompatibility and tuneable properties. In general, hydrogels are poor conductors of electric current, due to the insulating nature of commonly-used hydrophilic polymer chains. A number of biomedical applications require or benefit from an increased electrical conductivity. These include hydrogels used as scaffolds for tissue engineering of electroactive cells, as strain-sensitive sensors and as platforms for controlled drug delivery. The incorporation of conductive nanomaterials in hydrogels results in nanocomposite materials which combine electrical conductivity with the soft nature, flexibility and high water content of hydrogels. Here, we review the state of the art of such materials, describing the theories of current conduction in nanocomposite hydrogels, outlining their limitations and highlighting methods for improving their electrical conductivity.

Received 22nd September 2022,  
Accepted 3rd February 2023

DOI: 10.1039/d2tb02019j

rsc.li/materials-b

<sup>a</sup> CIRIMAT, Université de Toulouse, CNRS, INPT, UPS, 31062 Toulouse CEDEX 9, France. E-mail: emmanuel.flahaut@univ-tlse3.fr

<sup>b</sup> LAPLACE, Université de Toulouse, CNRS, INPT, UPS, 31062 Toulouse CEDEX 9, France. E-mail: zarel.valdez-nava@laplace.univ-tlse.fr

<sup>c</sup> IPBS, Université de Toulouse, NRS UMR, UPS, 31077 Toulouse CEDEX 4, France

<sup>d</sup> INU Champollion, Université de Toulouse, 81012 Albi, France

† Electronic supplementary information (ESI) available. See DOI: <https://doi.org/10.1039/d2tb02019j>

## 1. Introduction

### 1.1 Hydrogels

Hydrogels are three-dimensional, viscoelastic networks of hydrophilic polymer chains, cross-linked in an aqueous environment. The water-polymer network is gelled through the association of polymer chains to form a continuous structure, that immobilises water within it and becomes resistant to



From left to right: Georgios Kougkolos, Muriel Golzio, Lionel Laudebat, Zarel Valdez-Nava and Emmanuel Flahaut

Emmanuel Flahaut is a senior CNRS researcher in materials science. His research is focused on the synthesis and functionalization of carbon nanomaterials as well as their application in various fields ranging from materials science to biomedicine. All are affiliated to the University of Toulouse, France. They are all partners of a National (ANR) project on non-invasive drug delivery through skin electroporation, involving electrically conductive nanocomposite hydrogels.

Georgios Kougkolos is pursuing a PhD in materials science. His research interests lie in the interface between materials science and biomedicine and currently include nanocomposite hydrogels, drug delivery and electroporation.

Muriel Golzio is a senior CNRS researcher in biophysics. Her main research interests lie in the field of cell electroporation, nucleic acids electrotransfer and biomedical applications for cancer treatment and gene therapy.

Lionel Laudebat is an associate professor of electrical engineering and researcher. His main research interests include numerical simulation and modelling of power electronic materials and studies of dielectric materials. Zarel Valdez-Nava is a CNRS researcher in electrical engineering. His research concerns insulating and dielectric materials for high voltage and/or high temperature power electronics, focusing in identifying the relationship between processing and properties of composites and ceramics.





flow.<sup>1</sup> The association of polymer chains occurs through a variety of mechanisms that can be classified into physical or chemical. Mechanisms of physical cross-linking include the physical entanglement of individual polymer chains, typically induced by solubility alterations in response to temperature changes; macromolecular self-assembly through non-covalent bonding (hydrogen bonds, van der Waals forces, hydrophobic interactions); crystallization, the formation of microcrystals through a freeze-and-thaw process, which then act as a cross-linking site; ionic gelation, polymer chains surround ions forming a crosslinking site; and electrostatic interaction of polymer chains with opposite charges.<sup>2–5</sup> Chemical cross-linking involves the formation of covalent bonds between polymer chains through mechanisms including radical polymerization, chemical reactions of complementary groups (for example hydroxyl groups or amides with carboxylic acids), high energy irradiation, addition of chemical cross-linking agents (glutaraldehyde, epoxy compounds, isocyanates, metal ions) and enzymatic reactions.<sup>2–4,6</sup>

Physically cross-linked hydrogels are reversible, easy to produce and do not require the use of chemical cross-linking agents.<sup>3,4</sup> Chemically cross-linked hydrogels generally have higher mechanical strength and offer more possibilities for control of the cross-linking process and customised design.<sup>2,3</sup> However, they often make use of toxic cross-linkers which then have to be extracted to keep the hydrogel biocompatible.<sup>4</sup> The combination of physical and chemical cross-linking mechanisms offers the possibility for more precise control over the hydrogels' properties.<sup>2</sup>

Hydrogels can be further classified according to their polymeric composition as: (1) single polymer networks (homo-polymers), derived from one type of monomer unit; (2) copolymers, derived from the cross-linking of two or more types of monomers, arranged in alternating, block or random configuration on the polymer chain; (3) semi-interpenetrating polymer networks, where a linear polymer is contained within an independent, cross-linked polymer network; and (4) interpenetrating polymer networks, derived from two independent, cross-linked polymer networks interlocked together.<sup>4,5,7</sup> In each case, at least one of the monomers must be hydrophilic, to render the network water swellable.

Hydrogels are rich in water (typically 80 to 95% w/w but can span almost all range), flexible with viscoelastic behaviour and usually biocompatible.<sup>8–10</sup> These properties have fostered numerous applications in the domains of biomedicine, soft electronics and actuators.<sup>2</sup> Some of these properties can be straightforwardly modified to fit a specific application. For example, the rigidity and water content of hydrogels can be tuned by adjusting the polymer concentration and the cross-linking degree.<sup>11</sup> In an aqueous environment, a dynamic equilibrium exists between the interactions responsible for water sorption (capillary, osmotic and hydration forces) and the cross-linked polymer network resisting expansion.<sup>12</sup>

In addition, hydrogels can be highly responsive to external stimuli. Small changes in environmental conditions such as temperature, pH, pressure, electric field or chemical agents can induce unexpected and mostly reversible changes in hydrogel properties such as volume, swelling degree, conductivity or

permeability.<sup>13</sup> These stimuli-responsive or smart hydrogels can be engineered to sense external stimuli and transmit an electrical or optical signal, by modifying a readily readable property such as electrical conductivity or colour.<sup>13,14</sup> Many hydrogels used in motion sensing devices change their electrical conductivity when strained, giving an electrical signal to the device.<sup>13</sup> Hydrogel membranes can selectively allow the transfer of molecules by swelling to open or block their pores, according to biochemical signals.<sup>15</sup> More recently, 3D printing of hydrogels has opened new possibilities for customized design.<sup>16</sup>

Despite their remarkable properties and several possible applications, hydrogels have some important limitations. They generally have limited mechanical strength and are susceptible to irreversible deformation.<sup>17</sup> In addition, hydrogels from commonly used polymers intrinsically have very low electrical conductivity. These limitations make conventional hydrogels unsuitable for applications that require robustness or electrical conductivity.

## 1.2 Electrically conductive hydrogels

Electrical conductivity, in particular, is an important property of hydrogels in biomedical applications. Applications of electrically conductive hydrogels include hydrogels used as substrates for the growth of electroactive cells, hydrogels which function as flexible strain sensors for health monitoring and wearable devices and drug-loaded hydrogels used for electro-stimulated drug delivery.<sup>18</sup> There are three approaches to prepare electrically conductive hydrogels: (1) using a conducting polymer in the hydrogel matrix, (2) increasing the ionic conductivity of the aqueous phase and (3) incorporating a conductive material in the hydrogel.

Conducting polymers are organic macromolecules with intrinsic electrical conductivity. Conducting polymers commonly used for preparing hydrogels are polypyrrole (PPy), polyaniline (PANI) and poly-(3,4-ethylenedioxythiophene) (PEDOT).<sup>19</sup> They cannot form hydrogels themselves but have to be combined with a supporting polymer that provides hydrophilicity and mechanical strength.<sup>19</sup> They provide a conducting path of electronic conductivity due to the delocalized pi electrons of their conjugated systems, and can also increase the ionic conductivity of the aqueous phase by contributing ions.<sup>20,21</sup> Guo and Ma reviewed materials for tissue engineering with conducting polymers, including hydrogels<sup>22</sup> and Stejskal reviewed conducting polymer hydrogels with a focus on preparation methods.<sup>19</sup>

The ionic conductivity of the aqueous phase can be increased by preparing and/or swelling the hydrogel in an ion-rich aqueous solution. Free ions can be generated in water from acids, metal salts or ionic liquids.<sup>23</sup> Metal ions, in particular, can act both as cross-linking agents for polymer chains and electrolytes of ionic conductivity.<sup>24</sup> The cross-linking mechanism is metal-ligand interaction where the metal ions form coordinate covalent bonds with chelating agents (N, O, S) in the polymer chain.<sup>25</sup> In high concentrations, the free metal ions contribute to the ionic conductivity of the hydrogel.<sup>24</sup> Zhang *et al.* review the recent advances in metal ion hydrogels for biological applications.<sup>25</sup> Non-ionic polymer chains may impair the ionic conductivity of



hydrogels, compared to polyelectrolyte hydrogels.<sup>26</sup> Polyelectrolytes are polymers which contain ionic and/or ionizable groups in a substantial portion of their constitutional units.<sup>27</sup> They can be cationic, anionic or ampholytic (containing both negative and positive charges; also called zwitterionic, commonly when the positive and negative charges are located in the same pendant group).<sup>26,27</sup> In low concentration electrolyte solutions, polycationic and polyanionic hydrogels exhibit the highest ionic conductivity, due to high concentrations of mobile counterions. In high concentration electrolyte solutions, polyzwitterionic hydrogels promote fast ion dissociation and transport due to the highly charged polar side groups.<sup>26,28</sup> Wang *et al.* and Liu *et al.* reviewed polyelectrolyte<sup>29</sup> and polyzwitterionic<sup>30</sup> hydrogels for biomedical applications.

The incorporation of conductive materials aims to create a continuous network of electronic conduction throughout the hydrogel, through the dispersion of conductive nanomaterials and/or other conductive materials, such as metal microwires or carbon fibers, in the hydrogel framework.

The current review focuses on the incorporation of conductive nanomaterials in otherwise electrically insulating hydrogel polymer matrices. Each section is accompanied by illustrative examples of practical applications from the recent literature. Electrically conductive hydrogels are widely researched for applications in biomedicine and soft electronics including tissue engineering, strain sensors and controlled drug release (Fig. 1). In the following section, we present these practical applications and underline the relevance of electrical conductivity in each case. Section 2 lists the conductive nanomaterials commonly incorporated in hydrogels. In Sections 3–5 we delve into the electrical properties of nanocomposite hydrogels by

introducing electrical percolation, current conduction mechanisms and experimental electrical characterization techniques. Lastly, section 6 includes a comprehensive table and graph of conductive nanocomposite hydrogels and a discussion on some processing methods that can improve electrical conductivity.

### 1.3 Applications

**1.3.1 Tissue engineering.** Tissue engineering aims to develop artificial tissue and organs to restore functions of injured or malfunctioning organs *in vivo*, by cultivating cells on suitable substrates.<sup>31</sup> Hydrogels are particularly adequate as substrates because they can be biocompatible and biodegradable, have a similar water content and stiffness as natural organs and their porosity allows for sufficient nutrient transfer to the growing cells (Fig. 2).<sup>32,33</sup> The substrate is responsible for cell adhesion, proliferation and differentiation, functions physiologically performed by the extracellular matrix, the scaffold that provides structural and biochemical support to surrounding cells.<sup>34</sup>

Electrical conduction plays an important role in cell signalling and affects the differentiation and proliferation of cells. In particular, muscle and neural cells are excitable; they use rapid changes in membrane potential for cell-to-cell communication. Muscle tissue cells can contract, in response to electrical signals. Thus, substrates with an electrical conductivity near the conductivity of the native muscle deliver the most promising results.<sup>35</sup>

Navaei *et al.* developed a conductive, nanocomposite hydrogel to act as a cardiac tissue substrate for myocardial regeneration and repair. They synthesized gold nanorods which were incorporated into a methacrylated gelatin prepolymer solution and cross-linked it through UV radiation. A concentration of  $1.5 \text{ mg ml}^{-1}$  of gold nanorods reduced the electrical impedance of the hydrogel (measured by impedance spectroscopy) and improved both cell–cell signalling and electrical signal propagation on cells growing on the substrate, compared to the pristine hydrogel. This resulted in an improved cardiac tissue contractility with a lower excitation threshold (Fig. 3(A)).<sup>36</sup> Dong *et al.* reviewed the conductive biomaterials employed in muscle tissue engineering<sup>35</sup> while a review article of Li *et al.*

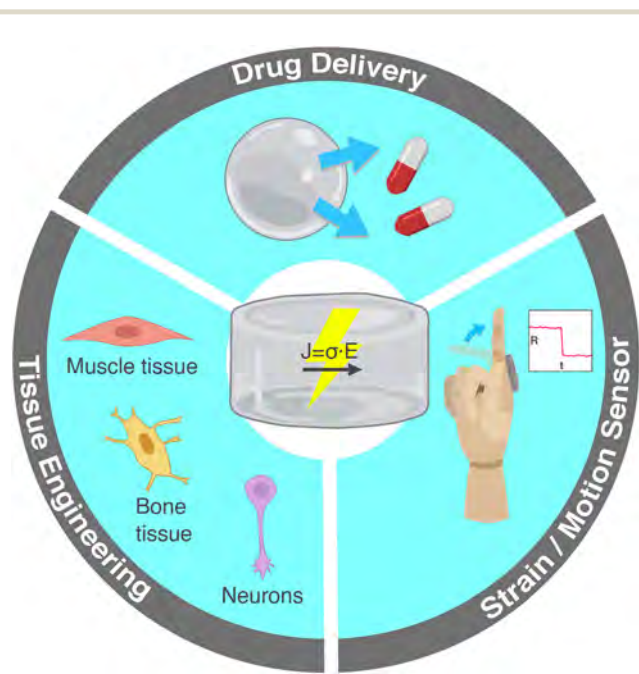


Fig. 1 Main applications of hydrogels with electrically conductive nanomaterials: tissue engineering of electroactive cells, controlled drug delivery and strain sensors for human motion monitoring.

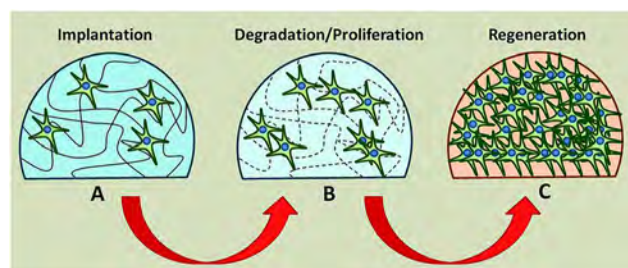


Fig. 2 Biodegradable hydrogel as a substrate for tissue regeneration. (A) Stem cells seeded on hydrogel. (B) Hydrogel degrades while cells proliferate and secrete their extracellular matrix. (C) Hydrogel has completely degraded leaving in place a new tissue composed of tissue and extracellular matrix. Reproduced from ref. 32 with permission from The Royal Society of Chemistry.





focused on the conductive biomaterials employed for cardiac repair.<sup>37</sup>

Nerve tissue is comprised of electroactive neural cells that transmit electrochemical signals. Conductive scaffolds, enhance the cellular activity and tissue regeneration of neural cells, compared to non-conductive substrates.<sup>38</sup> Liu *et al.* chemically cross-linked reduced graphene oxide (rGO) sheets and carbon nanotube (CNT) poly(ethylene glycol) acrylate to oligo(poly ethylene glycol) fumarate hydrogels, increasing their electrical conductivity from  $2 \times 10^{-4} \text{ S m}^{-1}$  to  $7.9 \times 10^{-4} \text{ S m}^{-1}$ . The nanoengineered conductive hydrogel was biocompatible and led to a higher proliferation of PC12 cells and increased neurite development (Fig. 3(B)).<sup>39</sup>

Bone regeneration and remodelling involves electrical fields generated by intrinsic piezoelectric properties of the bone tissue.<sup>33</sup>

Additionally, bone cell tissue engineering requires scaffolds with high mechanical strength to stimulate the differentiation of osteocytes.<sup>40</sup> Pelto *et al.* fabricated polylactide scaffolds to serve as a substrate for osteogenic differentiation and coated them with electrically conductive polypyrrole. The electrically conductive scaffold increased significantly the differentiation of human adipose stem cells compared to the insulating one.<sup>41</sup>

**1.3.2 Strain sensors.** Flexible and soft strain sensors are used in wearable devices that detect motion or pressure. This is relevant in the fields of health monitoring, prosthetics, soft robotics, electronic skin and human-machine communication.<sup>42</sup> Stimuli-responsive hydrogels are ideal materials for these applications because of their flexibility, stretchability, self-healing ability and biocompatibility.<sup>13,43</sup> Electrical conductivity is a readily measurable property of hydrogels and can be directly translated to electronic

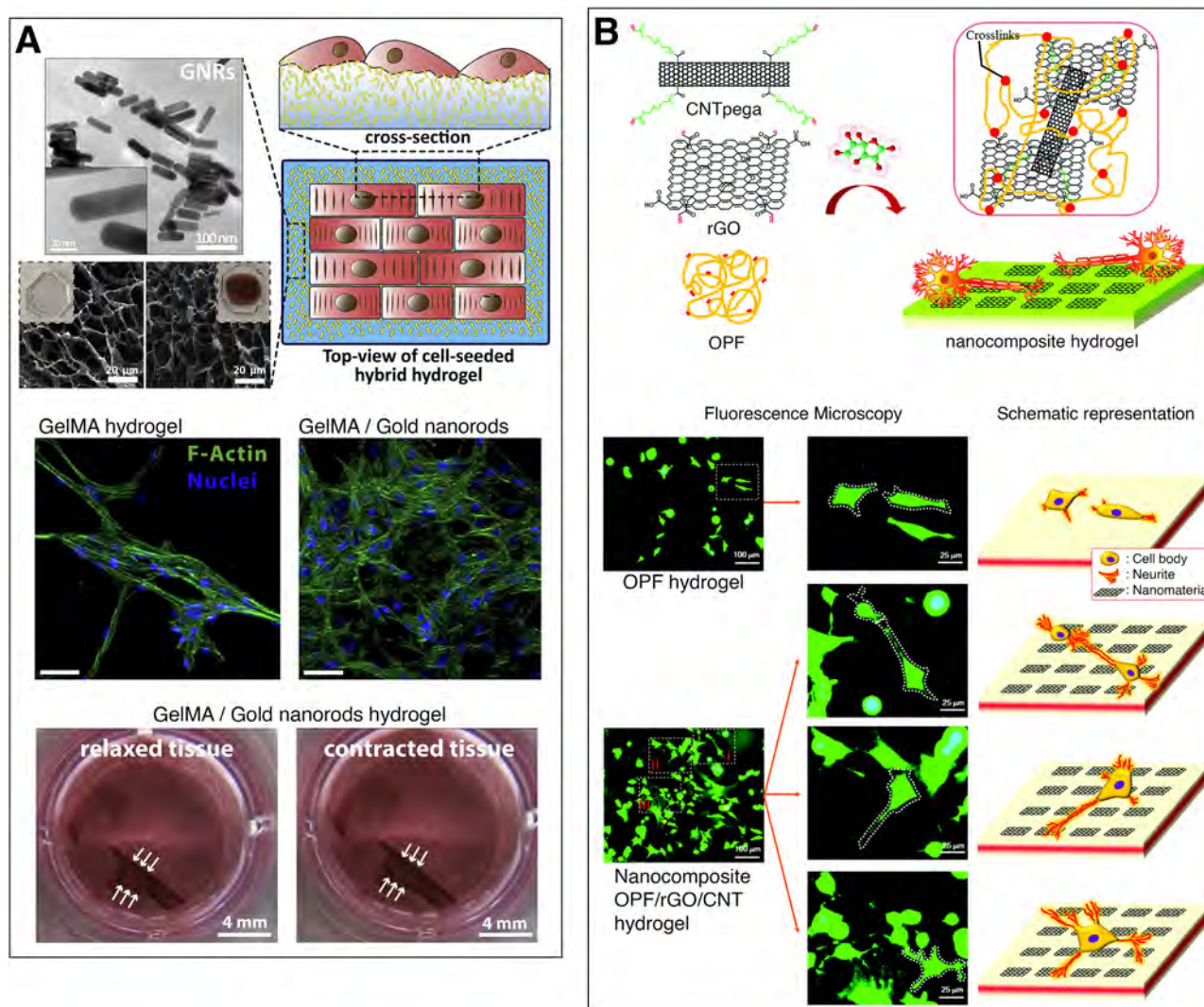


**Fig. 3** Electrically conducting hydrogels for tissue engineering. (A) Gelatin methacrylate hydrogel with gold nanorods for myocardial regeneration. The nanocomposite hydrogels illustrate highly packed cardiomyocytes with local alignment of fibers. A cell-loaded nanocomposite hydrogel displays contraction of the full hydrogel. Adapted from ref. 36, Copyright 2016, with permission from Elsevier. (B) Oligo(poly ethylene glycol) fumarate hydrogel with CNTs and rGO for neural tissue engineering. Fluorescence microscopy images and schemes of PC12 cells growing on plain and nanocomposite hydrogel, showing that neural cells growing on conductive substrates exhibit increased neurite development. Adapted from ref. 39 with permission from The Royal Society of Chemistry.



signals. Thus, strain-sensitive, electrically conductive hydrogels are extensively studied for their use as motion sensors.<sup>16</sup>

Xia *et al.* fabricated a conductive polyacrylamide/chitosan hydrogel with carboxylated multi-wall CNTs that functions as a

wearable, self-healable and adhesive sensor (Fig. 4(A)).<sup>44</sup> The incorporation of 1% w/w CNTs increased the conductivity of the hydrogel from 0.1 to 0.95 S m<sup>-1</sup> and more importantly improved the strain sensitivity of the hydrogel (the ratio of

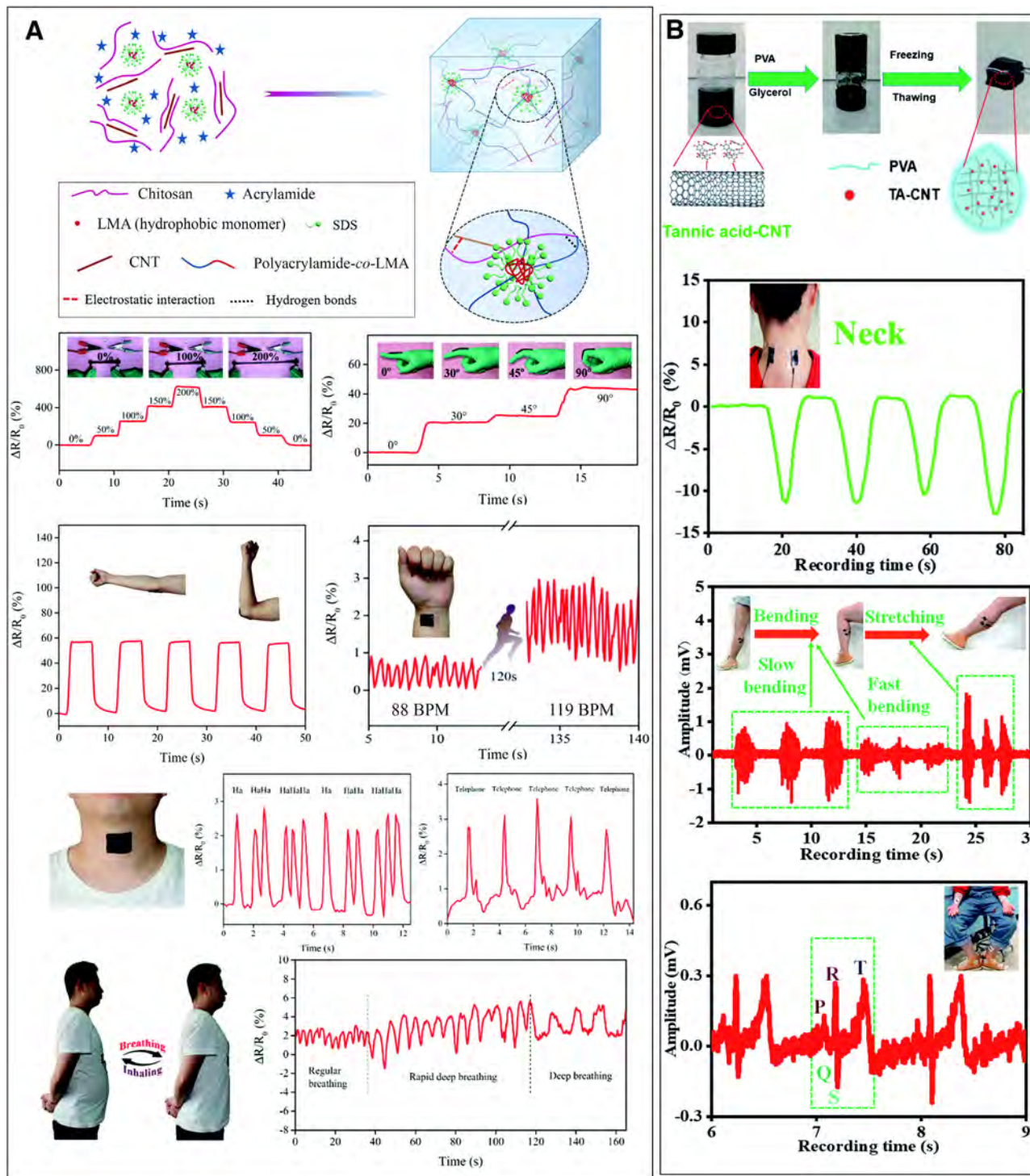


Fig. 4 Conductive nanocomposite hydrogels used as strain sensors for monitoring human motions and health. (A) A polyacrylamide-co-lauryl methacrylate/chitosan and carboxylated CNTs hydrogel changes its electrical resistance with strain. This property can be exploited to monitor movements such as finger and elbow flexion or even heart pulse, talking and breathing. Adapted from ref. 44 with permission from The Royal Society of Chemistry. (B) Polyvinyl alcohol/tannic acid-CNT hydrogel monitors joint movements such as neck bending and can also be used as an electrode for electrophysiological measurements (EMG and ECG). Adapted from ref. 46 with permission from The Royal Society of Chemistry.





resistance change over applied strain). The electrical resistance of the hydrogel increased with increasing stress and recovered fast (150 ms) after the stress was removed.<sup>44</sup> The strained hydrogel both reorganized the conductive nanomaterial network decreasing its electronic conductivity and densified the polymer network, restricting ion mobility and thus reducing ionic conductivity.<sup>44,45</sup> The hydrogel was tested for the monitoring of movements of human articulations (finger, wrist, elbow, knee) and was sensitive enough to monitor even subtle strains such as talking, breathing and pulse, placed on the neck, chest and inside of wrist, respectively (Fig. 4(A)).<sup>44</sup> He *et al.* developed a highly-sensitive, freeze-resisting strain sensor gel by incorporating tannic acid-CNTs into a polyvinyl alcohol water/glycerol gel. The nanomaterials increased the electrical conductivity from 0.19 to 5.13 S m<sup>-1</sup> and the gels could be used as strain sensors to detect joint movements and as flexible electrodes for the detection of electrophysiological signals (EMG and ECG, Fig. 4(B)).<sup>46</sup> Coupled with a wireless transmitter, such hydrogel materials can be useful in health and activity monitoring.<sup>45</sup> Three recent review publications summarised the latest developments regarding hydrogels used as strain sensors.<sup>13,42,43</sup>

Nanocomposite hydrogels used as biosensors are the ideal candidates to bridge the gap between humans and machines, in the context of biomedical engineering, diagnostics and wearable and implantable devices.<sup>47</sup> Both living organisms and electronic devices use electric signals to coordinate their activities. In living organisms, these signals are based on ionic conduction in a soft and water-rich environment. Small ions (Na<sup>+</sup>, K<sup>+</sup>, Cl<sup>-</sup>, Ca<sup>2+</sup>) rapidly flow through channels in the plasma membranes of cells, hyperpolarising and depolarising the transmembrane potential. In machines, electric signals are based on electronic conductivity in dry and rigid solids. Free electrons flow through the metallic or semi-conducting components of electronic devices. Nanocomposite hydrogels incorporate elements of both: they are viscoelastic materials with adjustable mechanical strength, high water content and solid-like behaviour, and the conduction mechanisms can combine ionic and electronic conductivity. Yuk *et al.* have reviewed conductive hydrogels in the interface between biology and electronics.<sup>47</sup>

**1.3.3 Drug delivery.** Conventional drug delivery has a number of drawbacks including high dosages, limited bioavailability, repeated administration and potential toxicity.<sup>48</sup> Controlling how, when and where drugs are available to cells and tissues can increase the drug's efficiency and reduce the frequency and concentration of the doses, limiting the toxicity and improving patient compliance and life quality. Hydrogels are some of the most promising and widely considered platforms for controlled drug delivery. They are hydrophilic, biocompatible, have a large water retention capacity and can be stimuli-responsive. Typical mesh sizes of hydrogels range from 10 to 100 nm.<sup>48</sup> This means that most molecules can diffuse freely within the porosity of the hydrogel network. The mesh size can be decreased by increasing the polymer concentration and cross-linking, to delay the release rate by steric hindrance.

To further reduce the release rate, active ingredients can form covalent, electrostatic or hydrophobic interactions with the polymer matrix.<sup>48</sup> Nanomaterials can also reduce the release rate of active ingredients.<sup>48,49</sup> Hydrophilic drugs can be readily diffused within hydrogels while hydrophobic drugs can associate with hydrophobic domains (aliphatic chains, cyclodextrin) in the polymer network or be encapsulated in nanovesicles.<sup>48,50</sup> Hydrogels can be engineered to release part of their water content according to environmental stimuli.<sup>51</sup> Pulsatile drug release, in particular, can mimic the natural patterns of *in vivo* release of endogenous chemicals such as insulin, growth hormone and oestrogen.<sup>48,52</sup> Externally applied electric fields can be used to control the release rate of drugs from conductive hydrogels. Servant *et al.* added ball-milled graphene nanosheets to methacrylic acid hydrogels, to improve their mechanical and electrical properties. A concentration of 0.2 mg ml<sup>-1</sup> of graphene nanosheets increased the electrical conductivity of the hydrogel from 2.9 × 10<sup>-6</sup> to 10<sup>-5</sup> S m<sup>-1</sup>. The nanocomposite conductive hydrogels demonstrated controlled, pulsatile release of a small molecule (sucrose) upon the intermittent application of an electrical field (Fig. 5(A)).<sup>53</sup> Additionally, nanomaterials can enhance electro-stimulated drug release. Liu *et al.* incorporated rGO into poly(vinyl alcohol) hydrogels and loaded them with a drug (lidocaine). With no external stimulation, the rGO nanomaterials acted as a barrier, retaining the drug within the hydrogel, while the application of an electric field triggered the release of the drug. The addition of rGO negatively charged the polymer matrix, enhancing electro-osmosis. In contrast, a control hydrogel without conductive nanomaterials did not change the drug release profile with electric field application (Fig. 5(B)).<sup>49</sup> Merino *et al.* reviewed the field of nanocomposite hydrogels for controlled drug delivery.<sup>51</sup>

## 1.4 Electrical conductivity targets

**1.4.1 Tissue engineering.** The electrical conductivity values aimed through the incorporation of conductive nanomaterials depend directly on the application. Hydrogels used as substrates for tissue engineering of electroactive cells require conductivity values close to native tissues. The conductivity values for tissues depend on the electrical measurement method, investigated species and if it was measured *in vivo* or *ex vivo*, and have been reported to range from 0.15 to 2.6 S m<sup>-1</sup> for muscle tissue,<sup>35,54</sup> 0.4 to 3 S m<sup>-1</sup> for nerves,<sup>54,55</sup> for bones the values range from 9 × 10<sup>-3</sup> S m<sup>-1</sup> (cortical bone) to 0.23 S m<sup>-1</sup> (bone marrow).<sup>56</sup> The electrical environment of cells plays an important role in the development of healthy tissues. In addition, conductive hydrogels used as substrates for tissue engineering can serve as electrodes for the application of external electrical stimulation to cells. Electric fields and currents affect tissue and cellular behaviour in a number of ways including interference in differentiation, migration, alignment, cytoskeleton organization, neurite growth in neurons, calcification of osteoblasts, collagen production from fibroblasts and wound healing.<sup>57-59</sup>

**1.4.2 Strain sensors.** Biosensors based on conductive hydrogels function by measuring a resistance change and correlating this change to a signal. The signal can be a motion,



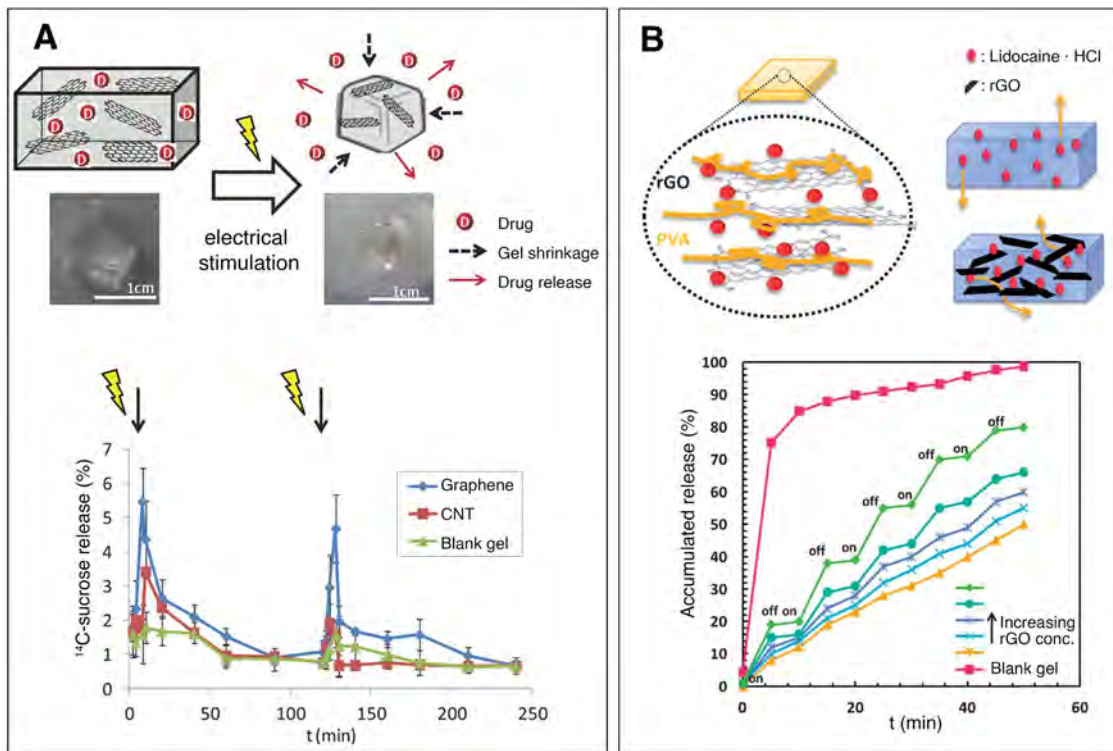


**Fig. 5** Conductive nanocomposite hydrogels for controlled drug delivery. (A) Electrical stimulation causes a methacrylic acid–graphene nanosheet hydrogel to shrink, releasing drug. *In vivo* release profile of  $^{14}\text{C}$  sucrose on the blood plasma of mice implanted with sucrose-loaded hydrogels. Hydrogels with no nanomaterials (green),  $0.2\text{ mg ml}^{-1}$  CNTs (red) and  $0.2\text{ mg ml}^{-1}$  graphene (blue) were tested. A tension of 10 V DC is applied for 1 minute with a time interval of 2 h. The graphene-loaded hydrogel (which also had the highest conductivity) demonstrated a pulsatile release of sucrose, controlled by the electric field. Adapted, with permission, from ref. 53. Copyright 2014 Wiley. (B) Reduced graphene oxide nanomaterials retain lidocaine hydrochloride within a polyvinyl alcohol hydrogel. Upon pulsatile electrical stimulation (on/off, 15 V DC) the nanocomposite hydrogels exhibit controlled drug release, while the blank gel does not change release profile. Adapted from ref. 49 with permission from The Royal Society of Chemistry.

as in strain sensors for health monitoring (joints movements, breath *etc.*) or a biosignal, such as the attachment of an antigen on the hydrogel.<sup>45,60</sup> The mechanism through which the resistance of a conductive nanocomposite hydrogel changes with strain is triple: firstly, a strain applied on the hydrogel changes the hydrogel's geometry, affecting the overall resistance. Secondly, the polymer matrix densifies (or loosens), affecting ion mobility. Thirdly, a strain changes the configuration of the conductive nanomaterial network within the hydrogel, breaching or creating electrical pathways. For this application, a hydrogel with a higher conductivity ensures a more reliable signal. The nanomaterial concentration ideally has to be maintained slightly higher than the percolation concentration.‡ A very high nanomaterial concentration risks to “saturate” the electrical network, resulting in minor conductivity changes under strain: a highly percolating network will remain percolated even with some elongation.

**1.4.3 Drug delivery.** In nanocomposite hydrogels for drug delivery, two approaches are distinguished: electro-responsive hydrogels that release a drug upon application of an external electric field and conductive hydrogels used as electrodes for transdermal drug delivery through skin electroporation.<sup>51,61</sup> Electro-responsive hydrogels shrink or bend upon the application

of an external electric field. A loaded drug is released through the contraction of the hydrogel as well as through electrophoretic forces. The electrically-induced contraction of hydrogels occurs through the combination of four mechanisms: (1) a stress gradient in the hydrogel, (2) electro-osmosis of water coupled with electrophoresis, (3) local pH changes near the electrodes due to water electrolysis and (4) a temperature gradient in the hydrogel due to resistive heating.<sup>51</sup> So far, there is no clear conductivity target for electro-responsive hydrogels in controlled drug release, however, the incorporation of conductive nanomaterials has been shown to enhance drug release.<sup>49,53</sup> In the case of conductive hydrogels for transdermal drug delivery, the hydrogel functions as an electrode, for the application of pulsed electric field on the skin.<sup>61</sup> A higher conductivity ensures a more efficient distribution of the electric field into the skin, a prerequisite for skin electroporation.<sup>61,62</sup> According to FEM simulations run on a skin model, a hydrogel conductivity higher than  $10^{-4}\text{ S m}^{-1}$  ensures a critical distribution of the pulsed electric field in the skin, for a side-to-side electrode configuration and 300 V potential difference.<sup>63</sup>

## 2. Conductive nanomaterials

The conductive nanomaterials incorporated in hydrogels to increase their electrical conductivity fall into three categories:

‡ More on electrical percolation in Section 3.



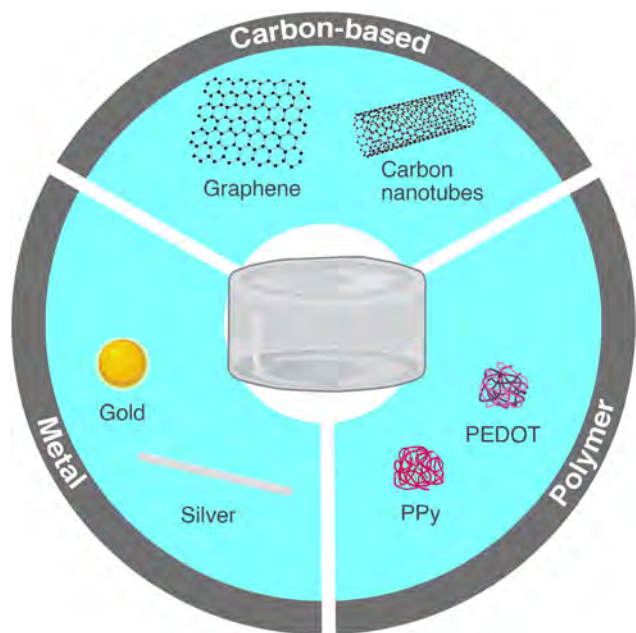


Fig. 6 Commonly used conductive nanomaterials in nanocomposite hydrogels.

carbon-based, polymeric and metals and metal oxides (Fig. 6). Throughout this review, the ISO definitions of nanomaterials and nanoparticles are used. A nanomaterial is defined as a material with any external dimension, internal structure or surface in the nanoscale, *i.e.* 1 to 100 nm. A nano-object is a discrete piece of material with one, two or three external

dimensions in the nanoscale while a nanoparticle has all three external dimensions in the nanoscale range.<sup>64</sup>

## 2.1 Carbon-based nanomaterials

Carbon-based nanomaterials have high mechanical strength, electrical conductivity, surface area and chemical stability and are available in a variety of allotropes and forms.<sup>65</sup> They can usually combine these properties, which is rather unique. The carbon nanomaterials most commonly employed to increase the electrical conductivity of hydrogels include carbon nanotubes (CNTs) and graphene-related materials (GRMs), and less often carbon black and graphite.

**2.1.1 Carbon nanotubes.** CNTs are one-dimensional, long, cylindrical nano-objects of  $sp^2$ -hybridized carbon atoms arranged in hexagonal arrays, with nanoscale diameters (Fig. 7(A)). They can be single-walled (SWNT) or multi-walled (MWNT), where multiple, concentric nanotubes with increasing diameters are held together by van der Waals forces. SWNTs can have diameters of 0.4 to 4 nm with most of them being around 1.4 nm.<sup>66</sup> Their length can range from a few hundreds of nm up to centimeters, with most nanotubes length on the micro scale.<sup>67</sup> CNTs are known to have remarkable physical properties, notably heat and electrical conductivity, mechanical strength, optical properties and a large surface area, with numerous potential applications in electronics, biomedicine, optics, composite materials and more.<sup>66–68</sup>

CNTs can be semi-conducting or metallic, depending on the diameter and the helicity of the nanotube. The electrical conductivity of isolated CNTs can reach values of  $10^5$ – $10^8$   $S\ m^{-1}$ .<sup>69,70</sup>

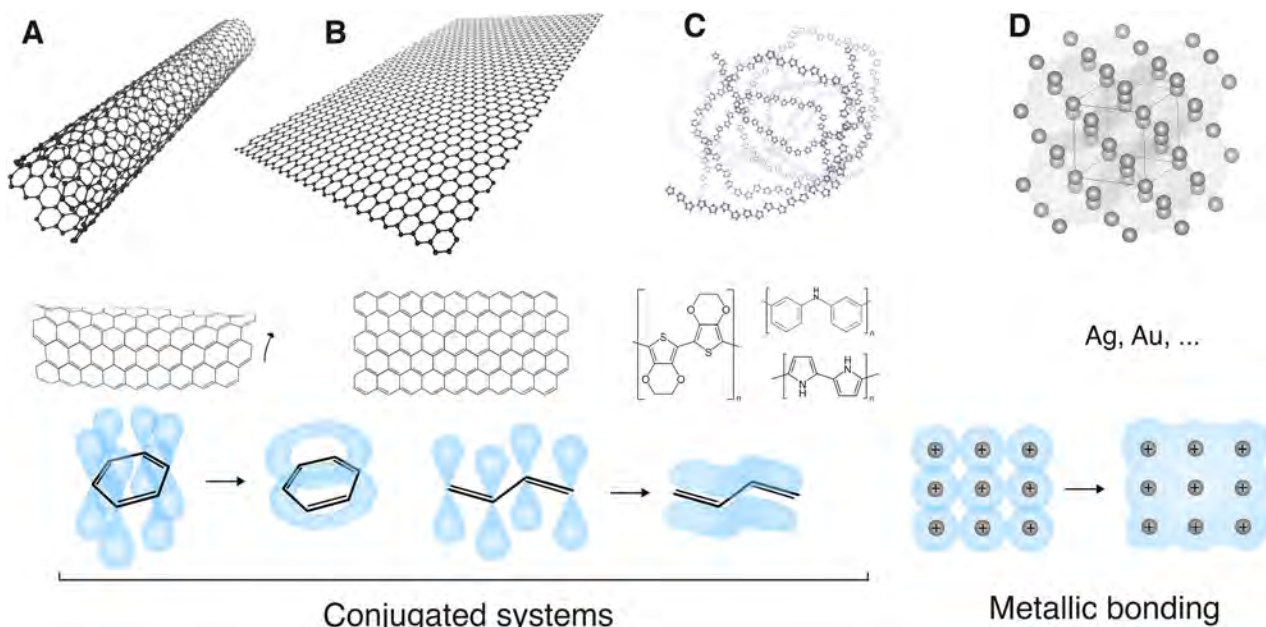


Fig. 7 Conductive nanomaterials. (A) Carbon nanotube; (B) graphene; (C) conducting polymer (polypyrrole); (D) metal (silver). A, B and C are conjugated systems. The pi orbitals of their hybridized  $sp^2$  bonds form a delocalized, overlapping and conducting pi electron orbital on a parallel plane over and under the sigma bonds. This is conventionally represented by alternating single and double bonds. D forms metallic bonding. Conduction electrons from the metal cations form a delocalized electron cloud all over the metal crystal structure. Software used: VMD<sup>81</sup> and VESTA.<sup>82</sup>





They are commonly implemented in nanocomposite hydrogels to increase their electrical conductivity because of their high intrinsic electrical conductivity, the ability to form percolation networks even at low concentration thanks to their high aspect ratio (typically from a few hundreds to tens of thousands) and the compliance with many polymer matrices.<sup>69</sup> Additionally, CNTs can also significantly reinforce the mechanical properties of nanocomposite hydrogels.<sup>71,72</sup>

Zhou *et al.* added SWNT into a gelatin hydrogel and cross-linked them with glutaraldehyde. The hydrogel served as a scaffold for engineered cardiac tissue, aimed to treat myocardial infarction. Adding 0.15% w/w of SWNT into a hydrogel with 7.5% w/w gelatin and 2.5% w/w glutaraldehyde increased the electrical conductivity from  $3 \times 10^{-8}$  to  $5 \times 10^{-5}$  S m<sup>-1</sup> and the shear modulus from 30 to 40 Pa. The SWNT concentration was chosen as a compromise between conductivity and cytotoxicity; hydrogel scaffolds with higher SWNT concentration significantly decreased cardiac cell viability. The conductive SWNTs enhanced the contractile muscle tissue function and the formation of gap junction and globally improved heart function after myocardial infarction, as tested on rats.<sup>73</sup>

Spizzirri *et al.* added MWNTs into gelatin microgels by emulsion polymerization, in the presence of sodium methacrylate and *N,N'*-ethylenebisacrylamide. The microgels served as a drug reservoir for electro-stimulated release on the skin surface. It was found that 0.8% w/w MWNTs increased the hydrogel conductivity from  $1.3 \times 10^{-7}$  to  $2.6 \times 10^{-7}$  S m<sup>-1</sup>. Lower concentrations of MWNT had no effect on the conductivity, indicating that a percolation network was not formed. The microgels with MWNTs showed no significant cytotoxic effect and increased the release rate of the drug, both with and without an external electric field.<sup>74</sup>

**2.1.2 Graphene-related materials.** Graphene is a two-dimensional, flat, one-layer sheet of sp<sup>2</sup>-hybridized carbon atoms arranged in a hexagonal lattice (Fig. 7(B)). The production of pure, flawless graphene is complex and costly. Mechanical exfoliation of graphite produces high-quality graphene sheets, with a very low yield. Graphene has high mechanical strength and electrical conductivity. The conductivity is affected by the interactions of graphene sheets with its substrate; suspended graphene sheets have a conductivity of up to  $6 \times 10^5$  S m<sup>-1</sup>.<sup>75</sup> Higher yields may be obtained at the cost of a lower selectivity in terms of number of layers (shifting to thicker nano-objects), ranging from few-layer graphene to multi-layer graphene and finally graphene platelets.<sup>76</sup>

Alternatively, the Hummers' method is used to oxidise graphite, which can then be exfoliated into graphene oxide (GO) in solution.<sup>77</sup> The covalent functionalization of graphene drastically reduces its conductivity to values around  $2 \times 10^{-2}$  S m<sup>-1</sup>, but GO has an easier production and can be dispersed in aqueous solutions. Then, GO can be chemically or thermally reduced to restore part of its electrical conductivity. Chemical reduction with reducing agents reaches conductivity values of  $6 \times 10^4$  S m<sup>-1</sup> and thermal reduction with high annealing temperatures can produce reduced graphene oxide (rGO) with conductivities up to  $2 \times 10^5$  S m<sup>-1</sup>.<sup>78</sup>

GRMs are incorporated into hydrogels to increase their electrical conductivity because of their high intrinsic conductivity and large aspect ratio, allowing for low percolation thresholds. They also simultaneously improve the mechanical properties of nanocomposite hydrogels.<sup>53</sup>

Wang *et al.* added rGO to increase the conductivity and mechanical resistance of a PVA-PDA (polyvinyl alcohol-polydopamine hydrochloride) hydrogel. The hydrogel was developed as a strain-sensitive human motion sensor. Blending in 5% GO/PVA slightly increased the conductivity from  $10^{-2}$  to  $2 \times 10^{-2}$  S m<sup>-1</sup>. However, reducing GO for 1 hour by mixing it with PDA and then adding the solution to the PVA hydrogel, in concentrations 5% w/w GO/PVA and 7.5% w/w PDA/PVA increased the conductivity of the hydrogel to 0.1 S m<sup>-1</sup>. Increasing the reduction time to 4 hours further increased the conductivity to 0.27 S m<sup>-1</sup>. The GO also increased the tensile strength of the hydrogels though the rGO reinforced the strength less than GO. This was attributed to the functional oxygen groups in GO, which physically interact with the polymer chains. The conductive hydrogels successfully changed their conductivity according to strain, as tested on a human wrist and knee joint.<sup>79</sup>

Alam *et al.* fabricated conductive, robust and pH-sensitive hydrogels by adding graphene to polyacrylic acid. Graphene was prepared from graphite powder, by oxidizing in an acidic environment with simultaneous ultrasonication. A thin film of the as-prepared graphene had a conductivity of 495 S m<sup>-1</sup>. The composite hydrogels were prepared by *in situ* polymerization. Adding 1% v/v graphene to the hydrogels increased their electrical conductivity from  $3 \times 10^{-14}$  to  $1.3 \times 10^{-5}$  S m<sup>-1</sup>, the compressive strength from 0.4 to 6.9 MPa and the Young's modulus from 1.6 to 19 MPa.<sup>80</sup>

## 2.2 Conducting polymers

Conducting (or conjugated) polymers are organic macromolecules with a backbone of alternating double and single bonds. The delocalized pi electrons of the double bonds, in combination with a dopant ion that is added to carry charges, confer them conducting or semiconducting properties (Fig. 7(C)).<sup>83</sup> The most common conducting polymers are polypyrrole (PPy), polyaniline (PANI), polythiophene and their derivatives, notably aniline oligomers and poly-(3,4-ethylenedioxythiophene) (PEDOT).<sup>22</sup>

Nanomaterials of conducting polymers can be prepared by post-polymerization dispersion or direct polymerization in disperse heterophase systems.<sup>84</sup> PPy nanomaterials are spherical with diameters ranging from 50 to 400 nm, depending on the stabilizer used and have a conductivity of  $10^2$ – $5 \times 10^3$  S m<sup>-1</sup>.<sup>84,85</sup> PANI nanomaterials can have diameters as small as 4 nm and up to 500 nm, in spherical or ellipsoid, rice-grain shape and have a conductivity of  $10$ – $10^7$  S m<sup>-1</sup>. PEDOT nanomaterials are often doped with anionic polyelectrolytes, such as poly(sodium-4-styrenesulfonate) (PSS), which serve as a charge balance. PEDOT:PSS nanomaterials are water soluble and have spherical size with diameters 35–100 nm and electrical conductivities of approx.  $10^5$  S m<sup>-1</sup>.<sup>84,85</sup>





Most conducting polymers can also be directly prepared by electropolymerisation on conducting substrates.

Conducting polymers are added to hydrogels to increase their conductivity, as an alternative to carbon-based or metal nanomaterials. They are mostly inexpensive, easy to process and biocompatible.<sup>22</sup> Additionally, surface functionalization and incorporation of dopant ions can further modulate their electrical properties.<sup>83</sup> However, conducting polymers are brittle and may decrease the overall mechanical strength of nanocomposite hydrogels.<sup>86</sup>

Li *et al.* synthesized a tough and conductive nanocomposite hydrogel by *in situ* polymerization of *N*-hydroxyethyl acrylamide in a solution containing PEDOT:PSS nanoparticles and LAPONITE<sup>®</sup> nanoplatelets. The polymer nanoparticles were added to increase the conductivity and the clay nanoplatelets to add mechanical strength. Adding 0.5% w/v PEDOT:PSS to the hydrogel increased the conductivity from 0.04 to 0.09 S m<sup>-1</sup>. The nanocomposite hydrogels exhibited strain-responsive conductivity and self-healing capacity, making them ideal candidates for applications in motion sensors.<sup>87</sup>

Wang *et al.* prepared a gelatin methacrylate hydrogel and integrated PPy nanoparticles into it with a dopamine cross-linker. The electrical conductivity of the hydrogels increased from 3.6 × 10<sup>-3</sup> S m<sup>-1</sup> (with 1 mg ml<sup>-1</sup> PPy) to 1.2 × 10<sup>-2</sup> S m<sup>-1</sup> with 4 mg ml<sup>-1</sup> PPy nanoparticles. The conductive hydrogel was then tested as an engineered cardiac patch to repair myocardial infarction in affected rat models, enhancing the functionalization of cardiomyocytes.<sup>88</sup>

### 2.3 Metal and metal oxide nanomaterials

These nanomaterials are nanoscale entities of pure metals or metal compounds, such as oxides (Fig. 7(D)). The most used metal nanomaterials for increasing the electrical conductivity of hydrogels are gold and silver nano-objects. Gold nano-objects are mostly spherical or rod-shaped, have diameters of 1–60 nm and a conductivity of 4.5 × 10<sup>7</sup> S m<sup>-1</sup>. Silver nano-objects can be spherical with diameters of 4–120 nm or nanowires, with diameters of 10–200 nm and lengths of 5–100 μm.<sup>85,89</sup> Silver has an electrical conductivity of 6.3 × 10<sup>7</sup> S m<sup>-1</sup>. Additionally, silver nano-objects are known to have antimicrobial properties, which can prove useful for some applications.<sup>90</sup> One major drawback of metal nano-objects is their propension to oxidation, leading to a decrease in performance over time.

Baei *et al.* synthesized a thermosensitive, conductive hydrogel by embedding gold nanoparticles into a chitosan matrix. The gold nanoparticles were spherical with an average diameter of 7 nm. A hydrogel with 0.016% w/v gold nanoparticles had a conductivity of 0.13 S m<sup>-1</sup>, close the conductivity of the native myocardium (0.16 S m<sup>-1</sup>), while the pristine chitosan hydrogel was not conductive. The conductive nanocomposite hydrogel stimulated the differentiation of mesenchymal stem cells into cardiomyocytes and was deemed promising for use as an injectable hydrogel to deliver cells and bioactive factors to the infarcted heart.<sup>91</sup>

### 2.4 MXenes

MXenes, two-dimensional sheets of transition metal carbides, carbonitrides or nitrides, represent a more recent class of conductive nanomaterials.<sup>92</sup> MXenes are prepared by selective chemical etching of the A element from MAX phases, layered ternary solids with a general formula of M<sub>n+1</sub>AX<sub>n</sub> (n = 1–4) where M is an early d-block transition metal, A is a main-group sp element and X is C, N or both.<sup>93</sup> They consist of sheets with a thickness of few atomic layers (3 to 9 atomic layers) and up to tens of microns in their lateral dimensions.<sup>92,94</sup> MXenes can have semiconducting or metallic conductivities with the highest values reported being 2.4 × 10<sup>6</sup> S m<sup>-1</sup> for a Ti<sub>3</sub>C<sub>2</sub> MXene.<sup>95</sup> MXene surfaces are commonly terminated with oxygen or hydroxyl groups, which render them hydrophilic.<sup>92,94</sup> Their hydrophilicity, high electrical conductivity and large aspect ratio make them suitable candidates for incorporation in conductive nanocomposite hydrogels.<sup>94</sup> For the moment, notable biomedical applications of MXene nanocomposite hydrogels have mostly focused on strain sensors.<sup>94,96</sup> An important limitation is that MXenes have a metastable character in aqueous media, *i.e.* they are prone to degradation.<sup>96,97</sup>

## 3. Electrical percolation

### 3.1 Percolation theory

Incorporation of a conducting filler in an insulating hydrogel matrix, increases the conductivity of the nanocomposite, with increasing filler concentration. Often, a point is observed where a small increase in filler concentration leads to a steep increase in conductivity, a shift of few orders of magnitude.<sup>69,98</sup> Further increase in filler concentration has a limited effect on conductivity. The resultant graph of conductivity *versus* filler concentration exhibits a sigmoidal shape (Fig. 8).

Percolation theory explains this jump-like transition. The conductivity increases steeply when the filler forms a continuous conducting network within the hydrogel. Individual clusters of filler particles come into contact with each other, to ultimately form a single cluster that extends throughout the system.<sup>98</sup> Electron transport takes place through the conductive filler network and the system's behaviour changes from insulating to conducting (Fig. 8). The corresponding critical filler concentration is called percolation threshold. The percolation threshold of different nanocomposite hydrogels varies widely and depends on the polymer matrix and the shape, size, orientation and dispersion of the filler.<sup>69</sup> Higher aspect ratios and better dispersions lead to lower percolation thresholds.

The electrical percolation threshold is an important parameter in percolating systems. Experimentally finding it and tuning it by changing the properties of the system can lead to the development of highly conductive nanocomposites with minimal filler concentration and desirable properties. For a random distribution of a well-dispersed filler, the statistical percolation theory can model the conductivity of composites.<sup>98,99</sup>

$$\sigma = \sigma_0(\Phi - \Phi_c)^t, \text{ for } \Phi > \Phi_c \quad (1)$$



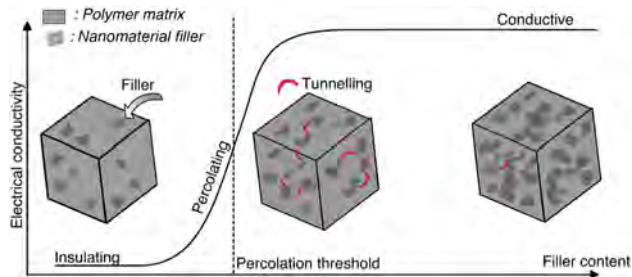


Fig. 8 Electrical conductivity vs. nanofiller content. Percolation has three phases: initially the concentration of the nanomaterial is not enough to form an interconnecting network and the conductivity remains low. As the concentration increases, electrons can hop through the nanofillers with tunnelling and the conductivity increases. When the concentration reaches the percolation threshold, a network is formed throughout the whole system and the conductivity reaches a high plateau. Adapted from ref. 78.

where  $\sigma$  is the electrical conductivity of the composite,  $\sigma_0$  the electrical conductivity of the filler in its bulk form,  $\Phi$  the filler volume fraction,  $\Phi_c$  the percolation threshold and  $t$  the critical power law exponent. The exponent  $t$  depends on the system dimensionality and takes values of *ca.* 1.3 for 2D systems and *ca.* 2 for 3D.<sup>78,100</sup> The electrical percolation threshold can be determined experimentally or numerically.

Experimentally, the electrical percolation threshold can be deduced from a graph of electrical conductivity with increasing filler concentration. The threshold is the middle point of the S-shaped part of the graph. It can also be calculated by fitting eqn (1) to experimental data.

Numerically, there are various models with increasing complexity for calculating the percolation threshold. The first studies of percolation assumed a lattice organisation of particles where a set of predefined spatial positions may be covered or be left empty.<sup>98</sup> In materials science though, the results of these studies can only be relevant for systems with a crystalline structure. The continuum percolation models can be applied for hydrogels, which have an amorphous structure and thus a random distribution of particles. The simplest models simulate the filler particles with interpenetrating objects. The electrical percolation threshold is calculated as the point where the filler particles form a continuous network, a cluster of particles that extends through the simulation space.

The calculated percolation thresholds from the above method can be higher than the experimental ones because it does not take into account two phenomena: the filler particles cannot penetrate into each other because of repulsive van der Waals interactions and the electrical percolation threshold can occur before the geometrical percolation, due to electron tunnelling.<sup>101</sup> Geometrical percolation is when the filler particles form a network with physical contact. Electrical percolation can occur at lower filler concentrations, as electrons can be transferred through a thin film of dielectric material that separates the filler particles. The electron tunnelling distance is in the order of few nm.<sup>102</sup>

The hard-core, soft-shell simulation model is used to represent more accurately the nanocomposite system. In this

model, the fillers are randomly distributed in a fixed space and are represented by impenetrable hard cores. The soft shells can overlap with the cores and with each other and represent the tunnelling distance.<sup>69,101</sup> Another factor that differentiates experimental from numerical results is the non-randomness of real dispersions. In numerical models, the particles will be randomly distributed within the system's boundaries while in experiments particles tend to agglomerate/cluster and align, affected by particle interactions, the dispersion method and the thermal or mechanical processing history of the material.<sup>103</sup> This clustering and non-random alignment of nanomaterials can have substantial effects on the percolation concentration of the system.<sup>103,104</sup>

### 3.2 Critical path approximation

Percolation models assume a sharp cut-off point of electrical conductivity. Two individual particles are either electrically connected or not. Subsequently, a cluster of particles passes from disconnected (insulating) to percolated (electrically conductive), when the percolation threshold is reached. Ambrosetti *et al.* argue that this approach is well suited to explain the electrical conductivity in the extreme cases of low filler concentration (particles with no electrical contact) and high filler concentration (particles “touching” each other throughout the system) but fails to account for the conductivity changes in the intermediate regime, around the percolation concentration.<sup>105</sup> They model the conductivity changes in nanocomposite systems by focusing on the tunnelling conductance between conductive particles.<sup>105,106</sup> The tunnelling conductance decays exponentially with distance, but does not include a sharp cut-off. This model can be solved numerically by simulating the conducting fillers as a network of particles that are all connected to each other through tunnelling processes (Global Tunnelling Network). An analytical solution for the conductivity  $\sigma$ , is given by the critical path approximation

$$\sigma \cong \sigma_0 \exp \left[ -\frac{2\delta_c(\varphi, a, b)}{\xi} \right] \quad (2)$$

where  $\sigma_0$  a constant,  $\xi$  the characteristic tunnelling length and  $\delta_c$  a critical distance, which depends on the filler concentration  $\varphi$  and the geometric characteristics of the particles  $a$  and  $b$  ( $a/b$  is the aspect ratio). The solution of eqn (2) reduces the conductivity of a nanocomposite system to the calculation of the geometrical parameter  $\delta_c$  and is in good accordance with the numerical solutions from the global tunnelling network model.<sup>105</sup>

The implications of the critical path approximation are that the transition from insulating to conducting is no longer described by a power law increase in conductivity after the percolation threshold concentration, but rather as a crossover between the insulating matrix conductivity and the interparticle tunnelling conductivity.<sup>105</sup>

### 3.3 Percolation of carbon nanotubes

CNTs have a high aspect ratio (generally *ca.* 1000 or higher), which allows for low percolation thresholds.<sup>69</sup> Kovacs *et al.* used the excluded volume concept to calculate a percolation



threshold of

$$\Phi_c = \frac{1}{\eta} = \frac{1}{1000} = 0.1\%w/w \quad (3)$$

where  $\eta$  is the aspect ratio of CNTs.<sup>100</sup> They argue that this percolation threshold is universal for CNTs in insulating polymer matrices (they reviewed solid nanocomposite polymers but their results are useful in the case of hydrogels too). Deviations with higher  $\Phi_c$  are attributed to poor dispersion and lower  $\Phi_c$  are attributed to kinetic percolation, a state where the particles are free to move through diffusion, convection, shearing or external fields and form a conducting network at lower concentrations. The critical exponent  $t$  for CNTs, calculated from fitting the experimental data into eqn (1) ranged from 0.9 to 7.6, peaking at  $t = 2$ .<sup>100</sup>

CNTs can be modelled as capped cylinders for the numerical simulations. The most sophisticated models take into account the electron tunneling distance, the non-random alignment, as well as the waviness of the nanotubes, which increases the percolation threshold.<sup>107</sup>

### 3.4 Percolation of graphene-related materials

The high specific surface area and aspect ratio of GRMs allow for low percolation thresholds. Zhang *et al.* compared the percolation threshold of graphene and graphite nanocomposites, to illustrate the influence of the aspect ratio and specific surface. They measured the conductivity of PET/graphene and PET/graphite with increasing filler concentrations and obtained a percolation threshold of 0.47% v/v for graphene and 3.5% v/v for graphite.<sup>108</sup>

Marsden *et al.* reviewed the electrical percolation threshold of GRM nanocomposites and the average percolation threshold was 0.5% v/v.<sup>78</sup> A high standard deviation though (0.7% v/v) indicates that the percolation threshold may vary widely according to the dispersion, shape parameters of the filler (aspect ratio and specific surface) and the polymer matrix.

### 3.5 Electrical percolation studies in hydrogels

Most conductive hydrogel studies presented in this review did not report a percolation threshold. The ones commenting on percolation threshold concentration are grouped here. Ferris and Panhuis found a percolation threshold of 1.3% w/w for gellan gum hydrogels containing multi-walled CNTs.<sup>109</sup> Mottet *et al.* report a percolation threshold of 0.5% w/w for alginate hydrogels with CNTs.<sup>110</sup> Cui *et al.* report a percolation threshold of 0.015% w/w for poly-ethyl acrylate hydrogels, with multi-walled CNTs.<sup>111</sup> Guillet *et al.* and Macdonald *et al.* found no percolation threshold for agarose – double-wall CNTs hydrogels for concentrations up to 1% w/w and for collagen – SWNTs for concentrations up to 0.008% w/w respectively.<sup>112,113</sup> Alam *et al.* reported a percolation threshold of 0.4% v/v for graphene incorporated in poly acrylic acid hydrogels.<sup>80</sup> Sayyar *et al.* and Qiu *et al.* both reported a percolation threshold of 0.1% w/w for rGO fillers in chitosan and poly-isopropyl acrylamide hydrogels.<sup>114,115</sup>

In contrast, in studies of solid nanocomposite polymers, there are more publications reporting a clear electrical percolation threshold. We explain this by four factors: (1) there are fewer studies in total for nanocomposite hydrogels, (2) carbon-based materials which generally exhibit low percolation thresholds are highly hydrophobic resulting in the formation of aggregates and poor dispersions in aqueous media, (3) polymer chains may tend to wrap around nano-objects, limiting direct contact between the conductive phase, and (4) hydrogels are more complex systems consisting of at least three components (polymer matrix, water, filler) and two conduction mechanisms (ionic and electronic). This complicates the investigation of the percolation threshold. Rather than a clear cut-off point of several orders of magnitude increase in conductivity, many nanocomposite hydrogels present modest augmentations with increasing nanofiller content.

### 3.6 Dispersion

Nanomaterials are introduced into nanocomposite hydrogels using one of three possible approaches: (1) dispersion of nanomaterials in an aqueous suspension of a monomer, followed by gelation, (2) dispersion of a nanomaterial precursor in an aqueous suspension of a monomer, followed by gelation and nanomaterial synthesis within the polymerized matrix, and (3) physical embedding of nanomaterials into a hydrogel matrix.<sup>116,117</sup> The nanomaterials can significantly alter the properties of the nanocomposite hydrogels, thanks to the multiple physical and/or chemical interactions between the nanomaterials and the polymer. These include hydrogen bonds, van der Waals interactions and electrostatic interactions.<sup>116</sup> The dispersion of nanomaterials in the hydrogel network affects the system's electrical and mechanical properties. Poor dispersions, leading to nanomaterial agglomeration undermine the property-enhancing features of nano-engineering.

Carbon-based nanomaterials have highly hydrophobic surfaces. They form agglomerates in aqueous suspensions and have low interfacial compatibility with polymer matrices.<sup>116,118</sup> The surface of carbon nanotubes and graphene sheets can be functionalized with hydrophilic groups, such as –COOH and –OH, facilitating their dispersion in water through electrostatic repulsion (at slightly acidic pH and above, the carboxylic function is present as a negatively charged carboxylate).<sup>119</sup> However, covalent functionalization disrupts the electronic structure of pristine carbon-based nanomaterials, deteriorating their electrical conductivity.<sup>116</sup> Another route is the addition of surfactants. Lastly, physical methods, such as polymer wrapping and cellulose-assisted dispersion have also been developed. Polymer wrapping and surfactants improve dispersion but also cover the surface of carbon nanomaterials and may increase the distance between the nanomaterials, decreasing electron tunnelling conductance and negatively affecting the conductivity of the nanocomposite hydrogel.<sup>118</sup>

Metal nanomaterials have high surface energy and strong dipole–dipole attractions. They form aggregates and precipitate in aqueous suspensions. Two approaches that achieve stable dispersions with fewer aggregates are the *in situ* growth of metal nanomaterials after gelation of the hydrogel and the use



of metal nanomaterials as reactive cross-linking agents to polymerize the hydrogel.<sup>116</sup>

Conducting polymers are hydrophobic in their undoped form.<sup>83</sup> Nanoparticles of conducting polymer, stabilized with a dopant, can be dispersed in aqueous solutions by stirring and sonicating. PEDOT is a hydrophobic, positively charged conjugated polymer. It is usually doped with PSS, a hydrophilic, negatively charged polyelectrolyte, to create stable water dispersions of PEDOT:PSS.<sup>120</sup> PEDOT:PSS nanoparticles have fairly good dispersibility in water.<sup>87</sup> Similarly, PANI is hydrophobic in its undoped form and hydrophilic when stabilized with a dopant such as camphor sulfonic acid.<sup>121,122</sup> Polypyrrole nanoparticles can be doped with iron(III) chloride or PSS and can be easily dispersed in aqueous solutions.<sup>123,124</sup>

## 4. Electrical conductivity and conduction mechanisms

### 4.1 Conductivity

Electrical conductivity is an intrinsic property of materials which measures how well they conduct electric current. It is the reciprocal of resistivity, the resistance of a material to the flow of electric current. When a potential difference is applied to a sample, an electric field  $E$  is created, and charges inside the sample have an electric force applied to them. For an isotropic conductivity and a homogenous electric field, the current density  $J$  that results, depends on the sample's conductivity  $\sigma$ .

$$J = \sigma \cdot E \quad (4)$$

Electric current is conducted by charge carriers, which can be ions, electrons and holes. Electrical conductivity depends on the product of charge carrier concentration and mobility.

### 4.2 Conduction mechanisms

When a sample is placed between two electrodes, charge is injected in it through the interface of the sample with the electrode materials, then passes through its volume and gets out again from the interface of the sample with the other electrode. Localised charge movements also result in a measurable current, even if the charge carrier does not exit the sample. The limiting conduction mechanism is the determining one and this can fall into one of two categories: interface-limited (or electrode-limited) and volume-limited (or bulk-limited).<sup>125</sup> Depending on the nature of the material and the applied electric field, one or more conduction mechanisms may contribute to the electric current transport.

Interface-limited conduction mechanisms depend on the electrical properties at the contact between the sample and the electrode. The most important parameters are the energy barrier height that the charge carrier has to overcome in order to get injected into the sample and the effective mass of the charge carriers.<sup>125,126</sup> Volume-limited conduction mechanisms depend on the electrical properties of the sample. The most important parameter in volume-limited conduction are traps, locations in solids which restrict the movement of charge

Table 1 Conduction mechanisms in solids and equations<sup>112,127</sup>

Volume-limited		Interface-limited	
Ohmic	$J = \sigma E$	Schottky	$J = AT^2 e^{\left(\frac{\Phi_0 - \beta_{sv}\sqrt{E}}{k_B T}\right)}$
Ionic (Hopping)	$J = J_0 \sinh\left(\frac{q l_i E}{k_B T}\right)$	Fowler-Nordheim-Tunneling effect	$J = AE^2 e^{\left(-\frac{\beta}{E}\right)}$
Poole-Frenkel	$J = J_0 e^{\frac{\Phi_0 - \beta_{PF}\sqrt{E}}{k_B T}}$		

carriers. Trap energy level, trap spacing and concentration all affect volume-limited conduction. Other parameters include the electrical mobility, the dielectric relaxation time and the density of states in the conduction band.<sup>125,126</sup> Table 1 summarizes the conduction mechanisms in solid materials and their equations, where  $J$  the current density,  $\sigma$  the conductivity,  $E$  the electric field,  $J_0$  the zero-field current density,  $q$  the electric charge,  $l_i$  the ion jump distance from one potential well to another,  $k_B$  the Boltzmann constant,  $T$  the temperature,  $\Phi_0$  the barrier height and  $A$  and  $\beta$  constants.

### 4.3 Ionic conduction

Ionic conduction occurs when the charge carriers are ions. It is the dominant conduction mechanism in electrolyte solutions but also contributes to the electrical conductivity of solids. Fast ion conductors and solid electrolytes are examples of solid materials where ionic conduction is the main conduction mechanism.<sup>128</sup> The ionic conduction mechanism consists of a series of jumps over potential barriers from one site to another.<sup>126</sup> Ions are several orders of magnitude bigger and heavier than electrons and consequently ion mobility, reduced by steric effects, is much lower than electron mobility. Ionic conduction depends on ion concentration, temperature, ion size and valency, electrical field magnitude, viscosity (in the case of solutions) and the height and spacing of potential barriers (in the case of solids).

### 4.4 Electric current

The movement of charge carriers under the influence of an electric field is the conduction current. There are two more current types that can be measured. The diffusion current is created by the movement of charge carriers under the influence of their concentration gradient. The displacement current is a transitory current due to the variation of the electric field and is not linked to a charge movement inside the sample. It includes the polarisation current, a transitory current that arises from the orientation of dipoles with the electric field. The total current can be written as the sum of the above current types

$$j(t) = \underbrace{qn(x,t) \mu(E,t) E(x,t)}_{\text{Conduction}} + \underbrace{-qD_n \frac{\partial n(x,t)}{\partial tx}}_{\text{Diffusion}} + \underbrace{\epsilon_0 \frac{\partial E}{\partial t} + \frac{\partial P}{\partial t}}_{\text{Polarisation Displacement}} \quad (5)$$

where  $j$  is the current density,  $q$  the elemental charge,  $n$  the charge carrier concentration,  $\mu$  the charge carrier mobility,  $E$





the electric field  $D_n$  the diffusion constant of the charge carriers,  $\epsilon_0$  the permittivity of vacuum and  $P$  is polarisation.

#### 4.5 Hydrogel water content and electrical conductivity

Nanocomposite hydrogels are complex systems consisting of at least three components: water, which comprises the largest part of the hydrogel, a cross-linked polymer network and the filler nanomaterials. The role of each constituent in the electrical conductivity of the system is still poorly understood. Deionised water is used for the fabrication of most hydrogel samples. Nevertheless, some ions will always be present, introduced to the system from the polymer, the nanomaterials and other impurities, the contact with air and labware and due to the non-perfect deionisation of water. These free ions contribute to the electrical conductivity of nanocomposite hydrogels by ionic conduction. However, the mobility of ions in hydrogels is restricted by the porous network of the polymer. The ion mobility inside a hydrogel depends on the concentration and charge of the polymer and the pore size and distribution and is significantly lower than the ion mobility in an aqueous solution. The total amount of water within hydrogels can be classified into three types, according to phase transition behaviour: (1) non-freezing (bound) water, in the primary hydration shell of the hydrophilic polymer chains, (2) freezing bound water, in the secondary hydration shell and (3) freezing free water, which does not interact with the polymer matrix.<sup>129,130</sup> These different states of water within the hydrogel framework can be distinguished through differential scanning calorimetry (DSC).<sup>131</sup> Ionic mobility is expected to be much lower in the bound water fraction.<sup>132,133</sup> Therefore, the ionic conductivity is mostly affected by the free water in the hydrogel matrix. The polymer network consists of electrically insulating polymer chains. The conduction mechanisms through it are expected to be equivalent to conduction through non-crystalline dielectric solids. Lastly, the nanomaterials studied in this review are embedded in hydrogels because of their metallic conduction properties. When they are present in a critically high concentration, they form a percolating network through the hydrogel allowing for a steep increase in the system's conductivity. The conduction mechanism through a percolating network of conductive nanomaterials is ohmic conduction.<sup>112</sup>

The water content of nanocomposite hydrogels directly affects their electrical conductivity. Lower water contents decrease ionic conduction by densifying the polymer network, leading to smaller pores and lower ion mobility. At the same time, a decrease in water content with the subsequent densification of the hydrogel, increases the volume fraction of the nanomaterials and thus the chances of forming a percolating network. Ferris and Panhuis measured the electrical conductivity of a gellan gum hydrogel embedded with multi-walled CNTs and a control gellan gum hydrogel (without nanomaterials), upon drying. They inserted the hydrogels between two electrodes, put it on a mass balance and placed all the system in a heated chamber, with the temperature increasing from 20 to 60 °C, over time. The device allowed for simultaneous mass and conductivity measurements. The initial conductivity for both

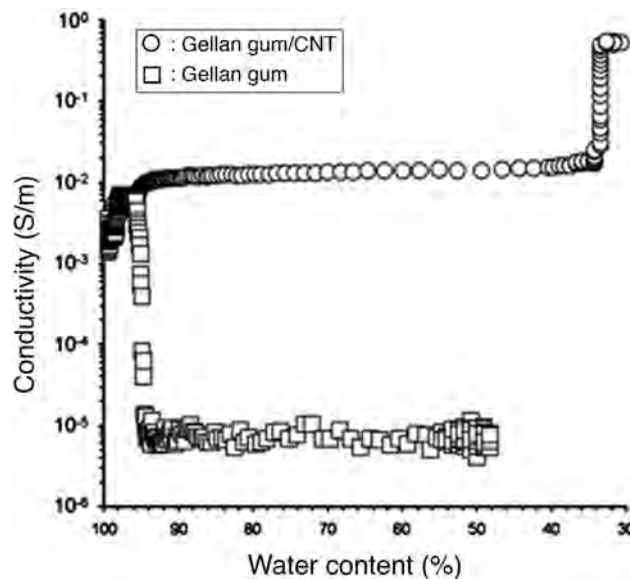


Fig. 9 Conductivity of gellan gum hydrogels with CNTs (circles) and without (squares), over decreasing water content. The loss of water content densifies the polymer network restricting ion mobility but simultaneously increases the nanomaterial volume fraction and leads to percolation. Adapted from ref. 109 with permission from The Royal Society of Chemistry.

hydrogels was  $10^{-3} \text{ S m}^{-1}$ . At 95% water content the conductivity of the nanocomposite hydrogel increased to  $10^{-2} \text{ S m}^{-1}$  while the conductivity of the control hydrogel decreased dramatically to  $10^{-5} \text{ S m}^{-1}$  (Fig. 9).<sup>109</sup> The initial hydrogel conductivity can be attributed to ionic conduction, while the differences in the behaviours for decreasing water content can be explained on the basis of electrical percolation of the CNTs and ion mobility restriction in the control hydrogel.

## 5. Measuring electrical properties

The electrical conductivity of hydrogels can be measured from the relation between voltage and current. First, the sample hydrogel is placed between two electrodes. Then, an electrical stimulus is applied to the electrodes (known voltage or current) and the response of the system is observed. The electrical response of the system depends on the transport of charges within the material and the transfer of electrons to or from the atoms and ions of the sample at the electrode-sample interface. The total current flow will depend on the resistance of the sample and the reaction rates at the interface between the sample and electrodes. In addition, the electrical response will be affected by impurities on the sample and electrodes, possibly leading to oxidation or reduction reactions. Typically, these measures apply low voltages to the sample (50 mV to 1 V). Care has to be taken to not apply over 1.23 V for an extended time period, which would lead to electrolysis of water molecules (oxidation, release of oxygen) and affect the results.

### 5.1 Two-point and four-point probe methods

The measuring device can be connected to the electrodes *via* a two-point or four-point system. Two-point probes are easier to



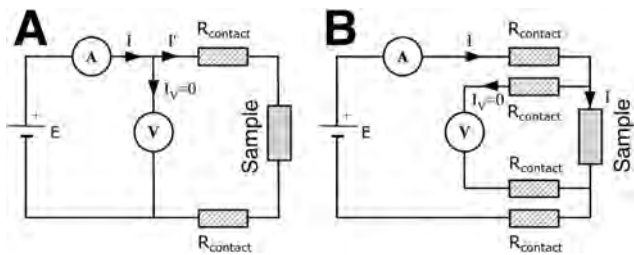


Fig. 10 Circuit diagrams of (A) two-point probe and (B) four-point probe method.

handle but also measure the contact resistance, *i.e.* the resistance at the interface between the cables and the electrodes (Fig. 10(A)). A four-point system measures directly the resistance of the sample. The electrical stimulus is applied through two probes and the sample's response is measured through the two other probes, avoiding the contact resistance (Fig. 10(B)). However, in most cases of nanocomposite hydrogels, the sample's resistance is several orders of magnitude higher than the contact resistance, so the choice of a two- or four-point probe is of negligible impact.

## 5.2 Direct current

**5.2.1 Ohmmeter.** An ohmmeter calculates the resistance  $R$  of a sample by applying a fixed DC current of few mA and measuring the corresponding voltage.

$$R = \frac{V}{I} \quad (6)$$

where  $V$  is the measured tension and  $I$  the applied current.

For an isotropic conductivity and a homogenous electric field, and with a simple sample geometry, the conductivity is calculated as the reciprocal of resistivity.

$$\left. \begin{aligned} R &= \rho \frac{l}{A} \\ \sigma &= \frac{1}{\rho} \end{aligned} \right\} \Rightarrow \sigma = \frac{l}{A} \cdot \frac{1}{R} \quad (7)$$

where  $\rho$  the resistivity,  $l$  the length and  $A$  the surface of the sample. DC conductivity measurement with a multimeter is the most simple and straightforward way to measure the conductivity of a sample hydrogel. However, it doesn't provide any information about capacitive and inductive behaviour. Most works reviewed here use this measurement, since they only seek to demonstrate an increased electrical conductivity through the incorporation of nanomaterials.

**5.2.2 Chronoamperometry.** In chronoamperometry, the electrical stimulus applied to the electrodes is a square-wave potential. The electrical response of the system is the current as a function of time  $I(t)$ . By applying a step potential difference on a hydrogel sample, a peak of current will be measured. This peak corresponds to the sum of the conduction current and the polarisation current, *i.e.* the orientation of water and other polar molecules in the direction of the electric field. The polarisation current exponentially decays and the current then reaches a plateau corresponding to the conduction current, *i.e.*

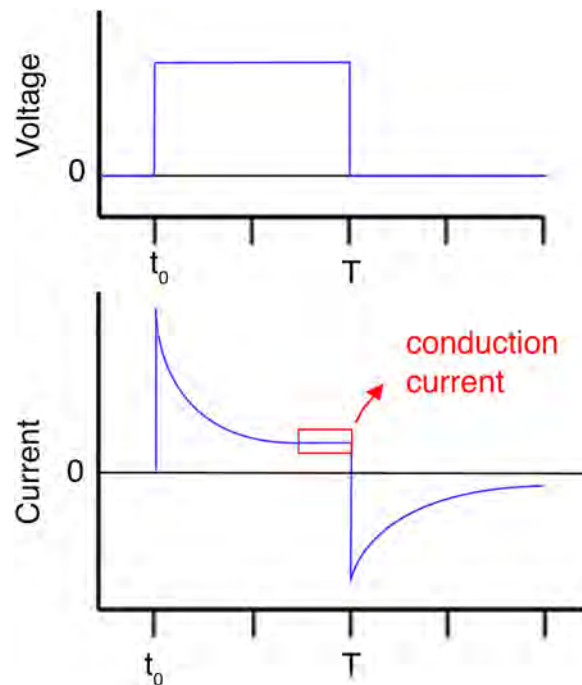


Fig. 11 Double-pulsed, controlled potential chronoamperometry. A square wave voltage initially causes a current peak, due to polarisation. The current then exponentially decays to the conduction current. The removal of the voltage may cause a brief reversed current peak.

the movement of ions and electrons within the hydrogel. When the step voltage is removed, the measured current may briefly exhibit a reverse peak, before decaying to zero. This reverse current is the result of the return of the electric dipoles (polar molecules) to a random orientation, after the removal of the electric field (Fig. 11).

From eqn (4), we have  $\sigma = \frac{J}{E}$  and for a simple geometry with the normal of the electric field perpendicular to it

$$\sigma = \frac{J}{E} = \frac{I/A}{V/l} = \frac{I \cdot l}{V \cdot A} \quad (8)$$

where  $V$  is the tension,  $I$  the current,  $l$  the length and  $A$  the surface of the sample hydrogel.

To calculate the conductivity, the conduction current (the time-invariant part of the  $I(t)$  graph) is inserted into eqn (8). Chronoamperometry also gives additional info about the sample's RC time constant.

Guillet *et al.* studied the conduction mechanism of agarose/CNTs nanocomposite hydrogels through chronoamperometry. They applied increasing voltage from 50 mV to 1.3 V and measured the current passing through the sample, *vs.* time. By plotting the conduction current density *vs.* the electric field (applied voltage divided by sample thickness) and comparing the graph with known equations of conduction mechanisms (Table 1), they suggested that pristine agarose hydrogels are dominated by an ionic conduction type, while nanocomposite hydrogels with CNTs most possibly exhibit a Poole-Frenkel conduction type.<sup>112</sup>





### 5.3 Alternating current

**5.3.1 Impedance spectroscopy.** In impedance spectroscopy, the electrical stimulus applied to the sample is a sinusoidal alternating voltage, over a range of frequencies (commonly between 0.1 and  $10^6$  Hz). The measured response of the system is the resulting current and the phase difference between signal and response.<sup>134</sup> For an electrical stimulus of  $v(t) = V_m \sin(\omega t)$ , with a frequency  $f = \omega/2\pi$ , the resulting current  $i(t) = I_m \sin(\omega t + \theta)$  is measured (for a linear behaviour). Here,  $\theta$  is the phase shift between the voltage and the current. It is equal to 0 for a purely resistive behaviour,  $\pi/2$  for a purely inductive and  $-\pi/2$  for purely capacitive. The conductive nanomaterials incorporated in hydrogels have a metallic conductivity, therefore phase shifts close to 0 degrees. In pristine hydrogels, ionic conductivity dominates and the values of  $\theta$  are near  $-30$  to  $-40$  degrees.

From the amplitude and phase shift measurement, a complex impedance  $Z$  is deduced with  $Z'$  the real part (resistance) and  $Z''$  the imaginary part (reactance). Impedance expands the notion of resistance by taking reactance into account. While resistance leads to the dissipation of energy as heat, reactance stores energy and releases it after  $\pi/2$ . Capacitive reactance stores energy in the form of an electric field and inductive reactance stores energy in the form of a magnetic field.

The analysis of impedance spectroscopy data provides information about the electrical properties of the sample hydrogel. Different excitation frequencies will elicit different electrical responses from the material. For example, in low frequencies, electrons, ions and dipoles of different sizes will all move responding to the electric field. In higher frequencies ions and bigger dipoles do not have the time to move; only electrons respond to a rapidly changing electric field. Plotting the impedance data into a Nyquist plot (Fig. 12) allows the visualization of electrical phenomena and the modelling of an equivalent circuit, *i.e.* a simplified theoretical model that retains all the electrical characteristics of the original, complex circuit.<sup>135</sup> The y-axis represents the negative of the imaginary part and the x-axis represents the real part of the complex impedance. The intersection of the curve with the x-axis designates the

resistance of the hydrogel.<sup>136</sup> The conductivity is then calculated from eqn (7).

In the case of nanocomposite hydrogels, the equivalent circuit seems to include a Warburg impedance element in series with a resistor.<sup>112,137,138</sup> The Warburg element models diffusion processes and is recognizable by a straight line with  $45^\circ$  slope, at low frequencies (Fig. 12(B)).

Warren *et al.* used impedance spectroscopy to investigate the percolation behaviour of CNT-loaded gellan gum hydrogels.<sup>137</sup> They prepared the hydrogels by dissolving gellan gum powder into warm ( $80^\circ\text{C}$ ) deionised water, dispersing CNTs in the solution through sonolysis and then cross-linking with  $\text{Ca}^{2+}$  ions. By varying the length of the hydrogel, they were able to distinguish between the sample's resistance and the contact resistance: the sample's resistance increases linearly with length, while the contact resistance remains invariable.

$$R_{\text{measured}} = \frac{1}{\sigma_{\text{sample}}} \frac{l}{A} + R_{\text{contact}} \quad (9)$$

where  $\sigma_{\text{sample}}$  the conductivity of the sample (hydrogel),  $l$  the length and  $A$  the cross section.

Three different carbon nanomaterials were employed, single-wall CNTs, multi-wall CNTs and vapour-grown carbon nanofiber. The impedance analysis for all three carbon nanomaterials in a 0.9% v/v concentration showed a similar modest increase in conductivity (final value  $0.12 \text{ S m}^{-1}$ ; the original conductivity of gellan gum is not mentioned here but is reported as  $10^{-3} \text{ S m}^{-1}$  in previous studies<sup>109</sup>). This concentration was deemed too low to have an effect on the conduction mechanism. The carbon filler concentration was further increased by selectively removing a part of the water content of the hydrogel, at a rate of  $0.43 \text{ g h}^{-1}$ , in a controlled temperature and humidity chamber. It was reported that at MWNT concentration of 1.4% v/v the impedance was no longer dependent on frequency and the Warburg coefficient value rapidly decreased, witnessing the formation of a percolating network and the transition between transport dominated by ions to transport dominated by electrons.<sup>137</sup>

**5.3.2 Conductivity meter.** Another way to measure the electrical conductivity of hydrogels is the use of a conductivity meter with an adequate probe. These devices are optimized for fast conductivity measurements of aqueous, ionic solutions but can also work in the case of hydrogels. In conductivity meters, the electrical stimulus applied is a single-frequency alternating current (or voltage) and the produced voltage (or current) is read. The conductivity meters are calibrated with solutions of known conductivity and their output is directly the conductivity value. Koppes *et al.* used a conductivity meter to evaluate changes in conductivity induced by the incorporation of single-wall CNTs into collagen type I hydrogels. For the measurements, they submerged the conductivity meter probe in the hydrogel precursor solution, cross-linked the hydrogel and then measured the conductivity. A concentration of 0.01% w/w of CNT increased the conductivity of collagen hydrogels from  $1.4$  to  $2.4 \text{ S m}^{-1}$ .<sup>139</sup>

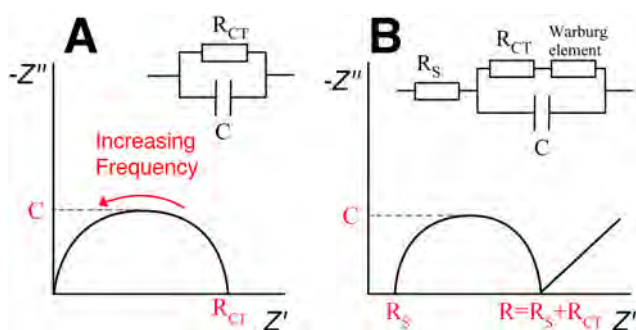


Fig. 12 Impedance spectroscopy results can be visualized with a Nyquist plot. (A) Typical Nyquist plot of simple RC circuit with one resistor and one capacitor in parallel. (B) Typical Nyquist plot of resistance in series with the parallel combination of a capacitance with a resistance and a Warburg diffusion element (also known as Randles circuit).



## 5.4 Hall effect

A Hall effect measurement system can be also used to measure a hydrogel's conductivity. When a sample is traversed by an electric current in one direction, and a magnetic field perpendicular to this direction is applied simultaneously, a potential difference will be produced along the sample.<sup>125,140</sup> This potential difference is called the Hall voltage. The Hall effect measurement also provides information about the charge carrier concentration and mobility.<sup>125</sup> Bu *et al.* prepared a sodium alginate and carboxymethyl chitosan hydrogel to use as a substrate for peripheral nerve regeneration. They doped the hydrogel with conductive PPy (In this case, not strictly a nanocomposite but a hybrid hydrogel) and measured its conductivity through a Hall effect testing system. The conductivity of the hydrogel increased from  $7.35 \times 10^{-6}$  to  $8 \times 10^{-3} \text{ S m}^{-1}$  by increasing the PPy mass ratio from 0.02 to 0.4, but no information was given on the charge carrier concentration and mobility.<sup>86</sup>

## 5.5 Conductive atomic force microscopy

Conductive atomic force microscopy (C-AFM) is a mode in AFM that allows for simultaneous measurement of the topography of a material and the electric current flow at the contact point of the probe with the sample.<sup>141</sup> In nanomaterials engineering, it can be used to evaluate the property-enhancement and dispersion of conductive nanomaterials on the surface of a sample. Annabi *et al.* fabricated an elastic, conductive hydrogel based on a human recombinant protein and GO. They dispersed  $2 \text{ mg ml}^{-1}$  GO nanomaterials in a methacryloyl-substituted tropoelastin prepolymer solution and then initiated UV photocrosslinking to obtain a biocompatible, highly elastic hydrogel for the regeneration of electroactive tissue. They conducted C-AFM measurements on a pristine and a nanocomposite hydrogel (Fig. 13). Impedance spectroscopy, C-AFM and excitation threshold measurements all

confirmed the higher electrical conductivity of the nanocomposite hydrogel.<sup>142</sup>

# 6. Discussion

## 6.1 Measured electrical conductivities of nanocomposite hydrogels

Conductive nanocomposite hydrogels are a relatively recent but rapidly expanding field of research. Virtually all publications covered in this review were published in the last 10 years. The main application that drives research are electrically conductive scaffolds for tissue engineering of electroactive cells. Other applications include strain sensors, biosensors, drug delivery, artificial skin, electrocardiography gel and electromagnetic interference shielding.<sup>74,143–145</sup> Table 2 presents a comprehensive summary of nanocomposite electrically conductive hydrogels, along with the nanomaterial concentrations employed and the highest conductivity value measured.

Impedance spectroscopy graphs give impedance or conductivity values over a range of AC frequencies. In some cases, when the low-frequency end of the graph forms a straight line, a DC conductivity value can be extrapolated (by expanding the line at 0 Hz). In most cases though, DC conductivity cannot be compared with AC impedance. Table 3 presents the nanocomposite hydrogels studied by impedance spectroscopy.

Some hydrogel studies incorporate conductive materials which are not strictly defined as nanomaterials, *e.g.* hydrogels with conductive oligomers. We provide a short table of such hydrogels as ESI† (Table S1). It contains hydrogels with the incorporation of aniline oligomers, hybrid hydrogels with polypyrrole polymer incorporation and metallic microwires.

The nanomaterial concentrations in hydrogels can be described in many ways:  $\text{mg ml}^{-1}$ , % w/w, w/v, v/v on the total

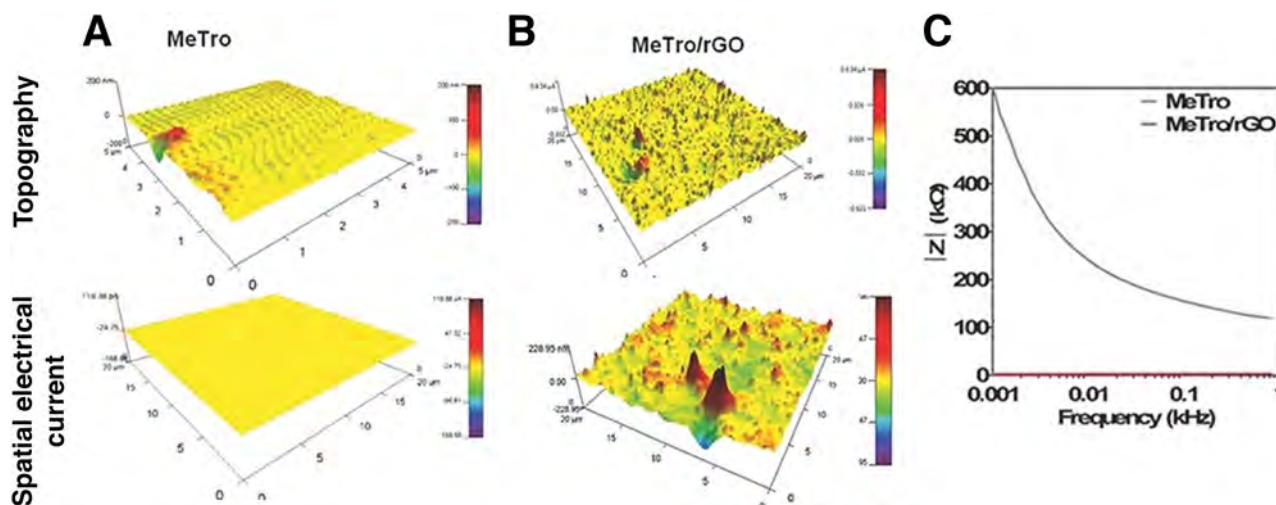


Fig. 13 Conductive atomic force microscopy (C-AFM) and impedance spectroscopy of methacryloyl-substituted tropoelastin (MeTro) – rGO hydrogel. Surface topography and spatial conductivity of (A) pristine and (B) nanocomposite hydrogel. The nanomaterial affected both the topography and the electrical conductivity of the hydrogel. Current spikes are visible on the nanomaterials' locations. (C). Impedance spectroscopy of pristine (green) and nanocomposite hydrogel (red). Reduced GO decreased impedance in all of the frequency range studied. Adapted with permission from ref. 142. Copyright 2015 Wiley.



Table 2 Electrical conductivity of nanocomposite hydrogels

Nanomaterial	Polymer matrix	Application	Nanomaterial conc.	Hydrogel cond. $\sigma_0$ ( $S m^{-1}$ ) (at 1 mg ml <sup>-1</sup> CNT)	$\sigma_{max}$ ( $S m^{-1}$ )	Notes	Ref.
CNT	OPF oligo(poly(ethylene glycol)fumarate)	Neural tissue engineering	10 mg ml <sup>-1</sup>	$3.7 \times 10^{-4}$	$2.04 \times 10^{-3}$		72
CNT	PAM/PAA polyacrylamide/polyacrylic acid	Biosignals/skin protection	0.36% w/v	0.25	8	Glycerol + water hydrogels. CNTs functionalized with dopamine	146
CNT	Gelatin	Skin treatment	0.4% w/w	$2.5 \times 10^{-2}$	$7.2 \times 10^{-2}$	CNTs functionalized with dopamine	147
CNT (SW)	Gelatin	Muscle tissue engineering	1.5 mg ml <sup>-1</sup>	$3 \times 10^{-8}$	$5 \times 10^{-5}$	Gelatin cross-linked with GA	73
CNT (SW)	Collagen type I	Tissue engineering	4% w/w polymer	0.3	0.7	Collagen seeded with HDF human dermal fibroblast cells	113
CNT (SW)	Collagen type I	Neural tissue engineering	0.01% w/w	1.4	2.4	CNTs oxidized. Measured cond. in prepolymer solution form	139
CNT (SW)	Collagen type I	Muscle tissue engineering	2% w/w polymer	0.25	0.61		148
CNT (SW)	Agarose	Motion sensor	15% w/w polymer	0.1 (at 5% CNT w/w of polymer)	0.3	CNTs functionalized with dopamine	145
CNT (DW)	Agarose	Drug delivery	40% w/w polymer	$7.4 \times 10^{-4}$	$2.7 \times 10^{-2}$		112
CNT (MW)	Agarose	Neural tissue engineering	0.1% w/w	0.94	1.46	Hydrogels lyophilized and then placed in a PBS solution before conductivity measurements	149
CNT (MW)	Gellan gum	Tissue engineering	0.1–0.5% w/v increased with drying	$10^{-3}$	$10^{-2}$ , up to 0.53 with decreasing water content		109
CNT (MW)	Gelatin	Drug delivery	8 mg ml <sup>-1</sup>	$1.3 \times 10^{-11}$	$2.6 \times 10^{-11}$		74
CNT (MW)	Alginate	Probe microbe electro-activity				Percolation at 0.5% w/w	110
CNT (MW)	PNIPAM poly <i>N</i> -isopropyl acrylamide	Motion sensor	4 mg ml <sup>-1</sup>		0.13	CNTs carboxylated. LAPO-NITE <sup>®</sup> nanoclay added for mechanical strength	150
CNT (MW)	PAM/CS polyacrylamide/chitosan	Motion sensor	0.125% w/v	0.1	0.95	CNTs carboxylated	44
CNT (MW)	PAM polyacrylamide	Artificial skin, Electromagnetic interference shielding	1% w/w	0.1	0.85	CNTs dispersed with cellulose nanofiber	143
CNT (MW)	poly(EA-MAA) ethyl acrylate – methacrylic acid		1% w/w	$4 \times 10^{-2}$	3		111
CNT (MW)	PEG polyethylene glycol	Neural tissue engineering	0.1% w/v	1.14	1.6		151
CNT (MW)	PEG polyethylene glycol	Neural tissue engineering	1.2% w/v	1.14	2		152
CNT (MW)	PEG/DFA polyethylene glycol/dimer fatty acid	Tissue engineering	6% w/w polymer	$2.4 \times 10$	$1.6 \times 10^{-2}$	CNTs oxidized	153
CNT (MW) + GO	OPF oligo(poly(ethylene glycol) fumarate)	Neural tissue engineering	10 mg ml <sup>-1</sup> rGO 10 mg ml <sup>-1</sup> CNT	$2 \times 10^{-4}$	$7.9 \times 10^{-4}$	CNTs functionalized with PEGA poly(ethylene glycol)acrylate	39
Carbon black	PGMA poly(glycerol methacrylate)	Bioelectronics	0.005% w/w	$10^{-4}$	0.1		154
Carbon black	PEGMA poly(ethylene glycol) dimethacrylate	Bioelectronics	0.005% w/w	$9.3 \times 10^{-5}$	$1.8 \times 10^{-2}$		154
Carbon black	PDEGMA poly(diethylene glycol) dimethacrylate	Bioelectronics	0.005% w/w	$8.9 \times 10^{-5}$	$1.2 \times 10^{-2}$		154
Carbon nanofibers	Chitosan	Muscle tissue engineering	1% w/v	0.03	0.04		155
GO	Chitosan	Tissue engineering	0.05% w/w	$5.7 \times 10^{-2}$	$1.22 \times 10^{-1}$	GO functionalized with dopamine	119
GO	Chitosan	Neural tissue engineering	3% w/w polymer	$10^{-8}$	$4 \times 10^{-2}$		156
GO	Chitosan	Tissue engineering	3% w/w polymer	$10^{-8}$	0.13	GO reduced	115



Table 2 (continued)

Nanomaterial	Polymer matrix	Application	Nanomaterial conc.	Hydrogel cond. $\sigma_0$ ( $S m^{-1}$ )	$\sigma_{max}$ ( $S m^{-1}$ )	Notes	Ref.
GO	PVA/PEG poly(vinyl alcohol)/polyethylene glycol	ECG acquisition	1.2% w/w	$8.5 \times 10^{-4}$	$5.1 \times 10^{-3}$		144
GO + PEDOT:PSS	PU polyurethane	Neural tissue engineering	14% w/w GO + PEDOT:PSS	0.13 (at 2% w/w GO + PEDOT:PSS)	0.62	Liquid crystals of reduced GO + PEDOT:PSS	157
GO	OPF oligo(poly(ethylene glycol) fumarate)	Muscle tissue engineering	1 mg ml <sup>-1</sup>	0.09	0.42		158
GO	PVA poly(vinyl alcohol)		0.5% w/w PVA	$10^{-4}$	0.27	GO reduced and functionalized with dopamine.	79
GO	Sodium polyacrylate		10% w/w polymer	$5.9 \times 10^{-4}$	$3.7 \times 10^{-3}$	GO reduced	159
GO	PNIPAM poly <i>N</i> -isopropyl acrylamide		0.23% v/v	0.7 (at 0.05% v/v, 100 Hz)	9 (at 100 Hz)	A reduced GO aerogel (monolith) is mixed with the polymer	114
GO	PAM polyacrylamide	Muscle tissue engineering	0.3% w/v	$1.8 \times 10^{-3}$	$1.3 \times 10^{-2}$	GO reduced	160
GO	PAM polyacrylamide		4% w/w polymer	$2.5 \times 10^{-2}$	10	GO reduced and functionalized with dopamine	161
Graphene	PAM polyacrylamide		2% w/w polymer	–	$10^{-6}$		162
Graphene	PAA poly(acrylic acid)		1.25% v/v	$3 \times 10^{-14}$	$1.6 \times 10^{-5}$		80
Ag nanowires	Agarose	Motion sensor	50 mg ml <sup>-1</sup>	0.01 (at 10 mg ml <sup>-1</sup> Ag nanowires)	300	Patterned silver nanowires	163
Ag	Collagen	Tissue engineering	$2.7 \times 10^{-7}$ % w/w	$4 \times 10^{-7}$	$8 \times 10^{-7}$		164
Au	Collagen	Tissue engineering	$4.9 \times 10^{-7}$ % w/w	$4 \times 10^{-7}$	$1.3 \times 10^{-6}$		164
Au	Chitosan	Muscle tissue engineering	1.5 w/w polymer	0.08	0.13		91
PANI nanofibers	PAA poly(acrylic acid)	Muscle tissue engineering	4.65% w/w		0.14	Doped with CSA camphor sulphonic acid	122
PANI	PVP poly( <i>N</i> -vinyl-2-pyrrolidone)		0.06% w/w	$5 \times 10^{-4}$	$10^{-3}$		138
PEDOT:PSS	GelMA gelatin methacrylate	Motion sensor	0.5% w/v	0.03	0.09	LAPONITE <sup>®</sup> nanoplatelets added for mechanical strength	87
PPy	GelMA gelatin methacrylate + PEGDA poly(ethylene glycol) diacrylate	Muscle tissue engineering	4 mg ml <sup>-1</sup>	$3.6 \times 10^{-3}$ (at 1.2 $\times 10^{-2}$ 1 mg ml <sup>-1</sup> Ppy)			88

mass of the nanocomposite hydrogel or as a ratio over the polymer concentration, for example 5% CNT w/w of gelatin. Nanomaterial concentration expressed as a ratio over the total hydrogel mass or volume (water + polymer + nanomaterial) is more relevant for the electrical properties of the system (electrical percolation, for example, depends on the % v/v concentration) but does not remain stable over different conditions, since the water content of hydrogels may change due to evaporation or swelling. Nanomaterial concentration expressed as a ratio over the polymer concentration has the advantage of remaining stable on different conditions but is less relevant for the properties of the system as a whole. In the following tables, we have chosen to keep the nanomaterial concentration as reported by the original authors, due to a lack of sufficient data that would allow us to homogenize the concentrations (notably polymer concentrations and/or water content).

## 6.2 Processing methods to increase electrical conductivity

**6.2.1 Nanomaterial alignment.** Nanomaterials with high aspect ratios, such as nanotubes, nanosheets and nanowires can be aligned within the polymer matrix to further increase

the conductivity in the alignment orientation. The conductive nanomaterial alignment introduces an anisotropic conductivity to the hydrogel, a property which can be exploited in specific applications such as biosensing and bioelectronics.<sup>170,171</sup> Oriented nanomaterials on scaffolds for tissue engineering can also allow to direct the growth and differentiation of skeletal cells.<sup>171,172</sup> For example, mesenchymal stem cells on a substrate with aligned CNTs stretch along the direction of the CNTs. According to Namgung *et al.* the elongated stem cells have higher cytoskeletal tension which triggers mechanotransduction pathways translating into increased proliferation and differentiation when compared with cells growing on a substrate with randomly distributed CNTs.<sup>173</sup> Nanomaterials embedded in hydrogels can be aligned through mechanical strain,<sup>174</sup> with electrospinning<sup>175</sup> or through the application of an external AC electric field, a technique known as dielectrophoresis.<sup>165,176</sup>

**6.2.2 Dielectrophoresis.** In dielectrophoresis, an AC electric field exerts a force on dielectric particles, due to the charge polarisation on the particles and the surrounding medium.<sup>165</sup> It can be used in hydrogel nanoengineering, to orientate nanomaterials within a polymer matrix.





Table 3 Nanocomposite hydrogels characterized by impedance spectroscopy

Nanomaterial	Polymer matrix	Application	Nanomaterial conc.	Conductivity	Notes	Ref.
CNT	GelMA gelatin methacrylate	Muscle tissue engineering	0.3 mg ml <sup>-1</sup>	Impedance decreased with increased CNT content. Even more for aligned CNTs	CNTs carboxylated and aligned with dielectrophoresis	165
CNT (MW)	GelMA gelatin methacrylate	Muscle tissue engineering, actuator	5 mg ml <sup>-1</sup>	Increasing CNT content decreases impedance	CNTs carboxylated	166
CNT (MW)	GelMA gelatin methacrylate	Muscle tissue engineering	1 mg ml <sup>-1</sup>	Impedance decreased with increased CNT content. Aligned CNTs decreased impedance even at lower concentration (0.25 mg ml <sup>-1</sup> )	CNTs carboxylated and aligned with dielectrophoresis	167
GO	GelMA gelatin methacrylate	Tissue engineering	2 mg ml <sup>-1</sup>	1 mg ml <sup>-1</sup> GO did not affect impedance. 2 mg ml <sup>-1</sup> GO decreased impedance		168
GO	Methacryloyl-substituted tropoelastin	Muscle tissue engineering	2 mg ml <sup>-1</sup>	GO decreased impedance. rGO even more		142
Au nanorods	GelMA gelatin methacrylate	Muscle tissue engineering	1.5 mg ml <sup>-1</sup>	Impedance decreased with increasing gold nanorod content	Gold nanorods aspect ratio 3.15	36
PEDOT:PSS	PHEA poly( <i>N</i> -hydroxyethyl acrylamide)	Muscle tissue engineering	0.3% w/v	Impedance decreased with increasing PEDOT:PSS content		169

Small and Paunov elaborated an agarose – silver nanowire composite gel with anisotropic electrical conductivity.<sup>60</sup> They dissolved 0.5% w/v agarose in hot water (70 °C) and added 0.5% w/v 50 nm long silver nanowires. An AC electric field of 50 to 300 V cm<sup>-1</sup> and frequency of 5 kHz was applied to assemble and align the nanowires into percolating microwires in the direction of the applied field, while the temperature was kept at 55 °C. When the silver nanowires had aligned, the temperature was lowered to allow the agarose to form a gel, thus entrapping the nanowires. In a subsequent study by the same authors, the silver nanowires were functionalised with an antibody (thiolated biotin) and the electrically anisotropic hydrogel was used as a proof of concept for biosignal detection (Fig. 14(A)). An antigen (streptavidin) that binds on the antibody, induces tighter packing of the silver nanowires and limits their Brownian motion leading to an increased conductivity.<sup>60</sup>

Ramón-Azcón *et al.* prepared a gelatin methacrylate hydrogel with 0.3 mg ml<sup>-1</sup> CNTs. An AC electric field of 20 V<sub>pp</sub> and frequency of 2 MHz was applied to dielectrophoretically align the CNTs (Fig. 14(B)). The gelatin methacrylate was polymerised after aligning the CNTs, thus freezing their orientation.<sup>165</sup> In further work, they showed how the nanocomposite hydrogel with aligned CNTs enhanced the cardiac differentiation of mouse embryoid bodies. An externally applied electric pulse stimulation (1 V, 10 ms, 1 Hz) significantly increased the beating frequency of embryoid bodies on the nanocomposite hydrogels with aligned CNTs, as compared to the pristine hydrogels or the nanocomposite hydrogels with randomly distributed CNTs.<sup>167</sup>

### 6.2.3 Mussel-inspired dopamine-coating of nanomaterials.

Efficient dispersion of nanomaterials is essential for their property-enhancing features. In particular, a substantial increase in electrical conductivity of nanocomposite hydrogels can only take place once the filler particles have formed a percolative network, and the agglomeration of nanomaterials dramatically increases the percolation threshold concentration.

Polydopamine coating is inspired by adhesive proteins secreted by mussels to attach to wet surfaces. Dopamine is a simple

structural mimic of *Mytilus Edulis* foot protein 5 (Mefp-5).<sup>177</sup> In an alkaline solution, it self-polymerizes into a thin surface-adherent polydopamine film through oxidation by dissolved oxygen.<sup>147,178</sup> Polydopamine adheres to a large number of varied surfaces through covalent (Michael reaction of catechol with an amine or thiol) and non-covalent (hydrogen bonds and  $\pi$ - $\pi$  stacking) interactions.<sup>178</sup> In nanocomposite hydrogels, polydopamine coating is used to facilitate nanomaterial dispersion and to confer self-healing and adhesive properties to the hydrogel.<sup>119,161</sup>

Han *et al.* exploited the surface properties of polydopamine to fabricate a conductive and adhesive nanocomposite hydrogel. They coated CNTs with polydopamine and noted that the coating facilitated the dispersion of CNTs in an aqueous suspension. Next, they dissolved acrylamide and acrylic acid monomers in the suspension, before adding glycerol to form a glycerol–water binary solvent that allows the gel to be manipulated in a very wide range of temperatures (–20 °C to 60 °C). The glycerol–water gel was then formed *in situ* by UV-initiation of polyacrylamide/polyacrylic acid copolymerization. The gels with polydopamine coated CNTs showed a significant increase in electrical conductivity compared to gels without dopamine (from 5 to 8.2 S m<sup>-1</sup> for hydrogels with 10% w/w of polymer CNTs). The resulting hydrogel can find applications in adhesive bioelectronics to detect biosignals.<sup>146</sup>

Jing *et al.* conceived a self-healing, adhesive and conductive nanocomposite hydrogel for cardiac tissue engineering. They used a chitosan polymer, reinforced with 0.5 mg ml<sup>-1</sup> GO. Dopamine was added to cross-link the chitosan gel, partially reduce the graphene oxide (the oxidative polymerization of dopamine releases electrons) and facilitate its dispersion by coating it (Fig. 14(C)). The nanocomposite hydrogel showed a twofold increase in electrical conductivity (from 0.06 S m<sup>-1</sup> to 0.12 S m<sup>-1</sup> for chitosan-dopamine hydrogels) and enhanced the viability and proliferation of human stem cell-derived cardiomyocytes.<sup>119</sup> Zhang *et al.* drew on the previous work and proposed a flexible, wearable sensor consisting of a poly(vinyl alcohol) hydrogel matrix embedded with GO. Dopamine was



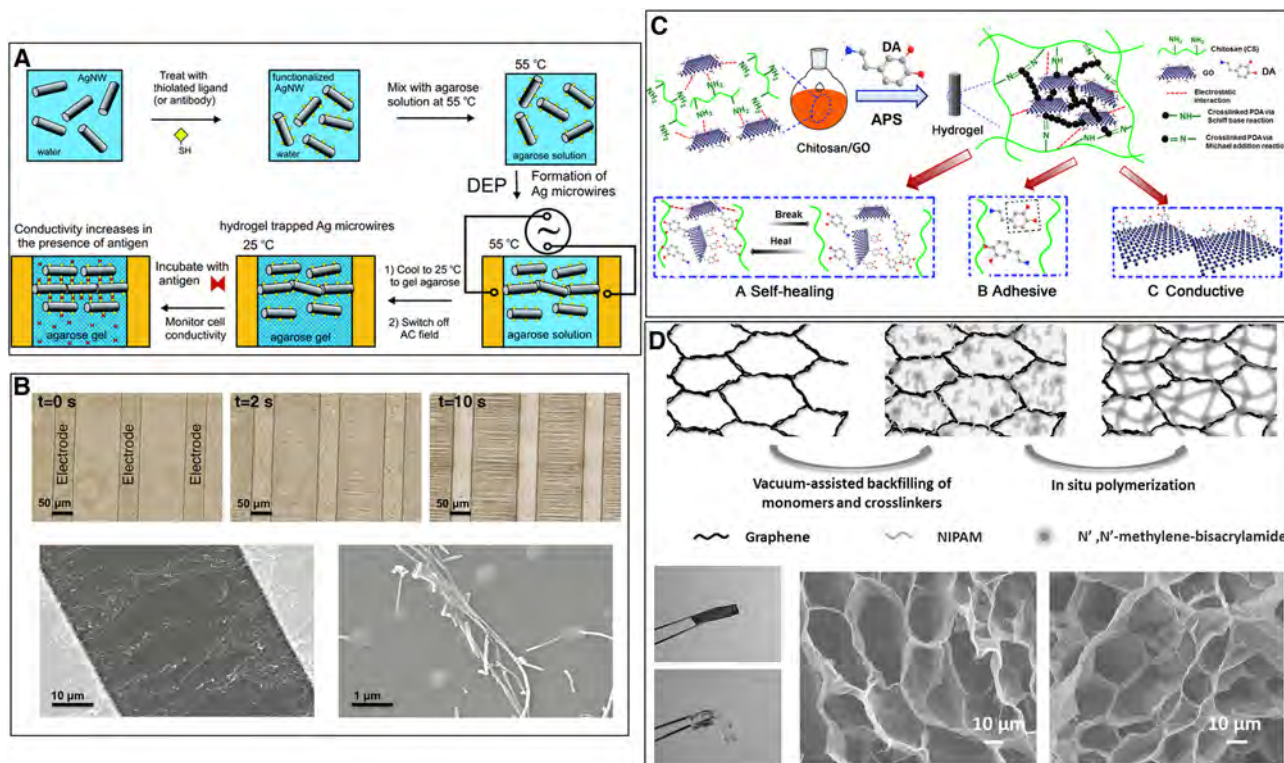


**Fig. 14** Processing methods to increase electrical conductivity of nanocomposite hydrogels. (A) Functionalized silver nanowires in warm water–agarose solution aligned through dielectrophoresis (DEP). After cooling down, agarose gelation occurs and a hydrogel with anisotropic electrical conductivity is formed. The conductivity increases in the presence of antigen due to the tighter packing of the functionalized silver nanowires. Reproduced from ref. 60 with permission from The Royal Society of Chemistry. (B) Nanocomposite hydrogel with chitosan, polydopamine and reduced GO. Self-healing mechanism attributable to the electrostatic interactions between GO and chitosan and the non-covalent bonding of catechol groups. Adhesiveness as a result of the catechol groups of polydopamine. Electrical conductivity through the reduced GO. Reprinted from ref. 119, Copyright 2016, with permission from Elsevier. Dielectrophoretic alignment of CNT between electrode bands. Phase images of CNT dielectrophoretic alignment over time. SEM images of dielectrophoretically aligned CNTs between two electrodes. Reprinted from ref. 167, Copyright 2017, with permission from Elsevier. (D) Graphene monolith – poly-*N*-isopropylacrylamide hydrogel. Photos of nanocomposite (dark and rigid) and pristine (transparent) hydrogel and SEM images of graphene monolith and freeze-dried nanocomposite hydrogel. Reprinted with permission from ref. 114. Copyright 2014 Wiley.

added to reduce and facilitate the dispersion of GO and the resulting hydrogel had a conductivity of  $0.5 \text{ S m}^{-1}$ . Small-scale movements of the human body (from joint movements to breathing) applied strain to the hydrogel, changing its electrical conductivity.<sup>179</sup>

Other applications of mussel-inspired conductive hydrogels include a patch to repair myocardial infarction,<sup>88</sup> wound dressing to promote the regeneration of infected skin,<sup>147,180</sup> a self-rolling hydrogel film biosensor<sup>181</sup> and an implantable biosensor for health monitoring.<sup>161</sup>

**6.2.4 Monolith (aerogel) conductive network.** Qiu *et al.* fabricated a cork-like, mechanically stable, elastic, graphene monolith (or aerogel) by freeze casting.<sup>182</sup> In following work, they developed a conductive hydrogel by inserting an aqueous solution of *N*-isopropylacrylamide monomers and polymerizing *in situ* (Fig. 14(D)). In contrast to conventional graphene nanocomposite hydrogels, where the percolation threshold is between 0.2 and 2% v/v, they reported a very low percolation threshold of 0.045% v/v. Additionally, no surface modification of graphene is required with this technique. Conventional nanocomposite hydrogels have a random distribution of

nanomaterials which also tend to form aggregates. The graphene monolith hydrogel was polymerized within an already percolated structure of graphene sheets.<sup>114</sup>

**6.2.5 Limitations of processing methods.** The above processing methods can increase the electrical conductivity of nanocomposite hydrogels by aligning the nanomaterials, improving their dispersion, and polymerizing a hydrogel within an already formed conductive network of nanomaterials. However, they do have some practical limitations. Alignment is only relevant for nanomaterials with high aspect ratios. It produces anisotropic conductivity, increasing the electrical conductivity in the direction of alignment and decreasing it in the perpendicular direction.<sup>171</sup> This may prove useful in some applications but disadvantageous for others. Polydopamine coating improves dispersion of hydrophobic nanomaterials but coating the surface of conductive nanomaterials with a polymer also decreases the electron tunnelling conductance. Lastly, not all nanomaterials can form self-standing 3D structures. CNTs and graphene are known to form monoliths which can then be vacuum-filled with a monomer solution and polymerized *in situ*. This may also be possible with metal nanowires but not with





spherical metal nanoparticles or conducting polymer nanomaterials. In addition, the precursor solution must have adequately low viscosity to enter the porous monoliths.

### 6.3 Comments and comparisons of electrical conductivities

Electrical conductivity of nanocomposite hydrogels varies by several orders of magnitude. The conductivity *vs.* nanomaterial concentration graph (Fig. 15) brings together the DC electrical conductivity values of nanocomposite hydrogels *vs.* nanomaterial concentration. It was compiled from the available literature data,<sup>44,72–74,87,88,91,109,111–115,119,144,146,147,151,152,155–160,164,183</sup> when enough information was available. Some observations can be made from these graphs and Table 2.

Nanomaterial concentrations employed to increase the conductivity of hydrogels were mostly within the range of 0.01 to 1% w/w. Some higher concentrations seen in the graph represent studies where nanocomposite hydrogels were partially dried, thus importantly increasing nanomaterial concentration.

Nanocomposite hydrogels can be classified as semi-conductors with their electrical conductivity spanning 6 orders of magnitude, from  $10^{-5}$  to  $10$  S  $m^{-1}$ . The conductivities of hydrogels of different polymers, without nanomaterials, already show an important variability. We can distinguish two main groups. Firstly, the more insulating hydrogels, with conductivities of  $10^{-6}$  up to  $2 \times 10^{-3}$  S  $m^{-1}$ . These are hydrogels made from agarose, alginate, hyaluronan, poly(vinyl alcohol), oligo(poly(ethylene glycol) fumarate) and polyacrylic acid. A second group of hydrogels have higher conductivities, even without nanomaterials, with values ranging from  $2 \times 10^{-2}$  up to  $1.4$  S  $m^{-1}$ . They are

made from polymers including chitosan, polyethylene glycol, collagen, gelatin and poly(ethyl acrylate). Some of these differences (though not all) can be explained on the basis of polymer material chemistry. Polymers with ionisable functional groups (like amines and carboxylic acids) will confer a higher ionic conductivity to the hydrogel and polymers with conjugated chains have free electrons that contribute to the electronic conductivity of the polymer. Different measuring methods and conditions also contribute to the observed variability. A third group, not presented here, concerns hydrogels of conducting polymers. Conducting polymers include PPy, PANI, polythiophene, aniline oligomers and PEDOT. The hydrogels formed from these polymers are conductive but are brittle, have poor mechanical properties and are not biodegradable.<sup>57</sup>

The majority of nanocomposite hydrogels use carbon-based nanoparticles. GRMs and CNTs combine superior mechanical strength and electrical conductivity with high aspect ratios, leading to low percolation thresholds. By plotting the conductivity *vs.* concentration of these two nanomaterials in separate graphs, a different story emerges. GRMs show a relatively linear relationship between concentration and conductivity, on a log-log graph (Fig. 15(C)). Higher concentrations lead to higher conductivities. In the case of CNTs, there is no dominant trend on the graph (Fig. 15(B)). This is accentuated by some hydrogels that have high conductivity even without nanomaterial percolation (collagen and polyethylene glycol) but even by removing them, the relationship between concentration and conductivity is less straightforward.

Our hypothesis is that CNT agglomeration partly explains this difference. CNTs are highly hydrophobic and tend to form

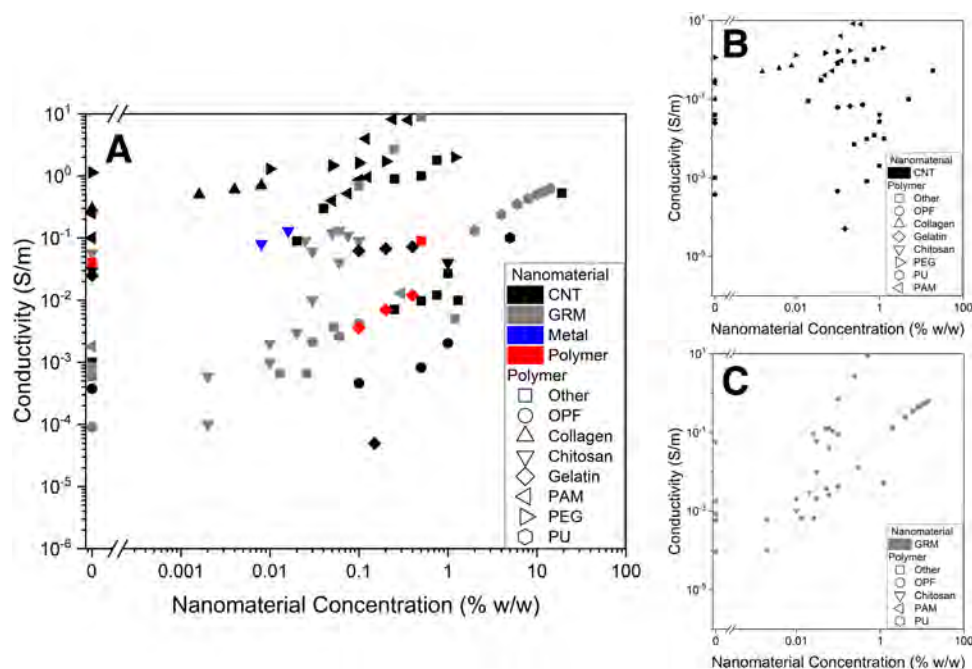


**Fig. 15** Nanocomposite hydrogel electrical conductivity *vs.* nanomaterial concentration. (A) All, (B) CNTs, (C) GRMs. A nanomaterial concentration of 0 represents the electrical conductivity of the pristine hydrogels (without conductive nanomaterials). OPF: oligo(poly(ethylene glycol) fumarate); PAM: polyacrylamide; PEG: polyethylene glycol; PU: polyurethane. Data extracted from ref. 44, 72–74, 87, 88, 91, 109, 111–115, 119, 144, 146, 147, 151, 152, 155–160, 164 and 183.



agglomerates in aqueous suspensions. Hydrogels where the CNTs form bundles instead of uniformly dispersing in the hydrogel matrix do not form a percolation network, even in high concentrations. At the same time, CNTs have high aspect ratio (approximately 1000 or higher) and can, on the principle, form a percolating network even at low concentrations, if they are well dispersed. We maintain that, concerning the electrical conductivity of CNT-loaded hydrogels, dispersion is a parameter at least as important as concentration, if not more. In GRMs, hydrogels with rGO dominate the graph. GO is well dispersed in aqueous suspensions. The hydroxyl and carboxylic/carboxylate groups are hydrophilic, facilitating GO dispersion. GO has a much lower conductivity than graphene, but GO reduction can restore part of it. Better dispersions lead to a straightforward relationship between concentration and conductivity. We did not find in literature a sufficient number of hydrogels with polymer and metal nanomaterials to extend this reasoning.

## 7. Conclusion – perspectives

Nanocomposite hydrogels are complex, polyphasic materials, consisting of at least three components: water, a polymer matrix and the nanomaterials. In most cases additional components are also present: hybrid hydrogels with a second polymer, cross-linkers, dispersants and other impurities. All these components contribute to the electrical properties of the hydrogel through adding charge carriers (ions and electrons) and restricting or facilitating their mobility.

Moreover, nanocomposite hydrogels are dynamic systems. In aqueous environments they reach a dynamic equilibrium and their mass remains constant. When removed from an aqueous environment, and if the atmosphere is not saturated with water vapours, hydrogels lose over time a part of their water content. The kinetics of drying depend on the nature of the polymer, the nanomaterials and the environmental conditions (temperature, humidity), but can be quite rapid for most hydrogels even in ambient conditions. Electrical characterization equipment is mostly adapted to either solid materials or liquids. Hydrogels are viscoelastic materials with a high water content, falling between these two categories. The water loss affects electrical conductivity in a number of ways. Water loss changes the organisation of the hydrogel, densifying the polymer matrix. This directly reduces ion mobility, decreasing ionic conductivity. At the same time, the concentration of all components increases, due to the water loss. The nanomaterial configuration changes and can lead to a more connected network, increasing electronic conductivity. An example of this complexity is that despite all the efforts that have been undertaken, the percolation studies for nanocomposite hydrogels fail to reproduce the clear cut-off values found in studies of solid nanocomposite materials.

Hydrogels find numerous applications in biomedicine thanks to their biocompatibility, high water content and resemblance to native tissues. Materials scientists have been working on tailoring their properties, such as mechanical strength, water absorption capacity, porosity, adhesiveness and self-healability

to custom fit specific applications. In parallel, hydrogels can be made stimuli-responsive, reacting to environmental cues like temperature, pH, antigen presence, electromagnetic fields, and more. The incorporation of conductive nanomaterials can confer electrical conductivity to—otherwise insulating—hydrogels, expanding their field of application. These nanocomposite conductive hydrogels are widely used in tissue engineering, strain sensors and drug delivery where their electrical properties play a crucial role. Their applications will continue to expand as we further understand the link between the materials, the processing methods and their electrical properties.

## Abbreviations

CNT	Carbon nanotubes
SWNT	Single-wall carbon nanotubes
MWNT	Multi-wall carbon nanotubes
GRM	Graphene-related materials
GO	Graphene oxide
rGO	Reduced graphene oxide
PPy	Polypyrrole
PANI	Polyaniline
PEDOT	Poly-(3,4-ethylenedioxythiophene)
PSS	Poly(sodium-4-styrenesulfonate)

## Author contributions

G. Kougkoulos: writing – original draft; M. Golzio: writing – review & editing; L. Laudebat: writing – review & editing, supervision; Z. Valdez-Nava: writing – review & editing, supervision; E. Flahaut: writing – review & editing, supervision, funding acquisition.

## Conflicts of interest

There are no conflicts to declare.

## Acknowledgements

The current work is funded by the French national research agency under the project CARBO2DERM –Carbon nanotubes for the transdermal delivery of therapeutic molecules (grant ANR-19-CE09-0007).

## References

- 1 M. J. Lewis, in *Physical Properties of Foods and Food Processing Systems*, ed. M. J. Lewis, Woodhead Publishing, 1996, pp. 137–166.
- 2 Y. S. Zhang and A. Khademhosseini, *Science*, 2017, **356**(6337), 1–10.
- 3 K. Varaprasad, G. M. Raghavendra, T. Jayaramudu, M. M. Yallapu and R. Sadiku, *Mater. Sci. Eng., C*, 2017, **79**, 958–971.
- 4 F. Ullah, M. B. H. Othman, F. Javed, Z. Ahmad and H. Md. Akil, *Mater. Sci. Eng., C*, 2015, **57**, 414–433.



- 5 N. A. Peppas and A. S. Hoffman, in *Biomaterials Science*, ed. W. R. Wagner, S. E. Sakiyama-Elbert, G. Zhang and M. J. Yaszemski, Academic Press, 4th edn, 2020, pp. 153–166.
- 6 W. Wagermaier and P. Fratzl, in *Polymer Science: A Comprehensive Reference*, ed. K. Matyjaszewski and M. Möller, Elsevier, Amsterdam, 2012, pp. 35–55.
- 7 E. M. Ahmed, *J. Adv. Res.*, 2015, **6**, 105–121.
- 8 J. P. Gong, *Soft Matter*, 2006, **2**, 544–552.
- 9 H. Li, Y. S. Choi, M. W. Rutland and R. Atkin, *J. Colloid Interface Sci.*, 2020, **563**, 347–353.
- 10 A. S. Hoffman, *Adv. Drug Delivery Rev.*, 2012, **64**, 18–23.
- 11 A. Doderio, L. Pianella, S. Vicini, M. Alloisio, M. Ottonelli and M. Castellano, *Eur. Polym. J.*, 2019, **118**, 586–594.
- 12 S. J. Buwalda, K. W. M. Boere, P. J. Dijkstra, J. Feijen, T. Vermonden and W. E. Hennink, *J. Controlled Release*, 2014, **190**, 254–273.
- 13 D. Zhang, B. Ren, Y. Zhang, L. Xu, Q. Huang, Y. He, X. Li, J. Wu, J. Yang, Q. Chen, Y. Chang and J. Zheng, *J. Mater. Chem. B*, 2020, **8**, 3171–3191.
- 14 G. Isapour and M. Lattuada, *Adv. Mater.*, 2018, **30**, 1707069.
- 15 I. Tokarev, V. Gopishetty, J. Zhou, M. Pita, M. Motornov, E. Katz and S. Minko, *ACS Appl. Mater. Interfaces*, 2009, **1**, 532–536.
- 16 T. Distler and A. R. Boccaccini, *Acta Biomater.*, 2020, **101**, 1–13.
- 17 N. Chirani, L. Yahia, L. Gritsch, F. L. Motta, S. Chirani and S. Faré, *J. Biomed. Sci.*, 2016, **4**(2.13), 1–23.
- 18 B. W. Walker, R. P. Lara, E. Mogadam, C. H. Yu, W. Kimball and N. Annabi, *Prog. Polym. Sci.*, 2019, **92**, 135–157.
- 19 J. Stejskal, *Chem. Pap.*, 2017, **71**, 269–291.
- 20 K. Liu, S. Wei, L. Song, H. Liu and T. Wang, *J. Agric. Food Chem.*, 2020, **68**, 7269–7280.
- 21 A. Malti, J. Edberg, H. Granberg, Z. U. Khan, J. W. Andreasen, X. Liu, D. Zhao, H. Zhang, Y. Yao, J. W. Brill, I. Engquist, M. Fahlman, L. Wågberg, X. Crispin and M. Berggren, *Adv. Sci.*, 2016, **3**, 1500305.
- 22 B. Guo and P. X. Ma, *Biomacromolecules*, 2018, **19**, 1764–1782.
- 23 Q. Peng, J. Chen, T. Wang, X. Peng, J. Liu, X. Wang, J. Wang and H. Zeng, *InfoMat*, 2020, **2**, 843–865.
- 24 D. Liang, G. Zhou, Y. Hu, C. Zhao and C. Chen, *J. Mater. Sci.*, 2021, **56**, 14531–14541.
- 25 X. Zhang, Y. Tang, P. Wang, Y. Wang, T. Wu, T. Li, S. Huang, J. Zhang, H. Wang, S. Ma, L. Wang and W. Xu, *New J. Chem.*, 2022, **46**, 13838–13855.
- 26 C.-J. Lee, H. Wu, Y. Hu, M. Young, H. Wang, D. Lynch, F. Xu, H. Cong and G. Cheng, *ACS Appl. Mater. Interfaces*, 2018, **10**, 5845–5852.
- 27 M. Hess, R. G. Jones, J. Kahovec, T. Kitayama, P. Kratochvíl, P. Kubisa, W. Mormann, R. F. T. Stepto, D. Tabak, J. Vohlídal and E. S. Wilks, *Pure Appl. Chem.*, 2006, **78**, 2067–2074.
- 28 J. Cardoso, A. Huanosta and O. Manero, *Macromolecules*, 1991, **24**, 2890–2895.
- 29 C.-G. Wang, N. E. B. Surat'man, J. J. Chang, Z. L. Ong, B. Li, X. Fan, X. J. Loh and Z. Li, *Chem. – Asian J.*, 2022, **17**, e202200604.
- 30 S. Liu, J. Tang, F. Ji, W. Lin and S. Chen, *Gels*, 2022, **8**, 46.
- 31 A. Khademhosseini and R. Langer, *Nat. Protoc.*, 2016, **11**, 1775–1781.
- 32 J. A. Hunt, R. Chen, T. van Veen and N. Bryan, *J. Mater. Chem. B*, 2014, **2**, 5319–5338.
- 33 Y. Luo, in *Principles of Tissue Engineering*, ed. R. Lanza, R. Langer, J. P. Vacanti and A. Atala, Academic Press, 5th edn, 2020, pp. 343–360.
- 34 M. Petreaca and M. Martins-Green, in *Principles of Tissue Engineering*, ed. R. Lanza, R. Langer, J. P. Vacanti and A. Atala, Academic Press, 5th edn, 2020, pp.93–117.
- 35 R. Dong, P. X. Ma and B. Guo, *Biomaterials*, 2020, **229**, 119584.
- 36 A. Navaei, H. Saini, W. Christenson, R. T. Sullivan, R. Ros and M. Nikkhah, *Acta Biomater.*, 2016, **41**, 133–146.
- 37 Y. Li, L. Wei, L. Lan, Y. Gao, Q. Zhang, H. Dawit, J. Mao, L. Guo, L. Shen and L. Wang, *Acta Biomater.*, 2022, **139**, 157–178.
- 38 P. Zarrintaj, A. M. Urbanska, S. S. Gholizadeh, V. Goodarzi, M. R. Saeb and M. Mozafari, *J. Colloid Interface Sci.*, 2018, **516**, 57–66.
- 39 X. Liu, A. L. M. Ii, S. Park, B. E. Waletzki, A. Terzic, M. J. Yaszemski and L. Lu, *J. Mater. Chem. B*, 2016, **4**, 6930–6941.
- 40 R. Eivazzadeh-Keihan, A. Maleki, M. de la Guardia, M. S. Bani, K. K. Chenab, P. Pashazadeh-Panahi, B. Baradaran, A. Mokhtarzadeh and M. R. Hamblin, *J. Adv. Res.*, 2019, **18**, 185–201.
- 41 J. Pelto, M. Björninen, A. Pälli, E. Talvitie, J. Hyttinen, B. Mannerström, R. Suuronen Seppänen, M. Kellomäki, S. Miettinen and S. Haimi, *Tissue Eng., Part A*, 2012, **19**, 882–892.
- 42 L. Tang, S. Wu, J. Qu, L. Gong and J. Tang, *Materials*, 2020, **13**, 3947.
- 43 Z. Chen, Y. Chen, M. S. Hedenqvist, C. Chen, C. Cai, H. Li, H. Liu and J. Fu, *J. Mater. Chem. B*, 2021, **9**, 2561–2583.
- 44 S. Xia, S. Song, F. Jia and G. Gao, *J. Mater. Chem. B*, 2019, **7**, 4638–4648.
- 45 M. Liao, P. Wan, J. Wen, M. Gong, X. Wu, Y. Wang, R. Shi and L. Zhang, *Adv. Funct. Mater.*, 2017, **27**, 1703852.
- 46 P. He, J. Wu, X. Pan, L. Chen, K. Liu, H. Gao, H. Wu, S. Cao, L. Huang and Y. Ni, *J. Mater. Chem. A*, 2020, **8**, 3109–3118.
- 47 H. Yuk, B. Lu and X. Zhao, *Chem. Soc. Rev.*, 2019, **48**, 1642–1667.
- 48 J. Li and D. J. Mooney, *Nat. Rev. Mater.*, 2016, **1**, 1–17.
- 49 H.-W. Liu, S.-H. Hu, Y.-W. Chen and S.-Y. Chen, *J. Mater. Chem.*, 2012, **22**, 17311–17320.
- 50 K. Elkhoury, P. Koçak, A. Kang, E. Arab-Tehrany, J. Ellis Ward and S. R. Shin, *Pharmaceutics*, 2020, **12**, 849.
- 51 S. Merino, C. Martín, K. Kostarelos, M. Prato and E. Vázquez, *ACS Nano*, 2015, **9**, 4686–4697.
- 52 S. Murdan, *J. Controlled Release*, 2003, **92**, 1–17.
- 53 A. Servant, V. Leon, D. Jasim, L. Methven, P. Limousin, E. V. Fernandez-Pacheco, M. Prato and K. Kostarelos, *Adv. Healthcare Mater.*, 2014, **3**, 1334–1343.
- 54 J. H. Lee, Y. C. Yoon, H. S. Kim, J. Lee, E. Kim, C. Findekle and U. Katscher, *Sci. Rep.*, 2022, **12**, 73.



- 55 F. A. Duck, in *Physical Properties of Tissues*, ed. F. A. Duck, Academic Press, London, 1990, pp. 167–223.
- 56 T. W. Balmer, S. Vesztegom, P. Broekmann, A. Stahel and P. Büchler, *Sci. Rep.*, 2018, **8**, 8601.
- 57 A. Saberi, F. Jabbari, P. Zarrintaj, M. R. Saeb and M. Mozafari, *Biomolecules*, 2019, **9**, 448.
- 58 M. Rouabhia, H. Park, S. Meng, H. Derbali and Z. Zhang, *PLoS One*, 2013, **8**, e71660.
- 59 S. Du, N. Zhou, Y. Gao, G. Xie, H. Du, H. Jiang, L. Zhang, J. Tao and J. Zhu, *Nano Res.*, 2020, **13**, 2525–2533.
- 60 W. R. Small and V. N. Paunov, *J. Mater. Chem. B*, 2013, **1**, 5798–5805.
- 61 J.-F. Guillet, E. Flahaut and M. Golzio, *ChemPhysChem*, 2017, **18**, 2715–2723.
- 62 J. Simon, B. Jouanmiquieu, M.-P. Rols, E. Flahaut and M. Golzio, *Pharmaceutics*, 2021, **13**, 1805.
- 63 G. Kougkolos, presented in part at SEEDS/JCGE22, Le Croisic, France, June 2022.
- 64 ISO/TR 18401:2017(en), Nanotechnologies—Plain language explanation of selected terms from the ISO/IEC 80004 series, <https://www.iso.org/obp/ui/#iso:std:iso:tr:18401:ed-1:v1:en>, (accessed 4 July 2022).
- 65 K. Zhou, *Carbon Nanomaterials: Modeling, Design, and Applications*, CRC Press, 2019.
- 66 M. Monthieux, P. Serp, E. Flahaut, M. Razafinimanana, C. Laurent, A. Peigney, W. Bacsá and J.-M. Broto, in *Springer Handbook of Nanotechnology*, ed. B. Bhushan, Springer, Berlin, Heidelberg, 2010, pp. 47–118.
- 67 M. F. L. D. Volder, S. H. Tawfick, R. H. Baughman and A. J. Hart, *Science*, 2013, **339**, 535–539.
- 68 J. Simon, E. Flahaut and M. Golzio, *Materials*, 2019, **12**, 624.
- 69 C.-W. Nan, Y. Shen and J. Ma, *Annu. Rev. Mater. Res.*, 2010, **40**, 131–151.
- 70 T. W. Ebbesen, H. J. Lezec, H. Hiura, J. W. Bennett, H. F. Ghaemi and T. Thio, *Nature*, 1996, **382**, 54–56.
- 71 F. Xie, P. Weiss, O. Chauvet, J. Le Bideau and J. F. Tassin, *J. Mater. Sci. Mater. Med.*, 2010, **21**, 1163–1168.
- 72 X. Liu, J. C. Kim, A. Lee Miller, B. E. Waletzki and L. Lu, *New J. Chem.*, 2018, **42**, 17671–17681.
- 73 J. Zhou, J. Chen, H. Sun, X. Qiu, Y. Mou, Z. Liu, Y. Zhao, X. Li, Y. Han, C. Duan, R. Tang, C. Wang, W. Zhong, J. Liu, Y. Luo, M. (Mengqiu) Xing and C. Wang, *Sci. Rep.*, 2014, **4**, 3733.
- 74 U. G. Spizzirri, S. Hampel, G. Cirillo, F. P. Nicoletta, A. Hassan, O. Vittorio, N. Picci and F. Iemma, *Int. J. Pharm.*, 2013, **448**, 115–122.
- 75 X. Du, I. Skachko, A. Barker and E. Y. Andrei, *Nat. Nanotechnol.*, 2008, **3**, 491–495.
- 76 P. Wick, A. E. Louw-Gaume, M. Kucki, H. F. Krug, K. Kostarelos, B. Fadeel, K. A. Dawson, A. Salvati, E. Vázquez, L. Ballerini, M. Tretiach, F. Benfenati, E. Flahaut, L. Gauthier, M. Prato and A. Bianco, *Angew. Chem., Int. Ed.*, 2014, **53**, 7714–7718.
- 77 J. Chen, B. Yao, C. Li and G. Shi, *Carbon*, 2013, **64**, 225–229.
- 78 A. J. Marsden, D. G. Papageorgiou, C. Vallés, A. Liscio, V. Palermo, M. A. Bissett, R. J. Young and I. A. Kinloch, *2D Mater.*, 2018, **5**, 032003.
- 79 M. Wang, Y. Chen, R. Khan, H. Liu, C. Chen, T. Chen, R. Zhang and H. Li, *Colloids Surf., A*, 2019, **567**, 139–149.
- 80 A. Alam, Q. Meng, G. Shi, S. Arabi, J. Ma, N. Zhao and H.-C. Kuan, *Compos. Sci. Technol.*, 2016, **127**, 119–126.
- 81 W. Humphrey, A. Dalke and K. Schulten, *J. Mol. Graphics*, 1996, **14**, 33–38.
- 82 K. Momma and F. Izumi, *J. Appl. Crystallogr.*, 2011, **44**, 1272–1276.
- 83 R. Ravichandran, S. Sundarajan, J. R. Venugopal, S. Mukherjee and S. Ramakrishna, *J. R. Soc., Interface*, 2010, **7**, S559–S579.
- 84 J. Pecher and S. Mecking, *Chem. Rev.*, 2010, **110**, 6260–6279.
- 85 J. H. Min, M. Patel and W.-G. Koh, *Polymers*, 2018, **10**, 1078.
- 86 Y. Bu, H.-X. Xu, X. Li, W.-J. Xu, Y. Yin, H. Dai, X. Wang, Z.-J. Huang and P.-H. Xu, *RSC Adv.*, 2018, **8**, 10806–10817.
- 87 Y. Li, X. Xiong, X. Yu, X. Sun, J. Yang, L. Zhu, G. Qin, Y. Dai and Q. Chen, *Polym. Test.*, 2019, **75**, 38–47.
- 88 L. Wang, J. Jiang, W. Hua, A. Darabi, X. Song, C. Song, W. Zhong, M. M. Q. Xing and X. Qiu, *Adv. Funct. Mater.*, 2016, **26**, 4293–4305.
- 89 P. Zhang, I. Wyman, J. Hu, S. Lin, Z. Zhong, Y. Tu, Z. Huang and Y. Wei, *Mater. Sci. Eng., B*, 2017, **223**, 1–23.
- 90 T. Bruna, F. Maldonado-Bravo, P. Jara and N. Caro, *Int. J. Mol. Sci.*, 2021, **22**, 7202.
- 91 P. Baei, S. Jalili-Firoozinezhad, S. Rajabi-Zeleti, M. Tafazzoli-Shadpour, H. Baharvand and N. Aghdami, *Mater. Sci. Eng., C*, 2016, **63**, 131–141.
- 92 M. Naguib, V. N. Mochalin, M. W. Barsoum and Y. Gogotsi, *Adv. Mater.*, 2014, **26**, 992–1005.
- 93 J.-C. Lei, X. Zhang and Z. Zhou, *Front. Phys.*, 2015, **10**, 276–286.
- 94 Y.-Z. Zhang, J. K. El-Demellawi, Q. Jiang, G. Ge, H. Liang, K. Lee, X. Dong and H. N. Alshareef, *Chem. Soc. Rev.*, 2020, **49**, 7229–7251.
- 95 A. S. Zeraati, S. A. Mirkhani, P. Sun, M. Naguib, P. V. Braun and U. Sundararaj, *Nanoscale*, 2021, **13**, 3572–3580.
- 96 Y. Zhang, M. Gong and P. Wan, *Matter*, 2021, **4**, 2655–2658.
- 97 A. Bhat, S. Anwer, K. S. Bhat, M. I. H. Mohideen, K. Liao and A. Qurashi, *npj 2D Mater. Appl.*, 2021, **5**, 1–21.
- 98 A. Aharony and D. Stauffer, *Introduction To Percolation Theory: Second Edition*, Taylor & Francis, 2018.
- 99 J. W. Essam, *Rep. Prog. Phys.*, 1980, **43**, 833.
- 100 W. Bauhofer and J. Z. Kovacs, *Compos. Sci. Technol.*, 2009, **69**, 1486–1498.
- 101 L. Berhan and A. M. Sastry, *Phys. Rev. E: Stat., Nonlinear, Soft Matter Phys.*, 2007, **75**, 041120.
- 102 J. R. Winkler and H. B. Gray, *J. Am. Chem. Soc.*, 2014, **136**, 2930–2939.
- 103 A. P. Chatterjee, *J. Phys.: Condens. Matter*, 2015, **27**, 315303.
- 104 A. P. Chatterjee, *J. Chem. Phys.*, 2013, **139**, 224904.
- 105 G. Ambrosetti, C. Grimaldi, I. Balberg, T. Maeder, A. Danani and P. Ryser, *Phys. Rev. B: Condens. Matter Mater. Phys.*, 2010, **81**, 155434.
- 106 V. Ambegaokar, B. I. Halperin and J. S. Langer, *Phys. Rev. B: Solid State*, 1971, **4**, 2612–2620.





- 107 L. Berhan and A. M. Sastry, *Phys. Rev. E: Stat., Nonlinear, Soft Matter Phys.*, 2007, **75**, 041121.
- 108 H.-B. Zhang, W.-G. Zheng, Q. Yan, Y. Yang, J.-W. Wang, Z.-H. Lu, G.-Y. Ji and Z.-Z. Yu, *Polymer*, 2010, **51**, 1191–1196.
- 109 C. John Ferris and M. in het Panhuis, *Soft Matter*, 2009, **5**, 3430–3437.
- 110 L. Mottet, D. L. Cornec, J.-M. Noël, F. Kanoufi, B. Delord, P. Poulin, J. Bibette and N. Bremond, *Soft Matter*, 2018, **14**, 1434–1441.
- 111 Z. Cui, M. Zhou, P. J. Greensmith, W. Wang, J. A. Hoyland, I. A. Kinloch, T. Freemont and B. R. Saunders, *Soft Matter*, 2016, **12**, 4142–4153.
- 112 J.-F. Guillet, Z. Valdez-Nava, M. Golzio and E. Flahaut, *Carbon*, 2019, **146**, 542–548.
- 113 R. A. MacDonald, C. M. Voge, M. Kariolis and J. P. Stegemann, *Acta Biomater.*, 2008, **4**, 1583–1592.
- 114 L. Qiu, D. Liu, Y. Wang, C. Cheng, K. Zhou, J. Ding, V.-T. Truong and D. Li, *Adv. Mater.*, 2014, **26**, 3333–3337.
- 115 S. Sayyar, E. Murray, B. C. Thompson, J. Chung, D. L. Officer, S. Gambhir, G. M. Spinks and G. G. Wallace, *J. Mater. Chem. B*, 2014, **3**, 481–490.
- 116 T. Chen, K. Hou, Q. Ren, G. Chen, P. Wei and M. Zhu, *Macromol. Rapid Commun.*, 2018, **39**, 1800337.
- 117 P. Thoniyot, M. J. Tan, A. A. Karim, D. J. Young and X. J. Loh, *Adv. Sci.*, 2015, **2**, 1400010.
- 118 A. Hajian, S. B. Lindström, T. Pettersson, M. M. Hamed and L. Wågberg, *Nano Lett.*, 2017, **17**, 1439–1447.
- 119 X. Jing, H.-Y. Mi, B. N. Napiwocki, X.-F. Peng and L.-S. Turng, *Carbon*, 2017, **125**, 557–570.
- 120 B. Lu, H. Yuk, S. Lin, N. Jian, K. Qu, J. Xu and X. Zhao, *Nat. Commun.*, 2019, **10**, 1043.
- 121 J. Alam, L. A. Dass, M. S. Alhoshan, M. Ghasemi and A. W. Mohammad, *Appl. Water Sci.*, 2012, **2**, 37–46.
- 122 S. Hosseinzadeh, S. M. Rezayat, E. Vashegani-Farahani, M. Mahmoudifard, S. Zamanlui and M. Soleimani, *Polymer*, 2016, **97**, 205–216.
- 123 A. Kisiel, D. Korol, A. Michalska and K. Maksymiuk, *Electrochim. Acta*, 2021, **390**, 138787.
- 124 M. Pishvaei, F. Najafi and M. Salami-Kalajahi, *J. Color Sci. Technol.*, 2016, **10**, 145–154.
- 125 C. Kittel, *Introduction to Solid State Physics*, Wiley, 8th edn, 2005.
- 126 F.-C. Chiu, *Adv. Mater. Sci. Eng.*, 2014, **204**, e578168.
- 127 S. M. Sze and K. K. Ng, *Physics of Semiconductor Devices*, Wiley, 3rd edn, 2006.
- 128 H. L. Tuller and P. K. Moon, *Mater. Sci. Eng., B*, 1988, **1**, 171–191.
- 129 C. Lin and I. Gitsov, *Macromolecules*, 2010, **43**, 3256–3267.
- 130 V. M. Gun'ko, I. N. Savina and S. V. Mikhailovsky, *Gels*, 2017, **3**, 37.
- 131 T. Hatakeyama and F. X. Quinn, *Thermal analysis: fundamentals and applications to polymer science*, Wiley, Chichester, New York, 2nd edn, 1999.
- 132 A. R. Khare and N. A. Peppas, *Polymer*, 1993, **34**, 4736–4739.
- 133 H. B. Lee, M. S. Jhon and J. D. Andrade, *J. Colloid Interface Sci.*, 1975, **51**, 225–231.
- 134 J. R. Macdonald and W. B. Johnson, *Impedance Spectroscopy*, John Wiley & Sons, Ltd, 2018, pp. 1–20.
- 135 N. Bonanos, B. C. H. Steele, E. P. Butler, J. R. Macdonald, W. B. Johnson, W. L. Worrell, G. A. Niklasson, S. Malmgren, M. Strømme, S. K. Sundaram, M. C. H. McKubre, D. D. Macdonald, G. R. Engelhardt, E. Barsoukov, B. E. Conway, W. G. Pell, N. Wagner, C. M. Roland and R. S. Eisenberg, *Impedance Spectroscopy*, John Wiley & Sons, Ltd, 2018, pp. 175–478.
- 136 P. Pissis and A. Kyritsis, *Solid State Ionics*, 1997, **97**, 105–113.
- 137 H. Warren, R. D. Gately, P. O'Brien, R. Gorkin and M. in het Panhuis, *J. Polym. Sci., Part B: Polym. Phys.*, 2014, **52**, 864–871.
- 138 C. Dispenza, C. L. Presti, C. Belfiore, G. Spadaro and S. Piazza, *Polymer*, 2006, **47**, 961–971.
- 139 A. N. Koppes, K. W. Keating, A. L. McGregor, R. A. Koppes, K. R. Kearns, A. M. Ziemba, C. A. McKay, J. M. Zuidema, C. J. Rivet, R. J. Gilbert and D. M. Thompson, *Acta Biomater.*, 2016, **39**, 34–43.
- 140 E. H. Hall, *Am. J. Math.*, 1879, **2**, 287–292.
- 141 G. Benstetter, A. Hofer, D. Liu, W. Frammelsberger and M. Lanza, *Conductive Atomic Force Microscopy*, John Wiley & Sons, Ltd, 2017, pp. 45–77.
- 142 N. Annabi, S. R. Shin, A. Tamayol, M. Miscuglio, M. A. Bakooshli, A. Assmann, P. Mostafalu, J.-Y. Sun, S. Mithieux, L. Cheung, X. (Shirley) Tang, A. S. Weiss and A. Khademhosseini, *Adv. Mater.*, 2016, **28**, 40–49.
- 143 W. Yang, B. Shao, T. Liu, Y. Zhang, R. Huang, F. Chen and Q. Fu, *ACS Appl. Mater. Interfaces*, 2018, **10**, 8245–8257.
- 144 X. Xiao, G. Wu, H. Zhou, K. Qian and J. Hu, *Polymers*, 2017, **9**, 259.
- 145 Q. Han, A. Wang, W. Song, M. Zhang, S. Wang, P. Ren, L. Hao, J. Yin and S. Bai, *ACS Appl. Bio Mater.*, 2021, **4**(8), 6148–6156.
- 146 L. Han, K. Liu, M. Wang, K. Wang, L. Fang, H. Chen, J. Zhou and X. Lu, *Adv. Funct. Mater.*, 2018, **28**, 1704195.
- 147 Y. Liang, X. Zhao, T. Hu, Y. Han and B. Guo, *J. Colloid Interface Sci.*, 2019, **556**, 514–528.
- 148 H. Sun, J. Zhou, Z. Huang, L. Qu, N. Lin, C. Liang, R. Dai, L. Tang and F. Tian, *Int. J. Nanomed.*, 2017, **12**, 3109–3120.
- 149 Z. Liu, M. Yushan, Y. Alike, Y. Liu, S. Wu, C. Ma and A. Yusufu, *BioMed Res. Int.*, 2020, **2020**, e4794982.
- 150 Z. Deng, T. Hu, Q. Lei, J. He, P. X. Ma and B. Guo, *ACS Appl. Mater. Interfaces*, 2019, **11**, 6796–6808.
- 151 M. Imaninezhad, K. Pemberton, F. Xu, K. Kalinowski, R. Bera and S. P. Zustiak, *J. Neural Eng.*, 2018, **15**, 056034.
- 152 K. Shah, D. Vasileva, A. Karadaghy and S. P. Zustiak, *J. Mater. Chem. B*, 2015, **3**, 7950–7962.
- 153 M. Mihajlovic, M. Mihajlovic, P. Y. W. Dankers, R. Masereeuw and R. P. Sijbesma, *Macromol. Biosci.*, 2019, **19**, 1800173.
- 154 P. Dutta, N. N. Dass and N. S. Sarma, *React. Funct. Polym.*, 2015, **90**, 25–35.
- 155 A. M. Martins, G. Eng, S. G. Caridade, J. F. Mano, R. L. Reis and G. Vunjak-Novakovic, *Biomacromolecules*, 2014, **15**, 635–643.





- 156 M. Jafarkhani, Z. Salehi and T. Nematian, *Mater. Today Proc.*, 2018, **5**, 15620–15628.
- 157 M. Javadi, Q. Gu, S. Naficy, S. Farajikhah, J. M. Crook, G. G. Wallace, S. Beirne and S. E. Moulton, *Macromol. Biosci.*, 2018, **18**, 1700270.
- 158 J. Zhou, X. Yang, W. Liu, C. Wang, Y. Shen, F. Zhang, H. Zhu, H. Sun, J. Chen, J. Lam, A. G. Mikos and C. Wang, *Theranostics*, 2018, **8**, 3317–3330.
- 159 R. Peng, Y. Yu, S. Chen, Y. Yang and Y. Tang, *RSC Adv.*, 2014, **4**, 35149–35155.
- 160 H. Jo, M. Sim, S. Kim, S. Yang, Y. Yoo, J.-H. Park, T. H. Yoon, M.-G. Kim and J. Y. Lee, *Acta Biomater.*, 2017, **48**, 100–109.
- 161 L. Han, X. Lu, M. Wang, D. Gan, W. Deng, K. Wang, L. Fang, K. Liu, C. W. Chan, Y. Tang, L.-T. Weng and H. Yuan, *Small*, 2017, **13**, 1601916.
- 162 S. Das, F. Irin, L. Ma, S. K. Bhattacharia, R. C. Hedden and M. J. Green, *ACS Appl. Mater. Interfaces*, 2013, **5**, 8633–8640.
- 163 Q. Han, Y. Chen, W. Song, M. Zhang, S. Wang, P. Ren, L. Hao, A. Wang, S. Bai and J. Yin, *Bio-Des. Manuf.*, 2019, **2**, 269–277.
- 164 K. Hosoyama, M. Ahumada, C. D. McTiernan, J. Bejjani, F. Variola, M. Ruel, B. Xu, W. Liang, E. J. Suuronen and E. I. Alarcon, *RSC Adv.*, 2017, **7**, 47704–47708.
- 165 J. Ramón-Azcón, S. Ahadian, M. Estili, X. Liang, S. Ostrovidov, H. Kaji, H. Shiku, M. Ramalingam, K. Nakajima, Y. Sakka, A. Khademhosseini and T. Matsue, *Adv. Mater.*, 2013, **25**, 4028–4034.
- 166 S. R. Shin, S. M. Jung, M. Zalabany, K. Kim, P. Zorlutuna, S. Bok Kim, M. Nikkhah, M. Khabiry, M. Azize, J. Kong, K. Wan, T. Palacios, M. R. Dokmeci, H. Bae, X. (Shirley) Tang and A. Khademhosseini, *ACS Nano*, 2013, **7**, 2369–2380.
- 167 S. Ahadian, S. Yamada, J. Ramón-Azcón, M. Estili, X. Liang, K. Nakajima, H. Shiku, A. Khademhosseini and T. Matsue, *Acta Biomater.*, 2016, **31**, 134–143.
- 168 S. R. Shin, B. Aghaei-Ghareh-Bolagh, T. T. Dang, S. N. Topkaya, X. Gao, S. Y. Yang, S. M. Jung, J. H. Oh, M. R. Dokmeci, X. (Shirley) Tang and A. Khademhosseini, *Adv. Mater.*, 2013, **25**, 6385–6391.
- 169 A. R. Spencer, A. Primbetova, A. N. Koppes, R. A. Koppes, H. Fenniri and N. Annabi, *ACS Biomater. Sci. Eng.*, 2018, **4**, 1558–1567.
- 170 S. J. Lee, G. L. Pishko, G. W. Astary, T. H. Mareci and M. Sarntinoranont, *J. Appl. Polym. Sci.*, 2009, **114**, 1992–2002.
- 171 S. Ahadian, J. Ramón-Azcón, M. Estili, X. Liang, S. Ostrovidov, H. Shiku, M. Ramalingam, K. Nakajima, Y. Sakka, H. Bae, T. Matsue and A. Khademhosseini, *Sci. Rep.*, 2014, **4**, 4271.
- 172 Z. J. Han, A. E. Rider, M. Ishaq, S. Kumar, A. Kondyurin, M. M. M. Bilek, I. Levchenko and K. (Ken) Ostrikov, *RSC Adv.*, 2013, **3**, 11058–11072.
- 173 S. Namgung, K. Y. Baik, J. Park and S. Hong, *ACS Nano*, 2011, **5**, 7383–7390.
- 174 C. M. Voge, M. Kariolis, R. A. MacDonald and J. P. Stegemann, *J. Biomed. Mater. Res., Part A*, 2008, **86A**, 269–277.
- 175 Y. Wu, L. Wang, B. Guo and P. X. Ma, *ACS Nano*, 2017, **11**, 5646–5659.
- 176 W. R. Small and V. N. Paunov, *J. Mater. Chem.*, 2008, **18**, 2082–2084.
- 177 H. Lee, S. M. Dellatore, W. M. Miller and P. B. Messersmith, *Science*, 2007, **318**, 426–430.
- 178 J. H. Ryu, P. B. Messersmith and H. Lee, *ACS Appl. Mater. Interfaces*, 2018, **10**, 7523–7540.
- 179 Y. Zhang, B. Liang, Q. Jiang, Y. Li, Y. Feng, L. Zhang, Y. Zhao and X. Xiong, *Smart Mater. Struct.*, 2020, **29**, 075027.
- 180 Y. Yang, Y. Liang, J. Chen, X. Duan and B. Guo, *Bioact. Mater.*, 2022, **8**, 341–354.
- 181 J. Jiang, Y. Huang, Y. Wang, H. Xu, M. Xing and W. Zhong, *Materials*, 2017, **10**, 964.
- 182 L. Qiu, J. Z. Liu, S. L. Y. Chang, Y. Wu and D. Li, *Nat. Commun.*, 2012, **3**, 1241.
- 183 J. W. Cho, J. W. Kim, Y. C. Jung and N. S. Goo, *Macromol. Rapid Commun.*, 2005, **26**, 412–416.



## Supplementary Information

**Table S1.** Electrical conductivity of hybrid hydrogels

Material	Polymer matrix	Application	Material Concentration	Hydrogel conductivity	$\sigma_{\max}$	Notes	Ref
Pd microwires	GelMA gelatin methacrylate	Muscle tissue engineering	1 mg/ml	9.50E-02	2.5	palladium-based metallic glass submicron wires	1
Aniline dimer	Gelatin	Neural tissue engineering. Drug delivery	10 % w/w gelatin	1.00E-04	1.00E-03	Aniline carboxylated	2
Aniline tetramer	HA-SH thiolated hyaluronic acid + PEGDA polyethylene glycol diacrylate	Muscle tissue engineering	7.5 % w/w	7.00E-06	2.30E-02		3
Aniline pentamer	Agarose	Neural tissue engineering	5.1% w/w	1.00E-03 (at 0.96 % w/w)	1.50E-02	Agarose aminated	4
PPy	sodium alginate (SA) + carboxymethyl chitosan (CMCS)	Neural tissue engineering	40 % w/w	7.40E-06 (at 0.02 % w/w)	8.00E-03		5
PPy	HA hyaluronic acid		3.35 mg/ml	1.20E-03	7.30E-03	1% w/v Ppy polymerizes directly on the backbone of the HA	6
PPy	Alginate	Tissue engineering	0.67 mg/ml	8.20E-04	1.00E-02		7

## References

- 1 S. Ahadian, R. B. Sadeghian, S. Yaginuma, J. Ramón-Azcón, Y. Nashimoto, X. Liang, H. Bae, K. Nakajima, H. Shiku, T. Matsue, K. S. Nakayama and A. Khademhosseini, *Biomater. Sci.*, 2015, **3**, 1449–1458.
- 2 P. Zarrintaj, A. M. Urbanska, S. S. Gholizadeh, V. Goodarzi, M. R. Saeb and M. Mozafari, *J. Colloid Interface Sci.*, 2018, **516**, 57–66.
- 3 W. Wang, B. Tan, J. Chen, R. Bao, X. Zhang, S. Liang, Y. Shang, W. Liang, Y. Cui, G. Fan, H. Jia and W. Liu, *Biomaterials*, 2018, **160**, 69–81.
- 4 P. Zarrintaj, B. Bakhshandeh, I. Rezaeian, B. Heshmatian and M. R. Ganjali, *Sci. Rep.*, 2017, **7**, 17187.
- 5 Y. Bu, H.-X. Xu, X. Li, W.-J. Xu, Y. Yin, H. Dai, X. Wang, Z.-J. Huang and P.-H. Xu, *RSC Adv.*, 2018, **8**, 10806–10817.
- 6 J. Yang, G. Choe, S. Yang, H. Jo and J. Y. Lee, *Biomater. Res.*, 2016, **20**, 31.
- 7 S. Yang, LindyK. Jang, S. Kim, J. Yang, K. Yang, S.-W. Cho and J. Y. Lee, *Macromol. Biosci.*, 2016, **16**, 1653–1661.



# Skin electroporation for transdermal drug delivery: Electrical measurements, numerical model and molecule delivery

Georgios Kougkoulos<sup>a,b</sup>, Lionel Laudebat<sup>b,c</sup>, Sorin Dinculescu<sup>b</sup>, Juliette Simon<sup>a,d</sup>,  
Muriel Golzio<sup>d,\*</sup>, Zarel Valdez-Nava<sup>b,\*</sup>, Emmanuel Flahaut<sup>a,\*</sup>

<sup>a</sup> CIRIMAT, Université de Toulouse, CNRS, INPT, UPS, Toulouse CEDEX 9 31062, France

<sup>b</sup> LAPLACE, Université de Toulouse, CNRS, INPT, UPS, Toulouse CEDEX 9 31062, France

<sup>c</sup> INU Champollion, Université de Toulouse, Albi 81012, France

<sup>d</sup> IPBS, Université de Toulouse, CNRS UMR, UPS, Toulouse CEDEX 4 31077, France

## ARTICLE INFO

### Keywords:

Skin electroporation  
Drug delivery  
Hydrogel  
FEM simulation  
Electrical properties  
Stratum corneum

## ABSTRACT

Skin electroporation for drug delivery involves the application of Pulsed Electric Fields (PEFs) on the skin to disrupt its barrier function in a temporary and non-invasive manner, increasing the uptake of drugs. It represents a potential alternative to delivery methods that are invasive (e.g. injections) or limited. We have developed a drug delivery system comprising nanocomposite hydrogels which act as a reservoir for the drug and an electrode for applying electric pulses on the skin. In this study, we employed a multi-scale approach to investigate the drug delivery system on a mouse skin model, through electrical measurements, numerical modeling and fluorescence microscopy. The Electrical properties indicated a highly non-linear skin conductivity behavior and were used to fine-tune the simulations and study skin recovery after electroporation. Simulation of electric field distribution in the skin showed amplitudes in the range of reversible tissue electroporation (400–1200 V/cm), for 300 V PEF. Fluorescence microscopy revealed increased uptake of fluorescent molecules compared to the non-pulsed control. We reported two reversible electroporation domains for our configuration: (1) at 100 V PEF the first local transport regions appear in the extracellular lipids of the stratum corneum, demonstrated by a rapid increase in the skin's conductivity and an increased uptake of lucifer yellow, a small hydrophilic fluorophore and (2) at 300 V PEF, the first permeabilization of nucleated cells occurred, evidenced by the increased fluorescence of propidium iodide, a membrane-impermeable, DNA intercalating agent.

## 1. Introduction

The skin represents an accessible and convenient route for non-invasive drug delivery. Medicine administered through the skin avoids the first-pass metabolism and the gastrointestinal tract [1]. Transdermal delivery platforms, such as nicotine patches, can effectively administer drugs through the epidermis in a controlled manner. Advantages include increased bioavailability, sustained steady-state blood concentration levels, painless self-administration and reduced frequency of dosing, which in turn improve patient compliance and quality of life [2]. However, the skin, and more specifically its outermost layer, the stratum corneum (SC), acts as a barrier protecting the organism from the penetration of exogenous substances and microbes and limiting water loss.

Passive diffusion of drugs through the skin is only achieved for low molecular weight (MW < 400–500 Da), relatively lipophilic molecules (logP around 2 to 3) [3]. Several chemical and physical methods are being developed, allowing bigger and/or hydrophilic molecules to cross the skin barrier. Among these, skin electroporation consists in applying electric field pulses with high voltage (50 to 3000 V) and short duration (5 μs to 100 ms) on the surface of the skin, permeabilizing the SC in a non-invasive and temporary manner [4–6].

In humans (and most mammals), the skin can be divided into three layers: the epidermis, the dermis and the hypodermis. The epidermis is a stratified epithelium consisting mainly of keratinocytes. These cells proliferate in the basal layer of the epidermis and progressively migrate outwards while terminally differentiating, forming the spinous layer, the

*Abbreviations:* PEF, Pulsed Electric Field; SC, Stratum Corneum; LTR, Local Transport Region; CNT, Carbon Nanotube; LY, Lucifer Yellow; PI, Propidium Iodide; FD4, Fluorescein isothiocyanate–dextran (MW: 4kDa).

\* Corresponding authors.

*E-mail addresses:* [muriel.golzio@ipbs.fr](mailto:muriel.golzio@ipbs.fr) (M. Golzio), [valdez@laplace.univ-tlse.fr](mailto:valdez@laplace.univ-tlse.fr) (Z. Valdez-Nava), [emmanuel.flahaut@univ-tlse3.fr](mailto:emmanuel.flahaut@univ-tlse3.fr) (E. Flahaut).

<https://doi.org/10.1016/j.jconrel.2024.01.036>

Received 3 November 2023; Received in revised form 12 January 2024; Accepted 17 January 2024

Available online 27 January 2024

0168-3659/© 2024 Published by Elsevier B.V.

granular layer and the stratum corneum (or cornified layer) [7]. The keratinocytes of the SC are 15–20 layers of flattened, dead cells with a cornified envelope replacing their plasma membrane, and they form the layer responsible for the barrier function of the skin. The extracellular space in the SC is occupied by lipids (ceramides, fatty acids, cholesterol and cholesterol esters) that are attached to the cornified envelope and are largely organized in stacks of lipid bilayers [8,9]. The dermis is a layer of connective tissue with collagen, fibroblasts and high water content that provides nutrients to the epidermis and protects the organism against mechanical injury [7]. Both the dermis and the epidermis are also traversed by skin appendages, notably hair follicles, sebaceous glands and eccrine glands [10]. The subcutaneous tissue (or hypodermis) is located below the dermis. It is composed of loose connective tissue, including collagen and elastin fibers, as well as adipose tissue. The dermis and the hypodermis have a rich blood supply, provided by a highly branched network of blood vessels [10].

Electroporation is a bioelectrical phenomenon where a lipid bilayer is permeabilized through the application of an external electric field [11,12]. Depending on the parameters of the electric field (strength, duration, waveform, number and frequency of repetitions in the case of PEF) and the electrode configuration, the permeabilization may be transient (reversible EP) or permanent (irreversible EP). Reversible electroporation has found numerous applications most notably in biotechnology, for inserting genes into cells (gene electro-transfer) [13] and for fusing cells (electrofusion) *in vitro* [14]; in medical applications for cancer treatment, through the uptake of membrane-impermeant drugs into cancer cells [15]; and in drug delivery through the needle-free transport of molecules across the epidermis [2] or drug and nucleic acid administration through injection of the agents (drugs, vaccines) into tissue, followed by PEF application [16,17].

Skin electroporation for non-invasive, transdermal drug delivery was first suggested by Prausnitz et al. in 1993. They demonstrated that the application of PEF on human skin, *ex vivo*, and hairless mouse skin, *in vivo*, lead to a temporary, multi-fold increase on the uptake of three small to medium-sized, negatively charged, fluorescent molecules (lucifer yellow, calcein, erythrosin derivative), compared to a non-pulsed control [9]. Since then, numerous studies have been published on skin electroporation for transdermal drug delivery, expanding the results to a wider range of molecules (charge and size) and testing different electrode configurations and pulse parameters, on a variety of skin models (mouse, pig, reconstructed human, human) [2,18–25]. However, very few studies have reached human *in vivo* testing of this delivery method [26,27]. A number of limitations prevent transdermal electroporation for drug delivery from reaching clinical trials. These include inconsistent drug delivery quantities, unpractical electrode configurations, unclear pain thresholds for PEFs, failure to deliver larger molecules and a general limited understanding of the underlying mechanisms. A successful non-invasive transdermal drug delivery has to be painless, practical, totally-reversible and must deliver consistent amounts of therapeutic molecules in relevant quantities, within reasonable timeframes.

The critical parameter in lipid bilayer electroporation is the electric potential difference across the bilayer. The application of an external electric field charges the bilayer, which has dielectric properties, up to a critical threshold, when electroporation is observed. For plasma membranes, this threshold is experimentally calculated to be approx. 250 mV, in eukaryotic cells [28]. Electroporation is observed through the loss of the barrier properties of the bilayer (transport of water and solutes through it) and a rapid potential decrease across it. While the exact mechanism of electroporation at the molecular level is not fully elucidated, it is proposed that it may be caused by structural rearrangement of the lipids, forming aqueous pores, electrically-induced chemical modifications of the lipid chains or a combination of these [12]. Molecular dynamics simulations of lipid bilayers under strong electric fields have pointed out towards the formation of short-lived aqueous pores [29]. On a tissue level, an electric field higher than 400 V/cm can

permeabilize the plasma membranes of cells within the tissue [30]. Starting at approx. 1200 V/cm and over, the PEF application may induce permanent permeabilization and cell death, *i.e.* the electroporation is irreversible [30].

At the skin level, the application of an external electric field can disrupt the barrier function of the SC by creating Local Transport Regions (LTRs), *i.e.* aqueous pathways through the skin [30,31]. LTRs are regions of increased ionic mobility and increased solute mass transfer, with enhanced electrical conductivity and permeability. Their appearance is accompanied by a rapid decrease in the resistivity of the SC (up to three orders of magnitude [32]), increase in transepidermal water loss, and increased permeability to hydrophilic compounds [6,24]. The high current density that circulates through LTRs causes Joule heating and melting of the lipids in their vicinity, further increasing their size for longer pulse durations. Higher applied voltages increase the density of LTRs and longer durations (pulse duration and number of repetitions) increase their diameter [2,31]. For certain electrical parameters, with voltage being the most important, these changes are mostly or fully reversible. Recently, Gupta and Rai visualized the pore formation on the extracellular lipid bilayers of the SC through molecular dynamics simulations [33].

Once LTRs are formed, drug delivery across the skin can take place. The driving forces for the mass transfer of solutes are (1) electrophoretic drag (for charged entities), (2) electro-osmosis and (3) concentration gradient [2]. In the case of skin electroporation for drug delivery, three pathways through the SC are possible: (1) the paracellular pathway, a tortuous pathway through the extracellular lipids of the SC; (2) the transcellular pathway, a more direct pathway through the corneocytes (implies permeabilization of their cornified envelopes), and (3) the transappendageal pathway, following the hair follicles or the sweat ducts of the SC [18,34]. Transport of molecules may include a combination of these pathways but the paracellular is generally accepted as the dominant one [2,24,33].

Several factors, both physical and chemical in nature —such as temperature, pH, and chemical enhancers— have an impact on skin permeability. These methods can be utilized in conjunction with skin electroporation to enhance its effectiveness. Their action mechanism can be categorized into three types, either independently or in combination: (1) reducing the electric field threshold required for forming Local Transport Regions (LTRs), (2) increasing the size of LTRs, and (3) extending the duration of LTRs. Moderately increased skin temperatures (40 to 45 °C), coupled with PEF application, increase the transport of molecules through the SC [35] and cell permeabilization [36]. Neutral and alkaline pH impedes the barrier function recovery of the skin, prolonging the duration of LTRs [37,38]. Surfactants (Sodium dodecyl sulfate [39]), anionic lipids (mixture of 1,2-dioleoyl-3-phosphatidylglycerol and 1,2-dioleoyl-3-phosphatidylcholine [40], 1,2-dimyristoyl-3-phosphatidylserine [41]), reducing agents (thiosulfate [42]) and charged macromolecules (heparin [43,44], dextran sulfate [44]) can be used to increase transdermal transport, in parallel with electroporation. These chemical enhancers have different proposed mechanisms. Surfactants interfere with the lipid bilayers of the SC. Combined with the application of a PEF, they facilitate barrier disruption and prolong the formed LTRs [39]. Anionic lipids and macromolecules stabilize the formed pathways and prolong their duration [40,43,44]. Reducing agents break the disulfide bonds of the corneocyte keratin matrix, enlarging the LTRs [42].

In the current work we chose to not include physical and chemical permeability enhancers, in order to study the interaction of increasing PEF voltages with the mouse skin. However, the application of an electric field on the tissue engenders some physical and chemical changes which can affect permeabilization such as temperature increase due to joule heating and pH changes due to water electrolysis. These are discussed in the results and discussion section.

The most common electrode configurations for skin electroporation are presented in Fig. 1. These include the two-chamber configuration

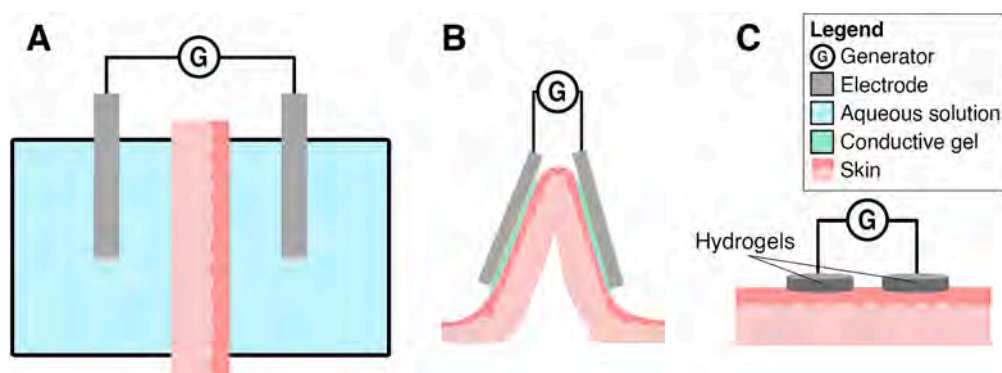


**Fig. 1.** Configurations for skin electroporation. (A) Two-chamber [9]. An *ex vivo* skin model is placed between two chambers, filled with an aqueous solution. The electrodes are immersed in the solutions. This configuration is only relevant for research purposes. (B) Pinched skin with conductive gel [45]. The skin model (*ex vivo* or *in vivo*) is pinched and placed between two electrodes. A Conductive gel placed between the metal electrodes and the skinfold ensures electrical contact. (C) Our configuration [46]. Side by side hydrogels functioning as drug reservoirs and electrodes.

[9], the skinfold configuration [45] and our configuration [46], two-in-one electrode-reservoir hydrogels, placed side by side. Some less common configurations include two cylindrical L-shaped electrodes side by side [47], multi-electrode arrays [48] and meander electrodes [49]. In general, the configurations include one (or more) positive electrode(s), one (or more) negative electrode(s), the model skin, the drug/model molecule formulation and (optionally) a conductive material to facilitate contact between the skin model and the electrodes. Some of these components may be combined. (See Fig. 2.)

We have developed a conductive nanocomposite hydrogel that functions both as a reservoir for a drug and an electrode for the application of electrical pulses to the skin (Fig. 1C), by incorporating conductive Carbon Nanotubes (CNTs) into a hydrophilic and biocompatible agarose polymer matrix. Electrically conductive, nanocomposite hydrogels are widely used in controlled drug delivery, due to their hydrophilicity, biocompatibility, retention capacity and potential responsiveness to stimuli [50]. Our configuration is efficient and practical, avoiding altogether problems arising from skin pinching, and the use of conductive gels and different drug formulations. Previously, we studied the absorption and release kinetics of the nanocomposite hydrogels [46], measured their electrical properties [51] and demonstrated the transdermal delivery of model molecules using fluorescence microscopy on histological tissue sections of mouse skin [23]. The drug delivery was

found to depend on the charge and size of the model molecule and the disruption of the skin's barrier function was reversible for PEFs of 300 V [23]. In the current work, we expanded our results with real-time electrical measurements during electroporation and numerical modeling of the system coupled with fluorescent molecule delivery for validation. First, we applied PEFs and measured the skin's resistance before, during and after the application of the pulses. Then, we used these results to adjust a numerical model of the system. Finally, we compared the model with transdermal delivery of fluorescent molecules and discussed on the mechanisms of skin electroporation. Employing fluorophores with different properties, we determined distinctly the threshold for disruption of the skin barrier function through the formation of LTRs in the extracellular lipids of the SC, and the threshold for permeabilization of the plasma membranes of viable cells in the epidermis and dermis.

## 2. Materials and methods

### 2.1. Skin models

The electroporation experiments were conducted on freshly-extracted, dorsal mouse skin. Two mice strains were used: female hairless SKH1 mice (Charles River, France) aged 8 to 16 weeks and weighing between 25 and 35 g, and male and female C57BL/6 mice, aged 8 to 16 weeks and weighing 20 to 30 g. With the latter, hair removal was performed two days before using a depilatory cream (Veet). The explanted mice skin had a thickness of  $0.46 \pm 0.07$  mm. They were cut into rectangles with average dimensions  $(14 \pm 1) \times (33 \pm 4)$  mm, for the electroporation experiments. All experiments were performed 15 min to 2 h after mice euthanasia and skin extraction.

### 2.2. Nanocomposite hydrogels

The nanocomposite hydrogels were prepared as previously described, but with an increased concentration of CNTs [46]. Briefly, 1.25 g of agarose (Sigma-Aldrich, CAS: 9012-36-6) were dissolved into 25 ml of deionized water at 90 °C, under magnetic stirring, while 125 mg of lab-produced double-wall CNTs were suspended into another 25 ml of deionized water through 1 h of probe sonication (Vibra Cell, Bioblock scientific, 12 mm diameter, 1 s ON/1 s OFF, 30% amplitude, 750 W max power) and with the addition of 12.5 mg of carboxymethyl cellulose (Fluka, CAS: 9004-32-4), used as a dispersant. The agarose solution and CNT suspension were then mixed together through 20 min of dispersion with a mini disperser (IKA ultra-turrax T10, 8000 rpm) and magnetic stirring, before being cast into silicone molds of 10 mm diameter and 2 mm height, and left to cool down for 5–10 min at room temperature. The resulting nanocomposite hydrogels were then dried (48 h, 30 °C,

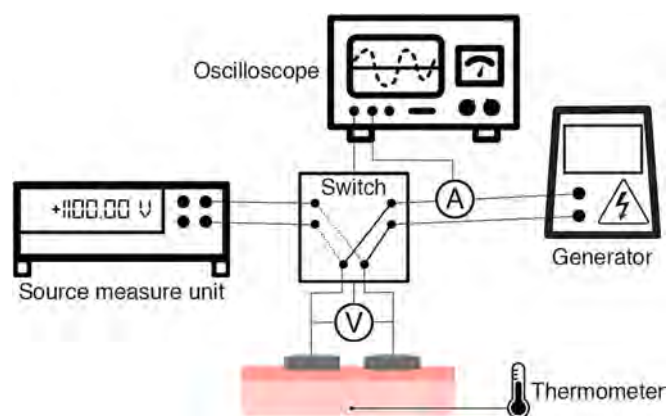


**Fig. 2.** Scheme of connections for *in situ* electrical measurements. Two hydrogels were placed on top of the skin model and connected to the pulse generator. An oscilloscope measured the voltage and current during the pulsed electric fields (PEF) application. Before, and after the PEF, the system was connected to a source-measuring unit (SMU) that measured the DC resistance. A manual switch allowed the transition between generator and SMU. The fiber optic temperature sensor was placed under the skin, at the center.



between two metal plates) and stored till use. Prior to use, the dry hydrogels were immersed for 24 h in electroporation buffer solution (8.1 mM  $K_2HPO_4$ , 1.9 mM  $KH_2PO_4$ , 1 mM  $MgCl$ , 250 mM saccharose;  $\sigma = 0.15$  S/m, pH = 7.4) with one or two types of fluorescent molecules. The fluorescent molecules used were Lucifer Yellow (LY, Sigma-Aldrich, CAS: 67769–47-5), at a concentration of 1 mM, Propidium Iodide (PI, Sigma-Aldrich, CAS: 25535–16-4) at a concentration of 0.1 mM, and Fluorescein isothiocyanate–dextran of average molecular weight 4 kDa (FD4, Sigma-Aldrich, CAS: 60842–46-8) at a concentration of 1 mM.

### 2.3. In situ electrical measurements

Freshly-extracted mouse skin was placed on a gauze soaked with commercial phosphate buffer saline (PBS without  $Ca^{2+}$  and  $Mg^{2+}$ , Eurobio Scientific), inside a plastic petri dish. An electrical heater under the petri dish kept the temperature of the skin at 32 °C, corresponding to the skin surface temperature of the human forearm [52]. Two hydrogel electrodes were placed on the surface of the skin, 14 mm apart (center-to-center). Stainless steel cylindrical electrical contacts were placed on top of each hydrogel and were connected to an electrical generator (ELECTRO cell B10 HVLV, Betatech). The PEF applied consisted of 8 square unipolar pulses of 20 ms duration, frequency of 1 Hz and voltage of 0 (control) to 400 V. The potential difference and the current passing through the system were monitored before, during and after the application of PEFs. A source-measuring unit (SMU, Keithley 2410) applied a constant DC voltage of 1 V and measured the resulting current before and after the PEF, while a digital oscilloscope (Tektronix MSO44), equipped with a high-voltage differential probe (Tektronix THDP0200) and an AC/DC current probe (Tektronix TCP0030A), measured the voltage applied on the electrodes and the current passing through the system during the application of the PEF. Instantaneous resistance is presented as voltage divided by current ( $r(t) = u(t)/i(t)$ ). The temperature of the skin was monitored with a fiber optic temperature sensor (Neoptix Qualitrol), placed at the center, between the skin and the wet gauze, at the point with the highest current density and temperature increase.

### 2.4. Numerical modeling

The current conservation continuity equation was solved with Finite Element Method (FEM) software (COMSOL Multiphysics, v. 6.1, AC/DC Module). The module solved the following set of equations in time domain:

$$\vec{E}(t) = -\vec{\nabla}V \quad (1)$$

$$\vec{J}(t) = \sigma \vec{E}(t) + \frac{\partial \vec{D}(t)}{\partial t} \quad (2)$$

With  $\vec{E}(t)$  the electric field,  $V$  the voltage,  $\vec{J}(t)$  the current density,  $\sigma$  the conductivity and  $\vec{D}(t)$  the electric displacement. The geometry is described in Fig. 5A (stacked layers). The boundary conditions were the voltages set on each cylindrical electrical contact: the left cylinder was set at 0 V (ground) and the right cylinder was set at 50 to 400 V. For the purposes of the numerical simulation, the mouse skin was simulated as stacked layers, with homogeneous and isotropic conductivity. The conductivity of the skin layer with the highest resistance, the stratum corneum, can be increased up to three orders of magnitude during electroporation conditions [30]. We used the electrical measurements to adjust the nonlinear conductivity of the SC for different electric fields, while remaining within the range of the reported literature values. The temporal simulation with nonlinear conductivity for a very thin layer (SC) was challenging, especially to have a well-adapted mesh, therefore the grid was refined during the simulation to get a convergence of the solution. Earlier works have simulated this layer in larger dimensions, and compensated by increasing its conductivity [32,53] or merged it

with the rest of the epidermis [30]. The conductivity of the other skin layers also decreases through electroporation, but to a much lesser extent (factor of 2 to 4) [30]. This was not included in the simulation to save on computing power and because the changes in the global resistance of the system would be minor (<10%). Geometry and electrical properties of mouse skin were found in refs. [53,54] (Table 1). In lack of data on the conductivity of specific mouse skin layers, the values from humans were used.

### 2.5. Fluorescence macroscopy

After PEF application, the fluorophore-loaded hydrogels were left in contact with the mouse skin for 15 min, allowing for post-pulse delivery through diffusion. Once this time interval elapsed, the hydrogels were removed, and the mouse skins were thoroughly rinsed with PBS to wash away the fluorescent molecules that had not penetrated into the skin. The skin surface was visualized with an upright, wide-field fluorescence microscope (MacroFluo with Light source EL6000, Leica Microsystems) equipped with a microscope camera (CoolSNAP HQ, Roper Scientific). The images, with magnifications of 0.57× up to 9.2×, were acquired through microscopy image analysis software (Metamorph, Molecular Devices) and treated through image processing software (ImageJ, National Institute of Health). A green filter cube (EX 480/40 nm, BS 505 nm, EM 527/30 nm; L5 filter, Leica Microsystems) was used for the FD4 and LY fluorophores, and a red filter cube (EX 560/40 nm, BS 585 nm, EM 630/75 nm; mCH/TR, Leica Microsystems) was used for PI. Exposure time was 1 s. Relative Fluorescence Intensity (RFI) is presented as a ratio between the mean fluorescence intensity of the treated area (full area under the hydrogel) divided by the mean fluorescence intensity of an untreated area of the mouse skin [23].

### 2.6. Statistics

The fluorescence data was tested for normality, with the Shapiro-Wilk test and the distribution was found to be Gaussian or approximately Gaussian in all cases. The variance of the results was tested for equality with the Brown-Forsythe test and was found to be unequal for LY and PI and equal for FD4. Comparisons between relative fluorescence intensities of different treatment groups were made using one-way ANOVA, followed by the Dunnett's T3 post-hoc test, for the samples with unequal variance and the Dunnett's test for the sample with equal variance, and differences were considered significant for  $p \leq 0.05$ . The Dunnett's and Dunnett's T3 post-hoc tests are suitable for small groups and unequal sample sizes, which is the case for our fluorescence data. The Dunnett's test compares all groups to a control, while the Dunnett's T3 test compares all possible pairwise group differences and both tests are relatively conservative (limit false positives) [55].

## 3. Results and discussion

### 3.1. Electrical properties of the skin under PEF application

The application of a PEF, over a threshold value, permeabilizes the skin, creating aqueous pathways through the skin layers. These pathways allow the delivery of hydrophilic entities, such as hydrophilic

**Table 1**  
Geometry and electrical properties of the different elements of the system.

	Thickness (m)	Conductivity (S/m)
Nanocomposite hydrogel	$4 \times 10^{-4}$	0.15
Stratum corneum	$9 \times 10^{-6}$	From $10^{-4}$ to $5 \times 10^{-2}$
Epidermis	$1.8 \times 10^{-5}$	0.2
Dermis	$1.8 \times 10^{-4}$	0.2
Hypodermis	$10^{-4}$	0.05
Muscle tissue	$1.4 \times 10^{-4}$	0.5
Gauze with PBS	$1 \times 10^{-3}$	1.5

drugs or fluorophores into the skin. At the same time, they also increase the conductivity of the skin by increasing the mobility of ions in the skin. Naturally present electrolytes ( $K^+$ ,  $Na^+$ ,  $Cl^-$  and others) give ionic conductive properties to tissues. However, in the SC, their mobility is

dramatically restricted by the tightly packed lipid layers, resulting in a high resistivity ( $\rho \approx 2000 \Omega \cdot m$ ). At the onset of electroporation, a measurable and rapid decrease in the instantaneous resistance of the system occurs.

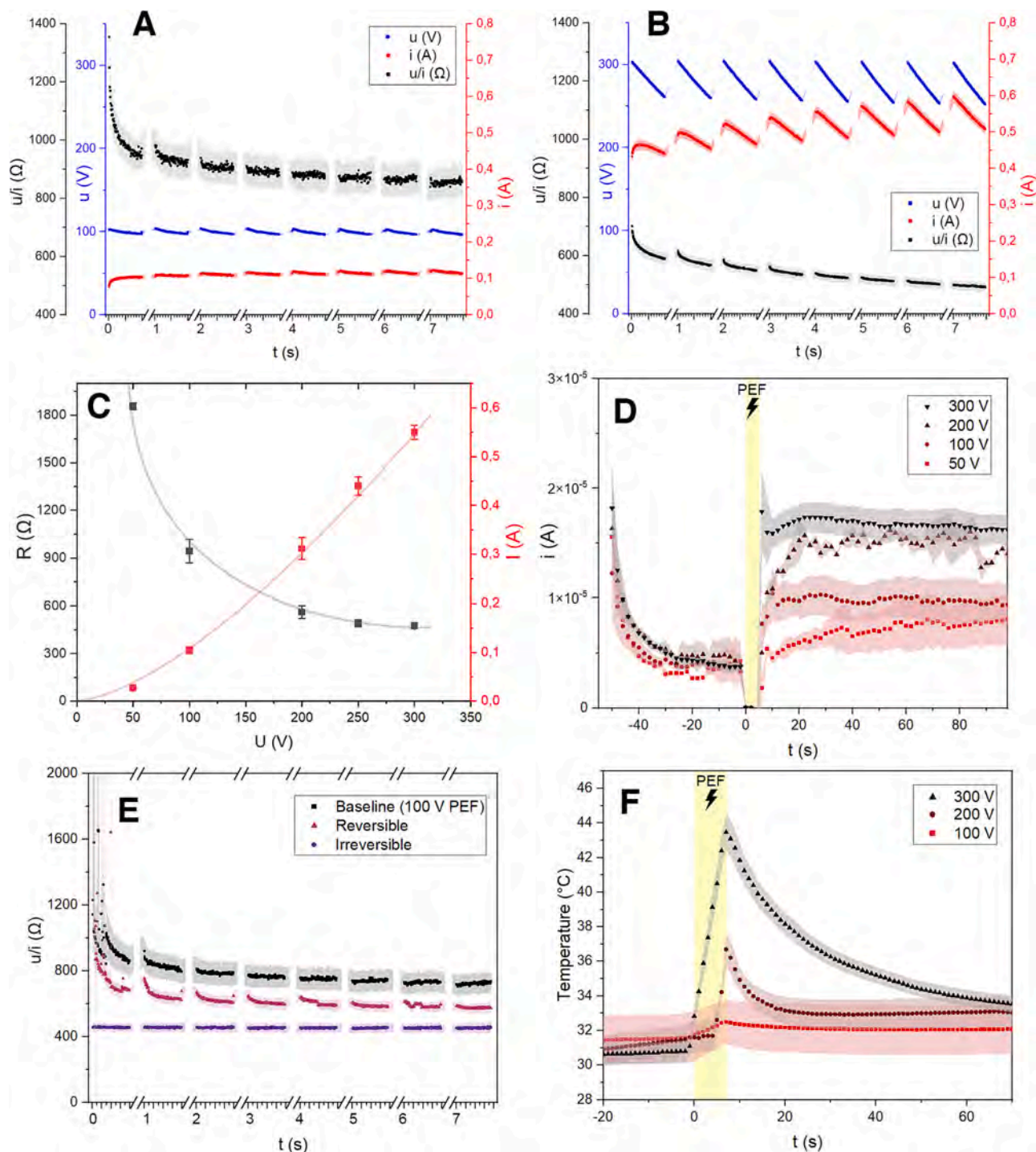


**Fig. 3.** Electrical properties and temperature increase of *ex vivo* mouse skin model, during PEF application. (A), (B) Voltage, current and instantaneous resistance ( $u/i$ ) of the systems during Pulsed Electric Fields (PEF) of 100 V ( $n = 5$ ) and 300 V ( $n = 12$ ). In both cases, the instantaneous resistance of the system decreases during pulse application, mostly for the first 5–7 ms. (C) I-V and R-V curves of the system, demonstrating non-linear behavior ( $n = 2$ –18). (D) Electric current resulting from the application of 1 V DC, before and after PEF ( $n = 2$ –11). Yellow shaded area corresponds to PEF application. After a PEF of 50 V, the current does not change substantially. After PEF of 100 to 300 V, an increase in electric current was observed. (E) Instantaneous resistance of *ex vivo* system at 100 V, for a series of PEF applications ( $n = 3$ –4). The instantaneous resistance of the skin after low-voltage PEF (up to 150 V) recovers near the baseline value. After, a series of high-voltage PEF (up to 400 V), the skin loses its dynamic character. (F) Temperature increase of the skin during PEF application ( $n = 3$ –9). Yellow shaded area corresponds to PEF application. The temperature increase is minimal for a PEF of 100 V, but increases considerably for 200 and 300 V. In all cases, shaded areas and error bars represent SEM. (For interpretation of the references to colour in this figure legend, the reader is referred to the web version of this article.)

We define the instantaneous resistance of the system as  $r(t) = u(t)/i(t)$ . The detailed electrical response obtained through the oscilloscope showed that the instantaneous resistance of the system decreased during the application of the pulses (Fig. 3A, Fig. 3B and Supplementary Info Fig. S1 for the full data). A control experiment confirmed that the decrease in the instantaneous resistance of the system is attributed specifically to the skin, and not to the hydrogels or other components (wet gauze, metal electrical contacts, cables): the instantaneous resistance of our system without the skin remained constant during the application of PEFs (Supplementary Info, Fig. S2). This rapid decrease of resistance was attributed to the formation of LTRs, aqueous pathways that greatly increased ionic mobility and allowed the passage of hydrophilic molecules. The largest resistance decrease was observed during the first 5–7 ms after PEF application. We therefore infer that the expansion of the LTRs occurs within these first milliseconds. Further (lesser) decrease in instantaneous resistance may be attributed to conductivity changes within already formed and expanded LTRs, due to local temperature increase and lipid phase transition. According to molecular dynamics simulations, the creation of pores in the lipid bilayers of the SC takes place very rapidly, within few tens of nanoseconds (1–100 ns) [33]. It is possible that pores appear in the nano- to micro-second range, but their expansion continues up to the millisecond range.

Moreover, the average resistance of the system varied considerably for different applied voltages. The  $I/U$  graph (Fig. 3C) shows the average current and average resistance of the system, during the last of 8 pulses. It ranged from  $1860 \pm 30 \Omega$  for PEF of 50 V, down to  $470 \pm 10 \Omega$  during the application of 300 V PEF, indicating a highly non-linear electric behavior. There was a rapid decrease of average resistance between PEF of 50 to 100 V, then a more modest decrease till 200 V and minor further decrease for PEF up to 300 V. This multi-fold increase in conductivity was indicative of the extent of skin electroporation. We support the hypothesis that higher PEF voltages increased the density (the surface coverage) of LTRs in the skin, therefore increasing the overall conductivity.

Through the electrical measurements, we have also confirmed that the nanocomposite hydrogels establish effective electrical contact between the metal electrodes and the skin. This eliminated the necessity of using a conductive gel, as the resistance of the system remained unchanged regardless of the presence of a conductive gel (Supplementary Info, Fig. S3).

In parallel to the electrical response during PEF, we measured the current flowing through the system, under a 1 V DC square step chronoamperometry, before and after the PEF (Fig. 3D). Upon DC voltage application, a brief current peak was observed, decaying swiftly to a steady value. This peak was attributed to the formation and charging of an electrical double layer at the interfaces and the polarization of the system, while the steady state value corresponded to the conduction current [50,56]. The current increased after the PEF treatment, indicating prolonged changes in the conductivity of the skin. The conduction current was equal to  $4.0 \pm 0.1 \mu\text{A}$  before PEF application. After PEF application, the current increased with the voltage applied: we measured  $4.4 \pm 1.1 \mu\text{A}$  (+10%, not significant) for 50 V,  $9.1 \pm 0.5 \mu\text{A}$  (+130%) for 100 V,  $13.6 \pm 1.2 \mu\text{A}$  (+240%) for 200 V, and  $16.3 \pm 0.3 \mu\text{A}$  (+310%) for 300 V. The current did not regress towards the baseline (current before PEF), even after up to 12 min following the application of PEF (Supplementary Info, Fig. S4).

Unexpectedly, the DC electrical properties of the skin did not recover, after PEF, even for the lower voltages tested (100 V; 50 V did not induce any significant changes). Similar studies have reported a rapid recovery (ca. 20 s for the essential part [57]). Some possible but unlikely explanations could be the *ex vivo* system, not attached to the living organism; an influence of the 1 V DC applied, inhibiting electrical recovery, or a recovery in a later period.

### 3.2. Recovery of electrical properties of the skin after electroporation

Next, we studied the reversibility of the electrical response after the PEF application, by applying the PEF sequence to the same skin model multiple times. The first PEF application at 100 V, served as a baseline. For the reversibility experiment, we applied two sequences of low-to-moderate voltage PEF from 100 up to 150 V. For the irreversibility experiment, we applied five sequences of high-voltage PEF from 200 up to 400 V. The skin models were then placed in an incubator at 37 °C and left to recover for one hour. After the recovery, subsequent PEF at 100 V were applied and the electrical response was compared to the baseline (Fig. 3E). The instantaneous resistance of the baseline measurement started at  $1200 \pm 200 \Omega$ , decreased to  $860 \pm 90 \Omega$  at the end of the 1st pulse and further decreased to  $730 \pm 60 \Omega$  at the last pulse. The reversible experiments revealed a similar behavior: the instantaneous resistance started at  $1100 \pm 100 \Omega$ , decreased to  $680 \pm 20 \Omega$  at the end of the 1st pulse and further decreased to  $580 \pm 30 \Omega$  at the last pulse. The baseline and the reversibility experiments resulted in a typical instantaneous resistance behavior, with a major decrease over the first pulse and lesser subsequent decrease over the next pulses (compare with Fig. 3A and Fig. 3B). Moreover, the reversibility experiments indicated that the electrical properties of the skin were recovered, albeit not to 100% of the baseline values ( $R/R_0 = 86\%$ ). The 14% loss in instantaneous resistance may include permanent formation of some conductive pathways, in the center of LTRs, due to local thermal damage or irreversible electrically-induced changes. On the contrary, after the irreversibility experiments, the skin exhibited a constant instantaneous resistance of  $460 \pm 20 \Omega$  throughout the duration of the pulses. The instantaneous resistance of the skin not only did not recover to the baseline value ( $R/R_0 = 37\%$ ), but also totally lost its dynamic character, and was assimilated to a resistive material with a constant resistance, such as our system without the skin (consisting only of a wet gauze and hydrogels, compare Fig. 3E with Fig. S2). We infer that in this case, permanent conductive pathways were formed by a combination of electrical and thermal effects, in such density and size, that no new pathways could be formed for a PEF of 100 V, *i.e.* most of the current traversing the system passed through the pre-formed pathways.

### 3.3. Temperature and pH changes upon PEF application

The baseline temperature of the skin model was  $31.2 \pm 0.4 \text{ }^\circ\text{C}$ . During PEF application, the temperature of the explanted mouse skins increased rapidly throughout the duration of the pulses, before regressing towards baseline within the next seconds (Fig. 3E). There was no measurable increase for a PEF of 50 V. The max temperature reached  $32.5 \pm 1.3 \text{ }^\circ\text{C}$  for 100 V,  $36.7 \pm 0.9 \text{ }^\circ\text{C}$  for 200 V and  $43.5 \pm 1 \text{ }^\circ\text{C}$  for 300 V. In all cases, the maximum temperature was reached just after the last pulse of the PEF. The temperature decreased to  $<35 \text{ }^\circ\text{C}$  within 3 s, in the case of 200 V; and within 36 s, in the case of 300 V.

Electroporation is generally understood to be a non-thermal phenomenon at the lipid bilayer level [58]. Yet Joule heating, local temperature increase and heat transfer play an important role during the application of PEFs on biological tissue. The current passing through the skin produces heat. At the place with the highest current density (according to our numerical model) we measured a maximum temperature increase of  $+12.3 \pm 1 \text{ }^\circ\text{C}$  for 300 V PEF, below the heat pain threshold on healthy human skin (50–55 °C [59]). For a fixed voltage, this increase can be minimized by decreasing the duration of the pulses and/or their frequency. *In vivo*, the temperature increase is expected to be lower, and the return to baseline faster, thanks to the mass of the organism that functions as a heat sink and blood circulation that contributes to thermoregulation. It must also be noted that the thermal properties of mouse and human (thicker) skins should differ. Electroporation also induces heat shock protein activation in healthy tissue, but to a lesser extent than the exposure of tissue to a warm bath (40–45 °C) for few minutes [60].

The current density through the skin is not homogeneous. During



PEF application, most of the SC retains its low conductivity, while LTRs have dramatically increased conductivities. As a result, the current density preferentially passes through these regions. The local temperature at the center of the transport regions may reach much higher values. According to Pliquett et al. [61] and Becker [62], the temperature locally rises to over 70 °C, the phase transition temperature of lipids, contributing to the thermal expansion of the LTR and the delivery of larger molecules. A local temperature increase as low as 45 °C can also contribute to the destabilization of the barrier function of the SC. At ~45 °C, the lipid packing transitions from orthorhombic to the less dense hexagonal packing [63]. In addition, Bulysheva et al. showed that moderately increased skin temperatures (43 °C) lead to more efficient cell permeabilisation, compared to a non-heated control (The temperature increase was independent from electric pulse application; they heated the skin through infrared laser heating) [36].

The exposure of an aqueous solution to a potential difference over 1.23 V causes pH changes due to water electrolysis. Higher voltages, such as the ones used in electroporation, accelerate the kinetics of electrolysis. We measured (qualitatively) the pH changes in the hydrogels and on the surface of the skin through the incorporation of phenol red in the hydrogels. The pH within the hydrogel buffer solution, and on the surface of the skin changed immediately after the PEF application, reaching values over 8.3 at the negative electrode and under 6.2 at the positive electrode (Supplementary Info, Fig. S5). In our configuration, the skin barrier function recovery would be impeded under the negative electrode, prolonging the duration of the LTRs. Neutral and alkaline pH hinder skin barrier recovery due to pH-related changes in the surface charge state of epidermal lipids, influencing their fusion rates [38] and/or impaired postsecretory lipid processing mediated by an acidic pH optimum of lipid-processing enzymes in the SC [37].

### 3.4. Numerical modeling of the skin upon PEF application

The numerical simulation allowed us to visualize the electric field distribution within the skin, during the PEF application. We used the  $I/U$  measurements (Fig. 3C) to adjust the relationship between the SC conductivity and the electric field,  $\sigma_{SC}(E)$ , until we got a satisfying agreement between the *ex vivo* results and the numerical model (Fig. 4), while remaining within the reported conductivity values for the SC under normal and electroporation conditions [32].

In all cases, the electric field was most intense in the areas directly

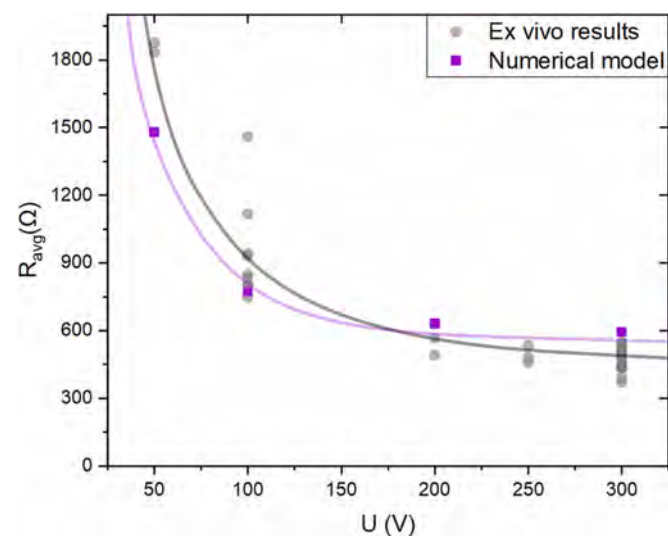


Fig. 4. Average resistance of the *ex vivo* system (grey circles) for applied PEF voltages from 50 to 300 V, compared with the results of the numerical model (purple squares). (For interpretation of the references to colour in this figure legend, the reader is referred to the web version of this article.)

under the hydrogels, reaching its highest values in the crescent-shaped areas where the electrodes face each other (Fig. 5). For PEFs at 50 and 100 V, the electric field in the viable skin layers (under the SC) did not reach sufficient levels for cell permeabilization. Starting at 200 V a very small part (6%) of the treated area (area under the hydrogels) had values over the permeabilization threshold (400 V/cm [30]). At 300 V, most of the treated area (83%) had values in the range of reversible permeabilization. At 400 V, all of the treated area had sufficiently high electric field, but the electric field exceeded the threshold for irreversible damage, in a small part of the treated area (7%). The results are presented in Fig. 5 and Table 3 (full data can be found in SI Fig. S6). As pointed out by Corovic et al., the inclusion of nonlinear conductivity of the SC (*i.e.* the conductivity is dependent on the electric field,  $\sigma(E)$ ) proves crucial for the electric field distribution [30]. With a constant conductivity, the electric field appeared to concentrate only on the SC, without reaching the viable skin layers (SI, Fig. S6).

The numerical model closely predicted the decrease in the average resistance of the system for increasing applied voltage, but we did not attempt to simulate the time-dependence of the instantaneous resistance decrease during the pulses, which is connected to the expansion of aqueous pathways in the skin.

Another limit was the macroscopic nature of the numerical simulations. The electrical conductivity of the skin is not homogeneous and isotropic, as simulated. The increased conductivity is localized in LTRs. It is possible to take into account individual LTRs but the incomplete literature data on LTR conductivity, shape and density, as well as the imposed decreased model size due to computer power limitations, present their own shortcomings [64,65]. Additionally, real skin contains imperfections, such as hair follicles and sweat ducts, which are areas of higher current density [66]. Moreover, the alignment of cells creates an anisotropic electrical conductivity. This is well established for muscle tissue, where the longitudinal conductivity can be up to 5 times higher than the transversal one [30], but the argument holds true for the cells of the SC too, and to a lesser extent, all of the skin. For these reasons, the exact values obtained from the simulations should be interpreted with caution.

### 3.5. Molecular delivery into skin after PEF application

Three fluorophores with different size, charge and properties were selected for the delivery tests assessed by fluorescence macroscopy (Table 2). For a range of PEF voltages studied, all three fluorophores demonstrated significantly higher fluorescence emission compared to the control. Lucifer Yellow (LY) is a small (442 Da), hydrophilic, negatively charged fluorophore. We used it as a marker of the integrity of the barrier function of the SC [67]. Under the positive electrode, there was no significant increase in the LY uptake for any of the PEF voltages tested. Under the negative electrode, LY exhibited a statistically significant ( $p = 0.03$ ; Dunnett's T3) increase in fluorescence ( $2.9 \pm 0.4$ ), compared to the control ( $1.4 \pm 0.1$ ), already at a PEF of 100 V. Further increase in the PEF voltage at 200 V resulted in an increased fluorescence emission ( $5.2 \pm 0.3$ ), while at 300 V, the fluorescence did not increase more ( $4.6 \pm 0.3$ , Fig. 6A). Propidium Iodide (PI) is a small (668 Da), hydrophilic, positively-charged, membrane-impermeable, DNA-intercalating fluorophore, used here as evidence of cell membrane permeabilization. PI showed a statistically significant ( $p = 0.0008$ ; Dunnett's T3) increase in fluorescence only under the positive electrode, for a PEF of 300 V ( $1.54 \pm 0.11$ , compared to  $1.01 \pm 0.02$  for the control, Fig. 6B). Fluorescein isothiocyanate–dextran (FD4), is a large (4000 Da average molecular weight), hydrophilic fluorophore, with sparse negative charges (fluorescein is negatively charged and the substitution rate is ca. 0.01 mol FITC per mol of glucose). We used it as a model molecule for insulin, that has a comparable molecular weight (5700 Da). FD4 was only tested at 300 V, and showed a statistically significant ( $p = 0.002$ ; Dunnett's) increase in fluorescence, under the negative electrode ( $2.3 \pm 0.3$ , compared to  $0.96 \pm 0.01$  for the control, Fig. 6C). It should be noted

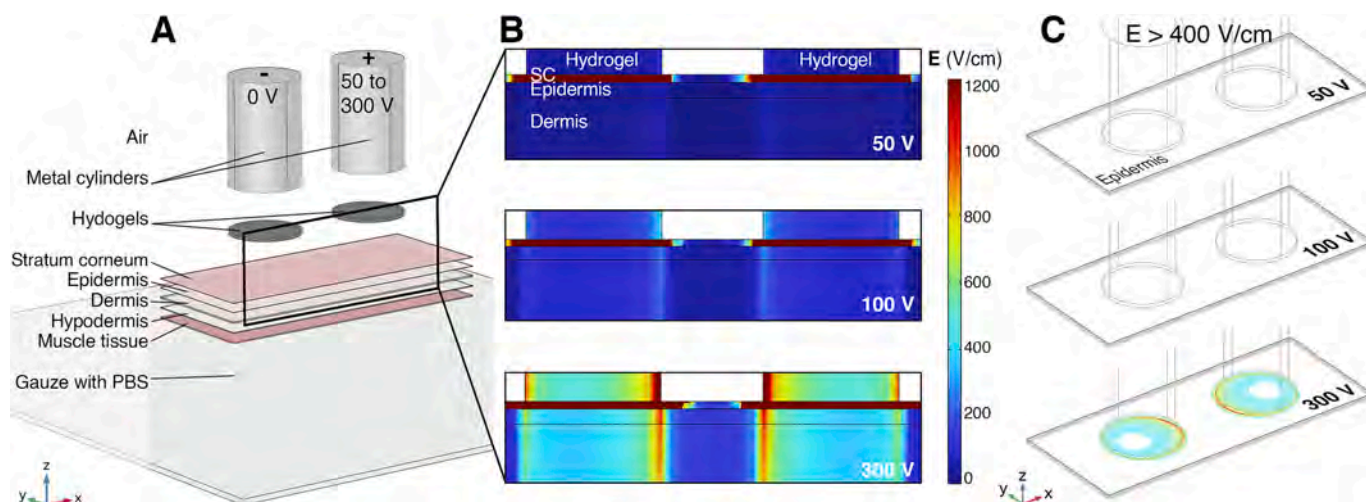


**Fig. 5.** Numerical simulation of mouse skin model during electrical stimulation. **(A)** The 3D drug delivery system (cascade layers preview, colored). **(B)** XZ slices of electric field distribution for a PEF of 50, 100 and 300 V. **(C)** Viable skin (Epidermis, under the SC) area where the electric field is over the threshold value for cell permeabilization in tissue ( $\sim 400$  V/cm), for PEF of 50, 100 and 300 V. The colour legend is common for B and C.

**Table 2**

Fluorescent molecules loaded into drug delivery hydrogels.

Fluorophore	Molar mass (Da)	Charge	Notes	Chemical structure
Lucifer Yellow (LY)	457 (443 without 2 Li <sup>+</sup> )	-2	Destabilization of extracellular matrix	
Propidium Iodide (PI)	668 (414 without 2 I <sup>-</sup> )	+2	Cell permeabilization	
Fluorescein isothiocyanate-dextran (FD4)	4000 (avg)	Slightly	Macromolecule delivery model	

that the luminescence intensity of fluorescein is reduced in acidic pH [68], and we measured an acidification of the solution in the positive electrode (SI, Fig. S8).

In all three cases, the charge of the fluorophore played a determining role in the delivery: negatively charged fluorophores marked the skin under the negative electrode and the positively charged PI mostly marked the skin under the positive electrode. This was true even for FD4, whose total electric charge was marginal. LY was the only fluorophore that exhibited some fluorescence in the control experiment. Indeed, the limit for passive diffusion through the SC, for hydrophilic molecules is approx. 500 Da. Molecules near this limit, like LY, have a very slow diffusion rate, but a small quantity can traverse the SC. However, the fluorescence of LY was greatly enhanced already with a PEF of 100 V. We hypothesized that the application of a PEF of 100 V, destabilized the extracellular lipids matrix between the corneocytes of the SC, allowing the fluorophore to pass through the paracellular pathway. An increase to 200 V nearly doubled the fluorescence intensity, while 300 V did not further increase it. The disorganization of the extracellular matrix peaked at 200 V, for our configuration.

However, there was no cell membrane permeabilization for PEF lower than 300 V. PI, a marker of cell permeabilization, only exhibited enhanced fluorescence at 300 V. PI is a DNA intercalating agent, increasing its fluorescence by 20- to 30-fold when it binds to DNA [69]. The cells of the SC do not contain a nucleus, thus the PI fluorescence originated in cells in deeper layers of the epidermis or the dermis. Lastly, FD4, a macromolecule of 4 kDa, exhibited significantly increased fluorescence, demonstrating the potential of skin electroporation for the delivery of therapeutic molecules of large size, such as insulin [23].

Visible light penetrates into the skin, at a depth of few hundred  $\mu\text{m}$ , typically 100  $\mu\text{m}$  to 1 mm, depending on the wavelength [70]. Therefore, fluorescence emission captured by the camera does not only originate from the SC, but also from deeper layers, at least down to parts of the dermis. Under the negative electrode, the fluorescence of LY appeared mostly concentrated at the regions between cells. Additionally, a diffuse, out-of-focus fluorescence was observed, originating from LY deeper into the skin (Fig. 7A). Under the positive electrode, where LY did not benefit from the electrophoretic force, it was clearly seen concentrated on the paracellular regions, with much less diffuse light



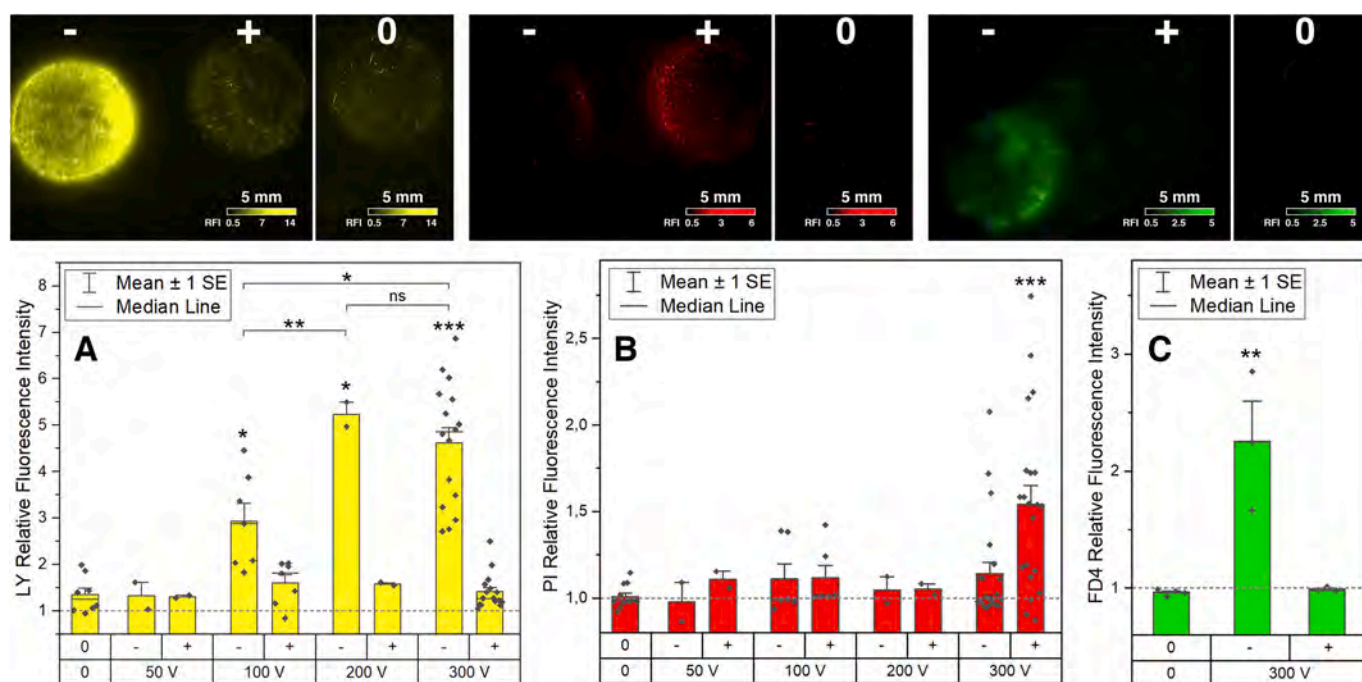


**Fig. 6.** Fluorescent molecule marking on skin model (top view) and relative fluorescence intensity quantification graphs. **(A)** Lucifer Yellow, a small (442 Da), negatively charged fluorophore penetrated the skin for PEF over 100 V ( $n = 2-16$ ). **(B)** Propidium Iodide, a small (668 Da), positively charged, DNA-intercalating fluorophore permeabilized nucleated cells for 300 V PEF ( $n = 2-20$ ). **(C)** Fluorescein isothiocyanate-dextran, a large (4000 Da), slightly negatively charged fluorophore was delivered through the skin with 300 V PEF ( $n = 3-4$ ). Error bars represent SEM. Statistical treatment: one-way ANOVA and Dunnett's T3 (A, B) or Dunnett's (C) post-hoc tests. Codes signification: \* =  $p \leq 0.05$ ; \*\* =  $p \leq 0.01$ ; \*\*\* =  $p \leq 0.001$ ; no symbol or ns = not significant difference ( $p > 0.05$ ). Means are compared to control (0), unless brackets indicate otherwise. (For interpretation of the references to colour in this figure legend, the reader is referred to the web version of this article.)

**Table 3**

Global resistance and electric field distribution in skin layers, for PEFs of 50 to 400 V. The threshold value for tissue electroporation is approx. 400 V/cm. For electric field values over 1200 V/cm, electroporation can be irreversible.

U (V)	R = U/I ( $\Omega$ )	E (V/cm) @Viable skin	Rev perm. E > 400 V/cm (% treated area)	Irrev. perm. E > 1200 V/cm (% treated area)
50	1860	20–60	0	0
100	940	100–250	0	0
200	560	250–600	6	0
300	470	350–1000	83	0
400	450	500–1400	100	7

from deeper layers (Fig. 7B). PI was observed within skin cells (Fig. 7C). The cells of the SC are anucleated, thus PI fluorescence originated from cells deeper in the epidermis and/or dermis. Similar to LY, FD4 appeared to fluoresce from the paracellular regions, with some diffuse light from deeper layers (Fig. 6D). In most cases, the fluorescence intensity was higher in the crescent-shaped areas where electrodes face each other. This can be explained by the electric field strength calculated through the simulations, which was higher in these areas (Fig. 5C).

### 3.6. Mechanisms of skin electroporation

We evaluated skin electroporation, for applied PEFs of 50 to 300 V, on four different levels: (1) electrical measurements during the pulses, (2) DC current before and after the pulses, (3) fluorescent microscopy of LY, a fluorophore indicating destabilization of skin's barrier properties, and (4) fluorescent microscopy of PI for cell membrane permeabilization. Combining our findings, we distinguish three voltage domains with different effects on the skin.

#### 3.6.1. Domain 1: low-voltage PEFs (<100 V) conductive pathway formation

In the initial domain, where PEFs were below 100 V, an increase in ionic mobility within the skin was observed. This was evidenced by a reduction in instantaneous resistance during PEFs and a decline in average resistance with increasing voltage. Remarkably, these effects were noticeable even at PEFs as low as 50 V. However, no molecule transfer through the skin occurred at voltages <100 V. We hypothesize that the conductive pathways formed within the skin increased the mobility of electrolytes but were too small in radius or limited in surface coverage to impact the skin's barrier properties (Fig. 8B). Additionally, the DC current measured before and after applying 50 V PEFs showed minimal alterations (not significant), suggesting that any changes in electrical properties were short-lived. It was challenging to establish a precise minimum PEF voltage threshold for pathway formation, based solely on electrical properties, as instantaneous resistance decreased even at the lowest voltages applied. According to Chizmadzhev et al., at low voltages (up to 30 V, equivalent to roughly 100 V in our configuration, see SI Fig. S7 for the equivalence calculation), electroporation of epithelial cells in appendageal ducts might contribute to the observed reduction in skin resistance. The appendageal ducts (hair follicles and sweat ducts) are areas of higher current density and are lined by only two layers of epithelial cells [66].

#### 3.6.2. Domain 2: moderate-voltage PEFs (100–200 V) – disruption of extracellular lipid matrix and molecule transport

Moving to the second domain, encompassing PEFs ranging from 100 to 200 V, we observed the transport of small hydrophilic molecules through the SC and enduring changes in the skin's passive electrical properties. At this stage, the applied PEF disrupted the organization of extracellular lipids in the SC, resulting in the formation of LTRs. Hydrophilic molecules with limited passive diffusion through the SC, such as LY, traversed the SC via the disorganized lipid bilayers in the

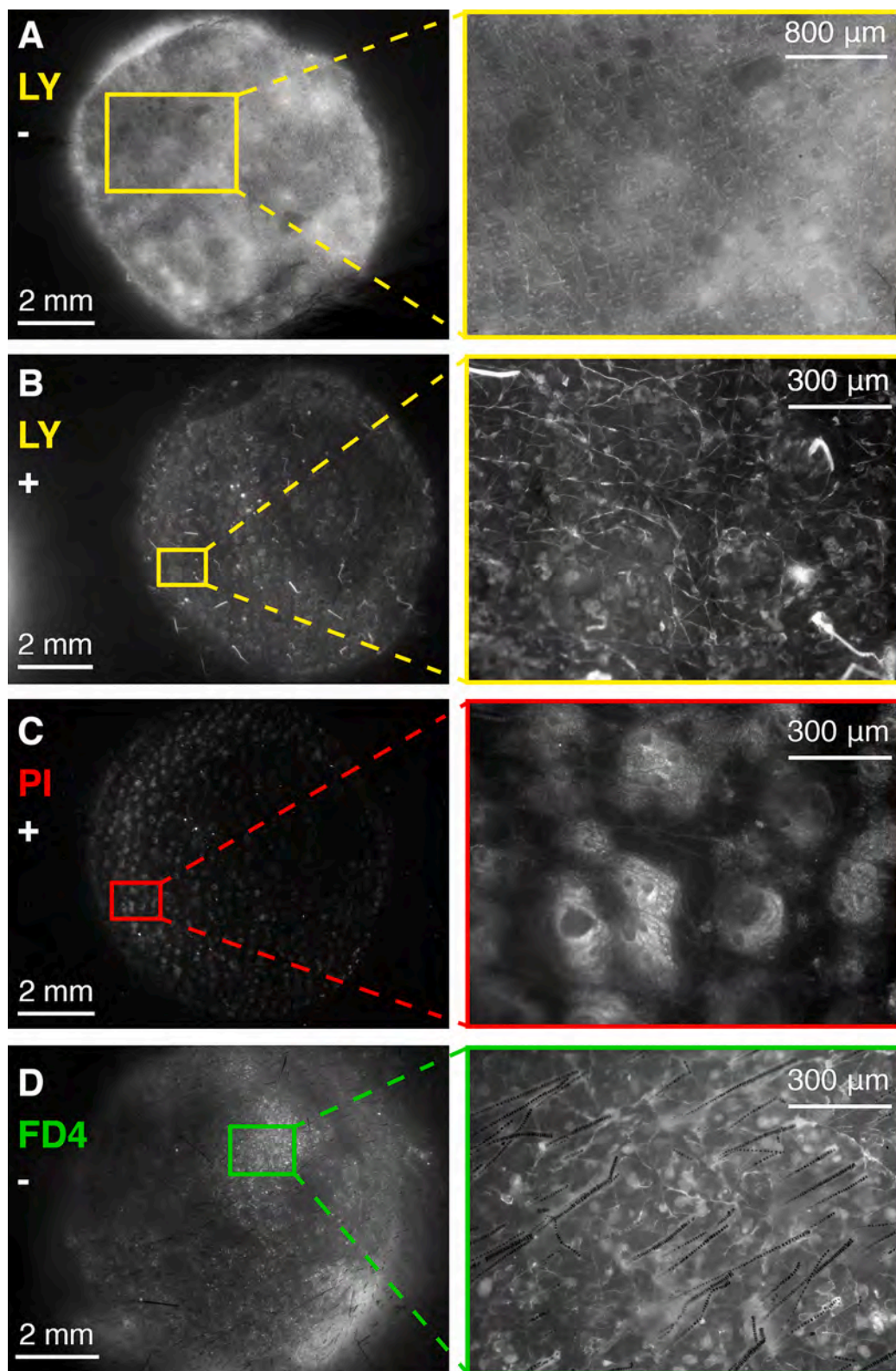


**Fig. 7.** Molecular delivery into skin model after PEF at 300 V. Images showing the patterns of fluorescence with (A) Lucifer Yellow (LY) under negative electrode with optical zoom of 1.25 $\times$  (left) and 3.2 $\times$  (right); (B) LY under positive electrode with optical zoom of 1.25 $\times$  (left) and 9.2 $\times$  (right); (C) Propidium Iodide (PI) under positive electrode with optical zoom of 1.25 $\times$  (left) and 9.2 $\times$  (right); (D) Fluorescein isothiocyanate–dextran under negative electrode with optical zoom of 1.25 $\times$  (left) and 9.2 $\times$  (right). LY fluorescence mostly originates from the paracellular space of the stratum corneum (B), while Propidium Iodide is located in the intracellular space of nucleated cells, in the viable skin (C). Brightness and contrast are customized for each capture. (For interpretation of the references to colour in this figure legend, the reader is referred to the web version of this article.)



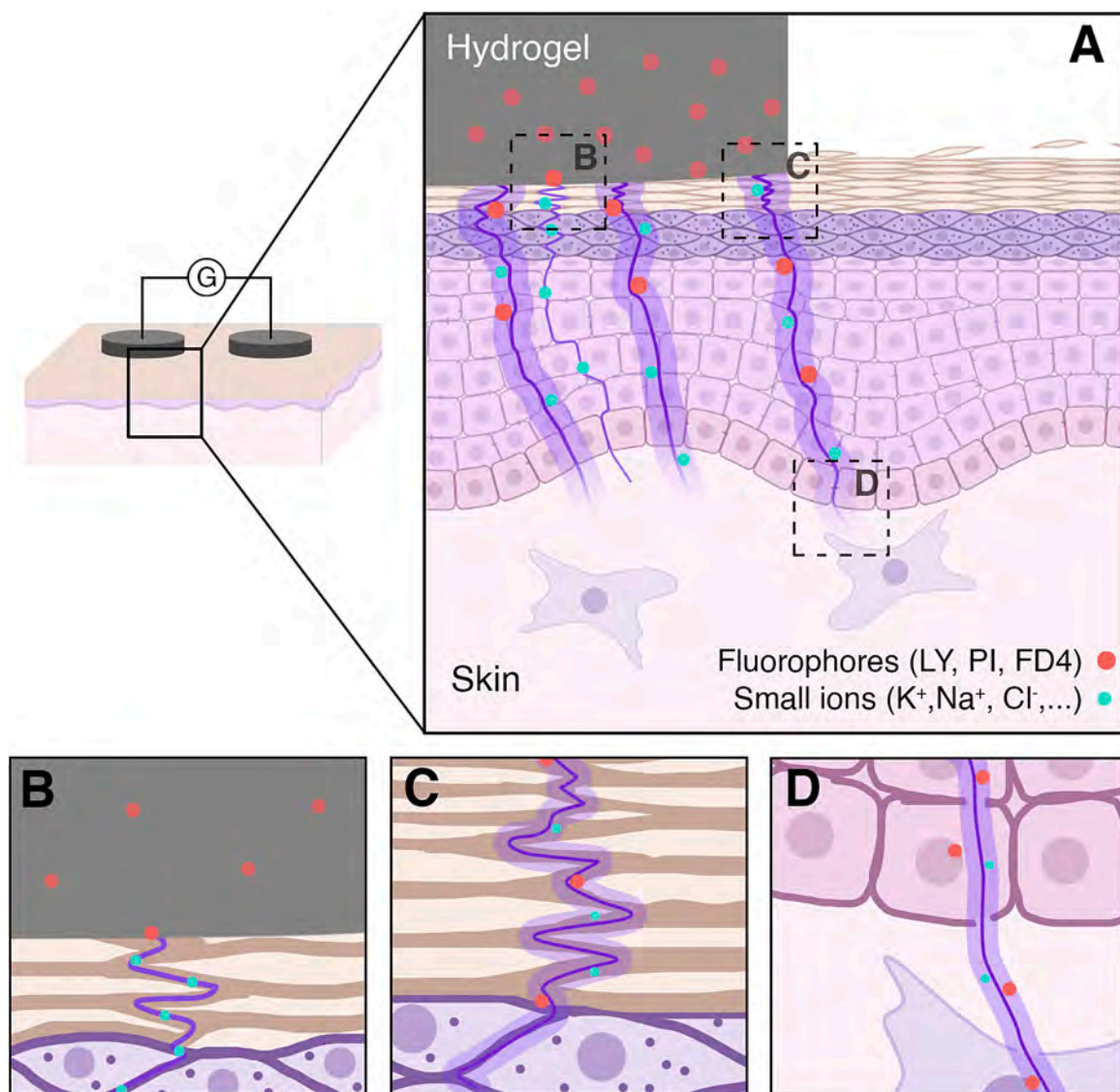


**Fig. 8.** Local transport regions (LTRs) and cell membrane permeabilization in skin. **(A)** Scheme of skin electroporation with electrode-reservoir hydrogel. **(B)** At PEF voltages lower than 100 V, conductive pathways were formed, increasing ionic mobility. **(C)** Starting at 100 V PEF, the creation of LTRs in the extracellular lipids of the stratum corneum, allowed the diffusion of fluorophores through the skin. **(D)** At 300 V PEF, the cell membranes of nucleated cells of the epidermis and/or dermis were permeabilized and fluorophores entered the cytoplasm.

paracellular region (Fig. 8C). Moreover, we noted an increase in the skin's DC current following PEF application, indicating the sustained creation of conductive pathways. Still, no permeabilization of cell membranes occurred within this domain.

### 3.6.3. Domain 3: high-voltage PEFs (300 V) cell membrane permeabilization

In the third domain, corresponding to PEFs of 300 V, we observed the permeabilization of cell membranes. At this point, the electric field at the viable skin layers reached values exceeding 400 V/cm. This resulted in a transmembrane potential within nucleated cells in the epidermis and/or dermis surpassing the threshold of 250 mV, leading to membrane permeabilization. This allowed the introduction of Propidium Iodide (PI) into the intracellular space, followed by its subsequent intercalation with DNA (Fig. 8D). Our numerical simulations, despite their simplifications, accurately predicted cell membrane permeabilization for 300 V PEFs. In previous work, we assessed the uptake of LY following PEF exposure and established that PEFs of 300 V, within our configuration, were largely reversible [23].

## 4. Conclusion

We have proposed a configuration for non-invasive drug delivery through skin electroporation, consisting of two conductive hydrogels, placed side-to-side, that contain the model medication and serve as electrodes for the application of electrical pulses on the skin. We applied a multi-scale approach to evaluate skin electroporation and drug delivery: *in situ* measurements of electrical properties and temperature before, during and after the application of PEFs, FEM simulation of our system and fluorescence microscopy to evaluate the delivery of model molecules (A schematic table with the summarized results is provided in SI, Fig. S8). The experimental setup proposed here can serve as a model for future investigations of skin electroporation.

Regarding the I-V measurements, there were two major observations: (1) the average resistance of the system decreased for increasing PEF voltages, and (2) the instantaneous resistance of the system decreased during the application of the electric pulses. We attributed the first observation to the formation of a larger number of LTRs with increasing applied voltage, and the second observation to the expansion of the LTRs during the electric field application. The current-voltage

graph of the system demonstrated the non-linear character of the skin's electrical conductivity. There was a substantial local temperature increase for PEFs over 200 V, but the skin temperature remained under the limits of human heat pain threshold, for PEFs up to 300 V. We used electrical measurements to evaluate the reversibility of PEF application on our configuration: low PEF voltages up to 150 V resulted in near-full recovery of the skin's instantaneous resistance, while multiple sequences of high PEF voltages up to 400 V, irreversibly damaged the skin and its dynamic electrical behavior.

The numerical model was adjusted with *ex vivo* results and accurately predicted the evolution of the average resistance of the system for increasing applied voltage. According to the model, the electric field reached levels of reversible cell permeabilization in the viable skin layers, for most of the treated area, at 300 V PEF. At 400 V, the field strength passed the threshold for irreversible electroporation (eventually leading to cell death), in parts of the treated area.

Even though the formation of LTRs within the SC was demonstrated for PEFs starting at 100 V, no permeabilization of nucleated cells was observed for PEFs lower than 300 V. These results showed the existence of two distinct (reversible) electroporation domains, one consisting in the formation of LTRs in the extracellular lipids of the SC and the accompanying increase in skin's conductivity, and a second one, consisting in the permeabilization of the plasma membranes of nucleated cells (*i.e.* cells in layers deeper than the SC). Both of these domains are relevant in the context of drug delivery through the skin. Some drugs such as lidocaine and corticosteroids can be administered locally, to the epidermis, for local anesthesia and to treat skin inflammation. Nucleic acid vaccinations have to enter the interior of cells in order to express the encoded antigen and elicit an immune response. Similarly, anti-tumor antibiotic medicine like bleomycin, have to permeabilize the cell membrane to have an effect. Fentanyl and insulin have to reach systemic circulation, through the vasculature of the dermis, to treat pain and regulate glucose metabolism. The exact parameters chosen for skin electroporation depend on the delivery target and the drug's physico-chemical properties (size, charge, hydrophilicity).

#### CRedit authorship contribution statement

**Georgios Koukoulos:** Writing – original draft, Visualization, Methodology, Investigation, Formal analysis, Conceptualization. **Lionel Laudebat:** Writing – review & editing, Methodology, Investigation, Conceptualization. **Sorin Dinculescu:** Writing – review & editing, Methodology. **Juliette Simon:** Methodology. **Muriel Golzio:** Writing – review & editing, Funding acquisition, Conceptualization. **Zarel Valdez-Nava:** Writing – review & editing, Supervision, Funding acquisition, Conceptualization. **Emmanuel Flahaut:** Writing – review & editing, Supervision, Funding acquisition, Conceptualization.

#### Declaration of competing interest

There are no conflicts to declare.

#### Data availability

Data will be made available on request.

#### Acknowledgements

The authors would like to thank the other members of the CARBO2DERM research project team, namely Geraldine Alberola, Jelena Kolosnjaj-Tabi, Anne-Marie Larssonneur Galibert, Marie-Pierre Rols, Brigitte Soula, Audrey Tourette and Alicia Weibel, for their insightful comments and critical discussions. The current work is funded by the French national research agency under the project CARBO2DERM - Carbon nanotubes for the transdermal delivery of therapeutic molecules (grant ANR-19-CE09-0007).

#### Appendix A. Supplementary data

Supplementary data to this article can be found online at <https://doi.org/10.1016/j.jconrel.2024.01.036>.

#### References

- [1] G.W. Cleary, Transdermal delivery systems: a medical rationale. In: V.P. Penetration, Shah H.I. Maibach (Eds.), *Topical Drug Bioavailability, Bioequivalence*. Springer: US, Boston, MA, 1993, pp. 17–68, [https://doi.org/10.1007/978-1-4899-1262-6\\_2](https://doi.org/10.1007/978-1-4899-1262-6_2).
- [2] A.-R. Denet, R. Vanbever, V. Pr at, Skin electroporation for transdermal and topical delivery, *Adv. Drug Deliv. Rev.* 56 (5) (2004) 659–674, <https://doi.org/10.1016/j.addr.2003.10.027>.
- [3] S. Wiedersberg, R.H. Guy, Transdermal drug delivery: 30+ years of war and still fighting!, *J. Control. Release* 190 (2014) 150–156, <https://doi.org/10.1016/j.jconrel.2014.05.022>, sept.
- [4] R. Vanbever, V. Pr at, In vivo efficacy and safety of skin electroporation, *Adv. Drug Deliv. Rev.* 35 (1) (1999) 77–88, [https://doi.org/10.1016/s0169-409x\(98\)00064-7](https://doi.org/10.1016/s0169-409x(98)00064-7).
- [5] M.R. Prausnitz, A practical assessment of transdermal drug delivery by skin electroporation, *Adv. Drug Deliv. Rev.* 35 (1) (1999) 61–76, [https://doi.org/10.1016/s0169-409x\(98\)00063-5](https://doi.org/10.1016/s0169-409x(98)00063-5).
- [6] J. Dermol-Cerme, E. Pirc, D. Miklavcic, Mechanistic view of skin electroporation – models and dosimetry for successful applications: an expert review, *Expert Opin. Drug Deliv.* 17 (5) (2020) 689–704, <https://doi.org/10.1080/17425247.2020.1745772>.
- [7] J.A. McGrath, R.A.J. Eady, F.M. Pope, in: *Anatomy and Organization of Human Skin*, Rook's Textbook of Dermatology, John Wiley & Sons, Ltd, 2004, pp. 45–128, <https://doi.org/10.1002/9780470750520.ch3>.
- [8] E. Candi, R. Schmidt, G. Melino, The cornified envelope: a model of cell death in the skin, *Nat. Rev. Mol. Cell Biol.* 6 (4) (2005) Art. 4, <https://doi.org/10.1038/nrm1619>.
- [9] M.R. Prausnitz, V.G. Bose, R. Langer, J.C. Weaver, Electroporation of mammalian skin: a mechanism to enhance transdermal drug delivery, *Proc. Natl. Acad. Sci.* 90 (22) (1993) 10504–10508, <https://doi.org/10.1073/pnas.90.22.10504>.
- [10] Y. Gilaberte, L. Prieto-Torres, I. Pastushenko, A. Juarraz, Chapter 1 - anatomy and function of the skin, in: M.R. Hamblin, P. Avci, T.W. Prow (Eds.), *Nanoscience in Dermatology*, Academic Press, Boston, 2016, pp. 1–14, <https://doi.org/10.1016/B978-0-12-802926-8.00001-X>.
- [11] E. Neumann, K. Rosenheck, Permeability changes induced by electric impulses in vesicular membranes, *J. Membr. Biol.* 10 (1) (1972) 279–290, <https://doi.org/10.1007/BF01867861>.
- [12] T. Kotnik, L. Rems, M. Tarek, D. Miklavcic, Membrane electroporation and Electropermeabilization: mechanisms and models, *Annu. Rev. Biophys.* 48 (1) (2019) 63–91, <https://doi.org/10.1146/annurev-biophys-052118-115451>.
- [13] S. Chabot, C. Rosazza, M. Golzio, A. Zumbusch, J. Teissie, M.-P. Rols, Nucleic acids electro-transfer: from bench to bedside, *Curr. Drug Metab.* 14 (3) (2013) 300–308, <https://doi.org/10.2174/1389200211314030005>.
- [14] I.P. Sugar, W. F rster, E. Neumann, Model of cell electrofusion: membrane electroporation, pore coalescence and percolation, *Biophys. Chem.* 26 (2) (1987) 321–335, [https://doi.org/10.1016/0301-4622\(87\)80035-9](https://doi.org/10.1016/0301-4622(87)80035-9).
- [15] L.M. Mir, et al., Effective treatment of cutaneous and subcutaneous malignant tumours by electrochemotherapy, *Br. J. Cancer* 77 (12) (1998) Art. no 12, <https://doi.org/10.1038/bjc.1998.388>.
- [16] S. Pedron-Mazoyer, J. Plou t, L. Hellaudais, J. Teissie, M. Golzio, New anti angiogenesis developments through electro-immunization: optimization by in vivo optical imaging of intradermal electro gene transfer, *Biochim. Biophys. Acta* 1770 (1) (2007) 137–142, <https://doi.org/10.1016/j.bbagen.2006.09.014>.
- [17] L. Pasquet, et al., Safe and efficient novel approach for non-invasive gene electrotransfer to skin, *Sci. Rep.* 8 (1) (2018) Art. no 1, <https://doi.org/10.1038/s41598-018-34968-6>.
- [18] B.M. Medi, B. Layek, J. Singh, Electroporation for dermal and transdermal drug delivery, in: N. Dragicevic, H.I. Maibach (Eds.), *Percutaneous Penetration Enhancers Physical Methods in Penetration Enhancement*, Springer, Berlin, Heidelberg, 2017, pp. 105–122, [https://doi.org/10.1007/978-3-662-53273-7\\_7](https://doi.org/10.1007/978-3-662-53273-7_7).
- [19] R. Vanbever, N. Lecouturier, V. Pr at, Transdermal delivery of metoprolol by electroporation, *Pharm. Res.* 11 (11) (1994) 1657–1662, <https://doi.org/10.1023/A:1018930425591>.
- [20] A. Jadoul, N. Lecouturier, J. Mesens, W. Caers, V. Pr at, Transdermal alniditan delivery by skin electroporation, *J. Control. Release* 54 (3) (1998) 265–272, [https://doi.org/10.1016/S0168-3659\(97\)00195-8](https://doi.org/10.1016/S0168-3659(97)00195-8).
- [21] V. Regnier, N. De Morre, A. Jadoul, V. Pr at, Mechanisms of a phosphorothioate oligonucleotide delivery by skin electroporation, *Int. J. Pharm.* 184 (2) (1999) 147–156, [https://doi.org/10.1016/S0378-5173\(98\)00085-4](https://doi.org/10.1016/S0378-5173(98)00085-4).
- [22] T.-W. Wong, T.-Y. Chen, C.-C. Huang, J.-C. Tsai, S.W. Hui, Painless skin electroporation as a novel way for insulin delivery, *Diabetes Technol. Ther.* 13 (9) (2011) 929–935, <https://doi.org/10.1089/dia.2011.0077>.
- [23] J. Simon, B. Jouanmiqu eou, M.-P. Rols, E. Flahaut, M. Golzio, Transdermal delivery of macromolecules using two-in-one nanocomposite device for skin electroporation, *Pharmaceutics* 13 (11) (2021) Art. no 11, <https://doi.org/10.3390/pharmaceutics13111805>.
- [24] N. Kis, A. Kov acs, M. Budai-Sz ucs, G. Er s, E. Cs anyi, S. Berk , The effect of non-invasive dermal electroporation on skin barrier function and skin permeation in

- combination with different dermal formulations, *J. Drug Deliv. Sci. Technol.* 69 (2022) 103161, <https://doi.org/10.1016/j.jddst.2022.103161>.
- [25] M. Madi, M.-P. Rols, L. Gibot, Efficient in vitro Electropermeabilization of reconstructed human dermal tissue, *J. Membr. Biol.* 248 (5) (2015) 903–908, <https://doi.org/10.1007/s00232-015-9791-z>.
- [26] M.S. Wallace, B. Ridgeway, E. Jun, G. Schulteis, D. Rabussay, L. Zhang, Topical delivery of lidocaine in healthy volunteers by electroporation, Electroincorporation, or iontophoresis: An evaluation of skin anesthesia, *Reg. Anesth. Pain Med.* 26 (3) (2001) 229–238, <https://doi.org/10.1053/rapm.2001.22633>.
- [27] U. Pliquett, J.C. Weaver, Feasibility of an electrode-reservoir device for transdermal drug delivery by noninvasive skin electroporation, *IEEE Trans. Biomed. Eng.* 54 (3) (2007) 536–538, <https://doi.org/10.1109/TBME.2006.886828>.
- [28] J. Teissié, M.P. Rols, An experimental evaluation of the critical potential difference inducing cell membrane electropermeabilization, *Biophys. J.* 65 (1) (1993) 409–413, <https://doi.org/10.1016/B978-0-12-802926-8.00001-X>.
- [29] M. Tarek, Membrane electroporation: a molecular dynamics simulation, *Biophys. J.* 88 (6) (2005) 4045–4053, <https://doi.org/10.1529/biophysj.104.050617>.
- [30] S. Corovic, I. Lackovic, P. Sustaric, T. Sustar, T. Rodic, D. Miklavcic, Modeling of electric field distribution in tissues during electroporation, *Biomed. Eng. Online* 12 (1) (2013) 16, <https://doi.org/10.1186/1475-925X-12-16>.
- [31] U.F. Pliquett, T.E. Zewert, T. Chen, R. Langer, J.C. Weaver, Imaging of fluorescent molecule and small ion transport through human stratum corneum during high voltage pulsing: localized transport regions are involved, *Biophys. Chem.* 58 (1) (1996) 185–204, [https://doi.org/10.1016/0301-4622\(95\)00098-4](https://doi.org/10.1016/0301-4622(95)00098-4).
- [32] N. Pavšelj, V. Prát, D. Miklavčič, A numerical model of skin Electropermeabilization based on in vivo experiments, *Ann. Biomed. Eng.* 35 (12) (2007) 2138–2144, <https://doi.org/10.1007/s10439-007-9378-7>.
- [33] R. Gupta, B. Rai, Electroporation of skin stratum Corneum lipid bilayer and molecular mechanism of drug transport: a molecular dynamics study, *Langmuir* 34 (20) (2018) 5860–5870, <https://doi.org/10.1021/acs.langmuir.8b00423>.
- [34] B. Zorec, V. Prát, D. Miklavčič, N. Pavšelj, Active enhancement methods for intra- and transdermal drug delivery: a review, *ZdravVestn* (2013), <https://doi.org/10.6016/1889>.
- [35] S. Narasimha Murthy, A. Sen, Y.-L. Zhao, S.W. Hui, Temperature influences the Postelectroporation permeability state of the skin, *J. Pharm. Sci.* 93 (4) (2004) 908–915, <https://doi.org/10.1002/jps.20016>.
- [36] A. Bulysheva, et al., Coalesced thermal and electrotransfer mediated delivery of plasmid DNA to the skin, *Bioelectrochem. Amst. Neth.* 125 (2019) 127–133, <https://doi.org/10.1016/j.bioelechem.2018.10.004>.
- [37] T. Mauro, et al., Barrier recovery is impeded at neutral pH, independent of ionic effects: implications for extracellular lipid processing, *Arch. Dermatol. Res.* 290 (4) (1998) 215–222, <https://doi.org/10.1007/s004030050293>.
- [38] S.N. Murthy, A. Sen, Y.-L. Zhao, S.W. Hui, pH influences the postpulse permeability state of skin after electroporation, *J. Control. Release* 93 (1) (2003) 49–57, <https://doi.org/10.1016/j.jconrel.2003.08.002>.
- [39] S.N. Murthy, A. Sen, S.W. Hui, Surface-enhanced transdermal delivery by electroporation, *J. Control. Release* 98 (2) (2004) 307–315, <https://doi.org/10.1016/j.jconrel.2004.05.006>.
- [40] A. Sen, Y. Zhao, L. Zhang, S.W. Hui, Enhanced transdermal transport by electroporation using anionic lipids, *J. Control. Release* 82 (2) (2002) 399–405, [https://doi.org/10.1016/S0168-3659\(02\)00164-5](https://doi.org/10.1016/S0168-3659(02)00164-5).
- [41] A. Sen, M.E. Daly, S.W. Hui, Transdermal insulin delivery using lipid enhanced electroporation, *Biochim. Biophys. Acta Biomembr.* 1564 (1) (2002) 5–8, [https://doi.org/10.1016/S0005-2736\(02\)00453-4](https://doi.org/10.1016/S0005-2736(02)00453-4).
- [42] T.E. Zewert, U.F. Pliquett, R. Vanbever, R. Langer, J.C. Weaver, Creation of transdermal pathways for macromolecule transport by skin electroporation and a low toxicity, pathway-enlarging molecule, *Bioelectrochem. Bioenerg.* 49 (1) (1999) 11–20, [https://doi.org/10.1016/S0302-4598\(99\)00056-2](https://doi.org/10.1016/S0302-4598(99)00056-2).
- [43] J.C. Weaver, R. Vanbever, T.E. Vaughan, M.R. Prausnitz, Heparin alters transdermal transport associated with electroporation, *Biochem. Biophys. Res. Commun.* 234 (3) (1997) 637–640, <https://doi.org/10.1006/bbrc.1997.6701>.
- [44] R. Vanbever, M.R. Prausnitz, V. Prát, Macromolecules as novel transdermal transport enhancers for skin electroporation, *Pharm. Res.* 14 (5) (1997) 638–644, <https://doi.org/10.1023/a:1012161313701>.
- [45] G.A. Hofmann, W.V. Rustrum, K.S. Suder, Electro-incorporation of microcarriers as a method for the transdermal delivery of large molecules, *Bioelectrochem. Bioenerg.* 38 (1) (1995) 209–222, [https://doi.org/10.1016/0302-4598\(95\)01827-2](https://doi.org/10.1016/0302-4598(95)01827-2).
- [46] J.-F. Guillet, E. Flahaut, M. Golzio, A hydrogel/carbon-nanotube needle-free device for Electrostimulated skin drug delivery, *ChemPhysChem* 18 (19) (2017) 2715–2723, <https://doi.org/10.1002/cphc.201700517>.
- [47] S. Mazères, et al., Non invasive contact electrodes for in vivo localized cutaneous electropulsation and associated drug and nucleic acid delivery, *J. Control. Release.* 134 (2) (2009) 125–131, <https://doi.org/10.1016/j.jconrel.2008.11.003>.
- [48] S. Guo, A. Donate, G. Basu, C. Lundberg, L. Heller, R. Heller, Electro-gene transfer to skin using a noninvasive multielectrode array, *J. Control. Release.* 151 (3) (2011) 256–262, <https://doi.org/10.1016/j.jconrel.2011.01.014>.
- [49] L. Zhang, L. Li, Z. An, R.M. Hoffman, G.A. Hofmann, In vivo transdermal delivery of large molecules by pressure-mediated electroincorporation and electroporation: a novel method for drug and gene delivery, *Bioelectrochem. Bioenerg.* 42 (2) (1997) 283–292, [https://doi.org/10.1016/S0302-4598\(96\)05128-8](https://doi.org/10.1016/S0302-4598(96)05128-8).
- [50] G. Kougkolos, M. Golzio, L. Laudebat, Z. Valdez-Nava, E. Flahaut, Hydrogels with electrically conductive nanomaterials for biomedical applications, *J. Mater. Chem. B* 11 (10) (2023) 2036–2062, <https://doi.org/10.1039/D2TB02019J>.
- [51] J.-F. Guillet, Z. Valdez-Nava, M. Golzio, E. Flahaut, Electrical properties of double-wall carbon nanotubes nanocomposite hydrogels, *Carbon* 146 (2019) 542–548, <https://doi.org/10.1016/j.carbon.2019.01.090>.
- [52] C.M. Lee, S.-P. Jin, E.J. Doh, D.H. Lee, J.H. Chung, Regional variation of human skin surface temperature, *Ann. Dermatol.* 31 (3) (2019) 349–352, <https://doi.org/10.5021/ad.2019.31.3.349>.
- [53] N. Pavšelj, D. Miklavcic, Numerical models of skin Electropermeabilization taking into account conductivity changes and the presence of local transport regions, *Plasma Sci. IEEE Trans. On* 36 (2008) 1650–1658, <https://doi.org/10.1109/TPS.2008.928715>.
- [54] K. Sato, K. Sugibayashi, Y. Morimoto, Species differences in percutaneous absorption of Nicorandil, *J. Pharm. Sci.* 80 (2) (1991) 104–107, <https://doi.org/10.1002/jps.2600800203>.
- [55] D.C. Sauder, C.E. DeMars, An updated recommendation for multiple comparisons, *Adv. Methods Pract. Psychol. Sci.* 2 (1) (2019) 26–44, <https://doi.org/10.1177/2515245918808784>.
- [56] Z. Stojek, The electrical double layer and its structure, in: Z. Stojek (Ed.), *Electroanalytical Methods: Guide to Experiments and Applications*, Springer, Berlin, Heidelberg, 2010, pp. 3–9, [https://doi.org/10.1007/978-3-642-02915-8\\_1](https://doi.org/10.1007/978-3-642-02915-8_1).
- [57] U. Pliquett, R. Langer, J.C. Weaver, Changes in the passive electrical properties of human stratum corneum due to electroporation, *Biochim. Biophys. Acta Biomembr.* 1239 (2) (1995) 111–121, [https://doi.org/10.1016/0005-2736\(95\)00139-T](https://doi.org/10.1016/0005-2736(95)00139-T).
- [58] U.F. Pliquett, G.T. Martin, J.C. Weaver, Kinetics of the temperature rise within human stratum corneum during electroporation and pulsed high-voltage iontophoresis, *Bioelectrochem. Amst. Neth.* 57 (1) (2002) 65–72, [https://doi.org/10.1016/S1567-5394\(01\)00177-3](https://doi.org/10.1016/S1567-5394(01)00177-3).
- [59] A. Pertovaara, T. Kaupilla, M.M. Hämäläinen, Influence of skin temperature on heat pain threshold in humans, *Exp. Brain Res.* 107 (3) (1996) 497–503, <https://doi.org/10.1007/BF00230429>.
- [60] T. Forjanic, et al., Electroporation-Induced Stress Response and Its Effect on Gene Electrotransfer Efficacy: In Vivo Imaging and Numerical Modeling, *IEEE Trans. Biomed. Eng.* 66 (9) (2019) 2671–2683, <https://doi.org/10.1109/TBME.2019.2894659>.
- [61] U. Pliquett, Ch. Gusbeth, R. Nuccitelli, A propagating heat wave model of skin electroporation, *J. Theor. Biol.* 251 (2) (2008) 195–201, <https://doi.org/10.1016/j.jtbi.2007.11.031>.
- [62] S. Becker, Transport modeling of skin electroporation and the thermal behavior of the stratum Corneum, *Int. J. Therm. Sci.* 54 (2011), <https://doi.org/10.1016/j.ijthermalsci.2011.10.022>.
- [63] N. Pavšelj, D. Miklavčič, Resistive heating and electropermeabilization of skin tissue during in vivo electroporation: a coupled nonlinear finite element model, *Int. J. Heat Mass Transf.* 54 (11) (2011) 2294–2302, <https://doi.org/10.1016/j.ijheatmasstransfer.2011.02.035>.
- [64] N. Pavšelj, D. Miklavcic, A numerical model of Permeabilized skin with local transport regions, *IEEE Trans. Biomed. Eng.* 55 (7) (2008) 1927–1930, <https://doi.org/10.1109/TBME.2008.919730>.
- [65] J. Dermol-Černe, D. Miklavčič, From cell to tissue properties—modeling skin electroporation with pore and local transport region formation, *IEEE Trans. Biomed. Eng.* (2018), <https://doi.org/10.1109/TBME.2017.2773126>.
- [66] Y.A. Chizmadzhev, A.V. Indenbom, P.I. Kuzmin, S.V. Galichenko, J.C. Weaver, R. O. Potts, Electrical properties of skin at moderate voltages: contribution of Appendageal macropores, *Biophys. J.* 74 (2) (1998) 843–856, [https://doi.org/10.1016/S0006-3495\(98\)74008-1](https://doi.org/10.1016/S0006-3495(98)74008-1).
- [67] E.A. Leclerc, A. Hucheq, S. Kezic, G. Serre, N. Jonca, Mice deficient for the epidermal dermokinase  $\beta$  and  $\gamma$  isoforms display transient cornification defects, *J. Cell Sci.* 127 (13) (2014) 2862–2872, <https://doi.org/10.1242/jcs.144808>.
- [68] M.M. Martin, L. Lindqvist, The pH dependence of fluorescein fluorescence, *JOL* 10 (6) (1975) 381–390, [https://doi.org/10.1016/0022-2313\(75\)90003-4](https://doi.org/10.1016/0022-2313(75)90003-4).
- [69] D.J. Arndt-Jovin, T.M. Jovin, Chapter 16 Fluorescence Labeling and Microscopy of DNA, in: D.L. Taylor, Y.-L. Wang (Eds.), *Methods in Cell Biology*, 30, Academic Press, 1989, pp. 417–448 *Fluorescence Microscopy of Living Cells in Culture Part B. Quantitative Fluorescence Microscopy—Imaging and Spectroscopy*, 30, [https://doi.org/10.1016/S0091-679X\(08\)60989-9](https://doi.org/10.1016/S0091-679X(08)60989-9).
- [70] L. Finlayson, et al., Depth Penetration of light into skin as a function of wavelength from 200 to 1000 nm, *Photochem. Photobiol.* 98 (4) (2022) 974–981, <https://doi.org/10.1111/php.13550>.



## Supplementary Info

### Skin electroporation for transdermal drug delivery: electrical measurements, numerical model and molecule delivery

Georgios Kougkoulos<sup>1,2</sup>, Lionel Laudebat<sup>2,3</sup>, Sorin Dinculescu<sup>2</sup>, Juliette Simon<sup>1,4</sup>, Muriel Golzio<sup>4\*</sup>,  
Zarel Valdez-Nava<sup>2\*</sup> and Emmanuel Flahaut<sup>1\*</sup>

1 CIRIMAT, Université de Toulouse, CNRS, INPT, UPS, 31062 Toulouse CEDEX 9, FRANCE

2 LAPLACE, Université de Toulouse, CNRS, INPT, UPS, 31062 Toulouse CEDEX 9, France

3 INU Champollion, Université de Toulouse, 81012 Albi, France

4 IPBS, Université de Toulouse, CNRS UMR, UPS, 31077 Toulouse CEDEX 4, FRANCE

\* Corresponding authors: Dr Muriel Golzio (muriel.golzio@ipbs.fr), Dr Zarel Valdez-Nava (valdez@laplace.univ-tlse.fr), Dr Emmanuel Flahaut (emmanuel.flahaut@univ-tlse3.fr)

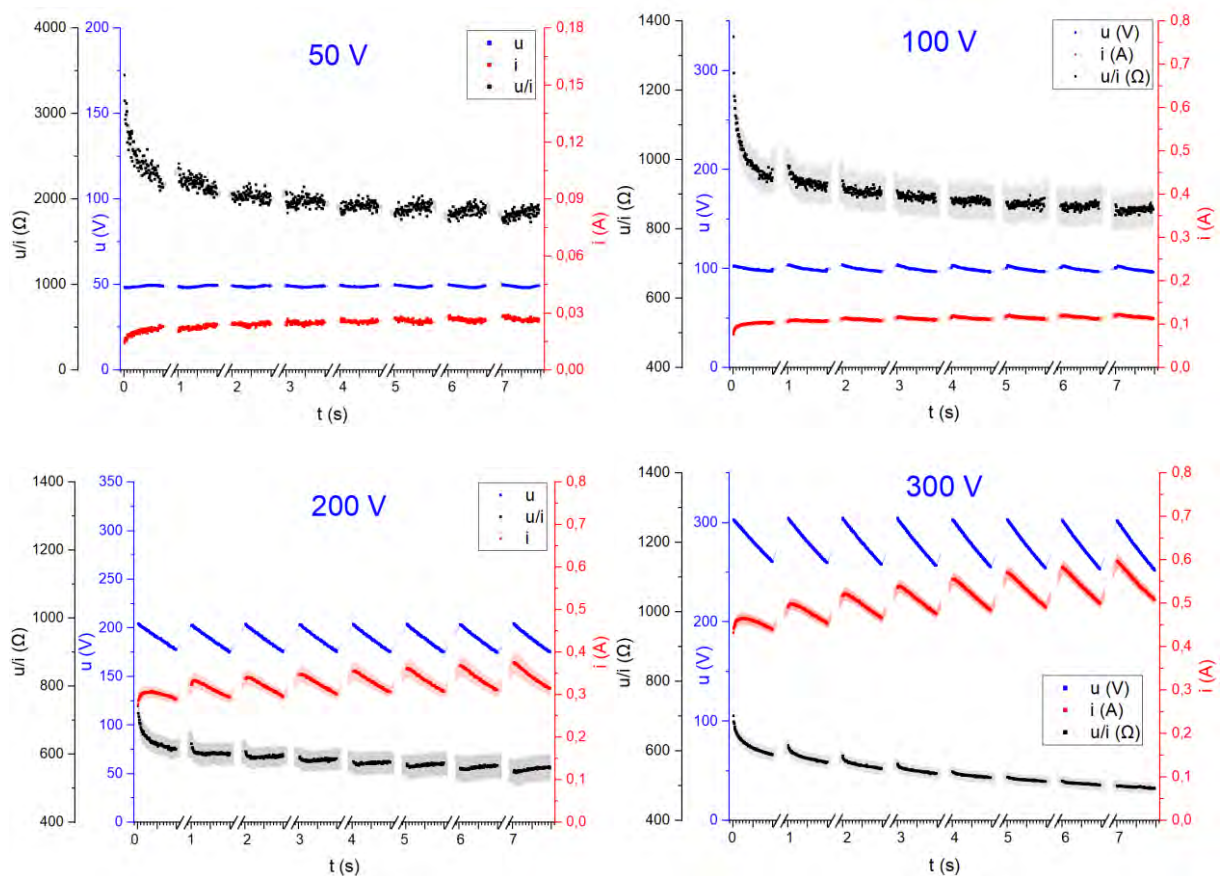


**Fig. S1.** Voltage, current and instantaneous resistance ( $u/i$ ) of drug delivery setup during Pulsed Electric Fields (PEF) of voltages from 50 to 300 V. Shaded areas represent SEM. (50V,200V:  $n=3$ ; 100V:  $n=5$ ; 300V:  $n=12$ ).

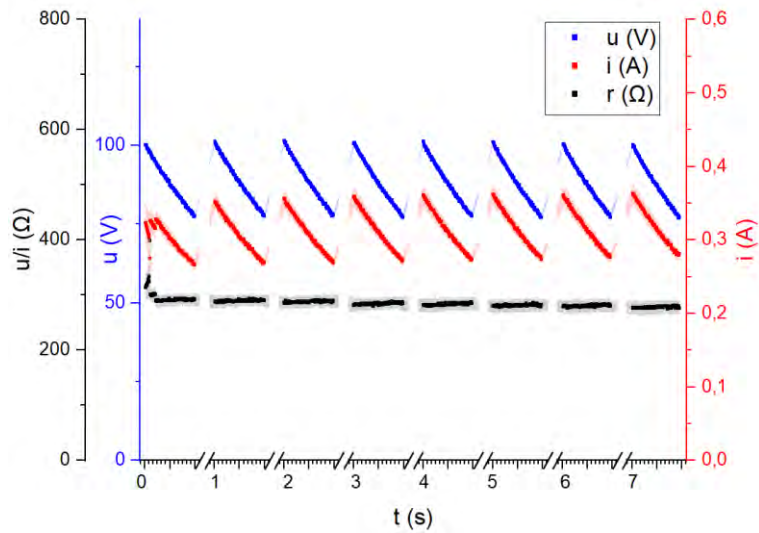


**Fig. S2.** Voltage and current of the system without mouse skin (only hydrogels and gauze). There was no variation of  $r(t)=u(t)/i(t)$  during PEF application. This showed that the resistance decrease was attributed to the skin. Shaded areas represent SEM.  $n=3$

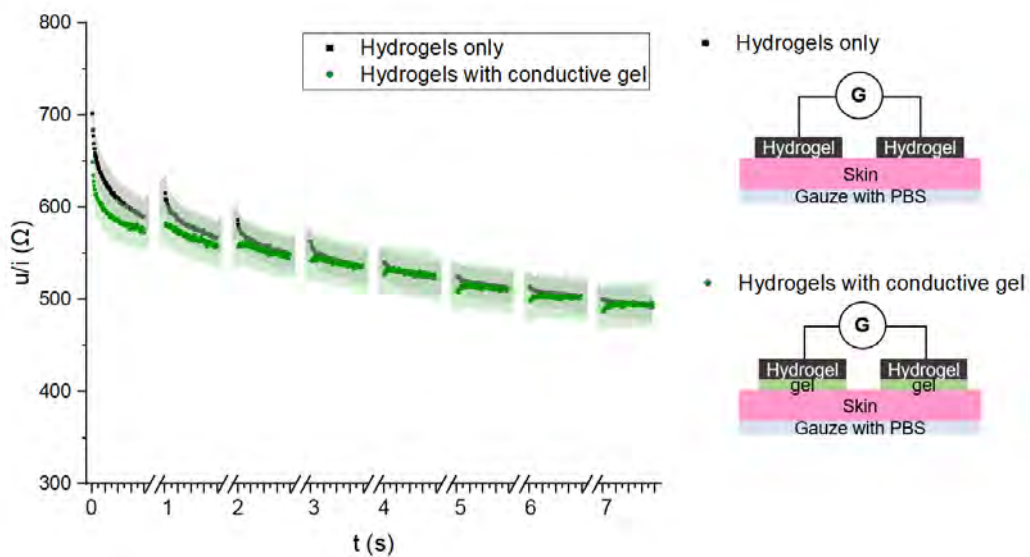


**Fig. S3.** Instantaneous resistance ( $r(t)=u(t)/i(t)$ ) of electroporation system with skin and hydrogels only (black,  $n=12$ ) and with skin, hydrogels and conductive gel between them (green,  $n=3$ ). Adding conductive gel between the hydrogels and the skin does not improve electrical contact, therefore it is rendered unnecessary, for our configuration. Shaded areas represent SEM.

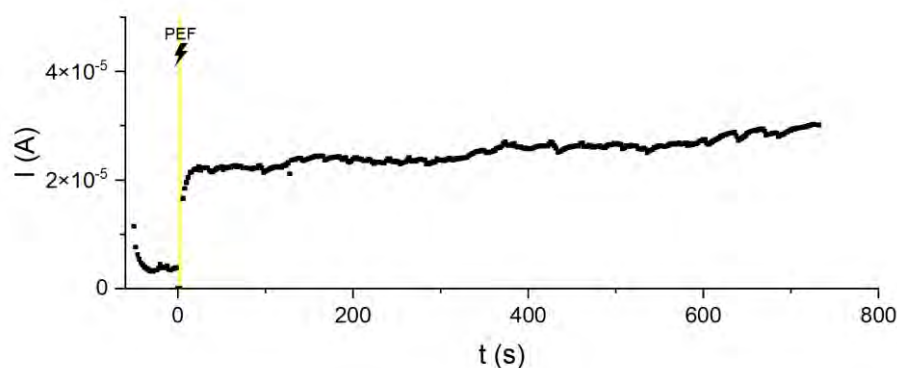


**Fig. S4.** Electric current resulting from the application of 1V DC, before and after PEF at 300 V. The DC resistance of the skin did not recover for up to 12 minutes. The change in the electrical properties of the skin appeared to be long-lived, or permanent, after 300 V PEF. Yellow shaded area corresponds to PEF application.

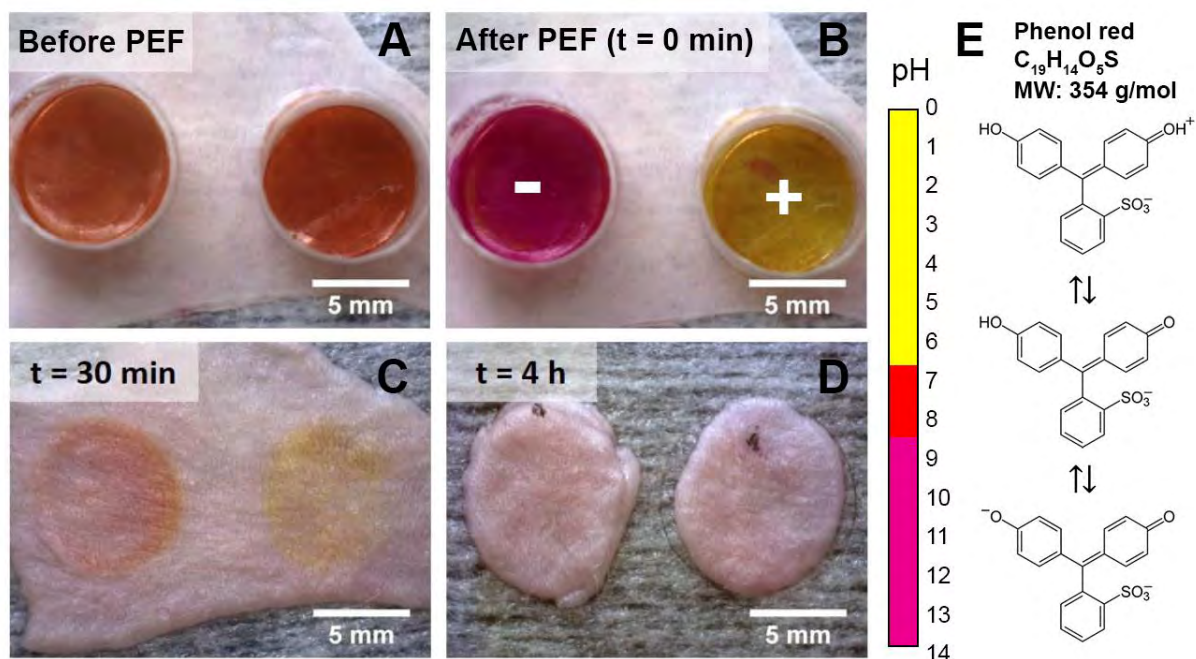


**Fig. S5.** Evaluation of pH changes in hydrogels and on the surface of the skin. A pH indicator, phenol red, was incorporated into two agarose hydrogels (without CNTs, to maintain their transparency), and a 300 V PEF was applied through them, on the surface of the skin. (A) Before PEF, the color of the dye was red orange, corresponding to a pH between 6.8 and 8.2. The hydrogels were buffered at pH=7.4. (B) Immediately after PEF application the color of the indicator shifted to magenta red in the negative electrode (pH>8.2) and yellow in the positive electrode (pH<6.8). (C) Phenol red was delivered into the mouse skin, under the influence of the PEF. (D) After few hours, pH changes were equilibrated, through diffusion. (E) Phenol red color scale with pH changes. The protocol for this experiment was the same as with the delivery of fluorescent molecules with the following changes: plain agarose hydrogels were used (without CNTs), no fluorophores were loaded in the hydrogels and the hydrogels were left in place for 30 minutes instead of 15, after PEF application.

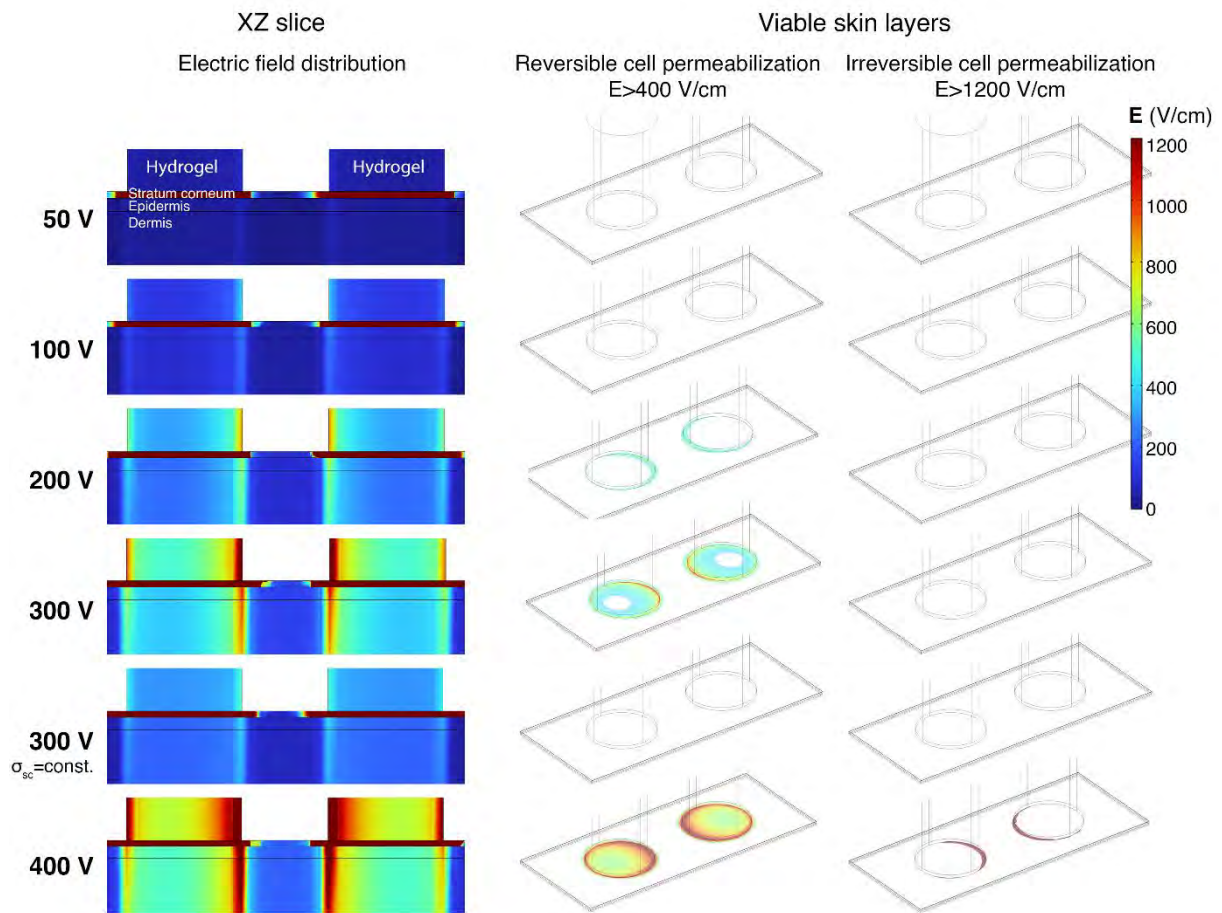


**Fig. S6.** Electric field distribution on skin for PEFs from 50 to 400 V, including 300 V PEF on skin with fixed conductivity  $\sigma_{sc}=5\times 10^{-4}$  S/m. XZ slices of electric field distribution and areas where the electric field reaches values over 400 V/cm and over 1200 V/cm on the viable skin (under the stratum corneum).

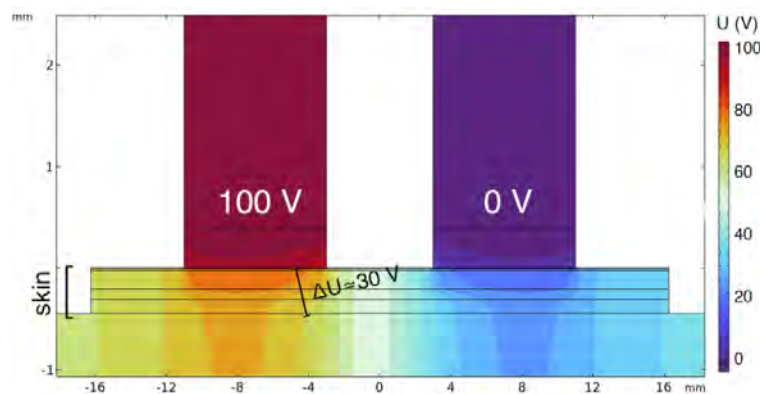


**Fig. S7.** Potential difference across skin for 100 V PEF. A 100 V PEF would result in an estimated potential difference of approximately 30 V across the skin. It's important to note that due to the non-uniform electric field resulting from the side-by-side electrode configuration, this estimation is approximate.



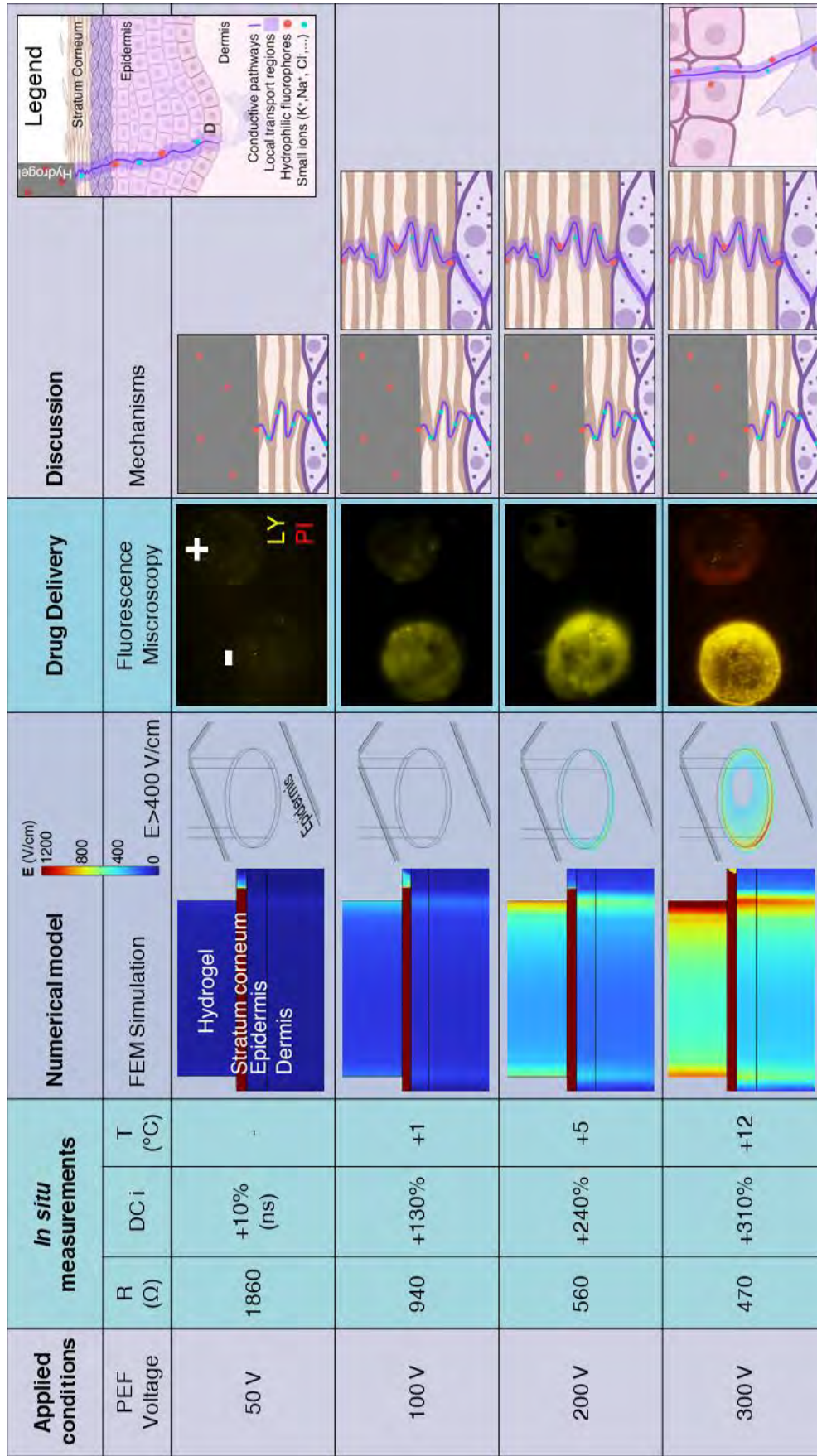


**Fig. S8.** Summary of experimental results on transdermal drug delivery, for applied PEFs of 50 to 300 V (8 pulses, 20 ms duration, 1 Hz). **In situ measurements.** Average resistance ( $U/I$ ) during last pulse, DC current change after PEF, Temperature increase (max) during PEF. **Numerical model.** Electric field distribution on the skin, through validated, nonlinear model. XZ slices of first skin layers and areas where  $E > 400$  V/cm (approximate threshold value for cell permeabilization in tissue) on viable skin layers. **Drug delivery.** Fluorescent marking of lucifer yellow (LY) and propidium iodide (PI) on skin, after PEF. **Discussion.** Proposed mechanisms for each voltage: creation of conductive pathways, formation of local transport regions and cell permeabilization.